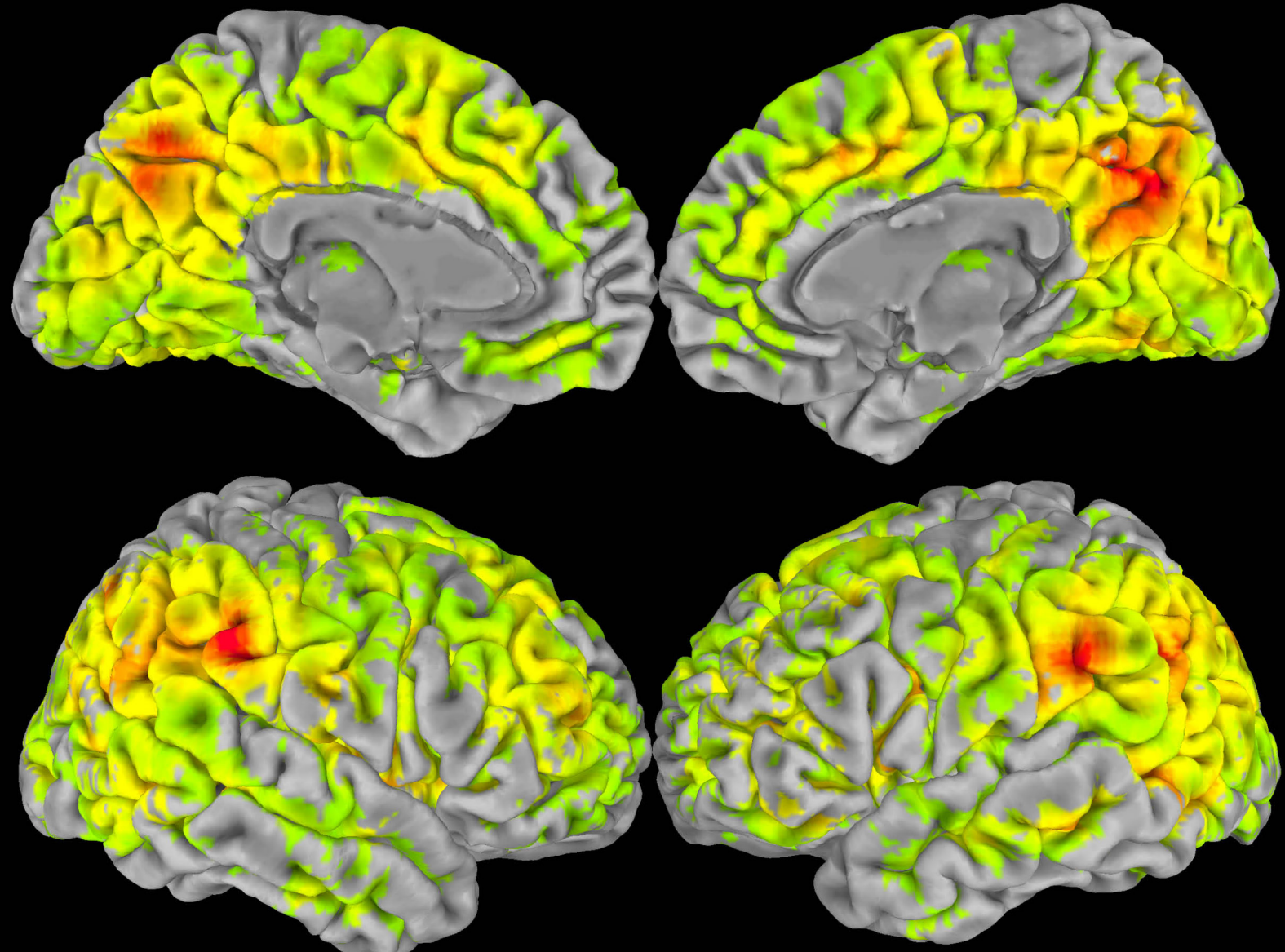


# PROCEEDINGS OF THE INTERNATIONAL SCHOOL ON MAGNETIC RESONANCE AND BRAIN FUNCTION – XII WORKSHOP

EDITED BY: Federico Giove and Itamar Ronen

PUBLISHED IN: Frontiers in Neuroscience and Frontiers in Physics





#### Frontiers Copyright Statement

© Copyright 2007-2018 Frontiers Media SA. All rights reserved.

All content included on this site, such as text, graphics, logos, button icons, images, video/audio clips, downloads, data compilations and software, is the property of or is licensed to Frontiers Media SA ("Frontiers") or its licensees and/or subcontractors. The copyright in the text of individual articles is the property of their respective authors, subject to a license granted to Frontiers.

The compilation of articles constituting this e-book, wherever published, as well as the compilation of all other content on this site, is the exclusive property of Frontiers. For the conditions for downloading and copying of e-books from Frontiers' website, please see the Terms for Website Use. If purchasing Frontiers e-books from other websites or sources, the conditions of the website concerned apply.

Images and graphics not forming part of user-contributed materials may not be downloaded or copied without permission.

Individual articles may be downloaded and reproduced in accordance with the principles of the CC-BY licence subject to any copyright or other notices. They may not be re-sold as an e-book.

As author or other contributor you grant a CC-BY licence to others to reproduce your articles, including any graphics and third-party materials supplied by you, in accordance with the Conditions for Website Use and subject to any copyright notices which you include in connection with your articles and materials.

All copyright, and all rights therein, are protected by national and international copyright laws.

The above represents a summary only. For the full conditions see the Conditions for Authors and the Conditions for Website Use.

ISSN 1664-8714  
ISBN 978-2-88945-554-6  
DOI 10.3389/978-2-88945-554-6

#### About Frontiers

Frontiers is more than just an open-access publisher of scholarly articles: it is a pioneering approach to the world of academia, radically improving the way scholarly research is managed. The grand vision of Frontiers is a world where all people have an equal opportunity to seek, share and generate knowledge. Frontiers provides immediate and permanent online open access to all its publications, but this alone is not enough to realize our grand goals.

#### Frontiers Journal Series

The Frontiers Journal Series is a multi-tier and interdisciplinary set of open-access, online journals, promising a paradigm shift from the current review, selection and dissemination processes in academic publishing. All Frontiers journals are driven by researchers for researchers; therefore, they constitute a service to the scholarly community. At the same time, the Frontiers Journal Series operates on a revolutionary invention, the tiered publishing system, initially addressing specific communities of scholars, and gradually climbing up to broader public understanding, thus serving the interests of the lay society, too.

#### Dedication to Quality

Each Frontiers article is a landmark of the highest quality, thanks to genuinely collaborative interactions between authors and review editors, who include some of the world's best academicians. Research must be certified by peers before entering a stream of knowledge that may eventually reach the public - and shape society; therefore, Frontiers only applies the most rigorous and unbiased reviews.

Frontiers revolutionizes research publishing by freely delivering the most outstanding research, evaluated with no bias from both the academic and social point of view. By applying the most advanced information technologies, Frontiers is catapulting scholarly publishing into a new generation.

#### What are Frontiers Research Topics?

Frontiers Research Topics are very popular trademarks of the Frontiers Journals Series: they are collections of at least ten articles, all centered on a particular subject. With their unique mix of varied contributions from Original Research to Review Articles, Frontiers Research Topics unify the most influential researchers, the latest key findings and historical advances in a hot research area! Find out more on how to host your own Frontiers Research Topic or contribute to one as an author by contacting the Frontiers Editorial Office: [researchtopics@frontiersin.org](mailto:researchtopics@frontiersin.org)

# PROCEEDINGS OF THE INTERNATIONAL SCHOOL ON MAGNETIC RESONANCE AND BRAIN FUNCTION – XII WORKSHOP

Topic Editors:

**Federico Govea**, Centro Fermi – Museo Storico Della Fisica e Centro di Studi e Ricerche Enrico Fermi, Fondazione Santa Lucia IRCCS, Rome, Italy

**Itamar Ronen**, Leiden University Medical Center, Netherlands

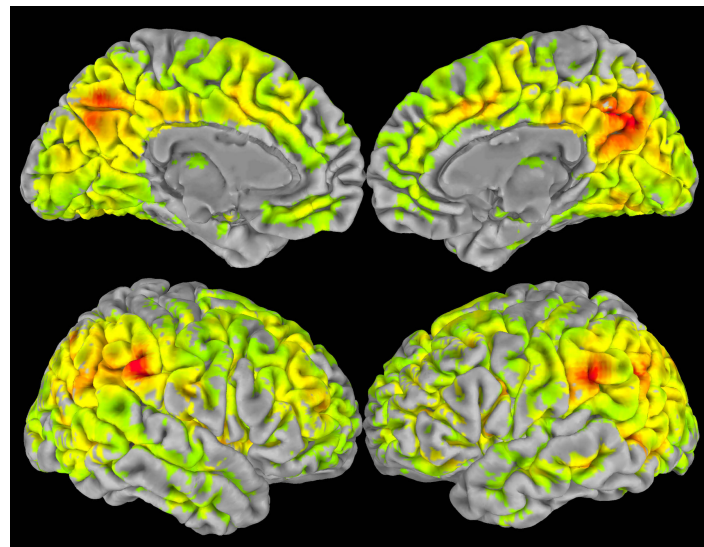


Image: Daniele Mascali, based on data from S. Tommasin, D. Mascali et al. Scale-invariant rearrangement of resting state networks in the human brain under sustained stimulation. Neuroimage 179:570-581 (2018)  
doi: 10.1016/j.neuroimage.2018.06.006

In the last thirty years, Magnetic Resonance has generated a wide revolution in biomedical research and in medical imaging in general. More recently, the “*in vivo*” studies of the human brain were extended by new original ways to the dynamic study of function and metabolism of the human brain. The enormous interest in expanding the investigation of the brain is emphasizing the search for new NMR methods capable of extracting information of so-far obscure aspects of the brain function. In fact, many quantitative approaches have been proposed in order to complement the information obtained by functional MRI, and several multimodal and multiparametric approaches have been developed to exploit the information, either functional or structural, made available by the flexible contrast generation typical of MRI, and to combine it with complementary information. The XII workshop of the International School on Magnetic Resonance and Brain Function, held in Erice between 17 April and 6 May, 2016, was specially devoted to novel approaches aimed at better structural characterization of brain diseases, and at investigating frontiers MRI approaches to better understand the brain function. The papers included in this eBook offer a broad overview of the subjects covered during the Workshop, including applications of multiparametric MRI to neurological diseases, multimodal combination of MRI with electrophysiology, advanced methods for the investigation of brain networks and of brain physiology, and perspectives towards brain state reading.

**Citation:** Govea, F., Ronen, I., eds (2018). Proceedings of the International School on Magnetic Resonance and Brain Function – XII Workshop. Lausanne: Frontiers Media.  
doi: 10.3389/978-2-88945-554-6

# Table of Contents

- 04 Editorial: Proceedings of the International School on Magnetic Resonance and Brain Function – XII Workshop**  
Federico Giove and Itamar Ronen
- 06 Multi-Modal Brain MRI in Subjects With PD and iRBD**  
Silvia Mangia, Alena Svatkova, Daniele Mascali, Mikko J. Nissi, Philip C. Burton, Petr Bednarik, Edward J. Auerbach, Federico Giove, Lynn E. Eberly, Michael J. Howell, Igor Nestrasil, Paul J. Tuite and Shalom Michaeli
- 18 Lysophosphatidyl Choline Induced Demyelination in Rat Probed by Relaxation Along a Fictitious Field in High Rank Rotating Frame**  
Lauri J. Lehto, Aloma A. Albors, Alejandra Sierra, Laura Tolppanen, Lynn E. Eberly, Silvia Mangia, Antti Nurmi, Shalom Michaeli and Olli Gröhn
- 32 Determining Excitatory and Inhibitory Neuronal Activity From Multimodal fMRI Data Using a Generative Hemodynamic Model**  
Martin Havlicek, Dimo Ivanov, Alard Roebroeck and Kamil Uludağ
- 52 Safety of Simultaneous Scalp or Intracranial EEG during MRI: A Review**  
Hassan B. Hawsawi, David W. Carmichael and Louis Lemieux
- 77 Type 1 Diabetes and Impaired Awareness of Hypoglycemia Are Associated With Reduced Brain Gray Matter Volumes**  
Petr Bednarik, Amir A. Moheet, Heidi Grohn, Anjali F. Kumar, Lynn E. Eberly, Elizabeth R. Seaquist and Silvia Mangia
- 85 Targeting Cognitive Impairment in Multiple Sclerosis—The Road Toward an Imaging-Based Biomarker**  
Jeroen Van Schependom and Guy Nagels
- 91 Task-Related Modulations of BOLD Low-Frequency Fluctuations Within the Default Mode Network**  
Silvia Tommasin, Daniele Mascali, Tommaso Gili, Ibrahim Eid Assan, Marta Moraschi, Michela Fratini, Richard G. Wise, Emiliano Macaluso, Silvia Mangia and Federico Giove
- 99 Graph Analysis and Modularity of Brain Functional Connectivity Networks: Searching for the Optimal Threshold**  
Cécile Bordier, Carlo Nicolini and Angelo Bifone
- 108 How Energy Metabolism Supports Cerebral Function: Insights From  $^{13}\text{C}$  Magnetic Resonance Studies In vivo**  
Sarah Sonnay, Rolf Gruetter and João M. N. Duarte
- 128 Graded Hypercapnia-Calibrated BOLD: Beyond the Iso-Metabolic Hypercapnic Assumption**  
Ian D. Driver, Richard G. Wise and Kevin Murphy
- 137 Reconstruction of Arm Movement Directions From Human Motor Cortex Using fMRI**  
Seungkyu Nam and Dae-Shik Kim



# Editorial: Proceedings of the International School on Magnetic Resonance and Brain Function – XII Workshop

Federico Giove<sup>1,2\*</sup> and Itamar Ronen<sup>3</sup>

<sup>1</sup> MARBILab, Centro Fermi – Museo Storico Della Fisica e Centro di Studi e Ricerche Enrico Fermi, Rome, Italy, <sup>2</sup> Fondazione Santa Lucia IRCCS, Rome, Italy, <sup>3</sup> C. J. Center for High Field MRI Research, Leiden University Medical Center, Leiden, Netherlands

**Keywords:** International School on Magnetic Resonance and Brain Function (ISMRBF), MRI and fMRI, MRI techniques, multimodal MRI, neuroscience

## Editorial on the Research Topic

### Proceedings of the International School on Magnetic Resonance and Brain Function – XII Workshop

This Special Research Topic includes the proceedings of the XII workshop of the International School on Magnetic Resonance and Brain Function (ISMRBF), held between April 30th and May, 6th 2016 in Erice (Italy) at the premises of the Ettore Majorana Foundation and Centre for Scientific Culture. ISMRBF is a biennial event that gathers scientists whose research is focused on the crucial intersection between technological advances in MRI and emerging applications in neuroscience.

Indeed, many recent improvements in MRI instrumentation and techniques have been triggered by the increasing demands from a vast community of neuroscientists, which are exploiting MRI as one the most powerful tools for non-invasive investigation of human brain structure and function. Another long lasting topic covered by ISMRBF is the use of multimodal and multiparametric approaches. MRI is intrinsically multiparametric, thanks to the flexibility of the framework for contrast generation, that can be made sensitive to multiple biophysical phenomena. MRI can be also combined with other distinct modalities, such as electrophysiology, optical imaging and PET based molecular imaging. Fusion of information within- and across modalities has shown an excellent potential to complement the strengths and weaknesses of MRI as a stand-alone technique.

The papers included in this Research Topic offer a broad overview of the subjects covered by the Workshop. Mangia et al. contributed a paper that shows the potential of multiparametric MRI in application to neurological diseases, characterizing how Parkinson's disease and idiopathic rapid eye movement sleep behavior disorder are associated with tissue properties in subcortical regions. The authors exploited a battery of conventional (diffusion tensor imaging, DTI) and non-conventional metrics (adiabatic and non-adiabatic rotating frame relaxation), and concluded that rotating frame relaxation combined with functional connectivity may provide sensitive and specific signatures of progression of neurological diseases. The paper by Lehto et al. used similar MRI approaches on rats. In this case, MRI outcomes were correlated with myelin content in pharmacologically induced demyelinating lesions. Techniques based on non-adiabatic rotating frame relaxation showed good specificity and excellent sensitivity in the detection of lesions, and good quantitative correlation with actual myelin content. In comparison, the sensitivity reached by a battery of more conventional MRI approaches was lower. Authors concluded that non-adiabatic rotating frame relaxation is a valuable technique for the investigation of demyelinating diseases.

## OPEN ACCESS

### Edited and reviewed by:

Ewald Moser,

Medizinische Universität Wien, Austria

### \*Correspondence:

Federico Giove

federico.giove@uniroma1.it

### Specialty section:

This article was submitted to

Biomedical Physics,

a section of the journal

Frontiers in Physics

**Received:** 07 February 2018

**Accepted:** 12 February 2018

**Published:** 06 March 2018

### Citation:

Giove F and Ronen I (2018) Editorial:

Proceedings of the International School on Magnetic Resonance and Brain Function – XII Workshop.

Front. Phys. 6:18.

doi: 10.3389/fphy.2018.00018

The contribution by Havlicek et al. expanded the multimodal approach to functional MRI. By combining multiple MRI and electrophysiological datasets from humans, non-human primates and cats, they discussed the generative model for BOLD (Blood-Oxygenation Level-Dependent) they recently introduced, and showed that it can explain the dynamic relationship between haemodynamic and neural events underlying the generation of the BOLD contrast. Hawsawi et al. dealt with multimodal combination of MRI and electrophysiological measurements in humans from the complementary point of view of patient safety. In their paper, the authors explored the safety issues related to simultaneous MRI and scalp or intracranial EEG, by identifying the physical phenomena that play a role in patient safety and reviewing the relevant literature. The authors concluded that risks can be managed, but that simultaneous invasive electrophysiology and MRI is characterized by a set of potential health hazards so complex, that careful case by case evaluation is needed.

The paper by Bednarik et al. is a retrospective study on patients affected by type 1 diabetes, investigating the connection between the pathology itself, impaired hypoglycaemia awareness, and cortical atrophy. Authors showed that type 1 diabetes is associated with gray matter atrophy compared to matched controls. The effect was larger in subjects with impaired hypoglycaemia awareness, likely because of increased exposure to hypoglycaemic episodes. Authors indicated that future studies should clarify whether the reported subtle reductions of gray matter volume are associated with cognitive impairment. The review by Van Schependom and Nagels discusses the relationship between neuroimaging and cognitive scores in multiple sclerosis (MS). The authors highlighted that improving the capability of neuroimaging-derived metric to assess pathology-related features can be useful not only for the characterization of the pathophysiological mechanisms underlying MS damage, but also to improve and speed-up the development of innovative therapies.

Tommasin et al. studied how the performance of a sustained cognitive stimulus affects the features of slow BOLD oscillations underlying functional connectivity within the Default Mode Network (DMN). They found that the stimulus reduced both amplitude of oscillation and functional connectivity within the DMN, but that the coupling between the reported changes was spatially heterogeneous and likely frequency specific. They concluded that the coupling between amplitude of BOLD fluctuations and functional connectivity is a potentially useful parameter to study brain networks. Bordier et al. presented a simulation work aimed at exploring optimal procedures for sparsification in graph theory analysis of topology of

functional networks. Sparsification is often needed to simplify the processing and the interpretation of networks, however it is prone to over-pruning the network, and the identification of an optimal threshold is an open issue. The authors used synthetic data to show that percolation data-driven approaches can be used to identify a threshold that maximize the information of the pruned network.

The next couple of papers deal with MR approaches to study neurophysiology and neurochemistry. Sonnay et al. reviewed the applications of  $^{13}\text{C}$ -MR to brain energetics, and in particular how the combination of advanced MR techniques, mathematical models of metabolism and nutrients transport, and increasing magnetic fields can help the understanding the specific metabolic response to stimulation within astrocytes and neurons, as well as the metabolic interactions between these cells. Driver et al. studied an important issue regarding the measurement of brain oxygen consumption ( $\text{CMRO}_2$ ) by MR via the so-called calibrated-BOLD method, i.e., the usual isometabolic assumption during hypercapnia. The authors showed that their new approach, using the most relaxed and physiologically sensible hypothesis of linear dependence between a graded hypercapnic challenge and  $\text{CMRO}_2$ , allows more accurate estimates of basal  $\text{CMRO}_2$  as well as activation-related  $\text{CMRO}_2$  change.

Finally, Nam and Kim tackled the issue of decoding brain states by fMRI, by showing that brain reading can be achieved non-invasively even in the motor domain. Specifically, they demonstrated that directional arm movement can be predicted in humans exploiting simple linear encoding models.

The next workshop of the ISMRBF will be held in Erice, April 22–29 2018. The focus will be, as usual, on brain functional and microstructural MRI and compatible approaches. Information about the workshop can be found at the website <http://ismrbf.marbilab.eu>.

## AUTHOR CONTRIBUTIONS

All authors listed have made an equal contribution to the work, and approved it for publication.

**Conflict of Interest Statement:** The authors declare that the research was conducted in the absence of any commercial or financial relationships that could be construed as a potential conflict of interest.

Copyright © 2018 Giove and Ronen. This is an open-access article distributed under the terms of the Creative Commons Attribution License (CC BY). The use, distribution or reproduction in other forums is permitted, provided the original author(s) and the copyright owner are credited and that the original publication in this journal is cited, in accordance with accepted academic practice. No use, distribution or reproduction is permitted which does not comply with these terms.



# Multi-modal Brain MRI in Subjects with PD and iRBD

**Silvia Mangia**<sup>1\*</sup>, **Alena Svatkova**<sup>2,3</sup>, **Daniele Mascali**<sup>4</sup>, **Mikko J. Nissi**<sup>5</sup>, **Philip C. Burton**<sup>1</sup>, **Petr Bednarik**<sup>1,3</sup>, **Edward J. Auerbach**<sup>1</sup>, **Federico Giove**<sup>4,6</sup>, **Lynn E. Eberly**<sup>7</sup>, **Michael J. Howell**<sup>8</sup>, **Igor Nestrasil**<sup>2</sup>, **Paul J. Tuite**<sup>8</sup> and **Shalom Michaeli**<sup>1</sup>

<sup>1</sup> Department of Radiology, Center for Magnetic Resonance Research (CMRR), University of Minnesota, Minneapolis, MN, United States, <sup>2</sup> Department of Pediatrics, University of Minnesota, Minneapolis, MN, United States, <sup>3</sup> Central European Institute of Technology (CEITEC), Masaryk University, Brno, Czechia, <sup>4</sup> MARBILab, Centro Fermi - Museo Storico Della Fisica e Centro di Studi e Ricerche Enrico Fermi, Rome, Italy, <sup>5</sup> Department of Applied Physics, University of Eastern Finland, Kuopio, Finland, <sup>6</sup> Fondazione Santa Lucia IRCCS, Rome, Italy, <sup>7</sup> Division of Biostatistics, University of Minnesota, Minneapolis, MN, United States, <sup>8</sup> Department of Neurology, University of Minnesota, Minneapolis, MN, United States

## OPEN ACCESS

### Edited by:

**Kevin J. Black**,  
Washington University in St. Louis,  
United States

### Reviewed by:

**Paolo Vitali**,

Fondazione Istituto Neurologico  
Nazionale Casimiro Mondino (IRCCS),  
Italy

**Anelyssa D'Abreu**,  
Brown University, United States

### \*Correspondence:

**Silvia Mangia**  
[mangia@umn.edu](mailto:mangia@umn.edu)

### Specialty section:

This article was submitted to  
Brain Imaging Methods,  
a section of the journal  
*Frontiers in Neuroscience*

**Received:** 20 April 2017

**Accepted:** 04 December 2017

**Published:** 19 December 2017

### Citation:

**Mangia S, Svatkova A, Mascali D, Nissi MJ, Burton PC, Bednarik P, Auerbach EJ, Giove F, Eberly LE, Howell MJ, Nestrasil I, Tuite PJ and Michaeli S (2017) Multi-modal Brain MRI in Subjects with PD and iRBD. *Front. Neurosci.* 11:709.**  
doi: 10.3389/fnins.2017.00709

Idiopathic rapid eye movement sleep behavior disorder (iRBD) is a condition that often evolves into Parkinson's disease (PD). Therefore, by monitoring iRBD it is possible to track the neurodegeneration of individuals who may progress to PD. Here we aimed at piloting the characterization of brain tissue properties in mid-brain subcortical regions of 10 healthy subjects, 8 iRBD, and 9 early-diagnosed PD. We used a battery of magnetic resonance imaging (MRI) contrasts at 3 T, including adiabatic and non-adiabatic rotating frame techniques developed by our group, along with diffusion tensor imaging (DTI) and resting-state fMRI. Adiabatic  $T_{1\rho}$  and  $T_{2\rho}$ , and non-adiabatic RAFF4 (Relaxation Along a Fictitious Field in the rotating frame of rank 4) were found to have lower coefficient of variations and higher sensitivity to detect group differences as compared to DTI parameters such as fractional anisotropy and mean diffusivity. Significantly longer  $T_{1\rho}$  were observed in the amygdala of PD subjects vs. controls, along with a trend of lower functional connectivity as measured by regional homogeneity, thereby supporting the notion that amygdalar dysfunction occurs in PD. Significant abnormalities in reward networks occurred in iRBD subjects, who manifested lower network strength of the accumbens. In agreement with previous studies, significantly longer  $T_{1\rho}$  occurred in the substantia nigra compacta of PD vs. controls, indicative of neuronal degeneration, while regional homogeneity was lower in the substantia nigra reticulata. Finally, other trend-level findings were observed, i.e., lower RAFF4 and  $T_{2\rho}$  in the midbrain of iRBD subjects vs. controls, possibly indicating changes in non-motor features as opposed to motor function in the iRBD group. We conclude that rotating frame relaxation methods along with functional connectivity measures are valuable to characterize iRBD and PD subjects, and with proper validation in larger cohorts may provide pathological signatures of iRBD and PD.

**Keywords:** **rotating frame MRI, Parkinson's disease, iRBD, functional connectivity, DTI**

## INTRODUCTION

Idiopathic rapid eye movement (REM) sleep behavior disorder (iRBD) is a sleep disorder associated with abnormal pontomedullary synuclein protein. iRBD evolves into Parkinson's disease (PD) or another synucleinopathy, e.g., dementia with Lewy bodies (LBD) or multiple system atrophy (MSA), in up to 90% of cases (Schenck et al., 1986, 1996; Boeve et al., 2001; Luk et al., 2012; Boeve, 2013; Bunzeck et al., 2013). Thus, iRBD may provide an opportunity to understand the evolution of neurodegeneration as well as a window in which to intervene with disease altering therapies. It is thought that the  $\alpha$ -synuclein pathology in more caudal brainstem regions in iRBD ascends to the substantia nigra (SN) of the midbrain as the disease evolves into PD or other synuclein disorders (Boeve, 2013). Iron, which is present in higher quantities in the substantia nigra and other structures, may also play a role in the loss of dopaminergic neurons through its pro-oxidant effects (Zecca et al., 2008; Kaur et al., 2009). In addition, several studies have demonstrated abnormalities in structural integrity and functional connectivity in patients with iRBD (Hanyu et al., 2012; Ellmore et al., 2013).

Magnetic resonance imaging (MRI) offers several non-invasive contrasts that are useful in evaluating the pathological hallmarks of patients with iRBD, and any MRI findings in iRBD patients can be compared with those in individuals with PD. Previous studies have focused on evaluating structural approaches such as diffusion tensor imaging (DTI) and voxel-based morphometry (VBM) in patients with PD. This has included work that showed changes in DTI fractional anisotropy (FA) (Menke et al., 2009, 2010; Vaillancourt et al., 2009; Peran et al., 2010; Du et al., 2011) and mean diffusivity (MD) (Kamagata et al., 2012) in the substantia nigra of patients with PD. Others have shown that DTI may be useful in differentiating PD from other degenerative parkinsonian disorders and may also have the potential to monitor for disease progression (Prodoehl et al., 2013). Additionally, VBM demonstrated non-dopaminergic brainstem alterations in iRBD (Scherfler et al., 2011). VBM and DTI have also provided insights into non-motor features such as depression (Feldmann et al., 2008; Kostic et al., 2010), smell (Ibarretxe-Bilbao et al., 2010; Rolheiser et al., 2011) and cognitive changes (Ibarretxe-Bilbao et al., 2009; Song et al., 2011) in PD. Therefore, DTI and VBM may prove useful in evaluating iRBD as it evolves into a Parkinsonian condition. So far, it has only been possible to show discriminative properties of the MRI methods using fairly large numbers of patients and controls, and these methods have not yet revealed if they are able to characterize the clinical severity of PD (Gorell et al., 1995; Martin et al., 2008). Therefore, our group previously employed novel microstructural imaging methods to map the SN (Michaeli et al., 2007; Nestrasil et al., 2010), as well as other brainstem and subcortical regions, in PD (Karagulle Kendi et al., 2008; Tuite et al., 2012).

In our current work, we employed several MRI modalities that are sensitive to various brain tissue properties, such as microstructural integrity, iron loads, and functional connectivity. Namely, we utilized novel rotating frame relaxation mapping methods developed in our group including adiabatic  $T_{1\rho}$

(Michaeli et al., 2006),  $T_{2\rho}$  (Michaeli et al., 2004) and RAFF4 (Relaxation Along a Fictitious Field in the rotating frame of rank 4) (Liimatainen et al., 2010, 2011, 2015), together with DTI and resting-state functional MRI (rsfMRI). Our previous studies conducted in PD (Michaeli, 2007; Michaeli et al., 2007; Nestrasil et al., 2010; Tuite et al., 2012) and other brain conditions (Sierra et al., 2008; Jokivarsi et al., 2009; Mangia et al., 2013; Satzer et al., 2015) have shown that the proposed rotating frame methods provide information on different relaxation mechanisms in the human brain.  $T_{2\rho}$  is sensitive to diffusion and exchange of water protons in environments with different local magnetic susceptibilities and reflects iron content with higher sensitivity than conventional  $T_2$  MRI (Michaeli et al., 2005, 2007).  $T_{1\rho}$  provides an indication of neuronal loss and can be used to assess PD nigral degeneration with a higher sensitivity than is possible with conventional  $T_1$ -based MRI (Michaeli et al., 2006, 2007). RAFF4 methodology, which is derived from adiabatic  $T_{1\rho}$  and  $T_{2\rho}$  (Liimatainen et al., 2010, 2011, 2015), has high sensitivity to myelin content (Satzer et al., 2015; Hakkainen et al., 2016), and thus could provide information on microstructural integrity.

Rotating frame relaxations offer a conceptual advantage as compared to free-precession relaxation methods for characterizing tissue properties thanks to their inherent sensitivity to slower motional regimes (Michaeli et al., 2008). Indeed, while water molecules undergo a large variety of motional regimes in tissue, the motions which are most sensitive to the intricate nature of tissue microstructure and composition are those in intermediate-slow regimes. Rotating frame relaxations during frequency swept pulses offer additional practical advantages as compared to continuous-wave  $T_{1\rho}$ , including a minimized sensitivity to  $B_1$  distributions and a capability to simultaneously tune the contrast to multiple effective frequencies (Mangia et al., 2009). Although not common for clinical studies of neurological disorders, rotating frame relaxations with frequency swept pulses were proven as robust and sensitive methods for a variety of *in vivo* investigations conducted by our group (Michaeli et al., 2007; Sierra et al., 2008; Jokivarsi et al., 2009; Nestrasil et al., 2010; Griffith et al., 2011; Liimatainen et al., 2012; Tuite et al., 2012; Mangia et al., 2013; Satzer et al., 2015; Hakkainen et al., 2016) and others (Andronesi et al., 2014; Casula et al., 2017; Okuaki et al., 2017).

Our previous applications of mapping adiabatic rotating frame relaxations in humans had been limited to single-slice acquisitions performed on a non-clinical 4 Tesla scanner (Michaeli et al., 2007; Nestrasil et al., 2010; Tuite et al., 2012; Mangia et al., 2013). With the present work, we piloted the extension of these methodologies to multi-slice acquisitions on a clinical 3 Tesla scanner, and we thus embarked on a small cross-sectional study of 10 healthy controls, 9 patients with iRBD, and 10 patients with PD. Rather than focusing on the endpoint of progression to a clinical PD diagnosis for iRBD subjects, the ultimate goal is to use 3 T MRI for characterizing the spectrum of abnormalities resulting from inexorable synuclein deposition and other pathological features in both PD and iRBD. Our study is a step forward for establishing biomarkers which can characterize PD and iRBD, and ultimately the development of parkinsonian syndromes from iRBD subjects.

## METHODS

### Subjects

PD and iRBD subjects were recruited from the University of Minnesota Movement Disorders Clinic. Ten healthy controls, 9 iRBD patients and 10 individuals with PD were recruited and underwent the MRI protocol. However, all data from one iRBD subject and one PD subject were entirely discarded due to major motion observed during the acquisition. All the other subjects successfully completed the MRI protocol (Table 1), except one control subject who did not finish the DTI acquisitions, and one PD subject who presented excessive motion during the resting-state acquisition.

Exclusion criteria included history of stroke, seizures, neurosurgical procedures, arrhythmias, Montreal cognitive assessment (MoCA) scores lower than 25, and incompatibility with MR safety criteria. This study was carried out in accordance with the recommendations of The Code of Federal Regulations, Institutional Review Board, with written informed consent from all subjects. All subjects gave written informed consent in accordance with the Declaration of Helsinki. The protocol was approved by the Institutional Review Board: Human Subjects Committee of the University of Minnesota. Clinical assessments were performed on anti-parkinsonian medications (for subjects on such treatment) and included the National Institute of Neurological Disorders and Stroke (NINDS) Common Data Element PD medical and family history, demographic information, the Hamilton Anxiety and Depression Rating Scales (Hamilton, 1959, 1960, 1980), United States version of the Parkinson disease questionnaire (PDQ-39) that reflects upon quality of life (Bushnell and Martin, 1999), the Unified Parkinson Disease Rating Scale (UPDRS), the Schwab and England, and Hoehn and Yahr (Fahn and Elton, 1987; Goetz et al., 2007, 2008; Dibble et al., 2010). In particular, we also used the UPDRS part III score to characterize our patient populations, as UPDRS part III represents an objective evaluation of motor symptoms. We assessed for features of iRBD with the validated REM sleep behavioral disorder questionnaire-Hong Kong (RBDQ-HK, English version) (Li et al., 2010) in all subjects. For cognitive function, we included the MoCA and the CogState (Nasreddine et al., 2005; Hoops et al., 2009; Gagnon et al., 2010).

For smell perception, we used the brief smell identification test (B-SIT) (Hawkes et al., 1997; Double et al., 2003; Bohnen et al., 2008; Silveira-Moriyama et al., 2009).

### Imaging Protocol

Studies were performed on a 3 T Siemens Prisma system using a 32-channel RF receive coil. Standard  $B_0$  shimming were performed at the beginning of the imaging session to minimize  $B_0$  inhomogeneities.

Adiabatic  $T_{1\rho}$ ,  $T_{2\rho}$  and non-adiabatic RAFF4 measurements were collected from 30 AC-PC aligned slices covering the brainstem and basal ganglia using a segmented GRE readout with 4 segments, voxel size =  $1.6 \times 1.6 \times 3.6 \text{ mm}^3$ , GRAPPA = 3, TE = 3.18 ms and TR = 2 s. For adiabatic relaxation measurements, hyperbolic secant (HS) pulses were used with BW = 1.6 kHz, pulse duration  $T_p = 6 \text{ ms}$ , peak power  $\omega_1^{\max}/(2\pi) = 800 \text{ Hz}$ , 5 acquisitions with number of pulses = 0, 4, 8, 12, 16 using MLEV4 phase cycling (Michaeli et al., 2004, 2005, 2006, 2008). In  $T_{2\rho}$  acquisitions, magnetization was on -z prior to readout. For RAFF4,  $T_p$  was 4.52 ms for one P-packet. The number of P-packets was 0, 4, 8, 12, 16 with  $\omega_1^{\max}/(2\pi) = 327 \text{ Hz}$ . RAFF4 acquisitions were separately conducted without and with a global inversion (achieved by the same HS pulse used for  $T_{1\rho}$ ) prior to the train of P-packets, to produce sampling of the recovery and decay curve, respectively, to the steady-state magnetization induced during RAFF4.

$T_1$ -weighted,  $T_2$ -weighted images, DTI and rsfMRI were collected covering the whole brain. For  $T_1$ -weighted acquisitions MPRAGE with TR = 2150 ms, TE = 2.47 ms, TI = 1,100 ms, voxel size =  $1 \times 1 \times 1 \text{ mm}^3$ , flip angle = 8 degrees and GRAPPA = 2 was used.  $T_2$ -weighted images were collected using SPACE sequence, voxel size =  $1 \times 1 \times 1 \text{ mm}^3$ , TE = 147 ms and GRAPPA = 2. Two DTI datasets were acquired with different phase encoding (i.e., anterior-posterior and posterior-anterior) utilizing TR = 2,820 ms, TE = 72.6 ms; multi band (MB) = 4 (<https://www.cmrr.umn.edu/multiband>), 7 non-diffusion weighed ( $b_0$ ) images, and 93 diffusion weighted images with  $b$ -value of  $750 \text{ s/mm}^2$  (47 images) and  $1,500 \text{ s/mm}^2$  (46 images) and voxel size =  $1.8 \times 1.8 \times 1.8 \text{ mm}^3$ . Finally, rsfMRI data was obtained using gradient echo Echo Planar Imaging (EPI) sequence, TR = 900 ms, multi band (MB) = 4; TE = 30 ms; voxel

**TABLE 1 |** Subjects' characteristics.

	Control mean $\pm$ SD (range)	iRBD mean $\pm$ SD (range)	PD mean $\pm$ SD (range)
n	10	8	9
Sex	7M/3F	4M/4F	4M/5F
Age (years)	$57.3 \pm 5.2$ (47.0–63.4)	$65.7 \pm 6.7$ (54.7–72.3)	$66.1 \pm 6.6$ (56.3–74.3)
Disease duration (years)	–	$9.1 \pm 14.1$ (0.1–15.0)	$2.4 \pm 1.9$ (0.1–4.5)
Onset side (PD)	–	–	4L/4R, 1NA
UPDRS	–	$11.6 \pm 6.2$ (3–21)	$36.8 \pm 11.2$ (26–58)
UPDRS-III	–	$6.9 \pm 4.9$ (0–14)	$20.3 \pm 5.5$ (15–32)
MoCA	–	$27.3 \pm 1.4$ (25–29)	$27.7 \pm 1.7$ (25–30)

Characteristics of subjects whose data underwent further analyses. All subjects completed the whole MRI protocol, except one control subject who did not finish the DTI acquisitions. One PD subject was later excluded from functional connectivity analyses, because the resting-state functional scans exceeded the established criteria for acceptable motion.

size =  $3 \times 3 \times 3$  mm $^3$ , matrix size =  $64 \times 64$ , 48 AC-PC aligned slices with interleaved slice acquisition, 502 volumes.

## Image Analysis and ROI Definition

Brain segmentation of the T<sub>1</sub>-weighted scan was carried out with FreeSurfer (FS) version 5.3.0 (<http://surfer.nmr.mgh.harvard.edu>) installed on the supercomputer at the Minnesota Supercomputing Institute. Automated processing has been described previously (Fischl et al., 2002). A trained operator visually inspected each subject's data to ensure accuracy of the segmentation.

The following region of interest (ROI) masks were derived from FS automatic labeling of each subject's brain anatomy: caudate nucleus, pallidum, putamen, accumbens, amygdala, thalamus, hippocampus, and brainstem. With the exception of the brainstem, separate left and right hemisphere ROIs were generated for each structure. The brainstem was then manually separated to midbrain and pons regions. Additionally, left and right ROIs encompassing the substantia nigra reticulata (SNr), and separately the substantia nigra compacta (SNC), were manually drawn on each subject's T<sub>2</sub>-weighted image using itkSNAP software v.3.2.0 (Yushkevich et al., 2006) following the methodology described in our previous paper (Nestrail et al., 2010). Representative examples of ROI selections are shown in Figures 1, 2.

Rigid-body motion correction was performed on adiabatic T<sub>1ρ</sub>, T<sub>2ρ</sub> and RAFF4 measurements using the MCFLIRT algorithm in FSL (Jenkinson et al., 2012) with default options (Jenkinson et al., 2002). For T<sub>1ρ</sub> and T<sub>2ρ</sub> measures, all acquired images were firstly co-registered to the first acquisition and then to the averaged volume. The same algorithm was also applied on the two separate decay and recovery RAFF4 datasets to minimize the effect of movement between the two acquisitions. Relaxation time constant maps were calculated with MATLAB (MathWorks, Natick, MA) using in-house written routines and the Aedes software package (<http://aedes.uef.fi>). In particular, we used a 2-parameters non-linear fitting for estimating M<sub>0</sub> and relaxation time in T<sub>1ρ</sub> and T<sub>2ρ</sub> acquisitions, and a 4-parameters non-linear fitting for estimating M<sub>0</sub>, M<sub>ss</sub> (steady state value of magnetization), -M<sub>z</sub> (initial magnetization value measured from the negative hemisphere) and relaxation time for RAFF4 acquisitions. The FreeSurfer BB-register algorithm (Greve and Fischl, 2009) was utilized to align the first acquired image of T<sub>1ρ</sub>, T<sub>2ρ</sub>, and RAFF4 measurements to the FS-preprocessed T1-weighted images. The transformation matrix was then applied to the parametric maps utilizing trilinear interpolation. The registration accuracy was visually verified. The quality of BB-register initialization was additionally quantified for the adiabatic relaxation maps by using the quality assessment value provided by the algorithm.

DTI datasets with opposite phase encoding were utilized to reduce susceptibility artifacts and field inhomogeneities using FSL TOPUP (Andersson et al., 2003). After motion and eddy-current correction (Andersson and Sotropoulos, 2016), data were skull-stripped (Smith, 2002) and BB-register was applied to co-register DTI data to the T1-weighted image (Greve and Fischl, 2009). The parameters utilized for BB-register matched

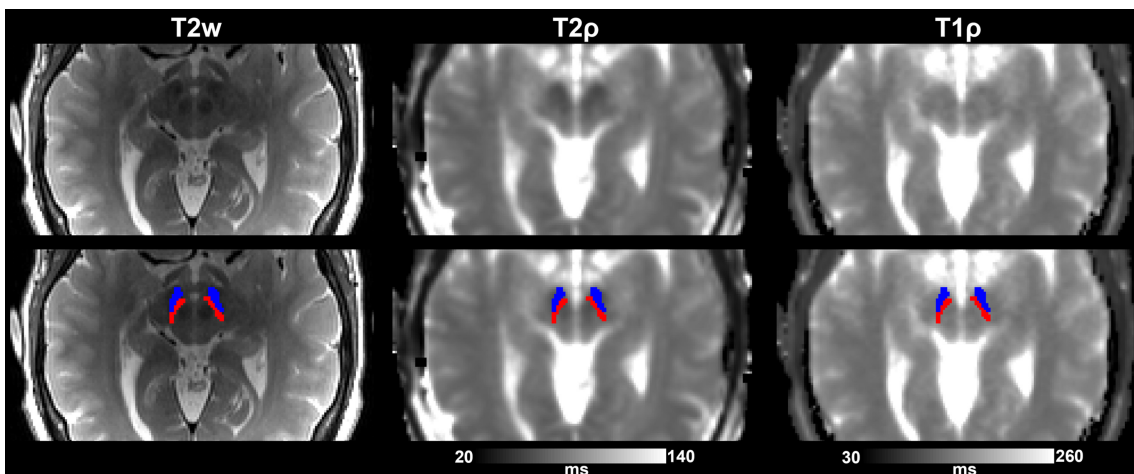
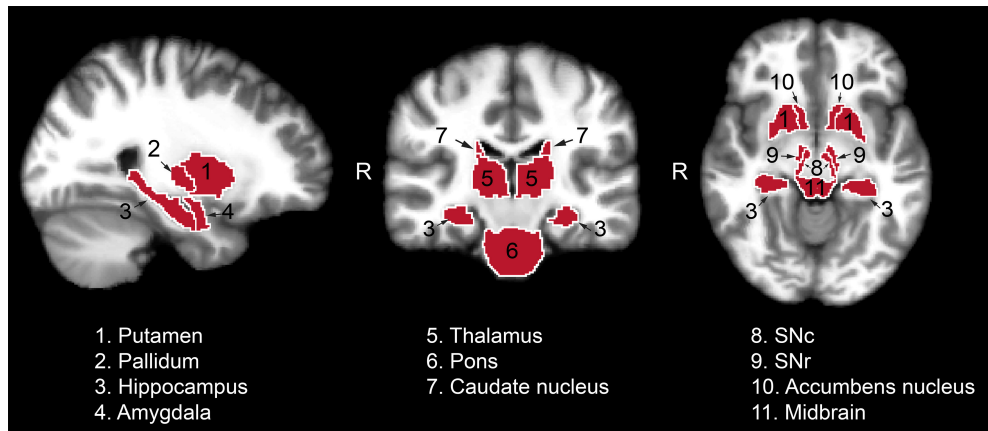
those used for motion-correcting the relaxation measurements, except that the first volume of relaxation measures was replaced by the b0 image in order to calculate the transformation matrix for DTI. The accuracy of registration was verified visually. The DTIFIT tensor model in FSL (Jenkinson et al., 2012) was fit to the co-registered DTI data to generate fractional anisotropy (FA) and mean diffusivity (MD) maps.

T<sub>1ρ</sub>, T<sub>2ρ</sub>, RAFF4, FA, and MD values of co-registered images were averaged across voxels within each ROI for each subject. Where applicable, the masked MRI ROIs extracted from the left and right hemispheres were combined before averaging. Representative examples of relaxation and DTI maps are shown in Figure 3.

## Resting State Functional Connectivity

### Pre-processing

Resting-state data were pre-processed and analyzed using AFNI (Cox, 1996), FS, and in-house routines based on Matlab R2013b. Data underwent the following pre-processing pipeline: (1) removal of first 10 volumes to allow for signal stabilization and for subjects to adapt to the new condition, (2) despiking (AFNI, 3dDespike), (3) slice-time correction (AFNI, 3dTshift), (4) realignment to the first EPI volume (AFNI, 3dvolreg), (5) coregistration of the first EPI volume to the FS-preprocessed T1-weighted image (FS, bbregister), and (6) normalization to  $2 \times 2 \times 2$  mm $^3$  MNI space (FS, mri\_vol2vol). To minimize data resampling, steps five and six were applied simultaneously, concatenating the two transformations (FS, mri\_vol2vol). In addition, a general linear model was constructed to regress out baseline drift, motion and spurious variance from MNI normalized data (AFNI, 3dTproject). The following regressors were included in the model: a second order Legendre polynomial, a basis of sine and cosine to model frequencies outside the band 0.01–0.1 Hz, the six estimated motion parameters and their first derivative, the first five eigenvectors from the time series inside WM (after two voxels erosion; FS mask) and the first five eigenvectors from the time series inside CSF (after one voxel erosion; FS mask), following the aCompCor approach (Behzadi et al., 2007). To further reduce the impact of motion, data were censored by removing time points with more than 0.33 mm of displacement (estimated as the Euclidian norm of motion parameter derivatives) along with each previous time point. Censoring was applied during the regression step, removing time points from both data and regressors. The censoring threshold of 0.33 mm was selected so that at least 20 degrees of freedom (DOF) remained in the data. One PD subject could not meet this criterion for any reasonable choice of the censoring threshold and was therefore excluded from any further connectivity analysis, leaving a total of 10 controls, 8 iRBD and 8 PD subjects. The remaining DOF did not differ among groups (controls:  $51.5 \pm 7.9$ , RBD:  $46.4 \pm 11.2$ , PD:  $48.1 \pm 7.8$ ; ANOVA  $p = 0.48$ ). Finally, conventional smoothing was not applied to the data since functional outcomes were not compared voxel-by-voxel but at the ROI level. However, since inter-subject variability in data smoothness, arising from different amounts of interpolation due to motion correction and/or spatial normalization, directly impacts local connectivity estimation, we



set the effective data smoothness to an isotropic Gaussian FWHM of 4 mm (Maximo et al., 2013). This step was accomplished with the AFNI program 3dBlurToFWHM with the non-default option to avoid local smoothness estimation (i.e., whole-brain estimation only), in order to preserve the neuronal related smoothness.

### Movement Assessment

Framewise displacement (FD), as defined in Power et al. (2012), was computed to index the subject's movements during the resting-state scan. There was no significant difference in FD between controls and PD (controls:  $0.15 \pm 0.06$  mm; PD:  $0.18 \pm 0.04$ ; control vs. PD  $p = 0.10$ ), however, iRBD subjects moved more than controls (iRBD:  $0.22 \pm 0.05$ ; iRBD vs. control  $p = 0.004$ ) and PD subjects (iRBD vs. PD  $p = 0.10$ ). To partially take into account this issue we included FD as a nuisance covariate in all statistical tests of the functional metrics.

### Metrics

Two functional metrics were calculated: seed-based functional connectivity (FC) and regional homogeneity (ReHo).

#### Seed-Based FC

Time series within each of the ROIs described previously were averaged, yielding a single time series that served as seed. The correlation (Pearson's  $r$ ) between the seed time series and the time series at each other voxel was then computed to quantify FC between the seed and the rest of the brain. To take into account the different number of DOF across subjects (due to the censoring procedure), correlation values were transformed in standard scores ( $Z$ ) dividing the Fisher transformed  $r$ -value by the standard error of the Fisher's distribution:

$$Z = \text{arctanh}(r) * \sqrt{\text{DOF} - 3}. \quad (1)$$

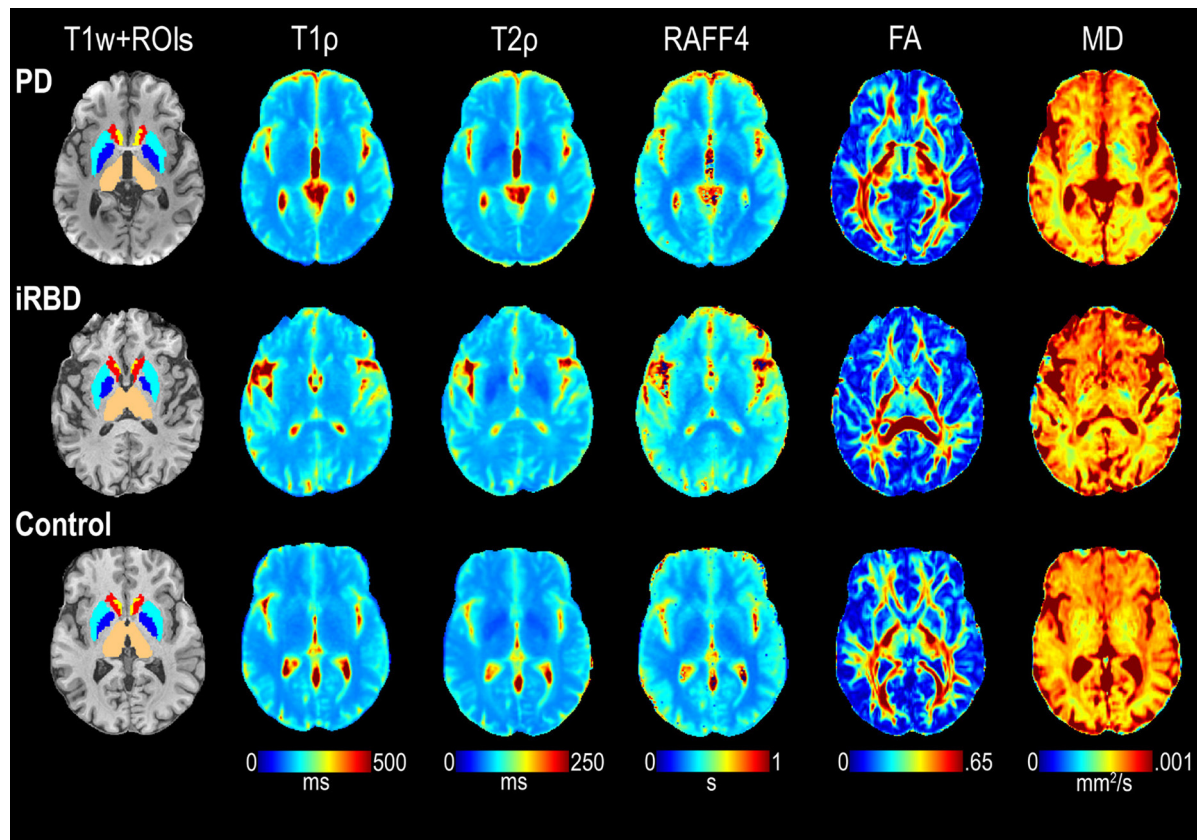


**FIGURE 3 |** Representative maps of  $T_{1\rho}$ ,  $T_{2\rho}$ , RAFF4, FA, and MD from one each of a control, iRBD and PD subject. ROIs of interest visible on the selected slices are also shown superimposed on the T1-weighted (T1w) images, including thalamus (beige), pallidum (dark blue), putamen (light blue), caudate (red), and accumbens (yellow).

For each subject and ROI, the seed-based FC was averaged within the functional network identified in the healthy control group. Specifically, the functional network was defined by a one-sample, one-tail, *t*-test on the seed-based FC maps of the healthy controls ( $p < 0.0005$ , minimum cluster size 20). We refer to this aggregate value of seed-based FC as network strength.

#### ReHo

Regional homogeneity was implemented as a metric to assess local connectivity (Zang et al., 2004). For each voxel in the brain, ReHo was computed as the Kendall's coefficient of concordance among the voxel time series and the time series of its 18 nearest neighbors (AFNI, 3dReHo). Resulting brain maps were then transformed into z-scores by subtracting the whole-brain mean and dividing by the whole-brain standard deviation. Aggregate ReHo values were finally extracted by averaging across voxels in each ROI previously described.

#### Statistical Analyses

Subject age, clinical characteristics, and movement (FD) were summarized by group with means and standard deviations (SD) and compared using linear models that allowed for group-specific variances and provided Holm-corrected *p*-values for

multiple comparisons among the groups (Holm, 1979); sex distribution was compared using Fisher's exact test. The average relaxation ( $T_{1\rho}$ ,  $T_{2\rho}$ , and RAFF4), diffusion (FA, MD) and functional connectivity (network strength and ReHo) parameters were analyzed per ROI. For each of the 11 ROIs separately, each MR parameter was summarized by group (PD, iRBD, controls) using means and standard deviations, and compared across groups using linear models which allowed group-specific variances; we fit models with and without correction for age. Per ROI, type I error was controlled with Holm's adjustment for the 2 comparisons (PD vs. control and iRBD vs. control) and false discovery rate correction (Benjamini and Hochberg, 1995) was used for multiple testing of the 7 MRI outcomes. Results are presented both without and with the multiple-comparisons and the multiple-testing corrections (Figure 4, Supplementary Table 1).

## RESULTS

Individuals enrolled in this study spanned from middle-age to older adults (Table 1). The age of PD and iRBD subjects was 66 years on average for both groups, while the healthy controls were on average 9 years younger ( $p < 0.02$ , corrected, for each of PD

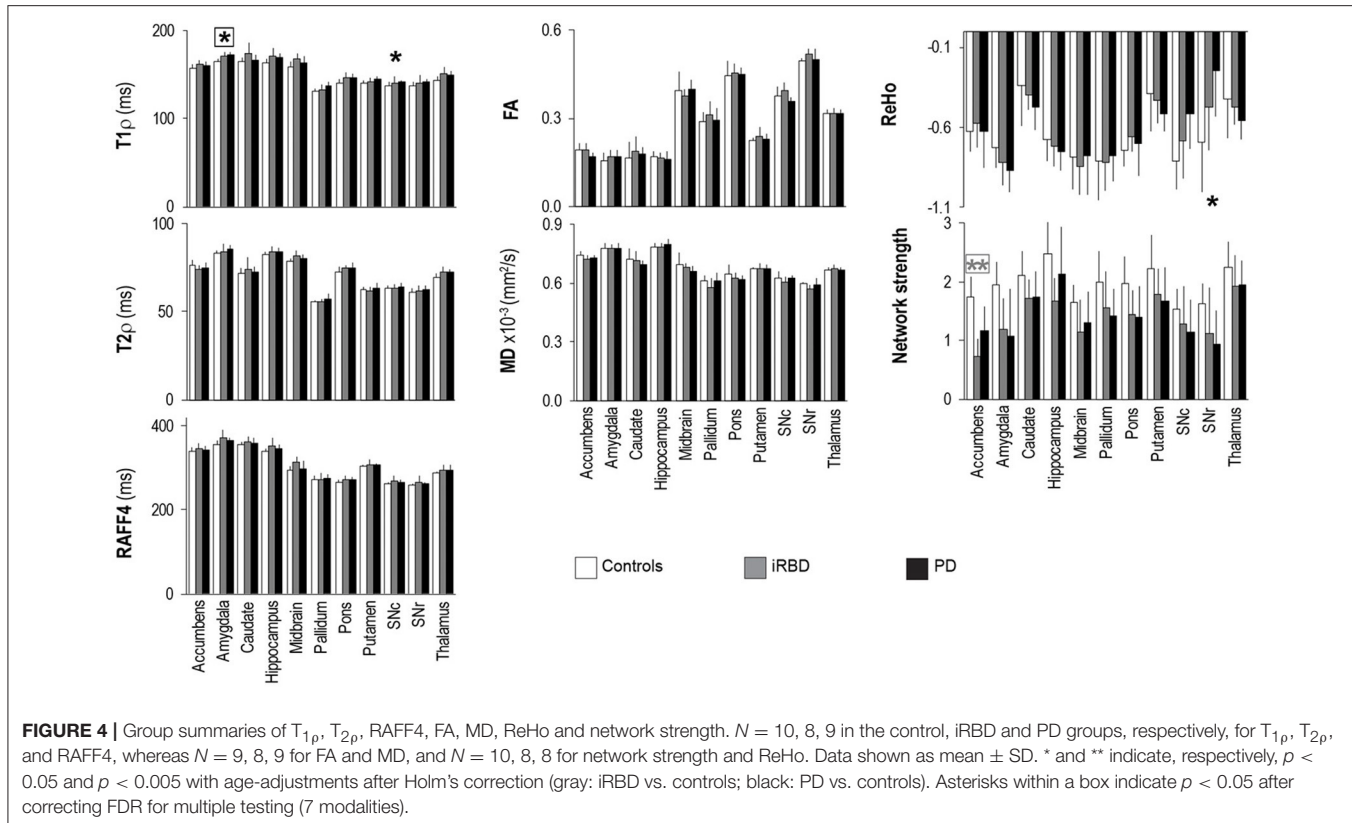


**FIGURE 4 |** Group summaries of  $T_{1p}$ ,  $T_{2p}$ , RAFF4, FA, MD, ReHo and network strength.  $N = 10, 8, 9$  in the control, iRBD and PD groups, respectively, for  $T_{1p}$ ,  $T_{2p}$ , and RAFF4, whereas  $N = 9, 8, 9$  for FA and MD, and  $N = 10, 8, 8$  for network strength and ReHo. Data shown as mean  $\pm$  SD. \* and \*\* indicate, respectively,  $p < 0.05$  and  $p < 0.005$  with age-adjustments after Holm's correction (gray: iRBD vs. controls; black: PD vs. controls). Asterisks within a box indicate  $p < 0.05$  after correcting FDR for multiple testing (7 modalities).

and iRBD vs. controls); the sex distribution was similar across all 3 groups. Disease duration spanned from 1 month to 4.5 years in the PD subjects, and from 1 to 15 years in the iRBD patients. As expected, PD subjects had significantly higher (worse) UPDRS scores and UPDRS-III scores than iRBD subjects ( $p = 0.00003$  and  $p = 0.00009$ , respectively), but their MoCA values were comparable.

The adiabatic relaxation maps were well-registered to the anatomical images, with an average value of quality assessment of  $0.21 \pm 0.04$  (normal range is between 0 and 1.1; 0 represents perfect registration initialization). The range of adiabatic  $T_{1p}$  ( $\sim 130$ – $180$  ms),  $T_{2p}$  ( $\sim 55$ – $90$  ms) and RAFF4 ( $\sim 240$ – $410$  ms) measured at 3 T from the gray matter structures of interest were in good agreement with previous studies conducted at 4 T (Michaeli et al., 2007; Nestrasil et al., 2010; Liimatainen et al., 2015). In addition, rotating frame relaxation maps were highly reproducible among subjects. Indeed, between-subject variations among healthy controls were 3% for adiabatic  $T_{1p}$ ,  $T_{2p}$ , and RAFF4 from the regions of interest. Diffusion parameters were more variable than relaxation parameters, with between-subjects variations of 9 and 4% for FA and MD, respectively. Between-subjects variations were considerably higher for functional connectivity parameters, namely 22 and 35% for network strength and ReHo, respectively.

Rotating frame relaxation parameters tended to be higher in patients than in controls for most of the ROIs (Figure 4, Supplementary Table 1). When age was not used as a covariate, significant Holm-corrected group-differences between

PD patients and controls were observed for  $T_{1p}$  in the amygdala ( $p = 0.0001$ ), hippocampus ( $p = 0.03$ ), pons ( $p = 0.011$ ), putamen ( $p = 0.014$ ), substantia nigra compacta ( $p = 0.018$ ), and thalamus ( $p = 0.013$ ), while between iRBD and controls  $T_{1p}$  differences occurred in the amygdala ( $p = 0.012$ ), hippocampus ( $p = 0.038$ ), midbrain ( $p = 0.016$ ), pons ( $p = 0.011$ ), and thalamus ( $p = 0.013$ ). Group differences between PD and controls were also observed for  $T_{2p}$  in the amygdala ( $p = 0.033$ ) and thalamus ( $p = 0.008$ ), while none of the RAFF4 findings were significant. Holm-corrected group differences between iRBD and controls occurred for  $T_{2p}$  and RAFF4 in the midbrain ( $p = 0.024$  and  $p = 0.005$ , respectively). On the other hand, diffusion parameters exhibited only one Holm-corrected group difference, namely MD in SNr of iRBD vs. controls ( $p = 0.001$ ). Network strengths were smaller in patients than in controls for most regions. Holm-corrected group differences were significant for the network of the accumbens of both patient groups vs. controls ( $p < 0.013$ ), and for the networks of the amygdala and SNr of PD vs. controls ( $p = 0.040$  and  $p = 0.028$ , respectively). Finally, differences in ReHo were observed only between PD and controls in the SNc ( $p = 0.021$ ) and SNr ( $p = 0.007$ ).

Including age as a covariate demonstrated that most of the above mentioned differences were largely accounted for by age (Figure 4, Supplementary Table 1), especially for  $T_{1p}$  outcomes. A lengthening of  $T_{1p}$  in the amygdala of PD patients as compared to controls was however still robustly detected with Holm-correction after age-adjustment ( $p = 0.005$ ). PD patients also

maintained a significantly longer  $T_{1\rho}$  in the SNc ( $p = 0.046$ ) as compared to controls. Between iRBD and controls, only trend-level group differences were observed after age-adjustments, namely for  $T_{1\rho}$  in the amygdala ( $p = 0.075$ ), and for  $T_{2\rho}$  and RAFF4 in the midbrain ( $p = 0.08$  and  $p = 0.064$ , respectively). Network strength was still lower in the accumbens of iRBD patients as compared to controls ( $p = 0.003$ ), but only a trend was observed between PD and controls ( $p = 0.085$ ). Moreover, age-adjustments and Holm-correction maintained a significantly lower ReHo in the SNr of PD vs. control ( $p = 0.035$ ), while only trend level differences were reached for the amygdala ( $p = 0.067$ ).

Finally, after additionally correcting FDR for multiple testing (7 modalities), the longer  $T_{1\rho}$  in the amygdala of PD vs. controls remained significant ( $p = 0.038$ ), along with the smaller network strength of the accumbens of iRBD vs. controls ( $p = 0.018$ ).

## DISCUSSION

In the current study we recruited an iRBD group in addition to a mild-moderately affected PD group with the ultimate goal of identifying similarities in MRI signatures of both diseases. Both patient groups were selected to have no diagnosis of dementia, with MoCA scores not less than 25 (Table 1, and Supplementary Figure 1). In addition, while iRBD subjects had findings on their UPDRS-III evaluations (Table 1, and Supplementary Figure 1), they were not thought to meet a clinical diagnosis of PD (Hughes et al., 1992) at enrollment. Motivated by the group-differences previously observed between PD subjects and controls when using adiabatic  $T_{1\rho}$  and  $T_{2\rho}$  (Michaeli et al., 2007; Nestrasil et al., 2010; Tuite et al., 2012), here we piloted a more extended imaging protocol which included  $T_{1\rho}$  and  $T_{2\rho}$ , RAFF4, DTI, and rsfMRI, and performed multi-slice acquisitions from the midbrain to characterize multiple subcortical brain regions rather than single slices of the brainstem as we used previously. Notably, multi-slice mapping of  $T_{1\rho}$ ,  $T_{2\rho}$ , and RAFF4 had never been implemented before, especially on a 3 Tesla clinical scanner. Here we demonstrate that 30-slices relaxation mapping is feasible with 5-min of acquisition time for each of  $T_{1\rho}$  and  $T_{2\rho}$  and 10-min for RAFF4. Thus the total acquisition time is similar to those employed for clinical MRI studies, and therefore such developments represent a critical step toward a future translation of the rotating frame methodologies to clinical trials. A multi-slice approach is needed for the purpose of obtaining more data that may allow an examination of regions involved in both motor and non-motor aspects of disease and that could be potentially useful in developing a prognostic biomarker (to predict whether iRBD patients are likely to develop PD) as well as a PD staging biomarker. With regard to the prognostic biomarker, based on clinical data, e.g., patients with greater cognitive impairment are more likely to have a different course than those without. If MRI methods can demonstrate pathology in sub-cortical regions involved in non-motor function, such as the amygdala or hippocampus, this information could be potentially useful in prognosis.

In principle, other MRI contrasts such as  $T_1$ -Magnetization Transfer (MT) signal (so-called neuromelanin-sensitive scan

Ogisu et al., 2013) and  $T_1$  relaxometry (Menke et al., 2009) could have been used, as they had been shown to reveal SN degeneration in PD. Such methods had been proven useful for visualizing and estimating the volumes of the SN structures. However, the neuromelanin-sensitive scan (Ogisu et al., 2013) is a qualitative approach based on signal intensity and it thus precludes a quantitative evaluation of SN tissue characteristics. On the other hand,  $T_1$ -relaxometry is a quantitative method that allows quantification of tissue relaxation properties. However, the  $T_1$  measured in the SN did not reveal a difference between PD and controls (Menke et al., 2009), consistent with a lower sensitivity of free-precession relaxations to detect tissue degeneration as compared to rotating frame relaxations.

An important finding of the current study is that rotating frame relaxation parameters provided more robust characterizations of brain tissue as compared to DTI metrics, both in terms of observed coefficient of variations and in terms of their sensitivity to detect age-related and disease-related differences. The most prominent observation was that PD and iRBD groups share a lengthening of  $T_{1\rho}$  in a region that is non-motor related and appears abnormal during cognitive impairment and depression, i.e., the amygdala. However, group differences vs. controls were clearly more pronounced in PD patients than in iRBD patients, as they remained robustly significant for PD patients also after age-adjustments and corrections for multiple testing, whereas they reached only trend level in comparisons of iRBD subjects vs. controls. Dysfunction in olfactory, cardiovascular, sleep, sensory and cognitive functions is often present during PD, and even can precede the motor symptoms and the disease onset (for example, see Jellinger, 2015). Therefore, the differences between PD and iRBD vs. controls in non-motor areas detected by rotating frame  $T_{1\rho}$  MRI further support the critical importance of considering non-motor abnormalities in PD and iRBD. The  $T_{1\rho}$  results obtained in the amygdala of PD patients were overall consistent with previous findings of structural amygdalar deterioration in these patients (Bouchard et al., 2008; van Mierlo et al., 2015; Vriend et al., 2016). Since significant differences of amygdalar volumes were not observed in the present study (data not shown), and our PD subjects did not have significant mood or cognitive impairments, one may speculate that  $T_{1\rho}$  MRI may detect subtle tissue changes in the amygdala which occur prior to structural changes and/or symptom manifestations. Interestingly, the lengthening of  $T_{1\rho}$  in the amygdala as well as in SN regions of PD vs. controls, which is suggestive of neuronal degeneration in these areas, was accompanied by a deterioration of local functional connectivity as revealed by regional homogeneity.

Group differences were seen in rotating frame MRI parameters for other regions such as the thalamus, although such differences were largely explained by age. It is, however, still interesting to note that motor dysfunction in PD has been related to the change in activity of thalamic neurons in the motor circuits (Halliday, 2009). The slight lengthening of  $T_{1\rho}$  in the SNc of PD patients as compared to controls is in agreement with previous studies (Michaeli et al., 2007; Nestrasil

et al., 2010), although the finding was not robust enough to survive after correcting FDR for multiple testing, most likely due to the limited number of subjects and/or due to lack of on-to-one age matching of PD and controls (although age was taken into account in the statistical analyses). Importantly, adiabatic  $T_{2\rho}$  was shown to pick up the difference in the SN of PD vs. control subjects in our previous studies conducted at 4 T (Michaeli et al., 2007; Nestrasil et al., 2010), but not in the current work. The differences in the outcomes among the current and previous studies could be attributed to the hardware used, i.e., higher magnetic field strength 4 T vs. 3 T (the lower field decreases sensitivity). Also, the multislice acquisition used in the current study may have impacted the efficiency of the contrast preparation module thus “diluting” the contrast as compared to the single slice used for the 4 T study. Importantly, in order to allow extended brain coverage, the spatial resolution used in this study was lower than previously used, thus leading to higher partial volume effects. Moreover, although the manual ROI segmentation of the SN was carefully performed, inaccuracies in placement are possible as there are unclear borders in  $T_2$ -weighted images (Bolding et al., 2013). Differences between current and previous studies may also be due to different subject characteristics, with the most notable being a shorter disease duration of the current cohort (on average 2.5 years) as compared to our previous studies (on average 5 years in Michaeli et al., 2007; and 7 years in Nestrasil et al., 2010). Similar arguments apply for the pons, where  $T_{1\rho}$  differences were previously observed (Tuite et al., 2012). In fact, in the present cohort we observed lengthening of  $T_{1\rho}$  in the pons of PD vs. controls only when comparisons were not adjusted for age.

Finally, the long-distance connectivity as measured by network strength was significantly lower for the accumbens of iRBD subjects relative to controls, while such difference was not noted for the PD subjects. On the other hand, rotating frame relaxation and DTI parameters did not show evident abnormalities in the accumbens. Another putative signature of iRBD subjects was a longer RAFF4 and  $T_{2\rho}$  in the midbrain, that could again be related to changes in non-motor features as opposed to motor function in the iRBD group.

In future studies, it would be important to follow the subjects for at least 3 years to identify iRBD patients who remain stable, those who progressed to PD, and those who progressed to LBD. Changes in nigrostriatal circuits are expected mainly in iRBD converted to PD, and to a lesser extent in iRBD converted to LBD. At the same time, it will be critical to fully characterize the iRBD and PD subjects with extensive behavioral and cognitive tests in order to fully understand the implications of the MRI findings. In addition, the lack in the present study of a complete age matching among controls and patients was a nuisance that had to be resolved with the inclusion of age-adjustments in the statistical analyses, and will have to be avoided in future investigations. Yet it allowed appreciating for the first time the interesting property that rotating frame relaxations may be exquisitely sensitive to age, a feature that may even be exploited in investigations that target aging itself. From an acquisition perspective, the rotating frame relaxation protocols also allow

great deal of flexibility. Depending on the hypothesis to be tested, for instance if a focus on only hippocampus and amygdala are desired, one may design a specific rotating frame multi-slice acquisition protocol that achieves high spatial resolution with a reduced number of slices, while guaranteeing full coverage of the selected regions of interest. If acquisition time is limited, one may choose to collect only adiabatic  $T_{1\rho}$  and resting-state fMRI, and skip entirely DTI which did not reveal sufficient sensitivity to detect group differences in this pilot investigation. On the other hand, other developments are currently underway to further optimize the acquisition times along with the intrinsic contrasts of the readout scheme. One promising direction is to implement magnetization preparation modules within a 3D readout sequence with virtually zero-echo times sequence, such as SWEEP Imaging with Fourier Transformation (SWIFT) (Idiyatullin et al., 2006). Initial steps in this directions of research have already been proven successful in animal studies (Zhang et al., 2016).

Assessment of PD and iRBD subjects through combined microstructural and functional approaches may be a platform for comprehensive analysis of ongoing neurodegeneration. In essence, this approach may allow for staging of degeneration. In the present study, several outcomes showed trend-level differences in multiple regions, indicating the need of larger cohorts in future studies. Therefore, further studies on large cohorts of patients including longitudinal investigations of how iRBD advance to PD are necessary to characterize the ability of MRI metrics to be used as biomarkers of progression of iRBD into PD or other neurodegenerative diseases.

## CONCLUSION

We piloted for the first time the multi-slice mapping of rotating frame adiabatic  $T_{1\rho}$  and  $T_{2\rho}$  and non-adiabatic RAFF4 on a 3 Tesla scanner for human brain studies, which here involved control subjects along with non-demented iRBD and PD subjects. Rotating frame relaxations provided greater sensitivity to detect tissue abnormalities compared to conventional diffusion modalities that are commonly used to characterize tissue microstructure. The most prominent abnormality observed was a lengthening of  $T_{1\rho}$  in the amygdala of PD subjects, indicating neuronal degeneration in a non-motor area. This finding was even more prominent than what was detected by  $T_{1\rho}$  in the substantia nigra, i.e., the area related to the typical motor symptoms of PD. Significantly smaller network strength of the accumbens was also observed for iRBD subjects as compared to controls.

## AUTHOR CONTRIBUTIONS

SiM participated in design of the work, acquisition, analysis, interpretation of the data and preparing the manuscript. AS participated in analysis and interpretation of the data, and preparing the manuscript. DM participated in analysis and interpretation of the data, and preparing the manuscript. MN participated in acquisition and analysis of the data,

and editing the manuscript. PCB participated in analysis and interpretation of the data, and editing the manuscript. PB participated in analysis and interpretation of the data, and editing the manuscript. EA participated in acquisition of the data, and editing the manuscript. FG participated in analysis and interpretation of the data, and editing the manuscript. LE participated in design of the work, analysis and interpretation of the data, and editing the manuscript. MH participated in design of the work, interpretation of the data, and editing the manuscript. IN participated in analysis and interpretation of the data, and editing the manuscript. PT participated in design of the work, interpretation of the data, and preparing the manuscript. SHM participated in design of the work, acquisition, interpretation of the data and preparing the manuscript.

## ACKNOWLEDGMENTS

We are grateful to the study coordinators and volunteers who participated in the study and thereby made this research possible. The authors acknowledge the Minnesota Supercomputing Institute (MSI) at the University of Minnesota for providing

resources that contributed to the research results reported within this paper. URL: <http://www.msi.umn.edu>. In addition, the authors would like to thank Karin Shmueli and Alejandra Sierra-Lopez for helpful discussions and feedback on the manuscript. Research reported in this publication was supported by the University of Minnesota Foundation, by the National Institutes of Health (Funding P41 EB015894, P30 NS076408, 1S10OD017974, UL1TR000114, and KL2TR000113), by the Academy of Finland (grant #285909) and by the Ministry of Education, Youth and Sports of the Czech Republic under the National Sustainability Programme II (project CEITEC 2020, LQ1601). This project has received funding from the European Union's Horizon 2020 research and innovation program under the Marie Skłodowska-Curie grant, agreement #691110 (MICROBRADAM). The content is solely the responsibility of the authors and does not necessarily represent the official views of the funding bodies.

## SUPPLEMENTARY MATERIAL

The Supplementary Material for this article can be found online at: <https://www.frontiersin.org/articles/10.3389/fnins.2017.00709/full#supplementary-material>

## REFERENCES

- Andersson, J. L., Skare, S., and Ashburner, J. (2003). How to correct susceptibility distortions in spin-echo echo-planar images: application to diffusion tensor imaging. *Neuroimage* 20, 870–888. doi: 10.1016/S1053-8119(03)00336-7
- Andersson, J. L., and Sotiroopoulos, S. N. (2016). An integrated approach to correction for off-resonance effects and subject movement in diffusion MR imaging. *Neuroimage* 125, 1063–1078. doi: 10.1016/j.neuroimage.2015.10.019
- Andronesi, O. C., Bhat, H., Reuter, M., Mukherjee, S., Caravan, P., and Rosen, B. R. (2014). Whole brain mapping of water pools and molecular dynamics with rotating frame MR relaxation using gradient modulated low-power adiabatic pulses. *Neuroimage* 89, 92–109. doi: 10.1016/j.neuroimage.2013.12.007
- Behzadi, Y., Restom, K., Liu, J., and Liu, T. T. (2007). A component based noise correction method (CompCor) for BOLD and perfusion based fMRI. *Neuroimage* 37, 90–101. doi: 10.1016/j.neuroimage.2007.04.042
- Benjamini, Y., and Hochberg, Y. (1995). Controlling the false discovery rate: a practical and powerful approach to multiple testing. *J. R. Stat. Soc. B* 57, 289–300.
- Boeve, B. F. (2013). Idiopathic REM sleep behaviour disorder in the development of Parkinson's disease. *Lancet Neurol.* 12, 469–482. doi: 10.1016/S1474-4422(13)70054-1
- Boeve, B. F., Silber, M. H., Ferman, T. J., Lucas, J. A., and Parisi, J. E. (2001). Association of REM sleep behavior disorder and neurodegenerative disease may reflect an underlying synucleinopathy. *Mov. Disord.* 16, 622–630. doi: 10.1002/mds.1120
- Bohnen, N. I., Gedela, S., Herath, P., Constantine, G. M., and Moore, R. Y. (2008). Selective hyposmia in Parkinson disease: association with hippocampal dopamine activity. *Neurosci. Lett.* 447, 12–16. doi: 10.1016/j.neulet.2008.09.070
- Bolding, M. S., Reid, M. A., Avsar, K. B., Roberts, R. C., Gamlin, P. D., Grawne, T. J., et al. (2013). Magnetic transfer contrast accurately localizes substantia nigra confirmed by histology. *Biol. Psychiatry* 73, 289–294. doi: 10.1016/j.biopsych.2012.07.035
- Bouchard, T. P., Malykhin, N., Martin, W. R., Hanstock, C. C., Emery, D. J., Fisher, N. J., et al. (2008). Age and dementia-associated atrophy predominates in the hippocampal head and amygdala in Parkinson's disease. *Neurobiol. Aging* 29, 1027–1039. doi: 10.1016/j.neurobiolaging.2007.02.002
- Bunzeck, N., Singh-Curry, V., Eckart, C., Weiskopf, N., Perry, R. J., Bain, P. G., et al. (2013). Motor phenotype and magnetic resonance measures of basal ganglia iron levels in Parkinson's disease. *Parkinsonism Relat. Disord.* 19, 1136–1142. doi: 10.1016/j.parkreldis.2013.08.011
- Bushnell, D. M., and Martin, M. L. (1999). Quality of life and Parkinson's disease: translation and validation of the US Parkinson's Disease Questionnaire (PDQ-39). *Qual. Life Res.* 8, 345–350. doi: 10.1023/A:1008979705027
- Casula, V., Nissi, M. J., Podlipska, J., Haapea, M., Koski, J. M., Saarakkala, S., et al. (2017). Elevated adiabatic T1rho and T2rho in articular cartilage are associated with cartilage and bone lesions in early osteoarthritis: a preliminary study. *J. Magn. Reson. Imaging* 46, 678–689. doi: 10.1002/jmri.25616
- Cox, R. W. (1996). AFNI: software for analysis and visualization of functional magnetic resonance neuroimages. *Comput. Biomed. Res.* 29, 162–173. doi: 10.1006/cbmr.1996.0014
- Dibble, L. E., Cavanaugh, J. T., Earhart, G. M., Ellis, T. D., Ford, M. P., and Foreman, K. B. (2010). Charting the progression of disability in Parkinson disease: study protocol for a prospective longitudinal cohort study. *BMC Neurol.* 10:110. doi: 10.1186/1471-2377-10-110
- Double, K. L., Rowe, D. B., Hayes, M., Chan, D. K., Blackie, J., Corbett, A., et al. (2003). Identifying the pattern of olfactory deficits in parkinson disease using the brief smell identification test. *Arch. Neurol.* 60, 545–549. doi: 10.1001/archneur.60.4.545
- Du, G., Lewis, M. M., Styner, M., Shaffer, M. L., Sen, S., Yang, Q. X., et al. (2011). Combined R2\* and diffusion tensor imaging changes in the substantia nigra in Parkinson's disease. *Mov. Disord.* 26, 1627–1632. doi: 10.1002/mds.23643
- Ellmore, T. M., Castriotta, R. J., Hendley, K. L., Aalbers, B. M., Furr-Stimming, E., Hood, A. J., et al. (2013). Altered nigrostriatal and nigrocortical functional connectivity in rapid eye movement sleep behavior disorder. *Sleep* 36, 1885–1892. doi: 10.5665/sleep.3222
- Fahn, S., and Elton, R. (1987). "Unified parkinson's disease rating scale," in *Recent Developments in Parkinson's Disease*, Vol. 2, eds S. Fahn, C. D. Marsden, D. B. Calne, and M. Goldstein (Florham Park, NJ: Macmillan Healthcare Information), 153–163.
- Feldmann, A., Illes, Z., Kosztolányi, P., Illes, E., Mike, A., Kover, F., et al. (2008). Morphometric changes of gray matter in Parkinson's disease with depression: a voxel-based morphometry study. *Mov. Disord.* 23, 42–46. doi: 10.1002/mds.21765

- Fischl, B., Salat, D. H., Busa, E., Albert, M., Dieterich, M., Haselgrove, C., et al. (2002). Whole brain segmentation: automated labeling of neuroanatomical structures in the human brain. *Neuron* 33, 341–355. doi: 10.1016/S0896-6273(02)00569-X
- Gagnon, J. F., Postuma, R. B., Joncas, S., Desjardins, C., and Latreille, V. (2010). The Montreal Cognitive Assessment: a screening tool for mild cognitive impairment in REM sleep behavior disorder. *Mov. Disord.* 25, 936–940. doi: 10.1002/mds.23079
- Goetz, C. G., Fahn, S., Martinez-Martin, P., Poewe, W., Sampaio, C., Stebbins, G. T., et al. (2007). Movement Disorder Society-sponsored revision of the Unified Parkinson's Disease Rating Scale (MDS-UPDRS): process, format, and clinimetric testing plan. *Mov. Disord.* 22, 41–47. doi: 10.1002/mds.21198
- Goetz, C. G., Tilley, B. C., Shaftman, S. R., Stebbins, G. T., Fahn, S., Martinez-Martin, P., et al. (2008). Movement Disorder Society-sponsored revision of the Unified Parkinson's Disease Rating Scale (MDS-UPDRS): scale presentation and clinimetric testing results. *Mov. Disord.* 23, 2129–2170. doi: 10.1002/mds.22340
- Gorell, J., Ordidge, R., and Brown, G. (1995). Increased iron-related MRI contrast in the substantia nigra in Parkinson's disease. *Neurology* 45, 1138–1143. doi: 10.1212/WNL.45.6.1138
- Greve, D. N., and Fischl, B. (2009). Accurate and robust brain image alignment using boundary-based registration. *Neuroimage* 48, 63–72. doi: 10.1016/j.neuroimage.2009.06.060
- Griffith, C. J., Wijdicks, C. A., Goerke, U., Michaeli, S., Ellermann, J., and LaPrade, R. F. (2011). Outcomes of untreated posterolateral knee injuries: an *in vivo* canine model. *Knee Surg. Sports Traumatol. Arthrosc.* 19, 1192–1197. doi: 10.1007/s00167-010-1358-z
- Hakkarainen, H., Sierra, A., Mangia, S., Garwood, M., Michaeli, S., Grohn, O., et al. (2016). MRI relaxation in the presence of fictitious fields correlates with myelin content in normal rat brain. *Magn. Reson. Med.* 75, 161–168. doi: 10.1002/mrm.25590
- Halliday, G. M. (2009). Thalamic changes in Parkinson's disease. *Parkinsonism Relat. Disord.* 15(Suppl. 3), S152–S155. doi: 10.1016/S1353-8020(09)70804-1
- Hamilton, M. (1959). The assessment of anxiety states by rating. *Br. J. Med. Psychol.* 32, 50–55. doi: 10.1111/j.2044-8341.1959.tb00467.x
- Hamilton, M. (1960). A rating scale for depression. *J. Neurol. Neurosurg. Psychiatry* 23, 56–62. doi: 10.1136/jnnp.23.1.56
- Hamilton, M. (1980). Rating depressive patients. *J. Clin. Psychiatry* 41(12 Pt 2), 21–24.
- Hanyu, H., Inoue, Y., Sakurai, H., Kanetaka, H., Nakamura, M., Miyamoto, T., et al. (2012). Voxel-based magnetic resonance imaging study of structural brain changes in patients with idiopathic REM sleep behavior disorder. *Parkinsonism Relat. Disord.* 18, 136–139. doi: 10.1016/j.parkreldis.2011.08.023
- Hawkes, C. H., Shephard, B. C., and Daniel, S. E. (1997). Olfactory dysfunction in Parkinson's disease. *J. Neurol. Neurosurg. Psychiatry* 62, 436–446. doi: 10.1136/jnnp.62.5.436
- Holm, S. (1979). A simple sequentially rejective Bonferroni test procedure. *Scand. J. Stat.* 6, 65–70.
- Hoops, S., Nazem, S., Siderowf, A. D., Duda, J. E., Xie, S. X., Stern, M. B., et al. (2009). Validity of the MoCA and MMSE in the detection of MCI and dementia in Parkinson disease. *Neurology* 73, 1738–1745. doi: 10.1212/WNL.0b013e3181c34b47
- Hughes, A. J., Daniel, S. E., Kilford, L., and Lees, A. J. (1992). Accuracy of clinical diagnosis of idiopathic Parkinson's disease: a clinico-pathological study of 100 cases. *J. Neurol. Neurosurg. Psychiatry* 55, 181–184. doi: 10.1136/jnnp.55.3.181
- Ibarretxe-Bilbao, N., Junque, C., Martí, M. J., Valdeoriola, F., Vendrell, P., Bargallo, N., et al. (2010). Olfactory impairment in Parkinson's disease and white matter abnormalities in central olfactory areas: a voxel-based diffusion tensor imaging study. *Mov. Disord.* 25, 1888–1894. doi: 10.1002/mds.23208
- Ibarretxe-Bilbao, N., Tolosa, E., Junque, C., and Martí, M. J. (2009). MRI and cognitive impairment in Parkinson's disease. *Mov. Disord.* 24(Suppl. 2), S748–S753. doi: 10.1002/mds.22670
- Idyatullin, D., Corum, C., Park, J. Y., and Garwood, M. (2006). Fast and quiet MRI using a swept radiofrequency. *J. Magn. Reson.* 181, 342–349. doi: 10.1016/j.jmr.2006.05.014
- Jellinger, K. A. (2015). Neuropathobiology of non-motor symptoms in Parkinson disease. *J. Neural. Transm.* 122, 1429–1440. doi: 10.1007/s00702-015-1405-5
- Jenkinson, M., Bannister, P., Brady, M., and Smith, S. (2002). Improved optimization for the robust and accurate linear registration and motion correction of brain images. *Neuroimage* 17, 825–841. doi: 10.1006/nimg.2002.1132
- Jenkinson, M., Beckmann, C. F., Behrens, T. E., Woolrich, M. W., and Smith, S. M. (2012). Fsl. *Neuroimage* 62, 782–790. doi: 10.1016/j.neuroimage.2011.09.015
- Jokivarsi, K. T., Niskanen, J. P., Michaeli, S., Grohn, H. I., Garwood, M., Kauppinen, R. A., et al. (2009). Quantitative assessment of water pools by T1 rho and T2 rho MRI in acute cerebral ischemia of the rat. *J. Cereb. Blood Flow Metab.* 29, 206–216. doi: 10.1038/jcbfm.2008.113
- Kamagata, K., Motoi, Y., Abe, O., Shimoji, K., Hori, M., Nakanishi, A., et al. (2012). White matter alteration of the cingulum in Parkinson disease with and without dementia: evaluation by diffusion tensor tract-specific analysis. *AJNR Am. J. Neuroradiol.* 33, 890–895. doi: 10.3174/ajnr.A2860
- Karagulle Kendi, A. T., Lehericy, S., Luciana, M., Ugurbil, K., and Tuite, P. (2008). Altered diffusion in the frontal lobe in Parkinson disease. *AJNR Am. J. Neuroradiol.* 29, 501–505. doi: 10.3174/ajnr.A0850
- Kaur, D., Lee, D., Ragapolan, S., and Andersen, J. K. (2009). Glutathione depletion in immortalized midbrain-derived dopaminergic neurons results in increases in the labile iron pool: implications for Parkinson's disease. *Free Radic. Biol. Med.* 46, 593–598. doi: 10.1016/j.freeradbiomed.2008.11.012
- Kostic, V. S., Agosta, F., Petrovic, I., Galantucci, S., Spica, V., Jecmenica-Lukic, M., et al. (2010). Regional patterns of brain tissue loss associated with depression in Parkinson disease. *Neurology* 75, 857–863. doi: 10.1212/WNL.0b013e3181f11c1d
- Li, S. X., Wing, Y. K., Lam, S. P., Zhang, J., Yu, M. W., Ho, C. K., et al. (2010). Validation of a new REM sleep behavior disorder questionnaire (RBDQ-HK). *Sleep Med.* 11, 43–48. doi: 10.1016/j.sleep.2009.06.008
- Liimatainen, T., Hakkarainen, H., Mangia, S., Huttunen, J. M., Storino, C., Idyatullin, D., et al. (2015). MRI contrasts in high rank rotating frames. *Magn. Reson. Med.* 73, 254–262. doi: 10.1002/mrm.25129
- Liimatainen, T., Mangia, S., Ling, W., Ellermann, J., Sorce, D. J., Garwood, M., et al. (2011). Relaxation dispersion in MRI induced by fictitious magnetic fields. *J. Magn. Reson.* 209, 269–276. doi: 10.1016/j.jmr.2011.01.022
- Liimatainen, T., Sierra, A., Hanson, T., Sorce, D. J., Yla-Herttuala, S., Garwood, M., et al. (2012). Glioma cell density in a rat gene therapy model gauged by water relaxation rate along a fictitious magnetic field. *Magn. Reson. Med.* 67, 269–277. doi: 10.1002/mrm.22997
- Liimatainen, T., Sorce, D. J., O'Connell, R., Garwood, M., and Michaeli, S. (2010). MRI contrast from relaxation along a fictitious field (RAFF). *Magn. Reson. Med.* 64, 983–994. doi: 10.1002/mrm.22372
- Luk, K. C., Kehm, V., Carroll, J., Zhang, B., O'Brien, P., Trojanowski, J. Q., et al. (2012). Pathological alpha-synuclein transmission initiates Parkinson-like neurodegeneration in nontransgenic mice. *Science* 338, 949–953. doi: 10.1126/science.1227157
- Mangia, S., Carpenter, A. F., Tyan, A. E., Eberly, L. E., Garwood, M., and Michaeli, S. (2013). Magnetization transfer and adiabatic T1rho MRI reveal abnormalities in normal-appearing white matter of subjects with multiple sclerosis. *Mult. Scler.* 20, 1066–1073. doi: 10.1177/1352458513515084
- Mangia, S., Liimatainen, T., Garwood, M., and Michaeli, S. (2009). Rotating frame relaxation during adiabatic pulses vs. conventional spin lock: simulations and experimental results at 4 T. *Magn. Reson. Imaging* 27, 1074–1087. doi: 10.1016/j.mri.2009.05.023
- Martin, W. R., Wieler, M., and Gee, M. (2008). Midbrain iron content in early Parkinson disease: a potential biomarker of disease status. *Neurology* 70(16 Pt 2), 1411–1417. doi: 10.1212/01.wnl.0000286384.31050.b5
- Maximo, J. O., Keown, C. L., Nair, A., and Muller, R. A. (2013). Approaches to local connectivity in autism using resting state functional connectivity MRI. *Front. Hum. Neurosci.* 7:605. doi: 10.3389/fnhum.2013.00605
- Menke, R. A., Jbabdi, S., Miller, K. L., Matthews, P. M., and Zarei, M. (2010). Connectivity-based segmentation of the substantia nigra in human and its implications in Parkinson's disease. *Neuroimage* 52, 1175–1180. doi: 10.1016/j.neuroimage.2010.05.086
- Menke, R. A., Scholz, J., Miller, K. L., Deoni, S., Jbabdi, S., Matthews, P. M., et al. (2009). MRI characteristics of the substantia nigra in Parkinson's disease: a combined quantitative T1 and DTI study. *Neuroimage* 47, 435–441. doi: 10.1016/j.neuroimage.2009.05.017

- Michaeli, S. (2007). Novel MRI contrasts measure *in vivo* characteristics of Parkinson's disease. *Nat. Clin. Pract. Neurol.* 3, 122–123. doi: 10.1038/ncpneuro0411
- Michaeli, S., Grohn, H., Grohn, O., Sorce, D. J., Kauppinen, R., Springer, C. S., et al. (2005). Exchange-influenced T2rho contrast in human brain images measured with adiabatic radio frequency pulses. *Magn. Reson. Med.* 53, 823–829. doi: 10.1002/mrm.20428
- Michaeli, S., Oz, G., Sorce, D. J., Garwood, M., Ugurbil, K., Majestic, S., et al. (2007). Assessment of brain iron and neuronal integrity in patients with Parkinson's disease using novel MRI contrasts. *Mov. Disord.* 22, 334–340. doi: 10.1002/mds.21227
- Michaeli, S., Sorce, D. J., and Garwood, M. (2008). T-2 rho and T-1 rho adiabatic relaxations and contrasts. *Curr. Anal. Chem.* 4, 8–25. doi: 10.2174/15734110878339115
- Michaeli, S., Sorce, D. J., Idiyatullin, D., Ugurbil, K., and Garwood, M. (2004). Transverse relaxation in the rotating frame induced by chemical exchange. *J. Magn. Reson.* 169, 293–299. doi: 10.1016/j.jmr.2004.05.010
- Michaeli, S., Sorce, D. J., Springer, C. S. Jr., Ugurbil, K., and Garwood, M. (2006). T1rho MRI contrast in the human brain: modulation of the longitudinal rotating frame relaxation shutter-speed during an adiabatic RF pulse. *J. Magn. Reson.* 181, 135–147. doi: 10.1016/j.jmr.2006.04.002
- Nasreddine, Z. S., Phillips, N. A., Bedirian, V., Charbonneau, S., Whitehead, V., Collin, I., et al. (2005). The Montreal Cognitive Assessment, MoCA: a brief screening tool for mild cognitive impairment. *J. Am. Geriatr. Soc.* 53, 695–699. doi: 10.1111/j.1532-5415.2005.53221.x
- Nestrasil, I., Michaeli, S., Liimatainen, T., Rydeen, C. E., Kotz, C. M., Nixon, J. P., et al. (2010). T1rho and T2rho MRI in the evaluation of Parkinson's disease. *J. Neurol.* 257, 964–968. doi: 10.1007/s00415-009-5446-2
- Ogiso, K., Kudo, K., Sasaki, M., Sakushima, K., Yabe, I., Sasaki, H., et al. (2013). 3D neuromelanin-sensitive magnetic resonance imaging with semi-automated volume measurement of the substantia nigra pars compacta for diagnosis of Parkinson's disease. *Neuroradiology* 55, 719–724. doi: 10.1007/s00234-013-1171-8
- Okuaki, T., Takayama, Y., Nishie, A., Ogino, T., Obara, M., Honda, H., et al. (2017). T1rho mapping improvement using stretched-type adiabatic locking pulses for assessment of human liver function at 3T. *Magn. Reson. Imaging* 40, 17–23. doi: 10.1016/j.mri.2017.03.006
- Peran, P., Cherubini, A., Assogna, F., Piras, F., Quattrocchi, C., Peppe, A., et al. (2010). Magnetic resonance imaging markers of Parkinson's disease nigrostriatal signature. *Brain* 133, 3423–3433. doi: 10.1093/brain/awq212
- Power, J. D., Barnes, K. A., Snyder, A. Z., Schlaggar, B. L., and Petersen, S. E. (2012). Spurious but systematic correlations in functional connectivity MRI networks arise from subject motion. *Neuroimage* 59, 2142–2154. doi: 10.1016/j.neuroimage.2011.10.018
- Prodoehl, J., Li, H., Planetta, P. J., Goetz, C. G., Shannon, K. M., Tangonan, R., et al. (2013). Diffusion tensor imaging of Parkinson's disease, atypical parkinsonism, and essential tremor. *Mov. Disord.* 28, 1816–1822. doi: 10.1002/mds.25491
- Rolheiser, T. M., Fulton, H. G., Good, K. P., Fisk, J. D., McKelvey, J. R., Scherfler, C., et al. (2011). Diffusion tensor imaging and olfactory identification testing in early-stage Parkinson's disease. *J. Neurol.* 258, 1254–1260. doi: 10.1007/s00415-011-5915-2
- Satzer, D., DiBartolomeo, C., Ritchie, M. M., Storino, C., Liimatainen, T., Hakkarainen, H., et al. (2015). Assessment of dysmyelination with RAFFn MRI: application to murine MPS I. *PLoS ONE* 10:e0116788. doi: 10.1371/journal.pone.0116788
- Schenck, C. H., Bundlie, S. R., Ettinger, M. G., and Mahowald, M. W. (1986). Chronic behavioral disorders of human REM sleep: a new category of parasomnia. *Sleep* 9, 293–308. doi: 10.1093/sleep/9.2.293
- Schenck, C. H., Bundlie, S. R., and Mahowald, M. W. (1996). Delayed emergence of a parkinsonian disorder in 38% of 29 older men initially diagnosed with idiopathic rapid eye movement sleep behaviour disorder. *Neurology* 46, 388–393. doi: 10.1212/WNL.46.2.388
- Scherfler, C., Frauscher, B., Schocke, M., Iranzo, A., Gschliesser, V., Seppi, K., et al. (2011). White and gray matter abnormalities in idiopathic rapid eye movement sleep behavior disorder: a diffusion-tensor imaging and voxel-based morphometry study. *Ann. Neurol.* 69, 400–407. doi: 10.1002/ana.22245
- Sierra, A., Michaeli, S., Niisanen, J. P., Valonen, P. K., Grohn, H. J., Yla-Herttuala, S., et al. (2008). Water spin dynamics during apoptotic cell death in glioma gene therapy probed by T1rho and T2rho. *Magn. Reson. Med.* 59, 1311–1319. doi: 10.1002/mrm.21600
- Silveira-Moriyama, L., Petrie, A., Williams, D. R., Evans, A., Katzenschlager, R., Barbosa, E. R., et al. (2009). The use of a color coded probability scale to interpret smell tests in suspected parkinsonism. *Mov. Disord.* 24, 1144–1153. doi: 10.1002/mds.22494
- Smith, S. M. (2002). Fast robust automated brain extraction. *Hum. Brain Mapp.* 17, 143–155. doi: 10.1002/hbm.10062
- Song, S. K., Lee, J. E., Park, H. J., Sohn, Y. H., Lee, J. D., and Lee, P. H. (2011). The pattern of cortical atrophy in patients with Parkinson's disease according to cognitive status. *Mov. Disord.* 26, 289–296. doi: 10.1002/mds.23477
- Tuite, P. J., Mangia, S., Tyan, A. E., Lee, M. K., Garwood, M., and Michaeli, S. (2012). Magnetization transfer and adiabatic R 1rho MRI in the brainstem of Parkinson's disease. *Parkinsonism Relat. Disord.* 18, 623–625. doi: 10.1016/j.parkreldis.2012.01.003
- Vaillancourt, D. E., Spraker, M. B., Prodoehl, J., Abraham, I., Corcos, D. M., Zhou, X. J., et al. (2009). High-resolution diffusion tensor imaging in the substantia nigra of *de novo* Parkinson disease. *Neurology* 72, 1378–1384. doi: 10.1212/01.wnl.0000340982.01727.6e
- van Mierlo, T. J., Chung, C., Foncke, E. M., Berendse, H. W., and van den Heuvel, O. A. (2015). Depressive symptoms in Parkinson's disease are related to decreased hippocampus and amygdala volume. *Mov. Disord.* 30, 245–252. doi: 10.1002/mds.26112
- Vriend, C., Boedhoe, P. S., Rutten, S., Berendse, H. W., van der Werf, Y. D., and van den Heuvel, O. A. (2016). A smaller amygdala is associated with anxiety in Parkinson's disease: a combined FreeSurfer-VBM study. *J. Neurol. Neurosurg. Psychiatry* 87, 493–500. doi: 10.1136/jnnp-2015-310383
- Yushkevich, P. A., Piven, J., Hazlett, H. C., Smith, R. G., Ho, S., Gee, J. C., et al. (2006). User-guided 3D active contour segmentation of anatomical structures: significantly improved efficiency and reliability. *Neuroimage* 31, 1116–1128. doi: 10.1016/j.neuroimage.2006.01.015
- Zang, Y., Jiang, T., Lu, Y., He, Y., and Tian, L. (2004). Regional homogeneity approach to fMRI data analysis. *Neuroimage* 22, 394–400. doi: 10.1016/j.neuroimage.2003.12.030
- Zecca, L., Casella, L., Albertini, A., Bellei, C., Zucca, F. A., Engelen, M., et al. (2008). Neuromelanin can protect against iron-mediated oxidative damage in system modeling iron overload of brain aging and Parkinson's disease. *J. Neurochem.* 106, 1866–1875. doi: 10.1111/j.1471-4159.2008.05541.x
- Zhang, J., Nissi, M. J., Idiyatullin, D., Michaeli, S., Garwood, M., and Ellermann, J. (2016). Capturing fast relaxing spins with SWIFT adiabatic rotating frame spin-lattice relaxation ( $T_{1\rho}$ ) mapping. *NMR Biomed.* 29, 420–430. doi: 10.1002/nbm.3474

**Conflict of Interest Statement:** The authors declare that the research was conducted in the absence of any commercial or financial relationships that could be construed as a potential conflict of interest.

Copyright © 2017 Mangia, Svatkova, Mascali, Nissi, Burton, Bednarik, Auerbach, Giove, Eberly, Howell, Nestrasil, Tuite and Michaeli. This is an open-access article distributed under the terms of the Creative Commons Attribution License (CC BY). The use, distribution or reproduction in other forums is permitted, provided the original author(s) or licensor are credited and that the original publication in this journal is cited, in accordance with accepted academic practice. No use, distribution or reproduction is permitted which does not comply with these terms.



# Lysophosphatidyl Choline Induced Demyelination in Rat Probed by Relaxation along a Fictitious Field in High Rank Rotating Frame

Lauri J. Lehto<sup>1,2</sup>, Aloma A. Albors<sup>1</sup>, Alejandra Sierra<sup>1</sup>, Laura Tolppanen<sup>3</sup>, Lynn E. Eberly<sup>4</sup>, Silvia Mangia<sup>2</sup>, Antti Nurmi<sup>3</sup>, Shalom Michaeli<sup>2</sup> and Olli Gröhn<sup>1,2\*</sup>

<sup>1</sup> Department of Neurobiology, A.I. Virtanen Institute for Molecular Sciences, University of Eastern Finland, Kuopio, Finland

<sup>2</sup> Department of Neurobiology, Center of Magnetic Resonance Research, University of Minnesota, Minneapolis, MN, United States, <sup>3</sup> Charles River Discovery Services, Kuopio, Finland, <sup>4</sup> Division of Biostatistics, University of Minnesota, Minneapolis, MN, United States

## OPEN ACCESS

### Edited by:

Federico Giove,  
Centro Fermi, Italy

### Reviewed by:

Kai-Hsiang Chuang,  
The University of Queensland,  
Australia

Li-Wei Kuo,

National Health Research Institutes,  
Taiwan

### \*Correspondence:

Olli Gröhn  
[olli.grohn@uef.fi](mailto:olli.grohn@uef.fi)

### Specialty section:

This article was submitted to  
Brain Imaging Methods,  
a section of the journal  
*Frontiers in Neuroscience*

Received: 24 March 2017

Accepted: 13 July 2017

Published: 03 August 2017

### Citation:

Lehto LJ, Albors AA, Sierra A, Tolppanen L, Eberly LE, Mangia S, Nurmi A, Michaeli S and Gröhn O (2017) Lysophosphatidyl Choline Induced Demyelination in Rat Probed by Relaxation along a Fictitious Field in High Rank Rotating Frame. *Front. Neurosci.* 11:433.  
doi: 10.3389/fnins.2017.00433

In this work a new MRI modality entitled Relaxation Along a Fictitious Field in the rotating frame of rank 4 (RAFF4) was evaluated in its ability to detect lower myelin content in lysophosphatidyl choline (LPC)-induced demyelinating lesions. The lesions were induced in two areas of the rat brain with either uniform or complex fiber orientations, i.e., in the corpus callosum (cc) and dorsal tegmental tract (dtg), respectively. RAFF4 showed excellent ability to detect demyelinated lesions and good correlation with myelin content in both brain areas. In comparison, diffusion tensor imaging metrics, fractional anisotropy, mean diffusivity and axonal and radial diffusivity, and magnetization transfer (MT) metrics, longitudinal relaxation during off-resonance irradiation and MT ratio, either failed to detect demyelination in dtg or showed lower correlation with myelin density quantified from gold chloride stained histological sections. Good specificity of RAFF4 to myelin was confirmed by its low correlation with cell density assessed from Nissl stained sections as well as its lack of sensitivity to pH changes in the physiological range as tested in heat denatured bovine serum albumin phantoms. The excellent ability of RAFF4 to detect myelin content and its insensitivity to fiber orientation distribution, gliosis and pH, together with low specific absorption rate, demonstrates the promise of rotating frame of rank  $n$  (RAFF $n$ ) as a valuable MRI technique for non-invasive imaging of demyelinating lesions.

**Keywords:** RAFF, DTI, relaxation, myelin, demyelination, white matter damage, lysophosphatidyl choline

## INTRODUCTION

The quantitative assessment of myelin in the brain is highly important for both diagnostic and monitoring purposes of a variety of disorders, including multiple sclerosis (MS), traumatic brain injury (TBI), and stroke. However, conventional magnetic resonance imaging (MRI) approaches currently used to detect demyelination are suboptimal in their ability to detect myelin. To date, the identification of specific pathological processes involving demyelination by conventional MRI methods is not possible. This is because many different pathological processes result in similarly-appearing lesions in conventional MR, e.g., inflammatory demyelination, infection, stroke or tumor may all appear as bright lesions on T<sub>2</sub>-weighted images.

Advanced MRI modalities such as diffusion tensor imaging (DTI) (Schmithorst et al., 2002), magnetization transfer (MT) (Does et al., 1998), T<sub>1</sub>/T<sub>2</sub> ratio (Glasser and Van Essen, 2011), multiexponential T<sub>2</sub> (McCreary et al., 2009), and direct detection using ultra-short echo time (Wilhelm et al., 2012) have potential in assessing tissue organization and myelin. However, these methodologies just partially address the problem of myelin detection (Glasser and Van Essen, 2011; Nossin-Manor et al., 2013). For instance, although DTI is sensitive to tissue microstructure, it is not specific to myelin (Le Bihan and Johansen-Berg, 2012), because metrics derived from DTI data are influenced also by the underlying macroscopic level organization of myelinated fibers. On the other hand, MT has contributions from T<sub>1</sub> in different water pools, and the results are dependent on experimental parameters such as off-resonance frequency and saturating B<sub>1</sub> field strength. For example, the MT ratio (MTR) showed equally strong correlations with both the degree of myelin loss and the extent of axonal loss in postmortem samples (Schmierer et al., 2004). T<sub>1</sub>/T<sub>2</sub> ratio has been shown to provide good correlation with myelin in normal gray matter (Glasser and Van Essen, 2011), but just like T<sub>1</sub> and T<sub>2</sub>, it is influenced by the change of multiple different factors such as edema and paramagnetic ion concentration in the pathological brain (Pirko and Johnson, 2008; Beer et al., 2016). Furthermore, in a recent study by Dula and co-workers (Dula et al., 2010), myelin water fraction, an often cited multiexponential T<sub>2</sub> relaxation metric, varied by almost a factor of 2 between two regions in the spinal cord while the myelin volume fractions differed by only approximately 12%. The proposed explanation for such observation relied on variation in microanatomy and intercompartmental water exchange. Overall, no currently available MRI technique or other noninvasive methods have proven capable of specifically signaling the myelin loss.

Recently, we introduced a novel MRI relaxation method entitled Release Along a Fictitious Field (RAFF) (Liimatainen et al., 2010, 2011) in the rotating frame of rank *n* (RAFF*n*) (Liimatainen et al., 2015). With RAFF*n*, the fictitious fields are created by a non-adiabatic modulation of the RF amplitude and frequency. The particular case of the fictitious fields H<sub>*n*</sub> of rank *n* which are stationary in the rotating frame of rank (*n*-1) was detailed in (Liimatainen et al., 2015). We have shown that frequency modulated pulses operating in the nonadiabatic regime in the 1st rotating frame, and thus producing a large fictitious magnetic field in the 2nd rotating frame, can be used for generating novel MRI contrast in living samples. RAFF*n* is conceptually different from more conventional rotating frame MRI methods. With continuous wave spin lock and adiabatic T<sub>1ρ</sub> and T<sub>2ρ</sub> methods, relaxations are governed solely by longitudinal or transverse relaxations in the rotating frame. On the other hand, relaxations during RAFF2 comprise contributions from both T<sub>1ρ</sub> and T<sub>2ρ</sub> relaxation pathways. Similarly, RAFF*n* comprises both T<sub>1ρ</sub>(*n*) and T<sub>2ρ</sub>(*n*) relaxation channels. Moreover, RAFF*n* is also conceptually different from chemical exchange saturation transfer (CEST) and/or MT since RAFF*n* is sensitive to all contributing relaxation mechanisms including dipole-dipole interactions,

diffusion in local field gradients and exchange between spins with different chemical shifts and the cross-relaxations. On the other hand, CEST and MT provide direct measure of the saturation transfer or exchange between off-resonance spins and water. We have shown that for adiabatic T<sub>1ρ</sub> the contribution of cross relaxations (origin of MT) between spins within the bandwidth of the adiabatic pulse is minor (Michaeli et al., 2008). The contribution of off-resonance saturation to RAFF*n* relaxation may originate also from side bands at frequencies defined by the duration of the RAFF*n* pulses (Liimatainen et al., 2015), a mechanism which may enhance sensitivity of RAFF*n* to multiple spin pools within the myelin component. These frequencies are determined by the assembling of the RAFF*n* pulses into P-packets, which refocuses the magnetization in the form of rotary echo (Solomon, 1959). Formation of the rotary echoes in the rotating frame during RAFF*n* pulses is an additional distinction from MT and CEST techniques.

RAFF*n* generates flexible MRI contrast with low specific absorption rate (SAR) and is thus particularly safe for human applications. We have demonstrated that by changing the rank of the rotating frame and the orientation of the fictitious field in the rotating frame of reference, RAFF*n* MRI contrast can be sensitized to various motional regimes. In particular, RAFF4 and RAFF5 are exquisitely sensitive to slow/ultra-slow motion characterized by the correlation times (τ<sub>c</sub>) in the millisecond time scale. This is important for sensitive and specific myelin detection as the highly organized structure of myelin contains multi-compartment water environments: myelinic, intra-axonal, and interaxonal. These pools are characterized by different molecular mobilities and T<sub>2</sub> relaxation components which correspond to ultra-short (50 μs–1 ms), short- (1–50 ms), intermediate (50 ms–0.5 s), and long-lived T<sub>2</sub> components (>0.5 s) (Does et al., 1998; Bonilla and Snyder, 2007). The short T<sub>2</sub> component is attributed mainly to myelin water, whereas an ultra-short component is thought to arise from carbon-bound methylene protons. Extensive experimental and theoretical studies by Mefed and coworkers have demonstrated that relaxation measurements in high-rank rotating frames of T<sub>1ρρ</sub> and T<sub>1ρρρ</sub> (second and third frame longitudinal relaxations, respectively) allow the probing of slow-ultra slow motion with the characteristic correlation times up to 10<sup>-1</sup>–10<sup>-3</sup> s (Mefed, 1999, 2001). Our previous analysis, in agreement with those by Mefed, also shows that the sensitivity of RAFF4 and RAFF5 is shifted to the motional regime in the millisecond time scale as compared to adiabatic T<sub>1ρ</sub> (Michaeli et al., 2006) which has a maximal sensitivity to the correlation times in the microsecond time scale (Satzer et al., 2015).

Utilizing the sensitivity of RAFF4 and 5 to slow molecular motion, we have recently embarked on measuring myelin content in the normal brain and in complex mucopolysaccharidosis type I (MPS-I) pathology including demyelination (Satzer et al., 2015; Hakkarainen et al., 2016). Importantly, the highest correlation between relaxation time constants and myelin content as assessed by quantitative histology was achieved with RAFF4 and RAFF5 techniques, as compared to other relaxation based contrasts (Satzer et al., 2015; Hakkarainen et al., 2016).

In the present work, we further focused on intracranial lysophosphatidyl choline (LPC) injections in the rat brain that have been used previously to model focal demyelination lesions in MS (Waxman et al., 1979; Ransohoff, 2012). LPC injection causes demyelination in the white matter within 3–5 days with only mild inflammatory response, thus allowing a clean model to study demyelination. Another important feature of the model is that location of the white matter lesion can be freely chosen, thus allowing to study the influence of underlying macroscopic structure of the myelinated fibers on MRI contrasts. The optimal MRI contrast for detection of demyelination would be sensitive to the amount of myelin regardless of macroscopic level anisotropy.

The aim of this study was to characterize the ability of RAFF4 to detect demyelination processes in presence of different underlying tissue macrostructure and to compare that with some of the approaches currently used to detect white matter lesions in advanced human studies. To achieve these goals, we induced demyelination by injecting LPC in the rat corpus callosum (cc) and dorsal tegmental tract (dtg), measured RAFF4, DTI and MT parameters, and performed histology validation to assess the ability of the various MRI modalities to detect demyelination. Furthermore, influence of pH on RAFF4 contrast was evaluated using bovine serum albumin containing phantoms.

## MATERIALS AND METHODS

### Animal Model

Male Sprague Dawley rats ( $n = 21$ , Charles River, Germany; 300–350 g) were used in the experiments. Rats were group housed with a preserved 12 h light/12 h dark cycle and *ad libitum* access to food and water. All animal procedures were approved by the Animal Ethics Committee of the Provincial Government of Southern Finland, and conducted in accordance with the guidelines set by the European Commission Directive 2010/63/EEC.

All surgical procedures were done under inhalation anesthesia using 1.8–2.2% isoflurane in 30%/70% O<sub>2</sub>/N<sub>2</sub>O. To induce demyelinated lesions, stereotaxic injections of the LPC solution (volume of 1.5  $\mu$ l; concentration: 10 mg/ml; L- $\alpha$ -lysophosphatidylcholine from egg yolk; L-4129 Sigma-Aldrich, St. Louis, USA) were performed in selected areas of the rat brain, chosen based on their myeloarchitecture. The injections were placed either in the cc ( $n = 6$  and  $n = 4$ , LPC and vehicle, respectively) at the stereotaxic coordinates: 0.4 mm posterior from bregma, 1.4 mm lateral from the midline, and 2.6 mm from the skull. For the dtg ( $n = 6$  and  $n = 4$ , LPC and vehicle, respectively) the injection coordinates were at 6.3 mm posterior from bregma, 0.8 mm lateral from the midline, and 4.3 mm from the skull. The cc represents a major white matter bundle with the parallel organization of myelin bundles, while dtg is a typical example of more complex myeloarchitecture with a high density of heterogeneously oriented axons. Control animals underwent identical protocol but were injected with 1.5  $\mu$ l of vehicle solution [0.1 M sodium phosphate buffer (PBS)] instead of LPC.

### MRI

All the animals were imaged 3 days after injection, when there is already significant demyelination in this animal model, while inflammatory reaction and remyelination typically develops later (Waxman et al., 1979). All MR experiments were performed using a horizontal 7 T magnet system (Bruker Pharmascan, Entlingen, Germany).

The sites of injections were localized using T<sub>2</sub>-weighted fast spin-echo (FSE) images with the following parameters: TR = 4 s, echo spacing 12 ms, TE<sub>eff</sub> = 48.0 ms, n<sub>echo</sub> = 8, FOV = 25.6  $\times$  25.6 mm<sup>2</sup>, matrix size = 256  $\times$  256, number of slices = 20 and slice thickness = 0.75 mm. The imaging slice for RAFFn, MT and DTI (middle slice) was centered to the FSE slice next to the injection site to avoid including mechanical damage induced by the injection.

### RAFFn Technique

A detailed description of the RAFFn technique was presented elsewhere (Liimatainen et al., 2015). We chose to use RAFF4, as RAFF4 and 5 showed highest correlation to myelin content in normal rat brain in our previous study (Hakkilainen et al., 2016), and as RAFF4 relaxation is faster than RAFF5 thus requiring shorter pulse train duration than RAFF5. With RAFFn, the *sine/cosine* pulses were used for the modulation of the amplitude and frequency, respectively. The orientation of the effective field of RAFFn in the rotating frame of rank (n-1) relative to the Z<sup>(n-1)</sup> axis of quantization is defined by the angle  $\alpha^{(n)}$ , as was previously detailed (Liimatainen et al., 2010, 2011, 2015). Here, the  $\alpha^{(n)}$  was set to 45° in each rotating frame of rank n-1, and the amplitude of the effective field H<sub>n</sub> was maintained at the same level. During RAFFn pulses, the rotary echoes are generated when using four pulse elements assembled into a P-packet according to the scheme PP<sup>-1</sup>P <sub>$\pi$</sub> P <sub>$\pi$</sub> <sup>-1</sup> (Liimatainen et al., 2010). An instantaneous flip of the effective field H<sub>n</sub> is indeed performed during each P-packet to ensure refocusing of M on the Z<sup>(n-1)</sup> axis and to form rotating frame rotary spin echo (Solomon, 1959). The peak RF amplitude of RAFF4 pulses was  $\gamma B_1 = 323$  Hz. The time duration of each PP<sup>-1</sup>P <sub>$\pi$</sub> P <sub>$\pi$</sub> <sup>-1</sup> packet defined as  $T_p = 4\pi/(\sqrt{2}\omega_1^{\max})$  was set to 4.525 ms. The signal intensity decay was measured by incremental pulse trains of P-packet, with an inversion pulse to account for steady state. RAFF4 pulse train durations were 0, 27, 54, 81, and 108 ms.

Fast spin-echo (FSE) was used as a readout pulse sequence with TR = 4 s, TE<sub>eff</sub> = 8.3 ms, n<sub>echo</sub> = 8, FOV = 32.0  $\times$  32.0 mm<sup>2</sup>, matrix size = 256  $\times$  256, number of slices = 1 and slice thickness = 0.5 mm, leading to total acquisition time 21 min 20 s for one relaxation time constant map.

### Comparator Techniques: DTI and MT

MT measurements were conducted using the same FSE readout sequence as described above for RAFF4. The modified inversion MT protocol with two consecutive acquisitions was used (Mangia et al., 2011). First, the signal decay during off-resonance irradiation with M oriented along +Z was acquired, and, second, the signal recovery was measured when M was inverted along -Z. A square saturation pulse with  $\gamma B_1 = 200$  Hz was placed 8 kHz off-resonance with an incrementing pulse duration of 0,

0.3, 0.6, 0.9, and 1.2 s. Total acquisition time was 21 min 20 s.  $T_{1\text{sat}}$ , steady state magnetization  $M_{\text{SS}}$  and magnetization in fully relaxed state,  $M_0$ , were solved using pixel-by-pixel analysis with monoexponential decay and rise functions to the same steady state value, as described in Mangia et al. (2011). MTR was calculated as  $\text{MTR} = 1 - M_{\text{SS}}/M_0$ .

For DTI, segmented spin-echo EPI was used with  $\text{TR} = 2$  s,  $\text{TE} = 30.0$  ms,  $n_{\text{shots}} = 6$ , number of averages = 12,  $\text{FOV} = 26.5 \times 18.0 \text{ mm}^2$ , matrix size =  $212 \times 144$ , number of slices = 9, slice thickness = 0.5 mm,  $b = 1,000 \text{ s/mm}^2$ , diffusion directions = 42 leading to total acquisition time of 1 h 55 min. Mean diffusivity (MD), fractional anisotropy (FA), radial and axial diffusivity (RD, AD) maps were calculated from DTI data.

## ROI Analysis with MRI

Relaxation time constant maps and parametric maps from MT and DTI data were calculated in MATLAB (MathWorks, Natick, MA). The regions of interest (ROIs) were hand-drawn using the Aedes software package (<http://aedes.uef.fi>). Six ROIs were drawn in the cc, three contralateral (1, 2, and 3) and three ipsilateral (4, 5, and 6) to the injection site (Figure 3). Mean values of ROI 4 further averaged over LPC or vehicle animals were used to evaluate the relative contrast (RC) of each of the different MRI metrics between LPC and vehicle injected animals. For metrics with lower intensity in vehicles,  $\text{RC} = [\text{LPC-vehicle}]/\text{LPC} * 100\%$ . For metrics with higher intensity in vehicles,  $\text{RC} = [\text{vehicle-LPC}]/\text{vehicle} * 100\%$ . This approach ensures that RC is comparable between techniques regardless of the direction of change between LPC and vehicle animals. Further, by dividing the difference with the higher value makes RC a conservative approach as it has a maximum of 100%. In addition, relative contrast-to-noise ratio (RCNR) was calculated so that  $\text{RCNR} = [\text{higher value-lower value}]/\text{SD}(\text{mean values of ROI4 of the vehicles})$ . To have a broader dynamic range of myelinated tissue, all 6 ROIs were used to calculate correlations between MRI and myelin content based on histological stainings as described below. For the dtg, an ROI covering the lesion was drawn and copied to the contralateral side to the corresponding anatomical location. For the vehicle injected animals, a 3-by-3 voxel ROI was drawn at the injection site and copied to the same anatomical location on the contralateral side. RC between LPC and vehicle injected animals were then calculated as for the cc, using the contralateral ROIs.

## Histological Procedures

Immediately after the MRI scans, all the animals were transcardially perfused with 0.9% NaCl (30 ml/min, 2 min, 4°C), followed by 4% paraformaldehyde (PFA) solution in 0.1 M phosphate buffer (pH 7.4, 30 ml/min, 25 min, 4°C). Fixed brains were removed from the skull, and post-fixed for 4 h in 4% PFA. Then, the brains were cryoprotected in 20% glycerol in 0.02 M potassium phosphate-buffered saline (pH 7.4) for 36 h, and frozen in dry ice. The frozen brains were stored at -70°C until sectioning.

The brains were cut in five series of 30- $\mu\text{m}$  thick coronal sections using a sliding microtome. The first series of sections was stored in 10% formalin, at room temperature. The series from

second to fifth were stored in a cryoprotectant tissue-collecting solution (30% ethylene glycol, 25% glycerol in 0.05 M PBS) at -20°C until further processing.

The first series of sections was stained with Nissl (thionin) to study cytoarchitecture, cell death and gliosis. The second series of sections was stained with gold chloride to assess the myeloarchitecture. For myelin staining, sections were mounted on gelatin-coated slides and dried at 37°C. They were then incubated in a 0.2% gold chloride solution ( $\text{HAuCl}_4 \bullet 3\text{H}_2\text{O}$ , G-4022 Sigma-Aldrich, St. Louis, USA) in 0.02 M PBS (pH 7.4) containing 0.09% NaCl for 7–8 h at room temperature in the dark. Then, the slides were washed twice for 4 min in 0.02 M PBS in 0.09% NaCl and placed in a 2.5% sodium thiosulfate solution for 5 min. After three 10 min washes in the buffer solution, sections were dehydrated through an ascending series of ethanol, cleared in xylene and coverslipped with DePeX (BDH, Laboratory Supplies, Dorset, UK).

## Histological Analyses

High-resolution photomicrographs of both myelin- and Nissl-stained sections of the cc and the dtg were obtained using a light microscope (Leica DMRB, Wetzlar, Germany) equipped with a digital camera (DXM1200F, Nikon Instruments Inc., Japan). Three consecutive sections of these areas were analyzed covering a volume of 450  $\mu\text{m}$  that corresponded to the slice thickness in MRI.

The optical density on myelin- and Nissl-stained sections was quantified using ImageJ software (version 1.41 <http://rsb.info.nih.gov/ij/>). For cc and dtg, ROIs were drawn corresponding in location, size and shape to the MRI ROIs. Optical density (OD) was averaged for each ROI over three consecutive sections to cover the volume analyzed in MRI. After conversion of the images to gray-scale, OD values were obtained from the ROIs. For correction of possible staining differences between sections and brains, OD values from healthy reference areas were obtained. For the cc lesions, white matter in the striatum was used as a reference and for dtg lesions, cc (in the sections of dtg) was used as a reference.

## Transmission Electron Microscopy (TEM)

One extra rat, injected with LPC as described above, was used to study the ultrastructure of the myelin sheaths in the corpus callosum 3 days after the LPC injection using TEM.  $T_2$ -weighted images were acquired to verify the presence and consistency of the demyelinated lesion. After MRI, the rat was perfused using 0.9% NaCl (30 ml/min) for 2 min followed by 4% PFA (30 ml/min) in 4°C for 50 min. The brain was removed from the skull, post-fixed in 4% PFA/1% glutaraldehyde overnight at 4°C, and sectioned in 1-mm thick coronal sections in a brain matrix. One 1-mm thick section matching the level of the MRI analysis was selected based on  $T_2$ -weighted images. The corpus callosum of this section was dissected into eight small portions from the level of the injection site to the same level on the healthy contralateral side. These corpus callosum samples were incubated with 4% PFA in 0.1 M cacodylate

buffer (pH 7.4) at 4°C for an overnight. Then, the samples were rinsed in 0.1 M cacodylate buffer 5 min three times, followed by a post-fixation in 1% osmium tetroxide ( $\text{OsO}_4$ ) in 0.1 M cacodylate buffer for 2 h. After that, the samples were again rinsed in 0.1 M cacodylate buffer for 5 min three times. Then, the samples were dehydrated in ascending percentage of alcohols for 10 min, and the last incubation was propylene oxide twice for 10 min. The samples were then infiltrated with a 1:1 mixture of propylene oxide and LX-112 resin (Ladd Research Industries Inc., USA) for 1 h, followed by incubation in LX-112 resin overnight. The embedding was done with fresh LX-112 resin in molds. The polymerization of the samples was done in an oven at 37°C for 24 h, and then at 60°C for 48 h.

Once the samples were embedded in the resin, four semi-thin sections of 1  $\mu\text{m}$  were sectioned and stained with Toluidine blue. Toluidine blue stained sections were used to study the cyto- and myeloarchitecture of the samples, and to guide TEM imaging. Six ultrathin sections were cut for TEM and mounted in three different grips. Imaging was done in a transmission electron microscope JEOL JEM-2100F using magnifications between 250 and 10,000x. Photomicrographs were taken using a digital camera connected to the microscope.

## Bovine Serum Albumin Phantoms

Heat denatured bovine serum albumin samples (BSA) were used to investigate influence of pH on RAFF4. Heat denatured BSA has been shown to provide a good model to study influence of pH modulated proton exchanges as relaxation mechanism in tissue, while glutaraldehyde crosslinking blocks a significant portion of exchangeable NH-groups in the protein (Mäkelä et al., 2001). BSA (fraction V, Sigma Chemicals, St. Louis, MO) was dissolved in 0.1 M Tris (pH 7.4) to yield a 10% solution. The pH was adjusted to be 6.2, 6.6, 7.0, 7.4, and 7.8 in five BSA samples, respectively, using HCl or NaOH. BSA phantoms were exposed to 65°C for 3 min for heat denaturation.

The pH phantoms were imaged using a horizontal 9.4 T magnet (Magnex Scientific Ltd., Abington, UK) interfaced to a Varian (Agilent) DirectDrive console (Agilent Technologies, Santa Clara, CA). RF transmission and signal reception were carried out using a single loop coil with 20 mm diameter.  $T_2$ -weighted FSE MR imaging was used as a readout with the parameters as follows: TR = 4 s, TE<sub>eff</sub> = 55 ms, matrix size 256 × 256, FOV = 25.6 × 25.6 mm<sup>2</sup>, 8 echoes with 8 ms echo spacing, initial TE = 10 ms, one slice with slice thickness 1 mm. The settings of RAFF4 were same as for *in vivo* studies described above.  $T_2$ -maps were measured using double spin-echo with two

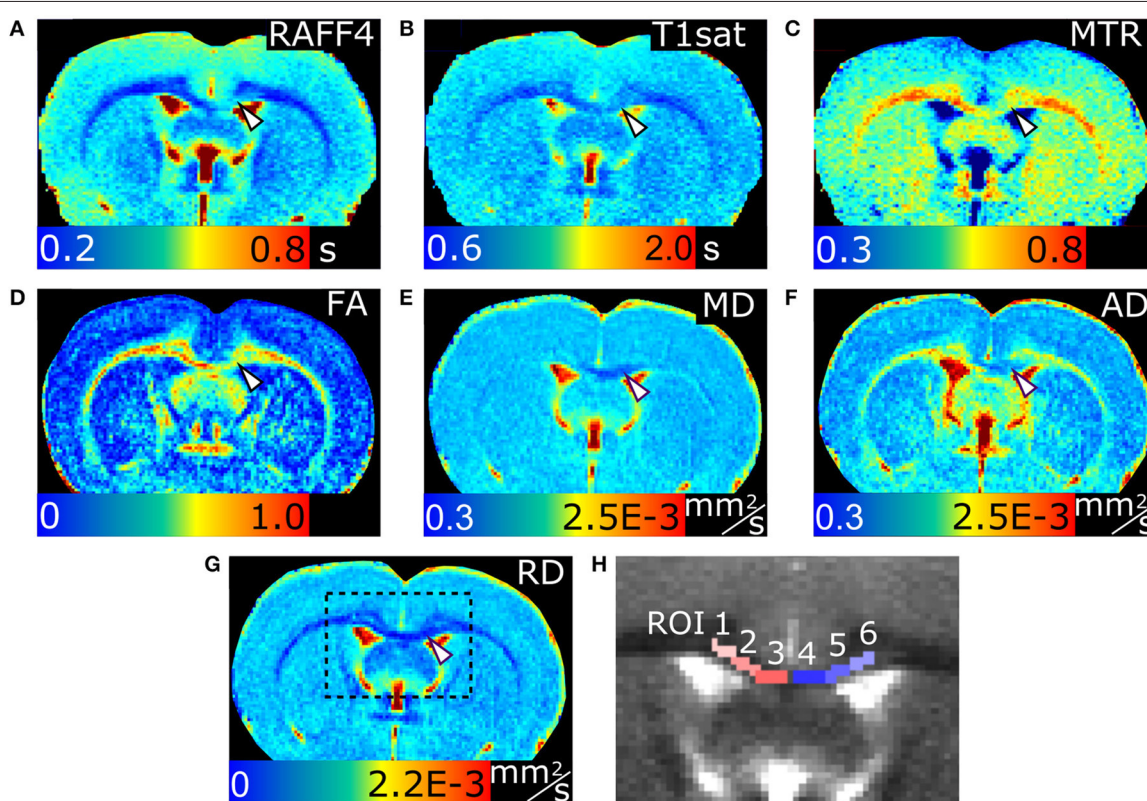


**FIGURE 1 |** MRI parameter maps of a representative rat, 3 days after an LPC injection into the corpus callosum. Relaxation time constant map of RAFF4 (A),  $T_{1\text{sat}}$  (B), magnetization transfer ratio, MTR (C), fractional anisotropy, FA (D), mean diffusivity, MD (E), and axial and radial diffusivity, AD and RD (F,G). Representative examples of ROIs for analyzing lesions in the corpus callosum are shown on a grayscale RAFF4 map in (H). White arrowhead points to demyelinated lesion in (A–G).

3 ms adiabatic full passage pulses and echo times of 5, 7, 15, 23, 31, 39, and 63 ms.

## Statistical Analyses

The Mann-Whitney *U*-test was used to compare LPC injected animals to vehicles. The contribution of myelinated axons and cell density to the MRI metrics was assessed using Pearson's linear correlation (two-tailed) between pooled

ROI analysis results from MRI and histology of myelin and Nissl stained sections, respectively. ROIs from both LPC and vehicle injected animals were included in the analysis including contralateral and ipsilateral ROIs. Correlation was calculated separately for all data, cc data and dtg data. False discovery rate (FDR) correction was done to adjust *p*-values for inflation of error due to multiple testing.

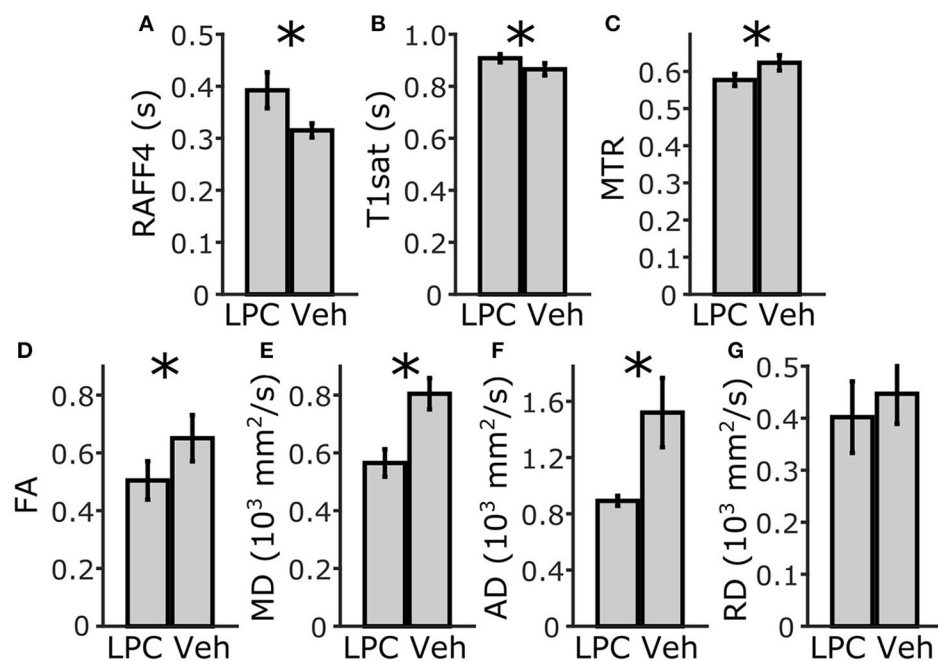


**FIGURE 2 |** ROI analysis of MRI parameters in the corpus callosum, ipsilateral side. Mean and SD using RAFF4 (A),  $T_{1\text{sat}}$  (B), magnetization transfer ratio, MTR (C), fractional anisotropy, FA (D), mean diffusivity MD (E), and axial and radial diffusivity, AD and RD (F,G) values obtained from LPC-induced lesion ROI 4 in the corpus callosum of LPC injected ( $n = 6$ ) rats and from the corresponding ROI in the vehicle injected ( $n = 4$ ) rats. Statistical significance; \*  $< 0.05$  (FDR adj. for testing 7 MRI parameters), Mann-Whitney *U*-Test.

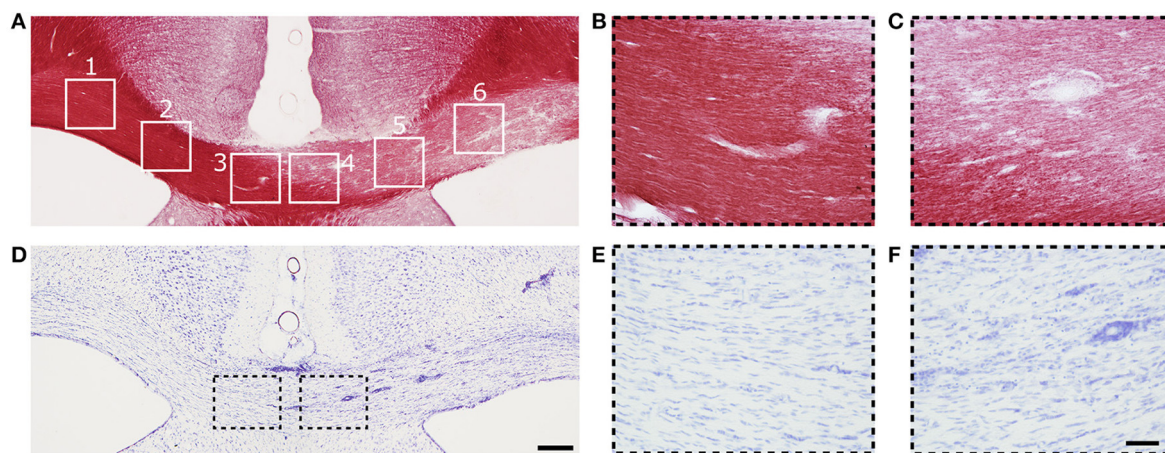


**FIGURE 3 |** (A) Representative photomicrograph of myelin-stained sections of the corpus callosum. (B,C) are high magnification images of ROIs 3 and 4 from (A). (D) Representative photomicrographs of Nissl-stained sections of the corpus callosum. (E,F) are high magnification images of ROIs 3 and 4 in (D). Scale bars: (D,F) 200 and 50  $\mu\text{m}$ , respectively.

## RESULTS

### Corpus Callosum–Demyelination in a Major white Matter Track with Parallel Axons MRI

Representative parametric maps from relaxation, MT and diffusion data obtained from a rat with LPC injection in the cc are shown in **Figure 1**. The imaging slice was chosen to be 0.75 mm posterior from the injection site to avoid the influence of mechanical damage caused by the injection needle. The lesion was clearly visible in all quantitative MRI maps as well as in myelin and Nissl stained histological slices on the ipsilateral site close to the injection site. In all animals, the lesion was located within the cc, extending ipsilaterally  $1.95 \pm 0.24$  mm (mean  $\pm$  SD; based on T<sub>2</sub>-weighted images) from the midline and

contralaterally  $0.05 \pm 0.15$  mm from the midline in mediolateral direction, due to diffusion of the LPC along the tract.

In the ROI analysis, all MRI metrics showed statistically significant differences ( $p < 0.05$ ) between lesions induced by LPC in the ipsilateral cc (ROI 4, in **Figure 3**) and the corresponding area in vehicle animals (**Figure 2**). The RC observed with RAFF4 was 19.7%. The RC of MTR and T<sub>1sat</sub> were 7.4 and 4.7%, respectively, thus exhibiting smaller RC than RAFF4. On the other hand, MD and FA showed the largest RC: 29.8 and 22.5%, respectively. Reduced MD and FA were explained by decrease in axial diffusivity (AD) by 41.3%, while radial diffusivity (RD) did not show a statistically significant difference, consistent with axonal damage and contradicting the typical pattern of diffusion changes often associated with demyelination (Song et al., 2005). While RC of DTI metrics were higher than that of RAFF4, RCNR

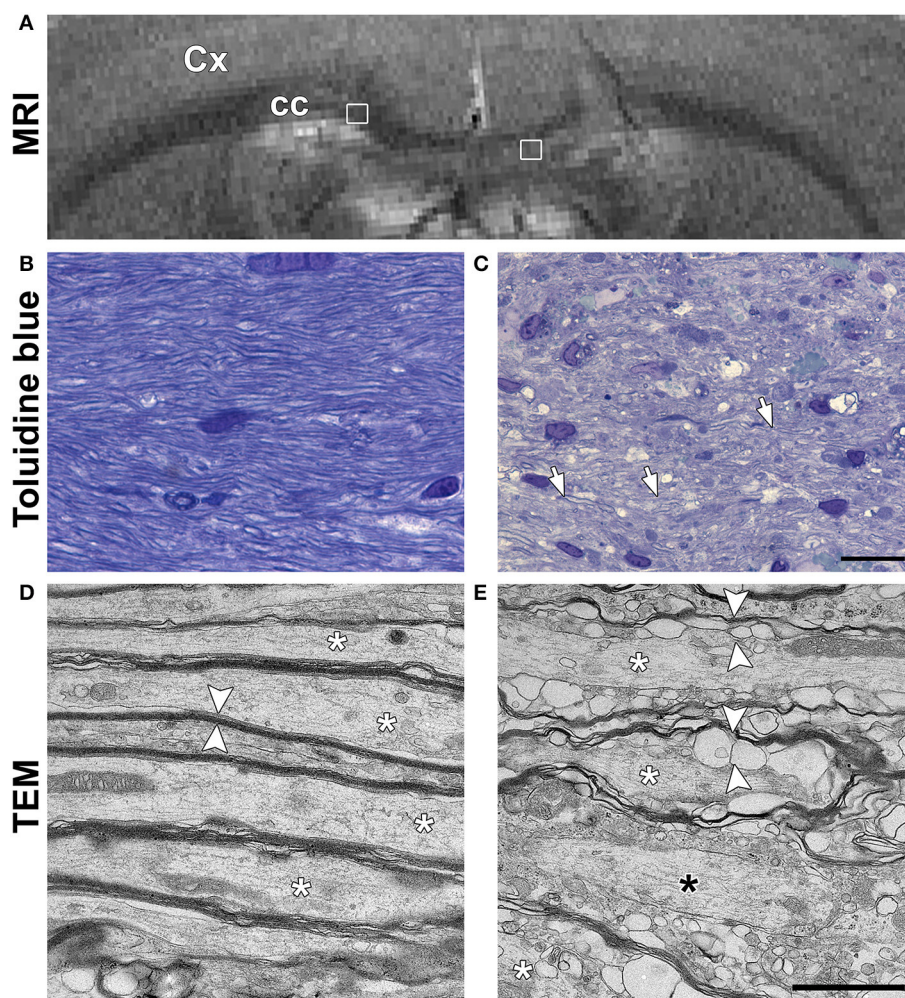


**FIGURE 4 | (A)** *In vivo* T<sub>2</sub>-weighted image of a rat used for the ultrastructural analysis using transmission electron microscopy (TEM). White squares indicate the location of the images shown in **(B,C)**. Representative photomicrographs of Toluidine blue stained sections of the normal corpus callosum **(B)** and demyelinating lesion **(C)**. White arrows in panel C point at axons with thin myelin sheath. Scale bar in **(B,C)** is 20  $\mu$ m. Representative photomicrographs obtained in TEM are shown for the normal corpus callosum **(D)** and demyelinated lesion **(E)**. White asterisks indicate individual axons in both **(D,E)**. In **(D)**, axons have normal and packed myelin sheaths (white arrowheads). In **(E)**, the myelin sheaths appear loosely packed and full of pockets (white arrowheads). A black asterisk indicates an axon without myelin sheath. Scale bar in **(D,E)** is 200 nm.

of RAFF4 was higher at 5.7 in comparison to 4.4, 1.8, and 2.6 of MD, FA and AD, respectively. Correspondingly, RCNR for MTR and  $T_{1\text{sat}}$  was 2.3 and 1.8 respectively.

### Histology and Electron Microscopy

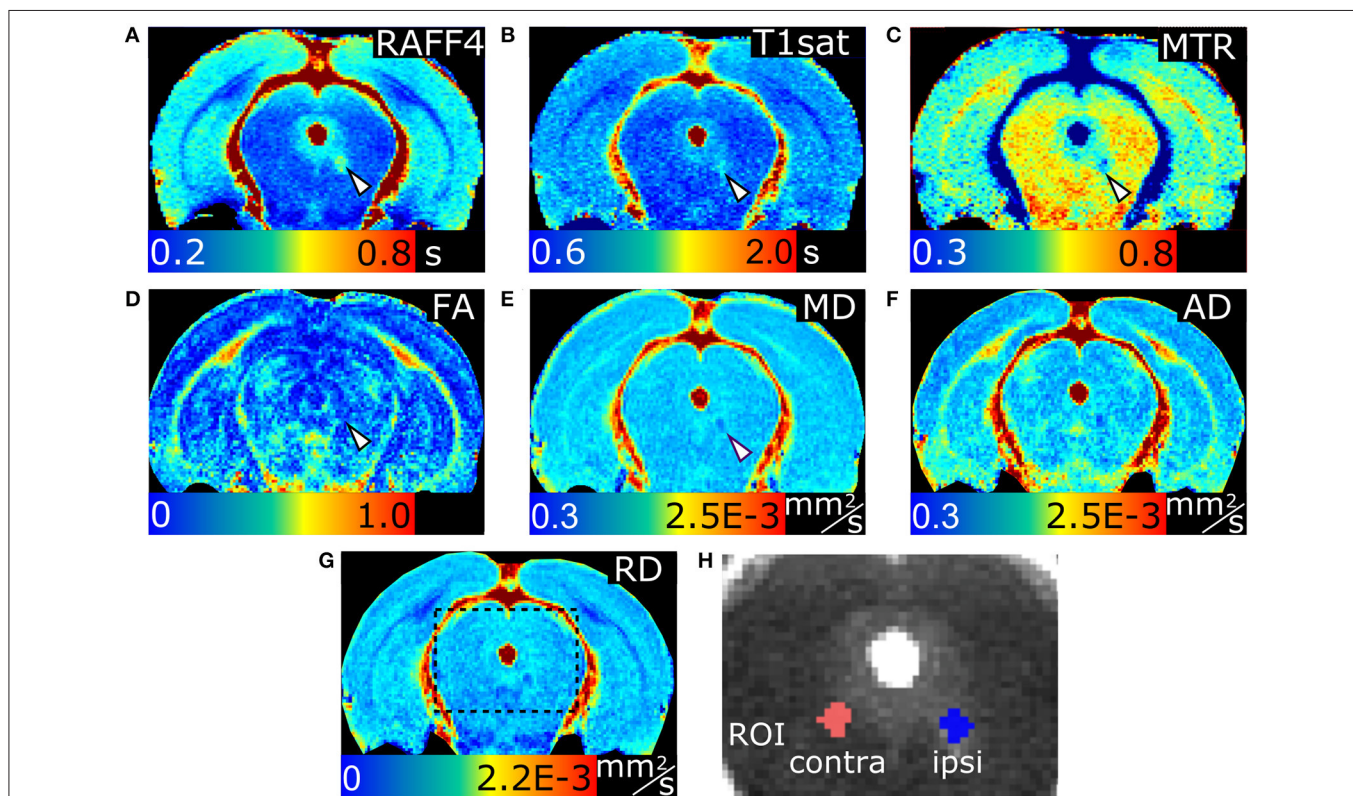
An example of myelin- and Nissl-stained section from the same animal as was presented for MRI in **Figure 1** is shown in **Figure 3**. Three days after LPC injection in the cc, a demyelinated area over the whole ipsilateral cc was observed (ROI 4 to 6) while the myelin content on the contralateral side appeared normal (ROI 1 to 3, **Figure 3A**). Also ROI 4, closest to the midline in the ipsilateral side still presented signs of demyelination (**Figure 3C**), which gradually decreased toward the contralateral side and ROI 3 (**Figure 3B**).

On Nissl-stained sections, a slightly increased cell density was observed on the demyelinated area (**Figure 3D**), which can be attributed to mild gliosis. The cell density was higher in ROI 6 and decreased toward the midline (ROI 4) and the contralateral side (ROI 3) (**Figure 3D**). Mild gliosis overlapped with the demyelinated area observed in myelin staining (**Figure 3A**). Gliosis was diffusely distributed; however, a high number of cells were found surrounding the blood vessels (**Figure 3F**). On the contralateral side to the injection site, the density and distribution of cells appeared normal (**Figure 3E**).

In order to understand the unexpected diffusion results in cc, samples from one additional animal underwent TEM.  $T_2$ -weighted imaging confirmed that the location and extent of the LPC lesion was comparable to lesions in other cc injected animals (**Figure 4A**). Toluidine blue staining showed clearly decreased staining intensity around the axons in the ipsilateral cc when compared to the contralateral cc, corroborating demyelination (**Figures 4B,C**). In TEM, axonal myelin sheaths appeared thick and tightly packed on the contralateral cc. Intra-axonal space appeared normal with only a few membranes or organelles, such as mitochondria, that could restrict diffusion along axons (**Figure 4D**). In the demyelinating ipsilateral cc, axons were either completely demyelinated or surrounded by thin and disorganized myelin sheaths (**Figure 4E**). In pockets between the myelin sheaths, vacuoles and myelin debris were observed around all the demyelinated axons, forming more boundaries along the axonal length.

### Dorsal Tegmental Tract-Demyelination in an Area with a Complex Myeloarchitecture MRI

Lesions with a width of  $0.59 \pm 0.18$  mm were clearly visible in RAFF4,  $T_{1\text{sat}}$  and MTR maps in the dtg (**Figure 5**). In ROI analysis of the dtg, RAFF4 and the MT MRI metrics showed a statistically significant difference ( $p < 0.05$ ) between lesions



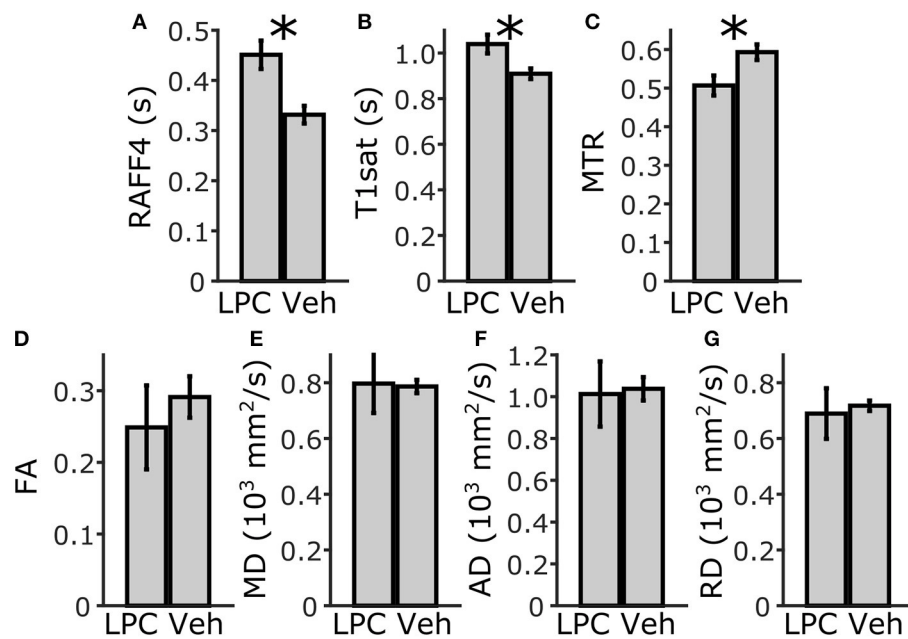


**FIGURE 6 |** ROI analysis of MRI parameters in the dorsal tegmental tract, ipsilateral side. Mean and SD of RAFF4 (A), T<sub>1sat</sub> (B), magnetization transfer ratio, MTR (C), fractional anisotropy, FA (D), mean diffusivity, MD (E), and axial and radial diffusivity, AD and RD (F,G) obtained from LPC induced lesion ROI in the dorsal tegmental tract of LPC injected ( $n = 6$ ) rats and from the corresponding injection site ROI in vehicle injected ( $n = 4$ ) rats. Statistical significance: \*  $< 0.05$  (FDR adj. for testing 7 MR parameters), Mann-Whitney U-Test.

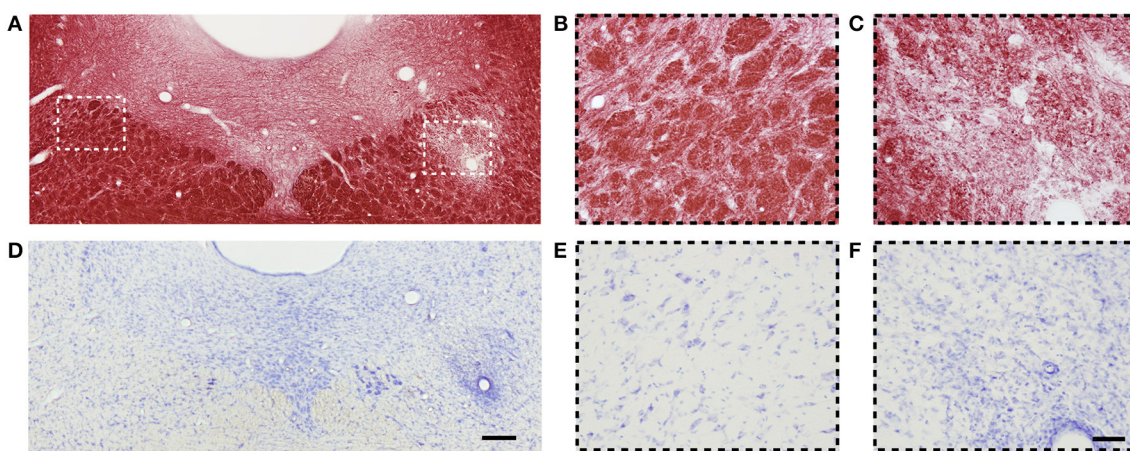


**FIGURE 7 |** (A) Representative photomicrograph of myelin-stained sections of the dorsal tegmental tract. (B,C) are high magnification images of contra- and ipsilateral ROIs from (A), respectively. (D) Representative photomicrographs of Nissl-stained sections of the dorsal tegmental tract. (E,F) are high magnification images of contra- and ipsilateral ROIs from (D), respectively. Scale bars: (D,F) 200 and 50  $\mu\text{m}$ , respectively.

induced by LPC and the corresponding area in vehicle injected animals, while the diffusion metrics did not show a significant difference (Figure 6). The RC of RAFF4 was 26.2% while the RCs of MTR and T<sub>1sat</sub> were lower at 16.4 and 12.5%, respectively. Corresponding RCNRs were 6.8, 4.8, and 5.6, respectively.

### Histology

Figure 7 shows myelin- and Nissl-stained sections of a rat 3 days after LPC injection in the dtg. We observed a

demyelinated area ipsilaterally to the injection (Figure 7C) while the myelin content on the contralateral side appeared normal (Figure 7B).

On Nissl-stained sections, we observed an increased cell density attributed to gliosis, which overlapped with the demyelinating area (Figure 7D). On the contralateral side to the injection site, the amount and distribution of cells were normal (Figure 7E). Similarly as in the cc lesion, gliosis was diffusely distributed, and a high

**TABLE 1 |** Pearson correlation of MRI parameters with optical density in myelin and Nissl stained sections including ipsilateral and contralateral ROIs and both LPC and vehicle injected animals.

		<b>RAFF4</b>	<b>MTR</b>	<b>T<sub>1sat</sub></b>	<b>FA</b>	<b>MD</b>	<b>AD</b>	<b>RD</b>
<b>MYELIN</b>								
cc	R	<b>-0.742</b>	<b>0.741</b>	<b>-0.741</b>	<b>0.662</b>	<b>0.708</b>	<b>0.714</b>	<b>0.257</b>
	95%, lower	-0.838	0.600	-0.837	0.490	0.553	0.562	0.003
	95%, upper	-0.601	0.837	-0.599	0.784	0.815	0.820	0.480
	upper-lower	0.237	0.237	0.238	0.294	0.262	0.257	0.476
	p	<0.001	<0.001	<0.001	<0.001	<0.001	<0.001	0.048
dtg	R	<b>-0.745</b>	<b>0.719</b>	<b>-0.705</b>	0.438	0.122	0.279	-0.079
	95%, lower	-0.893	0.405	-0.875	-	-	-	-
	95%, upper	-0.451	0.881	-0.382	-	-	-	-
	upper-lower	0.442	0.476	0.493	-	-	-	-
	p	0.001	0.001	0.001	0.053	0.610	0.233	0.739
Both	R	<b>-0.743</b>	<b>0.719</b>	<b>-0.700</b>	<b>0.473</b>	<b>0.591</b>	<b>0.648</b>	0.039
	95%, lower	-0.827	0.593	-0.797	0.282	0.426	0.499	-
	95%, upper	-0.625	0.811	-0.568	0.627	0.717	0.760	-
	upper-lower	0.203	0.218	0.229	0.350	0.291	0.260	-
	p	<0.001	<0.001	<0.001	<0.001	<0.001	<0.001	0.732
<b>NISSL</b>								
cc	R	0.217	-0.306	0.286	-0.245	-0.169	-0.208	0.036
	95%, lower	-	-	-	-	-	-	-
	95%, upper	-	-	-	-	-	-	-
	upper-lower	-	-	-	-	-	-	-
	p	0.149	0.107	0.107	0.149	0.225	0.149	0.782
dtg	R	<b>0.587</b>	<b>-0.562</b>	<b>0.580</b>	-0.412	-0.298	-0.396	-0.119
	95%, lower	0.195	-0.804	0.184	-	-	-	-
	95%, upper	0.817	-0.159	0.814	-	-	-	-
	upper-lower	0.6224	0.645	0.629	-	-	-	-
	p	0.026	0.026	0.026	0.112	0.230	0.112	0.616
Both	R	<b>0.343</b>	<b>-0.450</b>	<b>0.466</b>	<b>-0.415</b>	-0.066	<b>-0.292</b>	<b>0.295</b>
	95%, lower	0.134	-0.610	0.274	-0.582	-	-0.481	0.081
	95%, upper	0.524	-0.256	0.622	-0.215	-	-0.078	0.484
	upper-lower	0.390	0.354	0.348	0.367	-	0.404	0.403
	p	0.004	<0.001	<0.001	<0.001	0.564	0.009	0.008

Statistically significant R-values ( $p < 0.05$ , FDR adj. for testing 7 MRI parameters) are shown in bold.

Cc, corpus callosum; dtg, dorsal tegmental tract.

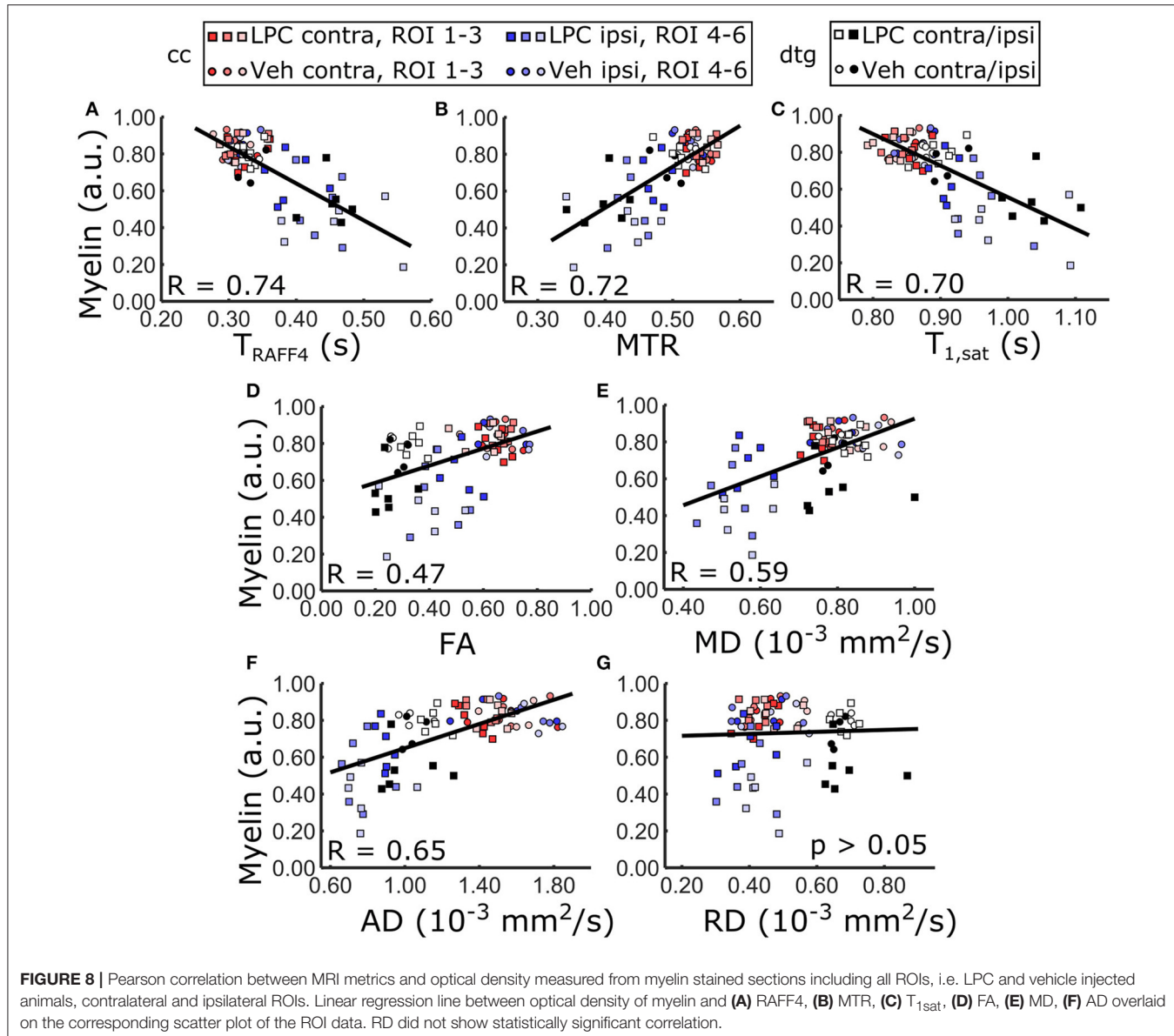
number of cells were found around blood vessels (**Figure 7F**).

## Correlation between MRI Parameters and Histology

RAFFn and MT parameters provided good correlation ( $R > 0.70$ ) with myelin staining optical density when data from both brain areas and all ROIs were pooled (**Table 1**, **Figure 8**), while the correlation with myelin density was clearly lower for FA ( $R = 0.47$ ) and for MD ( $R = 0.59$ ). When only ROIs in the cc were included in the correlation analysis, all MRI parameters, except RD, markedly correlated ( $R > 0.66$ ) with myelin density. However, the correlation

with diffusion parameters was lower than that of RAFFn or MT despite larger relative changes in diffusion parameters than RAFFn and MT (**Table 1**). Importantly, in the dtg, RAFF4 and MT parameters had excellent correlation with myelin staining ( $R > 0.70$ ), while there was no statistically significant correlation between diffusion parameters and myelin density.

There was a mild correlation between RAFF4 and Nissl staining intensity in the dtg ( $R < 0.59$ ), however no statistically significant correlation in the cc and a weak correlation overall ( $R < 0.35$ ). This indicates that cellularity is not the determining factor to contrast, but may have a small contribution for example in the case of profound gliosis (**Table 1**).



## Influence of pH in Protein Phantoms

Relaxation time maps were measured with different techniques from a BSA phantom with varying pH values. While  $T_2$  showed clear dependence on pH, due to altered proton exchange, as expected, RAFF4 was virtually unaffected by pH at values around a physiological pH of 7.4, in the range of 6.2–7.8 (Figure 9).

## DISCUSSION

In the present work, the value of the RAFF4 technique for detection of demyelination in the brain was investigated in a well-controlled LPC-injection rat model. Our major finding was that RAFF4 was able to robustly detect demyelination in both the cc and dtg, which have a different organization

of myelinated axons and had a different amount of gliosis after LPC injection. Furthermore, RAFF4 provided excellent correlation with myelin content in both cases, while DTI was unable to reliably assess demyelinated area in the dtg, likely due to its sensitivity to underlying cytoarchitecture and gliosis. Interestingly, MT parameters measured with a recently introduced modified inversion technique (Mangia et al., 2011) were able to detect demyelination in both the cc and dtg and showed good correlation with myelin content, though the overall ability of MT at detecting demyelination was slightly lower than that of RAFF4.

Excellent correlation of RAFF4 to myelin content can be attributed to sensitivity of RAFF:n to correlation time regime in the ms-range (Satzer et al., 2015; Hakkarainen et al., 2016), which likely corresponds to exchange and dipolar interaction

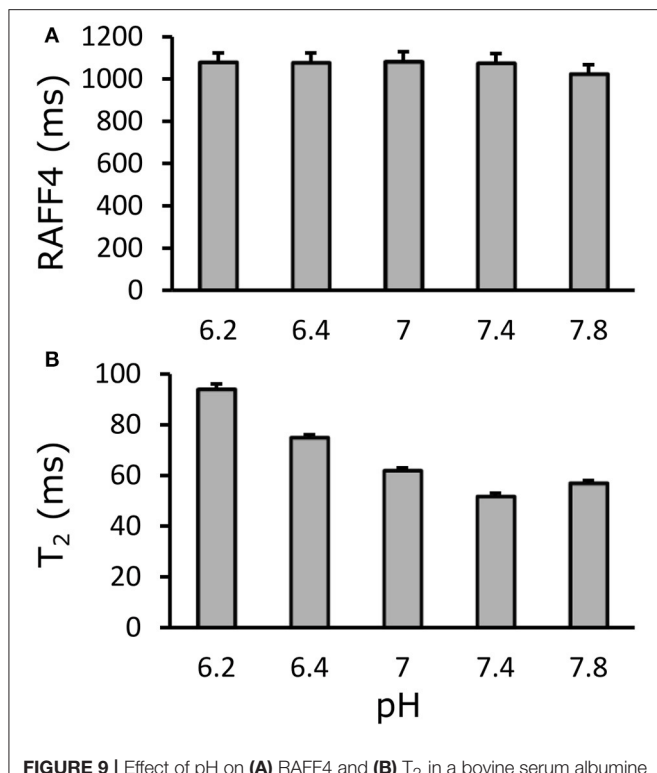


**FIGURE 9 |** Effect of pH on (A) RAFF4 and (B) T<sub>2</sub> in a bovine serum albumine phantom. RAFF4 is essentially unaffected by changing pH. Error bars indicate the standard deviation across voxels inside the ROI drawn in the phantom.

of myelin water and dipolar interaction with carbon-bound methylene protons. In our previous study, there was no significant difference between RAFF4 and RAFF5 in their ability to detect myelin in normal brain (Hakkarainen et al., 2016) indicating that contribution of myelin to spectral density function is relatively flat in this correlation time range. As RAFF4 has shorter relaxation time constant than RAFF5, and therefore requires shorter magnetization preparation pulse train, RAFF4 was chosen over RAFF5 for sensitizing MRI for myelin. In our previous studies, RAFF1-3 showed sensitivity to shorter correlation time regime than RAFF4-5, with reduced gray/white matter contrast and reduced sensitivity to myelin (Liimatainen et al., 2010; Satzer et al., 2015). The different sensitivities of RAFFn techniques indicate how these techniques can be tuned to detect different motional regimes corresponding to different cellular components and pathological processes.

A conventional DTI approach was used as a comparative method, as it is one of the most commonly used advanced MRI approaches in clinical settings for assessment of white matter abnormalities. In the cc, DTI was able to detect LPC lesion even better than RAFF4 based on contrast between LPC and vehicle injected animals. However, large variability of the DTI metrics led to worse contrast-to-noise ratio between the two groups in comparison to RAFF4. In addition, the pattern of diffusion changes was unexpected: decreased MD, which was associated with decreased AD, while RD was unchanged. Demyelination is classically associated with

increased RD (Song et al., 2005), as water molecules can pass axonal membranes more freely in the absence of myelin. In our study, demyelination, 3 days after LPC injection, was confirmed by quantitative analysis of myelin stained histological sections. Our results indicate substantial but not complete demyelination at this subacute time point. A previous electron microscopy study in LPC injected rats showed significant thinning of the myelin sheaths around axons, but not complete dissolution of myelin especially in the early time points (Foster et al., 1980). Our TEM data showed similar changes 3 days after LPC injection. In spite of clear demyelination, some disorganized myelin sheaths were still observed, which preserved RD close to normal. Furthermore, disorganized myelin sheaths with pockets, myelin debris, and vacuoles increased the number of diffusion restricting boundaries in the intra axonal space explaining the decreased AD, FA, and MD. These findings emphasize the complexity of using simple diffusion metrics as markers for a specific pathological feature such as demyelination. On the other hand, DTI, and especially more advanced high angular resolution diffusion-weighted imaging-type diffusion imaging approaches, clearly have potential to provide information that goes far beyond the myelin content and warrants further studies. The optimal MRI protocol to assess white matter pathology should contain both a technique with high sensitivity and specificity to myelin and capability to characterize microstructural changes.

Importantly, RAFF4 and RAFF5 have been shown to correlate with myelin density to a greater extent than MT in normal brain (Hakkarainen et al., 2016). Our results here show that using advanced MTR mapping (Mangia et al., 2011), MTR can also provide excellent correlation with myelin in LPC induced demyelination although lower than that of RAFF4. In addition to anisochronous and isochronous rotating frame relaxation pathways contributing to RAFF4 and 5, RAFF4 and 5 may share with MT cross-relaxation pathways. Therefore, these two techniques could provide complementary information for characterizing tissue integrity which could be utilized by proper modeling (Underhill et al., 2011).

A benefit of the LPC model is that it causes demyelination without significant edema formation and only mild to moderate gliosis. Therefore the LPC model allows assessment of demyelination without multiple simultaneous contributing factors. In practically all human pathological conditions, demyelination is co-localized with a number of other pathological processes including inflammation, edema and acidification. There was more gliosis in the dtg than in cc after LPC injections, which likely explains why there was statistically significant correlation with Nissl staining in dtg but not in cc. However, in both cases correlation with myelin content remained good, and in general RAFF4 correlation with myelin density was higher than with other MRI methods studied. Importantly, the correlation of RAFF4 with Nissl stain proves that mechanisms other than myelin must contribute to the RAFF4 contrast. Therefore, RAFF4 is not entirely specific to myelin, as expected for any relaxation parameters that unavoidably depends on multiple biological processes. Yet, the insensitivity of RAFF4

to at least some processes such as pH changes, along with the distinct feature of RAFF4 to detect slow and ultra-slow motional regimes typical in myelin, overall suggest also a better specificity of RAFF4 to myelin as compared to other methods.

A unique feature of RAFF4 is that sensitivity to slow molecular motion can be achieved within the SAR limits of human studies, making the RAFF4 technique readily applicable to clinical settings. Indeed, excellent gray/white matter contrast with high rank RAFF4 has already been demonstrated in human brain with reasonable acquisition times ( $\sim 10$  min) (Liimatainen et al., 2015). While sensitivity to ms-time range can be also achieved with conventional spin-lock techniques, such as continues-wave  $T_{1\rho}$  with spin-lock field in kHz range (Sepponen et al., 1985; Gröhn et al., 2000), human studies are compromised because of high SAR of on-resonance spin-lock pulses.

## CONCLUSION

The excellent ability of RAFF4 to detect myelin content in healthy and pathological tissues and its insensitivity to fiber orientation distribution, gliosis and pH together with low SAR, promises RAFFn to become a useful technique for visualizing demyelinating lesions. Future work will aim to investigate later time points after LPC-induced demyelination in order to follow the remyelination of the LPC injected animals and to test specificity of RAFF4 for myelin in other disease models with more complex pathology which for instance include edema.

## REFERENCES

- Beer, A., Biberacher, V., Schmidt, P., Righart, R., Buck, D., Berthele, A., et al. (2016). Tissue damage within normal appearing white matter in early multiple sclerosis: assessment by the ratio of T1- and T2-weighted MR image intensity. *J. Neurol.* 263, 1495–1502. doi: 10.1007/s00415-016-8156-6
- Bonilla, I., and Snyder, R. E. (2007). Transverse relaxation in rat optic nerve. *NMR Biomed.* 20, 113–120. doi: 10.1002/nbm.1090
- Does, M. D., Beaulieu, C., Allen, P. S., and Snyder, R. E. (1998). Multi-component T1 relaxation and magnetisation transfer in peripheral nerve. *Magn. Reson. Imaging* 16, 1033–1041. doi: 10.1016/S0730-725X(98)00139-8
- Dula, A. N., Gochberg, D. F., Valentine, H. L., Valentine, W. M., and Does, M. D. (2010). Multiexponential T2, magnetization transfer, and quantitative histology in white matter tracts of rat spinal cord. *Magn. Reson. Med.* 63, 902–909. doi: 10.1002/mrm.22267
- Foster, R. E., Kocsis, J. D., Malenka, R. C., and Waxman, S. G. (1980). Lysophosphatidyl choline-induced focal demyelination in the rabbit corpus callosum. Electron-microscopic observations. *J. Neurol. Sci.* 48, 221–231. doi: 10.1016/0022-510x(80)90202-6
- Glasser, M. F., and Van Essen, D. C. (2011). Mapping human cortical areas *in vivo* based on myelin content as revealed by T1- and T2-weighted MRI. *J. Neurosci.* 31, 11597–11616. doi: 10.1523/JNEUROSCI.2180-11.2011
- Gröhn, O. H. J., Kettunen, M. I., Mäkelä, H. I., Penttonen, M., Pitkänen, A., Lukkarinen, J. A., et al. (2000). Early detection of irreversible cerebral ischemia in the rat using dispersion of the magnetic resonance imaging relaxation time,  $T_{1\rho}$ . *J. Cerebr. Blood F. Met.* 20, 1457–1466. doi: 10.1097/00004647-200010000-00007
- Hakkarainen, H., Sierra, A., Mangia, S., Garwood, M., Michaeli, S., Gröhn, O., et al. (2016). MRI relaxation in the presence of fictitious fields correlates with myelin content in normal rat brain. *Magn. Reson. Med.* 75, 161–168. doi: 10.1002/mrm.25590
- Le Bihan, D., and Johansen-Berg, H. (2012). Diffusion MRI at 25: exploring brain tissue structure and function. *Neuroimage* 61, 324–341. doi: 10.1016/j.neuroimage.2011.11.006
- Liimatainen, T., Hakkarainen, H., Mangia, S., Huttunen, J. M., Storino, C., Idiyattullin, D., et al. (2015). MRI contrasts in high rank rotating frames. *Magn. Reson. Med.* 73, 254–262. doi: 10.1002/mrm.25129
- Liimatainen, T., Mangia, S., Ling, W., Ellermann, J., Sorce, D. J., Garwood, M., et al. (2011). Relaxation dispersion in MRI induced by fictitious magnetic fields. *J. Magn. Reson.* 209, 269–276. doi: 10.1016/j.jmr.2011.01.022
- Liimatainen, T., Sorce, D. J., O'Connell, R., Garwood, M., and Michaeli, S. (2010). MRI contrast from relaxation along a fictitious field (RAFF). *Magn. Reson. Med.* 64, 983–994. doi: 10.1002/mrm.22372
- Mäkelä, H. I., Gröhn, O. H., Kettunen, M. I., and Kauppinen, R. A. (2001). Proton exchange as a relaxation mechanism for T1 in the rotating frame in native and immobilized protein solutions. *Biochem. Biophys. Res. Commun.* 289, 813–818. doi: 10.1006/bbrc.2001.6058
- Mangia, S., De Martino, F., Liimatainen, T., Garwood, M., and Michaeli, S. (2011). Magnetization transfer using inversion recovery during off-resonance irradiation. *Magn. Reson. Imaging* 29, 1346–1350. doi: 10.1016/j.mri.2011.04.002
- McCreary, C. R., Bjarnason, T. A., Skihar, V., Mitchell, J. R., Yong, V. W., and Dunn, J. F. (2009). Multiexponential T2 and magnetization transfer MRI of demyelination and remyelination in murine spinal cord. *Neuroimage* 45, 1173–1182. doi: 10.1016/j.neuroimage.2008.12.071
- Mefed, A. (1999). Spectrometer for studying NMR and relaxation in the doubly rotating frame. *Appl. Magn. Reson.* 16, 411–426. doi: 10.1007/BF0316928
- Mefed, A. (2001). Nuclear spin-lattice relaxation in the triply rotating frame and ultraslow molecular motions in solids. *Appl. Magn. Reson.* 21, 127–145. doi: 10.1007/BF03162447

## AUTHOR CONTRIBUTIONS

LL, AA, and AS participated in design of the work, acquisition, analysis, interpretation of data and preparing the manuscript. LT participated in design of the work, acquisition and preparing the manuscript. LE participated in design of the work, analysis and preparing the manuscript. SMa participated in design of the work, interpretation of the data and preparing the manuscript. AN participated in design of the work and preparing the manuscript. SMi and OG participated in design of the work, analysis, interpretation of data and preparing the manuscript.

## FUNDING

The work was supported by EU H2020 Marie Skłodowska RISE project #691110 (MICROBRADAM), Academy of Finland grants #275453 and #298007, EU FP7-HEALTH project #602102 (EPITARGET), NIH BTRC grants, P41 EB015894, P30 NS057091. OG was supported by Professor Pool grant from Svenska Kulturfonden, SMi was supported by Fulbright-Saastamoinen Foundation Grant in Health and Environmental Science. LL was supported by MnDRIVE and the Emil Aaltonen Foundation.

## ACKNOWLEDGMENTS

Electron microscopy was performed utilizing Sib-labs infrastructure at the University of Eastern Finland.

- Michaeli, S., Sorce, D. J., and Garwood, M. (2008). T<sub>2ρ</sub> and T<sub>1ρ</sub> adiabatic relaxations and contrasts. *Curr. Anal. Chem.* 4, 8–25. doi: 10.2174/157341108783339115
- Michaeli, S., Sorce, D. J., Springer, C. S. Jr., Ugurbil, K., and Garwood, M. (2006). T1rho MRI contrast in the human brain: modulation of the longitudinal rotating frame relaxation shutter-speed during an adiabatic RF pulse. *J. Magn. Reson.* 181, 135–147. doi: 10.1016/j.jmr.2006.04.002
- Nossin-Manor, R., Card, D., Morris, D., Noormohamed, S., Shroff, M. M., Whyte, H. E., et al. (2013). Quantitative MRI in the very preterm brain: assessing tissue organization and myelination using magnetization transfer, diffusion tensor and T(1) imaging. *Neuroimage* 64, 505–516. doi: 10.1016/j.neuroimage.2012.08.086
- Pirkle, I., and Johnson, A. J. (2008). Neuroimaging of demyelination and remyelination models. *Curr. Top. Microbiol. Immunol.* 318, 241–266. doi: 10.1007/978-3-540-73677-6\_10
- Ransohoff, R. M. (2012). Animal models of multiple sclerosis: the good, the bad and the bottom line. *Nat. Neurosci.* 15, 1074–1077. doi: 10.1038/nn.3168
- Satzer, D., DiBartolomeo, C., Ritchie, M. M., Storino, C., Liimatainen, T., Hakkarainen, H., et al. (2015). Assessment of dysmyelination with RAFFn MRI: application to murine MPS I. *PLoS ONE* 10:e0116788. doi: 10.1371/journal.pone.0116788
- Schmierer, K., Scaravilli, F., Altmann, D. R., Barker, G. J., and Miller, D. H. (2004). Magnetization transfer ratio and myelin in postmortem multiple sclerosis brain. *Ann. Neurol.* 56, 407–415. doi: 10.1002/ana.20202
- Schmithorst, V. J., Wilke, M., Dardzinski, B. J., and Holland, S. K. (2002). Correlation of white matter diffusivity and anisotropy with age during childhood and adolescence: a cross-sectional diffusion-tensor MR imaging study. *Radiology* 222, 212–218. doi: 10.1148/radiol.2221010626
- Sepponen, R. E., Pohjonen, J. A., Sipponen, J. T., and Tanttu, J. I. (1985). A method for T<sub>1ρ</sub> imaging. *J. Comput. Assist. Tomogr.* 9, 1007–1011. doi: 10.1097/00004728-198511000-00002
- Solomon, I. (1959). Rotary spin echoes. *Phys. Rev. Lett.* 2:301. doi: 10.1103/PhysRevLett.2.301
- Song, S. K., Yoshino, J., Le, T. Q., Lin, S. J., Sun, S. W., Cross, A. H., et al. (2005). Demyelination increases radial diffusivity in corpus callosum of mouse brain. *Neuroimage* 26, 132–140. doi: 10.1016/j.neuroimage.2005.01.028
- Underhill, H. R., Rostomily, R. C., Mikheev, A. M., Yuan, C., and Yarnykh, V. L. (2011). Fast bound pool fraction imaging of the *in vivo* rat brain: association with myelin content and validation in the C6 glioma model. *Neuroimage* 54, 2052–2065. doi: 10.1016/j.neuroimage.2010.10.065
- Waxman, S. G., Kocsis, J. D., and Nitta, K. C. (1979). Lysophosphatidyl choline-induced focal demyelination in the rabbit corpus callosum. Light-microscopic observations. *J. Neurol. Sci.* 44, 45–53. doi: 10.1016/0022-510x(79)90221-1
- Wilhelm, M. J., Ong, H. H., Wehrli, S. L., Li, C., Tsai, P. H., Hackney, D. B., et al. (2012). Direct magnetic resonance detection of myelin and prospects for quantitative imaging of myelin density. *Proc. Natl. Acad. Sci. U.S.A.* 109, 9605–9610. doi: 10.1073/pnas.1115107109

**Conflict of Interest Statement:** The authors declare that the research was conducted in the absence of any commercial or financial relationships that could be construed as a potential conflict of interest.

Copyright © 2017 Lehto, Albors, Sierra, Tolppanen, Eberly, Mangia, Nurmi, Michaeli and Gröhn. This is an open-access article distributed under the terms of the Creative Commons Attribution License (CC BY). The use, distribution or reproduction in other forums is permitted, provided the original author(s) or licensor are credited and that the original publication in this journal is cited, in accordance with accepted academic practice. No use, distribution or reproduction is permitted which does not comply with these terms.



# Determining Excitatory and Inhibitory Neuronal Activity from Multimodal fMRI Data Using a Generative Hemodynamic Model

Martin Havlicek\*, Dimo Ivanov, Alard Roebroeck and Kamil Uludağ

Department of Cognitive Neuroscience, Faculty of Psychology and Neuroscience, Maastricht University, Maastricht, Netherlands

## OPEN ACCESS

### Edited by:

Itamar Ronen,  
Leiden University, Netherlands

### Reviewed by:

Nelson Jesús Trujillo-Barreto,  
University of Manchester,  
United Kingdom  
Fahmeed Hyder,  
Yale University, United States

### \*Correspondence:

Martin Havlicek  
[m.havlicek@maastrichtuniversity.nl](mailto:m.havlicek@maastrichtuniversity.nl)

### Specialty section:

This article was submitted to  
Brain Imaging Methods,  
a section of the journal  
*Frontiers in Neuroscience*

Received: 16 May 2017

Accepted: 23 October 2017

Published: 10 November 2017

### Citation:

Havlicek M, Ivanov D, Roebroeck A and Uludağ K (2017) Determining Excitatory and Inhibitory Neuronal Activity from Multimodal fMRI Data Using a Generative Hemodynamic Model. *Front. Neurosci.* 11:616.  
doi: 10.3389/fnins.2017.00616

Hemodynamic responses, in general, and the blood oxygenation level-dependent (BOLD) fMRI signal, in particular, provide an indirect measure of neuronal activity. There is strong evidence that the BOLD response correlates well with post-synaptic changes, induced by changes in the excitatory and inhibitory (E-I) balance between active neuronal populations. Typical BOLD responses exhibit transients, such as the early-overshoot and post-stimulus undershoot, that can be linked to transients in neuronal activity, but they can also result from vascular uncoupling between cerebral blood flow (CBF) and venous cerebral blood volume (venous CBV). Recently, we have proposed a novel generative hemodynamic model of the BOLD signal within the dynamic causal modeling framework, inspired by physiological observations, called P-DCM (Havlicek et al., 2015). We demonstrated the generative model's ability to more accurately model commonly observed neuronal and vascular transients in single regions but also effective connectivity between multiple brain areas (Havlicek et al., 2017b). In this paper, we additionally demonstrate the versatility of the generative model to jointly explain dynamic relationships between neuronal and hemodynamic physiological variables underlying the BOLD signal using multi-modal data. For this purpose, we utilized three distinct data-sets of experimentally induced responses in the primary visual areas measured in human, cat, and monkey brain, respectively: (1) CBF and BOLD responses; (2) CBF, total CBV, and BOLD responses (Jin and Kim, 2008); and (3) positive and negative neuronal and BOLD responses (Shmuel et al., 2006). By fitting the generative model to the three multi-modal experimental data-sets, we showed that the presence or absence of dynamic features in the BOLD signal is not an unambiguous indication of presence or absence of those features on the neuronal level. Nevertheless, the generative model that takes into account the dynamics of the physiological mechanisms underlying the BOLD response allowed dissociating neuronal from vascular transients and deducing excitatory and inhibitory neuronal activity time-courses from BOLD data alone and from multi-modal data.

**Keywords:** excitatory-inhibitory, multi-modal data, fMRI signal modeling, response transients, neuronal adaptation, post-stimulus BOLD undershoot, hemodynamic uncoupling, DCM

## INTRODUCTION

Functional magnetic resonance imaging (fMRI) is a widely used non-invasive technique to assess brain function. The fMRI signal reflects neuronal activity only indirectly through the measurements of accompanying hemodynamic processes at temporal resolution typically on the order of seconds and spatial resolution typically on the order of tens of cubic millimeters. In general, neuronal activation causes a series of physiological events, including localized changes in cerebral blood flow (CBF), cerebral metabolic rate of oxygen ( $\text{CMRO}_2$ ), cerebral blood volume (CBV), and deoxyhemoglobin content. These physiological variables form the basis of the blood oxygenation level-dependent (BOLD) signal (Ogawa et al., 1990), the most commonly used fMRI approach. However, CBF and CBV can also be directly measured with various fMRI techniques (e.g., see Wong et al., 1997; Lu et al., 2003; Liu and Brown, 2007; Huber et al., 2014b).

In many studies, it has been found that there is high correspondence between response properties measured in fMRI and other hemodynamic techniques and those measured from invasive electrical recordings, mostly acquired in non-human primates, cats and rodents (Logothetis et al., 2001, 2010; Kim et al., 2004; Niessing et al., 2005; Devor et al., 2007, 2013; Logothetis, 2008; Muckli, 2010; Boynton, 2011; Hillman, 2014). In particular, CBF and BOLD responses show better correlation with post-synaptic local field potentials (LFPs) than with spiking activity (multi-unit activity, MUA), suggesting that the hemodynamic response reflects stronger the input to a neuronal population in a brain area and intrinsic processing (Lauritzen, 2005) rather than the output of that area (Goense and Logothetis, 2008; Logothetis et al., 2010; Magri et al., 2012). Positive CBF and BOLD responses during stimulation are associated with an increase in neuronal activity and decrease in deoxyhemoglobin content, whereas negative CBF and BOLD responses are associated with a decrease in neuronal activity below baseline and increase in deoxyhemoglobin content (e.g., Shmuel et al., 2006 and references therein).

Typical positive BOLD responses to sustained stimulation display transients, such as response adaptation (also referred to as early-overshoot) and post-stimulus undershoot (Frahm et al., 1996; Krüger et al., 1996; Hoge et al., 1999). Similarly, neuronal responses to stimulation exhibit rapid rise followed by a decay (or adaptation) to a steady-state level and are often followed by a brief decrease below baseline after stimulus cessation (e.g., Logothetis et al., 2001). These neuronal transients (Boynton et al., 1996; Hoge et al., 1999; Bandettini and Ungerleider, 2001; Birn et al., 2001) are the result of changes in excitatory and inhibitory (E-I) balance between active neuronal populations, controlled by local micro-circuitry but also by long-range connections with other brain areas (Logothetis, 2002; Logothetis and Wandell, 2004; Shmuel et al., 2006; Hyder et al., 2010; Havlicek et al., 2017b). CBF reflects these neuronal transients in a temporally smoothed fashion (Hoge et al., 1999; Attwell and Iadecola, 2002; Uludağ et al., 2004; Sadaghiani et al., 2009; Attwell et al., 2010; Cauli and Hamel, 2010; Mayhew et al., 2014). Because of the complex underlying physiological processes, the BOLD response

can exhibit transients not only from neuronal sources, but also due to the properties of blood vessels: the BOLD response is dominated by signal contributions originating from the venous compartments, and venous CBV can be dynamically uncoupled from CBF (i.e., venous CBV lags behind CBF), influencing the amplitude of the early-overshoot and post-stimulus undershoot of the BOLD-response (Buxton et al., 1998b; Mandeville et al., 1999; Yacoub et al., 2006; Chen and Pike, 2009). Alternatively, dynamic uncoupling between CBF and  $\text{CMRO}_2$  (i.e.,  $\text{CMRO}_2$  lags behind CBF) could result in the same BOLD transients as well (Lu et al., 2004; Frahm et al., 2008; Donahue et al., 2009; Hua et al., 2011; Poser et al., 2011; van Zijl et al., 2012). However, we have recently argued, supported by modeling of experimental data, that the contribution of CBF- $\text{CMRO}_2$  uncoupling to BOLD signal transients is much lower than that of CBF-venous CBV uncoupling (Havlicek et al., 2017a). Thus, neuronal and hemodynamic responses in different areas (or voxels) and subjects exhibit dynamic features, which can be both due to changes in E-I balance or due to biomechanical properties of the vasculature.

In standard analysis of fMRI data, linear convolution is applied between a stick or box-car functions (representing the stimulation paradigm) and assumed canonical hemodynamic response function (representing the combined transform from stimulus time-course to neuronal signal and the measured BOLD response) (Friston et al., 1995). However, as indicated above, excitatory and inhibitory neuronal responses may be nonlinearly related to stimulation (e.g., see Boynton et al., 1996; Bandettini and Ungerleider, 2001; Birn et al., 2001; Grill-Spector and Malach, 2001; Kida and Yamamoto, 2008; Mullinger et al., 2013, 2014; Pérez-González and Malmierca, 2014; Havlicek et al., 2017a; Keller et al., 2017). Furthermore, vascular transients resulting from dynamic uncoupling induce additional nonlinearities between the input function and subsequent hemodynamic variables. Therefore, the linearity assumption in BOLD data analysis may not be sufficient in many experiments and, consequently, the inferred information about the neuronal activity changes obtained from hemodynamic signals using linear (de)convolution analysis might be confounded with vascular effects. In other words, to more accurately estimate neuronal responses from the BOLD signal, a nonlinear model that accounts for dynamic relationships between neuronal and hemodynamic physiological variables underlying the BOLD response is needed.

Recently, we have introduced a physiologically-informed generative model of the BOLD signal within the framework of dynamic causal modeling (Friston et al., 2003) (called P-DCM)<sup>1</sup>, linking excitatory and inhibitory neuronal activity to the BOLD response (Havlicek et al., 2015). In P-DCM, we employ: (i) an adaptive excitation-inhibition neuronal model that accounts for a wide range of neuronal time-course both during stimulation and post-stimulation periods; (ii) a neurovascular coupling (NVC) model that links neuronal activity to blood flow in a strictly

<sup>1</sup>As we have developed our novel generative model within the framework of the dynamic causal model (DCM) and applied it both to single ROI and to a network of ROIs, in this paper to avoid confusion, we use DCM and the generative model embedded within P-DCM interchangeably.

feedforward fashion; (iii) a balloon model (Buxton et al., 1998b) that can account for a vascular uncoupling between CBF and venous CBV; and (iv) field strength and sequence dependent parameterization of the BOLD signal equation. We compared P-DCM with other DCM models (Friston et al., 2003; Marreiros et al., 2008) and demonstrated significant improvements in the ability to model commonly observed neuronal and vascular response transients in single regions (Havlicek et al., 2015) and also within a network of several regions with task-driven activity changes (Havlicek et al., 2017b). In the latter case, we also showed a high fidelity of P-DCM to jointly explain CBF and BOLD responses simultaneously measured with the arterial spin labeling (ASL) fMRI technique, demonstrating the benefit of additional information provided by a CBF measurement for model inversion.

In general, multi-modal imaging is a powerful approach to study the relationship between neural activity and the BOLD fMRI signal. Measurements of different physiological variables can increase the ability to disambiguate neuronal and vascular effects present in the BOLD signal and potentially unravel limitations of the hemodynamic models. In the current work, we aim to explore the versatility of P-DCM to explain dynamic relationships between various combinations of measured physiological variables and to deduce the excitatory and inhibitory neuronal dynamics from hemodynamic data. This is done under the constraints of assumed physiological mechanisms and experimental manipulations. In particular, we use: (1) newly acquired CBF and BOLD responses to static and flickering stimuli in human subjects; (2) CBF, total CBV and BOLD response to square-wave grating stimulus acquired

in the cat brain from the study of Jin and Kim (2008); and (3) positive and negative neuronal and BOLD responses induced by rotating visual stimuli measured in the monkey brain from the study of Shmuel et al. (2006). In our modeling, we emphasize stimulus-type-dependent modulation of response transients that can be linked to a dynamic interplay between excitatory and inhibitory activity. In addition, we allow for differences between stimulation and post-stimulation response periods and account for vascular-, magnetic field strength-, and MRI sequence-dependent properties. The current approach can also be generalized to other invasive and non-invasive multimodal data, such as EEG-fMRI, provided generative models exist for both modalities.

## METHODS

### General Description of P-DCM

The generative model in P-DCM consists of four causally-linked components that define how the neuronal signal is transformed to the measured BOLD response (see **Figure 1** for an illustration and the summary of model equations). For a more detailed description of the model and its comparison with previous DCM models, please see (Havlicek et al., 2015, 2017b).

### Neuronal Model of E-I Balance

In this model, an exogenous input  $u(t)$  (e.g., sensory stimulus) drives the change in excitatory activity,  $n_E(t)$ , which is directly coupled with a change in inhibitory activity,  $n_I(t)$ . The strength of this input, expressed with the parameter  $c$ , scales the amplitude of the neuronal response. The shape of the neuronal response

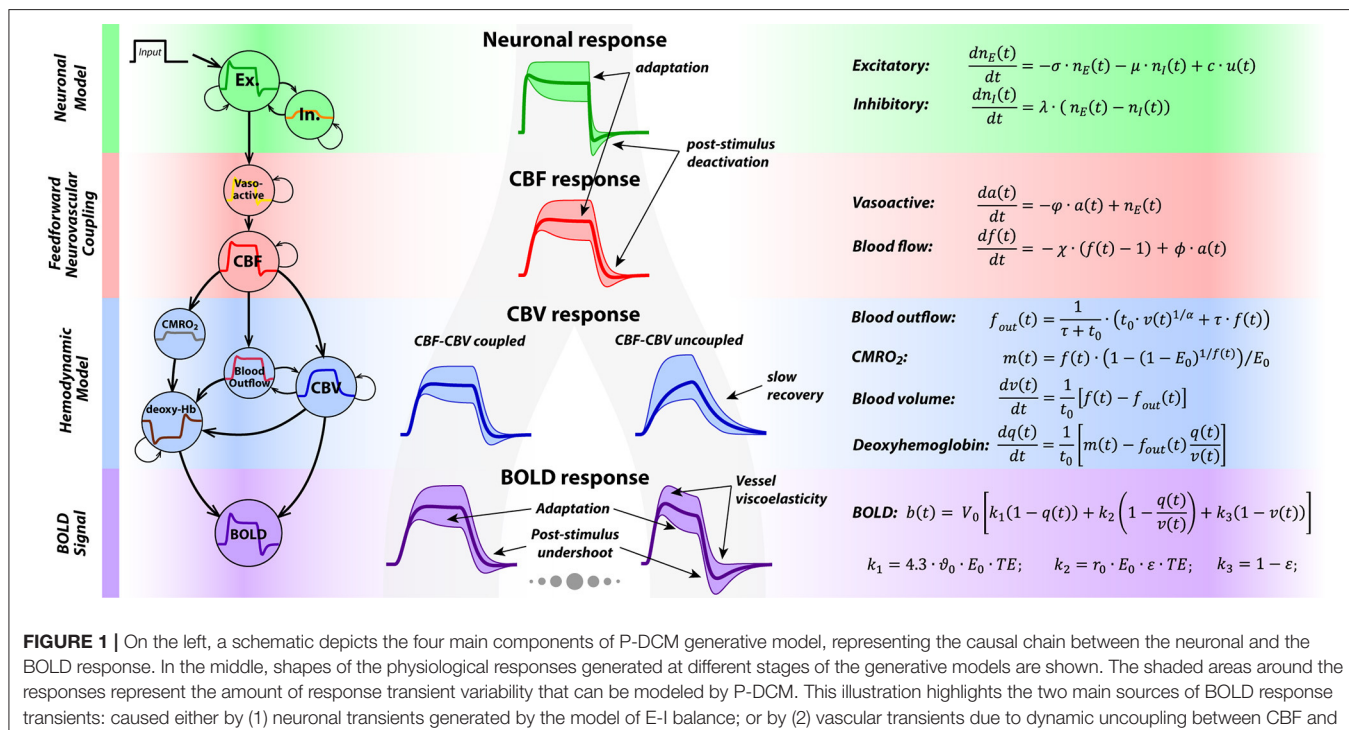


**FIGURE 1 |** On the left, a schematic depicts the four main components of P-DCM generative model, representing the causal chain between the neuronal and the BOLD response. In the middle, shapes of the physiological responses generated at different stages of the generative models are shown. The shaded areas around the responses represent the amount of response transient variability that can be modeled by P-DCM. This illustration highlights the two main sources of BOLD response transients: caused either by (1) neuronal transients generated by the model of E-I balance; or by (2) vascular transients due to dynamic uncoupling between CBF and venous CBV; or mixture of these two. On the right, a summary of all equations underlying P-DCM is provided.

is tuned by the transient imbalance between excitatory and inhibitory activity. In particular, the typical overshoot at the onset can be produced by gradually increasing inhibitory activity that modulates the excitatory activity via negative feedback. Next, persistence of the inhibitory activity following stimulus cessation can produce post-stimulus deactivation. This temporal evolution of excitatory and inhibitory activity, including their dynamic mismatch, is controlled by the parameters  $\sigma$  and  $\lambda$ , respectively, and the strength of the inhibitory activity modulating the excitatory activity is encoded by the parameter  $\mu$ . Optimization of these neuronal parameters allows modeling a broad repertoire of neuronal response adaptation profiles and of possible post-stimulus deactivations separately for the stimulation period (SP) and the post-stimulation period (PSP)<sup>2</sup>.

### Neurovascular Coupling (NVC):

The output of the neuronal model, i.e., the excitatory activity modulated by inhibitory activity, is transformed to CBF,  $f(t)$ , in a strictly feedforward fashion, via vasoactive signal  $a(t)$ . Neuronal excitation/inhibition leads to arterial vasodilatation/vasoconstriction associated with increased/decreased CBF (Devor et al., 2007). Thus, the modeled neuronal response transients are conveyed to a CBF response, albeit in a smooth version. Decay and delay of the CBF response with respect to the neuronal response is regulated with three constants,  $\varphi$ ,  $\phi$  and  $\chi$ , with only  $\chi$  being optimized during model inversion.

### Hemodynamic Model:

The hemodynamic model is represented by the balloon model (Buxton et al., 1998a,b). It models the mass balance of normalized changes in CBV,  $v(t)$ , and deoxyhemoglobin content,  $q(t)$ , as they pass through the venous compartment. Their changes are driven by changes in the inflowing CBF,  $f(t)$ , and CMRO<sub>2</sub>,  $m(t)$ , respectively. It is assumed that CBF and oxygen extraction fraction,  $E(t)$ , are dynamically coupled, thus  $m(t) = f(t) \cdot \frac{E(t)}{E_0}$ , where  $E_0$  is the value of oxygen extraction fraction at rest (please see discussion of this assumption in (Havlicek et al., 2015), and the Discussion section for more details). Furthermore, during steady-state, the blood leaving the venous compartment (i.e., the outflow,  $f_{out}(t)$ ) and the venous CBV are coupled via a power law relationship (Grubb et al., 1974), with exponent  $\alpha$ , whereas during the transient periods venous CBV and CBF can be uncoupled; i.e., venous CBV can evolve more slowly than CBF. This is due to the vessel's resistance to changes in venous CBV, described by the viscoelastic time constant,  $\tau$ . Theoretically, the viscoelastic time constant can have different values during SP and PSP,  $\tau_{SP}$  and  $\tau_{PSP}$ . The time dimension of changes in  $v(t)$  and  $q(t)$  is scaled by the mean transit time of the blood through the venous compartment at rest,  $t_0$ . Note that  $t_0$  is linked to the resting venous blood volume fraction  $V_0$  via the central volume principle,  $t_0 = \frac{V_0}{F_0}$ , where  $F_0$  is the blood flow at rest.

<sup>2</sup>Please note that we use PSP instead of PSU, as the sign of the post-stimulus BOLD response depends on whether it is preceded by negative or positive changes in neuronal activity during stimulation (as in Shmuel et al., 2006; whose data are investigated in the current study).

### BOLD Signal Equation:

The BOLD signal reflects changes in the deoxyhemoglobin content,  $q(t)$ , together with changes in the deoxyhemoglobin concentration,  $q(t)/v(t)$ , and venous CBV,  $v(t)$ . Their relative contribution is weighted by parameters that are magnetic field strength-, TE- and MRI sequence-dependent (Uludağ et al., 2009; Havlicek et al., 2015, 2017a).

In summary, as illustrated in **Figure 1**, P-DCM and its parameters allows the BOLD response to exhibit transients, such as response adaptation during stimulation and post-stimulus undershoot that can have both neuronal and vascular origins. As we show below, physiological origins of these transients can be tested under the constraints of concurrent multi-modal physiological data and experimental manipulations.

### Data Description

To demonstrate the utility and versatility of P-DCM, below we describe three different data-sets acquired from human, cat, and monkey brains. Each data-set consists of a different combination of physiological measurements: I. CBF and BOLD response; II. CBF, total volume CBV, and BOLD responses, published in Jin and Kim (2008); and III. neuronal and BOLD responses, published in Shmuel et al. (2006). Any additional physiological data, next to the BOLD data (and/or experimental manipulation), provide physiologically-informed constraints on the underlying mechanisms of the BOLD response. This can result in a more accurate inference on the changes in E-I balance forming the neuronal responses (Havlicek et al., 2017b) and potentially inform about the limitations of model structure and parameter assumptions.

### I. CBF and BOLD Responses

Four healthy volunteers (females, age range: 26–34) were scanned for the current study on a 3 T Siemens Prisma<sup>Fit</sup> MR scanner (Siemens Medical Solutions, Erlangen, Germany). For each subject, six functional runs and an anatomical scan were acquired. To obtain functional measurements of both CBF and BOLD signals, a multi-TE FAIR-Q2TIPS ASL sequence (Kim, 1995) was used with a gradient-echo echo-planar imaging (GE-EPI) readout and the following imaging parameters: TR = 2,200 ms; TI1/TI2 = 700/1,660 ms; TE1/TE2/TE3 = 8/21/33 ms; FOV = 192 × 192 mm<sup>2</sup>; nominal voxel size = 3 × 3 × 3 mm<sup>3</sup>, flip angle = 90°; matrix size = 64 × 64; 325 volumes (total scan duration 715 s); 10 oblique slices acquired in interleaved fashion, covering early visual areas. The anatomical MPRAGE scan was acquired with: 1 mm isotropic nominal voxel size; FOV = 224 × 224 mm<sup>2</sup>; matrix size = 224 × 224; TE = 2.1 ms; TR = 2,400 ms; TI = 1,040 ms.

The subjects were instructed to fixate on a small dot at the center of the screen throughout the experiments. Each of the EPI functional runs began with a 55 s resting period and continued with alternation of two static and two flickering checkerboard conditions (each 55 s long), interspersed with 110 s resting periods. Flickering checkerboards were presented at 4 Hz (eight reversals per second). The order of static and flickering conditions within a run was pseudo-randomized. For the static condition, a full-field, black-and-white radial

checkerboard was presented (Michelson contrast 1), whereas, for the flickering condition, reduced contrast (Michelson contrast 1/3) checkerboards were presented at 4 Hz (i.e., 8 reversal per second) (Sadaghiani et al., 2009). The resting periods consisted of a gray screen isoluminant with the mean luminance of the checkerboard. In order to maintain the subjects' attention, the color change of the fixation dot (altering between red and blue at three pseudo-random intervals within each stimulation block) was passively observed. For each subject, there were twelve trials per condition.

For each subject, the CBF time-series were derived from the ASL data acquired with TE = 8 ms using surround subtraction (Mumford et al., 2006). The BOLD time-series were obtained from the ASL data acquired with TE = 33 ms using surround averaging. The data were preprocessed using SPM12 (R6470) (<http://www.fil.ion.ucl.ac.uk/spm>). To correct for head motion, the realignment parameters with respect to the first volume were estimated using BOLD data and the same realignment parameters were applied to the corresponding volumes of CBF data. The mean BOLD image was coregistered to the anatomical image and the estimated spatial transformation matrix was applied to the functional BOLD and CBF data. CBF data were modeled voxel-wise using a general linear model (GLM). This model included main predictors representing the periods of static and flickering visual stimulation and additional predictors representing the stimulus onset and offset. All predictors (i.e., three per condition) were convolved with a gamma-variate hemodynamic response function ("spm\_Gpdf.m") with shape and scale parameters 4 and 0.5, respectively. The additional predictors were introduced to explain deviations of the hemodynamic response shape between conditions during stimulation and post-stimulation periods. The predictors were not orthogonalized in order to retain a direct interpretation of the model. Furthermore, data were high-pass filtered (cut-off = 1/256 s) to remove low frequency signal drifts and a first-order autoregressive model was used to remove serial correlations. Based on a conjunction analysis of the two main contrasts for static and flickering conditions, significant voxels within the gray matter of the left and right visual cortex ( $p < 0.05$ , corrected for family-wise errors) were selected from the CBF data. The same voxels were selected from the BOLD data. The statistically significant BOLD signal map (not reported) included the CBF ROI, but had a larger spatial spread. Voxel's time-courses from the CBF and BOLD data (~40 voxels per subject) were extracted, high-passed filtered (cut-off = 256 s), and the average responses in percent signal change were calculated for the two experimental conditions.

### CBF, Total CBV and BOLD Responses

Hemodynamic responses of CBF, total CBV, and BOLD signal were extracted from Figure 1 of the paper by Jin and Kim (2008) using Matlab (MathWorks, Inc.). These responses were measured using fMRI in the visual cortex of anesthetized cats at 9.4 T. In brief, they used 60 s visual stimulus of black and white square-wave gratings drifting with a temporal frequency of 2 cycles/s. This was always preceded by 20 s and followed by 60 s control condition represented by the same but stationary gratings. All data were acquired with GE-EPI readout. BOLD

and total CBV signals were acquired simultaneously with TR = 2 s and  $\sim 0.2 \times 0.2 \times 2 \text{ mm}^3$  voxel size and CBF signal was acquired during separate runs with TR = 3 s and  $\sim 0.3 \times 0.3 \times 2 \text{ mm}^3$  voxel size. However, the reported responses from Figure 1 were upsampled (using linear interpolation) to TR = 1 s. BOLD responses were derived from two TEs of 10 ms and 20 ms (by calculating the slope  $\Delta R_2^*$ , but displayed in average percent signal change). Furthermore, in Figure 1 by Jin and Kim, hemodynamic responses were reported for both the middle and top (superficial) part of the gray matter. We have taken CBF and total CBV responses from the middle gray matter and the BOLD response from the superficial area, where it exhibited the highest signal change. Note that CBF and total CBV are more localized to signal changes induced in the arterial blood compartment, while BOLD signal is mostly represented by the venous compartment, where the draining veins carry the signal from deeper gray matter structures toward the surface. Therefore, from the view of blood dynamics, the BOLD response measured at the surface mostly reflects the CBF and arterial CBV changes that occurred deeper in the gray matter. Finally, for all three hemodynamic responses, it is important to preserve the exact amounts of reported percent signal changes.

### III. Neuronal and BOLD Responses

Neuronal and BOLD responses were extracted from Figures 2A, 1D of the paper by Shmuel et al. (2006), respectively. These responses were measured simultaneously using invasive electrophysiological recording and fMRI in the visual cortex of anesthetized monkey brain at 4.7 T. In brief, 20 s visual stimuli consisting of high-contrast radial checkers rotating 60° per s were presented on gray background. The same background was used 5 s before and 25 s after the stimuli. Stimulation ring overlapping with the receptive field at V1 induced positive response in the vicinity of the electrode, while stimulus ring, which did not overlap with the receptive field, induced negative response in the same area. Neuronal responses were obtained by averaging the fractional change in power spectrum over the whole range of frequencies (4–3,000 Hz) with temporal resolution of 1 s. BOLD data were acquired with GE-EPI readout, TE = 20 ms, TR = 1 s and in-plane spatial resolution of  $0.75 \times 0.75 \times 2 \text{ mm}^3$ . Positive and negative BOLD responses induced by two stimuli were sampled and averaged over the same voxels within the ROI around the electrode.

### Model Specification

The multi-modal data from each study is used to identify the neuronal and vascular parameters of the generative model. Below, we specify the model assumptions for each study and form the observation equation to enable joint fitting to multiple physiological variables. In general, we aim to constrain the model estimation by at least two physiological measurements, experimental manipulations and properties of the venous blood compartment, the latter being independent of experimental manipulations, as it is given by the biomechanical properties of blood vessels. The assumptions about time-period-(i.e., stimulation or post-stimulation period) and experimental condition-specificity of certain model parameters were motivated

by three criteria: (1) we favor the minimum number of parameters that can sufficiently explain the dynamic behavior of the multi-modal experimental data; (2) we have prior knowledge from previous results that some parameters have to be time-period- and/or experimental condition-specific, e.g., vascular parameters are condition independent for the same voxels; (3) the first and second criteria should be consistent for all three experiments described above, i.e., the same assumptions about neuronal and vascular parameters have to hold for all three experiments. Furthermore, if available, the model is also constrained by the measured percent signal changes of CBF and BOLD responses.

### Experiment I: CBF and BOLD Responses:

To jointly model CBF and BOLD responses using P-DCM during both static and flickering conditions, we made the following specifications for the generative model in order to determine the transfer of condition-dependent neuronal changes to changes in the measured signals. Two independent inputs,  $u_S$  and  $u_F$ , in the form of box-car functions representing 55 s long static and flickering visual stimulation (whose strengths were controlled by two parameters  $c$ ), were used to drive the neuronal activity. To accommodate the assumption that each type of visual stimulus can result in a different adaptation profile during the stimulation period (SP) but also exhibit differences in neuronal adaptation during the post-stimulus period (PSP), parameters of the neuronal model,  $\sigma$  and  $\mu$ , were allowed to vary between the two phases but also between conditions. On the other hand,  $\lambda$  was allowed to vary only between the two conditions. This is because after the static stimulus the CBF response exhibits a slower return to the baseline without a post-stimulus undershoot, which is effectively modeled by setting the

parameter  $\mu$  close to zero. Thus, during this PSP, parameter  $\lambda$  does not have an effect on the shape of the neuronal response and becomes unidentifiable. Further, the NVC parameter  $\chi$ , was assumed to be the same for both conditions and SP and PSP. Within the hemodynamic model, the viscoelastic time constant,  $\tau$ , controlling the expansion and deflation of the venous compartment was allowed to vary between SP and PSP but not during the two conditions. The mean transit time at rest,  $t_0$ , was estimated together with the resting blood volume fraction,  $V_0$ , by assuming a blood flow value at rest,  $F_0 = 0.01 \text{ s}^{-1}$  (i.e., 60 ml/100 g/min, a typical value for human visual cortex; Donahue et al., 2006). All these free parameters and their usage during specific periods and conditions are summarized in **Table 1**. Next, the Grubb's exponent  $\alpha$  and the oxygen extraction fraction at rest,  $E_0$ , were fixed to 0.3 and 0.35, respectively. The BOLD signal equation was parameterized for 3 T magnetic field strength and the sequence parameters utilized in this study (see Table S1).

The modeled physiological variables were linked to measured (averaged) response at the level of CBF (i.e., the output of NVC) and BOLD signals. To enable their joint fitting, we considered a concatenated form of the observation equation:

$$\begin{bmatrix} y_f \\ y_b \end{bmatrix} = \begin{bmatrix} f - 1 \\ b \end{bmatrix} \cdot 100 + \begin{bmatrix} \varepsilon_f \\ \varepsilon_b \end{bmatrix}, \quad (1)$$

where  $y_f$  and  $y_b$  are measured CBF and BOLD responses to both static and flickering stimuli in percent signal changes, all concatenated to a single vector. The measured data were explained by modeled CBF and BOLD responses,  $f$  and  $b$ , respectively, with additive error terms  $\varepsilon_f$  and  $\varepsilon_b$ , constituting the “AR(1)+white noise” model (Friston et al., 2003).

**TABLE 1 |** Model parameters optimized during model inversion of the three data-sets.

Free parameters							
	Neuronal model				NVC	Hemodynamic model	
	$c$ (-)	$\sigma$ ( $\text{s}^{-1}$ )	$\mu$ ( $\text{s}^{-1}$ )	$\lambda$ ( $\text{s}^{-1}$ )	$\chi$ ( $\text{s}^{-1}$ )	$\tau$ (s)	$t_0$ (s), $V_0$ (%)
<b>CBF AND BOLD DATA:</b>							
SP	Static	■	■	■	■†	■	■
	Flicker	■	■	■	■‡		
PSP	Static	-	■	■	†		■
	Flicker	-	■	■	‡		
<b>CBF AND TOTAL CBV AND BOLD DATA:</b>							
SP	Gratings	■	■	■	■	■	■
PSP	-	■	■	■			
<b>NEURONAL AND BOLD DATA:</b>							
SP	Positive	■	■	■	■†	■†	■
	Negative	■	■	■	■‡	■‡	
PSP	Positive	-	■	■	†	†	■
	Negative	-	■	■	‡	‡	

■ Indicates parameter that is optimized within a certain time-period or condition.

†‡ Indicates optimized parameters that were consider the same between time-periods but different between conditions (e.g., † marks the static condition and ‡marks the flickering condition in the first experiment).

## Experiment II: CBF, Total CBV and BOLD Responses:

To jointly model CBF, total CBV and BOLD responses to the same visual stimulus, the generative model was specified as follows: the excitatory activity of the neuronal model was driven by a single input in the form of a box-car function representing 60 s stimulation duration, scaled by the parameter  $c$ . As in the previous experiment, the neuronal parameters  $\sigma$  and  $\mu$  were allowed to vary between SP and PSP periods, while a single  $\lambda$  was estimated for both periods. The NVC and hemodynamic model were also controlled in the same way as in the previous experiment (see Table 1). The BOLD signal equation was parameterized for 9.4 T magnetic field strength and specific sequence parameters (see Table S1). Since, we have additional measurements of the total CBV, the observation equation had the following form:

$$\begin{bmatrix} y_f \\ y_{\tilde{v}} \\ y_b \end{bmatrix} = \begin{bmatrix} f - 1 \\ \tilde{v} \\ b \end{bmatrix} \cdot 100 + \begin{bmatrix} \varepsilon_f \\ \varepsilon_{\tilde{v}} \\ \varepsilon_b \end{bmatrix}. \quad (2)$$

Here, the total CBV data,  $y_{\tilde{v}}$ , is modeled as a weighted sum of CBF (i.e., approximating the response shape of arterial CBV) and venous CBV,  $\tilde{v} = w_a \cdot (f - 1) + w_v \cdot (v - 1)$ , with weights  $w_a$  and  $w_v$  scaling the contribution of arterial CBV (i.e., proportional to CBF) and venous CBV. In other words, the measured BOLD data constraints the relative contributions of arterial and venous CBV to the measured total CBV data, as in the BOLD signal model only the venous CBV contributes to its time-course.

## Experiment III: Neuronal and BOLD Responses:

To jointly model positive and negative neuronal and BOLD responses to non-overlapping and overlapping visual stimuli, respectively, the generative model was specified as follows: Two independent inputs,  $u_P$  and  $u_N$ , scaled by the input strength parameters were used to induce positive and negative responses, respectively. The stimulus duration for the positive response was 25 s but 26 s for negative response as the measured neuronal response remained decreased  $\sim 1$  s after stimulus cessation. Furthermore, in contrast to the two experiments above, we assumed that NVC can differ for the positive and negative responses (i.e., a response-type-specific  $\chi$ ), as the mechanisms for NVC may differ for increases and decreases in CBF. On the other hand, similarly as before, the dynamic properties of venous blood compartment (i.e., the viscoelastic time constant  $\tau$ ) were assumed the same for the two response types but possibly different between SP and PSP periods. Thus, also a single mean transit time,  $t_0$ , and resting venous blood volume,  $V_0$ , were assumed across both conditions (see Table 1). The BOLD signal equation was parameterized for 4.7 T magnetic field strength and specific sequence parameters (see Table S1). Since in this experiment we also have access to neuronal recordings, the observation equation had the following form:

$$\begin{bmatrix} y_n \\ y_b \end{bmatrix} = \begin{bmatrix} w_n \cdot n_e \\ b \end{bmatrix} \cdot 100 + \begin{bmatrix} \varepsilon_n \\ \varepsilon_b \end{bmatrix}, \quad (3)$$

where  $y_n$  and  $y_b$  are the measured neuronal and BOLD responses to both types of stimuli (i.e., both positive and negative responses, concatenated to a single vector) in percent signal changes. Since the reported percent signal change of the measured neuronal responses in Shmuel et al. (2006) do not directly relate to the physiologically plausible range of CBF and BOLD signal changes in our model, the excitatory neuronal response,  $n_e$ , in the observation equation was additionally scaled with the parameter  $w_n$ .

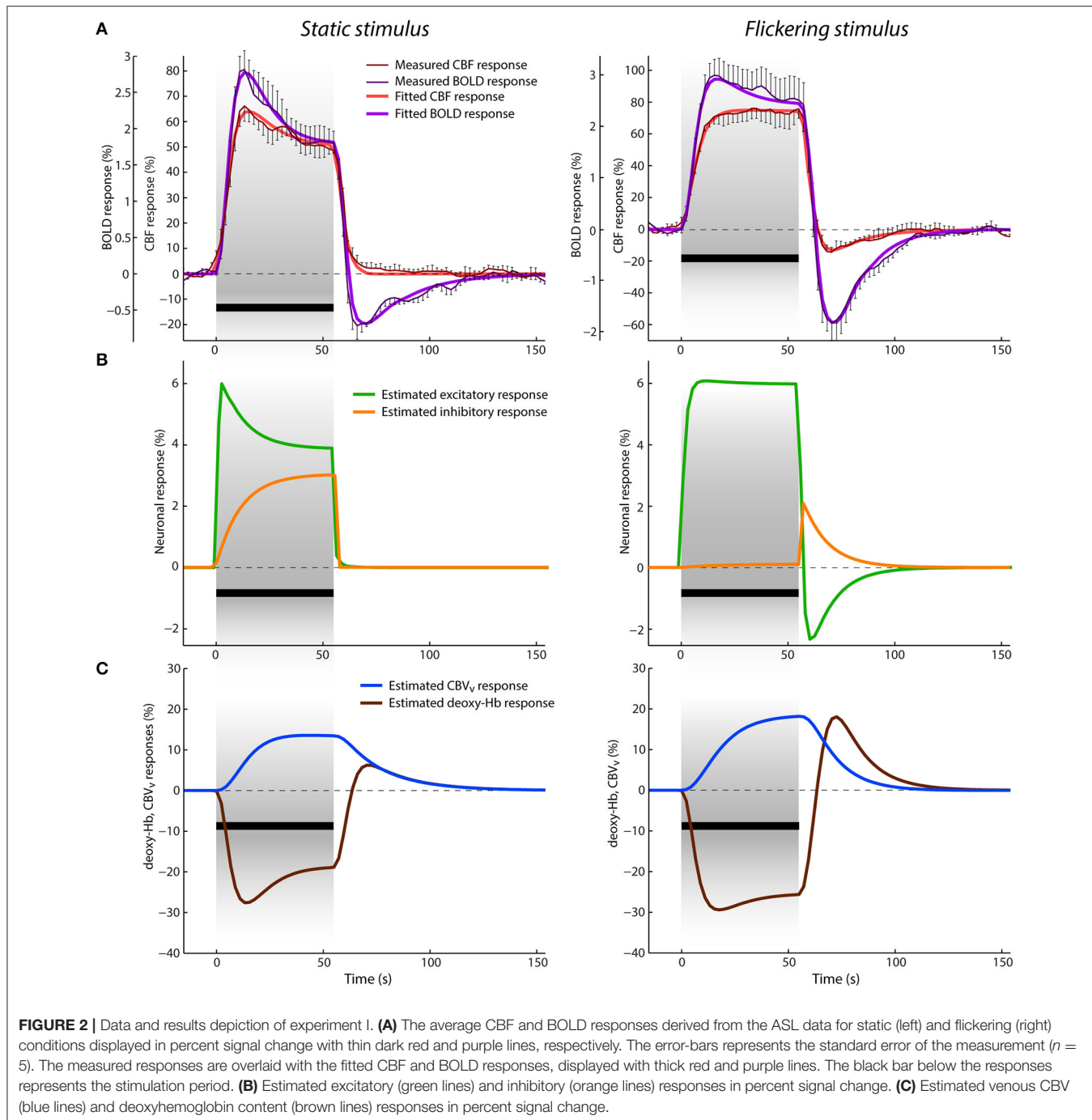
## Model Inversion

Modeled responses were calculated by a numerical integration of differential equations using a local linearization approach (Ozaki, 1992), with integration step  $\Delta t = 0.1$  s and later downsampled to match the TR of the measured data. Responses defined by the above observation equations were fitted to the measured data using variational Laplace (VL) optimization algorithm (Friston et al., 2007) as implemented in the SPM12 toolbox (“*spm\_nlsl\_GN.m*”). This is a Bayesian estimation procedure designed for the estimation of nonlinear dynamic models, where the model parameters are specified in terms of priors. It calculates posterior parameter estimates by iteratively maximizing the free energy (i.e., the approximation to the model log-evidence). Since the VL algorithm employs the Laplace assumption, all the parameters—prior and posterior—are defined using Gaussian distributions. As most of the physiological parameters included in the model can only have positive values, thus, their default values are scaled with a latent variable via the log-normal transformations; e.g.,  $\tau \cdot \exp(\tilde{\tau})$  (see Table S2). The prior means and variances of the latent variables are listed in Table S1.

## RESULTS

### CBF and BOLD Responses

Figure 2A shows the average CBF and BOLD responses to static and flickering stimuli in percent signal changes, respectively. With the onset of the static stimulus, the CBF response rises first and then the BOLD response follows slightly later. They both reach their maxima (i.e., 66% for CBF and 2.8% for BOLD) after  $\sim 13$  s and continue with a steady decrease toward the end of stimulation. This response adaptation has more pronounced character in the BOLD response. After stimulus offset, both responses rapidly decrease. The amplitude of the CBF response first drops quickly to  $\sim 10\%$  and then slowly recovers to the baseline. In contrast, the amplitude of the BOLD response drops below baseline, with a negative peak of  $-0.7\%$ , at  $\sim 11$  s after stimulus offset. This post-stimulus undershoot then recovers to the baseline in the next  $\sim 60$  s. The CBF and BOLD responses to the flickering stimulus differ substantially from the responses to the static stimulus. The CBF response reaches its maximum (i.e., 77%) only by the end of the stimulation, exhibiting mostly a flat plateau from  $\sim 22$  to 55 s. In contrast, the BOLD response peaks to 3% during an earlier phase of the stimulation, i.e., after 15 s, which is slightly later compared to the BOLD response to the static stimulus. From this time point, the BOLD response slightly and slowly decreases toward the end of the stimulation. After stimulus cessation, both CBF and BOLD responses drop below



baseline (reaching their negative peaks in  $\sim 15$  s after stimulus offset, at  $-15$  and  $-1.8\%$ , respectively) and then slowly recover to baseline. In general, the post-stimulus BOLD undershoot is much larger and peaks slightly later compared to the post-stimulus undershoot in the CBF response (both relative to their respective positive responses). Additionally, the post-stimulus BOLD undershoot recovery to baseline is steeper compared to the CBF response.

The results of jointly fitting CBF and BOLD responses using the P-DCM model are overlaid on the measured data in the

same **Figure 2A**. The estimated model parameters are listed in **Table 2**. One can see that the model was able to accurately explain the discrepancy in the response shape of the two hemodynamic variables, and also the response shape variation due to differences in the type of visual stimuli (see fitted CBF and BOLD responses depicted with thick red and purple lines, respectively).

The estimated excitatory and inhibitory neuronal responses are displayed in **Figure 2B**. The excitatory and not the inhibitory neuronal response mostly defines the shape of the CBF response. However, it evolves faster, with more pronounced transients,

**TABLE 2 |** Estimated values of model parameters.

Free parameters										
	Neuronal model				NVC	Hemodynamic model		Additional		
	c (-)	$\sigma$ ( $s^{-1}$ )	$\mu$ ( $s^{-1}$ )	$\lambda$ ( $s^{-1}$ )	$\chi$ ( $s^{-1}$ )	$\tau$ (s)	$t_0$ (s), $V_0$ (%)	$w_n$ (-)	$w_a$ (-)	$w_v$ (-)
<b>EXPERIMENT I: CBF AND BOLD RESPONSES</b>										
SP	Static	0.08	1.15	0.73	0.05 <sup>†</sup>	0.28	68.68	2.07	-	-
	Flicker	0.04	0.52	0.01	0.05 <sup>‡</sup>					
PSP	Static	-	0.25	0.00	†	69.49				
	Flicker	-	0.66	0.39	‡					
<b>EXPERIMENT II: CBF AND TOTAL CBV AND BOLD RESPONSES</b>										
SP	Gratings	0.17	2.80	7.30	0.02	0.27	59.91	2.06	-	0.12
PSP	-	-	2.13	1.95			41.11			0.19
<b>EXPERIMENT III: NEURONAL AND BOLD RESPONSES</b>										
SP	Positive	0.13	1.87	3.19	0.15 <sup>†</sup>	0.19 <sup>†</sup>	9.37	2.95	12.69 <sup>†</sup>	-
	Negative	-0.09	1.32	6.70	0.06 <sup>‡</sup>	0.85 <sup>‡</sup>			2.59 <sup>‡</sup>	
PSP	Positive	-	1.89	1.94	†	†	28.53		†	
	Negative	-	1.05	1.70	‡	‡			‡	

<sup>†‡</sup>Indicates optimized parameters that were considered the same between time-periods but different between conditions as described in Table 1.

such as response adaptation in the case of the static condition and post-stimulus deactivation in the case of the flickering condition. Response adaptation and post-stimulus deactivation were explained by an amplitude variation of the inhibitory neuronal response. This means that the more pronounced response adaptation during stimulation is caused by a larger, gradual increase of inhibitory activity above baseline and the post-stimulus deactivation solely reflects the sharp increase of inhibitory activity after stimulus cessation (followed by a slower return to baseline). Note that the inhibitory responses displayed in Figure 2B were modulated by the period and condition specific parameter  $\mu$  (i.e., the inhibitory-to-excitatory coupling). These experimental data and modeling results demonstrate that the type of stimulus modulates both the positive response and the post-stimulus undershoot, but in a different manner. This means that the E-I balance changes with time and can be very different between stimulation and post-stimulation periods, which is reflected in estimated neuronal parameters (i.e., in  $\sigma$  and  $\mu$ ).

The discrepancy between the measured CBF and BOLD responses was explained with uncoupling between the CBF and venous CBV responses. In Figure 2C, we can see that the venous CBV time-course evolves in a much slower fashion than the CBF time-course (Figure 2A). For example, for the static stimulus, the venous CBV response slowly increases during stimulation while the CBF response starts declining already after  $\sim 15$  s of stimulation. Similarly, the CBF response returns much faster to baseline after stimulus cessation than the venous CBV response. This dynamic uncoupling during the transient periods results in a more pronounced response transients in the BOLD response, which approximately represents the inverted deoxyhemoglobin response (see Figures 2A,C). The CBF-venous CBV uncoupling parameterized by the viscoelastic time constant was estimated separately for the stimulation and post-stimulation periods, but yielded almost identical values

$\tau_{SP} \approx 68$  s and  $\tau_{PSP} \approx 69$  s, respectively. These large values reflect the fact that  $\tau$  should scale with stimulus duration (see Uludağ and Blinder, 2017 and references therein). Importantly, the discrepancy between CBF and BOLD responses was explained with the same viscoelastic time constants for both the static and flickering conditions. This demonstrates that the passive mechanism of CBF-venous CBV uncoupling is independent of stimulus type (but dependent on the stimulus duration).

## CBF, Total CBV and BOLD Responses

Figure 3A shows the averaged CBF and BOLD responses in percent signal change to 60 s visual stimulation as reported by Jin and Kim (2008). The CBF response reaches its maximum peak (at 46%)  $\sim 12$  s after the stimulus onset. The BOLD response reaches the peak  $\sim 2$  s earlier (at 3.5%), even though the CBF response is faster immediately after stimulus onset. The average total CBV response (displayed in Figure 3C in percent signal change) rises with the BOLD response but its peak (at 6.5%) is  $\sim 3$  s delayed with respect to the BOLD response peak. After reaching their maxima, all three responses decrease toward the end of stimulation. While the BOLD response exhibits the steepest decay, the decrease of the total CBV response is the slowest. The amplitudes of CBF, total CBV and BOLD at the end of stimulation are 21, 3.6, and 1% (i.e., in ratios of 0.46, 0.55, and 0.29 with respect to their maximum peaks), respectively. After stimulus cessation, all responses drop below baseline and exhibit considerable post-stimulus undershoots. The ratios of the post-stimulus response undershoots with respect to the amplitudes at the end of the stimulation for CBF, total CBV, and BOLD are 0.57, 0.42, and 1.4, respectively. The BOLD response with the largest relative post-stimulus undershoot reaches the negative peak earliest (at  $-1.4\%$ ), i.e.,  $\sim 18$  s after stimulus onset, then CBF with smaller relative undershoot follows ( $-12\%$ , after 20 s), and the total CBV response has the smallest and most sluggish relative

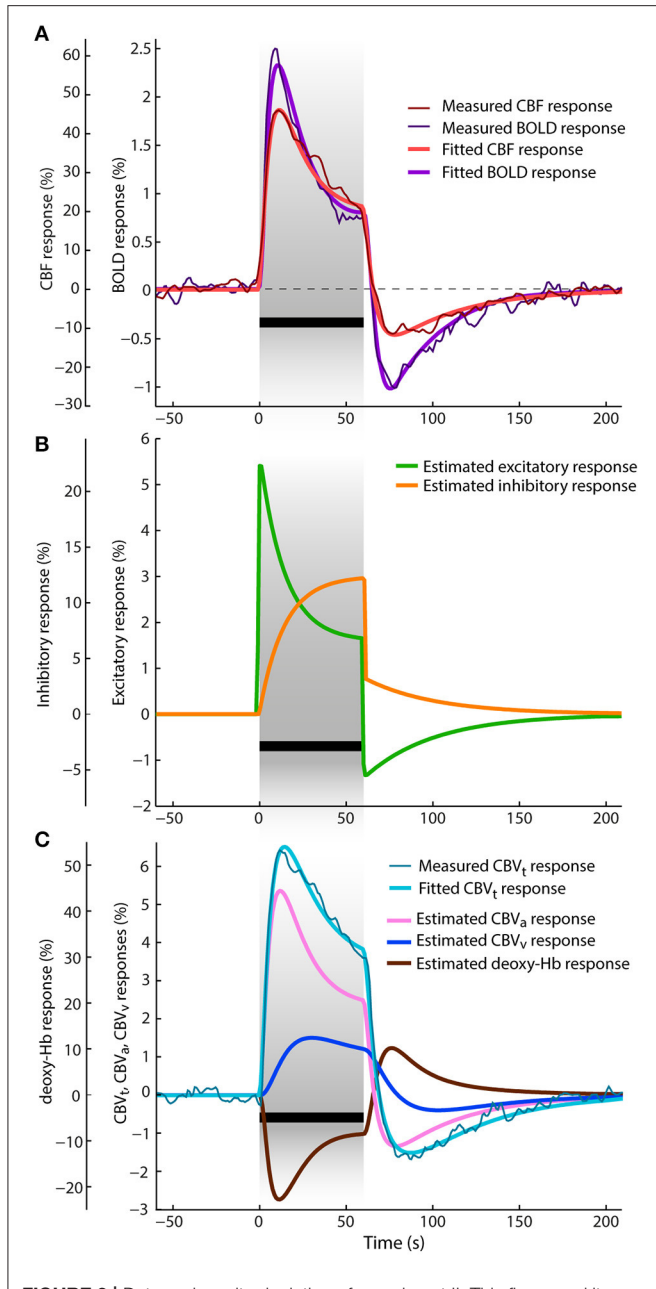


**FIGURE 3 |** Data and results depiction of experiment II. This figure and its sections follow the same plotting format as **Figure 2**. The average CBF, BOLD and total CBV responses are replotted versions of the data reported in Figure 1 of Jin and Kim (2008). **(A)** The fitted and average measured CBF and BOLD responses. **(B)** The estimated excitatory and inhibitory responses. **(C)** The average measured and fitted total CBV responses are displayed with dark thin and light thick cyan lines, respectively. Next, to the estimated venous CBV response and deoxyhemoglobin content responses, also the arterial CBV response is depicted (pink line).

post-stimulus undershoot ( $-1.5\%$ , after 27 s). All responses take almost 100 s to fully recover to baseline.

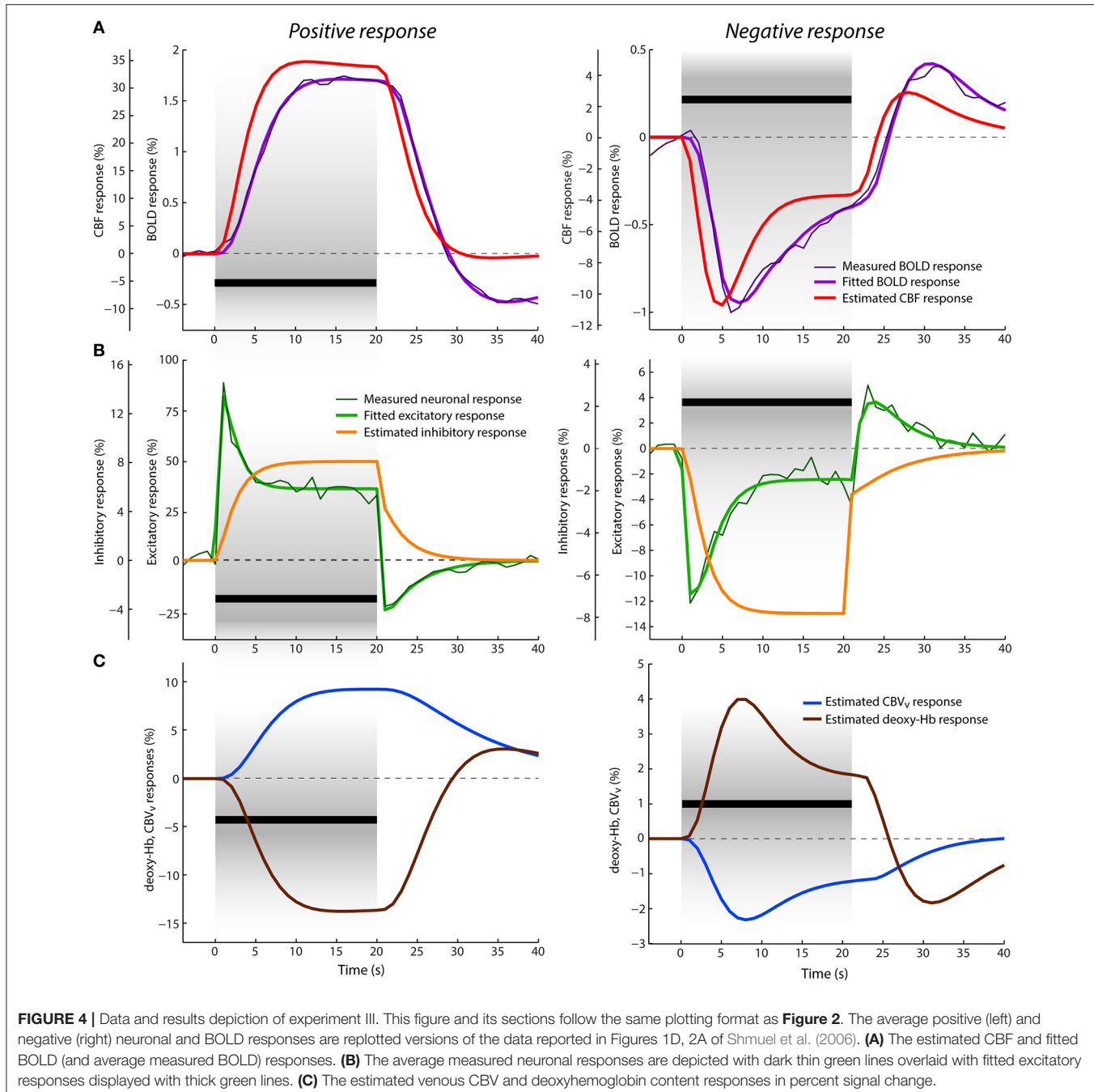
The results of jointly fitting CBF, total CBV and BOLD responses using the P-DCM model are overlaid on the measured data in the same **Figures 3A,C**. The estimated model parameters

are listed in **Table 2**. All fitted CBF, total CBV and BOLD responses follow very closely the dynamic changes observed in the experimental data. The estimated excitatory neuronal response depicted in **Figure 3B** shows a strong and fast adaptation during stimulation and drops significantly below baseline immediately after stimulus cessation, followed by a slow recovery to baseline. As in the previous study, neuronal response adaptation during stimulation and post-stimulus deactivation are modeled by dynamic changes in the inhibitory neuronal response. Inhibitory response modulates the excitatory response by different amounts during stimulation and post-stimulation periods (see **Table 2**, for differences in optimized period-specific neuronal parameters).

The dynamic relationship between CBF, total CBV, and BOLD signal was explained with the CBF-venous CBV uncoupling. Estimated arterial and venous CBV ( $\text{CBV}_a$  and  $\text{CBV}_v$ ) responses are displayed in **Figure 3C** in percent signal changes as they contribute to the predicted total CBV response (weighted by parameters  $w_a$  and  $w_v$ ). One can see that the arterial CBV change is larger than the venous CBV change (e.g., by a factor of  $\sim 2$  at the end of the stimulation) and that venous CBV evolves slower during the transient periods. The large dynamic uncoupling between CBF (or arterial CBV) and venous CBV, which differed between stimulation and post-stimulations periods ( $\tau_{SP} \cong 60$  s and  $\tau_{PSP} \cong 41$  s), was estimated to significantly contribute to the size of BOLD response transients. These  $\tau$  values provide a good explanation for the significantly more pronounced response adaptation and post-stimulus BOLD undershoot compared to the CBF and total CBV responses (as also reflected by the ratios mentioned above). As a consequence of CBF and arterial CBV responses exhibiting strong post-stimulus undershoots (due to the aforementioned decrease of excitatory activity below baseline during PSP), also venous CBV shows a post-stimulus undershoot, even though it is reduced and smoothed due to the viscoelastic properties of veins (i.e., large  $\tau$ ) (see **Figure 4C**). The same mechanism applies for the slower increase and strongly reduced adaptation profile of venous CBV during SP.

## Neuronal and BOLD Responses

Average positive and negative neuronal responses in percent signal changes to 20 s visual stimuli overlapping and non-overlapping with its receptive field, respectively, as reported in Shmuel et al. (2006), are displayed in **Figure 4B**. The corresponding average positive and negative BOLD responses (also in percent signal changes) are displayed in **Figure 4A**. The positive neuronal response reaches its maximum peak immediately after stimulus onset (given downsampling of the neuronal signal to  $\text{TR} = 1$  s). Then, within the next 5 s, it rapidly decreases to its lower plateau, where it remains till the end of the stimulation. In contrast, the positive BOLD response shows a rather slow increase, reaching its maximum  $\sim 15$  s after stimulus onset (at 1.75%) and it remains about this level until the end of the stimulation. After stimulus cessation, the neuronal response drops quickly below baseline, producing a strong post-stimulus deactivation followed by gradual return to baseline in the next  $\sim 13$  s. The BOLD response also decreases after stimulus cessation but in a much slower fashion, crossing the baseline  $\sim 9$  s after the



stimulus offset. Then it continues with a stronger post-stimulus BOLD undershoot, which is significantly delayed ( $\sim 15$  s) with respect to the neuronal post-stimulus deactivation. The limited post-stimulus period of 25 s did not allow for a full recovery of the BOLD undershoot to baseline. The negative neuronal response can be seen as an inverse of the positive response, but exhibiting significantly smaller signal change. After stimulus onset, there is an immediate decrease in neuronal activity below baseline followed by adaptation to the plateau of lower sustained amplitude during SP. After stimulus offset, it first slightly

decreases<sup>3</sup> (within 1 s) and then quickly increases, showing a post-stimulus activation above baseline, which is mostly in phase with the post-stimulus deactivation observed in the positive neuronal response. The negative BOLD response follows the course of the neuronal response more closely compared to the positive BOLD response. It reaches the minimum peak (at  $\sim 1\%$ )  $\sim 6$  s after the stimulus onset and keeps increasing almost linearly

<sup>3</sup>This is the reason why we extended the stimulation period for negative response by 1 s.

toward the end of the stimulation (to  $-0.4\%$ ). Afterwards, it crosses baseline  $\sim 4$  s earlier than the positive BOLD and exhibits a post-stimulus BOLD overshoot (with maximum at  $0.4\%$ ) that evolves significantly faster than the post-stimulus undershoot of the positive response.

The results of jointly fitting the positive and negative neuronal and BOLD responses with P-DCM are overlaid with the measured data in **Figures 4B,A**, respectively. The estimated model parameters are listed in **Table 2**. The fitted neuronal and BOLD responses follow very closely the dynamic changes observed in the experimental data. The estimated excitatory neuronal responses for both positive and negative responses provided an accurate representation of the transient features observed in the experimental data. As before, response adaption and post-stimulus deactivation profiles were modeled by a variable modulation of the excitatory activity by inhibitory activity (see **Figure 4A**). The dynamic features of the positive excitatory neuronal response are well comparable to the estimated neuronal response in the second experiment (or to the response features seen in the first experiment). The negative excitatory response was induced by the stimulus input function  $u_N(t)$  scaled by the negative  $c$  parameter. Thus, in contrast to the positive neuronal response, the inhibitory response gradually decreases below baseline during SP, which then causes an increase of the excitatory activity after its initial drop. After stimulus cessation, the inhibitory activity quickly increases up to  $\sim 1/4$  of the total decrease, and then slowly recovers to the baseline. This slow post-stimulus recovery of the inhibitory response below baseline causes an increase (i.e., overshoot) in the post-stimulus excitatory response.

Next, as the NVC could differ between the positive and negative responses, the estimated positive CBF response is significantly delayed with respect to the neuronal response, which smooths out the strong adaptation during SP and post-stimulus deactivation observed in the neuronal response. This slow evolution of the CBF response was achieved by slowing down the feedforward mechanism of NVC (i.e., by lowering the decay constant  $\chi$ ). On the other hand, the estimated CBF response following the negative neuronal response is much faster, closely resembling dynamic features of the neuronal response. This is because the NVC acts faster (by employing a higher decay constant  $\chi$ ).

Furthermore, the fitted positive BOLD response is even more delayed with respect to the CBF response, with mean transit time at rest,  $t_0 \cong 3$  s (see **Figure 4B**). The CBF-CBV uncoupling is smaller, with viscoelastic time constant,  $\tau_{SP} \cong 9$  s, (see **Figure 4C**). Therefore, no response adaptation is present during SP. Although the estimated CBF response exhibits a minimal post-stimulus undershoot, the stronger post-stimulus BOLD undershoot is well explained by a larger CBF-venous CBV uncoupling ( $\tau_{PSP} \cong 29$  s) during PSP. The venous CBV and deoxyhemoglobin responses are displayed in **Figure 4C**. The negative BOLD and CBF responses show similar response transients even though the same viscoelastic time constants, regulating CBF-venous CBV uncoupling during SP and PSP, were used as in the case of the positive response. Significant post-stimulus overshoot in the CBF response can account for a large

fraction of the post-stimulus BOLD overshoot. This is because the actual effect of CBF-CBV uncoupling on the post-stimulus BOLD undershoot for the negative response is smaller due to a generally lower amplitude level of venous CBV during recovery (see **Figure 4C**). Therefore, in contrast to the positive response, the main origin of post-stimulus BOLD overshoot is neuronal.

## DISCUSSION

The BOLD fMRI signal is an indirect reflection of neuronal activity. It has been suggested that it best correlates with the post-synaptic potentials, which—after mediation by metabolic and vascular processes—results in the characteristic hemodynamic delay and blurring relative to neuronal activity. Thus, the high complexity of tissue processes associated with brain activity, ranging from microscopic (i.e., molecular) to macroscopic (i.e., brain area) levels, is reduced to a spatially and temporally varying scalar number (i.e., the dynamic fMRI signal). That is, there is only reduced information about the excitatory and inhibitory neuronal activity available from the fMRI signal. As a result, temporal features of the BOLD signal, such as signal adaptation during stimulation or signal reduction after the stimulation, cannot be taken as a direct evidence of neuronal adaptation or post-stimulation deactivation, respectively. Recently, we have proposed, inspired by physiological observations, a novel generative hemodynamic model within the DCM framework, called P-DCM. We have demonstrated (using BOLD data and BOLD data combined with CBF) that P-DCM is superior in describing single ROI time-courses and also deducing the effective connectivity between brain areas (Havlicek et al., 2015, 2017b) compared to previous DCM models (Friston et al., 2003; Marreiros et al., 2008) and that the model inversion, in general, benefits from additional CBF data.

In this paper, we have additionally demonstrated the versatility of P-DCM to jointly explain dynamic relationships between neuronal, neurovascular and hemodynamic physiological variables underlying the BOLD signal using new and previously published multi-modal data. For this purpose, we utilized three data-sets of experimentally induced responses in primary visual areas measured in the brains of human, cat, and monkey, respectively: (1) CBF and BOLD responses to static and flickering stimuli acquired for this study; (2) CBF, total CBV and BOLD responses to square-wave grating stimulus (Jin and Kim, 2008); and (3) positive and negative neuronal and BOLD responses induced by overlapping and non-overlapping visual stimuli with the visual receptive field (Shmuel et al., 2006). The fitting of P-DCM to multi-modal data (i.e., the model inversion) was performed using a VB approach (Friston et al., 2007) under the constraint of assumed physiological mechanisms and experimental manipulations. Specifically, we assumed that the BOLD response transients, such as positive response adaptation and post-stimulus undershoot, can be due to two physiological mechanisms: (1) neuronal, due to changes in E-I balance caused by a dynamic interaction between excitatory and inhibitory neuronal populations (Hoge et al., 1999; Krekelberg et al., 2006; Shmuel et al., 2006; Logothetis, 2008; Sadaghiani

et al., 2009; Mullinger et al., 2013); and (2) vascular, due to dynamic uncoupling between CBF and venous CBV responses (Mandeville et al., 1998; Chen and Pike, 2009; Kim and Ogawa, 2012; Huber et al., 2014a; Havlicek et al., 2017a). We also assumed that the experimental manipulation can modulate the neuronal response transients by changing the E-I balance and that this can differ between SP and PSP. Similarly, the vascular uncoupling was allowed to vary between SP and PSP but was invariant with respect to the experimental manipulations. P-DCM provided accurate fits to all measured multi-modal responses and was able to shed a light on the dynamic relationships between the physiological processes underlying the BOLD response. The limitations of P-DCM due to its assumptions are discussed below.

In the first experiment using both CBF and BOLD responses, we were able to show that a 55 s long static and flickering stimuli induced different modulations of the CBF response transients during SP and PSP and that there was a large discrepancy in the size and form of transients between the CBF and BOLD transients, as commonly observed (see e.g., Sadaghiani et al., 2009; Havlicek et al., 2017a and references therein). P-DCM could explain the experimentally induced modulation of the CBF response transient by optimizing the balance between excitatory and inhibitory activity. The accurate fit of both CBF responses to static and flickering stimuli was achieved by allowing some of the neuronal model parameters ( $\sigma, \mu$ ) to be time-period- and condition-specific, while others ( $\lambda$ ) including the NVC parameter ( $\chi$ ) were considered condition- and period-invariant (see Table 2). Next, the large discrepancy in the size of transients between the measured CBF and BOLD responses was explained with a strong uncoupling between CBF and venous CBV responses, which was identified to be similar for SP and PSP ( $\tau_{SP} \cong 68$  s and  $\tau_{PSP} \cong 69$  s). More importantly, both BOLD responses to static and flickering stimuli could be explained by assuming the same vascular uncoupling for the two conditions. Additionally, these estimates compared quite well with our previous results obtained by applying P-DCM to the single-subject BOLD responses of the same experimental ASL data (Havlicek et al., 2015). Nevertheless, additional information about the shape of CBF responses incorporated in the current study provided more accurate estimation of the neuronal and vascular component contribution to the BOLD response transients (see Figure 6C in Havlicek et al., 2015).

By using P-DCM to explain the dynamic discrepancy in the shape of the CBF, total CBV and BOLD responses to a 60 s long square-wave grating visual stimulus provided by the second experiment (Jin and Kim, 2008), we were able to accurately jointly fit all measured responses. First, even though the response transients (i.e., early-overshoot and post-stimulus undershoot) were strongly present in both CBF and total CBV responses, the BOLD response transients were even more significantly pronounced (see Figure 3A). Thus, some additional mechanism next to the neuronal contribution is necessary to fully explain the BOLD response transients: As in the first study, the shape of CBF response was well explained by optimizing the E-I balance for the SP and PSP. Importantly, by having measurements of both CBF and total CBV responses underlying the BOLD response, we were

able to determine that arterial CBV has a larger contribution to the total CBV than the venous CBV, which is in good agreement with other experimental observations (Drew et al., 2011; Kim and Kim, 2011; Huber et al., 2014a; Gagnon et al., 2015), and that venous CBV evolves much slower compared to the CBF (or arterial CBV) due to a strong (but slightly different) CBF-venous CBV uncoupling between SP and PSP ( $\tau_{SP} \cong 60$  s and  $\tau_{PSP} \cong 41$  s) (Uludağ and Blinder, 2017). The strong neuronal transients are well reflected in both the CBF and arterial CBV responses, and also the venous CBV response transients reflect this neuronal modulation, albeit largely smoothed out by the strong CBF-venous CBV uncoupling (see Figure 3C). Therefore, even though the venous CBV does not exhibit the more typical slow increase during SP and slow return to baseline during PSP (Kim and Kim, 2011; Huber et al., 2014a), the vascular uncoupling still significantly contributes, in addition to the CBF post-stimulus deactivation, to the post-stimulus BOLD undershoot (having ~50% neuronal and 50% vascular origin). Thus, our modeling results agree with a suggestion by Jin and Kim (2008) that there is a significant contribution of CBF post-stimulus deactivation to the post-stimulus BOLD undershoot, but disagree with their suggestion that these multi-modal data do not support the contribution of the vascular uncoupling between CBF and venous CBV. It is incorrect to assume that the venous CBV must exhibit slow return to baseline after stimulus cessation in order to effectively contribute to the post-stimulus BOLD undershoot if there is a post-stimulus undershoot in CBF and total CBV.

The third experiment offered positive and negative neuronal and BOLD responses to 20 s long visual stimuli overlapping and non-overlapping with the receptive field of the voxels in the ROI (Shmuel et al., 2006). The electrophysiological recordings of neuronal activity in V1 demonstrated that the positive neuronal responses can indeed exhibit a very pronounced response adaptation (but see below) and significant deactivation/activation during SP and PSP, respectively, similarly as estimated by P-DCM from the hemodynamic responses in the two experiments above. By modeling the dynamic changes in E-I balance during both SP and PSP, P-DCM was also able to explain the negative neuronal response, including the post-stimulus increase in neuronal activity. Note that this was achieved under the assumption that the input arriving to the excitatory population in V1 from LGN is negative (i.e., already LGN exhibits negative response, see e.g., Gouws et al., 2014). Furthermore, the relationship between the positive neuronal and BOLD responses in this experimental data is very interesting as there is a strong adaptation in the neuronal response during SP but no sign of adaptation in the BOLD response. This seems to appear as a typical observation for the BOLD responses to stimuli with a comparable stimulus duration measured in the V1 area of anesthetized macaque monkey brain (Logothetis et al., 2001; Logothetis, 2002; Pfeuffer et al., 2004; Goense and Logothetis, 2006) but less common in anesthetized cats or rats (as shown above and, e.g., Zhao et al., 2007; Kida and Yamamoto, 2008; Kim et al., 2010). Moreover, the stronger neuronal deactivation during PSP invites the hypothesis that the post-stimulus BOLD response undershoot could be related to this decrease in neuronal activity. However, the estimate of

CBF response provided by P-DCM suggests that the neuronal adaptation and post-stimulus deactivations are almost entirely smoothed out by a slow rate of NVC (with  $\chi = 0.19$  Hz), which is also necessary to explain the smoothness of the observed BOLD response. This is in line with experimental observations from anesthetized macaque monkey brain reported in Pfeuffer et al. (2004), Zappe et al. (2008), and Zaldivar et al. (2014), albeit not explicitly described by the authors (see also discussion below for possible effects of anesthesia). Thus, in contrary to suggestion made in Shmuel et al. (2006), our modeling results suggest that the post-stimulus BOLD undershoot is not caused by the neuronal deactivation but by the vascular uncoupling (with  $\tau_{PSP} \cong 29$  s) with a slow return of venous CBV to baseline during PSP (but see also below). Note that this vascular uncoupling is smaller than in the first two experiments, which is in a good agreement with the fact that the size of the post-stimulus undershoot and thus also size of the vascular uncoupling is proportional to stimulus duration (Uludağ and Blinder, 2017).

On the other hand, the shape of the negative BOLD response follows very closely the shape of the negative neuronal response with a smaller delay of the negative peak with respect to the stimulus onset and the post-stimulus overshoot to stimulus offset compared to the positive BOLD response. The faster evolution of the negative BOLD response (with an earlier post-stimulus undershoot) compared to the positive BOLD response was also observed in other studies using human subjects (Shmuel et al., 2002; Pfeuffer et al., 2004; Huber et al., 2014a). As we assumed that the passive hemodynamic properties of the venous compartment are the same for both positive and negative responses (including the size of vascular uncoupling), P-DCM explained the dynamic relationship between neuronal and BOLD response by a faster NVC (with  $\chi = 0.85$  Hz) for decreases in neuronal activity. In contrast to the positive BOLD response, the neuronal transients are reflected in the BOLD signal time-course due to the fact that the relative change of neuronal amplitude between stimulus onset and offset is larger (close to baseline by the end of the stimulation) compared to the positive response. Note that theoretically, one could also explain the discrepancy between positive neuronal and BOLD responses by making the NVC faster, increasing the mean transit time ( $t_0$ ) and minimizing the vascular uncoupling ( $\tau$ ), which would result in the post-stimulus BOLD undershoot having mainly neuronal origin. However, this would lead to  $t_0 > 4.5$  s, which would have to significantly differ from the negative BOLD response. That is, we would not be able to assume the same hemodynamic (i.e., vascular) model for both negative and positive BOLD response in the same voxels, which is not physiologically plausible. In general, it is more likely that the main differences between the positive and negative BOLD responses are due to different control of NVC (Lauritzen, 2005). Whether the rate difference in NVC for positive and negative responses is a general distinctive feature will need to be clarified in future experiments.

In summary, the three experimental data-sets provided physiological measurements at different stages of the dynamic cascade between neuronal and BOLD responses. First, we demonstrated that P-DCM was able to estimate (excitatory and inhibitory) neuronal responses with different amount of response

adaptation during the stimulus period and post-stimulus deactivation/activation after the stimulation. We showed that the response adaptation during SP can vary from fast and strong (e.g., in the third experiment) to minimal (e.g., in the first experiment, response to flickering stimulus). Similarly, during PSP, the excitatory neuronal activity can slowly return to baseline (e.g., in the first experiment, after the response to the static stimulus) or it can decrease below baseline following the positive response (e.g., in the second experiment) or increase above baseline following the negative response. Second, the CBF response was shown to reflect the neuronal time-courses in a smoothed fashion via feedforward NVC, which can reduce or even completely eliminate neuronal transients (as in the third experiment for the positive CBF response). However, modeling of the NVC allows recovering excitatory and inhibitory neuronal transients from the CBF data. Additional transient phenomena in the BOLD response are induced by CBF-venous CBV uncoupling. That is, the discrepancy between the BOLD signal and CBF are due to venous CBV (or, alternatively, CMRO<sub>2</sub>, but see Havlicek et al., 2017a). That is, the presence or absence of dynamic features in the BOLD signal is not an unambiguous indication of the presence or absence of those features on the neuronal level. However, P-DCM applied to multi-modal data was able to dissociate between neuronal and vascular contributions to the BOLD response transients induced by different types and durations of stimuli. Furthermore, P-DCM accommodated the magnetic field strength and sequence parameters differences between experimental studies that also influence the size and nonlinearity of BOLD response transients (Havlicek et al., 2015, 2017a; Uludağ and Blinder, 2017). We think that P-DCM and its emphasis on response transients may be useful to also explain other combinations of multimodal data (e.g., neuronal activity recordings, CBF, CBV and BOLD) or to play an important role in combining EEG and fMRI data (Valdes Sosa et al., 2009; Riera and Sumiyoshi, 2010; Rosa et al., 2011; Butler et al., 2017; Friston et al., 2017). The neuronal mass activity of post-synaptic signals can be decomposed to non-overlapping frequency bands. The higher frequency band (gamma) is more associated with the main signal change of the hemodynamic response while lower frequency bands, such as alpha, and beta carry more information about changes in response transients (Magri et al., 2012; Mullinger et al., 2013, 2014; Ding et al., 2016).

Finally, it is important to realize that due to complexity of physiological mechanisms transforming the neuronal response to the BOLD response, the standard linear analysis (e.g., Friston et al., 1995, 1998) or (linear) deconvolution applied to BOLD data (e.g., Gaudes et al., 2011; Ryali et al., 2011; Smith et al., 2012; Bush and Cisler, 2013) cannot provide a reliable estimate of the underlying changes in neuronal activity in any of the three experiments. Our results highlight the necessity of nonlinear models, such as P-DCM, which account for dynamic uncoupling at both the neuronal and vascular levels and that can benefit from multi-modal data. In addition, nonlinear generative models, such as P-DCM, have the potential also to improve novel data analysis approaches, e.g., single-voxel and multi-voxel-pattern or representational similarity analysis approaches (e.g., Kriegeskorte et al., 2008; Haxby, 2012).

## Model Assumptions and Limitations

It is generally believed that modeling E-I balance—as the underlying source of the BOLD response (Logothetis, 2008)—is crucial for relating neuronal and hemodynamic responses. The applied neuronal model of E-I balance within P-DCM represents a large simplification of the underlying complex neuronal processes that operate at very fine temporal and spatial scales. The aim of this model is to mainly characterize regional post-synaptic changes in excitatory and inhibitory activity using a simple mathematical function that can be related to changes in the hemodynamic signal. It is assumed that the two-state neuronal model is driven by an exogenous input entering the excitatory state and the change in excitatory activity is followed by a (smaller) change in the inhibitory activity that subsequently modulates the excitatory activity via negative feedback and the E-I (im)balance eventually settles into a new balance state. Despite its simplicity, this model is able to represent dynamic change in E-I balance resulting in wide repertoire of neuronal response adaptions profiles (Hoge et al., 1999; Bandettini and Ungerleider, 2001; Logothetis et al., 2001), including more abrupt changes of E-I balance with stimulus cessation followed persistence of inhibitory activity that creates the post-stimulus deactivation (Sadaghiani et al., 2009; Mullinger et al., 2013, 2014, 2017). Therefore, P-DCM offers a new way to assess the neuronal origin of hemodynamic response transients by means of proxies for excitatory and inhibitory responses that can have high neuroscientific relevance.

Changes in the E-I balance were encoded in three neuronal parameters ( $\sigma$ ,  $\mu$ ,  $\lambda$ ). The temporal evolution of excitatory and inhibitory activity, including their dynamic mismatch, was controlled by the parameters  $\sigma$  and  $\lambda$ , respectively, and the strength of the inhibitory activity modulating the excitatory activity is encoded by the parameter  $\mu$ . In this paper, we have mostly commented on the shape of estimated neuronal response and emphasized possible differences in excitatory and inhibitory dynamics. However, the actual values of estimated parameters controlling the neuronal model are informative and significantly differed between the three experiments (especially  $\sigma$  and  $\mu$ ). It is possible that these differences can be attributed to the neuronal or stimulus properties, as described above (Kida and Yamamoto, 2008), but also to the fact that responses of the two animal experiments were acquired under anesthesia (see below). In addition, testing for significant differences in estimated neuronal parameters due to experimental modulation or between healthy and diseased subjects is potentially an important area for future P-DCM utilization (Stephan et al., 2017). Note that in this paper we have made the specific assumption that  $(\sigma, \mu)$  can vary between both SP and PSP but also between experimental conditions. On the other hand,  $\lambda$  was allowed to vary only between experimental conditions. This is because we favored a simpler model that was able to explain the observed neuronal responses in all three experiments, even with  $\lambda$  being only condition specific. Additionally, in the first experiment, the CBF response during PSP exhibits a slower return to the baseline without post-stimulus undershoot. This is effectively modeled by setting the parameter  $\mu$  (i.e., the influence of inhibitory to excitatory activity) close to zero, which means that during this

PSP, parameter  $\lambda$  does not have an effect on the shape of the neuronal response and becomes unidentifiable. Nevertheless, the inhibitory responses (as displayed in Figures 2–4) are modulated by the parameter  $\mu$ , which makes them time-period specific as well.

Furthermore, the assumption about the input entering the excitatory state is appropriate for the majority of cortical regions as the vast majority of long-range connections between regions are mediated by excitatory neurons (Markram et al., 2004). For an additional description how P-DCM can model long-range connections, please see Supplementary Material 3 in Havlicek et al. (2015). We have utilized the same assumption also for the negative neuronal response but with a negative input entering the excitatory state, as it was shown earlier that negative responses in primary visual areas may be preceded by negative responses in LGN (e.g., Gouws et al., 2014).

NVC in P-DCM transforms neuronal to CBF response using a feedforward mechanism. While the motivation for utilizing feedforward NVC is fully discussed in Havlicek et al. (2015), we have also demonstrated in Havlicek et al. (2017b) that NVC based on negative feedback mechanism (Friston et al., 2000) is suboptimal and that the feedforward NVC in conjunction with the two-state neuronal model of E-I balance is preferred for modeling fMRI data. NVC is controlled by three parameters ( $\varphi$ ,  $\phi$ ,  $\chi$ ), but optimizing only  $\chi$  is sufficient to adjust the smoothness and delay of CBF response with respect to the neuronal response (i.e., we prefer a parsimonious NVC model with a minimum number of free parameters). The NVC parameter  $\chi$  was assumed to vary between conditions. This is mainly because the third experiment involved a condition resulting in the negative response, and it was suggested earlier that the NVC of positive and negative hemodynamic response may differ (see e.g., Lauritzen, 2005; Huber et al., 2014a), which is supported here by our results obtained with constrained model inversion by multi-modal data. In fact, our fitting results of the first experiment showed that positive hemodynamic responses, although resulting from two different stimulus types and having different modulation of response transients, can have the same NVC parameter  $\chi$  (see Table 2).

In the hemodynamic model, P-DCM assumes that CBF and CMRO<sub>2</sub> are tightly coupled. There are three reasons to do so: (1) It is a common assumption in DCM literature that CBF is tightly coupled with CMRO<sub>2</sub> (Friston et al., 2003), and other papers showed that CBF and venous CBV are uncoupled (e.g., Mandeville et al., 1999; Kim and Kim, 2011; Huber et al., 2014a), as for longer stimuli venous CBV response exhibits much slower increase and return to baseline compared to the CBF response; (2) If one considers both CMRO<sub>2</sub> and venous CBV responses uncoupled from CBF response, then both can have similar impact on the transients of the BOLD response and the generative model becomes unidentifiable. From modeling (and model inversion) perspective, this is seen as redundancy and therefore it is preferable to fix one of these two mechanisms. This is because under normal conditions even with multimodal data (consisting of CBF, total CBV and BOLD) one cannot effectively disentangle these two mechanisms from each other; (3) We have recently provided a comprehensive proof using

multi-echo data (Havlicek et al., 2017a) that next to CBF (i.e., neuronal) contribution, the CBF-venous CBV uncoupling (and not the CBF-CMRO<sub>2</sub> uncoupling) is the mechanism behind the BOLD response transients. In this case, the specific echo-time dependence of the BOLD response transients (related to contribution from both extravascular and intravascular signals) together with a variable CBF response allowed us to identify the underlying mechanism.

In this paper, we have selected three multi-modal data-sets as illustrative examples to demonstrate the versatility of P-DCM to explain underlying causal relationships under the constraint of multiple physiological measurements. We aimed to include multi-modal data-sets acquired at different magnetic field strengths, containing different combinations of physiological variables next to the standard BOLD response, and possibly involving more than one level of experimental manipulation. Further, we favored averaged data with excellent signal-to-noise quality, which clearly manifest discrepancy between different physiological variables and between experimental conditions. There are certainly many more interesting published multi-modal data-sets that P-DCM could be further tested on. For example, we have limited our demonstration to human, monkey and cat data, however, there are many excellent multi-modal data measured in rodents (e.g., Kida et al., 2007; Boorman et al., 2010; Füchtemeier et al., 2010; Hyder et al., 2010; Hirano et al., 2011). Since a good correspondence was shown earlier between hemodynamic responses measured in cats and rats (see e.g., Zong et al., 2012) and in monkeys and rats (see e.g., Huber et al., 2015), we expect that P-DCM could perform well also if applied to rodent data. Furthermore, as model parameters are specified in terms of priors, it is also possible to account for interspecies differences in physiological parameters. For example, a higher baseline blood flow and volume influences the main transit time, which could be adjusted for different species (even though it was not necessary in our case, as the mean transit time was one of the free parameters).

All three data-sets represent evoked responses to longer sustained stimuli measured in the primary visual cortex. This choice allowed us to consider model assumptions that could be shared between all three experiments (as mentioned above) and fitting results obtained from these experiments could be more directly compared with each other. Additionally, in our previous aforementioned study (Havlicek et al., 2017a), the same static and flickering stimuli, including identical stimulus durations, provided high evidence that the BOLD response transients are mainly of neuronal and vascular origin (with negligible or zero contribution of CBF-CMRO<sub>2</sub> uncoupling). Therefore, we are in a good position to extend these results to the model assumptions applied in this paper, especially in the case of the first experiment. Similarly, the authors of the second experiment data-set showed in the independent study that with the same type of stimulus, the venous CBV response in the primary visual cortex of the cat exhibits much slower dynamics compared to the arterial CBV (Kim and Kim, 2011). Furthermore, other multi-modal data acquired in the primary visual cortex of monkey brain (i.e., comparable to the third experiment) showed that despite

deactivation of after stimulus cessation in the neuronal response, no or negligible post-stimulus undershoot was present in the CBF response but significantly present in the BOLD response (Pfeuffer et al., 2004; Zappe et al., 2008; Zaldivar et al., 2014). This supports our assumption and fitting result that CBF-venous CBV uncoupling can play important role in explaining the observed BOLD response transients also in third experiment. In general, the selected data may have revealed limitations of the structure of P-DCM and assumptions of specific parameters in the generative model. However, as the generative model was able to reproduce the experimental observations, P-DCM proves to be flexible enough to accommodate a wide range of multi-modal experimental data. Nevertheless, more work on novel data (including short stimuli and other brain regions) must be performed to further evaluate and develop current generative model used in P-DCM.

Finally, the second and third experiments were performed on anesthetized animals using isoflurane (i.e., a common anesthetic agent used in animal research). In general, anesthesia is known to influence the amplitude and shape of both neuronal and hemodynamic responses (Krautwald and Angenstein, 2012; Uludağ and Blinder, 2017). Under anesthesia using isoflurane, the neuronal baseline (i.e., the firing rate) is decreased and the neuronal responses exhibit smaller changes and can have more pronounced and faster adaptation compared to the awake state (Aksenov et al., 2015; Keller et al., 2017). This can potentially explain the large adaptation profiles of the neuronal responses in the second and third experiment, even though dynamic stimuli were applied (i.e., one would expect responses more comparable to responses to flickering rather than static stimuli in the first experiment). Having said this, larger differences in the shape of neuronal responses due to experimental modulations are expected during awake state (Haider et al., 2013; Bahmani et al., 2014; Keller et al., 2017), highlighting some benefits of human fMRI over animal studies under anesthesia. At the hemodynamic or NVC level, isoflurane based anesthesia leads to vasodilatation of mainly arteries and arterioles in the occipital areas, which results in increase of baseline CBF but even larger increase of baseline CBV; i.e., the mean transit time (in the microvasculature) is increased as well (Lorenz et al., 2001). Subsequently, the change in CBF due to activation is smaller and more delayed compared to awake state (Sicard et al., 2003; Pisauri et al., 2013). As a result, BOLD responses during anesthesia are also smaller. The anesthesia is expected to influence more the active mechanisms of the arterial compartment (in our model represented by CBF) than the passive mechanism of the venous compartment. Note that, theoretically, the same type of anesthetic agents could also have different effect on the neuronal responses and NVC between species, which could explain the large discrepancy between the second and third experiment (besides the obvious differences in stimulus type and stimulus duration). As P-DCM is able to optimize all stages of the physiological chain from the neuronal to the hemodynamic responses, it can also be useful in characterizing the differences in the physiological mechanisms during both anesthesia and the awake state.

## AUTHOR CONTRIBUTIONS

MH, KU, AR, and DI designed the experiment. MH and DI collected the data. MH and KU designed and performed data analysis. MH performed model inversions and created figures. MH, DI, AR, and KU wrote and revised the manuscript. All authors approved the final manuscript.

## ACKNOWLEDGMENTS

This work was financially supported by the VIDI grant (#452-11-002) of the Netherlands Organization for

Scientific Research (NWO). AR was supported by the European Research Council through an ERC Starting Grant (MULTICONNECT, #639938) and the Netherlands Organization for Scientific Research through a VIDI grant (#14637). All authors report no (financial) conflicts of interest.

## SUPPLEMENTARY MATERIAL

The Supplementary Material for this article can be found online at: <https://www.frontiersin.org/articles/10.3389/fnins.2017.00616/full#supplementary-material>

## REFERENCES

- Aksenov, D. P., Li, L., Miller, M. J., Iordanescu, G., and Wyrszcz, A. M. (2015). Effects of anesthesia on BOLD signal and neuronal activity in the somatosensory cortex. *J. Cereb. Blood Flow Metab.* 35, 1819–1826. doi: 10.1038/jcbfm.2015.130
- Attwell, D., Buchan, A. M., Charpak, S., Lauritzen, M., MacVicar, B. A., and Newman, E. A. (2010). Glial and neuronal control of brain blood flow. *Nature* 468, 232–243. doi: 10.1038/nature09613
- Attwell, D., and Iadecola, C. (2002). The neural basis of functional brain imaging signals. *Trends Neurosci.* 25, 621–625. doi: 10.1016/S0166-2236(02)02264-6
- Bahmani, H., Murayama, Y., Logothetis, N. K., and Keliris, G. A. (2014). Binocular flash suppression in the primary visual cortex of anesthetized and awake macaques. *PLoS ONE* 9:e107628. doi: 10.1371/journal.pone.0107628
- Bandettini, P. A., and Ungerleider, L. G. (2001). From neuron to BOLD: new connections. *Nat. Neurosci.* 4, 49–51. doi: 10.1038/nn0901-864
- Birn, R. M., Saad, Z. S., and Bandettini, P. A. (2001). Spatial heterogeneity of the nonlinear dynamics in the fMRI BOLD response. *Neuroimage* 14, 817–826. doi: 10.1006/nimg.2001.0873
- Boorman, L., Kennerley, A. J., Johnston, D., Jones, M., Zheng, Y., Redgrave, P., et al. (2010). Negative blood oxygen level dependence in the rat: a model for investigating the role of suppression in neurovascular coupling. *J. Neurosci.* 30, 4285–4294. doi: 10.1523/JNEUROSCI.6063-09.2010
- Boynton, G. M. (2011). Spikes, BOLD, attention, and awareness: a comparison of electrophysiological and fMRI signals in V1. *J. Vis.* 11:12 doi: 10.1167/11.5.12
- Boynton, G. M., Engel, S. A., Glover, G. H., and Heeger, D. J. (1996). Linear systems analysis of functional magnetic resonance imaging in human V1. *J. Neurosci.* 16, 4207–4221.
- Bush, K., and Cisler, J. (2013). Decoding neural events from fMRI BOLD signal: a comparison of existing approaches and development of a new algorithm. *Magn. Reson. Imaging* 31, 976–989. doi: 10.1016/j.mri.2013.03.015
- Butler, R., Bernier, P.-M., Lefebvre, J., Gilbert, G., and Whittingstall, K. (2017). Decorrelated input dissociates narrow band gamma power and BOLD in human visual cortex. *J. Neurosci.* 37, 5408–5418. doi: 10.1523/JNEUROSCI.3938-16.2017
- Buxton, R. B., Miller, K., Frank, L. R., and Wong, E. C. (1998a). “BOLD signal dynamics: the balloon model with viscoelastic effects,” in *Proceeding of ISMRM Conference* (Sydney, NSW), 1.
- Buxton, R. B., Wong, E. C., and Frank, L. R. (1998b). Dynamics of blood flow and oxygenation changes during brain activation: the balloon model. *Magn. Res. Med.* 39, 855–864. doi: 10.1002/mrm.1910390602
- Cauli, B., and Hamel, E. (2010). Revisiting the role of neurons in neurovascular coupling. *Front. Neuroenergetics* 2:9. doi: 10.3389/fnene.2010.00009
- Chen, J. J., and Pike, G. B. (2009). Origins of the BOLD post-stimulus undershoot. *NeuroImage* 46, 559–568. doi: 10.1016/j.neuroimage.2009.03.015
- Devor, A., Bandettini, P. A., Boas, D. A., Bower, J. M., Buxton, R. B., Cohen, L. B., et al. (2013). The challenge of connecting the dots in the B.R.A.I.N. *Neuron* 80, 270–274. doi: 10.1016/j.neuron.2013.09.008
- Devor, A., Tian, P., Nishimura, N., Teng, I. C., Hillman, E. M. C., Narayanan, S. N., et al. (2007). Suppressed neuronal activity and concurrent arteriolar vasoconstriction may explain negative blood oxygenation level-dependent signal. *J. Neurosci.* 27, 4452–4459. doi: 10.1523/JNEUROSCI.0134-07.2007
- Ding, N., Simon, J. Z., Shamma, S. A., and David, S. V. (2016). Encoding of natural sounds by variance of the cortical local field potential. *J. Neurosci.* 35, 2389–2398. doi: 10.1152/jn.00652.2015
- Donahue, M. J., Lu, H., Jones, C. K., Pekar, J. J., and Zijl, P. C. M. V. (2006). An account of the discrepancy between MRI and PET cerebral blood flow measures. A high-field MRI investigation. *NMR Biomed.* 19, 1043–1054. doi: 10.1002/nbm.1075
- Donahue, M. J., Stevens, R. D., de Boorder, M., Pekar, J. J., Hendrikse, J., and van Zijl, P. C. M. (2009). Hemodynamic changes after visual stimulation and breath holding provide evidence for an uncoupling of cerebral blood flow and volume from oxygen metabolism. *J. Cereb. Blood Flow Metab.* 29, 176–185. doi: 10.1038/jcbfm.2008.109
- Drew, P. J., Shih, A. Y., and Kleinfeld, D. (2011). Fluctuating and sensory-induced vasodynamics in rodent cortex extend arteriole capacity. *Proc. Natl. Acad. Sci. U.S.A.* 108, 8473–8478. doi: 10.1073/pnas.1100428108
- Frahm, J., Baudewig, J., Kallenberg, K., Kastrup, A., Merboldt, K. D., and Dechent, P. (2008). The post-stimulation undershoot in BOLD fMRI of human brain is not caused by elevated cerebral blood volume. *Neuroimage* 40, 473–481. doi: 10.1016/j.neuroimage.2007.12.005
- Frahm, J., Krüger, G., Merboldt, K. D., and Kleinschmidt, A. (1996). Dynamic uncoupling and recoupling of perfusion and oxidative metabolism during focal brain activation in man. *Magn. Reson. Med.* 35, 143–148. doi: 10.1002/mrm.1910350202
- Friston, K. J., Fletcher, P., Josephs, O., Holmes, A., Rugg, M. D., and Turner, R. (1998). Event-related fMRI: characterizing differential responses. *Neuroimage* 7, 30–40. doi: 10.1006/nimg.1997.0306
- Friston, K. J., Harrison, L., and Penny, W. (2003). Dynamic causal modelling. *Neuroimage* 19, 1273–1302. doi: 10.1016/S1053-8119(03)00202-7
- Friston, K. J., Mechelli, A., Turner, R., and Price, C. J. (2000). Nonlinear responses in fMRI: the balloon model, volterra kernels, and other hemodynamics. *NeuroImage* 12, 466–477. doi: 10.1006/nimg.2000.0630
- Friston, K. J., Preller, K. H., Mathys, C., Cagnan, H., Heinze, J., Razi, A., et al. (2017). Dynamic causal modelling revisited. *NeuroImage* doi: 10.1016/j.neuroimage.2017.02.045. [Epub ahead of print].
- Friston, K. J., Holmes, A. P., Worsley, K. J., Poline, J. P., Frith, C. D., and Frackowiak, R. S. J. (1995). Statistical parametric maps in functional imaging: a general linear approach. *Hum. Brain Mapp.* 2, 189–210. doi: 10.1002/hbm.460020402
- Friston, K., Mattout, J., Trujillo-Barreto, N., Ashburner, J., and Penny, W. (2007). Variational free energy and the Laplace approximation. *Neuroimage* 34, 220–234. doi: 10.1016/j.neuroimage.2006.08.035
- Füchtemeier, M., Leithner, C., Offenhauser, N., Foddis, M., Kohl-Bareis, M., Dirnagl, U., et al. (2010). Elevating intracranial pressure reverses the decrease in deoxygenated hemoglobin and abolishes the post-stimulus overshoot upon somatosensory activation in rats. *Neuroimage* 52, 445–454. doi: 10.1016/j.neuroimage.2010.04.237
- Gagnon, L., Sakadžić, S., Lesage, F., Musacchia, J. J., Lefebvre, J., Fang, Q., et al. (2015). Quantifying the microvascular origin of BOLD-fMRI from first

- principles with two-photon microscopy and an oxygen-sensitive nanoprobe. *J. Neurosci.* 35, 3663–3675. doi: 10.1523/JNEUROSCI.3555-14.2015
- Gaudes, C., Petridou, N., Dryden, I. L., Bai, L., Francis, S. T., and Gowland, P. A. (2011). Detection and characterization of single-trial fMRI BOLD responses: paradigm free mapping. *Hum. Brain Mapp.* 1418, 1400–1418. doi: 10.1002/hbm.21116
- Goense, J. B., and Logothetis, N. K. (2006). Laminar specificity in monkey V1 using high-resolution SE-fMRI. *Magn. Reson. Imaging* 24, 381–392. doi: 10.1016/j.mri.2005.12.032
- Goense, J. B. M., and Logothetis, N. K. (2008). Neurophysiology of the BOLD fMRI signal in awake monkeys. *Curr. Biol.* 18, 631–640. doi: 10.1016/j.cub.2008.03.054
- Gouws, A. D., Alvarez, I., Watson, D. M., Uesaki, M., Rodgers, J., and Morland, A. B. (2014). On the role of suppression in spatial attention: evidence from negative BOLD in human subcortical and cortical. *J. Neurosci.* 34, 10347–10360. doi: 10.1523/JNEUROSCI.0164-14.2014
- Grill-Spector, K., and Malach, R. (2001). fMR-adaptation: a tool for studying the functional properties of human cortical neurons. *Acta Psychol. (Amst)* 107, 293–321. doi: 10.1016/S0001-6918(01)00019-1
- Grubb, R. L., Raichle, M. E., Eichling, J. O., and Ter-Pogossian, M. M. (1974). The effects of changes in PaCO<sub>2</sub> cerebral blood volume, blood flow, and vascular mean transit time. *Stroke* 5, 630–639. doi: 10.1161/01.STR.5.5.630
- Haider, B., Häusser, M., and Carandini, M. (2013). Inhibition dominates sensory responses in the awake cortex. *Nature* 493, 2–8. doi: 10.1038/nature12370
- Havlicek, M., Ivanov, D., Poser, B. A., and Uludağ, K. (2017a). Echo-time dependence of the BOLD response transients—a window into brain functional physiology. *Neuroimage* 159, 355–370. doi: 10.1016/j.neuroimage.2017.07.034
- Havlicek, M., Roebroeck, A., Friston, K., Gardumi, A., Ivanov, D., and Uludağ, K. (2015). Physiologically informed dynamic causal modeling of fMRI data. *Neuroimage* 122, 355–372. doi: 10.1016/j.neuroimage.2015.07.078
- Havlicek, M., Roebroeck, A., Friston, K. J., Gardumi, A., Ivanov, D., and Uludağ, K. (2017b). On the importance of modeling fMRI transients when estimating effective connectivity: A dynamic causal modeling study using ASL data. *NeuroImage* 155, 217–233. doi: 10.1016/j.neuroimage.2017.03.017
- Haxby, J. V. (2012). NeuroImage multivariate pattern analysis of fMRI: The early beginnings. *Neuroimage* 62, 852–855. doi: 10.1016/j.neuroimage.2012.03.016
- Hillman, E. M. (2014). Coupling mechanism and significance of the BOLD signal: a status report. *Annu. Rev. Neurosci.* 37, 161–181. doi: 10.1146/annurev-neuro-071013-014111
- Hirano, Y., Stefanovic, B., and Silva, A. C. (2011). Spatiotemporal evolution of the functional magnetic resonance imaging response to ultrashort stimuli. *J. Neurosci.* 31, 1440–1447. doi: 10.1523/JNEUROSCI.3986-10.2011
- Hoge, R. D., Atkinson, J., Gill, B., Crelier, G. R., Marrett, S., and Pike, G. B. (1999). Stimulus-dependent BOLD and perfusion dynamics in human V1. *NeuroImage* 9(6 Pt 1), 573–585. doi: 10.1006/nimg.1999.0443
- Hua, J., Stevens, R. D., Huang, A. J., Pekar, J. J., and Zijl, P. C. M. V. (2011). Physiological origin for the BOLD poststimulus undershoot in human brain: vascular compliance versus oxygen metabolism. *J. Cereb. Blood Flow Metab.* 31, 1599–1611. doi: 10.1038/jcbfm.2011.35
- Huber, L., Goense, J., Kennerley, A. J., Ivanov, D., Krieger, S. N., Lepsiens, J., et al. (2014a). Investigation of the neurovascular coupling in positive and negative BOLD responses in human brain at 7T. *Neuroimage* 97, 349–362. doi: 10.1016/j.neuroimage.2014.04.022
- Huber, L., Goense, J., Kennerley, A. J., Trampel, R., Guidi, M., Reimer, E., et al. (2015). Cortical lamina-dependent blood volume changes in human brain at 7T. *Neuroimage* 107, 23–33. doi: 10.1016/j.neuroimage.2014.11.046
- Huber, L., Ivanov, D., Krieger, S. N., Streicher, M. N., Mildner, T., Poser, B. A., et al. (2014b). Slab-selective, BOLD-corrected VASO at 7 Tesla provides measures of cerebral blood volume reactivity with high signal-to-noise ratio. *Magn. Reson. Med.* 72, 137–148. doi: 10.1002/mrm.24916
- Hyder, F., Sanganahalli, B. G., Herman, P., Coman, D., Maandag, N. J. G., Behar, K. L., et al. (2010). Neurovascular and neurometabolic couplings in dynamic calibrated fMRI: transient oxidative neuroenergetics for block-design and event-related paradigms. *Front. Neuroenergetics* 2:18. doi: 10.3389/fnene.2010.00018
- Jin, T., and Kim, S.-G. (2008). Cortical layer-dependent dynamic blood oxygenation, cerebral blood flow and cerebral blood volume responses during visual stimulation. *Neuroimage* 43, 1–9. doi: 10.1016/j.neuroimage.2008.06.029
- Keller, A. J., Houlton, R., Kampa, B. M., Lesica, N. A., Mrsic-flogel, T. D., Keller, G. B., et al. (2017). Stimulus relevance modulates contrast adaptation in visual cortex. *Elife* 6, 4–15. doi: 10.7554/elife.21589
- Kida, I., Rothman, D. L., and Hyder, F. (2007). Dynamics of changes in blood flow, volume, and oxygenation: implications for dynamic functional magnetic resonance imaging calibration. *J. Cereb. Blood Flow Metab.* 27, 690–696. doi: 10.1038/sj.jcbfm.9600409
- Kida, I., and Yamamoto, T. (2008). Stimulus frequency dependence of blood oxygenation level-dependent functional magnetic resonance imaging signals in the somatosensory cortex of rats. *Neurosci. Res.* 62, 25–31. doi: 10.1016/j.neures.2008.05.006
- Kim, D.-S., Ronen, I., Olman, C., Kim, S.-G., Ugurbil, K., and Toth, L. J. (2004). Spatial relationship between neuronal activity and BOLD functional MRI. *Neuroimage* 21, 876–885. doi: 10.1016/j.neuroimage.2003.10.018
- Kim, S.-G. (1995). Quantification of relative cerebral blood flow change by flow-sensitive alternating inversion recovery (FAIR) technique: application to functional mapping. *Magn. Reson. Med.* 34, 293–301. doi: 10.1002/mrm.1910340303
- Kim, S.-G., and Ogawa, S. (2012). Biophysical and physiological origins of blood oxygenation level-dependent fMRI signals. *J. Cereb. Blood Flow Metab.* 32, 1188–1206. doi: 10.1038/jcbfm.2012.23
- Kim, T., and Kim, S.-G. (2011). Temporal dynamics and spatial specificity of arterial and venous blood volume changes during visual stimulation: implication for BOLD quantification. *J. Cereb. Blood Flow Metab.* 31, 1211–1222. doi: 10.1038/jcbfm.2010.226
- Kim, T., Masamoto, K., Fukuda, M., Vazquez, A., and Kim, S.-G. (2010). Frequency-dependent neural activity, CBF, and BOLD fMRI to somatosensory stimuli in isoflurane-anesthetized rats. *Neuroimage* 52, 224–233. doi: 10.1016/j.neuroimage.2010.03.064
- Krautwald, K., and Angenstein, F. (2012). Low frequency stimulation of the perforant pathway generates anesthesia-specific variations in neural activity and BOLD responses in the rat dentate gyrus. *J. Cereb. Blood Flow Metab.* 32, 291–305. doi: 10.1038/jcbfm.2011.126
- Krekelberg, B., Boynton, G. M., and van Wezel, R. J. A. (2006). Adaptation: from single cells to BOLD signals. *Trends Neurosci.* 29, 250–256. doi: 10.1016/j.tins.2006.02.008
- Kriegeskorte, N., Mur, M., and Bandettini, P. (2008). Representational similarity analysis—connecting the branches of systems neuroscience. *Front. Syst. Neurosci.* 2:4. doi: 10.3389/neuro.06.004.2008
- Krüger, G., Kleinschmidt, A., and Frahm, J. (1996). Dynamic MRI sensitized to cerebral blood oxygenation and flow during sustained activation. *Magn. Reson. Med.* 35, 4. doi: 10.1002/mrm.1910350602
- Lauritzen, M. (2005). Reading vascular changes in brain imaging: is dendritic calcium the key? *Nature reviews. Neuroscience* 6, 77–85. doi: 10.1038/nrn1589
- Liu, T. T., and Brown, G. G. (2007). Measurement of cerebral perfusion with arterial spin labeling: part 1. Methods. *J. Int. Neuropsychol. Soc.* 13, 517–525. doi: 10.1017/S1355617707070646
- Logothetis, N. K. (2002). The neural basis of the blood-oxygen-level-dependent functional magnetic resonance imaging signal. *Philos. Trans. R. Soc. Lond. Ser. B Biol. Sci.* 357, 1003. doi: 10.1098/rstb.2002.1114
- Logothetis, N. K. (2008). What we can do and what we cannot do with fMRI. *Nature* 453, 869–878. doi: 10.1038/nature06976
- Logothetis, N. K., Augath, M., Murayama, Y., Rauch, A., Sultan, F., Goense, J., et al. (2010). The effects of electrical microstimulation on cortical signal propagation. *Nat. Neurosci.* 13, 1283–1291. doi: 10.1038/nn.2631
- Logothetis, N. K., Pauls, J., Augath, M., Trinath, T., and Oeltermann, A. (2001). Neurophysiological investigation of the basis of the fMRI signal. *Nature* 412, 150–157. doi: 10.1038/35084005
- Logothetis, N. K., and Wandell, B. A. (2004). Interpreting the BOLD signal. *Annu. Rev. Physiol.* 66, 735–769. doi: 10.1146/annurev.physiol.66.082602.092845
- Lorenz, I. H., Kolbitsch, C., Hormann, C., Luger, T. J., Schocke, M., Felber, S., et al. (2001). Influence of equanaesthetic concentrations of nitrous oxide and isoflurane on regional cerebral blood flow, regional cerebral blood volume, and

- regional mean transit time in human volunteers. *Br. J. Anaesth.* 87, 691–698. doi: 10.1093/bja/87.5.691
- Lu, H., Golay, X., Pekar, J. J., and Van Zijl, P. C. M. (2003). Functional magnetic resonance imaging based on changes in vascular space occupancy. *Magn. Reson. Med.* 50, 263–274. doi: 10.1002/mrm.10519
- Lu, H., Golay, X., Pekar, J. J., and Van Zijl, P. C. M. (2004). Sustained poststimulus elevation in cerebral oxygen utilization after vascular recovery. *J. Cereb. Blood Flow Metab.* 24, 764–770. doi: 10.1097/01.WCB.0000124322.60992.5C
- Magri, C., Schridde, U., Murayama, Y., Panzeri, S., and Logothetis, N. K. (2012). The amplitude and timing of the BOLD signal reflects the relationship between local field potential power at different frequencies. *J. Neurosci.* 32, 1395–1407. doi: 10.1523/JNEUROSCI.3985-11.2012
- Mandeville, J. B., Marota, J. J. A., Ayata, C., Zaharchuk, G., Moskowitz, M. A., Rosen, B. R., et al. (1999). Evidence of a cerebrovascular postarteriole windkessel with delayed compliance. *J. Cereb. Blood Flow Metab.* 19, 679–689. doi: 10.1097/000004647-199906000-00012
- Mandeville, J. B., Marota, J. J., Kosofsky, B. E., Keltner, J. R., Weissleder, R., Rosen, B. R., et al. (1998). Dynamic functional imaging of relative cerebral blood volume during rat forepaw stimulation. *Magn. Reson. Med.* 39, 615–624. doi: 10.1002/mrm.1910390415
- Markram, H., Toledo-Rodriguez, M., Wang, Y., Gupta, A., Silberberg, G., and Wu, C. (2004). Interneurons of the neocortical inhibitory system. *Nature reviews. Neuroscience* 5, 793–807. doi: 10.1038/nrn1519
- Marreiros, A. C., Kiebel, S. J., and Friston, K. J. (2008). Dynamic causal modelling for fMRI: a two-state model. *Neuroimage* 39, 269–278. doi: 10.1016/j.neuroimage.2007.08.019
- Mayhew, S. D., Mullinger, K. J., Bagshaw, A. P., Bowtell, R., and Francis, S. T. (2014). Investigating intrinsic connectivity networks using simultaneous BOLD and CBF measurements. *Neuroimage* 99, 111–121. doi: 10.1016/j.neuroimage.2014.05.042
- Muckli, L. (2010). What are we missing here? Brain imaging evidence for higher cognitive functions in primary visual cortex v1. *Int. J. Imaging Syst. Technol.* 20, 131–139. doi: 10.1002/ima.20236
- Mullinger, K. J., Cherukara, M. T., Buxton, R. B., Francis, S. T., and Mayhew, S. D. (2017). Post-stimulus fMRI and EEG responses: Evidence for a neuronal origin hypothesised to be inhibitory. *Neuroimage* 157, 388–399. doi: 10.1016/j.neuroimage.2017.06.020
- Mullinger, K. J., Mayhew, S. D., Bagshaw, A. P., Bowtell, R., and Francis, S. T. (2013). Poststimulus undershoots in cerebral blood flow and BOLD fMRI responses are modulated by poststimulus neuronal activity. *Proc. Natl. Acad. Sci. U.S.A.* 110, 13636–13641. doi: 10.1073/pnas.122110
- Mullinger, K. J., Mayhew, S. D., Bagshaw, A. P., Bowtell, R., and Francis, S. T. (2014). Evidence that the negative BOLD response is neuronal in origin: a simultaneous EEG-BOLD-CBF study in humans. *Neuroimage* 94, 263–274. doi: 10.1016/j.neuroimage.2014.02.029
- Mumford, J. A., Hernandez-Garcia, L., Lee, G. R., and Nichols, T. E. (2006). Estimation efficiency and statistical power in arterial spin labeling fMRI. *Neuroimage* 33, 103–114. doi: 10.1016/j.neuroimage.2006.05.040
- Niessing, J., Ebisch, B., Schmidt, K. E., Niessing, M., Singer, W., and Galuske, R. A. W. (2005). Hemodynamic signals correlate tightly with synchronized gamma oscillations. *Science* 209, 948–951. doi: 10.1126/science.1110948
- Ogawa, S., Lee, T. M., Kay, A. R., and Tank, D. W. (1990). Brain magnetic resonance imaging with contrast dependent on blood oxygenation. *Proc. Natl. Acad. Sci. U.S.A.* 87, 9868–9872. doi: 10.1073/pnas.87.24.9868
- Ozaki, T. (1992). A bridge between nonlinear time series models and nonlinear stochastic dynamical systems: a local linearization approach. *Stat. Sin.* 2, 113–135.
- Pérez-González, D., and Malmierca, M. S. (2014). Adaptation in the auditory system: an overview. *Front. Integr. Neurosci.* 8:19. doi: 10.3389/fnint.2014.00019
- Pfeuffer, J., Merkle, H., Beyerlein, M., Steudel, T., and Logothetis, N. K. (2004). Anatomical and functional MR imaging in the macaque monkey using a vertical large-bore 7 Tesla setup. *Magn. Reson. Imaging* 22, 1343–1359. doi: 10.1016/j.mri.2004.10.004
- Pisauro, M. A., Dhruv, N. T., Carandini, M., and Benucci, A. (2013). Fast hemodynamic responses in the visual cortex of the awake mouse. *J. Neurosci.* 33, 18343–18351. doi: 10.1523/JNEUROSCI.2130-13.2013
- Poser, B. A., Mierlo, E. V., and Norris, D. G. (2011). Exploring the post-stimulus undershoot with spin-echo fMRI: implications for models of neurovascular response. *Hum. Brain Mapp.* 33, 141–153. doi: 10.1002/hbm.21003
- Riera, J. J., and Sumiyoshi, A. (2010). Brain oscillations: ideal scenery to understand the neurovascular coupling. *Curr. Opin. Neurol.* 23, 374–381. doi: 10.1097/WCO.0b013e32833b769f
- Rosa, M. J., Kilner, J. M., and Penny, W. D. (2011). Bayesian comparison of neurovascular coupling models using EEG-fMRI. *PLoS Comput. Biol.* 7:e1002070. doi: 10.1371/journal.pcbi.1002070
- Ryali, S., Supekar, K., Chen, T., and Menon, V. (2011). Multivariate dynamical systems models for estimating causal interactions in fMRI. *Neuroimage* 54, 807–823. doi: 10.1016/j.neuroimage.2010.09.052
- Sadaghiani, S., Ugurbil, K., and Uludağ, K. (2009). Neural activity-induced modulation of BOLD poststimulus undershoot independent of the positive signal. *Magn. Reson. Imaging* 27, 1030–1038. doi: 10.1016/j.mri.2009.04.003
- Shmuel, A., Augath, M., Oeltermann, A., and Logothetis, N. K. (2006). Negative functional MRI response correlates with decreases in neuronal activity in monkey visual area V1. *Nat. Neurosci.* 9, 569–577. doi: 10.1038/nn1675
- Shmuel, A., Yacoub, E., Pfeuffer, J., Van de Moortele, P. F., Adriany, G., Hu, X., et al. (2002). Sustained negative BOLD, blood flow and oxygen consumption response and its coupling to the positive response in the human brain. *Neuron* 36, 1195–1210. doi: 10.1016/S0896-6273(02)01061-9
- Sicard, K., Shen, Q., Brevard, M. E., Sullivan, R., Ferris, C. F., King, J. A., et al. (2003). Regional cerebral blood flow and BOLD responses in conscious and anesthetized rats under basal and hypercapnic conditions: implications for functional MRI studies. *J. Cereb. Blood Flow Metab.* 23, 472–481. doi: 10.1097/01.WCB.0000054755.93668.20
- Smith, J. F., Pillai, A., Chen, K., Horwitz, B., and Calhoun, V. D. (2012). Effective connectivity modeling for fMRI: six issues and possible solutions using linear dynamic systems. *Front. Syst. Neurosci.* 5:104. doi: 10.3389/fnsys.2011.00104
- Stephan, K. E., Schlagenhauf, F., Huys, Q. J. M., Raman, S., Aponte, E. A., Brodersen, K. H., et al. (2017). Computational neuroimaging strategies for single patient predictions. *Neuroimage* 145, 180–199. doi: 10.1016/j.neuroimage.2016.06.038
- Uludağ, K., Dubowitz, D. J., Yoder, E. J., Restom, K., Liu, T. T., and Buxton, R. B. (2004). Coupling of cerebral blood flow and oxygen consumption during physiological activation and deactivation measured with fMRI. *Neuroimage* 23, 148–155. doi: 10.1016/j.neuroimage.2004.05.013
- Uludağ, K., Müller-Bierl, B., and Ugurbil, K. (2009). An integrative model for neuronal activity-induced signal changes for gradient and spin echo functional imaging. *Neuroimage* 48, 150–165. doi: 10.1016/j.neuroimage.2009.05.051
- Uludağ, K., and Blinder, P. (2017). Linking brain vascular physiology to hemodynamic response in ultra-high field MRI. *NeuroImage*. doi: 10.1016/j.neuroimage.2017.02.063. [Epub ahead of print].
- Valdes Sosa, P. A., Sanchez Bornot, J. M., Sotero, R. C., Iturria Medina, Y., Aleman Gomez, Y., Bosch Bayard, J., et al. (2009). Model driven EEG/fMRI fusion of brain oscillations. *Hum. Brain Mapp.* 30, 2701–2721. doi: 10.1002/hbm.20704
- van Zijl, P. C. M., Hua, J., and Lu, H. (2012). The BOLD post-stimulus undershoot, one of the most debated issues in fMRI. *Neuroimage* 62, 1092–1102. doi: 10.1016/j.neuroimage.2012.01.029
- Wong, E. C., Buxton, R. B., and Frank, L. R. (1997). Implementation of quantitative perfusion imaging techniques for functional brain mapping using pulsed arterial spin labeling. *NMR Biomed.* 10, 237–249. doi: 10.1002/(SICI)1099-1492(199706/08)10:4/5<237::AID-NBM475>3.0.CO;2-X
- Yacoub, E., Ugurbil, K., and Harel, N. (2006). The spatial dependence of the poststimulus undershoot as revealed by high-resolution BOLD-

- and CBV-weighted fMRI. *J. Cereb. Blood Flow Metab.* 26, 634–644. doi: 10.1038/sj.jcbfm.9600239
- Zaldivar, D., Rauch, A., Whittingstall, K., and Logothetis, N. K. (2014). Report dopamine-induced dissociation of BOLD and neural activity in macaque visual cortex. *Curr. Biol.* 24, 2805–2811. doi: 10.1016/j.cub.2014.1.006
- Zappe, A. C., Pfeuffer, J., Merkle, H., Logothetis, N. K., and Goense, J. B. M. (2008). The effect of labeling parameters on perfusion-based fMRI in non-human primates. *J. Cereb. Blood Flow Metab.* 28, 640–652. doi: 10.1038/sj.jcbfm.9600564
- Zhao, F., Jin, T., Wang, P., and Kim, S.-G. (2007). Improved spatial localization of post-stimulus BOLD undershoot relative to positive BOLD. *Neuroimage* 34, 1084–1092. doi: 10.1016/j.neuroimage.2006.1.016
- Zong, X., Kim, T., and Kim, S.-G. (2012). Contributions of dynamic venous blood volume versus oxygenation level changes to BOLD fMRI. *Neuroimage* 60, 2238–2246. doi: 10.1016/j.neuroimage.2012.02.052

**Conflict of Interest Statement:** The authors declare that the research was conducted in the absence of any commercial or financial relationships that could be construed as a potential conflict of interest.

Copyright © 2017 Havlicek, Ivanov, Roebroeck and Uludağ. This is an open-access article distributed under the terms of the Creative Commons Attribution License (CC BY). The use, distribution or reproduction in other forums is permitted, provided the original author(s) or licensor are credited and that the original publication in this journal is cited, in accordance with accepted academic practice. No use, distribution or reproduction is permitted which does not comply with these terms.



# Safety of Simultaneous Scalp or Intracranial EEG during MRI: A Review

Hassan B. Hawsawi<sup>1,2,3\*</sup>, David W. Carmichael<sup>4</sup> and Louis Lemieux<sup>1,2</sup>

<sup>1</sup> Department of Clinical and Experimental Epilepsy, UCL Institute of Neurology, London, United Kingdom, <sup>2</sup> MRI Unit, Epilepsy Society, Chalfont St. Peter, United Kingdom, <sup>3</sup> Department of Medical Imaging, King Abdullah Medical City (KAMC), Makkah, Saudi Arabia, <sup>4</sup> Developmental Imaging and Biophysics Section, UCL Institute of Child Health, London, United Kingdom

## OPEN ACCESS

### Edited by:

Federico Giove,  
Centro Fermi, Italy

### Reviewed by:

Leonardo Angelone,  
United States Food and Drug  
Administration, United States  
Wim Van Paesschen,  
University Hospitals Leuven, Belgium

### \*Correspondence:

Hassan B. Hawsawi  
hassan.hawsawi.15@ucl.ac.uk

### Specialty section:

This article was submitted to  
Biomedical Physics,  
a section of the journal  
*Frontiers in Physics*

Received: 17 May 2017

Accepted: 04 September 2017

Published: 10 October 2017

### Citation:

Hawsawi HB, Carmichael DW and  
Lemieux L (2017) Safety of  
Simultaneous Scalp or Intracranial  
EEG during MRI: A Review.  
*Front. Phys.* 5:42.  
doi: 10.3389/fphy.2017.00042

Understanding the brain and its activity is one of the great challenges of modern science. Normal brain activity (cognitive processes, etc.) has been extensively studied using electroencephalography (EEG) since the 1930's, in the form of spontaneous fluctuations in rhythms, and patterns, and in a more experimentally-driven approach in the form of event-related potentials (ERPs) allowing us to relate scalp voltage waveforms to brain states and behavior. The use of EEG recorded during functional magnetic resonance imaging (EEG-fMRI) is a more recent development that has become an important tool in clinical neuroscience, for example for the study of epileptic activity. The purpose of this review is to explore the magnetic resonance imaging safety aspects specifically associated with the use of scalp EEG and other brain-implanted electrodes such as intracranial EEG electrodes when they are subjected to the MRI environment. We provide a theoretical overview of the mechanisms at play specifically associated with the presence of EEG equipment connected to the subject in the MR environment, and of the resulting health hazards. This is followed by a survey of the literature on the safety of scalp or invasive EEG-fMRI data acquisitions across field strengths, with emphasis on the practical implications for the safe application of the techniques; in particular, we attempt to summarize the findings in terms of acquisition protocols when possible.

**Keywords:** radiofrequency safety, gradient safety, thermal injury, MR safety, electroencephalography, implanted electrodes, epilepsy, neuroscience

## INTRODUCTION

Electroencephalography (EEG) is a technique to record the brain's electrical activity. Since its introduction by Berger in 1929 and replication by Adrian in 1934 [1], this technique has evolved from recording electrophysiological of the brain activities to clinical use including identification of epileptic seizures, non-epileptic seizures, migraine and movement disorders based on the spontaneous changes in the rhythms and shapes of the event-related potentials (ERPs). The activity of neurons, and to a lesser extent glial cells, produces electrical and magnetic fields [2]. In epilepsy, recording patients having a seizure using scalp EEG is a clinical tool of the utmost importance especially when used in conjunction with video recording to better identify the seizure onset. Two types of EEG are available: scalp EEG, the non-invasive tool capable of recording brain activity, mostly originating in the superficial neocortex, and intracranial EEG (icEEG), an invasive technique requiring surgery with exquisite sensitivity, although more restricted to the immediate

vicinity of the implanted electrodes [2–4]. According to Tao et al. [5], recognizable activity recorded on scalp EEG must originate from at least  $10\text{ cm}^2$  of cortical area. However, volume conduction and the attenuating effect of the skull make it difficult to relate these signals to their specific origin, forcing the investigator to make assumptions on the nature of the generator, combined with models of the associated fields: this is the inverse problem of EEG (MEG) [2]. IcEEG is capable of detecting activities generated in the mesial cortex during a seizure [6, 7]. In addition, icEEG has the ability to detect weaker brain activity that sometimes cannot be identified in scalp EEG and MEG and it can only detect activity occurring within a set of small brain regions defined by patient clinical needs [2, 3].

Functional brain imaging can help to localize regions responsible for epileptic discharges; this includes positron emission tomography (PET), single photon emission computed tomography (SPECT) and functional magnetic resonance imaging (fMRI). fMRI reveals changes in the blood oxygenation level [8] by measuring the local hemodynamic variations through detecting the changes in the blood oxygen level dependent (BOLD) signals that can be seen clearly during brain activities [9]. fMRI can be used to identify regions involved in the generation of epileptic discharges, particularly when combined with EEG: Simultaneous scalp EEG-fMRI [10, 11] or icEEG-fMRI [12–17]. However, as with all simultaneous multimodal data acquisitions methodologies, data quality can be compromised due to interactions between the two systems, and the subject [18].

The potential benefits of simultaneous scalp EEG-fMRI or icEEG-fMRI are plentiful. However, there are several risks associated with the three types of magnetic fields used by MRI: the static magnetic field ( $B_0$ ), time-varying magnetic gradient field and radiofrequency (RF) magnetic field ( $B_1$ ). The greatest risk is generally heating which is related to RF electromagnetic field-induced currents that cause increased power deposition in the tissue in the vicinity of metallic EEG or icEEG electrodes when applying concurrent fMRI [19]. In addition heating can also occur as a result of the induced currents by the switching magnetic fields [20]. These problems can cause tissue burns in the locations adjacent to the metallic electrodes [20, 21].

The main objective of this review is to provide a survey of the current knowledge regarding the safety of placing EEG electrodes in contact with or within human subjects, within the MRI scanner; although our primary interest is in the use of non-invasive (scalp) and invasive EEG electrodes, we consider studies of other brain implants such as electrodes for deep brain stimulation (DBS), to the extent that studies involving those are directly relevant to the topic of this review. Specifically, depth intra-cranial EEG electrodes are very similar to DBS electrodes, geometrically and in their composition, and therefore we believe that any published work on the safety implications of placing DBS electrodes in the MRI environment must be included in this review.

The article is structured as follows: first, we briefly review the health hazards that are associated with the technique of simultaneous scalp EEG-fMRI and icEEG-fMRI after which we discuss the main theoretical aspects of EEG equipment when subjected to MRI. Second, we list the factors that can affect the

increase of the heating of the scalp EEG and implanted electrodes inside the MRI that are subjects of previous and current research studies. Finally, we follow that by reviewing the appropriate acquisition protocol.

## HEALTH HAZARDS RELATED TO CURRENT FLOW IN, AND IN THE PRESENCE OF CONDUCTIVE ELECTRODES IN CONTACT WITH OR WITHIN, HUMAN TISSUE: A BRIEF SURVEY OF OBSERVATIONS

Observations from the use of diathermy show that electrical currents of the order of 1 A or greater may cause skin burns around metallic electrodes; similar effects have been observed in the vicinity of electrodes in contact with tissue placed in the MR environment [22–25]. Ulcers can be caused due to electrolysis from direct currents (DC) [20, 26]. Electro-motive forces and thermal skin damage are caused at the electric field of  $3,500\text{ V/m}$  [25, 27]. Electric shock or stimulation under the frequency of 100 KHz and tissue heating in the frequencies higher than 100 KHz occur as a result of current flow to the body in contact with a metallic objects [20, 28–31]. Human subjects reported mild neural stimulation when exposed to gradient field changes of  $61\text{ Ts}^{-1}$  [32]. Other health effects of the switching gradients in the body include nerve or muscle stimulation [33–35]. Schaefer et al. estimated that nerve simulation might occur during exposure to an electric field of  $0.0006\text{ Volts/m}$  or greater assuming the radius of the patient  $0.2\text{ m}$  [33]. Prolonged RF induced heating for up to  $5^\circ\text{C}$  (over the normal body temperature) would damage the neurons [34, 36] and that depends on the sensitivity of the tissue in the brain [37, 38].

We are not aware of any officially recorded report of significant injury directly linked to EEG recording inside the MR scanner in the scientific literature, European or North American regulatory authority databases or those of equipment manufacturers (Robert Stormer, Brain Products GmbH; personal communication). However, there are reports of ECG electrode-related burns sometimes placed during EEG-fMRI recording sessions [39].

## THE SOURCES OF HEALTH HAZARDS IN SIMULTANEOUS EEG AND FMRI: THEORETICAL CONSIDERATIONS

The sources of health hazards associated with the use of EEG during MRI scanning have been studied since the technique's first published demonstrations of feasibility of recording EEG on  $0.3\text{ T}$  MRI systems [40, 41] and then continued as EEG-fMRI was developed on  $1.5\text{ T}$  scanners [42–48]. The same general safety considerations apply to EEG-fMRI as for all applications of MR to human subjects. In summary, safety issues might arise not only from the physical forces or from magnetic fields on these foreign objects but also inductive interactions between magnetic fields and the body and other components placed within the field

[31]. In addition, capacitive interactions occur between the RF electrical field and the human body close to RF transmit coils in the form of (time varying) charge accumulation [20].

As with the introduction of any device not part of the MR system in the scanner, extra precautions are advised and careful consideration of any potential additional health hazard specifically related to the device should be given: ballistic (projectile) and electrical device safety issues and electromagnetic compatibility; these will not be the subject of this review and the reader should consult standard texts on MR safety and electrical device safety (as applied outside the MR environment), for example, [31, 49, 50]. In the case of EEG recording, we have the introduction of electrically conductive circuits consisting of powered amplifiers electrically connected to the patient via leads and electrodes attached to the patient's body and additional risks can arise from induced currents. Such electrically active components are the subject of electromagnetic compatibility regulations and standards such as produced by the International Electrotechnical Commission (IEC) ([www.iec.ch](http://www.iec.ch)), International Organization for Standardization (ISO) ([www.iso.org](http://www.iso.org)), the US Federal Communications Commission (FCC) ([www.fcc.gov](http://www.fcc.gov)) and the Society of Automotive Engineers (SAE) ([www.sae.org](http://www.sae.org)). The conductive loops in EEG equipment typically contain high impedance components in the amplifiers and low impedance segments [20].

Let us consider the exposure of conductive to the electromagnetic fields involved in the acquisition of MR images, namely the magnetic ( $B$ ) and electric ( $E$ ) fields. Interactions with different types of materials arise when EEG electrodes and leads are introduced in the three types of magnetic fields used in MRI. First, the strong and uniform static magnetic field ( $B_0$ ) interacts with different materials that have specific magnetic properties that include: diamagnetic, paramagnetic and ferromagnetic materials, resulting in mechanical forces (the aforementioned ballistic effects) or torques. Diamagnetic materials are repelled by magnetic field forces as a result of these forces. The paramagnetic or ferromagnetic materials are attracted by the forces of the magnetic fields. Second, RF electromagnetic fields, that are produced by RF coils during the MR sequence, contains two components; one magnetic ( $B_1$ ), and the second non-conservative electric component [20, 51]. For a circularly polarized  $B_1$ , the electrical component can be expressed as follows:

$$E_{RF} = \omega_0 B_1 (y \sin(\omega_0 t) + x \cos(\omega_0 t)) \hat{z} \quad (1)$$

Where  $\omega_0$  is the Larmor frequency (63.76 MHz and 127.7 for 1.5 T and 3 T, respectively) and  $\hat{z}$  is the unit vector along the scanner's long ( $B_0$ ) axis. Third, the gradient magnetic fields that modulate  $B_z$  produced by the scanner's gradient coils, for spatial encoding along the 3 orthogonal axes  $x$ ,  $y$  and  $z$  [52]:

$$Gx = \frac{dB_z}{dx}, Gy = \frac{dB_z}{dy} \text{ and } Gz = \frac{dB_z}{dz} \quad (2)$$

Therefore, induced currents can arise in circuits comprising of conductive loops (including body tissues) when exposed to a

time-varying magnetic field (gradient and RF) or when there are moving loops interacting with a spatially varying static magnetic field ( $B_0$ ) [19, 20]. The  $E_{RF}$  field can give rise to time-varying charge accumulation in extended linear conductors. The currents and charges resulting from such interactions increase with the strength and frequency of the applied fields (and/or the rate of motion within the fields) and require careful consideration in theory, and possibly experimentally.

## Theory of the Interaction between Closed Circuits (Loops) and the Switching Gradient Field

The interaction between conductive loops and a time-varying magnetic field follows Faraday's law:

$$V = -\frac{d}{dt} \int_A \vec{B} \cdot d\vec{S} \quad (3)$$

Where  $V$  is the induced electromotive force,  $(dS)$  is the infinitesimal area parameter which is also a factor of the moving surface area ( $A$ );  $B$  is the magnetic field. Equation (3) can be generalized to show the relationship between the electric and switching magnetic fields; Maxwell-Faraday's equation:

$$\nabla \times \vec{E} = -\frac{\partial}{\partial t} \vec{B} \quad (4)$$

Where  $\nabla$  is the curl operator,  $\vec{E}$  is the electric field and  $dB/dT$  is the rate of the magnetic field. In MRI terms, the maximum change in the magnetic field  $(dB/dT)_{max}$  corresponds to the gradient field's ( $S_{max}$ ) maximum slew rate at the position ( $z$ ) relative to the central axis of the gradient coils:

$$\left( \frac{dB}{dt} \right)_{max} = S_{max} \cdot z \quad (5)$$

The switching gradient field that is applied in three coordinates  $x$ ,  $y$ , and  $z$ , and used to modulate the resonance frequency, is an important element of MR scanning pulse sequences. The switching gradient field can interact with conducting loops causing one main issue for EEG-fMRI: the flow of the currents within the loop of tissues that depends on  $(dB/dT)$ , the conductivity of the body and the cross-section of the conducting loop [32].

## Interaction between the RF Field and Circuits (Loops and Linear Antennas)

At frequencies in the MHz range and above, and in contrast to the gradient fields, the electrical component of the EM field produced by coils becomes a primary element with significant safety implications.

Concerning the magnetic element,  $B_1$ , the following proportionality relationship applies the induced voltage,  $V$ , in a closed circuit:

$$V(t)_{RF} \approx -\omega_0 B_1(t) A \quad (6)$$

The exact relationship is a function of the circuit's geometry and location, and  $B_1$  distribution [20]. This occurs in loop antennas (inductive coupling).

The electrical part of the RF field can generate charges to flow and accumulate in extended wires (capacitive coupling) [20] according to Equation (1) for the  $E$  field for circularly polarized  $B_1$ . More generally the effect of EEG equipment can be considered as altering the electric field such that its overall power is increased both globally and in localized areas.

## Interaction between Moving Closed Circuits (Loops) and Static Magnetic Field ( $B_0$ )

Moving loops interaction with the static magnetic fields ( $B_0$ ) follows Equation (3) and the electromagnetic field and can be calculated by the following equation:

$$|V_{mov}| = B_0 \frac{dS}{dt} \quad (7)$$

Where  $(dS/dt)$  is the average of the loop area across the static magnetic field.

## Magnetic Forces and Torques

Another potential source of health hazard is the presence of magnetic forces and torques on any conductive or magnetic element because of the exposure to the temporary gradient magnetic field within the permanent magnetic fields; these forces are known as Lorentz forces that act on the icEEG implants and causes vibrations and displacement that can be directly dependent on the  $B_0$  (in the absence of the permanent magnetic parts) as well as the induced currents and the location from the iso-center of the  $B_0$  and inversely on the gradient ramp time [53–56].

In summary, the hazards related to EEG recording inside MRI fields that were listed in International Organization of Standardization [57] are:

- Heating which is induced by RF or gradient fields.
- Vibration as result of gradient switching fields.
- Force and torque due to  $B_0$ .
- Extrinsic electric potential as a result of lead voltage induced by gradient fields (is not the subject of this review).
- Rectification that is caused by lead voltage induced by RF (is not the subject of this review).
- Malfunction as a result of  $B_0$ , RF and gradient fields (is not the subject of this review).

## Experimental Factors that can Affect the Amount of Heating in the Vicinity of Electrodes in the Application of the EEG-fMRI

In this section, we start by describing the factors that are common to the safety of all MR scanning, and taking into consideration the presence of electrodes, starting with physiological, followed by the scanning process itself and associated MR technology. We then describe factors specifically related to experiments designed to assess the safety of MR scanning in the presence of electrodes.

## RF Energy Deposition

Although the type of sequence can be a general guide to RF-induced heating, the details of a MR scanning sequence are crucial in assessing the specific risks associated with its use, in the presence of conductive devices such as EEG electrodes. In the following, we discuss two common practical MR factors closely related to energy deposition: SAR and RF transmit coil type.

### Specific absorption rate

The specific absorption rate (SAR) is a measure of the amount of heat generated in a body due to exposure to RF fields through the Joule effect and is the most important parameter to quantify the risks associated with RF exposure during MR scanning [19, 58]. Furthermore, it can be empirically linked to the heating of implants and electrodes [59]. SAR is the relation between tissue exposure to the RF field and the absorbed energy in a certain mass [60, 61]. SAR in units of W/Kg can be related to the electric part of the RF field, as:

$$SAR = \frac{\sigma}{2\rho} |\vec{E}|^2 \quad (8)$$

Where  $\sigma$  is the material's electrical conductivity in (S/m),  $\rho$  is the mass density in the unit (kg/m<sup>3</sup>) and  $\vec{E}$  is the local RF electrical field magnitude. The SAR value can be calculated and expressed in several ways: averaged over a whole body, averaged over whole head and averaged over local or small volume that can be 1 g of tissue or 10 g of tissue or other values. (In this review, we use head-averaged SAR unless indicated otherwise) Under certain conditions, without heat dissipation, SAR can be expressed in-terms of temperature changes as follows [54]:

$$SAR = C_p \frac{dT}{dt} \quad (9)$$

Where  $C_p$  is the heat capacity in unit (4,186 J/C°.Kg for water) and  $dT/dt$  is the rate of temperature change.

The international safety guidelines for MRI scanning state that the increase in the temperature of human tissues must not exceed 1°C and that the SAR value should not exceed 10 W/Kg for the local SAR (using local transmit coils) [50, 60]. For the volume transmit coils such as head or body RF coils, whole-body SAR must not exceed 2 W/Kg and the whole-head SAR must not exceed 3.2 W/Kg for the head-average over 6 min [50]. For more information about thermal damage and thresholds, please refer to Sapareto and Dewey [37] and Yarmolenko et al. [38].

### Type of RF transmit coil

RF transmit coils vary greatly in geometry, size (anatomical coverage) and excitation mode, depending on the desired application and scanner design, with direct consequences for the  $E$  field distribution and power. Therefore the distribution and amount of tissue heating with or without any conductive components placed in or near the RF coil is greatly affected by the coil size and design. For example, SAR values can be decreased by careful transmit coil design [62–68]. Kangarlu and co-workers performed simulations and experiments to study the impact of coil length on localized heating at 8T, showing greater heating

for longer coils [69]. In practice, the volume of the coil is an important determinant of the total power required to produce the  $B_1$  field needed for a given pulse sequence with increased power requirements being associated with a greater risk of heating. Hence multiple studies have considered the type of coil coverage (head vs. body) in the presence of EEG electrodes and leads [19, 36, 55, 70, 71]. For example, Carmichael et al. [19] in a study at 1.5T in the presence of icEEG (depths or subdural grids and strips) electrodes found that the head transmit-receive coil results in significantly less localized heating compared to the body coil. The authors conclude that body transmit coil should be avoided when icEEG electrodes are present; this finding is in line with that of others, but in contradiction with Boucoussis et al. [36]. This could be explained by the different electrode and phantom configuration.

In addition, the use of multi-channel coils (such as an 8-channel system arranged in two rows positioned in the z-orientation) can help to reduce the required RF power and SAR values [64, 72–75]. Multi-transmit coils offer reduced power requirement to produce RF field and thus, a decreased SAR value [63–66, 73–78].

It is important to note that there is a complex relationship between the position of the body and the conductive components of the EEG system in relation to the RF coil and their coupling which is also field strength dependant. Therefore, generalizations are limited to the range of tested circumstances such as a particular spatial arrangement of EEG equipment tested in different RF coils.

### Type of MR Sequence

The type and parameters of an MR sequence are crucial factors for temperature elevation because of the obvious link between the amount of RF power deposited in the body, the power applied and heating; this deposited power, the SAR is a fundamental parameter in MR safety [55]. For structural and functional imaging of the brain in epilepsy, sequences typically used include spin echo (SE) and derived sequences such as fast spin echo (FSE) or turbo spin echo (TSE), gradient echo (GE) sequences with or without an inversion pulse for T1 weighted imaging and echo planar imaging (EPI) for functional imaging. SE involves the application of an excitation and refocusing RF pulse ( $90^\circ$  and  $180^\circ$ ) however it is rarely used due to long imaging times. In FSE or TSE, a series of multiple refocusing RF pulses are applied following the excitation pulse, which is termed the echo train length. A large power is required to produce the RF  $B_1$  field for refocusing pulses (that need to approach  $180^\circ$ ) and many are applied in a short time period (order 1 per 10 ms) that leads to high RF power levels. This then causes increases in the heating effects because of the coupling between E-field and B-field in the RF band [79]. Gradient echo sequences involve a single RF pulse followed by a gradient reversal [80], and generally have a much lower SAR than SE. In either case, the amount of heating can be controlled by changing parameters such as the flip angle and sequence repetition time (TR). EPI is a time efficient sequence where an entire image is obtained in a series of gradient echoes with differing phase encoding following a single RF pulse. This makes it typically a low RF power sequence. SE-EPI uses the

same readout following an excitation and refocusing pulse which increases its SAR.

Multi-band (MB) (also known as simultaneous multi-slice) sequence is a more recent development to speed the image acquisition by the use of excitations of multiple slices simultaneously [81]. This type of technique has recently become widely used in fMRI to allow faster temporal sampling than the single-banded acquisition pulse techniques. The requirements of exciting multiple slices can lead to greater RF power requirements, especially peak power and at high multiband factors. However, there are already a number of approaches to RF pulse design to limit this power requirement (e.g., Norris PINS pulses, transmit sense) [82]. In addition, for faster sampling (shorter TRs), optimal imaging requires smaller flip angles helping to limit power requirements. Nevertheless, these sequences repose the challenge of managing heating risks when higher SAR sequences are used together with EEG recording equipment particularly for high acceleration factors and high field strength MRI scanners [83].

In the context of studies focused on identifying the set of circumstances and image acquisition parameters that allow MRI in the presence of EEG electrodes (or other implants), SE sequences are often used to assess worst-case heating [20, 55, 70], and in comparison with other, less SAR intensive and more practically relevant sequences such as GE EPI used for fMRI. The former approach has the advantage of demonstrating the potential health impact of the wrong scanning protocol being used, for example through operator error, while allowing for risk assessment of lower SAR protocols. It is crucial to note that the calculation of SAR is scanner and software specific therefore to directly compare between pulse sequences across vendors  $B_{1\text{rms}}$  (root mean squared  $B_1$ ) provides a much more reliable metric independent of factors such as the RF coils used, body position or weight. SAR estimates for any given acquisition are model-based and scanner manufacturer-specific and are not designed to take any foreign body into consideration and therefore, caution is advised when using SAR in relation to the heating of implants [19].

### EEG Equipment-Related Factors

#### *Type, number and position of electrodes*

The general aim of most experiments on RF-induced electrode heating has been to identify the worst case scenario, which in effect means identifying the location of greatest heating for a given electrode/subject configuration. This approach is typically in accordance with the ASTM guidelines.

The types of EEG electrodes are factors that can theoretically affect the amount of localized heating in the presence of EEG electrodes in contact with human subjects in the MRI environment. EEG electrode types include scalp and icEEG (and for the purpose of this study, DBS electrodes which are extremely similar to depth EEG electrodes). The material used for the clinical and investigative scalp EEG electrode contacts range from Ag/AgCl, Au, plastic to stainless steel, each with greatly varying magnetic and conduction properties. Invasive (icEEG) electrodes are usually made of Pt-iridium (though steel and platinum are also used) and the conductive wires made

of nichrome (NiCr). At 4T, Stevens and co-workers reported no significant heating increases in three different types of scalp EEG electrodes: brass, silver, and conductive plastic of about 0.1, 0.0, and 0.1°C, respectively, when they are attached to an oil phantom without connection to the lead wires and EEG devices and without forming a resonant loop [84]. These temperature increases changed to 0.05, 0.04, and 0.06°C for the brass, silver and conductive plastic electrodes, respectively, when they were attached to an agarose phantom indicating the importance of choosing the proper phantom and electrode materials for heating measurements in the high magnetic fields [84]. Phantom composition will be explained in the following sections.

Angelone et al have found that the number of scalp EEG electrodes can affect the amount of heating using finite difference time domain (FDTD) computational simulations. In their simulations, SAR values of 0.59 W/kg without EEG and 0.77 W/kg were estimated in the skin with 124 scalp EEG electrodes at 3T [85]. The same trend was obtained for simulations at 7T where the results showed 0.29 W/kg without scalp EEGs, 0.35 W/kg with 16 electrodes, 0.41 W/kg with 31 electrodes and 0.43 W/kg with 62 electrodes [85]. However, outside the field of MR, a reduction in heating was observed experimentally when placing increased number of electrodes in the presence of GSM900 mobile phone (RF: 890–915 MHz) that depended on the location and angle of the electrode leads with respect to the RF [86]. Importantly the shielding effect of electrodes can result in a reduction in the local SAR [85, 86].

Concerning the distribution of RF-induced heating, Vasilios et al studied that with the scalp EEG electrodes according to the 10–20 international systems [87]. They measured heating of 1.09°C and 6.61°C in the CZ paste position and 0.87°C and 0.97°C 5 mm from Fp1 position when placing inkCap (thin nylon grommet contacts and thin polyester film) and the standard (gold/grass) scalp EEG electrodes, respectively [87].

Intracranial electrodes used for invasive monitoring in epilepsy patients are either strips or grids of disks that are designed to reside on the cortical surface (ECoG) or penetrating cylindrical electrodes (depth electrodes). Concerning studies of heating in the presence of icEEG, comparing depth electrodes with grid electrodes, the two electrodes tend to have similar heating [36, 55]. It has been shown that icEEG electrodes implanted coronally with their terminating wires positioned posteriorly to the magnet, showed heating below the standard allowed limits (<1°C); however, these terminating wires showed increased heating when positioned anteriorly to the magnet, and excessive heating can be seen in the parasagittal implant locations at 1.5T [70]. Therefore, it is recommended to apply EPI sequences in an orthogonal approach (perpendicular to the Z-axis of the magnet) [70]. The addition of multiple and different electrodes have been studied by Carmichael and Boucoussis but the total electrode number itself has not been identified as a critical factor determining heating.

#### **Connection cables (leads) and their configuration**

The conductive termination of wires can play a significant role in the amount of localized heating in the vicinity of EEG electrodes. For instance, Carmichael et al. have tested the effect of the

position of the terminal cables on heating and found that when these cables were positioned in the z-axis to the magnet, they produced high temperature of about 6°C and about 2.6°C when the cables are placed close to the body toward the feet (inside the bore) [55]. Heating can elevate above the permitted limits when the wires are shorted and placed in close proximity (effectively creating a short-circuit) [19, 36, 70].

It is well established that the length of electrode leads and cables plays a vital role in determining the amount of heating due to the possibility of resonant antenna effects, as a function of the relationship between effective length and the Larmor frequency (and therefore static field strength). This effect was investigated at 1.5T by Yeung et al. who determined that wires of a length of less than 0.6 m and around 2.6–3 m result in reduced heating [88]. Asseconti et al. also tested this phenomenon at 4T, observing a difference of 1.5°C temperature increase between two cable lengths [89].

#### **Static Field Strength ( $B_0$ )**

As noted above, scanner static magnetic field strength is an important factor for localized heating in itself, because the frequency of the RF is linearly related to field strength thus the power required for a given  $B_1$  amplitude is also increased and correspondingly the same pulse sequence results in higher SAR at higher field strengths. However, the higher SAR may not always result in greater heating for a given EEG system because the coupling between any conductive structure and the RF coil will depend on their respective resonant lengths. One research study that compared the heating effect on icEEG inside 1.5T and 3T MRI scanners was performed by Carmichael et al. [19] where they studied the effect of heating in three MR systems (1.5T GE, 3T GE Signa Excite and 3T Siemens TIM Trio) and found that in general the 3T MRI systems produces higher temperature elevation above the limits than 1.5T in the vicinity of metallic electrodes specifically when using structural sequences. The temperature increase also can be high even when the head transmit coil is used [55]. Another study showed that it may be possible to use the body transmit and head receive coil configuration in 3T and low SAR EPI sequences but the structural sequences such as FSE should be avoided because they produce heating above the standard limits [36].

Mullinger, Neuner and Jorge reported that using EEG cap connected with MR compatible EEG amplifier at ultrahigh field MRI scanners (7T and 9.4T) can be performed with acceptable risk under specific conditions [90–93].

#### **Gradient Fields**

The switching magnetic gradient fields can also affect the heating in the presence of metallic implants made of conducting materials [79]. The heating from the gradient switching fields can be determined by Faraday's law where the magnetic flux change produced by the scanner induces electrical eddy currents in conductive implants which is then converted to thermal energy. The magnitude of the flux change is strongly dependant on the position relative to the magnet's iso-center [20, 79]; however this effect is minimal for EEG electrodes [20, 55].

## Perfusion Process in the Human Body

Blood perfusion plays a vital role in temperature regulation and therefore is a consideration in devising safety tests, at least theoretically. Blood flow carries about 50–80% of the heat in or out the body tissues [94, 95]. There are many biophysical models that have been formulated to study temperature change or regulation by perfusion. It is noteworthy that some body parts are not normally perfused such as the eye [96]. Nonetheless, everything else being equal, perfusion should result in reduced heating compared to that observed in tests performed on (passive) phantoms and can therefore be cited as a mitigating effect although difficult to quantify or validate precisely due to the possible presence of other temperature regulating processes such as conduction, convection, radiation, metabolism and evaporation [97].

## Survey of the Experimental Literature on the Safety of Scalp EEG-fMRI and icEEG-fMRI

The main health-related effect that can be caused by the RF fields when scalp or intracranial EEG are within the MRI scanner during image acquisition are thermal as consequence of tissue absorption of RF energy that can be locally increased by the presence of the EEG system.

Summaries of the experimental research articles relevant to the topic can be found in **Tables 1, 2**. In the following, we describe some of the highlights and discuss important experimental factors for consideration when conceiving such experiments. One of the first safety studies using EEG within MRI was performed by Zhang et al. [98], where they studied the heating effect, resonant frequency and the RF power loss when placing nickel-chromium intracranial depth electrodes inside 1.5T MRI scanner. Zhang et al. found that the resonant frequency was 100 MHz and the RF power loss was  $-2$  dB when the electrode was in air, the resonant frequency decreased to 37 MHz and the RF power loss became  $-19$  dB when the electrode was placed inside saline solution. The RF power loss became  $-3$  dB at the frequency of 64 MHz (1.5T), and the heating increased to  $0.07^{\circ}\text{C}$  which was measured after each SE sequence [98]. The ASTM standard specifies the use of gel phantoms since saline can lead to significantly underestimated temperature increases due to the greater heat dissipation due to convection, which may partly explain the results of Zhang et al. [98]. We also note that the temperature measurements were performed after a delay following the scanning. Lemieux et al. also performed one of the early measurements of heating effect inside 1.5T MRI scanner examining the main factors of heat induction. It was performed by designing a loop from the wires of 15 EEG electrodes fitted with current limiting resistors in a square box shape surrounding a spherical head phantom in order to assess the effect of heating and suggest the appropriate resistor which was found to be around 5.6 k ohm for the maximum allowed specific air ratio (SAR) and 13 k ohm for the minimum heating of the fitted non-ferrous carbon resistors to achieve maximum heating of less than  $1^{\circ}\text{C}$  in the resistors for the non-loop and in the electrode [20]. While current-limiting resistors have been

used to reduce the heating from the currents that are induced by the gradient and RF field, some authors have found their effectiveness in limiting the heating associated with capacitive coupling (at 7T) to be doubtful [60]. Other authors such as Bonmassar and colleagues investigated the effect of MR induced heating by the addition of junction field effect transistor (JFET) in a circuit connected to the scalp EEG has been determined to produce isolated currents with less noise when it is in OFF mode [71]. The safety profile of scalp EEG have been further characterized using similar protocols and a range of different MRI protocols and clinical setups [84, 87, 89, 90, 99–102]. The summaries of the safety studies of scalp EEG in MRI are listed in **Table 1**.

In a similar vein, different groups have tested the MRI interactions with DBS devices. These typically consist of a pulse generator (housed in a metallic box), electrodes and connection wires. Overall at 0.35T [103] and 1.5T it has been found that risks can be managed under specific configurations (low SAR sequences and often a head transmit-receive coil) and the production of heating is less when DBS equipment are fully implanted [34, 59, 104–113]. In 3T MRI fields and higher [34, 59, 107, 109–111, 114–118], similar results in terms of heating have been obtained but more caution is required when dealing with DBS implants and wires as well as pulse sequences in general require greater SAR. The summaries of the safety studies of DBS external electrodes and implants in MRI are listed in **Table 2**.

A study by Carmichael et al focused on the safety of MRI in patients with icEEG electrodes used for epilepsy monitoring and presurgical evaluation. In this study, the mechanical forces on electrodes (types and positions), tissue heating and tissue stimulation were tested [19]. In addition, a study was performed to evaluate the safety of recording icEEG during fMRI where terminating cables positions and the use of different types of MRI scanners and RF coils were explored both on 1.5T MR scanners [55] and with the use of 3T MRI systems [19, 36, 55, 119]. In addition, studies by Shellock et al. [120], Nyenhuis et al. [121], and Bhattacharyya [122] were performed to assess the heating of metallic implants. Summaries of the safety research of icEEG and metallic implants in MRI are listed in **Table 1**.

Other groups [85, 93, 123, 124] have performed temperature and safety assessments when utilizing simultaneous EEG-fMRI and DBS techniques using finite difference time domain (FDTD) computing approaches. Yeung et al. performed heating assessments on conducting wires using the simulations of method of moments (MoM) [88]. Another technique known as finite element method (FEM) was used to study the heating effect on DBS electrodes and leads [125–128]. The summaries of the safety studies using computer simulation techniques when placing EEG, implants and DBS electrodes in MRI are found in **Table 3**. In principle, computer simulations offer the possibility of speeding up safety research by allowing the consideration of a variety of experimental scenarios (electrode configuration, subject, scanner design, sequence, etc.) the testing of which could be time consuming [85, 125]. However, this benefit is reliant on two considerations: computational speed and, most crucially, computational model accuracy. Therefore,

**TABLE 1 |** Summaries of the experimental research of scalp or external EEG-fMRI and implanted EEG-fMRI.

No.	Study	MR scanner and scanning protocols	Type of electrode(s)/implantations/No. of contacts	Positions and orientations of the electrodes	Safety hazard(s) considered	Methodology (test object and temperature measurement device)	Observations	Conclusions and recommendations	Safety standard: (reference and guidelines)
1	[98]	- 1.5T - Linear head coil - Spin echo sequence	- Depth electrodes - 8 contacts	The depth electrodes where positioned parallel to the scanner's longitudinal axis	- Temperature measurements - Resonant frequency - RF Power loss	- Phantom - Precision thermistor (model 4400SA, YSI inc., USA)	When using the spin echo, the temperature was about 0.07°C (Measured after the SE sequence)	It is safe to use the nickel-chromium electrodes inside the MRI under specific tested conditions. Using SE sequence is preferred than GE due to the presence of susceptibility artifacts in GE	N/A
2	[20]	- 1.5T - Quadrature birdcage head coil - 2D spin echo sequence	- Loop of wires and scalp EEG electrodes - 15 Scalp EEG electrodes	A loop was placed in positions from 0–15 in a clockwise positions around the edges of the head coil; 0 is located in the inferior periphery of the head coil	- RF voltage measurements - Temperature measurements - Suitable resistor	- Spherical head phantom - EEG- Fluoroptic thermometer (Luxtron, USA)	5.6 K ohm for the maximum SAR, and 13K ohm for minimum heating	In specific standard conditions, EEG-fMRI can be performed with extra caution by adding current-limiting resistors near the EEG electrodes	NRPB95 BS.5724 IEC601
3	[71]	- 3T - Head coil	Scalp EEG electrodes fitted N/A with junction field effect transistor (JFET) (a non-linear current limiting transistor)		- Temperature measurements - Resistor assessment	N/A	The addition of JFET to scalp EEG gives the noise immunity in the OFF mode	JFET resistors provide excellent current isolation	N/A
4	[121]	- 1.5T MRI system Signa (GE, USA) - Body RF transmit coil - FSE	Metallic implant	The implant was placed in the abdominal region of the phantom close to an implanted infusion pump. These insertions are made to resemble the clinical insertion in human	- Temperature measurements	- Phantom - Infusion pump (Medtronic, USA) - Fiber optic temperature thermometer (model 790, Luxtron, USA)	Using SE with SAR value of 0.95W/kg in the gel phantom, the heating was 0.23°C and 0.66°C without the implant and with the implant, respectively	It is possible to scan patients implanted with Synchronized pump in 1.5T systems without additional health hazards	N/A
5	[120]	- 1.5T - T1 spin-echo sequence and gradient echo sequence	- Titanium alloy implants - BioMesh, Large flexible burr hole cover, Large rigid burr hole cover, Large burr hole cover, Cranial screw, BioClip	The BioMesh implants were fixed into a plastic plane and placed in the edge of the phantom	- Induced torques assessment - Temperature measurements	- Phantom filled with gel - EEG- Fluoroptic thermometer (Luxtron)	Titanium alloy implants show 0.6°C heating inside the MRI	BioMesh implants have no safety issue when used in MRI under safe conditions and can be beneficial if they are implemented for neurosurgical and interventional MRI acquisitions	ASTM F 2182-02a
6	[99]	- 1.5T GE scanner - Head RF coil - T1, T2, DW, EPI, STIR, FLAIR, 3D-SPGR	- Silver Scalp EEG electrodes with a thick gold flash attached to thin copper wires with Teflon coating - 23 scalp EEG electrodes	The scalp EEG electrodes were positioned according to the 10-20 international system of EEG	- Artifact assessment - Temperature measurements	- Saline-filled spherical plastic phantom - Thermometer (FTI-10, FISO Technologies)	Maximum heating change was 20.45°C and the average head SAR was 1.6W/kg in the subjects	MR compatible EEG system can be utilized for concurrent EEG MRI recording safely with fewer artifacts by applying structural and functional sequences of $\leq 1.6\text{W/kg}$ SAR values	N/A

(Continued)

**TABLE 1 |** Continued

No.	Study	MR scanner and scanning protocols	Type of electrode(s)/implantations/No. of contacts	Positions and orientations of the electrodes	Safety hazard(s) considered	Methodology (Test object and temperature measurement device)	Observations	Conclusions and recommendations	Safety standard: (reference and guidelines)
7	[60]	- 1.5T GE MRI - Quadrature birdcage head coil, 3 head acquisitions, T1 weighted 3D- SPGR	- Two different types of EEG with 32 electrodes/leads were modeled and co-registered with the homogeneous head model - Modeled 32 scalp EEG electrode on 2D Mask (on MATLAB) - EEG electrodes with 10 k ohm resistor - 32 standard gold EEG and 32 Ag/AgCl EEG	Thirty-two leads were bundled on the Cz position, wrapped around the head and modal close to the neck. In addition, the electrodes/leads with 10 ohm and 32 resistors were modeled as a passive port directed along the lead	- SAR simulation - B1 field effect - Temperature measurements	- 32 EEG electrodes with and without resistors - Head mannequin anthropomorphic (CHEMA) and a computer designed phantom - EEG- Fluoroptic thermometer (Luxtron)	6°C in 30 min using the EEG paste, 1.22°C using Cz 15mm and 1.31°C using Cz 25mm	Caution should be taken when selecting EEG for simultaneous EEG-MRI and the use of high-resistive leads and solutions is recommended	NCRP Report No. 67 (1981), IEC Part 2-33 (2002)
8	[87]	- 7T MRI scanner (Siemens, Germany) - T2 TSE	- InkCap EEG Ag/AgCl electrodes - Standard EEG electrodes (QuickCap)	InkCap contains 32 non-magnetic gold EEG electrodes. QuickCap contains 32 EEG electrode noise	- Temperature measurements - EEG signal variance throughout EPI sequence - Ballisto-cardiogram noise	- Phantom (CHEMA) - Luxtron 3100 fluoroptic temperature sensors (Luxtron Co., USA)	At 7T, InkCap EEG electrodes presented five times decreased signal variance than the standard QuickCap EEG electrodes during EPI sequence. In addition, more heating was observed in the QuickCap EEG electrodes compared with InkCap EEG electrodes	InkCap electrodes are suitable for multi-channel EEG and high-field fMRI experiments. Patient movement artifacts can be minimized by using the lightweight InkCap EEG electrodes	IEC 60601-2-33 (2002)
9	[84]	- 4T Varian Unity Inova whole-body MR scanner contains Siemens shielded gradients - Quadrature birdcage RF coil - 3D multi-echo gradient echo (GE) sequence (RASTAMAP), T2-SE, and MRS pulse sequence (LASER)	- EEG electrodes made of brass, silver, and conductive plastic were tested	The electrodes were aligned parallel to the x-y axis of the scanner in order to determine the maximum field distortions around them	- B0 field distortion - Signal loss - Heating	- Hemispheric oil phantom - 15% agarose gel sphere - Fiber optic temperature probe (FTI-10; FISO Technologies Inc., USA)	The heating rate in the oil phantom was found 0.1, 0.1°C and 0.1°C for the brass, silver, and conductive plastic electrodes, respectively, and placed on the phantom without the leads and the adipose gel was 0.05, 0.04 and 0.06°C for the same electrodes respectively	No significant heating was observed in the three EEG electrodes made of brass, silver, and conductive plastic when they were placed on the phantom without the leads and the EEG equipment	N/A
10	[19]	- 1.5 GE Signa, 3 T GE Excite MR and 3 T Siemens TIM Trio - FSE sequence 2.4W/kg for head coil and 1.2W/kg for body coil	- Grids - Depths - Strip - 8 contacts electrode	The depth electrodes were placed in the left-right axis and perpendicular to the sagittal level. Electrodes' leads were placed along the side of the phantom with 10mm spacing, 6 contacts electrode with 10 mm spacing. Grid and strip electrodes (4 mm diameter PTFE disks and 2.3 mm exposed) within a silicon sheet and stainless steel wires	- Stimulation - RF-related heating	- Perspex phantom - Fluoroptic thermometer (Model 3100 Luxtron, USA)	At 1.5T, the maximum temperature change was within the safe limits (<1°C, <2.0°C) at 3T on GE scans and (<1°C) on the Siemens. The maximum heating was 6.7 °C using body coil	Intracranial electrode localization can be performed safely in 1.5 and 3T using head coil modifications of the imaging protocol (scan duration and number of slices) are needed to keep the heating changes within the safe limits	ASTM F 2118-202a

(Continued)

**TABLE 1 |** Continued

No.	Study	MR scanner and scanning protocols	Type of electrode(s)/implants/No. of contacts	Positions and orientations of the electrodes	Safety hazard(s) considered	Methodology (test object and temperature measurement device)	Observations	Conclusions and recommendations	Safety standard: (reference and guidelines)
11	[80]	- 7T Phillips Achieva MR scanner - Quadrature birdcage RF coil (Nova Medical, USA) - TSE and EPI GE	- EasyCap scalp EEG (Herrsching Germany) - 32 Ag/AgCl ring electrodes with plastic adapter and a 5-kΩ safety resistor	- International 10/20 system	- Heating measurements - Noise sources - EEG-MRI study on humans	- 20-cm-diameter, plastic spherical phantom with saline-and agar gel	Temperature measurements showed values less than 0.4°C during 20 min TSE sequence	EEG-MRI can be performed safely using commercial MR compatible EEG amplifier and EEG cap at 7T MRI scanner under tested standards	N/A
12	[55]	- Siemens 3 T Trio, 1.5 T Avanto and 3 T Signa Excite GE - Birdcage T/R coil (for the 1.5 T and 3 T Signa), T/R coil and body coil (for the 3 T Trio) - FSE and EPI sequences	- Strip electrode - Grid electrode - Depth electrode - Three depth implants of 2 models were inserted: 8 electrode contacts with 10 mm spacing, 6 electrode contacts with 10 mm spacing - One subdural grid and one strip electrode were used: 6-contact electrode with 10 mm spacing and the grid (6×8 contacts with 10 mm spacing, and tails)	The same setup as in Carmichael et al. [19]	- Voltage measurements - Heat measurements from the PF of the head and body transmit coils - The effect of cable position on tissue heating	- Perspex phantom according to (ASTM F 2182-02a, 2007 Model 3100 Luxtron, USA)	<1.0 °C using a head transmit RF coil. The measured gradient switching induced currents was 0.08 mA and the charge density 0.2 μC/cm <sup>2</sup> (all were within safety limits). The maximum heating was 6.9 °C using body coil	Heating was within the safe limits when using a head RF transmit coil, adding the extension cables, cautiously observing the length and position of the cables and applying low-SAR sequences	ASTM F 2182-02a, IEC (2002), IEC (2005) ICNIRP (2004), ICNIRP (1998), IEEE C95.1-1999,
13	[36]	- 3T GE Discovery - Body and head coil - SPGR, ASSET, FLAIR and Spiral GE, T2* GR-EPI and SS-FSE	- Subdural grid and strip electrodes - Depth electrodes - The grid electrodes 20 contacts (4.0-mm diameter discs, 10-mm spacing, enclosed in silicon) - Strip electrodes 8 contact (10-mm spacing) - Depth electrodes 4 or 6 contacts (10-mm spacing)	- In the first phantom, the grid was inserted in the top right side of the phantom simulating its placement in the right inferotemporal frontal lobe - In the second phantom, one depth electrode was inserted in a similar position to the right inferior frontal lobe. - In the third phantom, one grid and one depth electrodes were positioned on the left side of the phantom, and another grid and one strip electrode as well. On the left side of the phantom, similar positions to the first two phantoms were implemented in order to simulate the bilateral frontal insertions	- Device movements - Device temperature - Voltage - Gradient induced currents - Image quality	- Head phantom - Body phantom	Heating <1 °C in a typical icEEG-MRI setup that includes 60 min of continuous High SAR sequences (FSE) and the heating >2 °C and up to 10 °C on 3T MRI scanner	Simultaneous icEEG-MRI can be performed with low risk at 3T. High SAR sequences should be avoided. Consideration is given to the positioning the EEG cables toward the back of the scanner. Reduced heating is possible using head RF transmit coil rather than a body transmit coil. Calibrations scan for the parallel imaging (ASSET) should be avoided	ASTM (2000), (2008), (2009), (2011a), (2011b)

(Continued)

**TABLE 1 |** Continued

No.	Study	MR scanner and scanning protocols	Type of electrode(s)/implantations/No. of contacts	Positions and orientations of the electrodes	Safety hazard(s) considered	Methodology (test object and temperature measurement device)	Observations	Conclusions and recommendations	Safety standard: (reference and guidelines)
14	[70]	- Siemens Sonata whole-body 1.5T MRI System - Head coil, coil for rabbits, whole body coil - T1 True-FISP, T2-weighted FLAIR, EPI-FID	- 4 depth electrodes (0.8 mm diameter, 2 mm contact length and 1.5mm inter-contact interval)  - One sagittal electrode placed perpendicularly to the previous three  - All the three are placed mimicking the clinical setup: the two coronal adjacent electrodes (1 cm separation) on the left are simulating the amygdala and hippocampus placements, the third electrode is mimicking the left insular placement and the sagittal electrode is just perpendicular to the three electrodes	- Three electrodes were positioned coronally, two electrodes separated by 1 cm from each other and the third at 3 cm distance	Temperature measurements	- Head phantom - Torso phantom (ATSM) - White rabbits - Fiber optic thermometer (FOTEMP; USA)	Maximum of 0.6°C and 0.9°C in phantom and animals, respectively	- Using a 1.5T MRI, EPI sequence with intracranial electrodes showed similar heating as the conventional T1 and T2 sequences when using electrode implants in a perpendicular location to the z-axis of the magnet	ASTM F2503-05, ASTM F2213-06, ASTM F2052-06c1, ASTM 2182-02a, ASTM F2182-09
15	[100]	- 3T MRI: Philips Achieva - 8 channels head coil and Siemens Venio (12 channel head coil) - GE-EPI, TI-3D, T1-IR, Multi-echo SE, DTI and T2-TSE	- Scalp EEG caps (Brain Products, Germany). The sizes 52, 56, and 60 - The caps of the sizes 56 and 60 contained 64 electrodes, whereas the cap of the sizes 52 had 32 electrodes	N/A	Temperature measurements	Head Phantom	In the head phantom, the heating was 4.1 °C. In the volunteer, the mean heating change was 1.2 + 1.1 °C, 35.6 °C, and the maximum rise was 2.1 °C with the mean of 0.9 + 0.7 °C	Safe EEG-MRI protocol in IEC 60601-1 standard (2002)	3T can be achieved by following the standards of EEG provider and IEC protocols
16	[101]	- 3T Siemens Allegra head-only scanner and 7T Siemens scanner - Circularly polarized head coil for 3T and birdcage transmit head coil - 32-channel receive coil (for 7T) - TSE and GE	- dEEG scalp electrodes Ink-Net - AgCl-coated pellet scalp electrodes (Cu-Net) - 265 channels scalp EEG Cz, T7, T8, and the nasion	10–10 International System was used and the heating measurements were recorded in these locations: Cz, T7, T8, and the nasion	Heating Safety Assessment at 7T Data quality assessment at 3T	- ASTM 2182 agar-based conductive head phantom - 7 optical temperature probes (OSENSA Innovations Corp., USA)	TSE sequence in 7T scanners produced superficial heating values with Ink-Net, Cu-Net and with no net that were 1.02, 0.87, 0.99 °C, respectively, for acquisition time of 15 min and similar to those values for 30 min	High resistance polymer thick film can be placed in dEEG to improve the data quality of the structural and functional MRI following the tested protocol	ISO/TS 10974, ASTM 2182
17	[89]	- 4T MRI scanner (MedSpec, Bruker, Biospin head scanner and Siemens Magnetom) - Head birdcage transmitter and receiver - Prepared Rapid Gradient Echo, Single shot gradient echo, 2D Echo-Planar Imaging	- Scalp EEG cap - 63 Scalp EEG electrodes arranged based on the 10–20 system	63 EEG electrodes were arranged based on the 10–20 system	- Artifacts induced on phantom EEG and human EEG - Image analysis - Temperature measurements	- Spherical silicon oil phantom (170mm diameter) - Temperatures probes (LumaSense Technologies, USA)	The results showed 85% EEG noise decrease when using the short cables 60% of system sensitivity to noise and artifact can be achieved by using compact setup (using short cable connected to amplifier directly at the back of the head coil)	The heating is normal when applying the tested procedure. There is an advantage of less heating using short cables at 4T magnetic fields	N/A

(Continued)

**TABLE 1 |** Continued

No.	Study	MR scanner and scanning protocols	Type of electrode(s)/implantations/No. of contacts	Positions and orientations of the electrodes	Safety hazard(s) considered	Methodology (test object and temperature measurement device)	Observations	Conclusions and recommendations	Safety standard: (reference and guidelines)
18	[119]	- 3T (Skyra, Siemens, Germany) and 7T (Magnetom, Siemens, Germany) MR scanners - T2, T1, and fluid attenuated inversion recovery (FLAIR) in 3T and fast low-angle shot (FLASH) in 7T	- Electroenцеo-graphy (ECoG) grid with conductive nanoparticles in a polymeric thick film on an organic substrate (PTFEOS), - Two standard ECoG grids one with stainless steel platinum contacts and wires and the other with platinum contacts and wires - Both standard ECoG grids were 64 contacts	The electrodes were implanted over the cortex of mice and human's brain specimen	- Artifacts induced in mice and human's brain - Temperature measurements in a head phantom	- Head phantom - Two Mice - Brain specimen without skull	Temperature measurements showed increases of 3.84°, 4.05°, and 10.13° C for no grid, PTFEOS grid and standard grid, respectively	Heating profile can be minimized using PTFEOS grids compared with the conventional ECoG grids	N/A
19	[102]	1.5T MRI system Avanto (Siemens, Germany) - 3T MRI system Trio (Siemens, Germany) - Body transmit coil - MPAGE, EPI, DTI, HASTE, FLAIR and TSE	- Gold cup electrodes - Conductive plastic electrode	Three experiments were used: 1-by utilizing three wire configurations (short, medium and long). 2-Their length of the wires of the gold cup electrodes and the conductive plastic electrodes were shorted from the total 244 cm by 30.5 cm in each scan until the length became 30.5 cm. 3-Gold cup electrodes were placed on the head of human volunteer. All electrodes in the three experiments were positioned according to the international 10-20 system	- Heating measurements	- Phantom (watermelon) - Healthy volunteer - T1 fiber optic thermometer (Neoptix, Canada)	In experiment 1, the short wire for both electrodes produced heating of 15°C and the medium and the long wires produced heating below 4 °C. In experiment 2, the maximum heating was observed on the wires that have the odd multiples (fraction of 1/4 RF wavelength of 1.5T and 3T) and the minimum heating on the wires that have the even multiples (fraction of 1/4 RF wavelength of 1.5T and 3T). In experiment 3, the heating when using short cable was minimum in MPAGE and 2°C Using TSE and when using the long cable the heating was low for all sequences but a maximum heating was around the ECG electrodes	The influence of the antenna is important because the loop formation inside the MRI scanner can lead to high temperature increases around the EEG electrodes. Therefore, odd multiples (fraction of 1/4 RF wavelength of 1.5T and 3T) should not be utilized in patient scans due to its possible implications	IEC 60601-2-33 (2002)

(Continued)

**TABLE 1 |** Continued

No.	Study	MR scanner and scanning protocols	Type of electrode(s)/implantations/No. of contacts	Positions and orientations of the electrodes	Safety hazard(s) considered	Methodology (test object and temperature measurement device)	Observations	Conclusions and recommendations	Safety standard: (reference and guidelines)
20	[122]	- 1.5T MRI scanner (Tesla Espree, Siemens, Germany) - Receive array RF head coil - Localizer, T1-weighted FLASH, GE-EPI and T2-weighted TSE	- Two SEEG electrodes with 8–12 contacts (5 mm spacing, 2 mm long and 1 mm diameter)	- The electrodes were placed according to ASTM standards in the coronal position of the phantom; simulating surgical insertion locations	- Electrode heating measurements (using different sequences and different configurations)	- Gel phantom - Fluoroptic temperature device (model m330, Luxtron, USA)	Localizer, FLASH and EPI sequences showed heating of less than 2°C. Whereas, 12°C heating was observed when connecting the cable in different setups and can be significant heating if the extension cables were placed close to the scanner's bore and the body RF transmit coil. Very small temperature increase was noticed when extension cables were placed in the iso-center of the magnet in any MR sequence used	Simultaneous intracranial EEG-MRI is safe to perform with external stimulation equipment using localizer, FLASH, GE-EPI sequences without performing high SAR sequences	ASTM-F2182-02a, ISO/TS 10974, FDA (2014)

The table contains the studies that are ordered historically. The scanner type ranges in terms of field strength from 1.5T to 7T and the protocols are spin echo (SE), fast spin echo (FSE) or turbo spin echo (TSE), gradient echo (GE), diffusion weighted (DW), T1, T2, diffusion tensor imaging (DTI), echo planar imaging (EPI), fluid-attenuated inversion recovery (FLAIR), short-T1 inversion recovery (STIR), spoiled gradient recalled acquisition (SPGR), magnetization prepared rapid gradient echo (MPRAGE), array coil spatial sensitivity encoding (ASSET), robust automated shimming technique using arbitrary mapping acquisition parameters (RASTAMAP), true fast imaging with steady-state precession (True-FISP), single shot echo planar imaging (SS-EPI), localization by adiabatic selective refocusing (LASER), fast low angle shot (FLASH), saturation-prepared with 2 rapid gradient echoes (S2RAGE) and magnetic resonance spectroscopy (MRS). The safety hazards in the table are mostly related to temperature or heating measurements and the results can be in units of degree Celsius or in specific absorption ratio (SAR) unit W/kg. The other safety hazards such as resonant frequency, movements or others are not the main concentration here. The safety standard is related to the source of safety criteria that have been followed by the study.

computational simulations can be effective once the model has been subjected to exhaustive experimental validation.

Animal testing *in vivo* was performed by Ciumas et al. [70], Gorny et al. [110], Shrivastava et al. [114], Eryaman et al. [115], Shrivastava et al. [116], Eryaman et al. [117] and showed agreement with water-gel phantom experiments. The summaries of the safety researches of EEG and implants in MRI using animal samples are included in Table 1.

In the following we describe the experimental conditions in more depth.

## Phantom Composition and Geometry

ASTM has set the guidelines regarding the characteristics of phantom material for heating measurements which should have water mixed with sodium chloride and polyacrylic acid (PAA) or other materials such as hydroxyethylcellulose mixed with sodium chloride and water containing a conductivity of  $0.47 \pm 10\%$  S/m at temperature range from 20 to 25°C, specific heat of 4150 J/(kg K) at 21°C, diffusivity of approximately  $1.3 \times 10^{-7}$  m<sup>2</sup>/s and heat capacity of about 4,150 J/kg°C in order to simulate the human thermal properties of the tissues [49]. The phantom contents and its effect on heating in the application of EEG-fMRI has been addressed by Shellock research group where they filled a rectangular plastic phantom with a semi-solid gel containing hydroxyethylcellulose (HEC) and mixed with 91% of water and 0.12% of NaCl that simulates a conductivity of 0.8 S/m [120]. Other research has been performed by Mullinger et al. [91] that included mixing a heated solution of 4% Agar and 0.5% of NaCl. Boucoussis et al. have used a spherical phantom filled with 45 g of semi-solid agar gel, 1500 ml of distilled water and 6.75 g NaCl, which all mixed together in the sphere and surrounded by 0.9% NaCl solution in a small area isolated from the agar solution which is also surrounded by acrylic material from the outside to produce an electrical conductivity of 0.7 S/m and simulate the electrical conductivity of the gray matter [36]. The difference in phantom materials between studies is a potential source of error for temperature measurements that are carried out inside the MRI environment. The effect of the gelling-agent PAA, which controls the viscosity of the phantom material, with the heating increase was well characterized by Park and co-workers, finding that the more viscous the phantom material the more the localized heating which might be closer to “worst case” tissues with low perfusion in the human body [129].

## Location of the Temperature Probes

The location of the temperature-measuring devices relative to the EEG electrodes is another factor that affects the accuracy of temperature measurements. According to the ATSM safety standard, the temperature probes should be placed in the area which is suspected to experience the greatest heating, the temperature probe should have spatial resolution of less than 1 mm for the performance of heating calculations in all orientations [49]. Park and co-workers demonstrated the effect of taking temperature measurements on the tip of a DBS electrode, 5 mm lateral to the electrode and 5 mm above the electrode and determined different results in each setup [129]. Mattei et al. determined that there were underestimations of

**TABLE 2 |** Summaries of the experimental research of DBS external electrodes and internal implants using MRI and fMRI sequences.

No.	Study	MR scanner and scanning protocols	Type of electrode(s)/implantations/No. of contacts	Positions and orientations of the electrodes	Safety hazard(s) considered	Methodology (Test object and temperature measurement device)	Observations	Conclusions and recommendations	Safety standard: (reference and guidelines)
1	[103]	- 0.35T MRI scanner Signa (General Electric, USA) - 1.5T MRI Scanner Diasonics M/S (Diasonics Inc., USA)	Neurostimulator implant	The neurostimulator was placed in a position to mimic the patient implantation routine	- Voltage measurements - Temperature measurements	- Phantom (contains skull and trunk) - Fluoroptic sensor (model 750, Luxtron, USA)	The voltage amplitude of 6 V for the 0.35T scanner and 12 V for the 1.5T scanner that can harm the patient because the typical treatment amplitudes range from 1 to 5 V	- Under safety conditions, patients with specified neurostimulation implants could be scanned	N/A
2	[104]	- 1.5T Magnetom (Siemens, Germany) and a 3.0T MRI (Bruker, Germany) - Body RF coil	DBS electrodes	One DBS implant was used and located 1 cm from the surface of the head part of the phantom	- Temperature measurements	- Fiber optic temperature system (model 790, Luxtron, USA)	- Temperature measurements showed maximum value of 2.1°C at the tip of the electrode and it was less than that in the other parts of the implant	The temperature in this study was not very critical that might harm the patient. It is important to avoid the loops in order to minimize the temperature increases	N/A
3	[59]	1.5T scanner Vision (Siemens, Germany) - Body RF TR/R coil - Head RF TR/R coil - Sequences with different whole body and local SAR values	DBS electrodes	Two configurations have been used: 1- In the subthalamic nucleus, globus pallidus or ventralis intermedius 2- The DBS wires placed as a loop around the IPG device	- Temperature measurements	- Phantom (gel) - Fluoroptic thermometer probes (model 790, Luxtron, USA)	The highest heating ranges from 2.5°C to 25.3°C when scanning using body transmit coil, whereas the heating ranges from 2.3°C to 7.1°C when using head transmit receive coil	The type of the RF coil, SAR values and the location of the DBS wires affect the heating elevation	ECRI (1988), ECRI (1991)
4	[105]	- 1.5T MR system - Head RF TR/R coil - FSE: 3D magnetization prepared rapid acquisition GE, EPI, quantitative magnetization transfer and magnetization transfer suppressed angiography	DBS electrode	The electrodes are placed to mimic the clinical setup (subcutaneous pectoral insertion)	- Temperature measurements	- Fluoroptic thermometer (model 790, Luxtron, USA) - Phantom (filled with gel saline)	- The relationship between SAR and temperature increase (heating ≈ 0.9 local SAR) - Less than 1°C heating was found using FSE, magnetization prepared rapid acquisition GE and EPI, and high temperature changes (1–2°C) were found using magnetization transfer	Temperature increases are directly dependent on SAR values. MRI can be performed on patients with DBS implants and the heating can be less or equals 2°C when applying sequences of less than 2.4 W/kg local SAR and 0.9 W/kg whole body SAR	US-FDA (1998), US-FDA (1988), IEC 60601-2-33 (2002)
5	[34]	- 1.5T MRI Symphony (Siemens, Germany) - 2.35T MRI Biospec small bore (Bruker, Germany). In Symphony, diffusion-weighted SE, GE-EPI, FLASH, T2 SE and T2 TSE were applied - In Biospec, SE-EPI was applied	DBS electrodes (four contacts)	The DBS electrode was placed 5 cm away from the center of the bore (z direction)	- Voltage measurements - Temperature measurements - Forces on electrodes - Image quality	- Acrylic sphere phantom filled with NaCl and agar - Fluoroptic sensor (model 790, Luxtron, USA)	- The maximum resulted voltage during GE-EPI was 7 V and the frequency was 64 MHz. The loops (wires) created 13 V. The maximum heating was 15.6°C when using SE (13° electrode position). For the same setup, the heating was 2°C for EPI. In the 90° electrode configuration, the heating was 0.7–0.9°C for both GE-EPI and SE	- Patients implanted with DBS system can be imaged in MRI following safety precautions that include: connecting the electrodes should be avoided, leads need testing before any scan, the leads have to be away from the RF coils' edges and low SAR sequences are applied. Furthermore, the patient and the stimulator device have to be monitored during the scan and the stimulator setup has to be appropriately selected	N/A

(Continued)

**TABLE 2 |** Continued

No.	Study	MR scanner and scanning protocols	Type of electrode(s)/implantations/No. of contacts	Positions and orientations of the electrodes	Safety hazard(s) considered	Methodology (Test object and temperature measurement device)	Observations	Conclusions and recommendations	Safety standard: (reference and guidelines)
6	[106]	- 1.5T short bore MR Vision (Siemens, Germany) - 1.5T long bore MR Vision (Siemens, Germany) - Transmit / receive RF coil - FSE, T1-weighted SE, FSE inversion recovery	Bilateral DBS leads	The DBS system was placed to simulate the real clinical setup and the implantable pulse generators (IPG) were placed in the subcutaneous, subclavicular area similar to the real clinical setup	- Heating (units of whole body SAR)	- Phantom (ASTM) - Active tremor control (Medtronic, US) - IPG system (Medtronic, USA)	- The whole body SAR in Siemens Symphony is 90 times higher than Siemens Vision when using TR/R RF coil	- Apparent difference between two MR systems in terms of RF heating change in whole body SAR unit - SAR is unreliable indicator of the neurostimulation technique - There is a need to find more reliable safety indicators	ASTM (2002), US-FDA, IEC 60601-2-33 (2002)
7	[107]	- 1.5T Magnetom Vision (Siemens, USA) - 3T Magnetom Allegra (Siemens, USA) - In 1.5, TR/R RF body coil and in 3T, TR/R head coil - T1-weighted SE	Bilateral DBS device	Followed [106]	- Temperature measurements	- Gelled-Saline phantom - Fluoroptic thermometry probes (Model 3100, Luxtron, USA) - IPG (Medtronic, USA)	- Heating around DBS leads ranges from 0.8°C to 10.3°C in normal setup, however the heating reduces from 41% to 74% when placing a small concentric loop around the burr hole	- The placement of small central loops close to the burr hole seems to cause a decrease in the temperature change due to RF at 1.5T and 3T for the DBS implanted patients	US-FDA, IEC 60601-2-33 (2002)
8	[108]	- 1.5T MR Sonata (Siemens, Germany) - Transmit body RF coil and receive head RF coil - FSE, magnetization transfer contrast, EPI and GE	DBS leads	Followed [59] and [105]	- MRI-related temperature measurements - Whole body SAR calculations	- Phantom (semisolid gel) - Fluoroptic thermometry (Model 790, Luxtron, USA) - IPG (Medtronic, USA)	- Applying FSE, magnetization transfer contrast, EPI and GE presented calculated whole body SAR of 0.1 to 1.6 W/kg and the head SAR of 0.1 to 3.2 W/kg (temperature change was less than 1°C) - Applying the highest SAR in the previous sequences presented whole body SAR of 1.6 W/kg, local exposed body SAR 3.2 W/kg and local head SAR 2.9 W/kg (temperature change was 2.1°C)	Acceptable results and within the neurophysiological limits when applying clinically suitable techniques of MRI imaging under the conditions of limited SAR values	N/A
9	[109]	- 1.5T MR (Siemens, Germany) - 3T MR (Siemens, Germany) - Head RF transmit coil	DBS leads (with four contacts)	The DBS leads were positioned in areas that simulate the surgical placement locations (subclavicular regions)	- RF-related heating - Induced voltages - IPG function	- Perspex phantom - IPG system (Kinetra 7428, Medtronic, USA)	- When utilizing EPI with 0.4 W/kg, the temperature increase was 0.1°C at 1.5T and 0.5°C at 3T and when applying higher SAR sequences of 1.45W/kg at 1.5T and 2.34 W/kg at 3T, the temperature elevation was higher than the safety limits (>1°C)	FMRI sequences are safe to apply without restricting the experimental setup and more advantage is given to the patients who have internal implantation than the external implantation in terms of safety	MDA (2003), IEC 60601-2-33-2002, ICNRP (2003)

(Continued)

**TABLE 2 |** Continued

No.	Study	MR scanner and scanning protocols	Type of electrode(s)/implantations/No. of contacts	Positions and orientations of the electrodes	Safety hazard(s) considered	Methodology (Test object and temperature measurement device)	Observations	Conclusions and recommendations	Safety standard: (reference and guidelines)
10	[114]	- 9.4T MRI scanner - TR/R RF coil (for 9.4T systems)	Extracranial DBS	Two configurations were used: 1-The DBS electrode lead was placed parallel to the head coil (axial); 2-The DBS electrode lead was positioned perpendicular to the head coil (azimuthal)	- Heating measurements	- Phantom - Fluropic temperature probes (model m3000, Luxton, USA) - Animal sample (Porcine head model)	The axial orientation of the leads of the DBS electrodes produced temperature increase of 0–6°C that is significantly less than the azimuthal orientation that produced 1–27°C	In the ultra-high field system, it is possible to reduce the heating of the DBS electrodes by proper management of these electrodes and their leads	CDRH-FDA (2003)
11	[115]	- 3T MRI (Trio, Siemens, Germany) - Quadrature birdcage RF coil - Linear birdcage coil - Body RF coil - GRE sequence	Metallic implant	The implants were inserted in the phantom in two wire configurations: 1- straight. 2- curved	- Temperature measurements	- Commercial phantom (Dr. Oetker Jello, Turkey) - Fiber optic thermometer (Nepix, Canada)	Without affecting the sensitivity of the linear polarized birdcage RF coil, it is possible to create an area in the body that is free from electric fields by controlling the electric field distribution to allow safe use of metallic implants inside the MRI	N/A	
12	[116]	- 3T MRI system Trio (Siemens, Germany) - Head RF TR/R coil - TSE and GRE	Extracranial DBS	Four configurations of the electrode leads were implemented: 1-Looped at the top of the head; 2-Looped at the side of the head; 3-Looped at the back of the head. 4-Parallel to the head coil longitudinally (axial)	- Heating calculations	- Phantom - Fluropic temperature probes (model m3000, Luxton, USA) - Animal sample (Porcine head model)	Applying TSE with SAR of 3.16W/kg when the extracranial DBS leads were positioned in the longitudinal orientation, produced heating of 1.5–3.2°C which is quite less than the other orientations that produced heating of 5.1–24.7°C	The application of temperature modeling and MR thermometry sequences can provide direct safety information after an MRI scan and enhance the patient safety	CDRH-FDA (2003), ICNIRP (2004), IEC 60601-2-33 (2010)
13	[110]	- 1.5T and 3T MRI systems	DBS implant	The DBS implants were positioned in the subthalamic nucleus in the pig and similar location in the phantom to mimic the human insertion setup	- Heating measurements	- Phantom - Animal (pig) - Fluropic sensor (model 750, Luxtron, USA)	The maximum heating observed in the pig during low SAR testing was 0.46°C and during the high SAR was 1.3°C at 3T scanners. Phantom testing showed 2.56°C and 1.83°C for the high SAR sequence at 1.5T and 3T scanners, respectively, and 0.17°C and 0.27°C for the low SAR sequence at 1.5T and 3T scanners, respectively	ASTM Standard F2182 (2011a), IEC 60601-2-33, (1995) revised (2002)	

(Continued)

**TABLE 2 |** Continued

No.	Study	MR scanner and scanning protocols	Type of electrode(s)/implantations/No. of contacts	Positions and orientations of the electrodes	Safety hazard(s) considered	Methodology (test object and temperature measurement device)	Observations	Conclusions and recommendations	Safety standard: (reference and guidelines)
14	[117]	- 3T MRI system Trio (Siemens, Germany) - Dual-drive birdcage RF coil - GRE sequence	DBS lead	The DBS leads were positioned in two different measurements to extend out the cylindrical phantom (narrow placement) and in the third measurement to be confined within the phantom (wide placement)	- Temperature measurements - Animal experiment	- Commercial phantom (Dr. Oetker Jello, Turkey) - Fiber optic probes (Neoptix Inc., Canada)	- Utilizing dual-drive birdcage RF coil to manually control the distribution of the electric field minimizes the temperature of the lead and the tip to less than 0.3°C (4.4 W/kg SAR) - Utilizing quadrature excitation increases the temperature to more than 4.9°C	Animal and phantom tests showed that the application of dual-drive birdcage RF coil leads to reduced heating on the top of DBS metallic leads	N/A
15	[111]	- 1.5T Avanto (Siemens, Germany) - 3T Trio (Siemens, Germany) - Head TR/R coil - Body transmit coil - Head 12 channel receive coil - TSE sequence	DBS electrodes	Two DBS implants were inserted in the region of the nuclei through the drilled burholes in the phantom	- Heating calculations - Effect of phantom position in the body transmit coil - IPG function during the acquisition	- Phantom (poly-methyl-methacrylate) - Fiber optic thermometer (Neoptix, Canada) - IPG (Medtronic ActivaPC, USA)	During TSE sequence, head SAR was 0.2 W/kg and the heating ranges from 0.45°C to 0.79°C using 1.5T MRI scanner and 1.25°C to 1.44°C using 3T MRI scanner	3T MRI system induces heating that exceeds the international guidelines when using DBS system compared to 1.5T that can be safer to utilize even in case of poor patient positions	ASTM (2002), Medtronic (2010), HPA (2008)
16	[112]	- 1.5T MR Avanto (Siemens, Germany) - 1.5T MRI Aera (Siemens, Germany) - TR/R head coil - MPRAGE and T2-weighted	DBS electrode	29 patients were implanted: 25 patients implanted in the subthalamus and 4 patients implanted in the globus pallidus	- SAR measurements - Image quality	- 29 Patients	- In the Avanto system, the average SAR using MPRAGE sequence was 0.114 ± 0.021. In the Aera system using MPRAGE, the average SAR was 0.09 ± 0.001. In the Aera system, the average SAR using T2-weighted sequence was 1.037 ± 0.214 using Avanto system and 0.828 ± 0.091 using Aera system	If optimized imaging routine with reduced SAR values was implemented, DBS imaging can be performed without adverse events	N/A
17	[118]	3T MRI system Signa (GE, USA)	DBS implants	The DBS implants were placed in the head region of the phantom in the z-direction to mimic the human surgical implantation	- Temperature measurements	- Phantom - 10 patients - IPG (Activa, Medtronic Inc., USA)	Heating was 0.6°C when using body transmit coil with head receive coil. All the used sequences here produced heating of less than 1°C	This study is possibly the first to study the clinical safety of using 3T MRI scanner for DBS implanted patients. More safety tests are required to assess and confirm research findings	Medtronic (2015)

The table contains the studies that are ordered historically. The scanner type ranges in terms of field strength from 0.35T to 9.4T and the protocols are spin echo (SE), fast spin echo (FSE) or turbo spin echo (TSE), gradient echo (GE), T1, T2, diffusion tensor imaging (DTI), echo planar imaging (EPI), magnetization prepared rapid gradient echo (MPRAGE), fast relaxation fast spin echo (FLASE), fast spoiled gradient echo (FSPGR) and half-Fourier-acquired single-shot turbo spin echo (HASTE). The safety hazards in the table are mostly related to temperature or heating measurements and the results can be in units of degree Celsius or in specific absorption ratio (SAR) unit W/kg. The other safety hazards such as resonant frequency, movements or others are not the main concentration here. The safety standard is related to the source of safety criteria that have been followed by the study.

**TABLE 3 |** Summaries of the researches that utilized computer simulation platforms for studying the use of EEG and DBS electrodes inside the MRI.

No.	Study	MR scanner and scanning protocols	Type of electrode(s)/implantations/ No. of contacts	Positions and orientations of the electrodes	Safety hazard(s) considered	Methodology (Test object and temperature measurement device)	Observations	Conclusions and recommendations	Safety standard: (reference and guidelines)
1	[85]	- 1.5T MRI (GE, USA) - 3T MRI Trio (Siemens, Germany) - Quadrature TR/R head coil - Surface coil - T1 weighted 3d SPGR (in 1.5T) - T1 weighted MPRAGE (in 3T)	124 electrodes	The positions of the electrode and their leads were designed and applied in 3d software and FDTD simulation platform	SAR calculations	- XFDTD (REMCOM Co., USA) - Fastrack 3D digitizer (Polhemus, USA) - Scan 4.2 software (CompuMedics, USA) - 3DSpaceDX program (Neurosoft-Compumedics, USA) - Head computational models were extracted from two human subjects	- SAR values using the quadrature coil were significantly higher than that using surface coil - Compared to the reference values at 300 MHz, the simulation showed 4 times rise in average SAR of the bone marrow, 7 times of the skin and 5 times of the entire head	The existence of EEG electrodes and wires with application of 300 MHz can increase the average SAR up to 7/2 times. When applying RF exposures to EEG electrodes and cables, it is significant to reduce the SAR values to appropriate levels	NCRP (1981), FDA (2003)
2	[88]	- 1.5T System Signa (GE, USA) - Body RF transmit coil - Fast GE sequence	Conducting wire	The implants were positioned in medial position in the head region inside the phantom	Heating measurements (SAR)	- Phantom (3d computational model) - Method of moments (MoM) - EM field solver FEKO (EM software, USA) - Fiber optic thermometer (Fisco Technologies, Canada)	The temperature increase can be reduced if the wire length is reduced to less than 0.6 m and from about 2.4 m to 3 m. Furthermore, temperature increase can be decreased in case of using phantom (with similar density as the soft tissues if the wire placement is higher than 0.4 m and less than 0.13 m)	With the specified method, SAR safety can be achieved by proper estimation of heating change	US-FDA (1998), IEC 60601-2-33 (2002)
3	[123]	- 3T MRI system - Birdcage RF coil (16 rods)	DBS implants	Two DBS implants (with 19 leads each) were placed to simulate implantations in the right and left subthalamic nucleus of the human brain	- SAR calculations - Coil coupling - Effect of EM on lead resistivity	- 3d computational head model - XFDTD software (Remcom Co., USA)	Significant differences can be seen between 1 g averaged SAR and 10 g averaged SAR as result of EM simulations with respect to the electrode setup. With electrode leads, 1 g averaged SAR was 1080 W/kg and 10 g averaged SAR was 120 W/kg on the electrode tip. On the other hand, the results became very similar without electrode leads. 1 g averaged SAR was 0.5 W/kg and 10 g averaged SAR was 0.6 W/kg on the electrode tip	The results suggest that local SAR is important indication for safety of using DBS. The results can be used to improve the design and utilization of electrode lead	IEC-60601-2-33 (2002), NCRP (1981)
4	[124]	- 1.5T (GE, USA) - Quadrature birdcage RF transmit/receive head coil - T1-weighted 3D-SPGR	EEG electrode	19 and 32 EEG electrodes were placed on the head following the international standard 10-20	- SAR calculations - Antenna performance (dipole and mobile phone)	- 3d computational head model - XFDTD software (Remcom Co., USA) - Circuit Maker (Altium Inc., USA)	The results showed 20% differences in the whole head SAR and 10 g averaged SAR values in EM simulations with and without EEG leads. The values of the peak 1 g averaged SAR and 10 g averaged SAR were less than the ICNIRP and IEEE safety criteria	The results confirm the effect of the RF field on the EEG electrodes that can vary depending on the geometry of the EEG equipment and leads as well as their conductivity	NCRP (1981), ANSI Standard C95.1 (1982), (ANSI)/IEEE standard C95.1 (2006) IEEE standard 1528 (2003), ICNIRP (1998), FCC (2001), IEEE Standard P1528 (2009)

(Continued)

**TABLE 3 |** Continued

No.	Study	MR scanner and scanning protocols	Type of electrode(s)/implantations/ No. of contacts	Positions and orientations of the electrodes	Safety hazard(s) considered	Methodology (Test object and temperature measurement device)	Observations	Conclusions and recommendations	Safety standard: (reference and guidelines)
5	[113]	- 1.5T MRI scanner - Birdcage RF coil (16 rungs)	DBS electrode	The implants were placed inside the head of the 3d computational model. Two types of implant lead configuration were used: 1. Straight; 2. Helical	- SAR calculations - Temperature measurements	- ELIT1.5 phantom (3d computational model) - SEMCAD X V14 (FDTD) - Four 3d computational human models: Billie, Duke, Ella and Fats	Four-tier approach has been performed: Tier 1 has the highest overestimation of heating elevation and the safety margin used. Tier 2 has lower overestimation and safety margin than tier 1, tier 3 is lower than tier 2 and tier 4 is the lowest of all. The results of heating measurements showed that tier 1 was 1600°C, tier 2 was 220°C, tier 3 was 113°C and tier 4 was 18°C for the straight leads. For the helix lead, the heating increases were 300°C for tier 1, 44°C for tier 2, 21°C for tier 3 and 0.8°C for tier 4	This developed method presented for different types of overestimation and safety margins. It is recommended to use tier 3 and 4 for similar measurements. Tier 3 summarizes that straight DBS lead configuration would result in temperature increases of less than 3.5°C and helix DBS lead configuration would result in temperature increases of 0.1°C when exposed to 0.1W/kg MRI sequence	IEC 60601-2-33 (2008) ISO TS 10974 (2012), ASTM F2182-02 (2002), IEEE std C95.3 (2002)
6	[93]	- Siemens Magnetom 7T	- Scalp EasyCap 64 Ag/AgCl ring-type electrode	Arranged according to the international 10-20 system	- EEG cable noise contributions, - Electromagnetic simulations	- Agar Gel Phantom - Gel phantom (agar)	The temperature probe at the top of the phantom measured temperature increases from 19.7°C to 20.0°C when applying GE and then 20.3°C when applying SE. The heating increase on the EEG electrodes was 18.2°C to 18.7°C using GE and then to 19.1°C using SE. EEG amplifiers showed significant heating of 21.4°C to 22.8°C in GE sequence, and 27.9°C during SE sequence	The proposed setup is appropriate for simultaneous EEG-fMRI at 7T	Following published papers
7	[125]	- 3T MRI system Skyra (Siemens, Germany) - RF transmit coil	- DBS implants - Polymer thick-film (PTF) implants	The electrodes were placed in the head through burr holes to simulate the clinical setup	- Electrical conductivity measurements - SAR averaged over 10g of tissue calculations - Temperature measurements	- Phantom - Fiber optic temperature thermometer (Neoptix Inc., Canada) - IPG (Activa, Medtronic, USA)	Heating calculations in computer simulation technique of FEM showed three times decrease compared to the experimental measurements using DBS electrodes	PTF electrodes were tested (after being designed) using computer simulation and showed heating less than the Medtronic implants. The use of physical vapor deposition created wires might allow safe use of MRI for patients with DBS electrodes	ASTM-F2503-13 (2015), Medtronic (2010), ASTM-F2182-11 (2011), ANSI/AAMI-ISO-14708 (2-14), IEC-60601-2-33 (2002), Medtronic (2014)

(Continued)

**TABLE 3 |** Continued

No.	Study	MR scanner and scanning protocols	Type of electrode(s)/implantations/ No. of contacts	Positions and orientations of the electrodes	Safety hazard(s) considered	Methodology (Test object and temperature measurement device)	Observations	Conclusions and recommendations	Safety standard: (reference and guidelines)
8	[126]	- 1.5T and 3T MRI scanners - Head RF coil - All of these were used in finite element model (FEM) computer simulations - Different sequences with various SAR values	DBS electrode (3D computer design)	DBS electrodes were positioned in 5 head models: A- Eight-shape loop placed laterally; B- Semi-circular loop placed laterally; C- Semi-circular loop placed axially on the top; D- Without loop, short lead length (39cm); E- Without loop, long lead length (60cm)	- Local SAR calculations	- ANSYS Electronic Desktop 16.2 (ANSYS, USA)	The calculated local SAR values using FEM were as follows: Model A: 18.7±4.9W/kg, model B: 2.1±0.4 W/kg, model C: 46.2±16.8W/kg, model D: 207.3±68.7 W/kg and model E: 317±100.5 W/kg	At 3T (127 MHz), the SAR values can be reduced by proper placement of the electrode lead. For better surgical outcomes, more lead placement managements with extensive uncertainty assessment are recommended	Medtronic (2015), US-FDA (2015), IEEE-P1528.4/D1.0. (2014), ISO/TS 10974 (2012)
9	[127]	- 1.5T MRI scanner - Designed linear RF transmitter birdcage that has mechanical rotation capability - Close-fit 32 channels receive array	DBS electrode	DBS electrodes were positioned in the computational head model inside the designed rotating birdcage coil	- Local SAR calculations	- Phantom - 3D computer designed head model - ANSYS high frequency structure simulator (ANSYS, USA) - ANSYS Designer - ANSYS circuit analyzer	Null electric field area in 1.5T can fit the DBS leads with different distributions and loops. Maximum SAR (1 g) of about 1200 W/kg can be seen in the 0° orientation using the rotating birdcage coil and receive array and the minimum was 21 W/kg in 75°. The SAR value can be reduced when inserting the receive array with the other coil	Designed linear RF transmitter birdcage with mechanical rotation capabilities and close fitting receive array. 32 channel are new systems that might enhance the scanning for the patients implanted with DBS electrodes	Medtronic (2015), IEEE-P1528.4/D1.0. (2014)
10	[128]	- 1.5T MRI scanner - Designed linear polarized RF transmitter birdcage that has mechanical angular rotation (Reconfigurable coil) - Close-fit 32 channels receive array	DBS electrode	DBS electrodes were positioned the head model inside the designed rotating birdcage coil. The leads were distributed in 9 configurations in a patient extracted head model. 10 Coil settings were used	- Local SAR calculations - Image quality	- Anthropomorphic phantom - 3D computer designed head model - ANSYS high frequency structure simulator (ANSYS, USA) - ANSYS designer - ANSYS circuit analyzer	Heating in the head phantom during 15 min of scanning with the reconfigurable coil was less than 2°C. Maximum SAR of about 1414.8 W/kg can be seen in the 0° orientation using the linear polarized rotating birdcage coil and the minimum was 4.9 W/kg in 60°. Using the circular polarized rotating birdcage coil with the DBS implant produced SAR of 534.3 W/kg and without the DBS implant 0.9 W/kg	The use of linearly-polarized RF transmitter birdcage with mechanical rotation capabilities and close-fit receive array. 32 channel are useful to perform high resolution scanning for the patients implanted with DBS electrodes. More research is recommended to confirm their application	Medtronic (2003), Medtronic (2015), IEEE-P1528.4/D1.0. (2014)

The table contains the studies that are ordered historically. The scanner's field strength ranges from 1.5T to 7T and the protocols are gradient echo (GE), T1, T2, spoiled gradient recalled acquisition (SPGR) and magnetization prepared rapid gradient echo (MPRAGE). The safety hazards in the table are mostly related to temperature or heating measurements and the results can be in units of degree Celsius or in specific absorption ratio (SAR) unit W/kg. The computer simulation techniques are finite difference time domain (FDTD), finite element method (FEM) and method of moments (MoM). The safety standard is related to the source of safety criteria that have been followed by the study.

the measurements using Luxtron temperature probes of about 11 and 70% of the heating and SAR values, respectively at 1.5T when positioning the tip of the Luxtron temperature probe to the side of the contact and when positioning the tip of the Luxtron temperature probe to the tip of the contact [130]. The measurement of temperature and SAR values can be improved (less underestimation) by placing the active area of these particular probes (not the tip) in contact with the tip of the contact [130]. Therefore in general, care must be taken to consider the implant and probe geometry and sensitivity to ensure accurate temperature measurements are obtained.

## GENERAL CONCLUSIONS IN VIEW OF MINIMIZING THE ADDITIONAL HEALTH RISKS ASSOCIATED WITH SIMULTANEOUS EEG-FMRI

It must be emphasized that the safety of EEG recording in the MR environment (or conversely, MR scanning with EEG recording equipment) should always be treated as a non-standard procedure requiring extra care, and potentially require a site-specific risk assessment, even for non-invasive (scalp EEG) and *MR Conditional* labeled equipment, irrespective of field strength. Once implemented, it is strongly advised to monitor the subjects throughout the procedure. These considerations are more critical for the case of MR scanning in the presence of invasive, intracranial EEG electrodes, due to the greater risk of serious injury. MRI with invasive electrodes remains a relatively rare occurrence concentrated in specialized centers with only a few relevant publications dedicated to the study of the safety aspects. Although post-icEEG (and DBS) electrode implantation MR scanning (for electrode localization validation) is an established procedure in some clinical settings, to our knowledge this is usually performed under local safety rules and supervision. As things stand it seems unlikely that the icEEG-fMRI technique with electrodes attached to recording amplifiers will become standard clinical practice in the short to medium term and will not benefit from fully tested, commercially available turn-key solutions. Therefore site- (and scanner-) specific safety investigations are warranted for all applications of MR in the presence of implanted electrodes. For field strengths above 3T, this recommendation is even stronger and also applies to scalp EEG electrodes.

Nonetheless, it is possible to extract a summary of conclusions that may guide investigators wanting to implement EEG-fMRI. Firstly, follow the instructions provided by the providers/manufacturers of the (so-called) “MR-compatible” EEG equipment (from electrode, electrode cap, etc. to

amplifier/digitiser/signal transmitter) carefully; this advice usually comes in the form of a User’s Manual and *MR Conditional Statement* and may cover the details of the application of the electrodes, EEG equipment handling and positioning, MR scanner field strength, type of MR sequence, etc. In the specific case of icEEG-fMRI, no “MR-compatible” EEG equipment solution is available on the commercial market (as of July 2017) and therefore the type of guidance described above (for scalp EEG) does not exist. Secondly, we can provide the following general guidance, for the implementation of simultaneous EEG-fMRI in every local setting:

- High-SAR MR sequences (such as FSE) should always be avoided [36, 55].
- Excessive heating is more likely to occur when using body transmit RF coils than localized (e.g., head) transmit coils [14, 19, 55].
- Noxious effects are usually reduced by placing all leads and cables along the scanner’s central axis [36, 55].

At this time, given the huge variety of MR environments (scanner type and model, RF coil, etc.) it is not possible, nor wise in our opinion, to provide more specific guidelines for EEG-fMRI.

## CONCLUSIONS

Simultaneous scalp EEG-fMRI remains a significant tool for the detection, identification, and localization of epileptiform discharges. Simultaneous icEEG-fMRI is a more technically challenging, and much less widely applied technique, with potential for providing richer data on brain activity. The relative complexity and constant evolution of MRI instruments, with the numerous fields involved, combined with the quasi infinite number of possible EEG electrode and wire configurations provide the setting for a range of complex potential health hazards resulting from a number of mechanisms, i.e., physical interactions such as RF-induced heating due to the aforementioned factors (including lead orientations) and therefore require careful consideration and evaluation.

## AUTHOR CONTRIBUTIONS

HH has written the initial draft of the review which was then edited, corrected and improved (addition of proper sections and updated knowledge) by DC and LL.

## ACKNOWLEDGMENTS

The authors acknowledge the excellent suggestions from the reviewers. The authors also would like to thank Dr. Robert Stoermer for the valuable contribution to this review.

## REFERENCES

1. Millet D. The origins of EEG. *Int Soc Hist Neurosci.* (2002).
2. Da Silva F. EEG: origin and measurement. In: Mulert C, Lemieux L, editors. *EEG-fMRI: Physiological Basis, Technique and Applications*. Berlin: Springer Science & Business Media (2009). p. 19–39.
3. Kaur K, Shih JJ, Krusinski DJ. Empirical models of scalp-EEG responses using non-concurrent intracranial responses. *J Neural Eng.* (2014) **11**:035012. doi: 10.1088/1741-2560/11/3/035012
4. Enatsu R, Mikuni N. Invasive evaluations for epilepsy surgery: a review of the literature. *Neurol Med Chir.* (2016) **56**:221–7. doi: 10.2176/nmc.ra.2015-0319

5. Tao JX, Baldwin M, Hawes-Ebersole S, Ebersole JS. Cortical substrates of scalp EEG epileptiform discharges. *J Clin Neurophysiol.* (2007) **24**:96–100. doi: 10.1097/WNP.0b013e31803ecdaf
6. Hashiguchi K, Morioka T, Yoshida F, Miyagi Y, Nagata S, Sakata A, et al. Correlation between scalp-recorded electroencephalographic and electrocorticographic activities during ictal period. *Seizure* (2007) **16**:238–47. doi: 10.1016/j.seizure.2006.12.010
7. Zelmann R, Lina JM, Schulze-Bonhage A, Gotman J, Jacobs J. Scalp EEG is not a blur: it can see high frequency oscillations although their generators are small. *Brain Topogr.* (2014) **27**:683–704. doi: 10.1007/s10548-013-0321-y
8. Laufs H. A personalized history of EEG-fMRI integration. *Neuroimage* (2012) **62**:1056–67. doi: 10.1016/j.neuroimage.2012.01.039
9. Kesavadas C, Thomas B. Clinical applications of functional MRI in epilepsy. *Indian J Radiol Imaging* (2008) **18**:210. doi: 10.4103/0971-3026.41829
10. Cunningham CJ, Zaamout ME, Goodyear B, Federico P. Simultaneous EEG-fMRI in human epilepsy. *Can J Neurol Sci.* (2008) **35**:420–35. doi: 10.1017/S0317167100009070
11. Vulliemoz S, Carmichael DW, Rosenkranz K, Diehl B, Rodionov R, Walker MC, et al. Simultaneous intracranial EEG and fMRI of interictal epileptic discharges in humans. *Neuroimage* (2011) **54**:182–90. doi: 10.1016/j.neuroimage.2010.08.004
12. Vulliemoz S, Lemieux L, Daunizeau J, Michel CM, Duncan JS. The combination of EEG Source Imaging and EEG-correlated functional MRI to map epileptic networks. *Epilepsia* (2010) **51**:491–505. doi: 10.1111/j.1528-1167.2009.02342.x
13. Goebel R, Esposito F. The added value of EEG-fMRI in imaging neuroscience. In: Mulert C, Lemieux L, editors. *EEG-fMRI: Physiological Basis, Technique and Applications*. Berlin: Springer Science & Business Media (2009). p. 19–39.
14. Carmichael DW, Vulliemoz S, Rodionov R, Thornton JS, McEvoy AW, Lemieux L. Simultaneous intracranial EEG-fMRI in humans: protocol considerations and data quality. *Neuroimage* (2012) **63**:301–9. doi: 10.1016/j.neuroimage.2012.05.056
15. Murta T, Leite M, Carmichael DW, Figueiredo P, Lemieux L. Electrophysiological correlates of the BOLD signal for EEG-informed fMRI. *Hum. Brain Mapp.* (2015) **36**:391–414. doi: 10.1002/hbm.22623
16. Murta T, Hu L, Tierney TM, Chaudhary UJ, Walker MC, Carmichael DW, et al. A study of the electro-haemodynamic coupling using simultaneously acquired intracranial EEG and fMRI data in humans. *Neuroimage* (2016) **142**:371–80. doi: 10.1016/j.neuroimage.2016.08.001
17. Murta T, Chaudhary UJ, Tierney TM, Dias A, Leite M, Carmichael DW, et al. Phase-amplitude coupling and the BOLD signal: a simultaneous intracranial EEG (icEEG)-fMRI study in humans performing a finger-tapping task. *Neuroimage* (2017) **146**:438–51. doi: 10.1016/j.neuroimage.2016.08.036
18. Villringer A, Mulert C, Lemieux L. Principles of multimodal functional imaging and data integration. In: Mulert C, Lemieux L, editors. *EEG-fMRI: Physiological Basis, Technique, and Applications*. Berlin: Springer Science & Business Media (2009). p. 3–17.
19. Carmichael DW, Thornton JS, Rodionov R, Thornton R, McEvoy A, Allen PJ, et al. Safety of localizing epilepsy monitoring intracranial electroencephalograph electrodes using MRI: radiofrequency-induced heating. *J Magn Reson Imaging* (2008) **28**:1233–44. doi: 10.1002/jmri.21583
20. Lemieux L, Allen PJ, Franconi F, Symms MR, Fish DK. Recording of EEG during fMRI experiments: patient safety. *Magn Reson Med.* (1997) **38**:943–52. doi: 10.1002/mrm.1910380614
21. Lazeyras F, Zimine I, Blanke O, Perrig SH, Seeck M. Functional MRI with simultaneous EEG recording: feasibility and application to motor and visual activation. *J Magn Reson Imaging* (2001) **13**:943–8. doi: 10.1002/jmri.1135
22. Aigner N, Fialka C, Fritz A, Wruhs O, Zöch G. Complications in the use of diathermy. *Burns* (1997) **23**:256–64. doi: 10.1016/S0305-4179(96)00113-1
23. Hay DJ. Electrosurgery. *Surgery* (2005) **23**:73–5. doi: 10.1383/surg.23.2.73.60349
24. Dempsey MF, Condon B. Thermal injuries associated with MRI. *Clin Radiol.* (2001) **56**:457–65. doi: 10.1053/crad.2000.0688
25. Litvak E, Foster KR, Repacholi MH. Health and safety implications of exposure to electromagnetic fields in the frequency range 300 Hz to 10 MHz. *Bioelectromagnetics* (2002) **23**:68–82. doi: 10.1002/bem.99
26. Smallwood RH, Barker AT, Brydon J, Pay DA, Dowd WJ. *Hospital Physicists Association Topic Group Report Report 37 - Safe Design and Construction of Electromedical Equipment*. The Institute of Physical Sciences in Medicine, UK (1983).
27. Welch AJ. Laser irradiation of tissue. In: Eberhart RC and Shitzer A, editors. *Heat Transfer in Medicine and Biology*. New York, NY: Springer. (1985). p. 135–84.
28. National Radiological Protection Board (NRPB). *Board Statement on Clinical Magnetic Resonance Diagnostic Procedures*. Didcot: Chilton (1991).
29. Schaefer D. Bioeffects of MRI and patient safety. In: Bronskill MJ, Sprawls P, editors. *The Physics of MRI - 1992 AAPM Summer School Proceedings*. Woodbury, NY: AAPM (1993).
30. Rezai AR, Baker KB, Tkach JA, Phillips M, Hrdlicka G, Sharan AD, et al. Is magnetic resonance imaging safe for patients with neurostimulation systems used for deep brain stimulation? *Neurosurgery* (2005) **57**:1056–62. doi: 10.1227/01.NEU.0000186935.87971.2a
31. International Commission on Non-Ionizing Radiation Protection (ICNIRP). Guidelines for limiting exposure to time-varying electric and magnetic fields (1 Hz to 100 kHz). *Health Physics Society* (2010). **99**:818–36. doi: 10.1097/HP.0b013e3181f06c86
32. Cohen MS, Weisskoff RM, Rzedzian RR, Kantor HL. Sensory stimulation by time-varying magnetic fields. *Magn Reson Med.* (1990) **14**:409–14. doi: 10.1002/mrm.1910140226
33. Schaefer DJ, Bourland JD, Nyenhuis JA. Review of patient safety in time-varying gradient fields. *J Magn Reson Imaging* (2000) **12**:20–9. doi: 10.1002/1522-2586(200007)12:1<20::AID-JMRI3>3.0.CO;2-Y
34. Georgi JC, Stippich C, Tronnier VM, Heiland S. Active deep brain stimulation during MRI: a feasibility study. *Magn Reson Med.* (2004) **51**:380–8. doi: 10.1002/mrm.10699
35. Benksik M, Bowtell R, Bowley R. Electric fields induced in the human body by time-varying magnetic field gradients in MRI: numerical calculations and correlation analysis. *Phys Med Biol.* (2007) **52**:2337. doi: 10.1088/0031-9155/52/9/001
36. Boucouss SM, Beers CA, Cunningham CJ, Gaxiola-Valdez I, Pittman DJ, Goodyear BG, et al. Feasibility of an intracranial EEG-fMRI protocol at 3T: risk assessment and image quality. *Neuroimage* (2012) **63**:1237–48. doi: 10.1016/j.neuroimage.2012.08.008
37. Sapareto SA, Dewey WC. Thermal dose determination in cancer therapy. *Int J Radiat Oncol Biol Phys.* (1984) **10**:787–800.
38. Yarmolenko PS, Moon EJ, Landon C, Manzoor A, Hochman DW, Viglianti BL, et al. Thresholds for thermal damage to normal tissues: an update. *Int J Hyperther.* (2011) **27**:320–43. doi: 10.3109/02656736.2010.534527
39. Abdel-Rehim S, Bagirathan S, Al-Benna S, O'Boyle C. Burns from ECG leads in an MRI scanner: case series and discussion of mechanisms. *Ann Burns Fire Disast.* (2014) **27**:215–8
40. Lufkin R, Jordan S, Lylyck P, Vinuela F. MR imaging with topographic EEG electrodes in place. *Am J Neuroradiol.* (1988) **9**:953–4.
41. Duckwiler GR, Levesque M, Wilson CL, Behnke E, Babb TL, Lufkin R. Imaging of MR-compatible intracerebral depth electrodes. *Am J Neuroradiol.* (1990) **11**:353–4.
42. Ives JR, Warach S, Schmitt F, Edelman RR, Schomer DL. Monitoring the patient's EEG during echo planar MRI. *Electroencephalogr Clin Neurophysiol.* (1993) **87**:417–20. doi: 10.1016/0013-4694(93)90156-P
43. Belliveau JW, Baker JR, Kwong KK, Rosen BR, George JS, Aine CJ, et al. Functional neuroimaging combining fMRI, MEG, and EEG. In: *Proceedings of the International Society for Magnetic Resonance in Medicine*, Vol. 1. New York, NY (1993).
44. Huang-Hellinger FR, Breiter HC, McCormack G, Cohen MS, Kwong KK, Sutton JP, et al. Simultaneous functional magnetic resonance imaging and electrophysiological recording. *Hum. Brain Mapp.* (1995) **3**:13–23. doi: 10.1002/hbm.460030103
45. Warach S, Ives JR, Schlaug G, Patel MR, Darby DG, Thangaraj V, et al. EEG-triggered echo-planar functional MRI in epilepsy. *Neurology* (1996) **47**:89–93. doi: 10.1212/WNL.47.1.89
46. Seeck M, Lazeyras F, Michel CM, Blanke O, Gericke CA, Ives J, et al. Non-invasive epileptic focus localization using EEG-triggered functional MRI and electromagnetic tomography. *Electroencephalogr Clin Neurophysiol.* (1998) **106**:508–12. doi: 10.1016/S0013-4694(98)00017-0

47. Krakow K, Woermann FG, Symms MR, Allen PJ, Lemieux L, Barker GJ, et al. EEG-triggered functional MRI of interictal epileptiform activity in patients with partial seizures. *Brain* (1999) **122**:1679–88. doi: 10.1093/brain/122.9.1679
48. Portas CM, Krakow K, Allen P, Josephs O, Armony JL, Frith CD. Auditory processing across the sleep-wake cycle: simultaneous EEG and fMRI monitoring in humans. *Neuron* (2000) **28**:991–9. doi: 10.1016/S0896-6273(00)00169-0
49. ASTM F 2182-02a. *Standard Test Method for Measurement of Radio Frequency Induced Heating Near Passive Implants during Magnetic Resonance Imaging*. ASTM Committee F04 on Medical and Surgical Materials and Devices, Subcommittee F04.15 on Material Test Methods. West Conshohocken, PA: ASTM International (2007).
50. International Electrotechnical Commission (IEC). *Medical Electrical Equipment—Particular Requirements for the Safety of Magnetic Resonance Equipment for Medical Diagnosis*. Geneva: IEC (2010).
51. Hofman M, de Cock CC, van der Linden JC, van Rossum AC, Visser FC, Sprenger M, et al. Transesophageal cardiac pacing during magnetic resonance imaging: feasibility and safety considerations. *Magn Reson Med.* (1996) **35**:413–22. doi: 10.1002/mrm.1910350320
52. Glover PM. Interaction of MRI field gradients with the human body. *Phys Med Biol.* (2009) **54**:R99. doi: 10.1088/0031-9155/54/21/R01
53. Nyenhuis JA. Interactions of medical implants with the magnetic fields in MRI. In: *Engineering in Medicine and Biology Society, 2003. Proceedings of the 25th Annual International Conference of the IEEE*. Cancun, MX (2003). p. 3767–70.
54. Nyenhuis JA, Park SM, Kamondetdacha R, Amjad A, Shellock FG, Rezai AR. MRI and implanted medical devices: basic interactions with an emphasis on heating. *IEEE Trans Device Mater Reliabil.* (2005) **5**:467–80. doi: 10.1109/TDMR.2005.859033
55. Carmichael DW, Thornton JS, Rodionov R, Thornton R, McEvoy AW, Ordidge RJ, et al. Feasibility of simultaneous intracranial EEG-fMRI in humans: a safety study. *Neuroimage* (2010) **49**:379–90. doi: 10.1016/j.neuroimage.2009.07.062
56. Dal Molin R, Hecker B. Implantable medical devices MRI safe. In: Blobel B, Pharow P, Parv L, editors. *PHealth 2013: Proceedings of the 10th International Conference on Wearable Micro and Nano Technologies for Personalized Health*, Vol. 189. Amsterdam: IOS Press (2013). p. 96.
57. International Organization of Standardization (ISO). ISO TS 10974: *Assessment of the Safety of Magnetic Resonance Imaging for Patients with an Active Implantable Medical Device*. Geneva: International Organization for Standardization (2012).
58. Shellock FG. Comments on MR heating tests of critical implants. *J Magn Reson Imaging* (2007) **26**:1182–5. doi: 10.1002/jmri.21176
59. Rezai AR, Finelli D, Nyenhuis JA, Hrdlicka G, Tkach J, Sharan A, et al. Neurostimulation systems for deep brain stimulation: *in vitro* evaluation of magnetic resonance imaging-related heating at 1.5 tesla. *J Magn Reson Imaging* (2002) **15**:241–50. doi: 10.1002/jmri.10069
60. Angelone LM, Vassios CE, Wiggins G, Purdon PL, Bonmassar G. On the effect of resistive EEG electrodes and leads during 7 T MRI: simulation and temperature measurement studies. *Magn Reson Imaging* (2006) **24**:801–12. doi: 10.1016/j.mri.2006.01.006
61. Jin J. *Electromagnetic Analysis and Design in Magnetic Resonance Imaging*. Boca Ranton, FL: CRC Press (1998).
62. Barth M, Breuer F, Koopmans PJ, Norris DG, Poser BA. Simultaneous multislice (SMS) imaging techniques. *Magn Reson Med.* (2016) **75**:63–81. doi: 10.1002/mrm.25897
63. Poser BA, Anderson RJ, Guerin B, Setsompop K, Deng W, Mareyam A, et al. Simultaneous multislice excitation by parallel transmission. *Magn Reson Med.* (2014) **71**:1416–27. doi: 10.1002/mrm.24791
64. Fiedler TM, Ladd ME, Bitz AK. SAR simulations and safety. *Neuroimage* (in press). doi: 10.1016/j.neuroimage.2017.03.035
65. Restivo M, Raaijmakers A, van den Berg C, Luijten P, Hoogduin H. Improving peak local SAR prediction in parallel transmit using *in situ* S-matrix measurements. *Magn Reson Med.* (2017) **77**:2040–7. doi: 10.1002/mrm.26261
66. Tse DHY, Wiggins CJ, Poser BA. High-resolution gradient-recalled echo imaging at 9.4 T using 16-channel parallel transmit simultaneous multislice spokes excitations with slice-by-slice flip angle homogenization. *Magn Reson Med.* (2016) **78**:1050–8. doi: 10.1002/mrm.26501
67. Shajan G, Kozlov M, Hoffmann J, Turner R, Scheffler K, Pohmann R. A 16-channel dual-row transmit array in combination with a 31-element receive array for human brain imaging at 9.4 T. *Magn Reson Med.* (2014) **71**:870–9. doi: 10.1002/mrm.24726
68. Gilbert KM, Belliveau JW, Curtis AT, Gati JS, Klassen LM, Menon RS. A conformal transceive array for 7 T neuroimaging. *Magn Reson Med.* (2012) **67**:1487–96. doi: 10.1002/mrm.23124
69. Kangarlu A, Ibrahim TS, Shellock FG. Effects of coil dimensions and field polarization on RF heating inside a head phantom. *Magn Reson Imaging* (2005) **23**:53–60. doi: 10.1016/j.mri.2004.11.007
70. Ciomas C, Schaefers G, Bouvard S, Tailhades E, Perrin E, Comte JC, et al. A phantom and animal study of temperature changes during fMRI with intracerebral depth electrodes. *Epilepsy Res.* (2013) **108**:57–65. doi: 10.1016/j.eplepsyres.2013.10.016
71. Bonmassar G, Anami K, Belliveau JW. Improved subject's safety in simultaneous EEG and fMRI recordings using solid state switching devices on the electrodes. In: *Engineering in Medicine and Biology, 1999. 21st Annual Conference and the 1999 Annual Fall Meeting of the Biomedical Engineering Society] BMES/EMBS Conference, 1999. Proceedings of the First Joint, Vol. 2*, Atlanta, GA (1999) p. 898.
72. Brink WM, Gulani V, Webb AG. Clinical applications of dual-channel transmit MRI: a review. *J Magn Reson Imaging* (2015) **42**:855–69. doi: 10.1002/jmri.24791
73. Guérin B, Setsompop K, Ye H, Poser BA, Stenger AV, Wald LL. Design of parallel transmission pulses for simultaneous multislice with explicit control for peak power and local specific absorption rate. *Magn Reson Med.* (2015) **73**:1946–53. doi: 10.1002/mrm.25325
74. Zhu Y. Parallel excitation with an array of transmit coils. *Magn Reson. Med.* (2004) **51**:775–84 doi: 10.1002/mrm.20011
75. Wald LL, Adalsteinsson E. Parallel transmit technology for high field MRI. *MAGNETOM Flash* (2009) **40**:125–35.
76. Harvey PR, Hoogeveen RM. Multi transmit parallel RF transmission technology. *Koninklijke Philips Electron.* (2009).
77. Katscher U. Basic and tailored RF shimming in a multi-transmit whole body MR System. *PIERS Online* (2008) **4**:781–4. doi: 10.2529/PIERS07122114101
78. Sengupta S, Roebroeck A, Kemper VG, Poser BA, Zimmermann J, Goebel R, et al. A specialized multi-transmit head coil for high resolution fMRI of the human visual cortex at 7T. *PLoS ONE* (2016) **11**:e0165418. doi: 10.1371/journal.pone.0165418
79. Graf H, Steidle G, Schick F. Heating of metallic implants and instruments induced by gradient switching in a 1.5-Tesla whole-body unit. *J Magn. Reson. Imaging* (2007) **26**:1328–33. doi: 10.1002/jmri.21157
80. Elster AD. Gradient-echo MR imaging: techniques and acronyms. *Radiology* (1993) **186**:1–8. doi: 10.1148/radiology.186.1.8416546
81. Larkman DJ, Hajnal JV, Herlihy AH, Coutts GA, Young IR, Ehnholm G. Use of multicoil arrays for separation of signal from multiple slices simultaneously excited. *J. Magn. Reson. Imaging* (2001) **13**:313–7. doi: 10.1002/1522-2586(200102)13:2<313::AID-JMRI1045&gt;3.0.CO;2-W
82. Feinberg DA, Setsompop K. Ultra-fast MRI of the human brain with simultaneous multi-slice imaging. *J Magn Reson.* (2013) **229**:90–100. doi: 10.1016/j.jmr.2013.02.002
83. Auerbach EJ, Xu J, Yacoub E, Moeller S, Ugurbil K. Multiband accelerated spin-echo echo planar imaging with reduced peak RF power using time-shifted RF pulses. *Magn Reson Med.* (2013) **69**:1261–7. doi: 10.1002/mrm.24719
84. Stevens TK, Ives JR, Klassen LM, Bartha R. MR compatibility of EEG scalp electrodes at 4 Tesla. *J Magn Reson Imaging* (2007) **25**:872–7. doi: 10.1002/jmri.20872
85. Angelone LM, Potthast A, Segonne F, Iwaki S, Belliveau JW, Bonmassar G. Metallic electrodes and leads in simultaneous EEG-MRI: specific absorption rate (SAR) simulation studies. *Bioelectromagnetics* (2004) **25**:285–95. doi: 10.1002/bem.10198
86. Hamblin DL, Anderson V, McIntosh RL, McKenzie RJ, Wood AW, Iskra S, et al. EEG electrode caps can reduce SAR induced in the head by

- GSM900 mobile phones. *IEEE Trans Biomed Eng.* (2007) **54**:914–20. doi: 10.1109/TBME.2007.893486
87. Vasilios CE, Angelone LM, Purdon PL, Ahveninen J, Belliveau JW, Bonmassar G. EEG/(f) MRI measurements at 7 Tesla using a new EEG cap (“InkCap”). *Neuroimage* (2006) **33**:1082–92. doi: 10.1016/j.neuroimage.2006.07.038
  88. Yeung CJ, Karmarkar P, McVeigh ER. Minimizing RF heating of conducting wires in MRI. *Magn Reson Med.* (2007) **58**:1028–34. doi: 10.1002/mrm.21410
  89. Asseconti S, Lavallee C, Ferrari P, Jovicich J. Length matters: improved high field EEG-fMRI recordings using shorter EEG cables. *J Neurosci Methods* (2016) **269**:74–87. doi: 10.1016/j.jneumeth.2016.05.014
  90. Mullinger K, Brookes M, Stevenson C, Morgan P, Bowtell R. Exploring the feasibility of simultaneous electroencephalography/functional magnetic resonance imaging at 7 T. *Magn Reson Imaging* (2008) **26**:968–77. doi: 10.1016/j.mri.2008.02.014
  91. Mullinger K, Debener S, Coxon R, Bowtell R. Effects of simultaneous EEG recording on MRI data quality at 1.5, 3 and 7 tesla. *Int J Psychophys.* (2008) **67**:178–88. doi: 10.1016/j.ijpsycho.2007.06.008
  92. Neuner I, Warbrick T, Arrubla J, Felder J, Celik A, Reske M, et al. EEG acquisition in ultra-high static magnetic fields up to 9.4 T. *Neuroimage* (2013) **68**:214–20. doi: 10.1016/j.neuroimage.2012.11.064
  93. Jorge J, Grouiller F, Ipek Ö, Stoermer R, Michel CM, Figueiredo P, et al. Simultaneous EEG-fMRI at ultra-high field: artifact prevention and safety assessment. *Neuroimage* (2015) **105**:132–44. doi: 10.1016/j.neuroimage.2014.10.055
  94. Acharya S, Gurung DB, Saxena VP. Transient temperature distribution in human males and females body due to variation in perfusion effect. *Int J Appl Math.* (2014) **29**:1263–70.
  95. Acharya S, Gurung DB, Saxena VP. Human males and females body thermoregulation: perfusion effect analysis. *J Ther Biol.* (2014) **45**:30–6. doi: 10.1016/j.jtherbio.2014.07.006
  96. Athey T. A model of the temperature rise in the head due to magnetic resonance imaging procedures. *Magn Reson Med.* (1989) **9**:177–84. doi: 10.1002/mrm.1910090204
  97. Gokul KC, Gurung DB, Adhikary PR. Effect of blood perfusion and metabolism in temperature distribution in human eye. *Adv Appl Math Biosci.* (2013) **4**:13–23.
  98. Zhang J, Wilson CL, Levesque MF, Behnke EJ, Lufkin RB. Temperature changes in nickel-chromium intracranial depth electrodes during MR scanning. *Am J Neuroradiol.* (1993) **14**:497–500.
  99. Mirsatari SM, Lee DH, Jones D, Bihari F, Ives JR. MRI compatible EEG electrode system for routine use in the epilepsy monitoring unit and intensive care unit. *Clin. Neurophysiol.* (2004) **115**:2175–80. doi: 10.1016/j.clinph.2004.04.011
  100. Kuusela L, Turunen S, Valanne L, Sipilä O. Safety in simultaneous EEG-fMRI at 3 T: temperature measurements. *Acta Radiol.* (2015) **56**:739–45. doi: 10.1177/0284185114536385
  101. Poulsen C, Wakeman DG, Atefi SR, Luu P, Konya A, Bonmassar G. Polymer thick film technology for improved simultaneous dEEG/MRI recording: safety and MRI data quality. *Magn Reson Med.* (2016). **77**:895–903. doi: 10.1002/mrm.26116
  102. Balasubramanian M, Wells WM, Ives JR, Britz P, Mulkern RV, Orbach DB. RF heating of gold cup and conductive plastic electrodes during simultaneous EEG and MRI. *Neurodiagn J.* (2017) **57**:69–83. doi: 10.1080/21646821.2017.1256722
  103. Gleason CA, Kaula NF, Hricak H, Schmidt RA, Tanagho EA. The effect of magnetic resonance imagers on implanted neurostimulators. *Pacing Clin Electrophysiol.* (1992) **15**:81–94. doi: 10.1111/j.1540-8159.1992.tb02904.x
  104. Kainz W, Neubauer G, Überbacher R, Alesch F, Chan DD. Temperature measurement on neurological pulse generators during MR scans. *Biomed Eng Online* (2002) **1**:2. doi: 10.1186/1475-925X-1-2
  105. Finelli DA, Rezai AR, Ruggieri PM, Tkach JA, Nyenhuis JA, Hrdlicka G, et al. MR imaging-related heating of deep brain stimulation electrodes: *in vitro* study. *Am J Neuroradiol.* (2002) **23**:1795–802.
  106. Baker KB, Tkach JA, Nyenhuis JA, Phillips M, Shellock FG, Gonzalez-Martinez J, et al. Evaluation of specific absorption rate as a dosimeter of MRI-related implant heating. *J Magn Reson Imaging* (2004) **20**:315–20. doi: 10.1002/jmri.20103
  107. Baker KB, Tkach J, Hall JD, Nyenhuis JA, Shellock FG, Rezai AR. Reduction of magnetic resonance imaging-related heating in deep brain stimulation leads using a lead management device. *Neurosurgery* (2005) **57**:392–7. doi: 10.1227/01.NEU.0000176877.26994.0C
  108. Bhidayasiri R, Bronstein JM, Sinha S, Krahl SE, Ahn S, Behnke EJ, et al. Bilateral neurostimulation systems used for deep brain stimulation: *in vitro* study of MRI-related heating at 1.5 T and implications for clinical imaging of the brain. *Magn Reson Imaging* (2005) **23**:549–55. doi: 10.1016/j.mri.2005.02.007
  109. Carmichael DW, Pinto S, Limousin-Dowsey P, Thobois S, Allen PJ, Lemieux L, et al. Functional MRI with active, fully implanted, deep brain stimulation systems: safety and experimental confounds. *Neuroimage* (2007) **37**:508–17. doi: 10.1016/j.neuroimage.2007.04.058
  110. Gorny KR, Presti MF, Goerss SJ, Hwang SC, Jang DP, Kim I, et al. Measurements of RF heating during 3.0-T MRI of a pig implanted with deep brain stimulator. *Magn Reson Imaging* (2013) **31**:783–8. doi: 10.1016/j.mri.2012.11.005
  111. Kahan J, Papadaki A, White M, Mancini L, Yousry T, Zrinzo L, et al. The safety of using body-transmit MRI in patients with implanted deep brain stimulation devices. *PLoS ONE* (2015) **10**:e0129077. doi: 10.1371/journal.pone.0129077
  112. Franceschi AM, Wiggins GC, Mogilner AY, Shepherd T, Chung S, Lui YW. Optimized, minimal specific absorption rate MRI for high-resolution imaging in patients with implanted deep brain stimulation electrodes. *Am J Neuroradiol.* (2016) **37**:1996–2000. doi: 10.3174/ajnr.A4865
  113. Cabot E, Lloyd T, Christ A, Kainz W, Douglas M, Stenzel G, et al. Evaluation of the RF heating of a generic deep brain stimulator exposed in 1.5 T magnetic resonance scanners. *Bioelectromagnetics* (2013) **34**:104–13. doi: 10.1002/bem.21745
  114. Shrivastava D, Abosch A, Hanson T, Tian J, Gupte A, Iaizzo PA, et al. Effect of the extracranial deep brain stimulation lead on radiofrequency heating at 9.4 Tesla (400.2 MHz). *J Magn Reson Imaging* (2010) **32**:600–7. doi: 10.1002/jmri.22292
  115. Eryaman Y, Akin B, Atalar E. Reduction of implant RF heating through modification of transmit coil electric field. *Magn Reson Med.* (2011) **65**:1305–13. doi: 10.1002/mrm.22724
  116. Shrivastava D, Abosch A, Hughes J, Goerke U, DelaBarre L, Visaria R, et al. Heating induced near deep brain stimulation lead electrodes during magnetic resonance imaging with a 3 T transceive volume head coil. *Phys Med Biol.* (2012) **57**:5651. doi: 10.1088/0031-9155/57/17/5651
  117. Eryaman Y, Turk EA, Oto C, Algin O, Atalar E. Reduction of the radiofrequency heating of metallic devices using a dual-drive birdcage coil. *Magn Reson Med.* (2013) **69**:845–52. doi: 10.1002/mrm.24316
  118. Sammartino F, Krishna V, Sankar T, Fisico J, Kalia SK, Hodaie M, et al. 3-Tesla MRI in patients with fully implanted deep brain stimulation devices: a preliminary study in 10 patients. *J Neurosurg.* (2016) doi: 10.3171/2016.9.JNS16908. [Epub ahead of print].
  119. Ahmadi E, Katnani HA, Daftari Besheli L, Gu Q, Atefi R, Villeneuve MY, et al. An Electrocorticography grid with conductive nanoparticles in a polymer thick film on an organic substrate improves CT and MR imaging. *Radiology* (2016) **280**:595–601. doi: 10.1148/radiol.2016142529
  120. Shellock FG. Metallic neurosurgical implants: evaluation of magnetic field interactions, heating, and artifacts at 1.5-Tesla. *J Magn Reson Imaging* (2001) **14**:295–9. doi: 10.1002/jmri.1185
  121. Nyenhuis JA, Kildishev AV, Bourland JD, Foster KS, Gruber G, Athey TW. Heating near implanted medical devices by the MRI RF-magnetic field. *IEEE Trans Magn.* (1999) **35**:4133–5. doi: 10.1109/20.800779
  122. Bhattacharyya PK, Mullin J, Lee BS, Gonzalez-Martinez JA, Jones SE. Safety of externally stimulated intracranial electrodes during functional MRI at 1.5 T. *Magn Reson Imaging* (2017) **38**:182–8. doi: 10.1016/j.mri.2017.01.012
  123. Angelone LM, Ahveninen J, Belliveau JW, Bonmassar G. Analysis of the role of lead resistivity in specific absorption rate for deep brain stimulator leads at 3T MRI. *IEEE Trans Med Imaging* (2010) **29**:1029–38. doi: 10.1109/TMI.2010.2040624
  124. Angelone LM, Bit-Babik G, Chou CK. Computational electromagnetic analysis in a human head model with EEG electrodes and leads exposed to

- RF-field sources at 915 MHz and 1748 MHz. *Radiat Res.* (2010) **174**:91–100. doi: 10.1667/RR1933.1
125. Serano P, Angelone LM, Katnani H, Eskandar E, Bonmassar G. A novel brain stimulation technology provides compatibility with MRI. *Sci. Rep.* (2015) **5**:9805. doi: 10.1038/srep09805
126. Golestanirad L, Angelone LM, Iacono MI, Katnani H, Wald LL, Bonmassar G. Local SAR near deep brain stimulation (DBS) electrodes at 64 and 127 MHz: a simulation study of the effect of extracranial loops. *Magn Reson Med.* (2016). **78**:1558–65. doi: 10.1002/mrm.26535
127. Golestanirad L, Keil B, Angelone LM, Bonmassar G, Mareyam A, Wald LL. Feasibility of using linearly polarized rotating birdcage transmitters and close-fitting receive arrays in MRI to reduce SAR in the vicinity of deep brain stimulation implants. *Magn Reson Med.* (2016). **77**:1701–12. doi: 10.1002/mrm.26220
128. Golestanirad L, Iacono MI, Keil B, Angelone LM, Bonmassar G, Fox MD, et al. Construction and modeling of a reconfigurable MRI coil for lowering SAR in patients with deep brain stimulation implants. *Neuroimage* (2017) **147**:577–88. doi: 10.1016/j.neuroimage.2016.12.056
129. Park SM, Nyenhuis JA, Smith CD, Lim EJ, Foster KS, Baker KB, et al. Gelled versus nongelled phantom material for measurement of MRI-induced temperature increases with bioimplants. *IEEE Trans Magn.* (2003) **39**:3367–71. doi: 10.1109/TMAG.2003.816259
130. Mattei E, Calcagnini G, Triventi M, Censi F, Bartolini P, Kainz W, et al. MRI induced heating of pacemaker leads: effect of temperature probe positioning and pacemaker placement on lead tip heating and local SAR. In: *Engineering in Medicine and Biology Society*, 2006. EMBS'06. 28th Annual International Conference of the IEEE. New York, NY (2006). p. 1889–92.

**Conflict of Interest Statement:** The authors declare that the research was conducted in the absence of any commercial or financial relationships that could be construed as a potential conflict of interest.

Copyright © 2017 Hawsawi, Carmichael and Lemieux. This is an open-access article distributed under the terms of the Creative Commons Attribution License (CC BY). The use, distribution or reproduction in other forums is permitted, provided the original author(s) or licensor are credited and that the original publication in this journal is cited, in accordance with accepted academic practice. No use, distribution or reproduction is permitted which does not comply with these terms.



# Type 1 Diabetes and Impaired Awareness of Hypoglycemia Are Associated with Reduced Brain Gray Matter Volumes

Petr Bednarik<sup>1†</sup>, Amir A. Moheet<sup>2†</sup>, Heidi Grohn<sup>1</sup>, Anjali F. Kumar<sup>2</sup>, Lynn E. Eberly<sup>3</sup>, Elizabeth R. Seaquist<sup>2</sup> and Silvia Mangia<sup>1\*</sup>

<sup>1</sup> Department of Radiology, Center for Magnetic Resonance Research, University of Minnesota, Minneapolis, MN, United States, <sup>2</sup> Department of Medicine, University of Minnesota, Minneapolis, MN, United States, <sup>3</sup> Division of Biostatistics, University of Minnesota, Minneapolis, MN, United States

## OPEN ACCESS

### Edited by:

Itamar Ronen,  
Leiden University, Netherlands

### Reviewed by:

Jessica A. Church-Lang,  
University of Texas at Austin,  
United States  
Xiaoqi Huang,  
West China Hospital of Sichuan  
University, China

### \*Correspondence:

Silvia Mangia  
mangia@umn.edu

<sup>†</sup>These authors have contributed  
equally to this work.

### Specialty section:

This article was submitted to  
Brain Imaging Methods,  
a section of the journal  
Frontiers in Neuroscience

Received: 16 May 2017

Accepted: 11 September 2017

Published: 25 September 2017

### Citation:

Bednarik P, Moheet AA, Grohn H, Kumar AF, Eberly LE, Seaquist ER and Mangia S (2017) Type 1 Diabetes and Impaired Awareness of Hypoglycemia Are Associated with Reduced Brain Gray Matter Volumes. *Front. Neurosci.* 11:529.  
doi: 10.3389/fnins.2017.00529

In this study, we retrospectively analyzed the anatomical MRI data acquired from 52 subjects with type 1 diabetes (26M/26F,  $36 \pm 11$  years old,  $A1C = 7.2 \pm 0.9\%$ ) and 50 age, sex and BMI frequency-matched non-diabetic controls (25M/25F,  $36 \pm 14$  years old). The T1D group was further sub-divided based on whether subjects had normal, impaired, or indeterminate awareness of hypoglycemia ( $n = 31, 20$ , and  $1$ , respectively). Our goals were to test whether the gray matter (GM) volumes of selected brain regions were associated with diabetes status as well as with the status of hypoglycemia awareness. T1D subjects were found to have slightly smaller volume of the whole cortex as compared to controls ( $-2.7\%, p = 0.016$ ), with the most affected brain region being the frontal lobe ( $-3.6\%, p = 0.024$ ). Similar differences of even larger magnitude were observed among the T1D subjects based on their hypoglycemia awareness status. Indeed, compared to the patients with normal awareness of hypoglycemia, patients with impaired awareness had smaller volume of the whole cortex ( $-7.9\%, p = 0.0009$ ), and in particular of the frontal lobe ( $-9.1\%, p = 0.006$ ), parietal lobe ( $-8.0\%, p = 0.015$ ) and temporal lobe ( $-8.2\%, p = 0.009$ ). Such differences were very similar to those observed between patients with impaired awareness and controls ( $-7.6\%, p = 0.0002$  in whole cortex,  $-9.1\%, p = 0.0003$  in frontal lobe,  $-7.8\%, p = 0.002$  in parietal lobe, and  $-6.4\%, p = 0.019$  in temporal lobe). On the other hand, patients with normal awareness did not present significant volume differences compared to controls. No group-differences were observed in the occipital lobe or in the anterior cingulate, posterior cingulate, hippocampus, and thalamus. We conclude that diabetes status is associated with a small but statistically significant reduction of the whole cortex volume, mainly in the frontal lobe. The most prominent structural effects occurred in patients with impaired awareness of hypoglycemia (IAH) as compared to those with normal awareness, perhaps due to the long-term exposure to recurrent episodes of hypoglycemia. Future studies aimed at quantifying relationships of structural outcomes with functional outcomes, with cognitive performance, as well as with parameters describing glucose variability and severity of hypoglycemia episodes, will be necessary to further understand the impact of T1D on the brain.

**Keywords:** structural MRI, brain volumes, type 1 diabetes, hypoglycemia, hypoglycemia unawareness

## INTRODUCTION

Diabetes is a growing world epidemic, with an estimated projected number of more than 800 million people living with diabetes by 2,030 (Wild et al., 2004). Diabetes is a complex metabolic disorder that affects multiple systems in the body. Type 1 diabetes (T1D) is an autoimmune disease, characterized by destruction of insulin producing cells in the pancreas resulting in absolute deficiency of insulin (Standards of Medical Care in Diabetes, 2017). Although Type 1 diabetes can manifest at any age, it is usually diagnosed in children and young adults. In comparison, type 2 diabetes is characterized by variable degrees of insulin deficiency and reduced responsiveness to insulin action. It is usually diagnosed in middle age to older people and is associated with obesity. Diabetes is characterized by hyperglycemia (high blood glucose) and over time hyperglycemia can lead to development of complications such as eye problems, nerve damage and kidney disease (Standards of Medical Care in Diabetes, 2017). Treatment with exogenous insulin is needed in people with type 1 and advanced type 2 diabetes. Treatment with insulin to tightly control glucose can reduce the risk of long term complications of diabetes but also increases risk of hypoglycemia (low blood glucose).

It has been long recognized that diabetic patients may suffer from reduced cognitive function (Miles and Root, 1922; Cukierman-Yaffe, 2014). Both type 1 and type 2 diabetes are associated with cognitive impairment and structural changes in the brain. In particular, type 1 diabetes (T1D) has been linked to performance deficits in memory, attention, information processing and executive function (Kodl and Seaquist, 2008). The neuro-structural correlates of these clinical events remain uncertain.

Identification of brain damage induced by diabetes, particularly before cognitive symptoms appear, is critical for mitigating the long-term consequences of the disease on the brain. Various non-invasive and quantitative MRI neuroimaging approaches have been utilized to objectively characterize the impact of diabetes on brain structure and function, including structural MRI, diffusion tensor imaging (DTI), magnetic resonance spectroscopy (MRS) and functional MRI (fMRI) (Moheet et al., 2015b). Subjects with T1D have been found to have reductions in both white and gray matter (GM) volumes by MRI (Musen et al., 2006; Wessels et al., 2006, 2007). They have also been shown to have lower GM density, primarily in the regions of frontal, temporal, posterior, and cerebellar regions of the brain (Musen et al., 2006; Wessels et al., 2006; Hughes et al., 2013). Moreover, in children with T1D, greater exposure to severe hypoglycemia has been associated with enlargement of hippocampal GM volume compared to children without severe hypoglycemia (Hershey et al., 2010).

In the present study we retrospectively analyzed anatomical MRI data acquired in our laboratory from a sizable number of subjects with long-standing T1D and non-diabetic subjects. The T1D group was further sub-divided in two groups based on whether subjects had normal or impaired awareness of hypoglycemia (IAH).

The typical symptoms of hypoglycemia include sweating, hunger, shakiness/tremulousness, heart pounding, and nervousness/anxiety (Tesfaye and Seaquist, 2010). These warning symptoms are mediated by activation of the nervous system and are key for recognition of hypoglycemia so that the person can take corrective actions to stop the progression of hypoglycemia. Recognition of the onset of these symptoms constitutes awareness of hypoglycemia (McAulay et al., 2001; Geddes and Frier, 2007). Recurrent exposure to iatrogenic hypoglycemia can lead to development of IAH (Cryer, 2005). IAH is estimated to occur in 20% of patients with type 1 diabetes (Geddes et al., 2008). IAH is associated with a 6-fold increased risk of developing severe hypoglycemia (an event causing such neurological changes as to require the aid of another person) (Gold et al., 1994). Questionnaires have been developed to assess awareness of hypoglycemia in people with diabetes (Gold et al., 1994; Clarke et al., 1995; Pedersen-Bjergaard et al., 2001). In this study, we primarily utilized the Cox questionnaire to categorize the status of hypoglycemia awareness in participants with diabetes (Clarke et al., 1995). The Cox questionnaire comprises 8 questions that examine the glycemic threshold at which subjects develop symptoms of hypoglycemia. This questionnaire also characterizes the subject's exposure to episodes of moderate and severe hypoglycemia. A score of four or more implies IAH, while a score of two or less reflects normal awareness of hypoglycemia. A Cox score of three however indicates an indeterminate status of awareness, in which case one can consider an additional method, such as the Gold questionnaire to further characterize impaired awareness (Gold et al., 1994). The Gold scoring method is based on the response to a single question, "Do you know when your hypos are commencing?" Results are expressed in a 7-point Likert scale (from "Always aware" to "Never aware"), where a score of four or more indicates impaired awareness.

Our goal for this study was to estimate the group-differences in structural MRI outcomes available from our datasets. Whereas, other studies have investigated differences in brain volumes between diabetic and non-diabetic subjects (van Harten et al., 2006; Moheet et al., 2015b), a distinct novel aspect of the present work was to test, within the T1D group, whether the IAH is associated with altered brain volumes. In particular, we focused on the volume of the whole cortex, separate cortical lobes, and selected cortical and sub-cortical structures, namely the anterior cingulate cortex (ACC), the posterior cingulate cortex (PCC), the hippocampus, and the thalamus. The ACC and PCC are key brain regions involved in cognition and executive function (Nachev, 2006; Leech and Sharp, 2014), while the hippocampus, a brain structure located deep in the temporal lobe, plays an essential role in learning and memory processing (Scoville and Milner, 1957; Burgess et al., 2002; Squire et al., 2004). Our specific interest in the thalamus originated from recognizing that this area may be functionally involved in the development of IAH (Mangia et al., 2012). Indeed, the thalamus is one of the brain areas which manifest increased neuronal activity during hypoglycemia as measured by increases of blood flow in healthy controls. However, such response was observed to be blunted in a group of type 1 diabetic subjects with impaired awareness to hypoglycemia (Mangia et al., 2012).

## METHODS

### Subjects

Subjects were drawn from experiments that were conducted over a time-frame of 7 years from 2009 to 2016 within the context of multiple completed and on-going projects which generally aimed at describing the brain responses to hypoglycemia during hyperinsulinemic clamps (Mangia et al., 2012; Terpstra et al., 2014; Moheet et al., 2015a). Datasets that contained both T1-weighted (T1w) and T2-weighted (T2w) structural MRI of acceptable image quality as determined by visual inspection (e.g., no motion artifacts) were included in this analysis. Included T1D subjects were recruited for participation because they had T1D (defined on clinical grounds) and were between the ages of 18 and 67 years. The healthy control group was frequency matched to T1D based on age, sex, and BMI during the same time period. Recruited T1D subjects had hemoglobin A1C <8% in the 3 months before study participation, and did not have history of proliferative retinopathy or other microvascular complications. T1D subjects were also divided into two subgroups: T1D with IAH and T1D with normal awareness of hypoglycemia (NAH), as verified primarily by the Cox questionnaire (Clarke et al., 1995). In the few cases ( $n = 7$ ) that T1D subjects had a Cox score of three (i.e., indeterminate status), we used their Gold score (Gold et al., 1994) for determining their awareness status. For 1 of these 7 patients, Gold score was missing in the database, and therefore that subject was left as “indeterminate” and excluded from the analyses focused on hypoglycemia awareness. Other exclusion criteria for both groups included history of stroke, seizures, neurosurgical procedures, or arrhythmias, use of drugs that can alter glucose metabolism (other than insulin for the T1D subjects), alcohol abuse, history of renal insufficiency with serum creatinine levels above 1.5 mg/dL, pregnancy, breastfeeding, and incompatibility with MR safety criteria.

### Protocol

During the experimental MRI session, metabolic conditions were controlled by the use of a hyperinsulinemic (2 mu/kg/min) clamp to maintain blood glucose values around 95 mg/dL (normal glycemia). Only the data collected during normal glycemia are included in this analysis. Details regarding the protocol for this insulin clamp technique have been published elsewhere (Mangia et al., 2012; Moheet et al., 2015a). The studies were carried out in accordance with the Declaration of Helsinki and with the recommendations of The Code of Federal Regulations, Institutional Review Board. The protocol was approved by the Institutional Review Board: Human Subjects Committee of the University of Minnesota. Written informed consent was obtained from all subjects prior to the experimental session.

### MRI Measurements

MRI measurements were performed using either a 3 T Siemens Trio scanner (Siemens, Erlangen, Germany) or a 3 Tesla Siemens Prisma scanner (Siemens, Erlangen, Germany). Radiofrequency pulses were transmitted with the scanner body coil, while signal was received with either a 12-channels receive coil (for experiments conducted with the 3 T Trio) or a 20-channels receive coil (for experiments conducted with the 3 T Prisma).

Each subject's head was carefully fixed with padding and memory foam to prevent motion artifacts while assuring that subject was comfortable with the setup. In addition, the structural T1w and T2w images were always acquired at the beginning of the study session. High resolution T1w images were acquired with a MPRAGE sequence, with the following parameters:  $256 \times 256 \text{ mm}^2$  field of view, 160 slices, 1 mm isotropic resolution, repetition time (TR) = 2,150 ms, echo time (TE) = 2.47 ms, inversion time (TI) = 1,000 ms, with parallel acceleration factor (PAT) of 2 for a total scan time of ~5 min for each magnet. T2w scans were acquired with the T2-SPACE sequence at 1 mm isotropic resolution using the same imaging volume of the MPRAGE acquisition. For acquisitions on the 3T Trio, the T2-SPACE parameters were TR = 3,200 ms, TE = 201 ms, PAT 4, and for 3T Prisma TR = 3,200 ms, TE = 147 ms, PAT 4. Both T1w and T2w images were automatically corrected for the  $B_1^-$ -related spatial inhomogeneity utilizing coil sensitivity profile and “prescan normalize” routine implemented in the Siemens image acquisition/reconstruction algorithm.

### Data Processing

Segmentation of cortical and subcortical GM structures was performed with an identical pipeline for each subject based on FreeSurfer (version 5.3, <http://surfer.nmr.mgh.harvard.edu/>). In the first step, the masks resulting from subcortical segmentation (aseg) (Fischl et al., 2002) and cortical parcellation (aparc) (Desikan et al., 2006) were obtained in native subject space by using T1w images. In addition, the estimated intracranial volumes (eICV), later used to adjust volumes of brain GM regions to the head size (Buckner et al., 2004), were obtained per subject. The high contrast between cerebrospinal fluid (CSF) and cerebral cortex on T2w images was utilized to refine segmentation (Glasser et al., 2013). Finally the segmentation outputs were carefully manually edited in accordance with the FreeSurfer manual in several subsequent steps. The errors resulting from imperfect intensity normalization were corrected by adding control points. The remaining errors in white matter segmentation were fixed by editing of *wm.mgz* file. Finally, the pial surfaces were checked and edited where needed. All manual editing steps were performed by an experienced neuroradiologist (P.B.).

The selected nine cortical and subcortical regions of interest (ROIs) are listed in **Tables 2–4**, and are shown in **Figure 1**. In particular, the PCC corresponded to the brain areas identified by FreeSurfer as the isthmus cingulate, while the ACC corresponded to the rostral anterior cingulate. Volumes were calculated from each ROI separately for right and left hemisphere, so that two data points were obtained per subject per ROI. Volumes of the segmented brain structures were scaled (i.e., divided) by eICV per subject.

Finally, the operator performing the manual editing was blinded to the hypoglycemia awareness status of the T1D subjects, but was un-blinded to the diabetes status (controls or T1D). In order to assess the possible bias induced by the partial un-blinding of the operator, differences in the whole cortex volumes obtained before and after manual edits were calculated per subject, with positive numbers indicating volume reductions after editing.

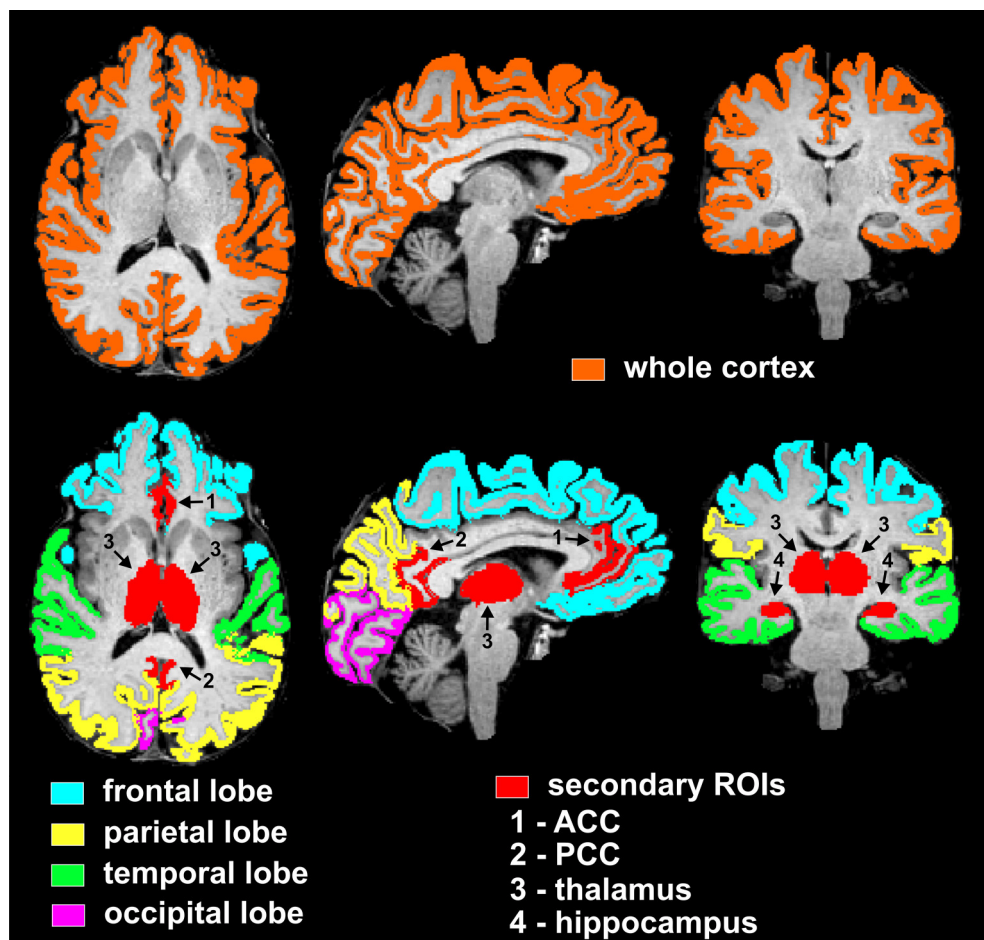


**FIGURE 1 |** Visualization of regions of interest subjected to volumetry analyses from one representative non-diabetic subject. The top row displays the mask of the whole supratentorial cortex, which includes lobes (frontal, parietal, temporal, occipital), insula and cingulum. Bottom row depicts masks of cortical lobar regions (frontal, parietal, temporal, occipital) and secondary cortical and subcortical regions of interest (ACC, PCC, thalamus, and hippocampus). In particular, the PCC and ACC corresponded to the brain areas identified by FreeSurfer as the isthmus cingulate and rostral anterior cingulate, respectively. ROIs are here shown as combined between the two hemispheres, however the statistical analyses used both right and left hemisphere data points per ROI per subject.

## Statistical Analyses

Subject age, BMI, A1c, and disease duration were summarized with means and standard deviations (SD) and compared between groups using linear models; sex and scanning protocol distribution were compared across groups using Fisher's exact test. For each of the nine ROIs separately, volumes (left and right hemispheres combined) were summarized by group using means and standard deviations. Group comparisons of GM volumes per ROI were tested (1) between all T1D subjects and controls, (2) between T1D with NAH and T1D with IAH, and (3) between controls and each of T1D with NAH and T1D with IAH. For such comparisons, linear mixed models were used that adjusted for age, sex, BMI, hemisphere, and protocol. For the NAH vs. IAH comparisons within the T1D group, we fit models with and without additional correction for duration of disease and A1c. Our primary test of interest was for the whole cortex. Within the whole cortex, false discovery rate (FDR) (Benjamini and Hochberg, 1995) correction was used for multiple testing of the 4 lobes, and separately for multiple testing of the

additional 4 cortical and subcortical ROIs (namely the ACC, PCC, hippocampus, and thalamus). When comparing controls to each of the groups of T1D subjects with NAH and with IAH, the FDR correction included the additional *p*-value correction for those two pairwise comparisons. Statistical significance results are presented both without and with the multiple-testing corrections. Finally, hemisphere by group interactions were evaluated (but were left out of the final models since they were non-significant for all ROIs), and differences in the whole cortex volumes obtained before and after manual edits were compared with unpaired two-tailed *t*-test between the controls and T1D subjects.

## RESULTS

A total of 102 datasets (50 from non-diabetic controls and 52 from T1D subjects) were evaluated. Subjects were evenly distributed among females and males in both control and T1D groups (Table 1). T1D subjects had good glycemic control, with

**TABLE 1 |** Subject characteristics.

Group	n	Age (years)	Sex (M/F)	BMI (kg/m <sup>2</sup> )	T1D duration (years)	A1C (%)	Protocol (Trio/Prisma)
Control	50	36 ± 14	25/25	25 ± 4	–	–	18/32
T1D	52	36 ± 11	26/26	26 ± 4	20 ± 11	7.2 ± 0.9	19/33
p-values*		0.86	0.99	0.25	–	–	0.99
T1D-NAH	31	32 ± 10	18/13	26 ± 4	17 ± 10	7.4 ± 0.8	10/21
T1D-IAH	20	43 ± 10	8/12	27 ± 5	25 ± 11	6.9 ± 0.8	9/11
p-values§		0.0005	0.26	0.45	0.008	0.042	0.39

\*Comparisons between control and T1D subjects.

§Comparisons between T1D-NAH and T1D-IAH subjects.

an average A1C of 7.2%, and their disease duration was 20 ± 11 years on average. Both T1D and control groups were 36 years old on average ( $p = 0.86$ ), while the T1D-NAH group was on average 11 years younger than the T1D-IAH group ( $p = 0.0005$ ). T1D-IAH subjects also tended to have slightly lower A1C as compared to the T1D-NAH group ( $p = 0.042$ ). No group-differences in BMI were observed. Image quality was high/excellent for all datasets, and no differences were observed among groups or between imaging protocols. In addition, on average, 0.04 ± 1.5% and 0.06 ± 1.1% of voxels were removed by the operator in controls and T1D subjects, respectively ( $p = 0.92$ ).

The GM volume of the whole cortex was slightly smaller for T1D subjects than controls (by –2.7%,  $p = 0.016$ ). Among the 4 lobes, the frontal cortex was the most affected (by –3.6%,  $p = 0.024$ , corrected), whereas only a trend of smaller volume was observed for the parietal lobe (by –2.9%,  $p = 0.081$ , corrected). No differences were observed when considering the other ROIs (**Table 2**).

When comparing IAH vs. NAH in T1D subjects (**Table 3**), the GM volume of the whole cortex was smaller by an even larger extent (namely –7.9%,  $p = 0.0009$ ) than what was observed between T1D subjects and controls. Smaller volumes were observed in particular in the frontal lobe (–9.1%,  $p = 0.006$ , corrected), parietal lobe (–8.0%,  $p = 0.015$ , corrected), and temporal lobe (–8.2%,  $p = 0.009$ , corrected). Such observations were not driven by differences in T1D duration and A1C among groups, since these models adjusting for T1D disease duration and A1C showed similar or even stronger statistical significance than when comparisons were not corrected for those parameters (**Table 3**). No volume differences in the other ROIs were observed.

Differences observed between T1D subjects with and without impaired awareness were very similar to those observed between T1D with IAH and controls (**Table 4**), namely –7.6% in whole cortex ( $p = 0.0002$ ), –9.1% in frontal lobe ( $p = 0.0003$ , corrected), –7.8% in parietal lobe ( $p = 0.002$ , corrected), and –6.4% in temporal lobe ( $p = 0.019$ , corrected). On the other hand, T1D with NAH did not present significant volume differences as compared to controls in any ROI.

Finally, no hemisphere by group interaction was observed for any ROI. Also, the two protocols were not found to impact the volumetric outcomes.

**TABLE 2 |** Volumetry comparisons between T1D subjects and controls.

Region	Group values (mean ± SD)		Group-comparisons		
	Control (n = 50)	T1D (n = 52)	Diff* (%)	unadj_p	fdr_p
Whole cortex	0.33 ± 0.02	0.32 ± 0.02	<b>–2.7</b>	0.016	0.016
Frontal lobe	0.119 ± 0.010	0.115 ± 0.009	<b>–3.6</b>	0.006	0.024
Occipital lobe	0.031 ± 0.003	0.030 ± 0.002	–3.4	0.084	0.112
Parietal lobe	0.079 ± 0.006	0.077 ± 0.006	–2.9	0.040	0.081
Temporal lobe	0.073 ± 0.005	0.072 ± 0.005	–1.3	0.345	0.345
ACC	0.0033 ± 0.0004	0.0033 ± 0.0004	–0.3	0.976	0.976
Hippocampus	0.0058 ± 0.0005	0.0058 ± 0.0005	0.0	0.800	0.976
PCC	0.0033 ± 0.0004	0.0032 ± 0.0004	–2.7	0.256	0.512
Thalamus	0.0104 ± 0.0009	0.0101 ± 0.0010	–2.6	0.131	0.512

Linear mixed models used for the comparisons included age, sex, BMI, hemisphere and protocol as covariates. False discovery rate correction was applied for the 4 lobes, and, separately, for the ACC, hippocampus, PCC, and thalamus. Shaded areas indicate  $p < 0.05$ , and bold numbers indicate group differences for which fdr\_p < 0.05. ACC (anterior cingulate cortex), PCC (posterior cingulate cortex), unadj\_p (unadjusted p-value), fdr\_p (p-value after false discovery rate correction).

\*Differences were calculated as T1D minus Control.

## DISCUSSION

This cross-sectional morphometric MRI study examined the association of T1D with GM volumes. In this study, we found that subjects with long standing T1D had smaller whole cortex and frontal lobe GM volumes compared to non-diabetic controls of similar age, sex and BMI. In this study, subjects with diabetes had good glycemic control based on A1C and did not have any severe microvascular complications. We also noted a trend toward T1D having smaller GM volume in the parietal region. Overall the magnitude of these differences was small, namely 3.6% in the frontal lobe and 2.7% in the whole cortex. However, structural effects of larger magnitude were present in T1D patients with IAH as compared to patients with NAH (e.g., 7.9 and 9.1% in whole cortex and frontal lobe, respectively), as well as compared to controls (e.g., 7.6 and 9.1% in whole cortex and frontal lobe, respectively). Interestingly, patients with NAH did not show volume reductions as compared to controls. These observations are novel because association between IAH and reduced brain volumes in patients with T1D diabetes has never been reported before.

The exact mechanisms underlying development of IAH are not known and could be related to alterations in both

**TABLE 3 |** Volumetry comparisons for T1D subjects between those with NAH and IAH.

Region	Group values (mean ± SD)			Group-comparisons			
			Diff* (%)	Without adjustment for T1D duration and A1C		With adjustment for T1D duration and A1C	
	T1D with NAH (n = 31)	T1D with IAH (n = 20)		unadj_p	fdr_p	unadj_p	fdr_p
Whole cortex	0.33 ± 0.01	0.30 ± 0.02	<b>-7.9</b>	0.002	0.002	0.0009	0.0009
Frontal lobe	0.120 ± 0.007	0.108 ± 0.008	<b>-9.1</b>	0.002	0.008	0.002	0.006
Occipital lobe	0.031 ± 0.002	0.029 ± 0.003	-3.8	0.593	0.593	0.342	0.342
Parietal lobe	0.079 ± 0.005	0.073 ± 0.006	<b>-8.0</b>	0.013	0.018	0.011	0.015
Temporal lobe	0.074 ± 0.004	0.069 ± 0.005	<b>-8.2</b>	0.008	0.016	0.005	0.009
ACC	0.0034 ± 0.0004	0.0032 ± 0.0005	-5.4	0.528	0.704	0.377	0.528
Hippocampus	0.0059 ± 0.0004	0.0057 ± 0.0006	-3.3	0.478	0.704	0.396	0.528
PCC	0.0033 ± 0.0004	0.0032 ± 0.0004	-2.7	0.966	0.966	0.876	0.876
Thalamus	0.0104 ± 0.0008	0.0097 ± 0.0011	-5.2	0.313	0.704	0.292	0.528

Linear mixed models used for the comparisons included age, sex, BMI, hemisphere and protocol as covariates, both without and with additional adjustment for disease duration and A1c. False discovery rate correction was applied for the 4 lobes, and, separately, for the ACC, hippocampus, PCC, and thalamus. Shaded areas indicate  $p < 0.05$ , and bold numbers indicate group differences for which  $fdr\_p < 0.05$ . ACC (anterior cingulate cortex), PCC (posterior cingulate cortex), unadj\_p (unadjusted p-value), fdr\_p (p-value after false discovery rate correction).

\*Differences were calculated as IAH minus NAH for the T1D subjects.

brain hypoglycemia sensing and impaired coordination of the counter-regulatory response. Alterations in neurotransmission, upregulation of brain glucose transport or availability of alternate fuels like lactate for brain metabolism (as a result of exposure to recurrent hypoglycemia) may contribute to development of IAH (Tesfaye and Seaquist, 2010). Strict avoidance of hypoglycemia may partially restore awareness of hypoglycemia (Dagogo-Jack et al., 1994; Fanelli et al., 1994; Leelarathna et al., 2013), however this is very challenging for insulin treated patients with diabetes to maintain long-term.

Importantly, our comparisons took into account age differences between the two patient populations (T1D subjects with IAH tend to be older than T1D subjects with NAH), along with differences in A1C (T1D subjects with IAH tend to have slightly lower A1C than T1D subjects with NAH) and differences in diabetes duration (T1D subjects with IAH tend to have longer disease duration than T1D subjects with NAH). Therefore, based on our results, we can rule out that our findings were driven by age or simply by disease duration. On the other hand, since T1D patients who develop IAH are generally those who experience episodes of hypoglycemia more frequently, one can speculate that the long-term exposure to recurrent hypoglycemia may be associated with reduced brain volumes. To test such hypothesis, future investigations should include objective measures of antecedent hypoglycemia episodes by means of continuous glucose monitoring.

Smaller brain volumes between T1D subjects and non-diabetic subjects are generally consistent with previous published literature. Musen et al. reported reduced GM density in the region of left and right superior temporal gyri, left angular gyrus, left middle temporal and middle frontal gyri, and left thalamus in subjects with T1D relative to control subjects (Musen et al., 2006). Another study reported reduced GM volume in the frontal lobe in subjects with T1D compared to controls (Hughes et al., 2013). Smaller GM volumes in T1D have been linked to poor

**TABLE 4 |** Volumetry comparisons of controls with T1D-NAH and T1D-IAH subjects.

Region	Group-comparisons					
	T1D-NAH vs. Controls			T1D-IAH vs. Controls		
	Diff* (%)	unadj_p	fdr_p	Diff* (%)	unadj_p	fdr_p
Whole cortex	0.4	0.632	0.632	<b>-7.6</b>	0.0001	0.0002
Frontal lobe	0.0	0.435	0.569	<b>-9.1</b>	0.00004	0.0003
Occipital lobe	-2.0	0.207	0.331	-5.7	0.118	0.237
Parietal lobe	-0.1	0.719	0.719	<b>-7.8</b>	0.0006	0.002
Temporal lobe	1.9	0.498	0.569	<b>-6.4</b>	0.007	0.019
ACC	-1.8	0.812	0.812	-3.7	0.794	0.812
Hippocampus	1.5	0.507	0.812	-2.0	0.810	0.812
PCC	1.4	0.255	0.812	-4.6	0.468	0.812
Thalamus	-0.6	0.371	0.812	-5.8	0.108	0.812

Linear mixed models used for the comparisons included age, sex, BMI, hemisphere and protocol as covariates. False discovery rate correction was applied for the 4 lobes and two pairwise comparisons, and, separately, for the ACC, hippocampus, PCC, thalamus and the two pairwise comparisons. Shaded areas indicate  $p < 0.05$ , and bold numbers indicate group differences for which  $fdr\_p < 0.05$ . ACC (anterior cingulate cortex), PCC (posterior cingulate cortex), unadj\_p (unadjusted p-value), fdr\_p (p-value after false discovery rate correction).

\*Differences were calculated as T1D-NAH or T1D-IAH subjects minus controls.

glycemic control, severe hypoglycemia and presence of severe microvascular complications (Moheet et al., 2015b).

In people with Type 2 diabetes, several studies have shown evidence of hippocampal atrophy and reduced performance on neurocognitive testing (den Heijer et al., 2003; Bruehl et al., 2009). In our study we did not see significant differences in hippocampal volumes of subjects with T1D compared to controls. These findings are consistent with previous small studies which also did not find evidence of hippocampal atrophy in subjects with long standing T1D (Lobnig et al., 2006;

Bednarik et al., 2015). Interestingly, whereas group differences were observed in the frontal and parietal lobes, our analysis did not reveal volume differences in two sub-regions of such lobes that constitute the major hubs of the default mode network, namely the ACC and PCC. Diabetes or hypoglycemia awareness status did not impact the thalamic volume either, despite this region has been suggested to be functionally involved in the development of hypoglycemia unawareness based on the blunted thalamic responses to hypoglycemia observed in IAH-T1D subjects as compared to non-diabetic controls (Mangia et al., 2012). These findings remind to apply general caution when anticipating structural group differences of a brain area based on functional group differences observed in that area.

MRI studies, including the present one, usually involve only limited numbers of subjects. Therefore, it remains a challenge to coherently describe how the many contributors such as age, diabetes duration, glucose control (i.e., A1C levels) and glucose variability, among others, mediate the impact of diabetes on the brain especially when analyses are performed at the voxel level, which is inherently more demanding in terms of multiple comparison corrections. To partially overcome such a challenge, in this study we chose a morphometry analysis based on estimating the volumes of aggregated large brain areas that were mostly automatically segmented by FreeSurfer routines and, most importantly, are maintained in the native space of the subject. Such an ROI-based approach allows a straightforward normalization of brain volumes based on the total intra-cranial volume of the subject and does not require excellent alignment of the normalized brains as is necessary for voxel-wise comparisons. Also, the use of automatic Freesurfer segmentation, and standardized operator routines to correct segmentation outcomes, allowed identifying the regions of interest with minimized operator biases. In addition, a distinct strength of our study design was the excellent matching in the frequency of age, sex, and BMI between T1D and non-diabetic subjects.

One obvious limitation of this study is its cross-sectional design. We do not have longitudinal A1C data or information about previous episodes of severe hypoglycemia, so we cannot assess the relationship of exposure to hyper- and hypoglycemia on GM volume. Another limitation of our study is that we did not perform neurocognitive testing in these subjects and cannot assess if these subtle reductions in GM volumes were associated with decline in cognitive function.

## REFERENCES

- Bednarik, P., Oz, G., Eberly, L. E., Kubisiak, K., Mangia, S., Kumar, A., et al. (2015). Volume of hippocampus and other subcortical brain structures in subjects with type 1 diabetes. in Proceedings of the 75th Scientific Session of the American Diabetes Association (ADA). Boston, MA. *Diabetes* 64(Suppl. 1):A108. doi: 10.13140/RG.2.2.12109.23521
- Benjamini, Y., and Hochberg, Y. (1995). Controlling the false discovery rate: a practical and powerful approach to multiple testing. *J. R. Stat. Soc. B.* 57, 289–300.

## CONCLUSIONS

We conclude that T1D is associated with a small but significant reduction of the whole cortex GM volume, mainly in the frontal lobe. Similar structural effects occur when comparing, within the T1D subjects, patients with IAH vs. those with normal awareness. The clinical significance of these subtle changes in GM volume is not clear. Future studies are needed to examine if these subtle reductions in GM volumes are associated with cognitive impairment.

## AUTHOR CONTRIBUTIONS

PB and AM have contributed equally to the work. PB participated in acquisition and analysis of the data, and in preparing the manuscript. AM participated in acquisition and interpretation of the data, and preparing the manuscript. HG and AK participated in acquisition of the data, and editing the manuscript. LE participated in design of the work, analysis and interpretation of the data, and in editing the manuscript. ES participated in design of the work, interpretation of the data, and editing the manuscript. SM participated in design of the work, acquisition, analysis, interpretation of the data, and preparing the manuscript.

## ACKNOWLEDGMENTS

The authors are grateful to the volunteers who participated in the study and thereby made this research possible. The authors are also grateful to the MRI support available at CMRR (namely Erik Solheid and Wendy Elvendahl). In addition, the authors would like to thank Dr. Alena Svatkova for helpful suggestions on data processing, and Nathan Rubin for help with data entry. The authors acknowledge the Minnesota Supercomputing Institute (MSI) at the University of Minnesota for providing resources that contributed to the research results reported within this paper (URL: <http://www.msi.umn.edu>). Research reported in this publication was supported by the National Institutes of Health (Award Numbers P41 EB015894, P30 NS076408, R01DK099137, and R56DK099137). Research reported in this publication was also supported by the National Center for Advancing Translational Sciences of the National Institutes of Health, Award Numbers KL2TR000113 and UL1TR000114. The content is solely the responsibility of the authors and does not necessarily represent the official views of the funding agencies.

- Bruehl, H., Wolf, O. T., Sweat, V., Tirsi, A., Richardson, S., and Convit, A. (2009). Modifiers of cognitive function and brain structure in middle-aged and elderly individuals with type 2 diabetes mellitus. *Brain Res.* 1280, 186–194. doi: 10.1016/j.brainres.2009.05.032
- Buckner, R. L., Head, D., Parker, J., Fotenos, A. F., Marcus, D., Morris, J. C., et al. (2004). A unified approach for morphometric and functional data analysis in young, old, and demented adults using automated atlas-based head size normalization: reliability and validation against manual measurement of total intracranial volume. *Neuroimage* 23, 724–738. doi: 10.1016/j.neuroimage.2004.06.018

- Burgess, N., Maguire, E. A., and O'Keefe, J. (2002). The human hippocampus and spatial and episodic memory. *Neuron* 35, 625–641. doi: 10.1016/S0896-6273(02)00830-9
- Clarke, W. L., Cox, D. J., Gonder-Frederick, L. A., Julian, D., Schlundt, D., and Polonsky, W. (1995). Reduced awareness of hypoglycemia in adults with IDDM. A prospective study of hypoglycemic frequency and associated symptoms. *Diabetes Care* 18, 517–522. doi: 10.2337/diacare.18.4.517
- Cryer, P. E. (2005). Mechanisms of hypoglycemia-associated autonomic failure and its component syndromes in diabetes. *Diabetes* 54, 3592–3601. doi: 10.2337/diabetes.54.12.3592
- Cukierman-Yaffe, T. (2014). Diabetes, dysglycemia and cognitive dysfunction. *Diabetes Metab. Res. Rev.* 30, 341–345. doi: 10.1002/dmrr.2507
- Dagogo-Jack, S., Rattarasarn, C., and Cryer, P. E. (1994). Reversal of hypoglycemia unawareness, but not defective glucose counterregulation, in IDDM. *Diabetes* 43, 1426–1434.
- den Heijer, T., Vermeer, S. E., van Dijk, E. J., Prins, N. D., Koudstaal, P. J., Hofman, A., et al. (2003). Type 2 diabetes and atrophy of medial temporal lobe structures on brain MRI. *Diabetologia* 46, 1604–1610. doi: 10.1007/s00125-003-1235-0
- Desikan, R. S., Segonne, F., Fischl, B., Quinn, B. T., Dickerson, B. C., Blacker, D., et al. (2006). An automated labeling system for subdividing the human cerebral cortex on MRI scans into gyral based regions of interest. *Neuroimage* 31, 968–980. doi: 10.1016/j.neuroimage.2006.01.021
- Fanelli, C., Pampanelli, S., Epifano, L., Rambotti, A. M., Di Vincenzo, A., Modarelli, F., Ciofetta, M., Lepore, M., Annibale, B., Torlone, E., and et al. (1994). Long-term recovery from unawareness, deficient counterregulation and lack of cognitive dysfunction during hypoglycaemia, following institution of rational, intensive insulin therapy in IDDM. *Diabetologia* 37, 1265–1276. doi: 10.1007/BF00399801
- Fischl, B., Salat, D. H., Busa, E., Albert, M., Dieterich, M., Haselgrave, C., et al. (2002). Whole brain segmentation: automated labeling of neuroanatomical structures in the human brain. *Neuron* 33, 341–355. doi: 10.1016/S0896-6273(02)00569-X
- Geddes, J., and Frier, B. M. (2007). Severe hypoglycaemia in insulin-treated Type 2 diabetes. *Diabet. Med.* 24, 327; author reply: 328. doi: 10.1111/j.1464-5491.2007.02084.x
- Geddes, J., Schopman, J. E., Zammitt, N. N., and Frier, B. M. (2008). Prevalence of impaired awareness of hypoglycaemia in adults with Type 1 diabetes. *Diabet. Med.* 25, 501–504. doi: 10.1111/j.1464-5491.2008.02413.x
- Glasser, M. F., Sotiroopoulos, S. N., Wilson, J. A., Coalson, T. S., Fischl, B., Andersson, J. L., et al. (2013). The minimal preprocessing pipelines for the Human Connectome Project. *Neuroimage* 80, 105–124. doi: 10.1016/j.neuroimage.2013.04.127
- Gold, A. E., MacLeod, K. M., and Frier, B. M. (1994). Frequency of severe hypoglycemia in patients with type 1 diabetes with impaired awareness of hypoglycemia. *Diabetes Care* 17, 697–703. doi: 10.2337/diacare.17.7.697
- Hershey, T., Perantie, D. C., Wu, J., Weaver, P. M., Black, K. J., and White, N. H. (2010). Hippocampal volumes in youth with type 1 diabetes. *Diabetes* 59, 236–241. doi: 10.2337/db09-1117
- Hughes, T. M., Ryan, C. M., Aizenstein, H. J., Nunley, K., Gianaros, P. J., Miller, R., et al. (2013). Frontal gray matter atrophy in middle aged adults with type 1 diabetes is independent of cardiovascular risk factors and diabetes complications. *J. Diabetes Complications* 27, 558–564. doi: 10.1016/j.jdiacomp.2013.07.001
- Kodl, C. T., and Seaquist, E. R. (2008). Cognitive dysfunction and diabetes mellitus. *Endocr. Rev.* 29, 494–511. doi: 10.1210/er.2007-0034
- Leech, R., and Sharp, D. J. (2014). The role of the posterior cingulate cortex in cognition and disease. *Brain* 137(Pt 1), 12–32. doi: 10.1093/brain/awt162
- Leelarathna, L., Little, S. A., Walkinshaw, E., Tan, H. K., Lubina-Solomon, A., Kumareswaran, K., et al. (2013). Restoration of self-awareness of hypoglycemia in adults with long-standing type 1 diabetes: hyperinsulinemic-hypoglycemic clamp substudy results from the HypoCOMPASS trial. *Diabetes Care* 36, 4063–4070. doi: 10.2337/dc13-1004
- Lobnig, B. M., Kromeke, O., Optenhostert-Porst, C., and Wolf, O. T. (2006). Hippocampal volume and cognitive performance in long-standing Type 1 diabetic patients without macrovascular complications. *Diabet. Med.* 23, 32–39. doi: 10.1111/j.1464-5491.2005.01716.x
- Mangia, S., Tesfaye, N., De Martino, F., Kumar, A. F., Kollasch, P., Moheet, A. A., et al. (2012). Hypoglycemia-induced increases in thalamic cerebral blood flow are blunted in subjects with type 1 diabetes and hypoglycemia unawareness. *J. Cereb. Blood Flow Metab.* 32, 2084–2090. doi: 10.1038/jcbfm.2012.117
- McAulay, V., Deary, I. J., and Frier, B. M. (2001). Symptoms of hypoglycaemia in people with diabetes. *Diabet. Med.* 18, 690–705. doi: 10.1046/j.1464-5491.2001.00620.x
- Miles, W. R., and Root, H. F. (1922). Psychologic tests applied to diabetic patients. *Arch. Intern. Med.* 30, 767–777. doi: 10.1001/archinte.1922.00110120086003
- Moheet, A., Mangia, S., Kumar, A., Tesfaye, N., Eberly, L. E., Bai, Y., et al. (2015a). Naltrexone for treatment of impaired awareness of hypoglycemia in type 1 diabetes: a randomized clinical trial. *J. Diabetes Complications* 29, 1277–1282. doi: 10.1016/j.jdiacomp.2015.08.004
- Moheet, A., Mangia, S., and Seaquist, E. R. (2015b). Impact of diabetes on cognitive function and brain structure. *Ann. N. Y. Acad. Sci.* 1353, 60–71. doi: 10.1111/nyas.12807
- Musen, G., Lyoo, I. K., Sparks, C. R., Weinger, K., Hwang, J., Ryan, C. M., et al. (2006). Effects of type 1 diabetes on gray matter density as measured by voxel-based morphometry. *Diabetes* 55, 326–333. doi: 10.2337/diabetes.55.02.06.db05-0520
- Nachev, P. (2006). Cognition and medial frontal cortex in health and disease. *Curr. Opin. Neurol.* 19, 586–592. doi: 10.1097/01.wco.0000247609.36482.ea
- Pedersen-Bjergaard, U., Agerholm-Larsen, B., Pramming, S., Hougaard, P., and Thorsteinsson, B. (2001). Activity of angiotensin-converting enzyme and risk of severe hypoglycaemia in type 1 diabetes mellitus. *Lancet* 357, 1248–1253. doi: 10.1016/S0140-6736(00)04405-6
- Scoville, W. B., and Milner, B. (1957). Loss of recent memory after bilateral hippocampal lesions. *J. Neurol. Neurosurg. Psychiatr.* 20, 11–21. doi: 10.1136/jnnp.20.1.11
- Squire, L. R., Stark, C. E., and Clark, R. E. (2004). The medial temporal lobe. *Annu. Rev. Neurosci.* 27, 279–306. doi: 10.1146/annurev.neuro.27.070203.144130
- Standards of Medical Care in Diabetes (2017). Standards of Medical Care in Diabetes-2017: Summary of Revisions. *Diabetes Care* 40, S4–S5. doi: 10.2337/dc17-S003
- Terpstra, M., Moheet, A., Kumar, A., Eberly, L. E., Seaquist, E., and Oz, G. (2014). Changes in human brain glutamate concentration during hypoglycemia: insights into cerebral adaptations in hypoglycemia-associated autonomic failure in type 1 diabetes. *J. Cereb. Blood Flow Metab.* 34, 876–882. doi: 10.1038/jcbfm.2014.32
- Tesfaye, N., and Seaquist, E. R. (2010). Neuroendocrine responses to hypoglycemia. *Ann. N. Y. Acad. Sci.* 1212, 12–28. doi: 10.1111/j.1749-6632.2010.05820.x
- van Harten, B., de Leeuw, F. E., Weinstein, H. C., Scheltens, P., and Biessels, G. J. (2006). Brain imaging in patients with diabetes: a systematic review. *Diabetes Care* 29, 2539–2548. doi: 10.2337/dc06-1637
- Wessels, A. M., Rombouts, S. A., Remijnse, P. L., Boom, Y., Scheltens, P., Barkhof, F., et al. (2007). Cognitive performance in type 1 diabetes patients is associated with cerebral white matter volume. *Diabetologia* 50, 1763–1769. doi: 10.1007/s00125-007-0714-0
- Wessels, A. M., Simsek, S., Remijnse, P. L., Veltman, D. J., Biessels, G. J., Barkhof, F., et al. (2006). Voxel-based morphometry demonstrates reduced grey matter density on brain MRI in patients with diabetic retinopathy. *Diabetologia* 49, 2474–2480. doi: 10.1007/s00125-006-0283-7
- Wild, S., Roglic, G., Green, A., Sicree, R., and King, H. (2004). Global prevalence of diabetes: estimates for the year 2000 and projections for 2030. *Diabetes Care* 27, 1047–1053. doi: 10.2337/diacare.27.5.1047
- Conflict of Interest Statement:** The authors declare that the research was conducted in the absence of any commercial or financial relationships that could be construed as a potential conflict of interest.
- Copyright © 2017 Bednarik, Moheet, Grohn, Kumar, Eberly, Seaquist and Mangia. This is an open-access article distributed under the terms of the Creative Commons Attribution License (CC BY). The use, distribution or reproduction in other forums is permitted, provided the original author(s) or licensor are credited and that the original publication in this journal is cited, in accordance with accepted academic practice. No use, distribution or reproduction is permitted which does not comply with these terms.



# Targeting Cognitive Impairment in Multiple Sclerosis—The Road toward an Imaging-based Biomarker

Jeroen Van Schependom<sup>1,2\*</sup> and Guy Nagels<sup>1,3</sup>

<sup>1</sup> Center for Neurosciences, Universitair Ziekenhuis Brussel, Vrije Universiteit Brussel, Brussels, Belgium, <sup>2</sup> Radiology, Universitair Ziekenhuis Brussel, Vrije Universiteit Brussel, Brussels, Belgium, <sup>3</sup> Neurology, National MS Center Melsbroek, Melsbroek, Belgium

Multiple Sclerosis (MS) is a neuro-degenerative and -inflammatory disease leading to physical and cognitive impairment, pathological fatigue and depression, and affecting patients' quality of life and employment status. The combination of inflammation, demyelination, and neurodegeneration leads to the emergence of MS lesions, reduced white and gray matter brain volumes, a reduced conduction velocity and microstructural changes in the so-called Normal Appearing White Matter (NAWM). Currently, there are very limited options to treat cognitive impairment and its origin is only poorly understood. Therefore, several studies have attempted to relate clinical scores with features calculated either using T1- and/or FLAIR weighted MR images or using neurophysiology. The aim of those studies is not only to provide an improved understanding of the processes that underlie the different symptoms, but also to develop a biomarker—sensitive to therapy induced change—that could be used to speed up therapeutic developments (e.g., cognitive training/drug discovery/...). Here, we provide an overview of studies that have established relationships between either neuro-anatomical or neurophysiological measures and cognitive outcome scores. We discuss different avenues that may help to improve the prediction of cognitive impairment, and how well we can expect them to predict cognitive scores.

## OPEN ACCESS

### Edited by:

Federico Giove,  
Centro Fermi, Italy

### Reviewed by:

Ranganatha Sitaram,  
Pontificia Universidad Católica de  
Chile, Chile  
Bruno Brochet,  
Université de Bordeaux, France

### \*Correspondence:

Jeroen Van Schependom  
jeroen.van.schependom@vub.ac.be

### Specialty section:

This article was submitted to  
Brain Imaging Methods,  
a section of the journal  
*Frontiers in Neuroscience*

**Received:** 26 January 2017

**Accepted:** 19 June 2017

**Published:** 30 June 2017

### Citation:

Van Schependom J and Nagels G (2017) Targeting Cognitive Impairment in Multiple Sclerosis—The Road toward an Imaging-based Biomarker.  
*Front. Neurosci.* 11:380.  
doi: 10.3389/fnins.2017.00380

**Keywords:** cognitive impairment, multiple sclerosis, biomarker, MRI and fMRI, neurophysiology

## INTRODUCTION

Cognitive impairment has been estimated to affect 1 out of every 2 multiple sclerosis (MS) patients (Rao et al., 1991) and affects different domains, most commonly information processing speed, working memory, long-term memory, attention, and executive functions (Langdon, 2011). In contrast to physical disability, which can be easily monitored with the Expanded Disability Status Scale (EDSS, Kurtzke, 1983), cognitive impairment is difficult to assess as (1) neuropsychological evaluation demands time and (2) test results can be influenced by practice-effects, i.e., an improvement of test scores even when the disease is stable as the patients get practiced in the specific tests.

Several attempts have been made to address these issues in order to facilitate and improve the reliability of cognitive follow-up. The Minimal Assessment of cognitive functioning in MS (MACFIMS, Benedict et al., 2002) and the Brief International Cognitive Assessment of MS (BICAMS, Langdon et al., 2012) have been developed in order to allow a less time-demanding cognitive assessment. Furthermore, even a single 5-min test can assess a patient's cognitive status

with a sensitivity of up to 0.9 at a specificity of about 0.6 (Van Schependom et al., 2014a). Although, the practice effect can be partially mitigated by using alternate versions of cognitive tests, patients can still learn certain strategies limiting the potential of these batteries to detect changes in clinical trials.

As part of the clinical follow-up, MS patients regularly undergo an MRI scan allowing the radiologist/neurologist to assess the number and volume of T1-hypointense, T2-hyperintense, and Gadolinium enhancing lesions. While the automated interpretation of MR images has not only led to a more reliable quantification of lesions (Jain et al., 2015), it provides objective insight in the brain's atrophy rate, which is significantly faster in MS than in healthy controls (De Stefano et al., 2015).

Despite improvements in the quantification of MR images, only a limited correlation is observed between the radiological findings and a patient's actual physical or cognitive disability. This lack of correlation is well-known and is known as the clinico-radiological paradox, which can be caused by a multitude of factors, amongst which: (1) Neglect of damage to the spine when assessing the correlation between brain lesion load and physical disability; (2) The quality of clinical ratings; (3) Differences in cognitive reserve defined as *differences in cognitive processes as a function of lifetime intellectual activities and other environmental factors that explain differential susceptibility to functional impairment in the presence of pathology or other neurologic insult* (Barulli and Stern, 2013), for which intelligence quotient and education level are often taken as indicators (Martins Da Silva et al., 2015); and (4) The assumption that white and gray matter appearing normal on T1 and T2 weighted images are unaffected by the disease process (Barkhof, 2002). Although, the use of diffusion tensor imaging has shown that both normal appearing white and gray matter (normal with respect to their appearance on T1 and T2 weighted MRI, NAWM/NAGM) are affected, their inclusion does not solve the clinico-radiological paradox (Hawellek et al., 2011; Moll et al., 2011).

Apart from the structural damage, neurophysiological changes have been described. Already in 2000, Leocani et al. showed a reduced alpha power and an increase of power at lower frequencies in 40–80% of the MS patients (Leocani et al., 2000). As neurophysiological functioning is not only influenced by structure but also by more widespread changes that might be too subtle to be picked up with conventional MR imaging, it might help to reduce the clinico-radiological paradox.

Given the prevalence of cognitive impairment in MS, the difficulties in cognitive assessment and the lack of disease modifying therapies targeting cognition, we aim at providing an overview of possible roads toward a biomarker for cognition in MS based on neuroanatomical and neurophysiological features acquired through MRI or magneto-/electroencephalography (M/EEG). A biomarker that is more objective and reliable than standard neuropsychological tests, easy to acquire and sensitive to interventions could substantially improve the follow-up and therapeutic development.

## NEURO-ANATOMY

In multiple sclerosis, MR imaging has provided a unique way of assessing the disease activity in the patient's brain *in vivo*. It has allowed identifying hypo-intense lesions on T1-weighted images, hyper-intense lesions on T2-weighted images (Li et al., 2003) and active breaches of the blood-brain-barrier using T1-weighted images after the administration of Gadolinium as contrast-enhancer (Soon et al., 2007). Whereas, T1-hypointense lesions indicate axonal loss, T2 hyperintense lesions are known to be sensitive yet unspecific markers of disease activity (van Waesberghe et al., 1999). As such, MR images have provided a way of assessing the disease activity and are increasingly being used as secondary outcome in pivotal clinical trials (Cohen et al., 2012).

However, despite the easy interpretability and despite the inclusion of MR imaging parameters in the revised 2010 McDonald criteria (Polman et al., 2011) for the diagnosis of MS, the relationship between the parameters extracted from MR images and clinical disability, expressed in EDSS or cognitive scores, remains surprisingly low.

One explanation for this clinico-radiological paradox may be the use of univariate linear techniques, whereas the relationship between MRI covariates and clinical covariates does not necessarily need to be linear. In Hackmack et al. (2012), the authors argued that using canonical correlation analysis and a searchlight procedure, they obtained correlations of up to 80% using standard MR images. Yet, it is important to note that many of the areas that allowed to predict the clinical status involved the periventricular white matter, a region that is difficult to coregister to a template. As such, we should make sure to understand what features drive more advanced techniques, especially when extending toward machine learning.

### Atrophy

MS-related cognitive impairment has been associated with both cortical (Benedict, 2002; Benedict et al., 2005; Morgen et al., 2006) and subcortical (Houtchens et al., 2007; Sicotte et al., 2008; Batista et al., 2012; Damjanovic et al., 2016; Preziosa et al., 2016; Rocca et al., 2016) gray matter atrophy and cortical lesions (Calabrese et al., 2009) explaining between 20 and 60% of the variance of a variety of cognitive tests assessing the most commonly affected cognitive domains using multilinear models.

The relationship between cortical atrophy and cognition should not come as a surprise, given that neuronal density, neuronal size, and axonal density all significantly predicted gray matter volume in 45 tissue blocks in a post-mortem study (Popescu et al., 2015). A more extensive review on this topic can be found in Filippi (2015).

### Microstructural Integrity

Apart from brain atrophy, MS leads to demyelination entailing a reduced structural connectivity. Normal appearing white matter typically shows decreased fractional anisotropy (FA), increased mean diffusivity (MD), and radial diffusivity (RD) demonstrating that the white matter appearing normal on T1 and T2 weighted

MR images is likely to be affected by the MS pathology (Vrenken et al., 2006; Roosendaal et al., 2009; Hawellek et al., 2011; Moll et al., 2011).

Apart from general reductions/increases in diffusion parameters, several studies have found microstructural abnormalities in specific tracts like the fornix (Roosendaal et al., 2009; Kern et al., 2012), the cingulum (Mesaros et al., 2012), and the uncinate fasciculus (Fink et al., 2010). Furthermore, several of these changes correlate with cognitive impairment: e.g., a reduced information processing speed was associated with reduced FA in the corpus callosum (Roosendaal et al., 2009) and higher FA in the fornix was related to better memory results (Kern et al., 2012). Yet, importantly, Mesaros et al. found that lesional damage (assessed by FA/MD) along cognitive related tracts (especially the cingulum) outperformed diffusion abnormalities in NAWM when discriminating cognitively preserved and impaired MS patients (Mesaros et al., 2012) on a variety of neuropsychological tests.

Furthermore, the addition of these measures to multilinear models did not result in a substantial improvement of the prediction of general cognitive impairment ( $R^2 = 0.2\text{--}0.5$ ) and does not seem to solve the clinico-radiological paradox (Daams et al., 2015; Preziosa et al., 2016). One explanation for this result could be that the interpretation of abnormal diffusion parameters is not straightforward. While decreased FA and increased MD tend to point to increased diffusion and thus a reduced fiber integrity, both increased/decreased FA/MD may indicate pathology-induced changes depending on the brain region and the underlying cellular structure (Soares et al., 2013). Finally, the magnetization transfer ratio, a measure related to microglia activation and—only in close proximity of lesions—to axonal degeneration (Moll et al., 2011), has been shown to be altered before the onset of clinical symptoms (Iannucci et al., 2000).

## NEUROPHYSIOLOGY

As functional connectivity (FC) is not only determined by the underlying structural connectivity matrix (Honey et al., 2009), it may provide additional and independent information on a patient's cognitive status and is therefore an important candidate biomarker for cognitive impairment in MS.

### Functional MRI

Based on the observation of the additional recruitment of adjacent brain areas during tasks in cognitively preserved MS patients as opposed to smaller activations in cognitively impaired MS patients (Staffen et al., 2002; Sweet et al., 2006), it has been suggested that the brain tries to compensate the reduced local processing power by recruiting adjacent areas leading to both increased activation and connectivity (Schoonheim et al., 2015).

However, recently, both increases (Hawellek et al., 2011; Faivre et al., 2012; Zhou et al., 2014) and decreases (Bonavita et al., 2011; Cruz-Gómez et al., 2013; Louapre et al., 2014) in resting-state FC of the default-mode network have been associated with cognitive impairment in MS. More specifically, Hawellek et al. observed an association between increased connectivity and impaired

cognitive functioning and suggested that the widespread white-matter damage precludes the brain from easily switching between different states resulting in an increased FC (Hawellek et al., 2011).

These contradicting results have led Schoonheim et al. to doubt the “compensation” hypothesis, proposing that this increased activation may also be interpreted as a maladaptive response of the brain following e.g., disinhibition or even an unrelated side-effect of the accumulating structural damage (Schoonheim et al., 2015).

A closer look at the MS cohorts on which these contradicting results are based, shows that studies observing a higher FC in MS and positive correlations between cognitive impairment and functional connectivity included patients in the very early stage of the disease (mean disease duration: 2, 1.1, and 2.8 years in Hawellek et al., 2011; Faivre et al., 2012; Zhou et al., 2014) as compared to studies observing lower FC and negative correlations (mean disease duration of 5.5, 4.5, and 11 years in Bonavita et al., 2011; Cruz-Gómez et al., 2013; Louapre et al., 2014, respectively). Therefore, we suggest that increased FC may be related with increased cognitive impairment in the very early stage of the disease but with increased cognitive abilities in later disease stages.

### Magneto-/Electroencephalography

All previously mentioned neurophysiological results are based on resting state functional MRI, which offers a high spatial resolution but does not capture the brain's rich temporal dynamics. Unfortunately, only few studies have assessed cognition in MS using resting-state assessed by electrophysiology (EEG) or magnetoencephalography (MEG).

The studies that have used rest EEG/MEG to assess MS patients, have found an increase in power density at low frequencies (delta, 2–4 Hz) and a decrease of power in the alpha band (Leocani et al., 2000; Babiloni et al., 2016), which allowed to distinguish between relapsing remitting and secondary progressive MS patients (Babiloni et al., 2016). Furthermore, Van der Meer et al. found a decrease in upper-alpha power (10–12 Hz) and an increase in lower-alpha power (8–10 Hz), which may relate to the slowing of the alpha-peak in Alzheimer's dementia (Goossens et al., 2017). Functional connectivity studies have observed an increase in functional connectivity in the beta band [assessed by the phase lag index (Tewarie et al., 2013), and synchronization likelihood (Schoonheim et al., 2013)] and the functional connectivity in the beta band correlated with an overall cognitive score (Tewarie et al., 2013).

With respect to task-related EEG/MEG, the most commonly applied paradigm is the P300, a paradigm in which the subject is asked to pay attention to a specific stimulus within a series of similar but more frequently occurring stimuli. Although, reduced amplitudes and increased latencies have been consistently found when comparing MS subjects with healthy controls (Piras et al., 2003; Magnano et al., 2006; Leocani et al., 2010), the accuracy of various features in detecting cognitive impairment in MS is limited: Van Schependom et al. reported accuracies of about 70% using a variety of machine learning techniques and features (Van Schependom et al., 2013, 2014c) with results highly depending

on the choice of connectivity measure (Van Schependom et al., 2014b).

## FUTURE DIRECTIONS

Given that both MRI and functional connectivity can only explain a small fraction of the observed variance, different approaches may be interesting to pursue.

One alternative approach to assessing the local connectivity of different structures is assessing the whole brain as one network. Based on this weighted or unweighted network—for a discussion on which metrics have been successfully applied cf. the EEG/MEG section above—different parameters can be calculated using graph theory. The most commonly defined parameters are the average shortest path length (also called the “integration”), the clustering coefficient and the modularity. Path length and clustering coefficient are typically normalized with respect to the mean of those parameters obtained by randomly permuting the adjacency matrix. The ratio of the normalized path length and clustering coefficient is called the small-worldness.

Graph theory approaches seem to point in the direction of a more regular topology as evidenced by an increase in path length and clustering coefficient in the alpha-band (Schoonheim et al., 2013) in rest and in the theta and delta band during an auditory oddball task (Van Schependom et al., 2014b).

An alternative option would be not to analyse the brain in terms of a frequency-decomposition, but rather to assess the brain in a non-static way. With regards to EEG, microstates—states that are stable for around 100 ms—have been shown to be relevant to schizophrenia (Kindler et al., 2011) and recently Gschwind et al. have shown differences in microstate properties in MS. Specifically, they found fewer short duration microstates and more frequent long duration states for the two microstates that have been suggested to represent the sensorimotor and the visual network (Gschwind et al., 2016). This finding could confirm the hypothesis put forward by Hawellek et al. of an impaired switching as the underlying mechanism of increased functional connectivity (Hawellek et al., 2011). Importantly, Gschwind et al. did not observe any correlation between the temporal dynamics and the patients’ cognitive scores. This approach could be extended to MEG, where Baker et al. showed the existence of stable states with lifetimes around 100–200 ms. As these states are defined in source space, they are easier to interpret (Baker et al., 2014; Vidaurre et al., 2016).

## FURTHER CONSIDERATIONS

Finally, we should be aware of the fact that the “golden truth” of a patient’s cognitive status cannot be directly observed but needs to be probed by the assessment of standardized neuropsychological tests. These tests have inherent limitations, e.g., some patients may have been subjected to similar tests previously and are better prepared than others. Furthermore, the results obtained on these tests may be influenced by a patient’s mood and fatigue level, two factors that may even be more difficult to assess than cognition. A final covariate that mostly cannot be taken into account is the influence of medication [e.g., the use of anti-cholinergics to

control bladder problems also influences cognitive functioning (Kersten et al., 2013) or the use of anti-epileptica (Ortinski and Meador, 2004)].

Therefore, a perfect correlation will never be reached. In order to provide a rough quantification of the correlation that we would be able to obtain, we assume (1) a true underlying cognitive profile that follows a Gaussian distribution across the MS population, (2) a simulated measured cognitive profile by adding extra Gaussian noise, and (3) a cognitive biomarker which is similarly composed of the sum of the true underlying cognitive profile and some Gaussian noise.

As Pearson’s correlation coefficient decreases with increasing standard deviation of the measured cognitive score and the biomarker, both of which are increased by the additive Gaussian noise, the maximal accuracy will decrease. As an example, we can use the values provided by Boringa et al. (2001) for the SDMT (mean = 52, standard deviation = 11). Assuming a standard deviation of 3 points on both measurements, the theoretical maximum for  $R^2$  is 0.86. The main limitation of this type of calculation is the assumption on the distribution of both the underlying cognitive profile and the noise caused by either imprecise cognitive batteries or imprecise biomarkers. Apart from its common use, there is no specific reason for which we have chosen a Gaussian distribution. However, the main point that we aim to convey in this paragraph, i.e., that we cannot expect an imaging biomarker to be perfect because the assessment of cognition is not expected to be perfect either, is independent from the specific distribution.

## CONCLUSION

In this perspective paper, we described—without providing an exhaustive review—the different imaging modalities (MRI/DTI/MTI/EEG/MEG) that have been applied with the aim of finding a correlate of cognitive impairment in MS. While the features deduced from different MRI modalities do not seem to overcome the clinico-radiological paradox, the generally increased interest in assessing whole-brain functional networks using EEG/MEG has found its way to MS. Although, it is more difficult to interpret changes in power at certain frequency bands or the “effectiveness” of a functional network than it is to interpret the changes in the volume of different brain structures, we feel that improved EEG/MEG features—whether or not in combination with MRI—may help to reduce the paradox and lead to assess cognitive functioning more objectively (without inter-rater variability) and therefore lead to improved patient-care.

## AUTHOR CONTRIBUTIONS

JVS and GN have both made substantial contributions to the design and critical revision of the manuscript, approve the final version, and agree to be accountable for all aspects of the work.

## FUNDING

JVS is a post-doctoral FWO fellow (grant no. 12I1817N).

## REFERENCES

- Babiloni, C., Del Percio, C., Capotosto, P., Noce, G., Infarinato, F., Muratori, C., et al. (2016). Cortical sources of resting state electroencephalographic rhythms differ in relapsing-remitting and secondary progressive multiple sclerosis. *Clin. Neurophysiol.* 127, 581–590. doi: 10.1016/j.clinph.2015.05.029
- Baker, A. P., Brookes, M. J., Rezek, I. A., Smith, S. M., Behrens, T., Probert Smith, P. J., et al. (2014). Fast transient networks in spontaneous human brain activity. *Elife* 3:e01867. doi: 10.7554/eLife.01867
- Barkhof, F. (2002). The clinico-radiological paradox in multiple sclerosis revisited. *Curr. Opin. Neurol.* 15, 239–245. doi: 10.1097/00019052-200206000-00003
- Barulli, D., and Stern, Y. (2013). Efficiency, capacity, compensation, maintenance, plasticity: emerging concepts in cognitive reserve. *Trends Cogn. Sci.* 17, 502–509. doi: 10.1016/j.tics.2013.08.012
- Batista, S., Zivadinov, R., Hoogs, M., Bergsland, N., Heininen-Brown, M., Dwyer, M. G., et al. (2012). Basal ganglia, thalamus and neocortical atrophy predicting slowed cognitive processing in multiple sclerosis. *J. Neurol.* 259, 139–146. doi: 10.1007/s00415-011-6147-1
- Benedict, R. H. (2002). Frontal cortex atrophy predicts cognitive impairment in multiple sclerosis. *J. Neuropsychiatr.* 14, 44–51. doi: 10.1176/jnp.14.1.44
- Benedict, R. H., Fischer, J. S., Archibald, C. J., Arnett, P. A., Beatty, W. W., Bobholz, J., et al. (2002). Minimal neuropsychological assessment of MS patients - a consensus approach. *Clin. Neuropsychol.* 16, 381–397. doi: 10.1076/clin.16.3.381.13859
- Benedict, R. H., Zivadinov, R., Carone, D. A., Weinstock-Guttman, B., Gaines, J., Maggiore, C., et al. (2005). Regional lobar atrophy predicts memory impairment in multiple sclerosis. *AJNR Am. J. Neuroradiol.* 26, 1824–1831.
- Bonavita, S., Gallo, A., Sacco, R., Corte, M. D., Bisecco, A., Docimo, R., et al. (2011). Distributed changes in default-mode resting-state connectivity in multiple sclerosis. *Mult. Scler.* 17, 411–422. doi: 10.1177/1352458510394609
- Boringa, J. B., Lazeron, R. H. C., Reuling, I. E. W., Ade, H. J., Pfennings, L., and Lindeboom, J. (2001). The brief repeatable battery of neuropsychological tests: normative values allow application in multiple sclerosis clinical practice. *Mult. Scler.* 7, 263–267. doi: 10.1177/135245850100700409
- Calabrese, M., Agosta, F., Rinaldi, F., Mattisi, I., Grossi, P., Favaretto, A., et al. (2009). Cortical lesions and atrophy associated with cognitive impairment in relapsing-remitting multiple sclerosis. *Arch. Neurol.* 66, 1144–1150. doi: 10.1001/archneuro.2009.174
- Cohen, J. A., Reingold, S. C., Polman, C. H., and Wolinsky, J. S. (2012). Disability outcome measures in multiple sclerosis clinical trials: current status and future prospects. *Lancet Neurol.* 11, 467–476. doi: 10.1016/S1474-4422(12)70059-5
- Cruz-Gómez, A. J., Ventura-Campos, N., Belenguer, A., Avila, C., and Forn, C. (2013). The link between resting-state functional connectivity and cognition in MS patients. *Mult. Scler.* 20, 338–348. doi: 10.1177/1352458513495584
- Daams, M., Steenwijk, M. D., Schoonheim, M. M., Wattjes, M. P., Balk, L. J., Tewarie, P. K., et al. (2015). Multi-parametric structural magnetic resonance imaging in relation to cognitive dysfunction in long-standing multiple sclerosis. *Mult. Scler.* 22, 608–619. doi: 10.1177/1352458515596598
- Damjanovic, D., Valsasina, P., Rocca, M. A., Stromillo, M. L., Gallo, A., Enzinger, C., et al. (2016). Hippocampal and deep gray matter nuclei atrophy is relevant for explaining cognitive impairment in MS: a multicenter study. *AJNR Am. J. Neuroradiol.* 38, 18–24. doi: 10.3174/ajnr.A4952
- De Stefano, N., Stromillo, M. L., Giorgio, A., Bartolozzi, M. L., Battaglini, M., Baldini, M., et al. (2015). Establishing pathological cut-offs of brain atrophy rates in multiple sclerosis. *J. Neurol. Neurosurg. Psychiatry* 87, 93–99. doi: 10.1136/jnnp.2014-309903
- Faivre, A., Rico, A., Zaaraoui, W., Crespy, L., Reuter, F., Wybrecht, D., et al. (2012). Assessing brain connectivity at rest is clinically relevant in early multiple sclerosis. *Mult. Scler.* 18, 1251–1258. doi: 10.1177/1352458511435930
- Filippi, M. (2015). MRI measures of neurodegeneration in multiple sclerosis: implications for disability, disease monitoring, and treatment. *J. Neurol.* 262, 1–6. doi: 10.1007/s00415-014-7340-9
- Fink, F., Eling, P., Rischkau, E., Beyer, N., Tomandl, B., Klein, J., et al. (2010). The association between California Verbal Learning Test performance and fibre impairment in multiple sclerosis: evidence from diffusion tensor imaging. *Mult. Scler.* 16, 332–341. doi: 10.1177/1352458509356367
- Gooossens, J., Laton, J., Van Schependom, J., Gielen, J., Struyfs, H., Van Moesvelde, S., et al. (2017). EEG dominant frequency peak differentiates between Alzheimer's disease and frontotemporal lobar degeneration. *J. Alzheimer's Dis.* 55, 53–58. doi: 10.3233/JAD-160188
- Gschwind, M., Hardmeier, M., Van De Ville, D., Tomescu, M. I., Penner, I. K., Naegelin, Y., et al. (2016). Fluctuations of spontaneous EEG topographies predict disease state in relapsing-remitting multiple sclerosis. *Neuroimage Clin.* 12, 466–477. doi: 10.1016/j.nicl.2016.08.008
- Hackmack, K., Weygandt, M., Wuferl, J., Pfueller, C. F., Bellmann-Strobl, J., Paul, F., et al. (2012). Can we overcome the “clinico-radiological paradox” in multiple sclerosis? *J. Neurol.* 259, 2151–2160. doi: 10.1007/s00415-012-6475-9
- Hawellek, D. J., Hipp, J. F., Lewis, C. M., Corbetta, M., and Engel, A. K. (2011). Increased functional connectivity indicates the severity of cognitive impairment in multiple sclerosis. *Proc. Natl. Acad. Sci. U.S.A.* 108, 19066–19071. doi: 10.1073/pnas.1110024108
- Honey, C. J., Honey, C. J., Sporns, O., Sporns, O., Cammoun, L., Cammoun, L., et al. (2009). Predicting human resting-state functional connectivity from structural connectivity. *Proc. Natl. Acad. Sci. U.S.A.* 106, 2035–2040. doi: 10.1073/pnas.0811168106
- Houthcens, M. K., Benedict, R. H., Killiany, R., Sharma, J., Jaisani, Z., Singh, B., et al. (2007). Thalamic atrophy and cognition in multiple sclerosis. *Neurology* 69, 1213–1223. doi: 10.1212/01.wnl.0000276992.17011.b5
- Iannucci, G., Tortorella, C., Rovaris, M., Sormani, M. P., Comi, G., and Filippi, M. (2000). Prognostic value of MR and magnetization transfer imaging findings in patients with clinically isolated syndromes suggestive of multiple sclerosis at presentation. *AJNR Am. J. Neuroradiol.* 21, 1034–1038.
- Jain, S., Sima, D. M., Ribbens, A., Cambron, M., Maertens, A., Van Hecke, W., et al. (2015). Automatic segmentation and volumetry of multiple sclerosis brain lesions from MR images. *Neuroimage Clin.* 8, 367–375. doi: 10.1016/j.nicl.2015.05.003
- Kern, K. C., Ekstrom, A. D., Suthana, N. A., Giesser, B. S., Montag, M., Arshana Palli, A., et al. (2012). Fornix damage limits verbal memory functional compensation in multiple sclerosis. *Neuroimage* 59, 2932–2940. doi: 10.1016/j.neuroimage.2011.09.071
- Kersten, H., Molden, E., Tolo, I. K., Skovlund, E., Engedal, K., and Wyller, T. B. (2013). Cognitive effects of reducing anticholinergic drug burden in a frail elderly population: a randomized controlled trial. *J. Gerontol. A Biol. Sci. Med. Sci.* 68, 271–278. doi: 10.1093/gerona/gls176
- Kindler, J., Hubl, D., Strik, W. K., Dierks, T., and Koenig, T. (2011). Resting-state EEG in schizophrenia: auditory verbal hallucinations are related to shortening of specific microstates. *Clin. Neurophysiol.* 122, 1179–1182. doi: 10.1016/j.clinph.2010.10.042
- Kurtzke, J. F. (1983). Rating neurologic impairment in multiple sclerosis: an expanded disability status scale (EDSS). *Neurology* 33, 1444–1452. doi: 10.1212/WNL.33.11.1444
- Langdon, D. W. (2011). Cognition in multiple sclerosis. *Curr. Opin. Neurol.* 24, 244–249. doi: 10.1097/WCO.0b013e328346a43b
- Langdon, D. W., Amato, M. P., Boringa, J., Brochet, B., Foley, F., Fredrikson, S., et al. (2012). Recommendations for a brief international cognitive assessment for multiple sclerosis (BICAMS). *Mult. Scler.* 18, 891–898. doi: 10.1177/1352458511431076
- Leocani, L., Gonzalez-Rosa, J. J., and Comi, G. (2010). Neurophysiological correlates of cognitive disturbances in multiple sclerosis. *Neurol. Sci.* 31, S249–S253. doi: 10.1007/s10072-010-0398-y
- Leocani, L., Locatelli, T., Martinelli, V., Rovaris, M., Falautano, M., Filippi, M., et al. (2000). Electroencephalographic coherence analysis in multiple sclerosis: correlation with clinical, neuropsychological, and MRI findings. *J. Neurol. Neurosurg. Psychiatry* 69, 192–198. doi: 10.1136/jnnp.69.2.192
- Li, B. S., Regal, J., Soher, B. J., Mannon, L. J., Grossman, R. I., and Gonon, O. (2003). Brain metabolite profiles of T1-hypointense lesions in relapsing-remitting multiple sclerosis. *AJNR Am. J. Neuroradiol.* 24, 68–74.
- Louapre, C., Perlberg, V., Garc, D., Urbanski, M., Benali, H., Assouad, R., et al. (2014). Brain networks disconnection in early multiple sclerosis cognitive deficits: an anatomicfunctional study. *Hum. Brain Mapp.* 35, 4706–4717. doi: 10.1002/hbm.22505
- Magnano, I., Aiello, I., and Piras, M. R. (2006). Cognitive impairment and neurophysiological correlates in MS. *J. Neurol. Sci.* 245, 117–122. doi: 10.1016/j.jns.2005.08.027

- Martins Da Silva, A., Cavaco, S., Moreira, I., Bettencourt, A., Santos, E., Pinto, C., et al. (2015). Cognitive reserve in multiple sclerosis: protective effects of education. *Mult. Scler.* 21, 1312–1321. doi: 10.1177/1352458515581874
- Mesaros, S., Rocca, M. A., Kacar, K., Kostic, J., Copetti, M., Stosic-Opincal, T., et al. (2012). Diffusion tensor MRI tractography and cognitive impairment in multiple sclerosis. *Neurology* 78, 969–975. doi: 10.1212/WNL.0b013e31824d5859
- Moll, N. M., Rietsch, A. M., Thomas, S., Ransohoff, A. J., Lee, J. C., Fox, R., et al. (2011). Multiple sclerosis normal-appearing white matter: pathology-imaging correlations. *Ann. Neurol.* 70, 764–773. doi: 10.1002/ana.22521
- Morgen, K., Sammer, G., Courtney, S. M., Wolters, T., Melchior, H., Blecker, C. R., et al. (2006). Evidence for a direct association between cortical atrophy and cognitive impairment in relapsing-remitting MS. *Neuroimage* 30, 891–898. doi: 10.1016/j.neuroimage.2005.10.032
- Ortinski, P., and Meador, K. J. (2004). Cognitive side effects of antiepileptic drugs. *Epilepsy Behav.* 5, 60–65. doi: 10.1016/j.yebeh.2003.11.008
- Piras, M., Magnano, I., Canu, E., Paulus, K., Satta, W., Soddu, A., et al. (2003). Longitudinal study of cognitive dysfunction in MS: neuropsychological, neuroradiological, and neurophysiological findings. *J. Neurol. Neurosurg. Psychiatry* 74, 878–885. doi: 10.1136/jnnp.74.7.878
- Polman, C. H., Reingold, S. C., Banwell, B., Clanet, M., Cohen, J. A., Filippi, M., et al. (2011). Diagnostic criteria for multiple sclerosis: 2010 revisions to the McDonald criteria. *Ann. Neurol.* 69, 292–302. doi: 10.1002/ana.22366
- Popescu, V., Klaver, R., Voorn, P., Galis-de Graaf, Y., Knol, D., Twisk, J., et al. (2015). What drives MRI-measured cortical atrophy in multiple sclerosis? *Mult. Scler.* 21, 1280–1290. doi: 10.1177/1352458514562440
- Preziosa, P., Rocca, M. A., Pagani, E., Stromillo, M. L., Enzinger, C., Gallo, A., et al. (2016). Structural MRI correlates of cognitive impairment in patients with multiple sclerosis. *Hum. Brain Mapp.* 37, 1627–1644. doi: 10.1002/hbm.23125
- Rao, S. M., Gary, J. L., Bernardin, L., and Unverzagt, F. (1991). Cognitive dysfunction in multiple sclerosis. I. Frequency, patterns, and prediction. *Neurology* 41, 685–691. doi: 10.1212/WNL.41.5.685
- Rocca, M. A., Morelli, M. E., Amato, M. P., Moiola, L., Ghezzi, A., Veggiani, P., et al. (2016). Regional hippocampal involvement and cognitive impairment in pediatric multiple sclerosis. *Mult. Scler.* 22, 628–640. doi: 10.1177/1352458515598569
- Roosendaal, S. D., Geurts, J. J., Vrenken, H., Hulst, H. E., Cover, K. S., Castelijns, J. A., et al. (2009). Regional DTI differences in multiple sclerosis patients. *Neuroimage* 44, 1397–1403. doi: 10.1016/j.neuroimage.2008.10.026
- Schoonheim, M. M., Geurts, J. J., Landi, D., Douw, L., Meer, M. L., Van Der Vrenken, H., et al. (2013). Functional connectivity changes in multiple sclerosis patients: a graph analytical study of MEG resting state data. *Hum. Brain Mapp.* 34, 52–61. doi: 10.1002/hbm.21424
- Schoonheim, M. M., Meijer, K. A., and Geurts, J. J. (2015). Network collapse and cognitive impairment in multiple sclerosis. *Front. Neurol.* 6:82. doi: 10.3389/fneur.2015.00082
- Sicotte, N. L., Kern, K. C., Giesser, B. S., Arshapall, A., Schultz, A., Montag, M., et al. (2008). Regional hippocampal atrophy in multiple sclerosis. *Brain* 131, 1134–1141. doi: 10.1093/brain/awn030
- Soares, J. M., Marques, P., Alves, V., and Sousa, N. (2013). A hitchhiker's guide to diffusion tensor imaging. *Front. Neurosci.* 7:31. doi: 10.3389/fnins.2013.00031
- Soon, D., Tozer, D. J., Altmann, D. R., Tofts, P. S., and Miller, D. H. (2007). Quantification of subtle blood-brain barrier disruption in non-enhancing lesions in multiple sclerosis: a study of disease and lesion subtypes. *Mult. Scler.* 13, 884–894. doi: 10.1177/1352458507076970
- Staffen, W., Mair, A., Zauner, H., Unterrainer, J., Niederhofer, H., Kutzelnigg, A., et al. (2002). Cognitive function and fMRI in patients with multiple sclerosis: evidence for compensatory cortical activation during an attention task. *Brain* 125, 1275–1282. doi: 10.1093/brain/awf125
- Sweet, L. H., Rao, S. M., Primeau, M., Durgerian, S., and Cohen, R. A. (2006). Functional magnetic resonance imaging response to increased verbal working memory demands among patients with multiple sclerosis. *Hum. Brain Mapp.* 27, 28–36. doi: 10.1002/hbm.20163
- Tewarie, P., Schoonheim, M. M., Stam, C. J., van der Meer, M. L., van Dijk, B. W., Barkhof, F., et al. (2013). Cognitive and clinical dysfunction, altered MEG resting-state networks and thalamic atrophy in multiple sclerosis. *PLoS ONE* 8:e69318. doi: 10.1371/journal.pone.0069318
- Van Schependom, J., D'Hooge, M., Cleynhens, K., D'Hooghe, M. B., De Keyser, J., and Nagels, G. (2013). "Detection of cognitive impairment in MS based on an EEG P300 paradigm," in *3rd International Workshop on Pattern Recognition in NeuroImaging* (Philadelphia, PA), 114–118.
- Van Schependom, J., D'hooge, M. B., Cleynhens, K., D'hooge, M., Haelewyck, M. C., De Keyser, J., et al. (2014a). The Symbol Digit Modalities Test as sentinel test for cognitive impairment in MS. *Eur. J. Neurol.* 21, 1219–1225, e71–e72. doi: 10.1111/ene.12463
- Van Schependom, J., Gielen, J., Laton, J., D'hooge, M. B., De Keyser, J., and Nagels, G. (2014b). Graph theoretical analysis indicates cognitive impairment in MS stems from neural disconnection. *Neuroimage Clin.* 4, 403–410. doi: 10.1016/j.nicl.2014.01.012
- Van Schependom, J., Gielen, J., Laton, J., D'hooge, M. B., De Keyser, J., and Nagels, G. (2014c). "SVM aided detection of cognitive impairment in MS," in *Proceedings of the 2014 International Workshop on Pattern Recognition in Neuroimaging* (Tübingen).
- van Waesberghe, J. H., Kamphorst, W., De Groot, C. J., van Walderveen, M. A., Castelijns, J. A., Ravid, R., et al. (1999). Axonal loss in multiple sclerosis lesions: magnetic resonance imaging insights into substrates of disability. *Ann. Neurol.* 46, 747–754. doi: 10.1002/1531-8249(199911)46:5<747::AID-ANA10>3.0.CO;2-4
- Vidaurre, D., Quinn, A. J., Baker, A. P., Dupret, D., Tejero-Cantero, A., and Woolrich, M. W. (2016). Spectrally resolved fast transient brain states in electrophysiological data. *Neuroimage* 126, 81–95. doi: 10.1016/j.neuroimage.2015.11.047
- Vrenken, H., Geurts, J. J., Knol, D. L., Polman, C. H., Castelijns, J. A., Pouwels, P. J., et al. (2006). Normal-appearing white matter changes vary with distance to lesions in multiple sclerosis. *AJNR Am. J. Neuroradiol.* 27, 2005–2011.
- Zhou, F., Zhuang, Y., Gong, H., Wang, B., Wang, X., Chen, Q., et al. (2014). Altered inter-subregion connectivity of the default mode network in relapsing remitting multiple sclerosis: a functional and structural connectivity study. *PLoS ONE* 9:e101198. doi: 10.1371/journal.pone.0101198

**Conflict of Interest Statement:** The authors declare that the research was conducted in the absence of any commercial or financial relationships that could be construed as a potential conflict of interest.

Copyright © 2017 Van Schependom and Nagels. This is an open-access article distributed under the terms of the Creative Commons Attribution License (CC BY). The use, distribution or reproduction in other forums is permitted, provided the original author(s) or licensor are credited and that the original publication in this journal is cited, in accordance with accepted academic practice. No use, distribution or reproduction is permitted which does not comply with these terms.



# Task-Related Modulations of BOLD Low-Frequency Fluctuations within the Default Mode Network

Silvia Tommasin<sup>1</sup>, Daniele Mascali<sup>1</sup>, Tommaso Gili<sup>1,2</sup>, Ibrahim Eid Assan<sup>3</sup>, Marta Moraschi<sup>1</sup>, Michela Fratini<sup>2,4</sup>, Richard G. Wise<sup>5</sup>, Emiliano Macaluso<sup>6</sup>, Silvia Mangia<sup>7</sup> and Federico Giove<sup>1,2\*</sup>

<sup>1</sup> MARBILab, Centro Fermi—Museo Storico Della fisica e Centro Studi e Ricerche Enrico Fermi, Rome, Italy, <sup>2</sup> Fondazione Santa Lucia IRCCS, Rome, Italy, <sup>3</sup> Dipartimento di Fisica, Sapienza Università di Roma, Rome, Italy, <sup>4</sup> Istituto di Nanotecnologia, Consiglio Nazionale delle Ricerche, Rome, Italy, <sup>5</sup> Cardiff University Brain Research Imaging Centre, School of Psychology, Cardiff University, Cardiff, United Kingdom, <sup>6</sup> ImpAct Team, Lyon Neuroscience Research Center, Lyon, France, <sup>7</sup> Center for Magnetic Resonance Research, University of Minnesota Twin Cities, Minneapolis, MN, United States

## OPEN ACCESS

**Edited by:**

Thomas Beyer,  
University of Vienna, Austria

**Reviewed by:**

Xiaoyun Liang,  
Florey Institute of Neuroscience and  
Mental Health, Australia  
Yunjie Tong,  
Purdue University College of  
Engineering, United States

**\*Correspondence:**

Federico Giove  
federico.giove@uniroma1.it

**Specialty section:**

This article was submitted to  
Biomedical Physics,  
a section of the journal  
Frontiers in Physics

**Received:** 15 May 2017

**Accepted:** 07 July 2017

**Published:** 25 July 2017

**Citation:**

Tommasin S, Mascali D, Gili T, Eid Assan I, Moraschi M, Fratini M, Wise RG, Macaluso E, Mangia S and Giove F (2017) Task-Related Modulations of BOLD Low-Frequency Fluctuations within the Default Mode Network. *Front. Phys.* 5:31.  
doi: 10.3389/fphy.2017.00031

Spontaneous low-frequency Blood-Oxygenation Level-Dependent (BOLD) signals acquired during resting state are characterized by spatial patterns of synchronous fluctuations, ultimately leading to the identification of robust brain networks. The resting-state brain networks, including the Default Mode Network (DMN), are demonstrated to persist during sustained task execution, but the exact features of task-related changes of network properties are still not well characterized. In this work we sought to examine in a group of 20 healthy volunteers (age  $33 \pm 6$  years, 8 F/12 M) the relationship between changes of spectral and spatiotemporal features of one prominent resting-state network, namely the DMN, during the continuous execution of a working memory n-back task. We found that task execution impacted on both functional connectivity and amplitude of BOLD fluctuations within large parts of the DMN, but these changes correlated between each other only in a small area of the posterior cingulate. We conclude that combined analysis of multiple parameters related to connectivity, and their changes during the transition from resting state to continuous task execution, can contribute to a better understanding of how brain networks rearrange themselves in response to a task.

**Keywords:** low frequency BOLD fluctuations, functional connectivity, DMN, working memory, fALFF

## INTRODUCTION

Spontaneous low-frequency fluctuations (LFFs) of the BOLD signal are thought to be a manifestation of the ongoing activity of the brain [1]. Such BOLD LFFs are spatially synchronized in the brain, identifying robust and reproducible connectivity patterns also known as resting-state networks [2]. Although, BOLD LFFs have been subject of intense research, the relationship between network connectivity and spectral features of the signal is still not completely characterized. Even less clear is how this relationship is influenced by the cognitive activity of the brain.

Of particular interest is the characterization of the spontaneous activity within the DMN, that is considered an intrinsic property of the human brain, relevant for brain physiology and pathology [3]. The specific interest for DMN is justified because features of slow BOLD fluctuations within the DMN have been linked to multiple brain processes (recently reviewed by [4]). Indeed, cognition has been shown to depend on the activity of the DMN itself

[5], as well as on the connectivity between DMN and other networks, such as the “task-positive” network [6]. Far from being a static property of the brain, connectivity within DMN and between DMN and other networks is influenced by behavior [7].

Task-related modulations of the DMN are not restricted to effects on connectivity. Indeed, the amplitude of BOLD LFFs within the DMN depends on the cognitive activity, decreasing during a working memory task [8] or after a continuous and prolonged attention task [9]. Level of activity in the DMN has been found to be modulated by working memory load both during and after task performance [10, 11]. The amplitude of LFFs has been proposed as a measure to assess the degree of intrinsic brain activity, offering insights into the physiological determinants of functional connectivity [12, 13]. Various metrics have been proposed to assess BOLD fluctuation amplitude, including ALFF (amplitude of LFF, [13, 14]) and its normalized version fALFF (fractional ALFF), less sensitive to noise [15]. ALFF has been found to be altered in several pathologies [14, 16, 17], and to be also influenced by the behavioral state or by the task [18, 19]. Moreover, the amplitude of fluctuations at rest has been shown to correlate with brain activation and deactivation in DMN during the execution of an N-back working memory task, and this correlation was found to be load dependent [20]. The load dependency of the relationship between rest and task fluctuations suggests that the involved regions are characterized by both a great capacity for enhancing flow and metabolism under stimulation, and a large fluctuation amplitude at rest.

The spectral amplitude of BOLD LFFs is often integrated over a relatively broad range (typically between 0.01 and 0.1 Hz), however it has been suggested that a finer spectral subdivision can allow a better grasp of the underlying physiological phenomena [21–23]. In particular, ALFF within the bands labeled slow-5 (0.01–0.027 Hz) and slow-4 (0.027–0.073 Hz) brings most of the neuronal-related information (compared to higher frequency ranges) and is characterized by distinct spatial patterns [23, 24].

BOLD response signals show a spatially segregated coupling with electrophysiological signals (e.g., [25–27]) and metabolism [28, 29], yet the connectivity patterns are only partially determined by anatomic constraints [30]. Brain spontaneous activity, embodied in functional connectivity, has been shown to account to up to 70% of the energy consumed by the brain [31], therefore, the local relationship between fluctuation amplitude and functional connectivity has the potential to clarify some basic features of functional networks. Accordingly, correlation between oscillation amplitude and functional connectivity has been found in healthy subjects at rest [32], and was reported to be decreased in Alzheimer’s disease patients [33]. Moreover, the temporal variance of dynamic local functional connectivity has been associated with the temporal variance of ALFF [34], and regional synchrony of BOLD fluctuations has been proposed as a determinant for neurovascular coupling variability [35].

In the present study, we sought to elucidate whether the relationship between amplitude and connectivity strength of BOLD fluctuations within the DMN can be modulated by behavior. For this purpose, we quantified spectral and spatiotemporal features of BOLD LFFs within the DMN during

resting state and during the sustained execution of a graded working memory task.

## MATERIALS AND METHODS

### Subjects

Twenty healthy Italian-speaking subjects (age  $33 \pm 6$  years, 8 female) participated in the present study. The study was carried out in accordance with a protocol approved by the Ethics Committee of Santa Lucia Foundation in Rome. Recruited subjects gave written informed consent in accordance with the Declaration of Helsinki and European Union regulations.

### Image Acquisition

Data were collected on a 3 T MRI system (Magnetom Allegra, Siemens Healthineers, Erlangen, Germany). Functional images were acquired via 2D gradient-echo planar sequence (TE = 30 ms, TR = 2,100 ms, FA =  $70^\circ$ , voxel size  $3 \times 3 \times 2.5 \text{ mm}^3$ ) lasting 24 min and 38 s for a total of 704 volumes (4 dummy scans included). Sagittal, T<sub>1</sub>-weighted structural data were acquired for tissue segmentation purpose (MPRAGE, TE = 4.38 ms, TR = 2,000 ms, FA =  $8^\circ$ , voxel size  $1.33 \times 1.33 \times 1 \text{ mm}^3$ ).

### Stimulation Paradigm

During the functional runs, subjects were presented with a stimulation paradigm consisting of alternated epochs of open-eyes resting state and sustained auditory working memory task (4 min and 54 s each, starting with resting-state epoch). The auditory working memory task involved continuous n-back trials administered in epochs either at “high” load (2-back) or “low” load (1-back). Each trial was composed of a 500-ms window, in which subjects were aurally presented with a pseudorandom vowel (A, E, or O), and a subsequent 1,600-ms window, in which subjects were asked to press a button every time the current vowel was the same as the one presented one stimulus prior (1-back) or two stimuli prior (2-back).

Two functional runs were acquired for each subject during the same experimental session, with epoch ordering: rest/1-back/rest/2-back/rest and rest/2-back/rest/1-back/rest. Run order was counterbalanced across subjects. The stimulation paradigm started after the second dummy scan (i.e., 2 scans before the first analyzed image) to roughly account for hemodynamic delay.

### Image Processing

Functional and structural MRI data were preprocessed using functional connectivity toolbox version 15.b [36] and analyzed with dedicated in-house routines based on MATLAB R2013a (The Mathworks, Natick, MA, USA) and AFNI [37]. T<sub>1</sub> weighted images were segmented in white matter (WM) and Cerebrospinal Fluid (CSF) probability maps to be later used for denoising. Functional data underwent standard preprocessing, including removal of the first four volumes of each fMRI run, realignment, slice-timing correction, normalization to MNI space (using as source volume the mean EPI image) and spatial smoothing with an isotropic Gaussian kernel ( $8 \times 8 \times 8 \text{ mm}^3$  FWHM). Several spurious sources of variance were removed from smoothed

functional data via regression analysis, including the estimated realignment parameters and their first derivative, signals from WM and CSF following the aCompCor approach [38] and outlier volumes detected using the Artifact Detection Tools (ART: [www.nitrc.org/projects/artifactdetect/](http://www.nitrc.org/projects/artifactdetect/)). Finally, a band-bass temporal filter in the range 0.008–0.09 Hz was applied to the residual time-series. An unfiltered time-series was also retained for fALFF computation.

Each functional run was then split in its five epochs, which were later used to extract epoch-related functional parameters (see below). A DMN mask was derived by independent component analysis (FSL MELODIC toolbox, [39]) of the first resting-state epoch and was used to constrain the subsequent analyses. The first resting-state epoch was then discarded, leaving 2 resting-state and 2 task epochs for each of the two functional runs.

A second dataset was obtained with the same procedures, but with isotropic Gaussian kernel at  $6 \times 6 \times 6 \text{ mm}^3$  FWHM for testing purposes. All the following results are referred to the  $8^3 \text{ mm}^3$  smoothing dataset, unless otherwise stated.

## Computation of Parameters

Each of the following parameters was computed separately in each functional epoch, thus they represent specific features of BOLD LFFs at specific steady-state conditions.

As a measure of average network strength, within-network functional connectivity (FC) was evaluated as the Pearson's correlation coefficient between each voxel's time course and the average time course of the whole DMN. Correlation maps were z-Fisher transformed to improve normality.

To quantify the amplitude of LFFs, fALFF was calculated for each voxel time series as the summation of the spectral amplitude in the selected low-frequency range (between 0.008 and 0.09 Hz) divided by the summation in the full frequency range [15]. The computation was performed via the AFNI program 3dRSFC [37]. Average contribution of different frequency bands was also evaluated by estimating the Power Spectral Density (PSD) of the average BOLD time course within the DMN. The PSD was estimated via the squared magnitude of the Fast Fourier Transform of the signal, and averaged separately in the slow-5 (0.01–0.027 Hz) and slow-4 (0.027–0.073 Hz) bands. PSD was also normalized by its integrated power.

## Analysis of Changes Associated with Sustained Working Memory Task

Stationary changes of each investigated parameter (fALFF and FC) between task and the resting epoch immediately following it were evaluated voxel by voxel (irrespectively of the task level) and tested for significance by paired *t*-test across subjects, after averaging separately the parameters of interest across the two functional runs of each subject.

Changes of the PSD profile were assessed by linearly fitting the normalized PSD of each epoch, and testing the resulting slopes via repeated measures ANOVA and *post-hoc* Bonferroni corrected paired *t*-test. Task-related changes of PSD integrated magnitude were assessed by 2-way repeated measures ANOVA and *post-hoc t*-tests (Bonferroni corrected), defining as factors the

stimulation condition (rest, 1-back, 2-back) and the frequency band (slow-5 and slow-4).

Finally, to test whether changes of functional connectivity are related to changes of amplitude of fluctuations we computed voxelwise Pearson correlation of the relevant quantities across subjects.

Statistical threshold for voxelwise comparisons was set to  $p < 0.05$  corrected for multiple comparisons at cluster level by Monte Carlo simulation (AFNI, 3dClustSim). The corrected threshold corresponded to a single-voxel  $p < 0.001$  and a minimum cluster size depending on the estimated smoothness of fit residuals and on the number of voxels within the DMN mask. Smoothness of fit residuals was estimated using a mixed model for autocorrelation function of noise [40, 41].

## RESULTS

fALFF and FC were significantly reduced within posterior areas of DMN during task execution, including the precuneus (bilaterally) and the posterior division of the cingulate (**Figures 1A,B**). The anterior portion of DMN showed significant task-related fALFF changes in the medial prefrontal cortex, but did not show any significant change of FC. Very similar results were obtained on the  $6 \times 6 \times 6 \text{ mm}^3$  smoothing dataset (not shown).

Spectral analysis revealed that the task-related fALFF decrement occurs with a reduction of fluctuations power at each

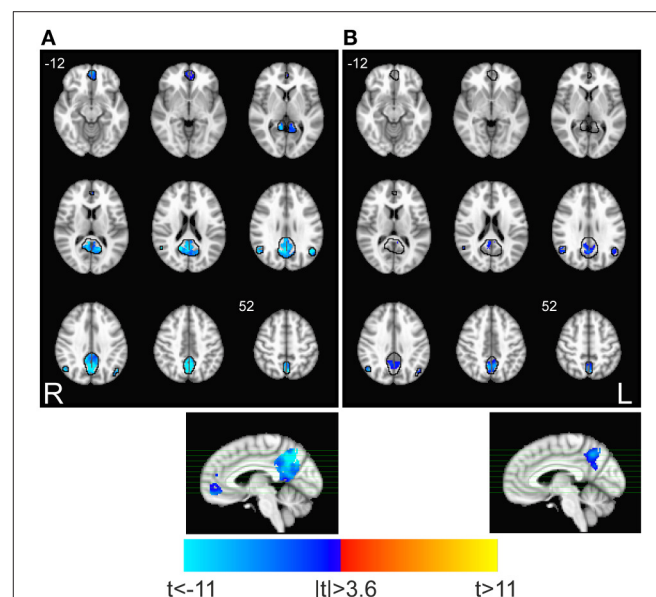


**FIGURE 1 |** Task-related changes in spectral and spatio-temporal parameters within DMN. Maps show the significant task-associated changes of **(A)** fALFF and **(B)** FC for the test TASK > REST (paired *t*-test,  $p < 0.05$  corrected). 3dClustSim parameters: single-voxel  $p < 0.001$ ; cluster size threshold, 10 and 18 voxels, for fALFF and FC, respectively). Black lines identify the boundaries of DMN as identified by ICA, where analysis was restricted. Task-related decrements of fALFF and FC are apparent in the posterior DMN, and in the anterior cingulate only for fALFF.

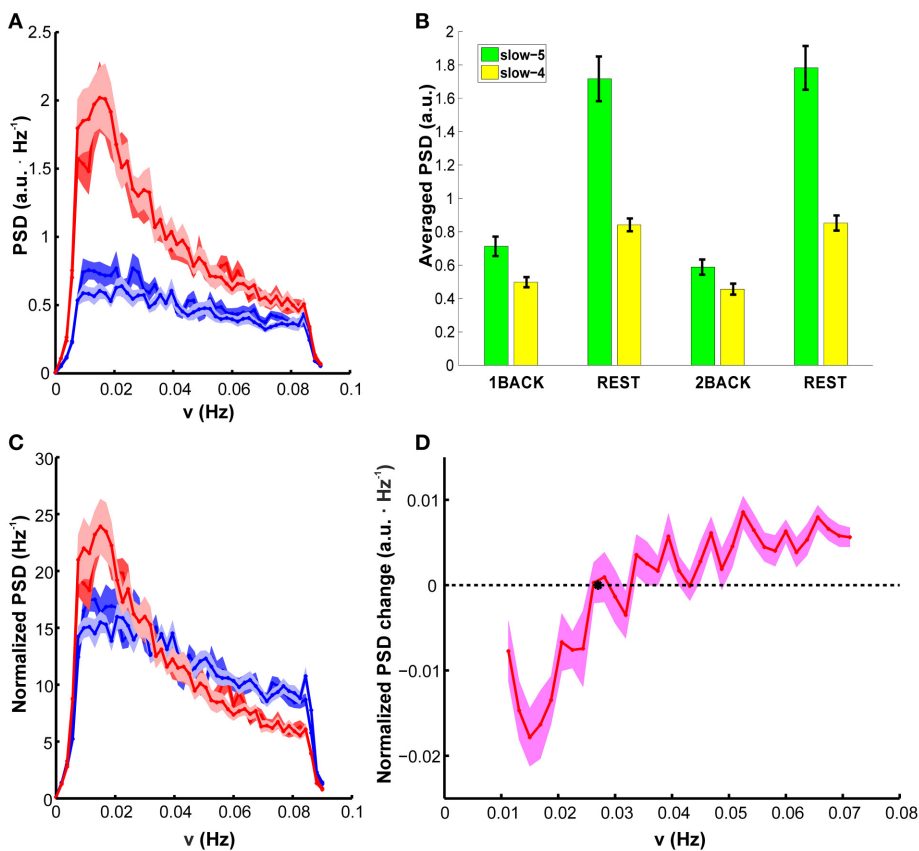


**FIGURE 2 |** PSD group results: **(A)** PSD of BOLD fluctuations in the DMN, averaged in each epoch. Resting-state epochs are represented in red, task epochs in blue (dark blue is 1 back, light blue is 2 back). Task-related changes in spectral power are visible. **(B)** PSD averaged in the slow-4 (green) and slow-5 (yellow) range. Slow-5 presents higher integrated power in all epochs. Power was always higher at rest than during task, but in a frequency specific manner (significant interaction stimulation condition  $\times$  frequency band). The two task levels were indistinguishable. See Results Section for *p*-values. **(C)** Normalized PSD. In normalized PSD a steeper dependence on frequency during resting state than during task performance is apparent. **(D)** Difference between normalized PSD during task execution and resting state as a function of frequency. All values are mean  $\pm$  SEM across subjects. SEM is computed after within-subject averaging of corresponding data from the two runs.

investigated frequency (**Figure 2A**). Comparison of error bands suggests that PSD of BOLD fluctuations is very reproducible between sessions at rest (compare light red and dark red lines in **Figure 2A**). Any possible effect of task level is confined to the lower part of frequency spectrum (below 0.02 Hz, light and dark blue lines in **Figure 2A**, see also **Supplementary Figure 1** for the confidence band of the PSD difference between task levels). Values averaged within slow-5 and slow-4 bands confirmed the result, showing a consistent task-related decrease of PSD, but no average effect of task level [**Figure 2B**, 2-way ANOVA,  $F_{(3, 57)} > 85$ ,  $p < 0.001$  for the factor “stimulation condition”; *post-hoc* Bonferroni paired *t*-test  $t > 10$ ,  $p < 0.001$ ,  $n = 20$  for task vs. rest;  $t < 1.4$ ,  $p > 0.9$ ,  $n = 20$  for differences between 1-back and 2-back].

The task-related decrement of fluctuation power was not uniform across the whole spectrum. Indeed, the reduction of PSD magnitude during task was less marked at the higher frequencies, both in absolute terms and in terms of fractional change compared to rest (compare changes in slow-4 and slow-5 bands, **Figure 2B**). This feature was demonstrated by a significant

interaction between factors (stimulation condition and frequency band) in 2-way ANOVA [ $F_{(3, 57)} > 32$ ,  $p < 0.001$ ]. Analysis of simple main effects confirmed that, in both bands, power change in task vs. rest comparison was always significant, and task (respectively rest) epochs were indistinguishable among them ( $p < 0.001$  for all significant comparisons,  $p > 0.8$  for all not significant comparisons). Accordingly, the normalized PSD highlighted an higher power contribution from the lower frequencies, but it was characterized by a steeper decrease of power with frequency during rest than during task; in other words, the normalized PSD became significantly flatter during task (**Figure 2C**). The change of normalized PSD shape between treatments was also confirmed by repeated measures ANOVA on the average slope [ $F_{(3, 57)} > 46$ ,  $p < 0.001$ ; **Table 1**]; relevant *post-hoc* tests indicated that the LFFs normalized spectrum was remarkably reproducible between rest epochs ( $t < 1.3$ ,  $p > 0.9$ ,  $n = 20$ ) and between task epochs, irrespectively of the task level ( $t < 1.8$ ,  $p > 0.4$ ,  $n = 20$ ). The slope was however reduced by task ( $t > 6.6$ ,  $p < 0.001$ ,  $n = 20$  for all comparisons).

**TABLE 1 |** Slope of normalized PSD.

	1-back	Rest after 1-back	2-back	Rest after 2 back
Slope	-0.284	-0.468	-0.235	-0.503
SEM	0.027	0.026	0.021	0.033

Values of the slope of normalized PSD averaged across subjects, separately calculated during task epochs and during rest epochs immediately following each task epoch. The shape is significantly flatter during task than rest [repeated measures ANOVA,  $F_{(3, 57)} > 46, p < 0.001$  between treatments]. Slopes are consistent across resting epochs, as well as across task epochs (Bonferroni paired t-test,  $t < 1.3, p > 0.9, n = 20$  and  $t < 1.8, p > 0.4$ , respectively;  $n = 20$ ). Slopes are reduced between task and the immediately following rest epoch ( $t > 6.6, p < 0.001, n = 20$  and  $t > 9.6, p < 0.001, n = 20$  for 1-back and 2-back, respectively). Slopes are also reduced between task and the chronologically unmatched rest ( $t > 8.4, p < 0.001, n = 20$  for 2-back vs. rest after 1 back, and  $t > 7.8, p < 0.001, n = 20$  for 1-back vs. rest after 2 back). SEM, Standard Error of the Mean.

In agreement with this finding, the difference between the pooled task and rest conditions showed an overall increase with frequency (Figure 2D); interestingly, the difference crosses zero (thus the normalized PSD at rest and task are equal) at a frequency roughly compatible with the boundary between slow-4 and slow-5 bands.

Finally, the voxel-wise analysis within the DMN revealed that the decrement of FC (Figure 1A) was correlated to the decrease of fALFF (Figure 1B) in a small area in the posterior cingulate (Figure 3, unthresholded correlation map is reported in Supplementary Figure 2). Equivalent results were obtained on the  $6 \times 6 \times 6 \text{ mm}^3$  smoothing dataset (not shown).

## DISCUSSION

In this work we sought to test whether changes in connectivity during a working memory task are mirrored by changes in fluctuation amplitude within the DMN, and if task-related changes of the two parameters are correlated. We found a remarkably homogeneous reduction of both fALFF and FC during sustained working memory task in the posterior areas of DMN, while changes in the anterior cingulate were less marked (Figures 1A,B).

Task-related reductions in fluctuation amplitude, as indexed by fALFF metric, were also evident in the power spectrum within the DMN mask. Task epochs showed a pronounced reduction in power at each investigated frequency, in a consistent and reproducible manner across different task loads (Figure 2A). However, the decrease in fluctuation power within the DMN was not uniform across the explored frequency range. Indeed, while both rest and task states showed higher fluctuation power in the slow-5 band compared to the slow-4 band, consistently with the known 1/f power distribution of BOLD LFFs [42, 43], the trend was less marked during tasks (Figure 2B). Accordingly, normalized spectral power showed state-dependent trends for slow-5 and slow-4 bands, suggesting that the switch to task state has a major impact on the lower frequency component, or (possibly) that the lower frequency component is more relevant to the switch of brain function.

The reduced power of LFFs during the task execution is in agreement with previous studies [8, 43, 44]. Indeed, power

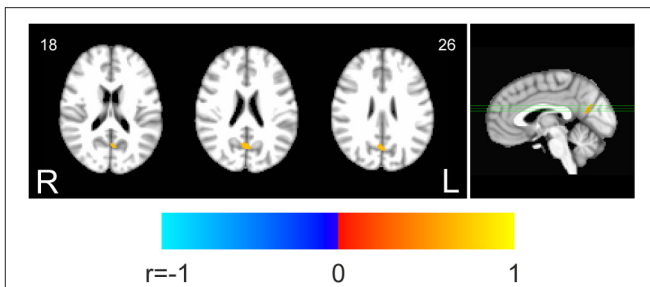


**FIGURE 3 |** Correlation between fALFF and FC changes within the DMN. The map shows the voxelwise thresholded results of correlation analysis between task-related changes of fALFF and FC. Decrease of fALFF was correlated to decrease of FC in a small single cluster within the posterior DMN areas ( $p < 0.05$  corrected. 3dClustSim parameters: single-voxel  $p < 0.001$ ; cluster size threshold, 16 voxels).

distributions of both task and rest states have shown to follow a power law, with significant reduced exponent during task states [43], compatible with the task-related decrease of PSD we reported. Moreover, reduced BOLD fluctuations were observed within the DMN during a working memory task, which, similarly to our results, were more notable in posterior regions [8]. At odds with our results, Zhang et al. have reported mainly decrements of fALFF during a stop signal task within the DMN [45]. While several factors might contribute to explain the discrepancy with our results (e.g., different task condition and the use of task-residual instead of a continuous and prolonged acquisition of task state), more likely it might be explained by the transformation of fALFF in z-score which removes the mean difference across states.

The reduction in fluctuation amplitude mirrors the tendency of the DMN to reduce its spontaneous activity during cognitive engagement. This result shows that task execution affects brain regions within the DMN inducing both a time-locked functional deactivation, as shown in countless task-based experiments, and a modulation of spontaneous fluctuations toward low level of activity. In addition, several studies have demonstrated that DMN deactivation increases with cognitive load [10, 11] indicating that cognitive resources are reallocated according to task demand and that endogenous processes need to be inhibited at different levels for successful execution. This could be interpreted as a redistribution of cognitive ability but also as a neuronal correlate of mental fatigue [11], self-referential processes [46], or mind-wandering [47]. In our case, aggregate values of LFFs power spectral density within slow-4 and slow-5 bands (Figure 2B) did not reveal any effect of load, while spectral decomposition suggested that any effect of load is confined to the lowest spectral range, below 0.02 Hz (about half of the slow-5 band, Figure 2A and Supplementary Figure 1). These results suggest that amplitude of fluctuations and DMN deactivation react differently to an increase of cognitive activity. Incidentally, the inhomogeneous response of PSD to task within the slow-5 band suggests that a further subdivision of slow-5 into 2 or more bands can help to identify subtle frequency-specific effects on the amplitude of BOLD LFFs.

Functional connectivity and ALFF during resting state have shown region specific couplings in elderly populations [32, 33] which were suggested to be of physiological relevance being disrupted in degenerative dementia [33]. While these studies have shown inter-subject associations between connectivity and amplitude at rest, others have also found within-subject synchronized fluctuations of the two parameters [34]. We found that the task-related decreases of fALFF and FC are highly correlated within a small area of the DMN (**Figure 3**), supporting a physiological relation between the two parameters, even within the DMN, which is not directly involved in the execution of the task. This result suggests that a change of functional connectivity reflects a change of amplitude of fluctuations at least in spatially segregated regions within posterior DMN areas. Taking into account a connection between amplitude of fluctuations and underlying electrophysiological activity [25, 27], this result overall suggests the neural origin of changes of functional connectivity within the DMN.

The correlation between variation of FC and fALFF within the DMN was not observed uniformly across the whole network. We hypothesize that this finding is related to an intrinsic heterogeneity of the coupling between FC and fALFF changes. Indeed, unthresholded data (**Supplementary Figure 2**) showed a smooth change of correlation with some local maxima (of which only one exceeds statistical threshold). This feature suggests spatially segregated coupling between FC and fALFF changes. However, the fact that the effect is confined in the areas of most significant FC and fALFF changes (compare **Figures 1A,B** with **Figure 3**) may also indicate a possible lack of sensitivity of our experimental design. The lack of generalized correlation between FC and fALFF changes also implies that fALFF changes are not the only determinants of FC changes, a notion that confirms the utility of exploiting both parameters in functional connectivity studies. An intriguing hypothesis, that deserves further analysis, is that the changes of connectivity and of fluctuation amplitude do not share the same spectral sensitivity profile. Indeed, in a previous study we reported band-specific spatial patterns of correlation between FC and ALFF at rest, even if the effect was mainly present outside the DMN [33]. However, in the present study, we found that the amplitude of fluctuation is substantially more affected by task execution in the lower range of frequencies (the slow-5 band), suggesting that, differently for the coupling during resting states, a frequency specific relationship may exist. This hypothesis is also in line with previous resting-state studies that have repeatedly shown frequency-specific alterations in fluctuation amplitude [16, 48, 49] and connectivity [48] during pathological states.

## REFERENCES

- Rogers BP, Morgan VL, Newton AT, Gore JC. Assessing functional connectivity in the human brain by fMRI. *Magn Reson Imaging* (2007) **25**:1347–57. doi: 10.1016/j.mri.2007.03.007
- Damoiseaux JS, Rombouts SA, Barkhof F, Scheltens P, Stam CJ, Smith SM, et al. Consistent resting-state networks across healthy subjects. *Proc Natl Acad Sci USA*. (2006) **103**:13848–53. doi: 10.1073/pnas.0601417103

In conclusion, in this work we reported that amplitude and connectivity of BOLD low-frequency fluctuations within the DMN are affected by the sustained performance of a cognitive task. With the exception of the very low frequency component, different cognitive loads were associated with similar modulations in fluctuation amplitude. Task-related modulations of amplitude of fluctuations and connectivity strength are not independent within the DMN. The results we obtained suggest that the correlation between amplitude of BOLD fluctuations and connectivity strength can be exploited to gather insights into the physiology of brain function.

## AUTHOR CONTRIBUTIONS

TG, EM, and FG designed research. ST, TG, IE, MM, and MF performed experiments. ST, DM, and IE analyzed data. ST, DM, TG, MM, RW, EM, SM, and FG interpreted results of experiments. ST wrote the main manuscript text and drafted the figures. All authors edited, reviewed, and approved the manuscript.

## ACKNOWLEDGMENTS

The present work was supported by Regione Lazio, grant PAMINA (to FG) and by the National Institutes of Health, award number R01DK099137 (to SM). This project has received funding from the European Union’s Horizon 2020 research and innovation programme under the Marie Skłodowska-Curie grant agreement No 691110 (MICROBRADAM). The content is solely the responsibility of the authors and does not necessarily represent the official views of the funding bodies.

## SUPPLEMENTARY MATERIAL

The Supplementary Material for this article can be found online at: <http://journal.frontiersin.org/article/10.3389/fphy.2017.00031/full#supplementary-material>

**Supplementary Figure 1** | PSD difference between 1 back and 2 back. The figure reports the 95% confidence band for the difference of LFFs power spectral density between task levels 1-back and 2-back. The confidence band does not overlap zero only below 0.02 Hz.

**Supplementary Figure 2** | Correlation between fALFF and FC changes within the DMN, unthresholded. Unthresholded map of the correlation between fALFF and FC changes within the DMN (unthresholded version of **Figure 3**). Correlation was generally around 0, except some clusters of positive correlation. Only one of them reached statistical significance (highlighted by black outline, corresponding to **Figure 3**).

- Fox MD, Snyder AZ, Vincent JL, Corbetta M, Van Essen DC, Raichle ME. The human brain is intrinsically organized into dynamic, anticorrelated functional networks. *Proc Natl Acad Sci USA*. (2005) **102**:9673–8. doi: 10.1073/pnas.0504136102
- Mak LE, Minuzzi L, MacQueen G, Hall G, Kennedy SH, Milev R. The default mode network in healthy individuals: a systematic review and meta-analysis. *Brain Connect.* (2017) **7**:25–33. doi: 10.1089/brain.2016.0438

5. Esposito F, Bertolino A, Scarabino T, Latorre V, Blasi G, Popolizio T, et al. Independent component model of the default-mode brain function: assessing the impact of active thinking. *Brain Res. Bull.* (2006) **70**:263–69. doi: 10.1016/j.brainresbull.2006.06.012
6. Hampson M, Driesen N, Roth JK, Gore JC, Constable RT. Functional connectivity between task-positive and task-negative brain areas and its relation to working memory performance. *Magn Reson Imaging* (2010) **28**:1051–7. doi: 10.1016/j.mri.2010.03.021
7. Bluhm RL, Clark CR, McFarlane AC, Moores KA, Shaw ME, Lanius RA. Default network connectivity during a working memory task. *Hum Brain Mapp.* (2011) **32**:1029–35. doi: 10.1002/hbm.21090
8. Fransson P. How default is the default mode of brain function? Further evidence from intrinsic BOLD signal fluctuations. *Neuropsychologia* (2006) **44**:2836–45. doi: 10.1016/j.neuropsychologia.2006.06.017
9. Gui D, Xu S, Zhu S, Fang Z, Spaeth AM, Xin Y, et al. Resting spontaneous activity in the default mode network predicts performance decline during prolonged attention workload. *Neuroimage* (2015) **120**:323–30. doi: 10.1016/j.neuroimage.2015.07.030
10. McKiernan KA, Kaufman JN, Kucera-Thompson J, Binder JR. A parametric manipulation of factors affecting task-induced deactivation in functional neuroimaging. *J Cogn Neurosci.* (2003) **15**:394–408. doi: 10.1162/089892903321593117
11. Pyka M, Beckmann CF, Schoning S, Hauke S, Heider D, Kugel H, et al. Impact of working memory load on fMRI resting state pattern in subsequent resting phases. *PLoS ONE* (2009) **4**:e7198. doi: 10.1371/journal.pone.0007198
12. Biswal B, Yetkin FZ, Haughton VM, Hyde JS. Functional connectivity in the motor cortex of resting human brain using echo-planar MRI. *Magn Reson Med.* (1995) **34**:537–41. doi: 10.1002/mrm.1910340409
13. Kiviniemi V, Kantola JH, Jauhainen J, Tervonen O. Comparison of methods for detecting nondeterministic BOLD fluctuation in fMRI. *Magn Reson Imaging* (2004) **22**:197–203. doi: 10.1016/j.mri.2003.09.007
14. Zang YF, He Y, Zhu CZ, Cao QJ, Sui MQ, Liang M, et al. Altered baseline brain activity in children with ADHD revealed by resting-state functional MRI. *Brain Dev.* (2007) **29**:83–91. doi: 10.1016/j.braindev.2006.07.002
15. Zou QH, Zhu CZ, Yang Y, Zuo XN, Long XY, Cao QJ, et al. An improved approach to detection of amplitude of low-frequency fluctuation (ALFF) for resting-state fMRI: fractional ALFF. *J Neurosci Methods* (2008) **172**:137–41. doi: 10.1016/j.jneumeth.2008.04.012
16. Zhang J, Wei L, Hu X, Zhang Y, Zhou D, Li C, et al. Specific frequency band of amplitude low-frequency fluctuation predicts Parkinson's disease. *Behav Brain Res.* (2013) **252**:18–23. doi: 10.1016/j.bbr.2013.05.039
17. Liu J, Ren L, Womer FY, Wang J, Fan G, Jiang W, et al. Alterations in amplitude of low frequency fluctuation in treatment-naïve major depressive disorder measured with resting-state fMRI. *Hum Brain Mapp.* (2014) **35**:4979–88. doi: 10.1002/hbm.22526
18. Yang H, Long XY, Yang Y, Yan H, Zhu CZ, Zhou XP, et al. Amplitude of low frequency fluctuation within visual areas revealed by resting-state functional MRI. *Neuroimage* (2007) **36**:144–52. doi: 10.1016/j.neuroimage.2007.01.054
19. Zhang S, Li CS. Task-related, low-frequency task-residual, and resting state activity in the default mode network brain regions. *Front Psychol.* (2012) **3**:172. doi: 10.3389/fpsyg.2012.00172
20. Zou Q, Ross TJ, Gu H, Geng X, Zuo XN, Hong LE, et al. Intrinsic resting-state activity predicts working memory brain activation and behavioral performance. *Hum Brain Mapp.* (2013) **34**:3204–15. doi: 10.1002/hbm.22136
21. Penttonen M, Buzsaki G. Natural logarithmic relationship between brain oscillators. *Thalamus Relat Syst.* (2003) **2**:142–52. doi: 10.1016/S1472-9288(03)00007-4
22. Buzsaki G, Draguhn A. Neuronal oscillations in cortical networks. *Science* (2004) **304**:1926–9. doi: 10.1126/science.1099745
23. Zuo XN, Di Martino A, Kelly C, Shehzad ZE, Gee DG, Klein DF, et al. The oscillating brain: complex and reliable. *Neuroimage* (2010) **49**:1432–45. doi: 10.1016/j.neuroimage.2009.09.037
24. Gohel SR, Biswal BB. Functional integration between brain regions at rest occurs in multiple-frequency bands. *Brain Connect.* (2015) **5**:23–34. doi: 10.1089/brain.2013.0210
25. Laufs H, Krakow K, Sterzer P, Eger E, Beyerle A, Salek-Haddadi A, et al. Electroencephalographic signatures of attentional and cognitive default modes in spontaneous brain activity fluctuations at rest. *Proc Natl Acad Sci USA.* (2003) **100**:11053–8. doi: 10.1073/pnas.1831638100
26. Shmuel A, Augath M, Oeltermann A, Logothetis NK. Negative functional MRI response correlates with decreases in neuronal activity in monkey visual area V1. *Nat Neurosci.* (2006) **9**:569–77. doi: 10.1038/nn1675
27. Hiltunen T, Kantola J, Abou Elseoud A, Lepola P, Suominen K, Starck T, et al. Infra-slow EEG fluctuations are correlated with resting-state network dynamics in fMRI. *J Neurosci.* (2014) **34**:356–62. doi: 10.1523/JNEUROSCI.0276-13.2014
28. Von Pfostl V, Li J, Zaldivar D, Goense J, Zhang X, Serr N, et al. Effects of lactate on the early visual cortex of non-human primates, investigated by pharmaco-MRI and neurochemical analysis. *Neuroimage* (2012) **61**:98–105. doi: 10.1016/j.neuroimage.2012.02.082
29. Bednarik P, Tkac I, Giove F, Dinuzzo M, Deelchand DK, Emir UE, et al. Neurochemical and BOLD responses during neuronal activation measured in the human visual cortex at 7 Tesla. *J Cereb Blood Flow Metab.* (2015) **35**:601–10. doi: 10.1038/jcbfm.2014.233
30. Buckner RL, Krienen FM, Yeo BT. Opportunities and limitations of intrinsic functional connectivity MRI. *Nat Neurosci.* (2013) **16**:832–7. doi: 10.1038/nn.3423
31. Tomasi D, Wang GJ, Volkow ND. Energetic cost of brain functional connectivity. *Proc Natl Acad Sci USA.* (2013) **110**:13642–7. doi: 10.1073/pnas.1303346110
32. Di X, Kim EH, Huang CC, Tsai SJ, Lin CP, Biswal BB. The influence of the amplitude of low-frequency fluctuations on resting-state functional connectivity. *Front Hum Neurosci.* (2013) **7**:118. doi: 10.3389/fnhum.2013.00118
33. Mascali D, Dinuzzo M, Gili T, Moraschi M, Fratini M, Maraviglia B, et al. Intrinsic patterns of coupling between correlation and amplitude of low-frequency fMRI fluctuations are disrupted in degenerative dementia mainly due to functional disconnection. *PLoS ONE* (2015) **10**:e0120988. doi: 10.1371/journal.pone.0120988
34. Tomasi D, Shokri-Kojori E, Volkow ND. Temporal changes in local functional connectivity density reflect the temporal variability of the amplitude of low frequency fluctuations in gray matter. *PLoS ONE* (2016) **11**:e0154407. doi: 10.1371/journal.pone.0154407
35. Yuan R, Di X, Kim EH, Barik S, Rypma B, Biswal BB. Regional homogeneity of resting-state fMRI contributes to both neurovascular and task activation variations. *Magn Reson Imaging* (2013) **31**:1492–500. doi: 10.1016/j.mri.2013.07.005
36. Whitfield-Gabrieli S, Nieto-Castanon A. Conn: a functional connectivity toolbox for correlated and anticorrelated brain networks. *Brain Connect.* (2012) **2**:125–41. doi: 10.1089/brain.2012.0073
37. Cox RW. AFNI: software for analysis and visualization of functional magnetic resonance neuroimages. *Comput Biomed Res.* (1996) **29**:162–73. doi: 10.1006/cbmr.1996.0014
38. Behzadi Y, Restom K, Liau J, Liu TT. A component based noise correction method (CompCor) for BOLD and perfusion based fMRI. *Neuroimage* (2007) **37**:90–101. doi: 10.1016/j.neuroimage.2007.04.042
39. Jenkinson M, Beckmann CF, Behrens TE, Woolrich MW, Smith SM. Fsl. *Neuroimage* (2012) **62**:782–90. doi: 10.1016/j.neuroimage.2011.09.015
40. Cox RW, Chen G, Glen DR, Reynolds RC, Taylor PA. FMRI clustering and false positive rates. *Proc Natl Acad Sci USA.* (2017a) **114**:E3370–1. doi: 10.1073/pnas.1614961114
41. Cox RW, Chen G, Glen DR, Reynolds RC, Taylor PA. FMRI clustering in AFNI: false positive rates redux. *Brain Connect.* (2017b) *arXiv:1702.04845*
42. Fox MD, Raichle ME. Spontaneous fluctuations in brain activity observed with functional magnetic resonance imaging. *Nat Rev Neurosci.* (2007) **8**:700–11. doi: 10.1038/nrn2201
43. He BJ. Scale-free properties of the functional magnetic resonance imaging signal during rest and task. *J Neurosci.* (2011) **31**:13786–95. doi: 10.1523/JNEUROSCI.2111-11.2011
44. Duff EP, Johnston LA, Xiong J, Fox PT, Mareels I, Egan GF. The power of spectral density analysis for mapping endogenous BOLD signal

- fluctuations. *Hum Brain Mapp.* (2008) **29**:778–90. doi: 10.1002/hbm.20601
45. Zhang S, Li CS. A neural measure of behavioral engagement: task-residual low-frequency blood oxygenation level-dependent activity in the precuneus. *Neuroimage* (2010) **49**:1911–8. doi: 10.1016/j.neuroimage.2009.09.004
46. Northoff G, Heinzel A, De Grecq M, Bermpohl F, Dobrowolny H, Panksepp J. Self-referential processing in our brain—a meta-analysis of imaging studies on the self. *Neuroimage* (2006) **31**:440–57. doi: 10.1016/j.neuroimage.2005.12.002
47. Mason MF, Norton MI, Van Horn JD, Wegner DM, Grafton ST, MacRae CN. Wandering minds: the default network and stimulus-independent thought. *Science* (2007) **315**:393–5. doi: 10.1126/science.1131295
48. Liu X, Wang S, Zhang X, Wang Z, Tian X, He Y. Abnormal amplitude of low-frequency fluctuations of intrinsic brain activity in Alzheimer's disease. *J Alzheimers Dis.* (2014) **40**:387–97. doi: 10.3233/JAD-131322
49. La C, Mossahebi P, Nair VA, Young BM, Stamm J, Birn R, et al. Differing patterns of altered slow-5 oscillations in healthy aging and ischemic stroke. *Front Hum Neurosci.* (2016) **10**:156. doi: 10.3389/fnhum.2016.00156

**Conflict of Interest Statement:** The authors declare that the research was conducted in the absence of any commercial or financial relationships that could be construed as a potential conflict of interest.

Copyright © 2017 Tommasin, Mascali, Gili, Eid Assan, Moraschi, Fratini, Wise, Macaluso, Mangia and Giove. This is an open-access article distributed under the terms of the Creative Commons Attribution License (CC BY). The use, distribution or reproduction in other forums is permitted, provided the original author(s) or licensor are credited and that the original publication in this journal is cited, in accordance with accepted academic practice. No use, distribution or reproduction is permitted which does not comply with these terms.



# Graph Analysis and Modularity of Brain Functional Connectivity Networks: Searching for the Optimal Threshold

Cécile Bordier\*, Carlo Nicolini and Angelo Bifone \*

Center for Neuroscience and Cognitive Systems, Istituto Italiano di Tecnologia, Rovereto, Italy

Neuroimaging data can be represented as networks of nodes and edges that capture the topological organization of the brain connectivity. Graph theory provides a general and powerful framework to study these networks and their structure at various scales. By way of example, community detection methods have been widely applied to investigate the modular structure of many natural networks, including brain functional connectivity networks. Sparsification procedures are often applied to remove the weakest edges, which are the most affected by experimental noise, and to reduce the density of the graph, thus making it theoretically and computationally more tractable. However, weak links may also contain significant structural information, and procedures to identify the optimal tradeoff are the subject of active research. Here, we explore the use of percolation analysis, a method grounded in statistical physics, to identify the optimal sparsification threshold for community detection in brain connectivity networks. By using synthetic networks endowed with a ground-truth modular structure and realistic topological features typical of human brain functional connectivity networks, we show that percolation analysis can be applied to identify the optimal sparsification threshold that maximizes information on the networks' community structure. We validate this approach using three different community detection methods widely applied to the analysis of brain connectivity networks: Newman's modularity, InfoMap and Asymptotical Surprise. Importantly, we test the effects of noise and data variability, which are critical factors to determine the optimal threshold. This data-driven method should prove particularly useful in the analysis of the community structure of brain networks in populations characterized by different connectivity strengths, such as patients and controls.

## OPEN ACCESS

### Edited by:

Federico Giove,  
Centro Fermi, Italy

### Reviewed by:

Veena A. Nair,

University of Wisconsin-Madison,  
United States  
Andrea Soddu,  
University of Western Ontario, Canada

### \*Correspondence:

Cécile Bordier  
cecile.bordier@iit.it  
Angelo Bifone  
angelo.bifone@iit.it

### Specialty section:

This article was submitted to  
Brain Imaging Methods,  
a section of the journal  
Frontiers in Neuroscience

Received: 09 March 2017

Accepted: 19 July 2017

Published: 03 August 2017

### Citation:

Bordier C, Nicolini C and Bifone A (2017) Graph Analysis and Modularity of Brain Functional Connectivity Networks: Searching for the Optimal Threshold. *Front. Neurosci.* 11:441.  
doi: 10.3389/fnins.2017.00441

## INTRODUCTION

In recent years, considerable efforts have been made to study the complex structure of brain connectivity, marking the inception of the “connectomic era” in brain neuroscience. Functional Magnetic Resonance Imaging (fMRI) and other neuroimaging methods have shown that spontaneous fluctuation in brain activity, as measured with a subject lying in the scanner without being engaged in any specific task, are organized in coherent patterns, thus suggesting that resting state functional connectivity reflects the functional architecture of the brain (Damoiseaux et al., 2006).

Several methods have been developed and applied to study these patterns of synchronization, including multivariate approaches (e.g., Principal Component or Independent Component Analysis) (Beckmann et al., 2005; Damoiseaux et al., 2006) and graph theoretical methods (Bullmore and Sporns, 2009).

Graph theory provides a general and powerful framework to investigate the topological organization of the brain connectivity. A number of graph theoretical studies have revealed a small-world, rich-club structure (van den Heuvel and Sporns, 2011) of functional connectivity networks, and the presence of hub regions defined by high connectivity and network centrality. Moreover, community detection methods have been widely applied to investigate the modular structure of many natural networks, including brain functional connectivity networks. The presence modules, i.e., clusters of nodes that are more densely connected among them than with the rest of the network, reflects functional segregation within the integrated network, and is thought to confer robustness and adaptability to brain connectivity networks (Bullmore and Sporns, 2009).

For these analyses, the brain is represented as a network of nodes interconnected by links. Commonly, the nodes correspond to anatomically defined brain areas and links to a measure of inter-regional interaction or similarity between the nodes. For resting state functional connectivity networks, edge weights are typically computed as temporal correlations in the fluctuations of the BOLD signals in different areas, resulting in a correlation adjacency matrix (Eguiluz et al., 2005).

Sparsification procedures are normally applied to remove weaker links, which are most affected by experimental noise (van den Heuvel and Fornito, 2014), and to reduce the density of the graph, thus making it computationally more tractable. In the literature, it is common practice to fix the density of the adjacency matrix *a priori*, and to identify the threshold that preserves the target density of edges (Bassett et al., 2008; Lynall et al., 2010). Stability analyses exploring a range of densities are often performed to assess how critically topological parameters derived from the sparsified adjacency matrix depend on the choice of threshold. Sparsification schemes based on the computation of graph Minimum Spanning Trees prior to thresholding have also been proposed to prevent disruption of local connectivity by global removal of weak links (Alexander-Bloch et al., 2010).

Here, we address the problem of computing the optimal threshold for community detection in brain connectivity networks. Specifically, we propose the use of percolation analysis, a method rooted in statistical physics, to identify a sparsification threshold that maximizes information on the network modular structure. This data driven procedure, first introduced by Gallos et al. (2012), iteratively removes the weakest edges and computes the largest connected component. The percolation threshold corresponds to the point where the largest component starts breaking apart. We entertain the hypothesis that the percolation threshold strikes the optimal balance between information gained by cutting off noise, and lost by removing potentially genuine weak connections. To test this hypothesis, we apply three different community detection methods (Newman's modularity Newman, 2006), InfoMap Rosvall and Bergstrom,

2008; Kawamoto and Rosvall, 2015, and Asymptotical Surprise Nicolini and Bifone, 2016; Nicolini et al., 2017) to synthetic networks endowed with a ground truth modular structure, and with topological features, levels of noise and variability similar to those observed in functional connectivity experimental data. We compare the retrieved and planted modular structures by using Normalized Mutual Information, an information theoretic measure of similarity, as a function of sparsification threshold. We find that this information can be maximized by an appropriate choice of threshold, and we assess the use of percolation analysis as a data-driven method for optimal sparsification. Finally, we discuss the application of this approach to compare networks characterized by different noise levels and connectivity strengths, such as those observed in cross-sectional studies assessing brain connectivity in different populations, e.g., patients and healthy controls.

## MATERIALS AND METHODS

Synthetic networks are a useful tool to test the effect of threshold on community detections, and the ability to retrieve a pre-determined ground-truth modular structure. We ran two types of simulations: simulation of Lancichinetti-Fortunato-Radicchi (LFR) networks (Lancichinetti et al., 2008) and simulation of complex LFR including intersubject variability and different level of noise. The latter made it possible to assess the influence of noise or data variability, thus mimicking realistic experimental dataset.

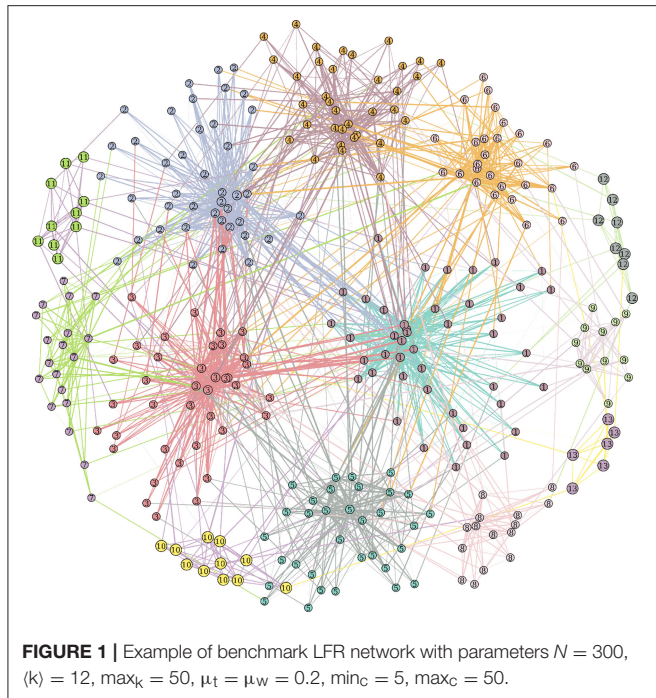
The main goal of these simulations is the validation of a method that can be used in the analysis of functional connectivity networks as measured by resting state fMRI. As shown in Nicolini and Bifone (2016), brain functional connectivity networks are composed of modules with heterogeneous size distributions. This structure can be mimicked using the LFR approach, which can generate synthetic networks with power law degree distributions and community sizes akin to those observed in natural networks, such as functional connectivity networks (Lancichinetti et al., 2008).

### Simulation 1

The Lancichinetti-Fortunato-Radicchi (LFR) benchmark algorithm generates networks with *a priori* known communities and node degree distributions. Community size and node degree follow power law distributions (for example see **Figure 1**).

The mixing of the communities is controlled by the topological mixing parameter  $\mu_t$ . Each node shares a fraction  $1-\mu_t$  of edges with nodes in its same community and a fraction  $\mu_t$  with nodes in other communities:  $0 \leq \mu_t \leq 1$ . Similarly, a weight mixing coefficient  $\mu_w$  controls, on average for each node, the balance between the incident edge weights coming from internal and external communities.

The LFR synthetic networks were built for  $N = 600$  nodes, sampling nodes degree from a power-law with exponent  $\tau_d = 2$ , average degree  $\langle k \rangle = 12$  and maximum degree  $\max_k = 50$ . We set the topological and weight mixing coefficient, i.e., the average fraction of intra-cluster and intercluster degree and strengths, to  $\mu_t = \mu_w = 0.2$ . Planted community sizes ranged from 5 to



50 nodes and were sampled from a power law with exponent  $\tau_c = 1$ . This simulation was run 9 times for each value of  $\mu_t = \mu_w$ . The Matlab code to generate LFR synthetic network is available at [github.com/carlonicolini/lfrwmx](https://github.com/carlonicolini/lfrwmx). The function takes the parameters described above as inputs, and returns the equivalent to a weighted connectivity matrix that can be directly analyzed by community detection approaches.

## Simulation 2

This simulation makes use of the output matrix from the LFR function described above to generate artificial resting state fMRI datasets. The general idea is that, starting from an adjacency matrix with a given modular structure, we can generate time-courses for each of the nodes whose pairwise correlations reproduce the edge structure of the original matrix. Schematic of this procedure is shown in **Figure 2**.

To this end, we first calculate the closest positive-definite matrix  $C \in \mathbb{R}^{n \times n}$  from the adjacency matrix of the original LFR network (Higham, 1988). We then exploit the properties of the Cholesky decomposition and the techniques described in Nicolini et al. (2017) to calculate time-courses for the individual nodes. This approach makes it possible to generate correlated random variables, i.e., following the weights of our original connectivity matrix, by decomposing the closest positive definite matrix  $C \in \mathbb{R}^{n \times n}$  into the product of a lower triangular matrix  $L \in \mathbb{R}^{n \times n}$  and its transpose such that  $C = LL^T$ . By multiplication of  $L$  with random standardized time series  $X \in \mathbb{R}^{n \times m}$  (our synthetic BOLD signals), we obtain new time series  $Y = LX$  whose covariance matrix is exactly  $C$  as one can verify that  $C = E(YY^T) = E[(LX)(LX)^T] = E[(LX)X^T L^T] = L E[XX^T]L^T = L^T L = C$ . The random time series were generated with 150

points and a base-line value set to 100. Both the random resting state time series  $X$  and the added noise were generated using the R package NeuRosim (Welvaert et al., 2011).

The generation of multiple sample of random time series simulates the effects of intersubject variability, and Rician-noise (Welvaert and Rosseel, 2013) is added to mimic fMRI resting state data. The definition of Signal-to-Noise (SNR) used in the rest of this paper is:  $\text{SNR} = \bar{S}/\sigma_N$  where  $\bar{S}$  is the average magnitude of the signal generated by NeuroSim and  $\sigma_N$  is the standard deviation of the noise (Krüger and Glover, 2001). An example of synthetic time-course is shown in the Supplementary Information section, Figure S1.

The last step results in 600 times series of 150 points with different levels of noise for each of the simulated subjects. Datasets were generated for populations of 20, 40, and 60 subjects and for a SNR equal to 35 and 70. The procedure has been run 5 times for each different parameter to produce different networks and datasets.

## Connectivity Matrix

The connectivity matrix is the weighted matrix representing the links between two nodes. In Simulation 1, the matrix was generated directly by the LFR model. In Simulation 2, using the same approach as in fMRI experiment, we computed pairwise Pearson correlations between time-series from pairs of nodes in each dataset (subject), resulting in a matrix  $M$  of size  $N \times N$  with  $N$  the number of nodes and with  $M(i,j)$  the correlation coefficient between the time series of the node  $i$  and the node  $j$ . Average group matrices were calculated by Fisher transformation and subsequent averaging of individual matrices.

## Sparsification and Percolation Threshold

Sparsification procedures are normally applied to remove weaker links, which are most affected by experimental noise (van den Heuvel and Fornito, 2014), and to reduce the density of the graph, thus making it computationally more tractable.

The method of our choice for the sparsification was motivated by a model to describe phase transitions of connected subgraphs in random networks called percolation analysis (Callaway et al., 2000; Goerdt, 2001). We applied thresholds on the original network at different levels of edge weights, and identified the largest connected components of the thresholded graphs via breadth-first search (Leiserson et al., 2009). The critical point where the largest component starts breaking apart is identified as the percolation threshold at which the network's structure is preserved while discarding potential effects of noise. **Figure 3** represents an example of the size of the largest component with respect to the threshold in a benchmark LFR network.

## Community Detection

To assess whether the efficacy of the sparsification procedure depends on the community detection approach, we applied three different methods, based on conceptually different principles that have been extensively applied to the analysis of resting state fMRI data. The first one, probably the most widely used, is Newman's modularity (Newman, 2006). We also tested InfoMap (Rosvall and Bergstrom, 2008) and Asymptotical Surprise (Nicolini and

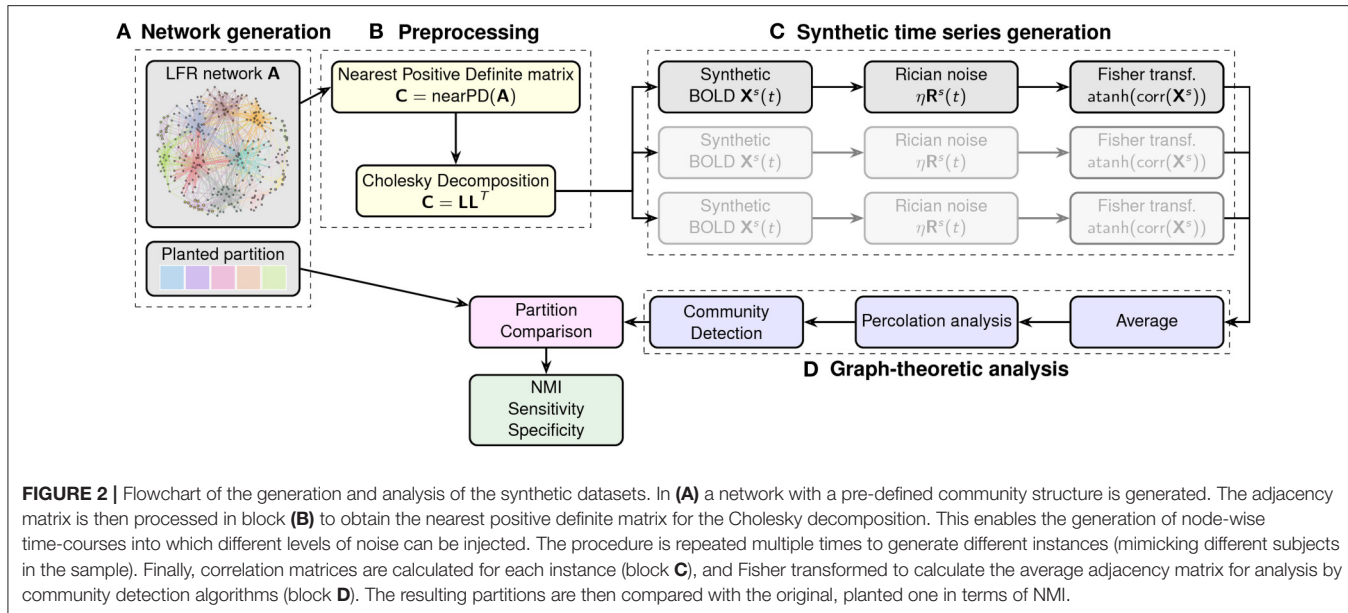


**FIGURE 2 |** Flowchart of the generation and analysis of the synthetic datasets. In **(A)** a network with a pre-defined community structure is generated. The adjacency matrix is then processed in block **(B)** to obtain the nearest positive definite matrix for the Cholesky decomposition. This enables the generation of node-wise time-courses into which different levels of noise can be injected. The procedure is repeated multiple times to generate different instances (mimicking different subjects in the sample). Finally, correlation matrices are calculated for each instance (block **C**), and Fisher transformed to calculate the average adjacency matrix for analysis by community detection algorithms (block **D**). The resulting partitions are then compared with the original, planted one in terms of NMI.

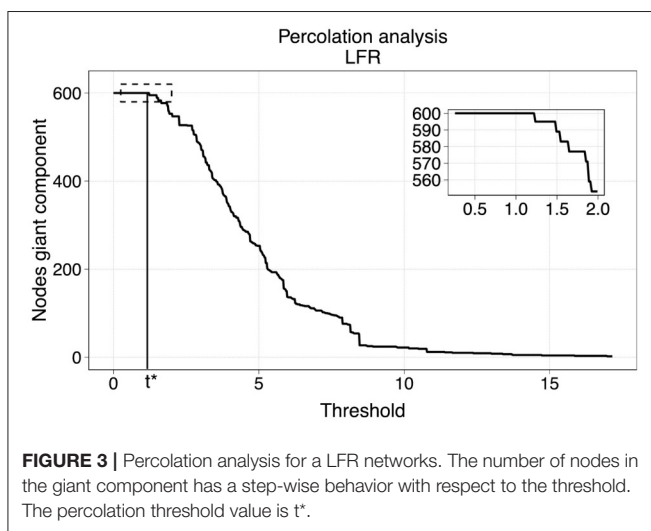


**FIGURE 3 |** Percolation analysis for a LFR networks. The number of nodes in the giant component has a step-wise behavior with respect to the threshold. The percolation threshold value is  $t^*$ .

Bifone, 2016; Nicolini et al., 2017), as they have been shown to resolve community structures at a finer level than Newman's modularity, which is affected by a resolution limit that prevents detection of modules that are smaller than a scale determined by the size of the entire network.

Briefly, Newman's modularity seeks optimal partition by maximizing intra-cluster edge-density against that of a null model based on random edge rewiring. Optimization of this fitness function is typically performed using the Louvain method (Blondel et al., 2008), a greedy agglomerative clustering algorithm that works on hierarchical refinements of the network's partitions. Here we used the Louvain implementation available in the Brain Connectivity toolbox (Rubinov and Sporns, 2010).

The idea behind Infomap is the minimization, through a set of heuristics, of the description length (Rissanen, 1978) of

a random walker defined on the network. For this study we used the Infomap implementation available in the igraph-0.7.1 package (Csárdi and Nepusz, 2006).

Finally, Asymptotical Surprise is a recently developed approach rooted in information theory that aims at maximizing the relative entropy between the observed intracluster density and the expected intracluster density, on the basis of the Erdos-Renyi null model (Traag et al., 2015). Surprise was recently shown to be quasi-resolution-limit free, and to provide improved means to resolve the modular structure of complex networks of brain functional connectivity (Nicolini and Bifone, 2016; Nicolini et al., 2017). Optimization of Asymptotical Surprise was carried out by means of PACO (PArtitioning Cost Optimization), an iterative agglomerative algorithm built on a variation of the Kruskal algorithm for minimum spanning trees (Nicolini and Bifone, 2016; Nicolini et al., 2017). We have shown that maximization of Asymptotical Surprise enables detection of communities of widely different sizes, thus making it possible to resolve differences in the modular organization of different networks representing functional connectivity in different subjects or experimental groups (Nicolini and Bifone, 2016). A Matlab toolbox including binary and weighted versions of Surprise optimization is available upon request at <http://forms.iit.it/view.php?id=68447>. An example of adjacency matrix for an LFR network with the node indexes reordered by membership and the modular partition demarcated by a red line is shown in the Supplementary Information section, Figure S2.

## Evaluation of Retrieved Partition

The advantage to know in advance the ground truth community is that we can quantify differences between the planted community and the extracted ones. Three coefficients were used to evaluate the results of the community detection methods at different levels of threshold of our synthetic networks. First,

the Normalized Mutual Information (NMI) (Danon et al., 2005; Meilă, 2007), a measure of the similarity between structures is defined as:

$$NMI(A, B) = \frac{-2 \sum_{i=1}^{C_A} \sum_{j=1}^{C_B} N_{ij} \log \left( \frac{N_{ij}N}{N_i N_j} \right)}{\sum_{i=1}^{C_A} N_i \log \left( \frac{N_i}{N} \right) + \sum_{j=1}^{C_B} N_j \log \left( \frac{N_j}{N} \right)} \quad (1)$$

where  $A$  and  $B$  are the community structures of two networks,  $C_A$  and  $C_B$  are the number of community in partition  $A$  and  $B$  respectively,  $N$  the total number of nodes in the networks (which is the same in  $A$  and  $B$ ) and  $N_{ij}$  is the overlap between  $A$ 's community  $i$  and  $B$ 's community  $j$ ; i.e., the number of common nodes. Finally,  $N_i$  and  $N_j$  are the total number of nodes in community  $i$  of  $A$  and  $j$  of  $B$  respectively. The NMI ranges from 0 to 1, where 0 indicates that the retrieved community structure does not convey information about the planted partition, and 1 when the two partitions correspond perfectly. Indeed,  $NMI = 0$  corresponds to the situation of  $N_{ij}=0$ , i.e., to a void intersection group between  $A$ 's and  $B$ 's communities, and  $NMI = 1$  to complete identity.

In order to gain information about the origin of mismatches between planted and retrieved partitions, we also computed Sensitivity and Specificity, assessing the levels of false positives and false negatives incurred by the community detection algorithms. For each community we identified the biggest overlap between the ground truth and the retrieved modules to establish a correspondence between the partitions. Subsequently, we identified the nodes that were correctly assigned (true positives = TP) and wrongly assigned (false positives = FP) to a selected community. We also identified nodes that were correctly assigned (true negatives = TN) or erroneously assigned (false negative = FN) to a different community. These values were used to calculate Sensitivity and Specificity for each community:

$$Sensitivity = \frac{TP}{TP + FN} \quad (2)$$

$$Specificity = \frac{TN}{TN + FP} \quad (3)$$

and subsequently averaged over the partition. The values for Sensitivity and Specificity range from 0 to 1, with 1 denoting the perfect match.

## Benchmark Resting State Functional Connectivity Network

To illustrate the effects of threshold choice on the partition of resting state fMRI functional connectivity networks, we used a benchmark dataset described by Crossley et al. (2013). Detailed experimental and image processing procedures are described in the original paper, alongside with the ethical statements. In short, fMRI data were acquired from 27 healthy volunteers at 3 T. Gradient echo-planar imaging data were acquired for 5 min (TR = 2 s, TE = 13). Time series were extracted from 638 brain regions defined by a template also described in Crossley et al. (2013), and band-passed (0.01–0.1 Hz). Functional connectivity was defined as pairwise Pearson correlation at a subject's level, and group-level functional connectivity matrix was calculated by averaging individuals' matrices after Fisher- transform. We used BrainNetViewer as a tool for the visualization of the communities on brain templates.

## RESULTS

### Simulation 1

The benchmark created for this first test did not involve any variation coming from noise or subject variability. The community detections methods were applied directly to the matrix generated by the LFR function. **Figure 4** shows the NMI calculated between the structure extracted by Newman modularity, InfoMap and Asymptotical Surprise, and the ground truth for  $\mu_t = \mu_w = 0.2$ , as a function of threshold.

The gray zone on the graphics indicates the range of sparsification thresholds obtained by percolation analysis calculated in different runs. These graphics demonstrate the deleterious effects of excessive removal of weak edges. In the case of noiseless networks, percolation analysis identifies the threshold corresponding to the departure from optimal performance of the community detection algorithm. This is in keeping with the fact that the percolation threshold is the minimum threshold value that preserves connectedness of the giant component. However, it should be noticed in this noiseless scenario all links correspond to true correlations, and no spurious edges are contemplated.

### Simulation 2

In the second simulation we assessed the effects of noise and variability in the correlation structure of the networks. We

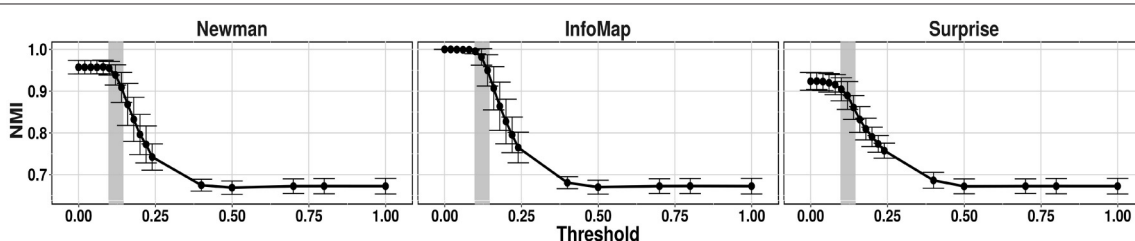


**FIGURE 4 |** NMI between ground truth community structure and the results of the 3 community detection algorithms applied to an LFR networks ( $\mu_t = \mu_w = 0.2$ ).

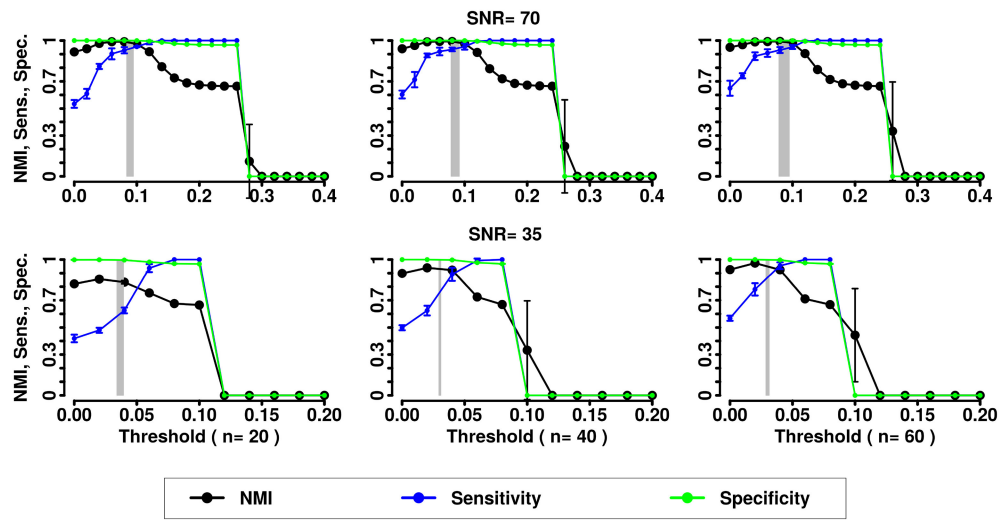


**FIGURE 5 |** NMI (in black), Sensitivity (in blue), and Specificity (in green) of the Newman community detection algorithm applied to LFR networks ( $\mu_t = \mu_w = 0.2$ ). Two different signal to noise ratio (SNR) are represented on the lines (top line SNR = 70, lower line SNR = 35), Number of subjects varies depending of the column (respectively from left to right 20, 40, and 60 subjects).

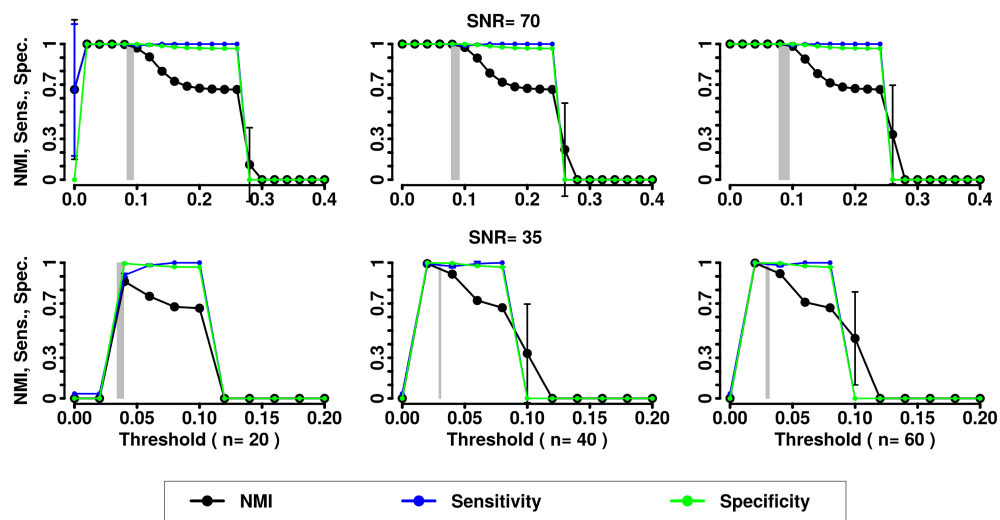


**FIGURE 6 |** NMI (in black), Sensitivity (in blue), and Specificity (in green) of the InfoMap community detection algorithm applied to LFR networks ( $\mu_t = \mu_w = 0.2$ ). Two different signal to noise ratio (SNR) are represented on the lines (top line SNR = 70, lower line SNR = 35), Number of subjects varies depending of the column (respectively from left to right 20, 40, and 60 subjects).

computed NMI, the Sensitivity and Specificity for the partitions obtained by the 3 methods (Newman, InfoMap and Asymptotical Surprise) with the different SNRs and numbers of subjects (see Figures 5–7).

In the presence of variability, we observe a first increase in NMI for increasing threshold, followed by a subsequent drop. We interpret the first rise as a regime in which weak links are mostly determined by spurious correlations, and carry little information about the structure of the network. As threshold increases, removal of additional edges decreases the ability to retrieve the planted modular structure

by removing structurally relevant correlations. This picture is confirmed by the observation that maxima in NMI correspond to simultaneously large values of Sensitivity and Specificity.

The percolation threshold values appear to consistently fall in the vicinity of maximum NMI for all three community detection methods. The general conclusion from these simulations is that percolation analysis detects a quasi-optimal value of sparsification threshold, thus enabling optimal detection of community structure in the presence of experimental noise and data variability.

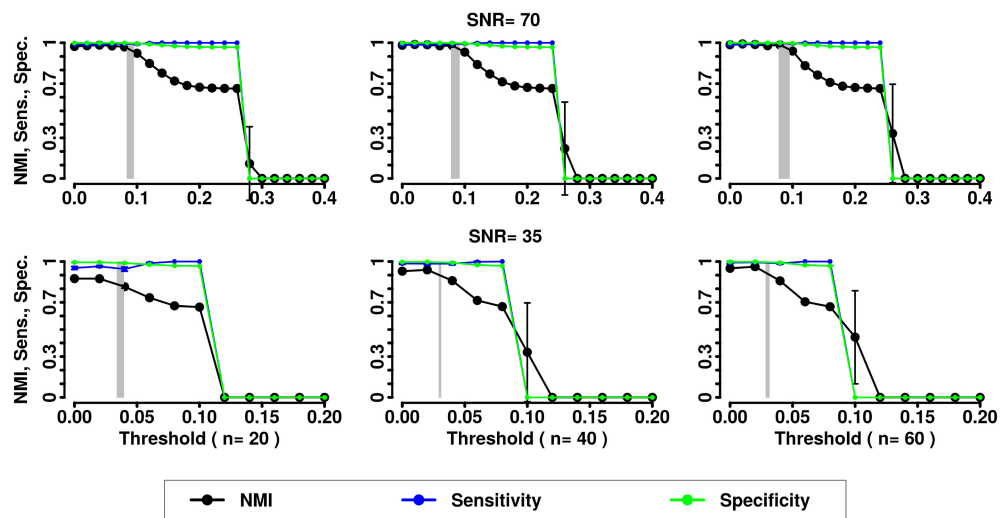


**FIGURE 7 |** NMI (in black), Sensitivity (in blue), and Specificity (in green) of the Asymptotical Surprise community detection algorithm applied to LFR networks ( $\mu_t = \mu_w = 0.2$ ). Two different signal to noise ratio (SNR) are represented on the lines (top line SNR = 70, lower line SNR = 35), Number of subjects varies depending of the column (respectively from left to right 20, 40, and 60 subjects).

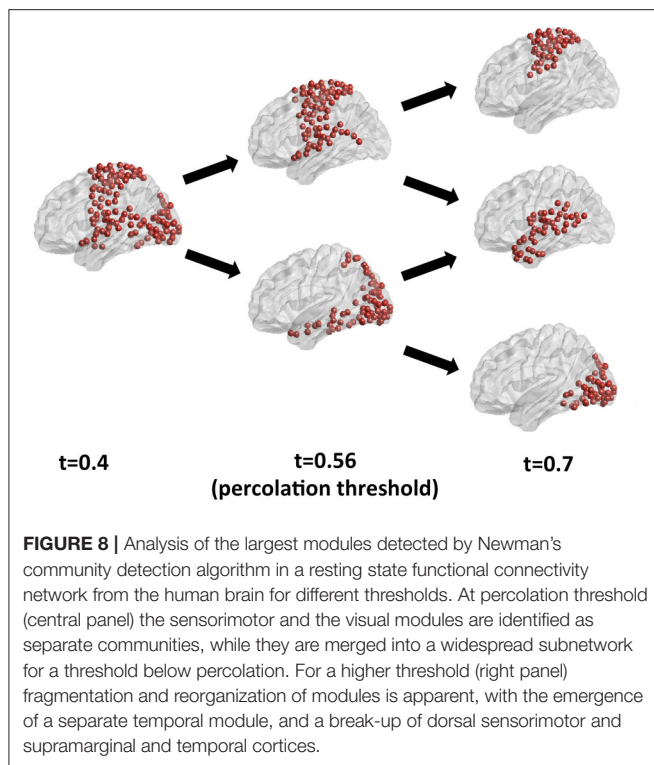
## Effects of Threshold in Resting State Brain Networks

A ground-truth community structure for functional connectivity networks from the human brain remains to be established, as different community detection approaches retrieve different partitions depending on the characteristics of the fitness function and optimization algorithm. A discussion of the ultimately valid partition for functional connectivity networks and of the best algorithm for its retrieval is beyond the scope of this paper, which focuses on the information theoretical foundations of the choice of the optimal sparsification threshold. We have recently compared various community detection methods as applied to the study of human brain functional connectivity in Nicolini et al. (2017). Here, to illustrate the effects of the choice of threshold on community detection, we have applied Newman's modularity, probably the most established community detection algorithm in network neuroscience, to a benchmark resting state functional connectivity network for different threshold values. Figure 8 shows the largest module identified by Newman's modularity at a threshold below percolation (left panel), and its partitions for increasing thresholds. Below percolation threshold, a widely distributed subnetwork comprising sensorimotor, auditory and visual cortices is detected as a single community. At percolation threshold, this broad community breaks up into a sensorimotor module, which also includes the superior temporal gyrus, and an occipital module, including visual cortices as well as the ventral and dorsal visual streams. As the threshold is further increased, the algorithm retrieves a different modular organization, with a dorsal sensorimotor module separated from the supramarginal and temporal nodes, which merge with other temporal nodes to form an independent community. Hence, the effects of the choice of threshold are not limited to fragmentation of modules for increasing

thresholds, but can also result in the mixing and merging of nodes from different communities into potentially spurious modules. This example further emphasizes the importance of a judicious choice of sparsification threshold. Our results in synthetic networks suggest that percolation analysis enables the identification of threshold that maximizes information on the network modular structure. A detailed description of the community structure of resting state functional connectivity brain networks at the percolation threshold is reported in Nicolini et al. (2017).

## DISCUSSION

An open problem in the analysis of brain connectivity is the optimal choice of threshold when comparing different groups, e.g., patients and healthy controls in cross-sectional studies assessing the effects of disease on functional connectivity. Typically, identical sets of nodes are defined for the two groups, and the comparison is based on edge distribution and strength. Many studies tend to fix the same edge density in the connectivity graphs of the groups to be compared. Indeed, certain global topological parameters (e.g., global efficiency, Rubinov and Sporns, 2010) depend on edge density, and comparisons at constant density make it possible to assess differences related to the topological reorganization of links, rather than to their number and strength. On the other hand, constant edge density may bias group comparisons when graphs exhibit intrinsic differences in connectivity strength. By way of example, neuropsychiatric diseases like Schizophrenia and Autism have been associated with disruption and overall reduction of functional and structural connectivity. Imposing equal densities for graphs describing connectivity in patients and controls may lead to the inclusion of a greater number of weak,



potentially spurious links in the group with weaker connectivity, and to the exclusion of important links in the group with stronger connectivity. A higher proportion of spurious connection results in a more random network topology, and intergroup differences may just reflect different levels of noise, rather than genuine topological differences (van den Heuvel and Fornito, 2014).

The present study may provide a strategy to overcome this problem. Indeed, community detection determines the membership of each node to a certain module. This is not dependent on overall edge density, but on the local balance between edges linking the node to other members of the same module, or to other nodes in different modules. The optimal sparsification threshold is the one that maximizes information about community structure, and is network-specific, as it depends on the structure and noisiness of each network. Hence, independent thresholding of the networks to be compared

## REFERENCES

- Alexander-Bloch, A. F., Gogtay, N., Meunier, D., Birn, R., Clasen, L., Lalonde, F., et al. (2010). Disrupted modularity and local connectivity of brain functional networks in childhood-onset schizophrenia. *Front. Syst. Neurosci.* 4:147. doi: 10.3389/fnsys.2010.00147
- Bassett, D. S., Bullmore, E., Verchinski, B. A., Mattay, V. S., Weinberger, D. R., Meyer-Lindenberg, A., et al. (2008). Hierarchical organization of human cortical networks in health and schizophrenia. *J. Neurosci.* 28, 9239–9248. doi: 10.1523/JNEUROSCI.1929-08.2008
- Beckmann, C. F., DeLuca, M., Devlin, J. T., and Smith, S. M. (2005). Investigations into resting-state connectivity using independent component analysis. *Philos. Trans. R. Soc. Lond. B Biol. Sci.* 360, 1001–1013. doi: 10.1098/rstb.2005.1634

based on percolation analysis maximizes information about memberships in the two groups.

## CONCLUSION

In conclusion, we have explored the use of percolation analysis, a method based on statistical physics, to determine the sparsification threshold in synthetic networks endowed with a ground-truth modular structure, and topological features akin to those of real world networks like brain connectivity graphs. We find that the percolation threshold, i.e., the highest threshold that preserves connectedness of the giant component, corresponds to the maximum information that can be retrieved by various community detection algorithms on the planted modular structure in the presence of noise and intersubject variability. Intuitively, this threshold corresponds to the optimal balance between information lost by removing genuine edges and spurious correlations introduced by noise. These findings provide evidence of the existence of an optimal sparsification threshold, and a solid theoretical basis for its identification by means of a data driven method like percolation analysis.

## AUTHOR CONTRIBUTIONS

AB conceived the study, CB analyzed the dataset, CB, CN, and AB wrote the paper and reviewed the analysis. All authors reviewed the manuscript.

## ACKNOWLEDGMENTS

This project has received funding from the European Union's Horizon 2020 Research and Innovation Program under grant agreement No 668863. The authors are grateful to Prof. Edward Bullmore and Prof. Nicolas Crossley for providing the weighted, unthresholded functional connectivity network derived from resting state fMRI in healthy volunteers.

## SUPPLEMENTARY MATERIAL

The Supplementary Material for this article can be found online at: <http://journal.frontiersin.org/article/10.3389/fnins.2017.00441/full#supplementary-material>

- Blondel, V. D., Guillaume, J.-L., Lambiotte, R., and Lefebvre, E. (2008). Fast unfolding of communities in large networks. *J. Stat. Mech. Theory Exp.* 10008:6. doi: 10.1088/1742-5468/2008/10/P10008
- Bullmore, E. T., and Sporns, O. (2009). Complex brain networks: graph theoretical analysis of structural and functional systems. *Nat. Rev. Neurosci.* 10, 186–198. doi: 10.1038/nrn2575
- Callaway, D. S., Newman, M. E. J., Strogatz, S. H., and Watts, D. J. (2000). Network robustness and fragility: percolation on random graphs. *Phys. Rev. Lett.* 85, 5468–5471. doi: 10.1103/PhysRevLett.85.5468
- Crossley, N. A., Mechelli, A., Vértes, P. E., Winton-Brown, T. T., Patel, A. X., Ginestet, C. E., et al. (2013). Cognitive relevance of the community structure of the human brain functional coactivation network. *Proc. Natl. Acad. Sci. U.S.A.* 110, 11583–11588. doi: 10.1073/pnas.1220826110

- Csárdi, G., and Nepusz, T. (2006). The igraph software package for complex network research. *Interf. Complex Syst.* 1695:1695.
- Damoiseaux, J. S., Romboots, S. A. R. B., Barkhof, F., Scheltens, P., Stam, C. J., Smith, S. M., et al. (2006). Consistent resting-state networks across healthy subjects. *Proc. Natl. Acad. Sci. U.S.A.* 103, 13848–13853. doi: 10.1073/pnas.0601417103
- Danon, L., Guilera, A. D., Duch, J., and Arenas, A. (2005). Comparing community structure identification. *J. Stat. Mech. Theory Exp.* 9:P09008. doi: 10.1088/1742-5468/2005/09/P09008
- Eguiluz, V. M., Chialvo, D. R., Cecchi, G. A., Baliki, M., and Apkarian, A. V. (2005). Scale-free brain functional networks. *Phys. Rev. Lett.* 94:18102. doi: 10.1103/PhysRevLett.94.018102
- Gallois, L. K., Makse, H. A., and Sigman, M. (2012). A small world of weak ties provides optimal global integration of self-similar modules in functional brain networks. *Proc. Natl. Acad. Sci. U.S.A.* 109, 2825–2830. doi: 10.1073/pnas.1106612109
- Goerdt, A. (2001). The giant component threshold for random regular graphs with edge faults. *Theor. Comput. Sci.* 259, 307–321. doi: 10.1016/S0304-3975(00)00015-3
- Higham, N. J. (1988). Computing a nearest symmetric positive semidefinite matrix. *Linear Algebra Appl.* 103, 103–118. doi: 10.1016/0024-3795(88)90223-6
- Kawamoto, T., and Rosvall, M. (2015). Estimating the resolution limit of the map equation in community detection. *Phys. Rev. E* 91:10. doi: 10.1103/PhysRevE.91.012809
- Krüger, G., and Glover, G. H. (2001). Physiological noise in oxygenation-sensitive magnetic resonance imaging. *Magn. Reson. Med.* 46, 631–637. doi: 10.1002/mrm.1240
- Lancichinetti, A., Fortunato, S., and Radicchi, F. (2008). Benchmark graphs for testing community detection algorithms. *Phys. Rev. E* 78:46110. doi: 10.1103/PhysRevE.78.046110
- Leiserson, C. C. E., Rivest, R. R. L., Stein, C., and Cormen, T. H. (2009). *Introduction to Algorithms*, 3rd Edn. Cambridge, MA: The MIT Press.
- Lynall, M. E., Bassett, D. S., Kerwin, R., McKenna, P. J., Kitzbichler, M., Muller, U., et al. (2010). Functional connectivity and brain networks in schizophrenia. *J. Neurosci.* 30, 9477–9487. doi: 10.1523/JNEUROSCI.0333-10.2010
- Meilă, M. (2007). Comparing clusterings—an information based distance. *J. Multivar. Anal.* 98, 873–895. doi: 10.1016/j.jmva.2006.11.013
- Newman, M. E. (2006). Modularity and community structure in networks. *Proc. Natl. Acad. Sci. U.S.A.* 103, 8577–8582. doi: 10.1073/pnas.0601602103
- Nicolini, C., and Bifone, A. (2016). Modular structure of brain functional networks: breaking the resolution limit by Surprise. *Sci. Rep.* 6:19250. doi: 10.1038/srep19250
- Nicolini, C., Bordier, C., and Bifone, A. (2017). Modular organization of weighted brain networks beyond the resolution limit. *Neuroimage* 146, 28–39. doi: 10.1016/j.neuroimage.2016.11.026
- Rissanen, J. (1978). Modeling by shortest data description. *Automatica* 14, 465–471. doi: 10.1016/0005-1098(78)90005-5
- Rosvall, M., and Bergstrom, C. T. (2008). Maps of random walks on complex networks reveal community structure. *Proc. Natl. Acad. Sci. U.S.A.* 105, 1118–1123. doi: 10.1073/pnas.0706851105
- Rubinov, M., and Sporns, O. (2010). Complex network measures of brain connectivity: uses and interpretations. *Neuroimage* 52, 1059–1069. doi: 10.1016/j.neuroimage.2009.10.003
- Traag, V. A., Aldecoa, R., and Delvenne, J. C. (2015). Detecting communities using asymptotic surprise. *Phys. Rev. E Stat. Nonlinear Soft. Matter Phys.* 92:002816. doi: 10.1103/PhysRevE.92.022816
- van den Heuvel, M., and Fornito, A. (2014). Brain networks in schizophrenia. *Neuropsychol. Rev.* 24, 32–48. doi: 10.1007/s11065-014-9248-7
- van den Heuvel, M. P., and Sporns, O. (2011). Rich-club organization of the human connectome. *J. Neurosci.* 31, 15775–15786. doi: 10.1523/JNEUROSCI.3539-11.2011
- Welvaert, M., Durnez, J., Moerkerke, B., Verdoollaeghe, G., and Rosseel, Y. (2011). neuRosim: an R package for generating fMRI data. *J. Stat. Softw.* 44, 1–18. doi: 10.18637/jss.v044.i10
- Welvaert, M., and Rosseel, Y. (2013). On the definition of signal-to-noise ratio and contrast-to-noise ratio for fmri data. *PLoS ONE* 8:e77089. doi: 10.1371/journal.pone.0077089

**Conflict of Interest Statement:** The authors declare that the research was conducted in the absence of any commercial or financial relationships that could be construed as a potential conflict of interest.

Copyright © 2017 Bordier, Nicolini and Bifone. This is an open-access article distributed under the terms of the Creative Commons Attribution License (CC BY). The use, distribution or reproduction in other forums is permitted, provided the original author(s) or licensor are credited and that the original publication in this journal is cited, in accordance with accepted academic practice. No use, distribution or reproduction is permitted which does not comply with these terms.



# How Energy Metabolism Supports Cerebral Function: Insights from $^{13}\text{C}$ Magnetic Resonance Studies *In vivo*

Sarah Sonnay<sup>1</sup>, Rolf Gruetter<sup>1,2,3</sup> and João M. N. Duarte<sup>1\*</sup>

<sup>1</sup> Laboratory for Functional and Metabolic Imaging, École Polytechnique Fédérale de Lausanne, Lausanne, Switzerland,

<sup>2</sup> Department of Radiology, University of Lausanne, Lausanne, Switzerland, <sup>3</sup> Department of Radiology, University of Geneva, Geneva, Switzerland

## OPEN ACCESS

### Edited by:

Federico Giove,  
Centro Fermi, Italy

### Reviewed by:

Mauro DiNuzzo,  
University of Copenhagen, Denmark  
Anant Bahadur Patel,  
Centre for Cellular and Molecular  
Biology (CSIR), India

### \*Correspondence:

João M. N. Duarte  
joao.duarte@epfl.ch

### Specialty section:

This article was submitted to  
Brain Imaging Methods,  
a section of the journal  
*Frontiers in Neuroscience*

Received: 02 February 2017

Accepted: 04 May 2017

Published: 26 May 2017

### Citation:

Sonnay S, Gruetter R and Duarte JMN  
(2017) How Energy Metabolism  
Supports Cerebral Function: Insights  
from  $^{13}\text{C}$  Magnetic Resonance  
Studies *In vivo*.  
*Front. Neurosci.* 11:288.  
doi: 10.3389/fnins.2017.00288

Cerebral function is associated with exceptionally high metabolic activity, and requires continuous supply of oxygen and nutrients from the blood stream. Since the mid-twentieth century the idea that brain energy metabolism is coupled to neuronal activity has emerged, and a number of studies supported this hypothesis. Moreover, brain energy metabolism was demonstrated to be compartmentalized in neurons and astrocytes, and astrocytic glycolysis was proposed to serve the energetic demands of glutamatergic activity. Shedding light on the role of astrocytes in brain metabolism, the earlier picture of astrocytes being restricted to a scaffold-associated function in the brain is now out of date. With the development and optimization of non-invasive techniques, such as nuclear magnetic resonance spectroscopy (MRS), several groups have worked on assessing cerebral metabolism *in vivo*. In this context,  $^1\text{H}$  MRS has allowed the measurements of energy metabolism-related compounds, whose concentrations can vary under different brain activation states.  $^1\text{H}$ -[ $^{13}\text{C}$ ] MRS, i.e., indirect detection of signals from  $^{13}\text{C}$ -coupled  $^1\text{H}$ , together with infusion of  $^{13}\text{C}$ -enriched glucose has provided insights into the coupling between neurotransmission and glucose oxidation. Although these techniques tackle the coupling between neuronal activity and metabolism, they lack chemical specificity and fail in providing information on neuronal and glial metabolic pathways underlying those processes. Currently, the improvement of detection modalities (i.e., direct detection of  $^{13}\text{C}$  isotopomers), the progress in building adequate mathematical models along with the increase in magnetic field strength now available render possible detailed compartmentalized metabolic flux characterization. In particular, direct  $^{13}\text{C}$  MRS offers more detailed dataset acquisitions and provides information on metabolic interactions between neurons and astrocytes, and their role in supporting neurotransmission. Here, we review state-of-the-art MR methods to study brain function and metabolism *in vivo*, and their contribution to the current understanding of how astrocytic energy metabolism supports glutamatergic activity and cerebral function. In this context, recent data suggests that astrocytic metabolism has been underestimated. Namely, the rate of oxidative metabolism in astrocytes is about half of that in neurons, and it can increase as much as the rate of neuronal metabolism in response to sensory stimulation.

**Keywords:** brain energy metabolism, neurotransmitter metabolism, neuron-glia interaction, neuronal activity, MRS, fMRI, mathematical modeling

## INTRODUCTION

Cerebral function requires the cooperative interaction between different cell types, namely neurons, astrocytes, microglia and oligodendrocytes, and depends on high metabolic activity supported by continuous supply of oxygen and glucose from the blood (Siesjö, 1978). Blood flow is indeed directly related to the cerebral metabolic rate of glucose consumption ( $\text{CMR}_{\text{glc}}$ ) (Sokoloff, 1978). Although the adult human brain represents only 2% of the total body weight, it consumes up to 20% of the total glucose metabolism under normal resting physiological conditions (e.g., Rolfe and Brown, 1997). Since the mid-twentieth century the idea that brain energy metabolism is coupled to neuronal activity has emerged (McIlwain et al., 1951; Van den Berg et al., 1969), and a number of studies supported this hypothesis (Pellerin and Magistretti, 1994; Poitry-Yamate et al., 1995; Tsacopoulos et al., 1997). Notably, in the 90's, brain energy metabolism was demonstrated to be compartmentalized between neurons and astrocytes, and astrocytic glycolysis was proposed to serve the energetic demands of glutamatergic activity (Pellerin and Magistretti, 1994; Poitry-Yamate et al., 1995; Tsacopoulos et al., 1997).

Ogawa et al. reported in 1992 the changes in the apparent transverse relaxation time  $T_2^*$  due to variations in local blood oxygen consumption ( $\text{CMR}_{\text{O}_2}$ ), cerebral blood flow (CBF) and cerebral blood volume (CBV; Ogawa et al., 1992). This discovery formed the basis of a powerful technique used nowadays to study brain activity: blood oxygenation level-dependent (BOLD) functional magnetic resonance imaging (fMRI). Under the assumption of brain metabolism being segregated into two main

compartments, neurons and astrocytes (which is valid for cortical gray matter), and based on measurements of the glutamate-glutamine cycle and glucose oxidation rates, a quantitative interpretation of functional imaging by integrating oxidative neuroenergetics of neuronal processes was thereafter suggested (Shulman and Rothman, 1998). In this context, the main metabolic costs underlying neuronal activity involved not only the maintenance of the glutamate-glutamine cycle, but also the generation and propagation of action potentials, uptake and recycling of neurotransmitters from the synaptic cleft, and restoration and maintenance of resting membrane potential (reviewed in Attwell and Laughlin, 2001). However, besides the proposed coupling between neurotransmission and neuronal oxidative metabolism, data acquired during the past decades in other experimental conditions and models suggested substantial astrocytic contribution to metabolism (Gruetter et al., 2001 and reviewed in Lanz et al., 2013) and blood flow regulation (reviewed in Attwell et al., 2010). A recent analysis on  $K^+$ -dependent stimulation of astrocytic metabolism suggests that the actual glial contribution to total energy metabolism has been long underestimated (DiNuzzo et al., 2017).

This article reviews the biochemical mechanisms associated with energy metabolism in brain cells, and provides a critical review of the traditional view of astrocytes being glycolytic and neurons oxidative, which has been challenged over the past years by evidence pointing to important rates of oxidative respiration in astrocytes, namely during increased brain activity.  $^{13}\text{C}$  MRS along with infusion of  $^{13}\text{C}$ -labeled substrates and the use of compartment models as tools to probe glial and neuronal metabolism will then be described. Data recently acquired in our laboratory (Sonny et al., 2016, 2017) assessing the matter of glial and neuronal oxidative metabolism coupled to neuronal activity is then presented and potential usage of the mitochondrial ATP production in astrocytes is further discussed.

## BRAIN GLUCOSE UPTAKE AND METABOLISM

The brain can consume several substrates, such as lactate (Bouzier et al., 2000; Wyss et al., 2011), acetate (Cerdan et al., 1990), fatty acids (Kuge et al., 1995) and ketone bodies (Künnecke et al., 1993), but energy metabolism in the adult brain primarily relies on glucose provided from the blood to fuel activity both in the resting and activated states (reviewed in Sokoloff, 2004).

Uptake of monocarboxylates, such as lactate, pyruvate, and ketone bodies, is mediated by monocarboxylate transporters (MCT) along with the co-transport of one  $^1\text{H}$  for each molecule. The isoform MCT1 is expressed in the endothelial cells and in astrocytes (reviewed in Pierre and Pellerin, 2005), MCT4 in astrocytes and MCT2 in neurons (Bergersen et al., 2002; and reviewed in Barros and Deitmer, 2010).

In mammalian brain cells, glucose transport and utilization is predominantly mediated by facilitated diffusion through glucose transporters GLUT1 and GLUT3 that belong to the Solute Carrier Family 2 (SLC2). GLUT1 is present in all brain cells, with high density in astrocytes and endothelial cells of the

**Abbreviations:** 20-HETE, 20-hydroxyeicosatetraenoic acid; AA, arachidonic acid; ADP, adenosine 5'-diphosphate; AMPA,  $\alpha$ -amino-3-hydroxyl-5-methyl-4-isoxazole-propionate; ANLS, astrocyte-neuron lactate shuttle; AST, aspartate transaminase; ATP, adenosine 5'-triphosphate; BBB, blood-brain barrier; BOLD, blood oxygenation level-dependent; cAMP, cyclic adenosine monophosphate; CBF, cerebral blood flow; CBV, cerebral blood volume;  $\text{CMR}_{\text{glc}}$ , cerebral metabolic rate of glucose;  $\text{CMR}_{\text{O}_2}$ , cerebral metabolic rate of oxygen; COX, cyclooxygenase; DNP, dynamic nuclear polarization; EAAT, excitatory amino acid transporters; EET, epoxieicosatrienoic acid;  $\text{FADH}_2$ , flavin adenine dinucleotide (reduced form); FE, fractional enrichment; fMRI, functional magnetic resonance imaging; fMRS, functional magnetic resonance spectroscopy; FRET, fluorescence resonance energy transfer; GDH, glutamate dehydrogenase; GDP, guanosine diphosphate; GLS, glutaminase; GLUT, glucose carrier; GS, glutamine synthetase; GTP, guanosine triphosphate; IP<sub>3</sub>, inositol 1,4,5-triphosphate; K<sub>t</sub>, apparent Michaelis constant of glucose transport; MCT, monocarboxylate transporters; ME, malic enzyme; mGluR, metabotropic glutamate receptor; MR, magnetic resonance; MRP, multidrug resistance proteins; MRS, magnetic resonance spectroscopy; NADH, nicotinamide adenine dinucleotide (reduced form); NMDA, N-methyl-D-aspartate; NO, nitric oxide; NOS, nitric oxide synthase; Nrf2, nuclear factor-erythroid 2-related factor-2; OAA, oxaloacetate; OG, 2-oxoglutarate; P2Y, purinergic receptors; PC, pyruvate carboxylase; PDH, pyruvate dehydrogenase complex; PEPCK, phosphoenolpyruvate carboxykinase; PET, positron emission tomography; PFK, phosphofructokinase-1; PFKFB3, fructose-2,6-bisphosphatase-3; PGE<sub>2</sub>, prostaglandins E<sub>2</sub>; PK, pyruvate kinase; PLA<sub>2</sub>, phospholipase A<sub>2</sub>; PLC, phospholipase C; SA, system A transporter; sGC, soluble guanylate cyclase; SLC2, solute carrier family 2; SN, system N transporter; SNARE, soluble *N*-ethylmaleimide-sensitive factor activating protein receptor; CA, tricarboxylic acid cycle; T<sub>max</sub>: apparent maximum transport rate of glucose transport; VGLUT, vesicular glutamate transporter; VSOAC, volume-sensitive organic osmolyte-anion channel.

capillaries, but less in neurons (reviewed in Maher et al., 1994). In contrast, GLUT3 expression is almost restricted to neurons (Maher et al., 1992, 1996). GLUT1 is thus the main carrier involved in the import of glucose into the brain from the blood, and its apparent affinity for glucose transport is lower than that of GLUT3 (discussed in Simpson et al., 2007). These two facilitative carriers mediate energy-independent transport of glucose bidirectionally along a concentration gradient, which is maintained by continuous phosphorylation of intracellular glucose by the glycolytic enzyme hexokinase, and exist in sufficient density to ensure that glucose transport is not rate-limiting for CMR<sub>glc</sub> (Gruetter et al., 1998b; Barros et al., 2007; Duarte et al., 2009). GLUT4 in neurons (Ashrafi et al., 2017) and GLUT2 in both neurons and astrocytes (Thorens, 2015) have also been shown to transport glucose. However, GLUT2 and GLUT4 are carriers involved in specific functions in certain brain areas, and are likely to have a minor role on glucose uptake for cellular fueling.

After entering the cells, glucose is converted via glycolysis to two molecules of pyruvate with net formation of 2 ATP and 2 NADH in the cytosol. Pyruvate can then be reduced to lactate mediating NAD<sup>+</sup> formation, transaminated to alanine or enter mitochondria via the mitochondrial pyruvate carrier, where it is decarboxylated to acetyl-CoA by the pyruvate dehydrogenase complex (PDH) with formation of CO<sub>2</sub> and NADH (Patel and Korotchkina, 2001). Acetyl-CoA condenses with oxaloacetate entering therefore oxidative metabolism via the tricarboxylic (TCA) cycle. Each turn of the TCA cycle yields 3 NADH, 1 FADH<sub>2</sub> and 1 GTP molecules. The electron-transfer chain generates a gradient of H<sup>+</sup> across the mitochondrial membrane, which is used by the ATP synthase for ATP production. As each NADH and FADH<sub>2</sub> molecules generates 2.5 and 1.5 ATP respectively, complete oxidation of one molecule of glucose produces 30 or 32 ATP, depending on the transport of cytosolic NADH to mitochondria either in the malate-aspartate or in the glycerol 3-phosphate mitochondrial shuttles (Voet and Voet, 1995).

Oxidation of glucose-derived pyruvate through the TCA cycle not only provides the bulk of energy produced to support cerebral function (reviewed in Hertz and Dienel, 2002), but also involves the generation of *de novo* amino acids, namely glutamate (reviewed in Gruetter, 2002). Neurons extensively release glutamate and need therefore a replenishment system to ensure adequate neurotransmitter levels. Namely, synthesis of *de novo* oxaloacetate from pyruvate is catalyzed by the glial-specific enzyme pyruvate carboxylase (PC; Gamberino et al., 1997), mediating CO<sub>2</sub> fixation in an energy-dependent manner, increasing therefore the number of carbon skeletons in the TCA cycle. Oxaloacetate formed through pyruvate carboxylation condenses with acetyl-CoA to produce new glutamate molecules (Waagepetersen et al., 2001). In addition, under low acetyl-CoA concentration, pyruvate can be produced cataplerotically from TCA cycle intermediates (pyruvate recycling): from oxaloacetate, mediated by the combined action of phosphoenolpyruvate carboxykinase (PEPCK) and pyruvate kinase (PK; Cruz et al., 1998), occurring in astrocytes (Sonnewald et al., 1996) and to less extent in neurons (Cruz et al., 1998), and

from malate by the malic enzyme (ME; Bakken et al., 1997; Cruz et al., 1998; Sonnewald, 2014).

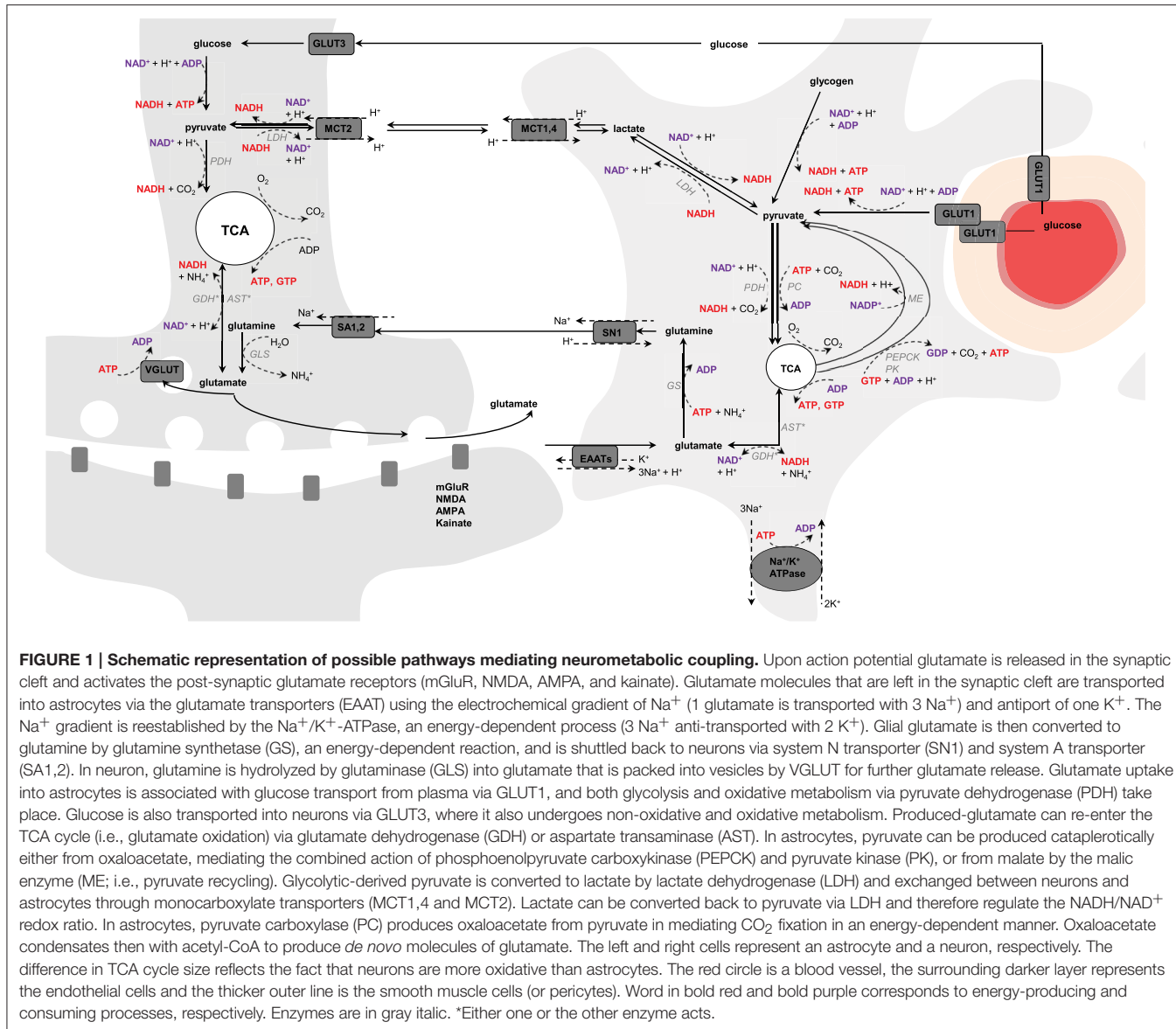
Once glutamate is taken by astrocytes, it can be converted to glutamine in an energy-dependent manner via the glial-specific enzyme, glutamine synthetase (GS; Derouiche and Frotscher, 1991). Glutamine is then transported to neurons via the System N transporter (SN1) in astrocytes (Chaudhry et al., 1999) and the System A transporters (SA1 and SA2) in neurons (Chaudhry et al., 2002), and converted to glutamate by glutaminase (GLS), completing therefore the glutamate-glutamine cycle (Shen et al., 1999; Zwingmann and Leibfritz, 2003), which is now accepted as a major mechanism for maintaining synaptic transmission. Therefore, while about 90% of the brain's glutamate resides in neurons (estimated between 5 and 16% in glia of the rodent brain; Tiwari et al., 2013; Lanz et al., 2014), most of the glutamine has been localized to astrocytes (Ottersen et al., 1992; Cruz and Cerdan, 1999). Glutamate can also re-enter the TCA cycle (Qu et al., 2001; Hertz et al., 2007; Sonnewald, 2014) notably by the reversible aspartate transaminase (AST) or the glial-abundant reversible enzyme glutamate dehydrogenase (GDH; Karaca et al., 2015), being oxidized for further energy or amino acid production. Consequently, the glutamate-glutamine cycle is not a stoichiometric process, as a number of amino acid molecules can be used in other metabolic pathways depending on cellular requirements (McKenna, 2007). Glutamine can diffuse out of the brain parenchyma and be used for ammonia detoxification (Zwingmann and Leibfritz, 2003). In addition, glutamate can have other fates than being converted to glutamine, such as formation of GABA and glutathione, and be synthesized from other substrates than glucose, namely lactate or ketone bodies. Amino acids can also be used for biosynthetic pathways and derived from protein degradation (McKenna, 2007; **Figure 1**).

## GLIAL SUPPORT TO CEREBRAL FUNCTION

### Scaffold-Associated Role of Astrocytes

The term *astrocyte* originates etymologically from the Greek words *astron* (star) and *cyte* (cell). They belong to the general group of macroglia cells (Kettenmann and Verkhratsky, 2008), where *glia* is derived from the Greek word *gliok* (glue). Astrocytes were initially described in the middle of the nineteenth century by Rudolf Virchow (Virchow, 1856), who named *nervenkitt* (*nerve-putty*) the “gelatinous” substance in the brain, and later by Camillo Golgi, who hypothesized a role of astrocytes in nutrient distribution to the brain parenchyma (Golgi, 1886).

Several cytological studies on rats (Kacem et al., 1998; Mathiisen et al., 2010) and mice (Halassa et al., 2007) have shown that astrocytes are anatomically polarized cells that associate both with neurons and the vasculature: whereas perisynaptic processes contact neurons, vascular processes (or endfeet) surround intraparenchymal blood vessels (i.e., blood-brain barrier, BBB; Kacem et al., 1998). Perisynaptic processes largely express glutamate transporters (EAAT1 and EAAT2), while endfeet are more specialized in nutrient uptake and express large amounts of glucose transporters (GLUT1; Iadecola and Nedergaard, 2007). Therefore, the etymology reflects what astrocytes have



traditionally been considered, satellite housekeeping cells of the brain, whose sole purpose is to serve neuronal cells in creating a favorable environment for the neurons to function efficiently. In this conventional view, astrocytes control pH and local ion homeostasis, deliver nutrients and clean neuronal waste (Nedergaard et al., 2003).

## Compartmentalization of Brain Energy Metabolism

However, the role of astrocytes extends beyond physically supporting neurons. Interconnected via gap junctions, astrocytes form a complex functional network that detects and modulates neuronal activity, integrates and transmits surrounding signals, controls brain vasculature for nutrient delivery, and regulates and metabolizes energy substrates. Astrocytes transport glucose via GLUT1 transporters (reviewed in Maher et al., 1994). Compared to neurons, astrocytes express high levels

of 6-phosphofructose-2-kinase/fructose-2,6-bisphosphatase-3 (PFKFB3), producing fructose-2,6-bisphosphate, activating in turn phosphofructokinase-1 (PFK) (Almeida et al., 2004; Herrero-Mendez et al., 2009). Astrocytes are, therefore, prone to aerobic glycolysis (Barros and Deitmer, 2010) and early studies have supported that glycolysis can be stimulated by neuronal activity (Kasischke et al., 2004), astrocytic glutamate uptake (Pellerin and Magistretti, 1994; Takahashi et al., 1995; Tsacopoulos et al., 1997) and extracellular  $\text{K}^+$  (Peng et al., 1994). Recently, using the genetically encoded fluorescence resonance energy transfer (FRET) lactate sensor Laconic, a lactate gradient from astrocytes to neurons was demonstrated *in vivo* (Mächler et al., 2016). The two ATPs glycolytically-produced have been proposed to serve the energetic demands associated with glutamatergic activity in fueling both the  $\text{Na}^+/\text{K}^+$ -ATPase pump coupled to glutamate transport (consuming one ATP) and the glutamine synthetase (consuming another

ATP) for the maintenance of the glutamate-glutamine cycle (Pellerin and Magistretti, 1994). On the other hand, neurons constantly degrade PFKFB3 (Almeida et al., 2004; and reviewed in Bolaños et al., 2010) and neuronal activation of PFKFB3 was shown to lead to oxidative stress and neuronal apoptosis (Herrero-Mendez et al., 2009). Astrocytic-produced lactate was therefore proposed to alternatively fuel neurons for oxidative metabolism during neuronal activity, in line with stimulation of glycolysis by  $K^+$  (Peng et al., 1994; Bittner et al., 2011), by glutamate (Pellerin and Magistretti, 1994), and increased lactate efflux by  $K^+$  (Sotelo-Hitschfeld et al., 2015) and  $NH^{+4}$  (Provent et al., 2007; Lerchundi et al., 2015), while neuronal glucose to be diverted into the pentose phosphate pathway for antioxidant defense during enhanced work at the respiratory chain (Bouzier-Sore and Bolaños, 2015). The study by Sibson et al. in the rat brain suggesting 1:1 stoichiometry between neuronal glucose oxidation and the glutamate-glutamine cycle rate (Sibson et al., 1998) provided support to this early view of compartmentation of brain metabolism. However, this hypothesis did not consider (or exclude) stimulation of glial oxidative metabolism to support increased neurotransmission rates. Yet, hexokinase was shown to be highly expressed in neurons as compared to astrocytes (Lundgaard et al., 2015), which is consistent with the ability of neurons to rapidly upregulate their glycolytic activity to fuel energy demand. In line with this, it was reported that increased glycolysis occurs for example in nerve terminals of bicuculline-treated rats (Patel et al., 2014), and in cultured neurons exposed to high  $K^+$  (Peng and Hertz, 2002).

## Stimulation of Glial Oxidative Metabolism *In vitro*

Although glycolytic activity is higher in glia than in neurons, astrocytes express an important number of enzymes involved in the TCA cycle, suggesting substantial oxidative capacity. In particular, about 45 and 16% of gene expression in astrocytes is dedicated to energy homeostasis and energy substrate transport, respectively, and TCA cycle related genes (i.e., citrate synthase, aconitase, isocitrate dehydrogenase, oxoglutarate dehydrogenase, dihydrolipoamide s-succinyltransferase, succinyl-CoA ligase, succinate dehydrogenase, fumarase, malate dehydrogenase) have larger expression in astrocytes than in neurons (Lovatt et al., 2007). Moreover, an important amount of small mitochondria was detected in the fine astrocytic processes (Derouiche et al., 2015) and shown to co-localize with EAAT (Genda et al., 2011; Jackson et al., 2014), which might facilitate coupling of astrocytic respiration with glutamate uptake (Eriksson et al., 1995). Additionally, elevation in astrocytic  $Ca^{2+}$  coincide with mitochondria position within the processes (Jackson and Robinson, 2015), and a rise in mitochondrial  $Ca^{2+}$  concentration might stimulate TCA cycle activity and thus ATP production (Wan et al., 1989; Denton, 2009). Consistent with glial metabolic activation by neuronal activity (Eriksson et al., 1995) and stimulation of  $Na^+/K^+$ -ATPase by extracellular  $K^+$  (Hajek et al., 1996; Honegger and Pardo, 1999), the fraction of glutamate that is metabolized through glial TCA cycle was reported to increase

with extracellular glutamate application to astrocytes (McKenna et al., 1996).

## Glial Oxidative Metabolism *In vivo*

A few *in vivo* studies have investigated the metabolic involvement of glia during neuronal activation. In particular, autoradiography studies using the glial-specific energy substrate acetate demonstrated increased glial oxidative metabolism during both acoustic (Cruz et al., 2005) and photic (Dienel et al., 2007b) stimulations in awake rats. Similarly, positron emission tomography (PET) along with [ $1-^{11}C$ ]acetate infusion showed increased astrocytic oxidative metabolism during infraorbital nerve stimulation of anesthetized rats and visual stimulation in humans (Wyss et al., 2009). Using dual photon fluorescence confocal microscopy, Lind et al. showed that during trigeminal nerve stimulation of anesthetized mice about 70% of astrocytes respond to stimulation with  $Ca^{2+}$  increase (Lind et al., 2013). With the same methodology the glial activation map was reported to resemble that of neurons during rat paw stimulation, suggesting both neuronal, and glial topographical representation of the body in the cortex (Ghosh et al., 2013), and pointing to significant glial activation during neuronal activity.

While these techniques present high spatial resolution, they are associated with some disadvantages, such as the need of radioactive tracers and ionizing radiations (PET, autoradiography), invasiveness (dual photon fluorescence confocal microscopy, FRET, autoradiography), potential cellular toxicity (FRET), the lack of absolute quantification in the case of FRET (as signal magnitude directly rely on the number of molecules of interest binding the sensor), and the lack of chemical specificity (PET, autoradiography) for providing quantitative information on metabolic pathways underlying oxidative metabolism. Currently, the development of tracers detectable by MRS, such as  $^{13}C$ -labeled substrates, the improvement of detection modalities (Henry et al., 2003), the progress in building adequate mathematical models (Gruetter et al., 2001) along with the increase in magnetic field strength render possible detailed compartmentalized metabolic flux characterization *in vivo* in a non-invasive manner and with minimal assumptions (Duarte et al., 2011; Duarte and Gruetter, 2013; Dehghani et al., 2016; Sonny et al., 2016, 2017). In particular direct detection of  $^{13}C$ -labeled compounds ( $^{13}C$  MRS) provides quantitative assessment of major metabolic pathways including glycolysis, TCA cycle, glutamate-glutamine cycle and pyruvate carboxylase (Gruetter et al., 2001; Henry et al., 2006; Duarte et al., 2011). Direct detection of  $^{13}C$ -labeled compounds is a technique that has been robustly implemented and can be applied to small animal metabolism studies in the whole brain (Duarte et al., 2011) or in specific cerebral regions (Patel et al., 2005a; Sonny et al., 2016, 2017).

## DYNAMIC $^{13}C$ MAGNETIC RESONANCE SPECTROSCOPY ( $^{13}C$ MRS)

Nuclear magnetic resonance (NMR) is a non-ionizing and non-invasive technique based on the magnetic properties of spin-containing nuclei. This methodology can be used in both clinical

settings (e.g., Prichard et al., 1991; Rothman et al., 1992; Gruetter et al., 1994, 1998a, 2001; Shen et al., 1999; Gruetter, 2002; Lebon et al., 2002; de Graaf et al., 2004; Mangia et al., 2007; Oz et al., 2007, 2015; Lin et al., 2012; Schaller et al., 2013, 2014; Bednářík et al., 2015) and pre-clinical studies (e.g., Mason et al., 1992; Hyder et al., 1996, 1997; Sibson et al., 1998, 2001; Choi et al., 2002; Henry et al., 2002; Patel et al., 2004, 2005a; Deelchand et al., 2009; Duarte and Gruetter, 2013; Duarte et al., 2011, 2015; Mishkovsky et al., 2012; Just et al., 2013; Bastiaansen et al., 2013, 2015; Lanz et al., 2014; Sonny et al., 2015, 2016, 2017). However, in most animal applications it requires anesthesia, which can modify the coupling between neuronal activity, brain metabolism and vascular regulation of blood flow (Masamoto and Kanno, 2012; Sonny et al., 2017, and references therein).

Several nuclei can be used to investigate brain metabolism, notably  $^1\text{H}$ ,  $^{31}\text{P}$ , or  $^{13}\text{C}$ . In the case of phosphorus,  $^{31}\text{P}$  MRS is used to investigate energy metabolism by providing information on the energy status of endogenous phosphate compounds, namely ATP, ADP, and PCr (e.g., Zhu et al., 2009).  $^1\text{H}$  MRS is based on local environment-dependent  $^1\text{H}$  present in metabolites (discarding water that is several orders of magnitude more concentrated) and assesses changes in total metabolite concentrations (generally in the mM range) involved in energy metabolism, osmoregulation, membrane metabolism and myelination (reviewed in Duarte et al., 2012). The main challenge associated with  $^1\text{H}$  MRS is the complexity of the neurochemical profile composed of several overlapping metabolite signals on a relatively small frequency range (i.e., 4–5 ppm) that is to be analyzed (de Graaf, 1998). An extension of this technique is  $^1\text{H}$  functional MRS (fMRS) that focuses on time-dependent changes in metabolite concentrations, which are associated with metabolic pathways during brain activity (Prichard et al., 1991; Mangia et al., 2007; Lin et al., 2012; Just et al., 2013; Schaller et al., 2013, 2014; Bednářík et al., 2015). The difficulty associated with the detection of small concentration changes occurring during neuronal activation can yet be overcome by using high magnetic field MR system ( $\geq 9.4$  T) to increase spectral resolution and sensitivity.

Direct  $^{13}\text{C}$  MRS can measure  $^{13}\text{C}$  isotope incorporation (or fractional enrichment, FE) over time into different molecules and into specific positions within the same molecule (i.e.,  $^{13}\text{C}$  isotopomers), with signals distributed over a large chemical shift range, namely about 200 ppm. Since the  $^{13}\text{C}$  isotope has a natural low abundance (1.1%), a low background signal is detected. However, as  $^{13}\text{C}$  gyromagnetic ratio is  $\frac{1}{4}$  of that of  $^1\text{H}$ ,  $^{13}\text{C}$  MRS is an insensitive technique as compared with  $^1\text{H}$  MRS. This is the reason why  $^{13}\text{C}$  tracers are infused in a substantial amount to enable proper signal detection. The  $^{13}\text{C}$  MRS detection threshold *in vivo* is typically in the mM range and it is usually not possible to measure TCA cycle intermediates that are present in smaller quantities. However, amino acids (e.g., glutamate, glutamine, and aspartate), which are in exchange with TCA cycle intermediates, are present at higher concentrations and can, therefore, be measured and used for metabolic modeling and thus for estimation of fluxes across major biochemical pathways.

On the other hand, dynamic nuclear polarization (DNP) can be used to increase  $^{13}\text{C}$  polarization of  $^{13}\text{C}$ -labeled substrates,

and thus offers potentially tremendous signal enhancement and detection of  $^{13}\text{C}$  labeling in tissue's TCA cycle intermediates, such as 2-oxoglutarate in the brain (Mishkovsky et al., 2012), or citrate in the heart (Schroeder et al., 2009; Bastiaansen et al., 2015). While such a technique can probe metabolism *in vivo* with high sensitivity and a time resolution of 1 s, the acquisition window is limited to approximately a minute (Comment, 2016), since MR acquisition needs to be performed within the time decay (seconds) of the enhanced nuclear polarization, and detection of downstream compounds depends notably on the turnover rates and on the concentration of labeled metabolites produced within the recording period (discussed in Mishkovsky et al., 2012). Moreover, further developments are required to actually translate the detection and measurement of hyperpolarized  $^{13}\text{C}$  *in vivo* to quantification of metabolic fluxes (Bastiaansen et al., 2013).

The strong heteronuclear scalar coupling between  $^{13}\text{C}$  and  $^1\text{H}$  nuclei complicates the spectra (i.e., splitting of  $^{13}\text{C}$  resonances in multiplets with reduced peak height) and reduces the sensitivity, so that additional hardware is required for  $^1\text{H}$  decoupling during acquisition (discussed in Henry et al., 2006). Homonuclear  $^{13}\text{C}$  couplings are also observable and the presence of  $^{13}\text{C}$  multiplets depends on the simultaneous presence of  $^{13}\text{C}$  spins in the same molecule at adjacent positions. Although assessment of  $^{13}\text{C}$  multiplets with high temporal resolution is challenging because of low signal amplitude, their inclusion in mathematical modeling (i.e., bonded cumomer approach) improves reliability and independency of the estimated brain metabolic fluxes (Shestopalov et al., 2012; Tiret et al., 2015; Dehghani et al., 2016).

The evaluation of  $^{13}\text{C}$  enrichment curves over time of carbon containing molecules requires the use of multi-compartment models describing best the data (de Graaf et al., 2003, 2004; Patel et al., 2004, 2005a, 2010; Henry et al., 2006; Lanz et al., 2013). As a simplified view of the real biochemical network, a model is a set of metabolite pools interconnected by the major biochemical reactions that are associated with metabolic fluxes. Each pool is associated with certain labeling positions in the atomic chain of one metabolite synthesized downstream from the infused compound: therefore there are at least as many labeling equations as carbon positions. The model contains the measurable entities and the non-measurable pools that are present in lower concentrations (e.g., TCA cycle intermediates) and that reach steady-state labeling much faster than larger pools, such as amino acids (Uffmann and Gruetter, 2007). The model can combine isoenzymes, parallel pathways that result in the same labeled pools, intermediate pools that equilibrate rapidly (e.g., pyruvate/lactate) or which enzymes are assumed not to be involved in other processes (e.g., glycolysis). According to the complexity to reach, the model can assess reversibility of reactions, sub-compartmentation or transport across membranes (reviewed in Henry et al., 2006). Based on the known biochemical reactions, a model should, therefore, be as simple as possible and as complex as necessary to describe measured parameters, focusing on the relevant pathways leading to metabolic observations and neglecting the influence of others (e.g., presence of cofactors, much slower reactions).

Derivation of metabolic fluxes is usually performed using dynamic positional enrichment (total amount of label

accumulated at individual position without distinguishing within multiplets; de Graaf et al., 2004; Duarte et al., 2011; Sonnay et al., 2016, 2017). The metabolic model describing  $^{13}\text{C}$  labeling is solved mathematically by a set of coupled linear differential mass-balance equations describing the system at equilibrium (i.e., metabolic but not isotopic steady-state). It assumes mass and energy conservation (i.e., constant fluxes and pool size over time), instant and uniformly labeling of the pools, and equal probability for a labeled or non-labeled molecule to enter and leave a pool (Mason et al., 1992 and see Lanz et al., 2013 for mathematical details). This latter assumption is plausible given that the biochemical reactions are fast compared to the temporal resolution of the MR acquisition techniques. Note that the metabolic steady-state assumption might not necessarily hold under certain conditions (Lanz et al., 2014).

## Isotopomers from $[1,6-^{13}\text{C}_2]$ Glucose

An extensively used substrate for two-compartment (i.e., neurons vs. astrocytes) brain metabolism investigation is  $[1,6-^{13}\text{C}_2]$ glucose (Lanz et al., 2013). On a general principle,  $[1,6-^{13}\text{C}_2]$ glucose crosses the BBB through facilitate glucose transporters (GLUT), is taken up by neurons and astrocytes, and 1 mole of glucose is metabolized through glycolysis (cytosolic reaction) to produce 2 moles of  $[3-^{13}\text{C}]$ pyruvate (1 mole of  $[1-^{13}\text{C}]$ glucose only produces 1 mole of  $[3-^{13}\text{C}]$ pyruvate, resulting in two-fold reduced  $^{13}\text{C}$  labeling of pyruvate). Two moles of  $[2-^{13}\text{C}]$ acetyl-CoA is then synthetized by PDH. Then in the first turn of the mitochondrial TCA cycle,  $[2-^{13}\text{C}]$ acetyl-CoA will label position C4 of 2-oxoglutarate. Due to the transimtochondrial exchange mediated notably by GDH and AST, cytosolic glutamate C4 is in turn labeled (the carbon positions are maintained). Due to the symmetry of the succinate and fumarate molecules, half of the labeling in position C4 of 2-oxoglutarate is transferred with equal probability to positions C2 and C3 of oxaloacetate, leading to the formation of  $[2-^{13}\text{C}]$ aspartate and  $[3-^{13}\text{C}]$ aspartate from oxaloacetate by AST. In the second turn of the TCA cycle, labeled molecules of oxaloacetate combine again with (labeled or unlabeled) molecules of acetyl-CoA, resulting in the formation of  $[2-^{13}\text{C}]$ glutamate and  $[3-^{13}\text{C}]$ glutamate. Then in the third turn of the TCA cycle, half of the carbons of position C3 of 2-oxoglutarate are transferred to position C2, while the other half stays at position C3. Meanwhile carbons at position C2 are transferred to position C1 of 2-oxoglutarate or lost as  $\text{CO}_2$ . The aspartate pool is enriched at position C1, C2, C3 and C4. In astrocytes,  $[3-^{13}\text{C}]$ oxaloacetate can be formed from  $[3-^{13}\text{C}]$ pyruvate by PC, leading to the formation of  $[2-^{13}\text{C}]$ 2-oxoglutarate and  $[2-^{13}\text{C}]$ glutamate. Therefore,  $[1,6-^{13}\text{C}_2]$ glucose, as  $[1-^{13}\text{C}]$ glucose, allows differentiating astrocytes and neurons in labeling positions C2 and diluting positions C3 (with  $^{12}\text{C}$ ) of glutamate via the glial specific enzyme PC, but enhances signal detection at a given resonance by two-fold compared to  $[1-^{13}\text{C}]$ glucose (two times more  $[3-^{13}\text{C}]$ pyruvate at the end of glycolysis). In the glutamate-glutamine cycle, the carbon positions are maintained. As the labeling persists in the TCA cycle, multiple carbon positions become labeled (Figure 2).

Other labeled substrates can be used to study brain metabolism by direct  $^{13}\text{C}$  MRS *in vivo* depending on the labeling pattern. For instance,  $[2-^{13}\text{C}]$ glucose in the human brain allowed labeling the carboxyl groups of glutamate and glutamine (i.e., positions C1 and C5), and aspartate (i.e., positions C1 and C4; Li et al., 2016). However, half of labeling is rapidly lost as  $\text{CO}_2$ . Using uniformly labeled glucose ( $[U-^{13}\text{C}]$ glucose) increases the splitting of the resonance C4 of glutamate and glutamine due to J-coupling with position C5 (Henry et al., 2003).  $[3-^{13}\text{C}]$ lactate can be used as an alternative to  $[1,6-^{13}\text{C}_2]$ glucose, but results in a reduced amount of labeling molecules because of a lower lactate entry into the brain as compared to  $[1,6-^{13}\text{C}_2]$ glucose (Duarte et al., 2015).  $[2-^{13}\text{C}]$ acetate has the particularity of being metabolized almost exclusively in glia. It produces  $[2-^{13}\text{C}]$ acetyl-CoA and the large neuronal glutamate pool becomes labeled via glial  $[4-^{13}\text{C}]$ glutamine. Therefore,  $[2-^{13}\text{C}]$ acetate allows increasing the sensitivity of the measurements of glial oxidative metabolism and the glutamate-glutamine cycle in minimizing the bias toward the large neuronal glutamate pool (Patel et al., 2010; Lanz et al., 2014). To obtain more precise measurements on neuronal and glial oxidative metabolism,  $[1,6-^{13}\text{C}_2]$ glucose can be co-infused with  $[1,2-^{13}\text{C}_2]$ acetate. However, advanced modeling approaches are needed to account for the additional homonuclear coupling brought by this double infusion (Deelchand et al., 2009).

## Compartmental Models of Brain Metabolism

### One-Compartment Model

The one-compartment model (Figure 3A) was the first metabolic model used to describe the turnover curves following infusion

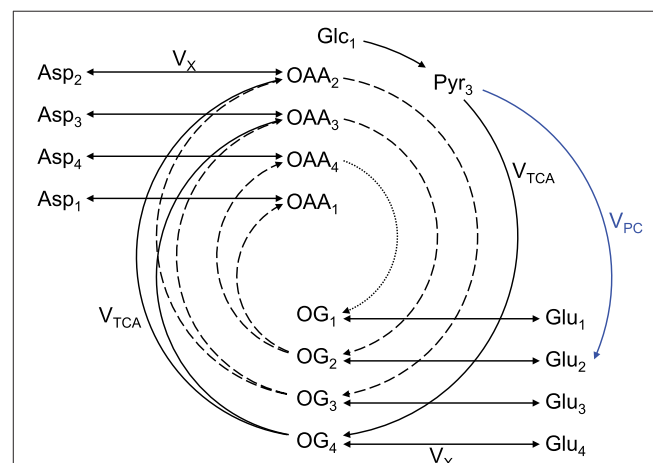
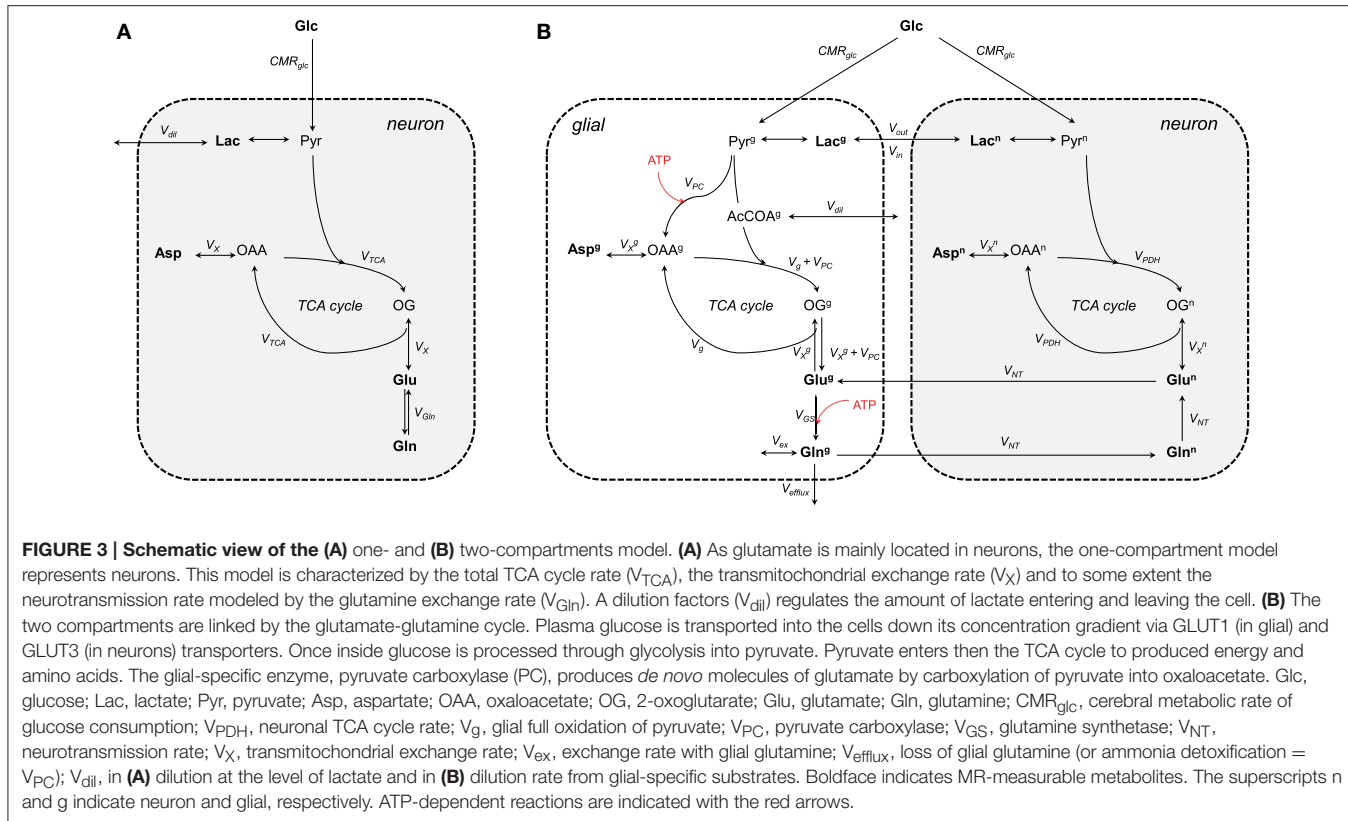


**FIGURE 2 | Schematic overview of labeling transfer during  $[1,6-^{13}\text{C}_2]$ glucose or  $[1-^{13}\text{C}]$ glucose infusion.** The splitting of the labeling after OG is due to the symmetry at the succinate and fumarate level. The indexes represent the carbon positions that become labeled. The first, second, and third turns of the TCA cycle are represented by solid, dashed, and dotted lines, respectively. The glial specific reaction driven by pyruvate carboxylase ( $V_{\text{PC}}$ ) labels position C2 and dilutes position C3. Glc, glucose; Lac, lactate; Pyr, pyruvate; Asp, aspartate; OAA, oxaloacetate; OG, 2-oxoglutarate; Glu, glutamate; Gln, glutamine;  $V_{\text{TCA}}$ , TCA cycle rate;  $V_x$ , transimtochondrial exchange rate (modified from Lanz et al., 2013).



of [ $1-^{13}\text{C}$ ]glucose along with  $^1\text{H}-[^{13}\text{C}]$  MRS (i.e., detection of  $^1\text{H}$  attached to  $^{13}\text{C}$ ; Mason et al., 1992; Rothman et al., 1992; Hyder et al., 1996). As most of the glutamate is located in neurons (Ottersen et al., 1992), this model is assumed to mainly represent neuronal TCA cycle activity. It allows assessing the TCA cycle rate ( $V_{TCA}$ ), the trans-mitochondrial flux ( $V_X$ ) and a dilution flux at the level of lactate ( $V_{dil}$ ), accounting for the utilization of unlabeled substrates (Mason et al., 1992) from fitting glutamate and glutamine C4, and Glx (glutamate+glutamine) C3. Although the astrocytic compartment is not represented in this model, the neurotransmission rate can be modeled with a glutamine exchange rate ( $V_{Gln}$ ; Henry et al., 2002). While  $^1\text{H}-[^{13}\text{C}]$  MRS studies provided an initial measure of local oxidative metabolism, they were limited to the number of detected  $^{13}\text{C}$  isotopomers and were dependent on several assumptions regarding glial fluxes (Patel et al., 2004; de Graaf et al., 2004). With the rapid improvement of MRS methodology and sensitivity (Gruetter et al., 1994, 1998a; Henry et al., 2003, 2006), detection of carbon position C2, C3, and C4 (and their splitting) of glutamate and glutamine became possible (i.e., direct detection of  $^{13}\text{C}$ -labeled compounds) resulting to the development of two-compartment models with minimum assumptions regarding glial fluxes (Gruetter et al., 2001).

## Two-Compartment Models

Two-compartment models describe compartmentalization of brain energy metabolism between glutamatergic neurons and

astrocytes linked by the glutamate-glutamine cycle (Figure 3B). In contrast to the one-compartment model, this model can estimate up to nine independent fluxes from the labeling curves of glutamate, glutamine, and aspartate (Duarte et al., 2011; Sonnay et al., 2016, 2017) resulting in up to thirteen parameters that can be assessed when combining some of the fitted fluxes. More precisely, the fitted parameters are the neurotransmission rate ( $V_{NT}$ ; i.e., glutamate-glutamine cycle representing neurotransmission), the neuronal and glial TCA cycle (i.e.,  $V_{PDH}$  and  $V_g$ , representing glial full pyruvate oxidation), pyruvate carboxylase activity ( $V_{PC}$ ), the trans-mitochondrial exchange rates describing the combined effects of AST, GDH and transport across mitochondrial membrane occurring in neurons ( $V_X^n$ ) and in glia ( $V_X^g$ ), glial glutamine exchange ( $V_{ex}$ ), pyruvate/lactate influx from plasma ( $V_{in}$ ) and dilution from glial specific substrates (i.e., acetate and fatty acids) ( $V_{dil}$ ). In addition, calculated fluxes are total glial TCA cycle activity ( $V_{TCA}^g = V_g + V_{PC}$ ), the glutamine synthetase rate ( $V_{GS} = V_{NT} + V_{PC}$ ), the total cerebral metabolic rate of glucose oxidation ( $\text{CMR}_{\text{glc(ox)}} = [V_{TCA}^g + V_{TCA}^n + V_{PC}]/2$ ) and the pyruvate/lactate out-flux from the brain parenchyma ( $V_{out} = 2\text{CMR}_{\text{glc}} - 2\text{CMR}_{\text{glc(ox)}} + V_{in}$ ).  $\text{CMR}_{\text{glc}}$  is the cerebral metabolic rate of glucose and is usually determined together with the apparent maximum transport ( $T_{max}$ ) and the apparent Michaelis constant of glucose transport  $K_t$  using labeling of plasma and brain glucose (Duarte et al., 2011; Sonnay et al., 2016, 2017). In glial cells, GLS is neglected because the net  $^{13}\text{C}$  labeling follows the direction of glutamine synthesis.  $V_{ex}$

can exchange with unlabeled glutamine of undefined origin (Oz et al., 2004) or the proposed  $^1\text{H}$  MR invisible but  $^{13}\text{C}$  labeled glutamine pool (Duarte and Gruetter, 2013). Besides the contribution to amino acid synthesis,  $V_{\text{PC}}$  also represents glutamine efflux ( $V_{\text{efflux}}$ ) from the brain (i.e., ammonia disposal) and maintains the mass balance in the glial TCA cycle (Lee et al., 1998). Glutamate oxidation in the model is possible through  $V_X$  (composite representation of AST and GDH). Note that both  $V_{\text{Gln}}$  and  $V_{\text{NT}}$  represent the glutamate-glutamine cycle. One is rather used in the one-compartment model ( $V_{\text{Gln}}$ ) as an exchange rate between glutamate and glutamine, while the other in the two-compartment model ( $V_{\text{NT}}$ ).

### Flux Information Brought by the Turnover Curves of Amino Acids

Labeling of a particular nucleus depends on pool size and the numbers of upstream and downstream fluxes (Henry et al., 2006), affecting therefore the shapes of the turnover curves differently. Glutamate is the most concentrated amino acid observed by  $^{13}\text{C}$  MRS (Figure 4). Glutamate labeling depends on both  $V_{\text{TCA}}$  and  $V_X$ , meaning that these two fluxes play an important role in defining glutamate turnover. While glutamate C4 relies on the composite flux  $V_{\text{gt}}$ , that is  $V_X \cdot V_{\text{TCA}} / (V_X + V_{\text{TCA}})$ , glutamate C3 and C2 depend on independent contribution of  $V_{\text{gt}}$ ,  $V_X$ , and  $V_{\text{TCA}}$  (reviewed in Lanz et al., 2013), because they are labeled in the second turn of the TCA cycle. Therefore, the information concerning  $V_X$  is mainly stored in the initial slopes of the turnover curves of position C4, C3, and C2 of glutamate (for  $V_X^n$ ) and glutamine (for  $V_X^g$ ). In the special case of  $V_X^g$ , this flux is particularly difficult to estimate, because labeled molecules from the glial TCA cycle into glial glutamate can also be transferred via  $V_{\text{PC}}$  (Figure 2). The value of  $V_X$  has been matter of debate for a long time, as it has been considered by some to be much larger than  $V_{\text{TCA}}$  (Mason et al., 1992; Patel et al., 2004; Yang et al., 2009), but it was also estimated to be on the same order of magnitude of  $V_{\text{TCA}}$ , as reflected in a delay in the C3 and C2 labeling relative to C4 (Gruetter et al., 2001; Oz et al., 2004; Duarte et al., 2011; Duarte and Gruetter, 2013; Lanz et al., 2014; Sonnay et al., 2016).

The neurotransmission rate,  $V_{\text{NT}}$ , represents the conversion of glutamate to glutamine and vice versa. In this process the carbon positions are maintained. Therefore,  $V_{\text{NT}}$  mostly depends on the relative steady-state enrichment of the turnover curves of glutamate and glutamine: the closer they are to each other, the faster  $V_{\text{NT}}$ .

The first turn of the TCA cycle results in label transfer from glucose to glutamate (via  $V_X$ ). Usually glutamate C4 is the first detectable peak in a spectrum during an experiment, as it appears within the first 5 min of infusion (Patel et al., 2005a; Duarte et al., 2011; Sonnay et al., 2016 and reviewed in de Graaf et al., 2003). Then, in the subsequent TCA cycle label is transferred from position C4 to C3 and C2. In neurons,  $V_{\text{PDH}}$  will therefore rely on the slope and the steady-state enrichment of the turnover curves of position C4, C3, and C2 of glutamate and glutamine, as labeling from glutamate is transferred to glutamine. As aspartate is mainly labeled via transamination of the TCA cycle intermediate oxaloacetate, the slope and the steady-state enrichment of position C3 and C2 of aspartate are further affected

by  $V_{\text{PDH}}$ . The slopes of the labeling curves reflect, the rate of  $V_{\text{PDH}}$ . In glia the situation is different, since label dilution due to  $V_{\text{PC}}$  can occur.  $V_{\text{PC}}$  dilutes position C3 and labels position C2 of glutamate and glutamine. Therefore, fast  $V_g$  results in a relatively high and steep glutamine C3 turnover curve ( $V_g$  has to be fast to counterbalance the loss due to  $V_{\text{PC}}$ ).

Diluting position C3 and labeling position C2 of glutamate and glutamine, the measurement of  $V_{\text{PC}}$  relies on the relative curves of position C3 and C2 of glutamate and glutamine, and the assumption that glutamate is mainly neuronal and glutamine mainly glial. High C3 and low C2 labeling is associated with slow  $V_{\text{PC}}$ , while high C2 and low C3 labeling reflect rather increased  $V_{\text{PC}}$ . Therefore, when the FE of glutamine C2 approaches that of C4, either PC activity is high compared to PDH, and/or glial-specific dilution of acetyl-CoA ( $V_{\text{dil}}$ ) occurs.

As mentioned above,  $V_{\text{dil}}$  reflects dilution of the acetyl-CoA pool with specific unlabeled glial substrates. Notably,  $V_{\text{dil}}$  dilutes glial acetyl-CoA  $^{13}\text{C}$  labeling relative to its precursor pyruvate. As the position C4 of glutamate and glutamine only receives labeling from acetyl-CoA, dilution at this point would lead to a lower (steady-state) C4 labeling. Since glutamate and glutamine are mainly present in neurons and glia, respectively,  $V_{\text{dil}}$  is also responsible for lower FE of position C4, C3, and C2 of glutamine compared to glutamate. However, the effect of  $V_{\text{dil}}$  on enhancing the labeling difference between glutamate and glutamine is counteracted by  $V_{\text{NT}}$ , which represents the glutamate-glutamine cycle. The faster the rate of  $V_{\text{NT}}$ , the more similar will be the labeling of glutamate and glutamine. Note that  $V_{\text{dil}}$  in glial acetyl-CoA can result in glutamine C2 being similar or larger than glutamine C4, which has been observed in some studies (discussed in Duarte et al., 2011).

$V_{\text{ex}}$  represents an exchange between two putative glutamine pools, one of which is not released to neurons and may account for a continuous slow increase in FE over time (Duarte and Gruetter, 2013).  $V_{\text{ex}}$  can be in exchange with a  $^1\text{H}$  MR invisible but  $^{13}\text{C}$  labeled glutamine pool (Hancu and Port, 2011) or with unlabeled amino acids from the blood (i.e., glutamine), as astrocytes envelop capillaries (Oz et al., 2004). This second glutamine pool could be associated with biosynthetic pathways, which have rates much slower than mitochondrial energy metabolism (McKenna, 2007). The effect of  $V_{\text{ex}}$  is in practice observable near the end of an experiment, when the labeling of glutamine still increases, while glutamate is at steady-state.

The difference  $V_{\text{out}} - V_{\text{in}}$  directly reflects whether the labeling from plasma glucose is enough to fuel the whole downstream metabolism since  $V_{\text{out}} - V_{\text{in}} = 2\text{CMR}_{\text{glc}} - 2\text{CMR}_{\text{glc(ox)}}$ . Therefore, if mitochondrial metabolism is faster than glycolysis, oxidation of additional substrates, such as lactate, must occur under certain conditions (Sonnay et al., 2017). In resting human brain, however, the brain exports lactate to the blood stream (discussed in Dienel, 2012).

The above descriptions are purely indicative of what happens for each flux independently. Experimental data is a linear combination of many fluxes, which will adjust during fitting process to best describe the turnover curves.

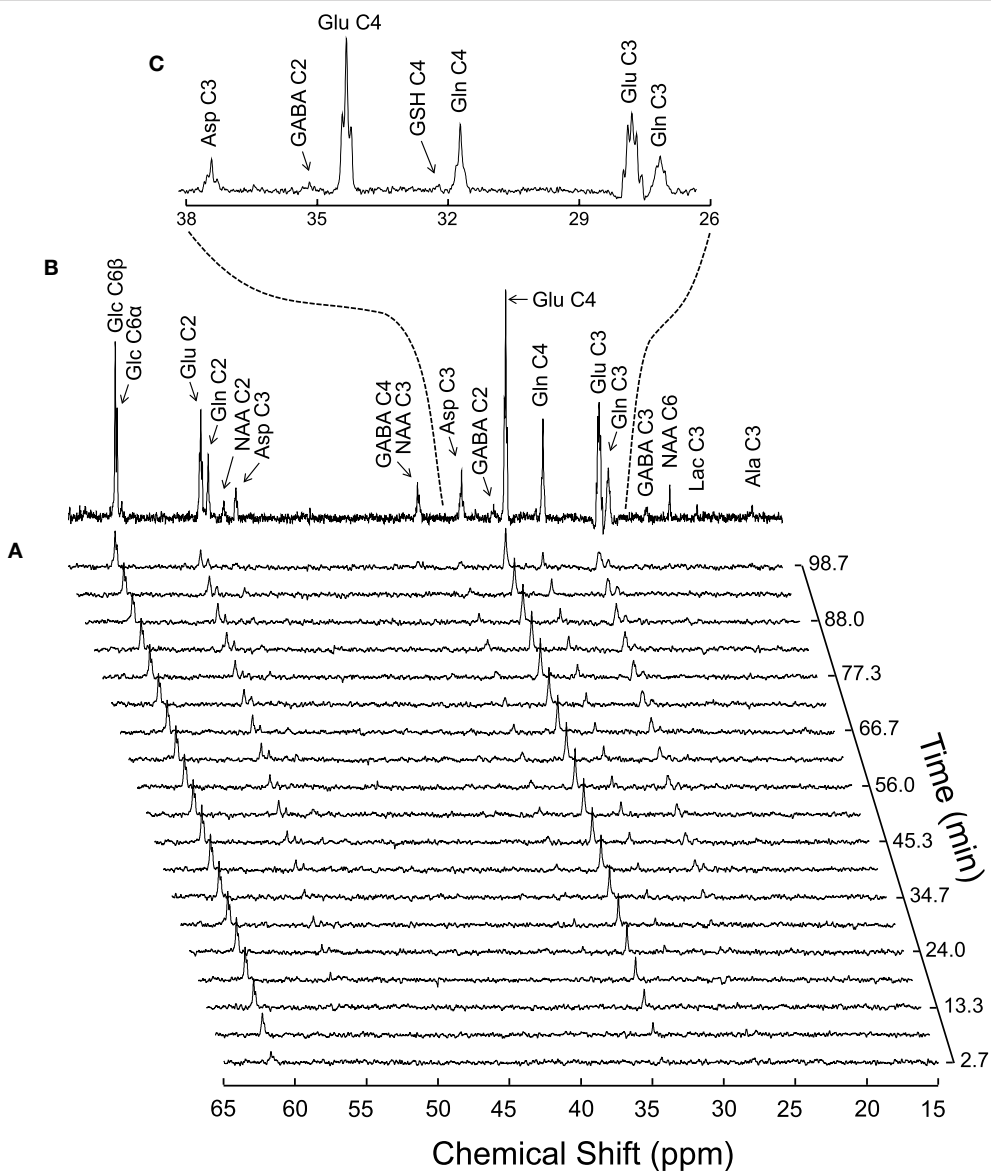


**FIGURE 4 |** Typical  $^{13}\text{C}$  MRS spectra acquired *in vivo* in the rat brain during  $[1,6-^{13}\text{C}_2]\text{glucose}$  infusion at 14.1T (reproduced from Duarte et al., 2011). Panel (A) shows a time course of  $^{13}\text{C}$  labeling with a temporal resolution of 5.3 min. The spectrum in (B) was acquired for 1.8 h, starting 3.5 h after the infusion onset. Panel (C) is an expansion of B depicting multiplets originated from isotopomers of glutamine (Gln), glutamate (Glu) and aspartate (Asp).

## INCREASED GLIAL AND NEURONAL GLUCOSE OXIDATION WITH NEURONAL ACTIVITY ASSESSED BY $^{13}\text{C}$ MRS

The first  $^{13}\text{C}$  MRS data acquired *in vivo* upon stimulus-induced brain activity were modeled using a one-compartment model and reported a marked increase in total TCA cycle activity in the somatosensory cortex of stimulated rats compared to rest (Hyder et al., 1996, 1997). The following experiment consisted on measuring neuronal  $\text{CMR}_{\text{glc}(\text{ox})}$  under three different anesthesia-induced activity states, namely pentobarbital (deep),  $\alpha$ -chloralose (moderate) and morphine (light) (Sibson et al., 1998). In this

study, energy metabolism was found to be coupled to the rate of the glutamate-glutamine cycle (representing glutamatergic neurotransmission,  $V_{\text{NT}}$  in Figure 3) in a proportion of 1:1 above isoelectricity, and the main assumption of the model was driven by the astrocyte-neuron lactate shuttle (ANLS) hypothesis according to which two glycolytic ATP are rapidly produced to fuel both glutamate uptake via the  $\text{Na}^+/\text{K}^+$ -ATPase and glutamine synthetase (Pellerin and Magistretti, 1994). According to this model, no stimulation of oxidative metabolism should occur in glia, in contrast to neurons. Later several studies in rat brain (Patel et al., 2004, 2005a; de Graaf et al., 2004), assuming  $V_{\text{PC}}$  as a fixed fraction of  $V_{\text{GS}}$  (Sibson et al., 2001) and  $V_{\text{TCA}}^{\text{g}}$

as a fraction of total  $V_{TCA}$  (van den Berg and Garfinkel, 1971; Lebon et al., 2002), corroborated the stoichiometry. However, it should be noted that constraining the value of  $V_{PC}$  to  $V_{GS}$  and  $V_{TCA}^g$  to the total  $V_{TCA}$  implies an effective coupling between glial oxidative metabolism and neuronal function.

Indeed, the astrocytic processes engulfing synapses are capable of sensing increased synaptic activity (Iadecola and Nedergaard, 2007; Cheung et al., 2014) and to stimulate metabolism in local mitochondria (Eriksson et al., 1995; Jackson et al., 2014). The  $^{13}\text{C}$  MRS study by Gruetter et al. (2001) in the human brain, modeling for the first time the occurrence of glucose oxidation in the glial compartment, indeed demonstrated that a significant fraction ( $\approx 21\%$ ) of glucose is also oxidized in astrocytes (Gruetter et al., 2001). Using a similar model, glial oxidation and pyruvate carboxylase activity was shown to significantly contribute also to total glucose oxidation in awake animals (Oz et al., 2004), and rats anesthetized with  $\alpha$ -chloralose (Duarte et al., 2011), pentobarbital (Choi et al., 2002) and thiopental (Sonny et al., 2017). In these rodent studies, going from the awake state to deep anesthesia, glial metabolism was found to account for 30–40% of total oxidative metabolism.

Recently, our group further addressed the issue of glial and neuronal oxidative metabolism coupled to neuronal activity. In particular, we first measured the cortical changes in metabolic fluxes induced by electrical stimulation of the four paws of rats. We observed a similar increase (in absolute terms) of both glial and neuronal oxidative metabolism resulting from the increase in glutamate-glutamine cycle rate (Figure 5; Sonny et al., 2016). Moreover, about 37% of total glucose oxidation, i.e.,  $\text{CMR}_{\text{glc(ox)}}$ , occurred in astrocytes at rest, 39% during stimulation and  $\Delta \text{CMR}_{\text{glc(ox)}}/\Delta V_{NT} \approx 1$ . Interestingly in this study, as well as in Patel et al. (2005b), PC did not vary with  $V_{NT}$ , suggesting that *de novo* synthesis of amino acids is not required for increases of the glutamate-glutamine cycle, neither there is increase in glutamine loss from the cortical tissue. Indeed Patel and Tilghman reported that glutamate can stimulate pyruvate carboxylation (Patel and Tilghman, 1973). Instead, glutamate could be oxidized in astrocytes to compensate for the high cost of glutamate uptake during neurotransmission (McKenna, 2013).

In the study by Sonny et al. (2016) the resulting incremental ATP produced by glucose oxidation was in excess of the increase in ATP required by the glutamate-glutamine cycle *per se* (i.e., glial  $\text{Na}^+/\text{K}^+$ -ATPase extrusion of  $\text{Na}^+$  that is co-transported with glutamate and glial glutamine synthetase activity). While the fate of neuronal ATP is likely involved in supporting other functions than the glutamate-glutamine cycle, such as stabilization of membrane potentials and restoration of ion ( $\text{Na}^+$ ,  $\text{K}^+$ , and  $\text{Ca}^{2+}$ ) gradients across the cell membrane (Attwell and Laughlin, 2001), the role of the considerable amount of ATP produced in glial cells (as estimated from recent  $^{13}\text{C}$  MRS experiments in rodents; Duarte et al., 2011, 2015; Sonny et al., 2016, 2017) is still unclear and likely extends beyond fueling glutamine synthetase, the  $\text{Na}^+/\text{K}^+$ -ATPase and the  $\text{Ca}^{2+}$ -ATPase (Fresu et al., 1999).  $\text{K}^+$  uptake has been recently suggested to fully account for astrocytic energy consumption (DiNuzzo et al., 2017). However, the simulations by DiNuzzo et al. are still unable to account for substantial  $V_{TCA}^g$  in cases of low glutamate-glutamine cycle rate.

To summarize, in addition to the proposed coupling of neuronal oxidative metabolism and neurotransmission, astrocytes increase their oxidative metabolism too, resulting in a large production of ATP. It is, therefore, important to investigate the exact fate of the ATP produced. In this context, the ATP produced in glia might notably support blood flow regulation (Zonta et al., 2003; Metea and Newman, 2006), neuronal activity modulation (Volterra and Meldolesi, 2005) and protection against oxidative stress (Borst and Elferink, 2002; Dringen and Hirrlinger, 2003). Glycogenolysis might moreover provide energy to support neurotransmission (i.e., release and uptake of glutamate; Sickmann et al., 2009).

## FUNCTIONS OF ASTROCYTES IN THE BRAIN

### Blood Flow Regulation

Brain vasculature is rich in arterioles and fine capillaries (Reina-De La Torre et al., 1998), and CBF regulation is mainly controlled by relaxation and constriction of these blood vessels (Attwell et al., 2010). In this context astrocytes and neurons are

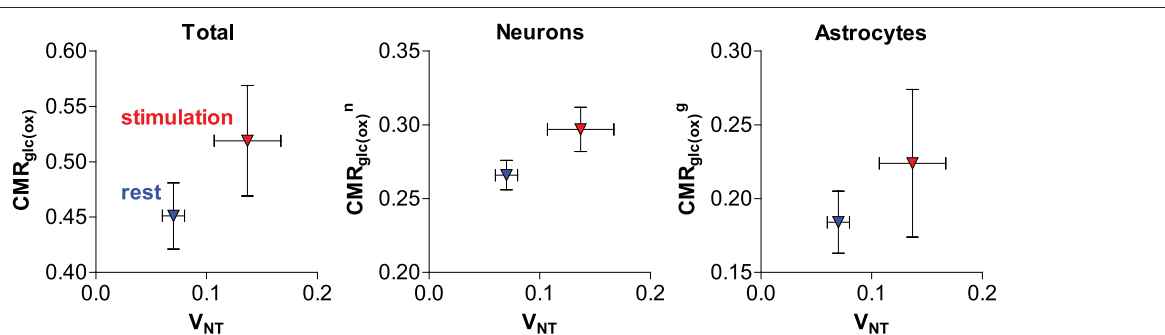
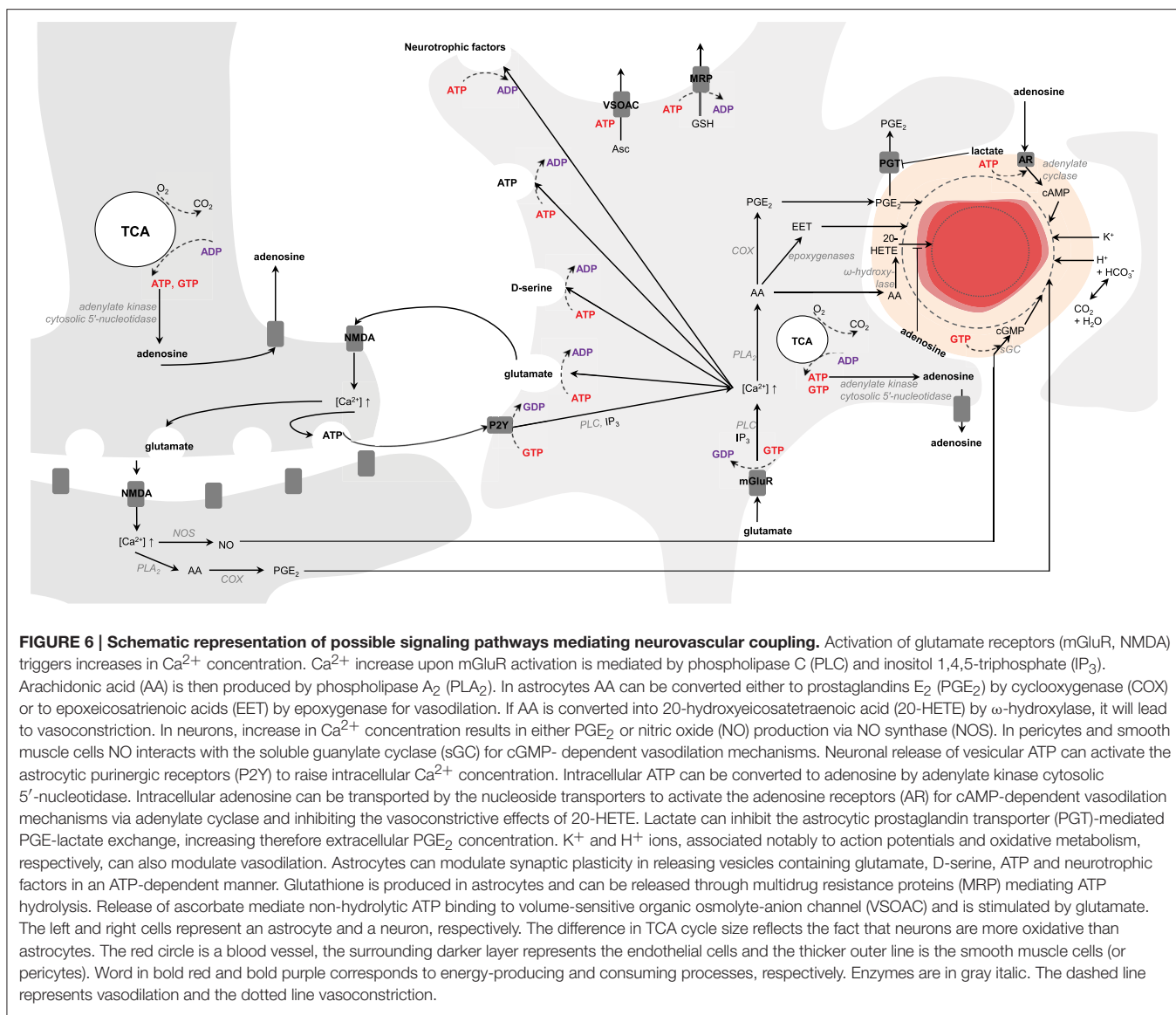


**FIGURE 5 | Relation of estimated total, neuronal and glial glucose oxidative metabolism to the glutamate-glutamine cycle in the rat cortex anesthetized with  $\alpha$ -chloralose (originally reported in Sonny et al., 2016).** Metabolic fluxes are in  $\mu\text{mol/g/min}$ . Average fluxes across the resting (in blue) and stimulated (in red) group are shown with associated SD.

presumed to play a key role in modulating CBF to match energy demands. In neurons, upon NMDA activation intracellular  $\text{Ca}^{2+}$  concentration increases, which activate phospholipase A<sub>2</sub> (PLA<sub>2</sub>) in the cytosol that then produces arachidonic acid (AA). In astrocytes, activation of mGluR by glutamate triggers the translocation of the  $\alpha$ -subunit of the receptors to phospholipase C (PLC) mediating the conversion of GTP to GDP (Bockaert et al., 1993). Activated PLC cleaves membrane phosphatidylinositol 4,5-bisphosphate (PIP<sub>2</sub>) to diacylglycerol (DAG) and inositol 1,4,5-triphosphate (IP<sub>3</sub>) that triggers  $\text{Ca}^{2+}$  increase. In neurons, cyclooxygenase (COX) converts AA into prostaglandins E<sub>2</sub> (PGE<sub>2</sub>) leading to vessel dilation (Wang et al., 2005). In astrocytes, AA can be converted either to PGE<sub>2</sub> by COX (Zonta et al., 2003) or to epoxecicosatrienoic acids (EET) by epoxygenase, which diffuse through pericytes (Hamilton et al., 2010; or smooth muscle cells for arteries) for blood vessel dilation. If AA is converted into 20-hydroxyeicosatetraenoic

acid (20-HETE) by  $\omega$ -hydroxylase in pericytes, it will cause vasoconstriction (Metea and Newman, 2006). New line of evidence suggest moreover that the astrocytic production of PGE<sub>2</sub> might be dependent on glutathione levels (Howarth et al., 2017, and references therein). In neurons activation of ionotropic glutamate receptors located on the post-synaptic zone (i.e., NMDA) also activates nitric oxide synthase (NOS), which in turn produces NO. Interaction of NO with soluble guanylyl cyclase (sGC) triggers cGMP dependent vasodilation mechanisms (Laranjinha et al., 2012; Lourenço et al., 2014). Moreover, neuronal vesicular ATP can be released and act on astrocytic purinergic receptors (P2Y) to raise intracellular  $\text{Ca}^{2+}$  concentrations mediating the conversion of GTP to GDP and PLC activation (reviewed in Erb and Weisman, 2012; Bazargani and Attwell, 2016). Alternatively, ATP can also intracellularly be converted to adenosine by adenylate kinase cytosolic 5'-nucleotidase (reviewed in Iadecola, 2004). Intracellular adenosine



can be released extracellularly by nucleoside transporters (Iliff et al., 2003), which can in turn act on adenosine receptors located on pericytes (Iliff et al., 2003; Gordon et al., 2008) and trigger the activation of adenylyl cyclase (in mediating the conversion of GTP to GDP) that converts ATP to cAMP (Suzuki et al., 1988). Increase in cAMP leads to vasodilation and inhibits the vasoconstrictive effects of 20-HETE (Koehler et al., 2006; **Figure 6**).

Other lines of evidence suggest that the transfer of excess electrons from NADH to O<sub>2</sub> by NADH oxidase (Wolin, 1996) can generate O<sub>2</sub><sup>-</sup>, which raises intracellular Ca<sup>2+</sup> levels (Ikebuchi et al., 1991) activating in turn NOS for NO production (Ido et al., 2001).

Two different dynamics of Ca<sup>2+</sup> signaling have been proposed to initiate and sustain hemodynamic responses. First, brief (100 ms) Ca<sup>2+</sup> responses in astrocytic end-feet, occurring downstream neuronal activation and scaling with the level of neuronal activity, triggers vessel dilation onset. Second, a slower and long lasting (seconds) Ca<sup>2+</sup> elevation contributes to a prolonged blood vessel dilation (Lind et al., 2013). Yet, the observation that astrocytic Ca<sup>2+</sup> can lag a few seconds arteriolar dilation supports the hypothesis that astrocytic Ca<sup>2+</sup>-dependent mechanisms may not be a prerequisite for CBF response initiation (Nizar et al., 2013). Local CBF response could be immediately regulated by fast (400 ms) feed-forward mechanisms directly related to neuronal activity (e.g., neuronal NO production (Buerk et al., 2003), action potential-associated K<sup>+</sup> current (Paulson and Newman, 1987), neuronal arachidonic pathway activation Zonta et al., 2003; Metea and Newman, 2006), rather than feedback mechanisms associated with metabolism (e.g., lactate, astrocytic mGluR-related signaling, ATP-derived adenosine signaling), that probably occur at longer time scales (seconds) to match CBF with energy demands (discussed in Buxton, 2010). In this context the fact that the CBF/CMRO<sub>2</sub> ratio varies between brain regions, as well with stimulus frequency (discussed in Buxton, 2010) and length (Lin et al., 2009), further suggests regulation of this ratio by notably neuronal activity-associated mechanisms (discussed in Buxton, 2010). Recent data further address this controversy in suggesting Ca<sup>2+</sup>-dependent signaling for modulation of capillary but not arteriolar diameter (Biesecker et al., 2016). Because CO<sub>2</sub>, one of the end products of oxidative metabolism, can diffuse out of the cells and is in rapid equilibrium with HCO<sub>3</sub><sup>-</sup>, extracellular H<sup>+</sup> ions can also locally contribute to CBF regulation (Kuschinsky and Wahl, 1978).

## Neuronal Activity Modulation and Synaptic Plasticity

Although astrocytes do not generate action potentials *per se* they can actively modulate synaptic transmission and neuronal synchronization in mediating notably the release of vesicles containing neurotransmitters and neuromodulators, such as glutamate, ATP, adenosine, and D-serine. Glutamate-containing microvesicles are present in astrocytes and upon Ca<sup>2+</sup> signaling glutamate molecules are released and can target post-synaptic receptors (i.e., NMDA, AMPA, mGluR, and kainate) to fine

tune firing threshold (Volterra and Meldolesi, 2005). In the extracellular space ATP can be converted to adenosine by the dephosphorylating action of the ectonucleotidase anchored at the plasma membrane (Joseph et al., 2003). Adenosine can activate adenosine receptors and therefore modulate neuronal activity by triggering K<sup>+</sup> efflux (e.g., Newman, 2003), as well as intermediary metabolism (Haberg et al., 2000; Hammer et al., 2001; Duarte et al., 2016) and blood flow (Blood et al., 2003; Iliff et al., 2003; Gordon et al., 2008). D-serine that can be released from astrocytes was also shown to modulate electrical neurotransmission by acting at the glycine binding site of NMDA receptor (Stevens et al., 2003). Moreover, the production of neurotrophic factors was shown to promote the formation and the function of synapses (Pfrieger and Barres, 1997), and to regulate intracellular Ca<sup>2+</sup> homeostasis upon stimulation of the glutamate receptors and thus to preserve the activity of the mitochondrial electrochemical gradient and therefore energy metabolism (El Idrissi and Trenkner, 1999). Glutamate, D-serine, ATP and neurotrophic factors are notably released exocytotically, mediating Ca<sup>2+</sup> signaling and ATP-dependent soluble N-ethylmaleimide-sensitive factor activating protein receptor (SNARE) disassembly (Goda, 1997; Parpura and Zorec, 2010), resulting in energy consumption (**Figure 6**). The delivery of these vesicles to the plasma membrane involves cytoskeleton assembly/disassembly (Potokar et al., 2007) requiring ATP hydrolysis (Korn et al., 1987; Le Clainche et al., 2003). Interestingly, the number of astrocytic processes, as well as their contact with active synapses, are stimulated by extracellular glutamate and also involve actin-independent mechanisms (Cornell-Bell et al., 1990) requiring ATP hydrolysis (Korn et al., 1987; Le Clainche et al., 2003).

## Protection against Oxidative Stress

The use of NADH through the electron transport chain for ATP production and mitochondrial Ca<sup>2+</sup> influx results in reactive oxygen species (ROS) production (Boveris and Chance, 1973; and reviewed in Görlach et al., 2015). Yet, the cooperative action of astrocytes in culture was shown to protect neurons against ROS toxicity (Desagher et al., 1996), and astrocytes express larger amounts of antioxidant molecules and ROS-detoxifying enzymes than neurons (Makar et al., 1994). The thiol group of the glutathione molecule acts as an important electron donor. While both neurons and astrocytes synthesize glutathione, neuronal glutathione levels are higher in the presence of astrocytes (Dringen et al., 1999), probably because of shuttling of cysteine-glycine (glutathione precursor) from astrocytes to neurons (Dringen and Hirrlinger, 2003). Glutathione transport across cells is notably mediated by multidrug resistance proteins (MRP) that belong to the subgroup ABCC of the ATP-binding cassette transporters, which mediate passage via ATP hydrolysis (Borst and Elferink, 2002; Dringen and Hirrlinger, 2003; **Figure 5**). Activation of astrocytic glutamate receptors was shown to translocate nuclear factor-erythroid 2-related factor-2 (Nrf2) (present in lower concentrations in neurons) into the nucleus and to trigger the expression of antioxidant genes, notably related to glutathione metabolism (Jimenez-Blasco et al., 2015).

Astrocytes synthesize large amount of hydrogen sulfide, which was demonstrated to not only have neuroprotective properties (Lee et al., 2009), but also act as neuromodulator in enhancing NMDA responses (Abe and Kimura, 1996) and modulating glial Ca<sup>2+</sup> waves (Nagai et al., 2004).

Ascorbate is also another important antioxidant anion in the brain and glutamate was demonstrated to stimulate its release from astrocytes (Wilson et al., 2000), suggesting an essential protecting role of the ascorbate flux from astrocytes to neurons during synaptic activity (Acuña et al., 2013). Astrocytes are responsible for the recycling of the neuronal extracellularly released dehydroascorbic acid (the oxidized form of ascorbate) into ascorbate, which can be exported to neurons (Covarrubias-Pinto et al., 2015). Extracellular transport of ascorbate from astrocytes is believed to be mediated by volume-sensitive organic osmolyte-anion channel (VSOAC) that requires non-hydrolytic ATP binding (Jackson et al., 1994; Covarrubias-Pinto et al., 2015; **Figure 6**). Considering the fact that efficacy of the mechanisms stimulated by astrocytic glutamate uptake depends on the density of the transporters at the plasma membrane (Robinson, 2002), efficient trafficking of EAAT2-containing vesicles and exocytosis must moreover take place (Stenovec et al., 2008).

## Glycogenolysis

Glycogen constitutes a glucose storage in the form of highly branched polysaccharide molecules (Preiss and Walsh, 1981) found in high concentrations in the liver and in skeletal muscle, although smaller but significant levels (6–8 μmol/g) are also estimated in the human brain (Oz et al., 2015). Glycogenesis (glycogen production from glucose 1-phosphate by glycogen synthase) and glycogenolysis (glycogen breakdown to glucose 6-phosphate by the combined action of glycogen phosphorylase and phosphoglucomutase) mainly occurs in astrocytes (Dringen et al., 1993; **Figure 1**), and the latter can be stimulated by extracellular glutamate and K<sup>+</sup> (Hertz et al., 2015). In line with this, glycogen levels were found to increase with anesthesia (Morgenthaler et al., 2006) and decrease during somatosensory (Swanson et al., 1992) and visual (Dienel et al., 2007a) stimulation. However, no change in brain glycogen level was measured during visual stimulation in humans (Oz et al., 2007). While glycogen-derived lactate has been demonstrated to have a pivotal role in memory formation and consolidation (Gibbs and Hertz, 2005; Suzuki et al., 2011; Boury-Jamot et al., 2016), learning mechanism and synaptic strength (Duran et al., 2013), and neuronal function (Tekköl et al., 2005), the role of glycogen is unlikely limited to fuel neuronal metabolism. Recently, astrocytic glycogenolysis was shown to provide energy to sustain glutamatergic neurotransmission (i.e., glutamate uptake and release; Sickmann et al., 2009). Glycogen might act as a substrate for *de novo* formation of glutamate (Gibbs et al., 2007) and glycogen-derived energy might be required over glucose-derived energy for pyruvate carboxylation (Sickmann et al., 2012),

suggesting that astrocytic glycogen metabolism might be crucial to maintain proper brain function.

## CONCLUSION

While the essential role of astrocytes to cerebral function is now widely accepted, quantitative assessment of their actual contribution to energy metabolism has been missing, notably because the methodologies did not allow differentiating between neurons and astrocytes. Direct <sup>13</sup>C MRS along with advanced metabolic modeling can provide measurements of both neuronal and glial metabolism in specific brain regions and under various activation states. In this context, new data indicate that the rate of astrocytic metabolism is about half of that in neurons, and can be activated by sensory stimulation and that the astrocytic response amplitude can be, in absolute terms, as large as in neurons, suggesting that the changes in ATP requirements associated with the glutamate-glutamine cycle are coupled with the ATP produced by glucose oxidation in both compartments.

Increase in neuronal metabolism likely supports neurotransmission-associated functions, such as restoration of ion gradients caused by action potentials, post-synaptic currents, and transport of glutamate into vesicles. Adaptation of glial metabolism also provides energy for neurotransmission besides housekeeping tasks, likely fueling the production and action of modulators of neuronal activity and of synaptic plasticity, supply of antioxidant molecules and neurotrophic factors that are necessary for adequate brain function, and regulation of blood flow and volume. Astrocytes are moreover important source of glycogen that can be used specifically for neurotransmission support.

Progress in MR detection methods of <sup>1</sup>H and non-<sup>1</sup>H nuclei is a promising direction for more detailed and complete metabolic dataset acquisition. While this provides insights into cellular function *in vivo*, it also requires improvement of current metabolic models describing best energy metabolism. Simultaneous acquisition of other types of data, such as electrical activity and blood flow, might contribute to more precise characterization of the coupling between brain function and energy metabolism by MRS.

## AUTHOR CONTRIBUTIONS

SS and JD wrote the manuscript. RG revised the manuscript.

## ACKNOWLEDGMENTS

The authors' research is supported by the Swiss National Science Foundation (148250 to JD and 149983 to RG); the National Competence Center in Biomedical Imaging (NCCBI); and by Centre d'Imagerie BioMédicale (CIBM) of the UNIL, UNIGE, HUG, CHUV, EPFL, and the Leenaards and Jeantet Foundations.

## REFERENCES

- Abe, K., and Kimura, H. (1996). The possible role of hydrogen sulfide as an endogenous neuromodulator. *J. Neurosci.* 16, 1066–1071.
- Acuña, A., Esparza, M., Kramm, C., Beltrán, F., Parra, A., Cepeda, C., et al. (2013). A failure in energy metabolism and antioxidant uptake precede symptoms of Huntington's disease in mice. *Nat. Commun.* 4, 2917. doi: 10.1038/ncomms3917
- Almeida, A., Moncada, S., and Bolaños, J. (2004). Nitric oxide switches on glycolysis through the AMP protein kinase and 6-phosphofructo-2-kinase pathway. *Nat. Cell Biol.* 6, 45–51. doi: 10.1038/ncb1080
- Ashrafi, G., Wu, Z., Farrell, R. G., and Ryan, T. A. (2017). GLUT4 mobilization supports energetic demands of active synapses. *Neuron* 93, 606–615. doi: 10.1016/j.neuron.2016.12.020
- Attwell, D., Buchan, A., Charpkas, S., Lauritzen, M., Macvicar, B., and Newman, E. (2010). Glial and neuronal control of brain blood flow. *Nature* 468, 232–243. doi: 10.1038/nature09613
- Attwell, D., and Laughlin, S. (2001). An energy budget for signaling in the grey matter of the brain. *J. Cereb. Blood Flow Metab.* 21, 1133–1145. doi: 10.1097/00004647-200110000-00001
- Bakken, I., Sonnewald, U., Clark, J., and Bates, T. (1997). [ $U-^{13}\text{C}$ ]glutamate metabolism in rat brain mitochondria reveals malic enzyme activity. *Neuroreport* 8, 1567–1570. doi: 10.1097/00001756-199705060-00004
- Barros, L., Bittner, C., Loaiza, A., and Porras, O. (2007). A quantitative overview of glucose dynamics in the glovascular unit. *Glia* 55, 1222–1237. doi: 10.1002/glia.20375
- Barros, L., and Deitmer, J. (2010). Glucose and lactate supply to the synapse. *Brain Res. Rev.* 63, 149–159. doi: 10.1016/j.brainresrev.2009.10.002
- Bastiaansen, J., Cheng, T., Lei, H., Gruetter, R., and Comment, A. (2015). Direct noninvasive estimation of myocardial tricarboxylic acid cycle flux *in vivo* using hyperpolarized  $^{13}\text{C}$  magnetic resonance. *J. Mol. Cell Cardiol.* 87, 129–137. doi: 10.1016/j.yjmcc.2015.08.012
- Bastiaansen, J., Cheng, T., Mishkovsky, M., Duarte, J. M. N., Comment, A., and Gruetter, R. (2013). *In vivo* enzymatic activity of acetylCoA synthetase in skeletal muscle revealed by  $^{13}\text{C}$  turnover from hyperpolarized [ $1-^{13}\text{C}$ ]acetate to [ $1-^{13}\text{C}$ ]acetyl carnitine. *Biochim. Biophys. Acta* 1830, 4171–4178. doi: 10.1016/j.bbagen.2013.03.023
- Bazargani, N., and Attwell, D. (2016). Astrocyte calcium signaling: the third wave. *Nat. Neurosci.* 19, 182–189. doi: 10.1038/nn.4201
- Bednářík, P., Tkáč, I., Giove, F., DiNuzzo, M., Deelchand, D. K., Emir, U., et al. (2015). Neurochemical and BOLD responses during neuronal activation measured in the human visual cortex at 7 Tesla. *J. Cereb. Blood Flow Metab.* 35, 601–610. doi: 10.1038/jcbfm.2014.233
- Bergersen, L., Rafiki, A., and Ottersen, O. (2002). Immunogold cytochemistry identifies specialized membrane domains for monocarboxylate transport in the central nervous system. *Neurochem. Res.* 27, 89–96. doi: 10.1023/A:1014806723147
- Biesecker, K. R., Srienc, A. I., Shimoda, A. M., Bergles, D. E., Kofuji, P., and Newman, E. A. (2016). Glial cell calcium signalling mediates capillary regulation of blood flow in the retina. *J. Neurosci.* 36, 9435–9445. doi: 10.1523/JNEUROSCI.1782-16.2016
- Bittner, C., Valdebenito, R., Ruminot, I., Loaiza, A., Larenas, V., Sotelo-Hitschfeld, T., et al. (2011). Fast and reversible stimulation of astrocytic glycolysis by  $K^+$  and a delayed and persistent effect of glutamate. *J. Neurosci.* 31, 4709–4713. doi: 10.1523/JNEUROSCI.5311-10.2011
- Blood, A. B., Hunter, C. J., and Power, G. G. (2003). Adenosine mediates decreased cerebral metabolic rate and increased cerebral blood flow during acute moderate hypoxia in the near-term fetal sheep. *J. Physiol.* 553, 935–945. doi: 10.1113/jphysiol.2003.047928
- Bockaert, J., Pin, J., and Fagni, L. (1993). Metabotropic glutamate receptors: an original family of G protein-coupled receptors. *Fundam. Clin. Pharmacol.* 7, 473–485. doi: 10.1111/j.1472-8206.1993.tb00252.x
- Bolaños, J., Almeida, A., and Moncada, S. (2010). Glycolysis: a bioenergetic or a survival pathway? *Trends Biochem. Sci.* 35, 145–149. doi: 10.1016/j.tibs.2009.10.006
- Borst, P., and Elferink, R. (2002). Mammalian ABC transporters in health and disease. *Annu. Rev. Biochem.* 71, 537–592. doi: 10.1146/annurev.biochem.71.102301.093055
- Boury-Jamot, B., Carrard, A., Martin, J., Halfon, O., Magistretti, P., and Bourtrel, B. (2016). Disrupting astrocyte-neuron lactate transfer persistently reduces conditioned responses to cocaine. *Mol. Psychiatry* 21, 1070–1076. doi: 10.1038/mp.2015.157
- Bouzier, A., Thiaudiere, E., Biran, M., Rouland, R., Canioni, P., and Merle, M. (2000). The metabolism of [ $3-^{13}\text{C}$ ]lactate in the rat brain is specific of a pyruvate carboxylase-deprived compartment. *J. Neurochem.* 75, 480–486. doi: 10.1046/j.1471-4159.2000.0750480.x
- Bouzier-Sore, A., and Bolaños, J. (2015). Uncertainties in pentose-phosphate pathway flux assessment underestimate its contribution to neuronal glucose consumption: relevance for neurodegeneration and aging. *Front. Aging Neurosci.* 7:89. doi: 10.3389/fnagi.2015.00089
- Boveris, A., and Chance, B. (1973). The mitochondrial generation of hydrogen peroxide. General properties and effect of hyperbaric oxygen. *Biochem. J.* 134, 707–716. doi: 10.1042/bj1340707
- Buerk, D., Ances, B., Greenberg, J., and Detre, J. (2003). Temporal dynamics of brain tissue nitric oxide during functional forepaw stimulation in rats. *Neuroimage* 18, 1–9. doi: 10.1006/nimg.2002.1314
- Buxton, R. (2010). Interpreting oxygenation-based neuroimaging signals: the importance and the challenge of understanding brain oxygen metabolism. *Front. Neuroenergetics* 2:8. doi: 10.3389/fnene.2010.00008
- Cerdan, S., Künecke, B., and Seelig, J. (1990). Cerebral metabolism of [ $1,2-^{13}\text{C}_2$ ]acetate as detected by *in vivo* and *in vitro*  $^{13}\text{C}$  NMR. *J. Biol. Chem.* 265, 12916–12926.
- Chaudhry, F., Reimer, R., Krizaj, D., Barber, D., Storm-Mathisen, J., Copenhagen, D., et al. (1999). Molecular analysis of system N suggests novel physiological roles in nitrogen metabolism and synaptic transmission. *Cell* 99, 769–780. doi: 10.1016/S0092-8674(00)81674-8
- Chaudhry, F., Schmitz, D., Reimer, R., Larsson, P., Gray, A., Nicoll, R., et al. (2002). Glutamine uptake by neurons: interaction of protons with system a transporters. *J. Neurosci.* 22, 62–72. Available online at: <http://www.jneurosci.org/content/22/1/62/tab-article-info>
- Cheung, G., Chever, O., and Rouach, N. (2014). Connexons and pannexons: newcomers in neurophysiology. *Front. Cell Neurosci.* 8:348. doi: 10.3389/fncel.2014.00348
- Choi, I., Lei, H., and Gruetter, R. (2002). Effect of deep pentobarbital anesthesia on neurotransmitter metabolism *in vivo*: on the correlation of total glucose consumption with glutamatergic action. *J. Cereb. Blood Flow Metab.* 22, 1343–1351. doi: 10.1097/01.WCB.0000040945.89393.46
- Comment, A. (2016). Dissolution DNP for *in vivo* preclinical studies. *J. Magn. Reson.* 264, 39–48. doi: 10.1016/j.jmr.2015.12.027
- Cornell-Bell, A., Thomas, P., and Smith, S. (1990). The excitatory neurotransmitter glutamate causes filopodia formation in cultured hippocampal astrocytes. *Glia* 3, 322–334. doi: 10.1002/glia.440030503
- Covarrubias-Pinto, A., Acuña, A., Beltrán, F., Torres-Díaz, L., and Castro, M. (2015). Old things new view: ascorbic acid protects the brain in neurodegenerative disorders. *Int. J. Mol. Sci.* 16, 28194–28217. doi: 10.3390/ijms161226095
- Cruz, F., and Cerdan, S. (1999). Quantitative  $^{13}\text{C}$  NMR studies of metabolic compartmentation in the adult mammalian brain. *NMR Biomed.* 12, 451–462.
- Cruz, F., Scott, S., Barroso, I., Santisteban, P., and Cerdán, S. (1998). Ontogeny and cellular localization of the pyruvate recycling system in rat brain. *J. Neurochem.* 70, 2613–2619. doi: 10.1046/j.1471-4159.1998.70062613.x
- Cruz, N., Lasater, A., Zielke, H., and Dienel, G. A. (2005). Activation of astrocytes in brain of conscious rats during acoustic stimulation: acetate utilization in working brain. *J. Neurochem.* 92, 934–947. doi: 10.1111/j.1471-4159.2004.02935.x
- Deelchand, D. K., Nelson, C., Shestov, A., Üğurbil, K., and Henry, P. G. (2009). Simultaneous measurement of neuronal and glial metabolism in rat brain *in vivo* using co-infusion of [ $1,6-^{13}\text{C}_2$ ]glucose and [ $1,2-^{13}\text{C}_2$ ]acetate. *J. Magn. Reson.* 196, 157–163. doi: 10.1016/j.jmr.2008.11.001
- de Graaf, R. A. (1998). *In vivo NMR Spectroscopy: Principles and Techniques*. England: Wiley.
- de Graaf, R. A., Mason, G. F., Patel, A. B., and Rothman, D. L. (2003). *In vivo*  $^1\text{H}-[^{13}\text{C}]$ -NMR spectroscopy of cerebral metabolism. *NMR Biomed.* 16, 339–357. doi: 10.1002/nbm.847
- de Graaf, R. A., Mason, G. F., Patel, A. B., Rothman, D. L., and Behar, K. L. (2004). Regional glucose metabolism and glutamatergic neurotransmission

- in rat brain *in vivo*. *Proc. Natl. Acad. Sci. U.S.A.* 101, 12700–12705. doi: 10.1073/pnas.0405065101
- Dehghani, M., Lanz, B., Duarte, J. M. N., Kunz, N., and Gruetter, R. (2016). Refined analysis of brain energy metabolism using *in vivo* dynamic enrichment of  $^{13}\text{C}$  multiplets. *ASN Neuro*. 8:2. doi: 10.1177/1759091416632342
- Denton, R. (2009). Regulation of mitochondrial dehydrogenases by calcium ions. *Biochim. Biophys. Acta* 1787, 1309–1316. doi: 10.1016/j.bbabiobio.2009.01.005
- Derouiche, A., and Frotscher, M. (1991). Astroglial processes around identified glutamatergic synapses contain glutamine synthetase: evidence for transmitter degradation. *Brain Res.* 552, 346–350. doi: 10.1016/0006-8993(91)90103-3
- Derouiche, A., Haseleu, J., and Korf, H. (2015). Fine astrocyte processes contain very small mitochondria: glial oxidative capability may fuel transmitter metabolism. *Neurochem. Res.* 40, 2402–2413. doi: 10.1007/s11064-015-1563-8
- Desagher, S., Glowinski, J., and Premont, J. (1996). Astrocytes protect neurons from hydrogen peroxide toxicity. *J. Neurosci.* 16, 2553–2562.
- Dienel, G. A. (2012). Brain lactate metabolism: the discoveries and the controversies. *J. Cereb. Blood Flow Metab.* 32, 1107–1138. doi: 10.1038/jcbfm.2011.175
- Dienel, G. A., Ball, K., and Cruz, N. (2007a). A glycogen phosphorylase inhibitor selectively enhances local rates of glucose utilization in brain during sensory stimulation of conscious rats: implications for glycogen turnover. *J. Neurochem.* 102, 466–478. doi: 10.1111/j.1471-4159.2007.04595.x
- Dienel, G. A., Schmidt, K., and Cruz, N. (2007b). Astrocyte activation *in vivo* during graded photic stimulation. *J. Neurochem.* 103, 1506–1522. doi: 10.1111/j.1471-4159.2007.04859.x
- DiNuzzo, M., Giove, F., Maraviglia, B., and Mangia, S. (2017). Computational flux balance analysis predicts that stimulation of energy metabolism in astrocytes and their metabolic interactions with neurons depend on uptake of K<sup>+</sup> rather than glutamate. *Neurochem. Res.* 42, 202–216 doi: 10.1007/s11064-016-2048-0
- Dringen, R., and Hirrlinger, J. (2003). Glutathione pathways in the brain. *Biol. Chem.* 384, 505–516. doi: 10.1515/BC.2003.059
- Dringen, R., Pfeiffer, B., and Hamprecht, B. (1999). Synthesis of the antioxidant glutathione in neurons: supply by astrocytes of CysGly as precursor for neuronal glutathione. *J. Neurosci.* 19, 562–569.
- Dringen, R., Schmoll, D., Cesár, M., and Hamprecht, B. (1993). Incorporation of radioactivity from [ $^{14}\text{C}$ ]lactate into the glycogen of cultured mouse astroglial cells. Evidence for gluconeogenesis in brain cells. *Biol. Chem. Hoppe Seyler* 374, 343–347. doi: 10.1515/bchm3.1993.374.1-6.343
- Duarte, J. M. N., Cunha, R. A., and Carvalho, R. A. (2016). Adenosine A<sub>1</sub> receptors control the metabolic recovery after hypoxia in rat hippocampal slices. *J. Neurochem.* 136, 947–957. doi: 10.1111/jnc.13512
- Duarte, J. M. N., Girault, F.-M., and Gruetter, R. (2015). Brain energy metabolism measured by  $^{13}\text{C}$  magnetic resonance spectroscopy *in vivo* upon infusion of [3- $^{13}\text{C}$ ]lactate. *J. Neurosci. Res.* 93, 1009–1018. doi: 10.1002/jnr.23531
- Duarte, J. M. N., and Gruetter, R. (2013). Glutamatergic and GABAergic energy metabolism measured in the rat brain by  $^{13}\text{C}$  NMR spectroscopy at 14.1 T. *J. Neurochem.* 126, 579–590. doi: 10.1111/jnc.12333
- Duarte, J. M. N., Lanz, B., and Gruetter, R. (2011). Compartmentalized Cerebral Metabolism of [1,6- $^{13}\text{C}$ ]Glucose Determined by *in vivo*  $^{13}\text{C}$  NMR Spectroscopy at 14.1 T. *Front. Neuroenergetics* 3:3. doi: 10.3389/fnene.2011.00003
- Duarte, J. M. N., Lei, H., Mlynárik, V., and Gruetter, R. (2012). The neurochemical profile quantified by *in vivo*  $^1\text{H}$  NMR spectroscopy. *Neuroimage* 61, 342–362. doi: 10.1016/j.neuroimage.2011.12.038
- Duarte, J. M. N., Morgenthaler, F., Lei, H., Poitry-Yamate, C., and Gruetter, R. (2009). Steady-state brain glucose transport kinetics re-evaluated with a four-state conformational model. *Front. Neuroenergetics* 1:6. doi: 10.3389/neuro.14.006.2009
- Duran, J., Saez, I., Gruart, A., Guinovart, J., and Delgado-García, J. (2013). Impairment in long-term memory formation and learning-dependent synaptic plasticity in mice lacking glycogen synthase in the brain. *J. Cereb. Blood Flow Metab.* 33, 550–556. doi: 10.1038/jcbfm.2012.200
- El Idrissi, A., and Trenkner, E. (1999). Growth factors and taurine protect against excitotoxicity by stabilizing calcium homeostasis and energy metabolism. *J. Neurosci.* 19, 9459–9468.
- Erb, L., and Weisman, G. (2012). Coupling of P2Y receptors to G proteins and other signaling pathways. *Wiley Interdiscip. Rev. Membr. Transp. Signal.* 1, 789–803. doi: 10.1002/wmts.62
- Eriksson, G., Peterson, A., Iverfeldt, K., and Walum, E. (1995). Sodium-dependent glutamate uptake as an activator of oxidative metabolism in primary astrocyte cultures from newborn rat. *Glia* 15, 152–156. doi: 10.1002/glia.440150207
- Fresu, L., Dehpour, A., Genazzani, A., Carafoli, E., and Guerini, D. (1999). Plasma membrane calcium ATPase isoforms in astrocytes. *Glia* 28, 150–155.
- Gamberino, W., Berkich, D., Lynch, C., Xu, B., and LaNoue, K. (1997). Role of pyruvate carboxylase in facilitation of synthesis of glutamate and glutamine in cultured astrocytes. *J. Neurochem.* 69, 2312–2325. doi: 10.1046/j.1471-4159.1997.69062312.x
- Genda, E., Jackson, J., Sheldon, A., Locke, S., Greco, T., O'Donnell, J., et al. (2011). Co-compartmentalization of the astroglial glutamate transporter, GLT-1, with glycolytic enzymes and mitochondria. *J. Neurosci.* 31, 18275–18288. doi: 10.1523/JNEUROSCI.3305-11.2011
- Ghosh, A., Wyss, M., and Weber, B. (2013). Somatotopic astrocytic activity in the somatosensory cortex. *Glia* 61, 601–610. doi: 10.1002/glia.22458
- Gibbs, M., and Hertz, L. (2005). Importance of glutamate-generating metabolic pathways for memory consolidation in chicks. *J. Neurosci. Res.* 81, 293–300. doi: 10.1002/jnr.20548
- Gibbs, M., Lloyd, H., Santa, T., and Hertz, L. (2007). Glycogen is a preferred glutamate precursor during learning in 1-day-old chick: biochemical and behavioral evidence. *J. Neurosci. Res.* 85, 3326–3333. doi: 10.1002/jnr.21307
- Goda, Y. (1997). SNAREs and regulated vesicle exocytosis. *Proc. Natl. Acad. Sci. U.S.A.* 94, 769–772. doi: 10.1073/pnas.94.3.769
- Golgi, C. (1886). *Sulla Fina Anatomia Degli Organi Centrali del Sistema Nervoso*. Milano: Hoepli.
- Gordon, G., Choi, H., Rungta, R., Ellis-Davies, G., and MacVicar, B. (2008). Brain metabolism dictates the polarity of astrocyte control over arterioles. *Nature* 456, 745–749. doi: 10.1038/nature07525
- Görlach, A., Bertram, K., Hudecová, S., and Krizanová, O. (2015). Calcium and ROS: a mutual interplay. *Redox. Biol.* 6, 260–271. doi: 10.1016/j.redox.2015.08.010
- Gruetter, R. (2002). *In vivo*  $^{13}\text{C}$  NMR studies of compartmentalized cerebral carbohydrate metabolism. *Neurochem. Int.* 41, 143–154. doi: 10.1016/S0197-0186(02)00034-7
- Gruetter, R., Novotny, E., Boulware, S. D., Mason, G. F., Rothman, D. L., Shulman, G. I., et al. (1994). Localized  $^{13}\text{C}$  NMR spectroscopy in the human brain of amino acid labeling from D-[1- $^{13}\text{C}$ ]glucose. *J. Neurochem.* 63, 1377–1385. doi: 10.1046/j.1471-4159.1994.63041377.x
- Gruetter, R., Seaquist, E. R., Kim, S., and Ugurbil, K. (1998a). Localized *in vivo*  $^{13}\text{C}$ -NMR of glutamate metabolism in the human brain: initial results at 4 tesla. *Dev. Neurosci.* 20, 380–388. doi: 10.1159/000017334
- Gruetter, R., Seaquist, E. R., and Ugurbil, K. (2001). A mathematical model of compartmentalized neurotransmitter metabolism in the human brain. *Am. J. Physiol. Endocrinol. Metab.* 281, E100–E112. Available online at: <http://ajpendo.physiology.org/content/281/1/E100.article-info>
- Gruetter, R., Ugurbil, K., and Seaquist, E. R. (1998b). Steady-state cerebral glucose concentrations and transport in the human brain. *J. Neurochem.* 70, 397–408. doi: 10.1046/j.1471-4159.1998.70010397.x
- Haberg, A., Qu, H., Haraldseth, O., Unsgård, G., and Sonnewald, U. (2000). *In vivo* effects of adenosine A<sub>1</sub> receptor agonist and antagonist on neuronal and astrocytic intermediary metabolism studied with *ex vivo*  $^{13}\text{C}$  NMR spectroscopy. *J. Neurochem.* 74, 327–333. doi: 10.1046/j.1471-4159.2000.0740327.x
- Hajek, I., Subbarao, K., and Hertz, L. (1996). Acute and chronic effects of potassium and noradrenaline on Na<sup>+</sup>,K<sup>+</sup>-ATPase activity in cultured mouse neurons and astrocytes. *Neurochem. Int.* 28, 335–342. doi: 10.1016/0197-0186(95)00081-X
- Halassa, M., Fellin, T., Takano, H., Dong, J., and Haydon, P. (2007). Synaptic islands defined by the territory of a single astrocyte. *J. Neurosci.* 27, 6473–6477. doi: 10.1523/JNEUROSCI.1419-07.2007
- Hamilton, N. B., Attwell, D., and Hall, C. N. (2010). Pericyte-mediated regulation of capillary diameter: a component of neurovascular coupling in health and disease. *Front. Neuroenergetics* 2:5. doi: 10.3389/fnene.2010.00005
- Hammer, J., Qu, H., Haberg, A., and Sonnewald, U. (2001). *In vivo* effects of adenosine A<sub>2</sub> receptor agonist and antagonist on neuronal and astrocytic intermediary metabolism studied with *ex vivo*  $^{13}\text{C}$  MR spectroscopy. *J. Neurochem.* 79, 885–892. doi: 10.1046/j.1471-4159.2001.00622.x
- Hancu, I., and Port, J. (2011). The case of the missing glutamine. *NMR Biomed.* 24, 529–535. doi: 10.1002/nbm.1620

- Henry, P. G., Adriany, G., Deelchand, D. K., Gruetter, R., Marjanska, M., Oz, G., et al. (2006). *In vivo*  $^{13}\text{C}$  NMR spectroscopy and metabolic modeling in the brain: a practical perspective. *Magn. Reson. Imaging* 24, 527–539. doi: 10.1016/j.mri.2006.01.003
- Henry, P. G., Lebon, V., Vaufrey, F., Brouillet, E., Hantraye, P., and Bloch, G. (2002). Decreased TCA cycle rate in the rat brain after acute 3-NP treatment measured by *in vivo*  $^1\text{H}$ - $[^{13}\text{C}]$  NMR spectroscopy. *J. Neurochem.* 82, 857–866. doi: 10.1046/j.jn.1471-4159.2002.01006.x
- Henry, P. G., Tkáč, I., and Gruetter, R. (2003).  $^1\text{H}$ -localized broadband  $^{13}\text{C}$  NMR spectroscopy of the rat brain *in vivo* at 9.4 T. *Magn. Reson. Med.* 50, 684–692. doi: 10.1002/mrm.10601
- Herrero-Mendez, A., Almeida, A., Fernández, E., Maestre, C., Moncada, S., and Bolaños, J. (2009). The bioenergetic and antioxidant status of neurons is controlled by continuous degradation of a key glycolytic enzyme by APC/C-Cdh1. *Nat. Cell Biol.* 11, 747–752. doi: 10.1038/ncb1881
- Hertz, L., and Dienel, G. A. (2002). Energy metabolism in the brain. *Int. Rev. Neurobiol.* 51, 1–102. doi: 10.1016/S0074-7742(02)51003-5
- Hertz, L., Peng, L., and Dienel, G. A. (2007). Energy metabolism in astrocytes: high rate of oxidative metabolism and spatiotemporal dependence on glycolysis/glycogenolysis. *J. Cereb. Blood Flow Metab.* 27, 219–249. doi: 10.1038/sj.jcbfm.9600343
- Hertz, L., Xu, J., Song, D., Du, T., Li, B., Yan, E., et al. (2015). Astrocytic glycogenolysis: mechanisms and functions. *Metab. Brain Dis.* 30, 317–333. doi: 10.1007/s11011-014-9536-1
- Honegger, P., and Pardo, B. (1999). Separate neuronal and glial  $\text{Na}^+$ ,  $\text{K}^+$ -ATPase isoforms regulate glucose utilization in response to membrane depolarization and elevated extracellular potassium. *J. Cereb. Blood Flow Metab.* 19, 1051–1059. doi: 10.1097/00004647-199909000-00013
- Howarth, C., Sutherland, B., Choi, H. B., Martin, C., Lind, B. L., Khennouf, L., et al. (2017). A critical role for astrocytes in hypercapnic vasodilation in brain. *J. Neurosci.* 37, 2403–2414. doi: 10.1523/JNEUROSCI.0005-16.2016
- Hyder, F., Chase, J., Behar, K. L., Mason, G. F., Siddeek, M., Rothman, D. L., et al. (1996). Increased tricarboxylic acid cycle flux in rat brain during forepaw stimulation detected with  $^1\text{H}$ - $[^{13}\text{C}]$ NMR. *Proc. Natl. Acad. Sci. U.S.A.* 93, 7612–7617. doi: 10.1073/pnas.93.15.7612
- Hyder, F., Rothman, D. L., Mason, G. F., Rangarajan, A., Behar, K. L., and Shulman, R. G. (1997). Oxidative glucose metabolism in rat brain during single forepaw stimulation: a spatially localized  $^1\text{H}$ - $[^{13}\text{C}]$  nuclear magnetic resonance study. *J. Cereb. Blood. Flow Metab.* 17, 1040–1047. doi: 10.1097/00004647-199710000-00005
- Iadecola, C. (2004). Neurovascular regulation in the normal brain and in Alzheimer's disease. *Nat. Rev. Neurosci.* 5, 347–360. doi: 10.1038/nrn1387
- Iadecola, C., and Nedergaard, M. (2007). Glial regulation of the cerebral microvasculature. *Nat. Neurosci.* 10, 1369–1376. doi: 10.1038/nn2003
- Ido, Y., Chang, K., Woolsey, T., and Williamson, J. (2001). NADH: sensor of blood flow need in brain, muscle, and other tissues. *FASEB J.* 15, 1419–1421. doi: 10.1096/fj.00-0652fje
- Ikebuchi, Y., Masumoto, N., Tasaka, K., Koike, K., Kasahara, K., Miyake, A., et al. (1991). Superoxide anion increases intracellular pH, intracellular free calcium, and arachidonate release in human amniotic cells. *J. Biol. Chem.* 266, 13233–13237.
- Iliff, J., D'Ambrosio, R., Ngai, A., and Winn, H. (2003). Adenosine receptors mediate glutamate-evoked arteriolar dilation in the rat cerebral cortex. *Am. J. Physiol. Heart. Circ. Physiol.* 284, H1631–H1637. doi: 10.1152/ajpheart.00909.2002
- Jackson, J., O'Donnell, J., Takano, H., Coulter, D., and Robinson, M. (2014). Neuronal activity and glutamate uptake decrease mitochondrial mobility in astrocytes and position mitochondria near glutamate transporters. *J. Neurosci.* 34, 1613–1624. doi: 10.1523/JNEUROSCI.3510-13.2014
- Jackson, J., and Robinson, M. (2015). Reciprocal regulation of mitochondrial dynamics and calcium signaling in astrocyte processes. *J. Neurosci.* 35, 15199–15213. doi: 10.1523/JNEUROSCI.2049-15.2015
- Jackson, P., Morrison, R., and Strange, K. (1994). The volume-sensitive organic osmolyte-anion channel VSOAC is regulated by nonhydrolytic ATP binding. *Am. J. Physiol.* 267(5 Pt 1), C1203–C1209.
- Jimenez-Blasco, D., Santofimia-Castaño, P., Gonzalez, A., Almeida, A., and Bolaños, J. (2015). Astrocyte NMDA receptors' activity sustains neuronal survival through a Cdk5-Nrf2 pathway. *Cell Death Differ.* 22, 1877–1889. doi: 10.1038/cdd.2015.49
- Joseph, S., Buchakjian, M., and Dubyk, G. (2003). Colocalization of ATP release sites and ecto-ATPase activity at the extracellular surface of human astrocytes. *J. Biol. Chem.* 278, 23331–23342. doi: 10.1074/jbc.M302680200
- Just, N., Xin, L., Frenkel, H., and Gruetter, R. (2013). Characterization of sustained BOLD activation in the rat barrel cortex and neurochemical consequences. *Neuroimage* 74, 343–351. doi: 10.1016/j.neuroimage.2013.02.042
- Kacem, K., Lacombe, P., Seylaz, J., and Bonvento, G. (1998). Structural organization of the perivascular astrocyte endfeet and their relationship with the endothelial glucose transporter: a confocal microscopy study. *Glia* 23, 1–10.
- Karaca, M., Frigerio, F., Migrenne, S., Martin-Levilain, J., Skyyt, D., Pajecza, K., et al. (2015). GDH-dependent glutamate oxidation in the brain dictates peripheral energy substrate distribution. *Cell Rep.* 13, 365–375. doi: 10.1016/j.celrep.2015.09.003
- Kasischke, K., Vishwasrao, H., Fisher, P., Zipfel, W., and Webb, W. (2004). Neural activity triggers neuronal oxidative metabolism followed by astrocytic glycolysis. *Science* 305, 99–103. doi: 10.1126/science.1096485
- Kettenmann, H., and Verkhratsky, A. (2008). Neuroglia: the 150 years after. *Trends Neurosci.* 31, 653–659. doi: 10.1016/j.tins.2008.09.003
- Koehler, R., Gebremedhin, D., and Harder, D. (2006). Role of astrocytes in cerebrovascular regulation. *J. Appl. Physiol.* 100, 307–317. doi: 10.1152/japplphysiol.00938.2005
- Korn, E., Carlier, M., and Pantalon, D. (1987). Actin polymerization and ATP hydrolysis. *Science* 238, 638–644. doi: 10.1126/science.3672117
- Kuge, Y., Yajima, K., Kawashima, H., Yamazaki, H., Hashimoto, N., and Miyake, Y. (1995). Brain uptake and metabolism of  $[1-^{11}\text{C}]$ octanoate in rats: pharmacokinetic basis for its application as a radiopharmaceutical for studying brain fatty acid metabolism. *Ann. Nucl. Med.* 9, 137–142. doi: 10.1007/BF03165040
- Künnecke, B., Cerdan, S., and Seelig, J. (1993). Cerebral metabolism of  $[1,2-^{13}\text{C}_2]$ glucose and  $[\text{U}-13\text{C}4]3$ -hydroxybutyrate in rat brain as detected by  $^{13}\text{C}$  NMR spectroscopy. *NMR Biomed.* 6, 264–277. doi: 10.1002/nbm.1940060406
- Kuschinsky, W., and Wahl, M. (1978). Local chemical and neurogenic regulation of cerebral vascular resistance. *Physiol. Rev.* 58, 656–689.
- Lanz, B., Gruetter, R., and Duarte, J. M. N. (2013). Metabolic flux and compartmentation analysis in the brain *in vivo*. *Front. Endocrinol.* 4:156. doi: 10.3389/fendo.2013.00156
- Lanz, B., Xin, L., Millet, P., and Gruetter, R. (2014). *In vivo* quantification of neuroglial metabolism and glial glutamate concentration using  $^1\text{H}$ - $[^{13}\text{C}]$  MRS at 14.1T. *J. Neurochem.* 128, 125–139. doi: 10.1111/jnc.12479
- Laranjinha, J., Santos, R., Lourenço, C., Ledo, A., and Barbosa, R. (2012). Nitric oxide signaling in the brain: translation of dynamics into respiration control and neurovascular coupling. *Ann. N. Y. Acad. Sci.* 1259, 10–18. doi: 10.1111/j.1749-6632.2012.06582.x
- Lebon, V., Petersen, K., Cline, G., Shen, J., Mason, G. F., Dufour, S., et al. (2002). Astroglial contribution to brain energy metabolism in humans revealed by  $^{13}\text{C}$  nuclear magnetic resonance spectroscopy: elucidation of the dominant pathway for neurotransmitter glutamate repletion and measurement of astrocytic oxidative metabolism. *J. Neurosci.* 22, 1523–1531. Available online at: <http://www.jneurosci.org/content/22/5/1523/tab-article-info>
- Le Clainche, C., Pantalon, D., and Carlier, M. F. (2003). ATP hydrolysis on actin-related protein 2/3 complex causes debranching of dendritic actin arrays. *Proc. Natl. Acad. Sci. U.S.A.* 100, 6337–6342. doi: 10.1073/pnas.1130513100
- Lee, M., Schwab, C., Yu, S., McGeer, E., and McGeer, P. (2009). Astrocytes produce the antiinflammatory and neuroprotective agent hydrogen sulfide. *Neurobiol. Aging* 30, 1523–1534. doi: 10.1016/j.neurobiolaging.2009.06.001
- Lee, W., Hawkins, R., Viña, J., and Peterson, D. (1998). Glutamine transport by the blood-brain barrier: a possible mechanism for nitrogen removal. *Am. J. Physiol.* 274(4 Pt 1), C1101–C1107.
- Lerchundi, R., Fernández-Moncada, I., Contreras-Baeza, Y., Sotelo-Hitschfeld, T., Mächler, P., Wyss, M., et al. (2015).  $\text{NH}_4^+$  triggers the release of astrocytic lactate via mitochondrial pyruvate shunting. *Proc. Natl. Acad. Sci. U.S.A.* 112, 11090–11095. doi: 10.1073/pnas.1508259112
- Li, S., An, L., Yu, S., Ferraris Araneta, M., Johnson, C., Wang, S., et al. (2016).  $^{13}\text{C}$  MRS of human brain at 7 Tesla using  $[2-^{13}\text{C}]$ glucose infusion and low power broadband stochastic proton decoupling. *Magn. Reson. Med.* 75, 954–961. doi: 10.1002/mrm.25721

- Lin, A., Fox, P., Yang, Y., Lu, H., Tan, L., and Gao, J. (2009). Time-dependent correlation of cerebral blood flow with oxygen metabolism in activated human visual cortex as measured by fMRI. *Neuroimage* 44, 16–22. doi: 10.1016/j.neuroimage.2008.08.029
- Lin, Y., Stephenson, M., Xin, L., Napolitano, A., and Morris, P. (2012). Investigating the metabolic changes due to visual stimulation using functional proton magnetic resonance spectroscopy at 7 T. *J. Cereb. Blood Flow Metab.* 32, 1484–1495. doi: 10.1038/jcbfm.2012.33
- Lind, B., Brazhe, A., Jessen, S., Tan, F., and Lauritzen, M. (2013). Rapid stimulus-evoked astrocyte  $\text{Ca}^{2+}$  elevations and hemodynamic responses in mouse somatosensory cortex *in vivo*. *Proc. Natl. Acad. Sci. U.S.A.* 110, E4678–E4687. doi: 10.1073/pnas.1310065110
- Lourenço, C., Santos, R., Barbosa, R., Cadenas, E., Radi, R., and Laranjinha, J. (2014). Neurovascular coupling in hippocampus is mediated via diffusion by neuronal-derived nitric oxide. *Free Radic. Biol. Med.* 73, 421–429. doi: 10.1016/j.freeradbiomed.2014.05.021
- Lovatt, D., Sonnewald, U., Waagepetersen, H., Schousboe, A., He, W., Lin, J., et al. (2007). The transcriptome and metabolic gene signature of protoplasmic astrocytes in the adult murine cortex. *J. Neurosci.* 27, 12255–12266. doi: 10.1523/JNEUROSCI.3404-07.2007
- Lundgaard, I., Li, B., Xie, L., Kang, H., Sanggaard, S., Haswell, J., et al. (2015). Direct neuronal glucose uptake heralds activity-dependent increases in cerebral metabolism. *Nat. Commun.* 6, 6807. doi: 10.1038/ncomms7807
- Mächler, P., Wyss, M., Elsaied, M., Stobart, J., Gutierrez, R., von Faber-Castell, A., et al. (2016). *In vivo* evidence for a lactate gradient from astrocytes to neurons. *Cell Metab.* 23, 94–102. doi: 10.1016/j.cmet.2015.10.010
- Maher, F., Davies-Hill, T., and Simpson, I. A. (1996). Substrate specificity and kinetic parameters of GLUT3 in rat cerebellar granule neurons. *Biochem. J.* 315(Pt 3), 827–831. doi: 10.1042/bj3150827
- Maher, F., Vannucci, S. J., and Simpson, I. A. (1994). Glucose transporter proteins in brain. *FASEB J.* 8, 1003–1011.
- Maher, F., Vannucci, S. J., Takeda, J., and Simpson, I. A. (1992). Expression of mouse-GLUT3 and human-GLUT3 glucose transporter proteins in brain. *Biochem. Biophys. Res. Commun.* 182, 703–711. doi: 10.1016/0006-291X(92)91789-S
- Makar, T., Nedergaard, M., Preuss, A., Gelbard, A., Perumal, A., and Cooper, A. (1994). Vitamin, E, ascorbate, glutathione, glutathione disulfide, and enzymes of glutathione metabolism in cultures of chick astrocytes and neurons: evidence that astrocytes play an important role in antioxidative processes in the brain. *J. Neurochem.* 62, 45–53. doi: 10.1046/j.1471-4159.1994.620045.x
- Mangia, S., Tkác, I., Gruetter, R., Van de Moortele, P., Maraviglia, B., and Ügurbil, K. (2007). Sustained neuronal activation raises oxidative metabolism to a new steady-state level: evidence from  $^1\text{H}$  NMR spectroscopy in the human visual cortex. *J. Cereb. Blood Flow Metab.* 27, 1055–1063. doi: 10.1038/sj.jcbfm.9600401
- Masamoto, K., and Kanno, I. (2012). Anesthesia and the quantitative evaluation of neurovascular coupling. *J. Cereb. Blood Flow Metab.* 32, 1233–1247. doi: 10.1038/jcbfm.2012.50
- Mason, G. F., Rothman, D. L., Behar, K. L., and Shulman, R. G. (1992). NMR determination of the TCA cycle rate and alpha-ketoglutarate/glutamate exchange rate in rat brain. *J. Cereb. Blood Flow Metab.* 12, 434–447. doi: 10.1038/jcbfm.1992.61
- Mathiisen, T., Lehre, K., Danbolt, N., and Ottersen, O. (2010). The perivascular astroglial sheath provides a complete covering of the brain microvessels: an electron microscopic 3D reconstruction. *Glia* 58, 1094–1103. doi: 10.1002/glia.20990
- McIlwain, H., Anguiano, G., and Cheshire, J. (1951). Electrical stimulation *in vitro* of the metabolism of glucose by mammalian cerebral cortex. *Biochem. J.* 50, 12–18. doi: 10.1042/bj0500012
- McKenna, M. (2007). The glutamate-glutamine cycle is not stoichiometric: fates of glutamate in brain. *J. Neurosci. Res.* 85, 3347–3358. doi: 10.1002/jnr.21444
- McKenna, M. (2013). Glutamate pays its own way in astrocytes. *Front. Endocrinol. (Lausanne)* 4:191. doi: 10.3389/fendo.2013.00191
- McKenna, M., Sonnewald, U., Huang, X., Stevenson, J., and Zielke, H. (1996). Exogenous glutamate concentration regulates the metabolic fate of glutamate in astrocytes. *J. Neurochem.* 66, 386–393. doi: 10.1046/j.1471-4159.1996.66010386.x
- Metea, M., and Newman, E. (2006). Glial cells dilate and constrict blood vessels: a mechanism of neurovascular coupling. *J. Neurosci.* 26, 2862–2870. doi: 10.1523/JNEUROSCI.4048-05.2006
- Mishkovsky, M., Comment, A., and Gruetter, R. (2012). *In vivo* detection of brain Krebs cycle intermediate by hyperpolarized magnetic resonance. *J. Cereb. Blood Flow Metab.* 32, 2108–2113. doi: 10.1038/jcbfm.2012.136
- Morgenthaler, F., Koski, D., Kraftsik, R., Henry, P. G., and Gruetter, R. (2006). Biochemical quantification of total brain glycogen concentration in rats under different glycemic states. *Neurochem. Int.* 48, 616–622. doi: 10.1016/j.neuint.2005.12.034
- Nagai, Y., Tsugane, M., Oka, J., and Kimura, H. (2004). Hydrogen sulfide induces calcium waves in astrocytes. *FASEB J.* 18, 557–559. doi: 10.1096/fj.03-1052fje
- Nedergaard, M., Ransom, B., and Goldman, S. (2003). New roles for astrocytes: redefining the functional architecture of the brain. *Trends Neurosci.* 26, 523–530. doi: 10.1016/j.tins.2003.08.008
- Newman, E. A. (2003). Glial cell inhibition of neurons by release of ATP. *J. Neurosci.* 23, 1659–1666. Available online at: <http://www.jneurosci.org/content/23/5/1659/tab-article-info>
- Nizar, K., Uhlirova, H., Tian, P., Saisan, P. A., Cheng, Q., Reznichenko, L., et al. (2013). *In vivo* stimulus-induced vasodilation occurs without  $\text{IP}_3$  receptor activation and may precede astrocytic calcium increase. *J. Neurosci.* 33, 8411–8422. doi: 10.1523/JNEUROSCI.3285-12.2013
- Ogawa, S., Tank, D., Menon, R., Ellermann, J., Kim, S., Merkle, H., et al. (1992). Intrinsic signal changes accompanying sensory stimulation: functional brain mapping with magnetic resonance imaging. *Proc. Natl. Acad. Sci. U.S.A.* 89, 5951–5955. doi: 10.1073/pnas.89.13.5951
- Ottersen, O., Zhang, N., and Walberg, F. (1992). Metabolic compartmentation of glutamate and glutamine: morphological evidence obtained by quantitative immunocytochemistry in rat cerebellum. *Neuroscience* 46, 519–534. doi: 10.1016/0306-4522(92)90141-N
- Oz, G., Berkich, D., Henry, P. G., Xu, Y., LaNoue, K., Hutson, S., et al. (2004). Neuroglial metabolism in the awake rat brain:  $\text{CO}_2$  fixation increases with brain activity. *J. Neurosci.* 24, 11273–11279. doi: 10.1523/JNEUROSCI.3564-04.2004
- Oz, G., DiNuzzo, M., Kumar, A., Moheet, A., and Seauquist, E. R. (2015). Revisiting glycogen content in the human brain. *Neurochem. Res.* 40, 2473–2481. doi: 10.1007/s11064-015-1664-4
- Oz, G., Seauquist, E. A., Kumar, A., Criego, A., Benedict, L., Rao, J., et al. (2007). Human brain glycogen content and metabolism: implications on its role in brain energy metabolism. *Am. J. Physiol. Endocrinol. Metab.* 292, E946–E951. doi: 10.1152/ajpendo.00424.2006
- Parpura, V., and Zorec, R. (2010). Gliotransmission: Exocytotic release from astrocytes. *Brain Res. Rev.* 63, 83–92. doi: 10.1016/j.brainresrev.2009.11.008
- Patel, A. B., Chowdhury, G. M., de Graaf, R. A., Rothman, D. L., Shulman, R. G., and Behar, K. L. (2005b). Cerebral pyruvate carboxylase flux is unaltered during bicuculline-seizures. *J. Neurosci. Res.* 79, 128–138. doi: 10.1002/jnr.20311
- Patel, A. B., de Graaf, R. A., Mason, G. F., Kanamatsu, T., Rothman, D. L., Shulman, R. G., et al. (2004). Glutamatergic neurotransmission and neuronal glucose oxidation are coupled during intense neuronal activation. *J. Cereb. Blood Flow Metab.* 24, 972–985. doi: 10.1097/01.WCB.0000126234.16188.71
- Patel, A. B., de Graaf, R. A., Mason, G. F., Rothman, D. L., Shulman, R. G., and Behar, K. L. (2005a). The contribution of GABA to glutamate/glutamine cycling and energy metabolism in the rat cortex *in vivo*. *Proc. Natl. Acad. Sci. U.S.A.* 102, 5588–5593. doi: 10.1073/pnas.0501703102
- Patel, A. B., de Graaf, R. A., Rothman, D. L., Behar, K. L., and Mason, G. F. (2010). Evaluation of cerebral acetate transport and metabolic rates in the rat brain *in vivo* using  $^1\text{H}-[^{13}\text{C}]$ -NMR. *J. Cereb. Blood Flow Metab.* 30, 1200–1213. doi: 10.1038/jcbfm.2010.2
- Patel, A. B., Lai, J. C., Chowdhury, G. M., Hyder, F., Rothman, D. L., Shulman, R. G., et al. (2014). Direct evidence for activity-dependent glucose phosphorylation in neurons with implications for the astrocyte-to-neuron lactate shuttle. *Proc. Natl. Acad. Sci. U.S.A.* 111, 5385–5390. doi: 10.1073/pnas.1403576111
- Patel, M., and Korotchkina, L. (2001). Regulation of mammalian pyruvate dehydrogenase complex by phosphorylation: complexity of multiple phosphorylation sites and kinases. *Exp. Mol. Med.* 33, 191–197. doi: 10.1038/emm.2001.32

- Patel, M., and Tilghman, S. (1973). Regulation of pyruvate metabolism via pyruvate carboxylase in rat brain mitochondria. *Biochem. J.* 132, 185–192. doi: 10.1042/bj1320185
- Paulson, O., and Newman, E. (1987). Does the release of potassium from astrocyte endfeet regulate cerebral blood flow? *Science* 237, 896–898. doi: 10.1126/science.3616619
- Pellerin, L., and Magistretti, P. (1994). Glutamate uptake into astrocytes stimulates aerobic glycolysis: a mechanism coupling neuronal activity to glucose utilization. *Proc. Natl. Acad. Sci. U.S.A.* 91, 10625–10629. doi: 10.1073/pnas.91.22.10625
- Peng, L., and Hertz, L. (2002). Amobarbital inhibits K<sup>+</sup>-stimulated glucose oxidation in cerebellar granule neurons by two mechanisms. *Eur. J. Pharmacol.* 446, 53–61. doi: 10.1016/S0014-2999(02)01794-6
- Peng, L., Zhang, X., and Hertz, L. (1994). High extracellular potassium concentrations stimulate oxidative metabolism in a glutamatergic neuronal culture and glycolysis in cultured astrocytes but have no stimulatory effect in a GABAergic neuronal culture. *Brain Res.* 663, 168–172. doi: 10.1016/0006-8993(94)90475-8
- Pfrieger, F., and Barres, B. (1997). Synaptic efficacy enhanced by glial cells *in vitro*. *Science* 277, 1684–1687. doi: 10.1126/science.277.5332.1684
- Pierre, K., and Pellerin, L. (2005). Monocarboxylate transporters in the central nervous system: distribution, regulation and function. *J. Neurochem.* 94, 1–14. doi: 10.1111/j.1471-4159.2005.03168.x
- Poitry-Yamate, C., Poitry, S., and Tsacopoulos, M. (1995). Lactate released by Müller glial cells is metabolized by photoreceptors from mammalian retina. *J. Neurosci.* 15(7 Pt 2), 5179–5191.
- Potokar, M., Kreft, M., Li, L., Daniel Andersson, J., Pangrsic, T., Chowdhury, H., et al. (2007). Cytoskeleton and vesicle mobility in astrocytes. *Traffic* 8, 12–20. doi: 10.1111/j.1600-0854.2006.00509.x
- Preiss, J., and Walsh, D. A. (1981). “The comparative biochemistry of glycogen and starch metabolism and their regulation,” in *Biology of Complex Carbohydrates*, ed V. Ginsburg (New York, NY: John Wiley and Sons), 199–314.
- Prichard, J. W., Rothman, D. L., Novotny, E., Petroff, O., Kuwabara, T., Avison, M., et al. (1991). Lactate rise detected by <sup>1</sup>H NMR in human visual cortex during physiologic stimulation. *Proc. Natl. Acad. Sci. U.S.A.* 88, 5829–5831. doi: 10.1073/pnas.88.13.5829
- Provent, P., Kickler, N., Barbier, E., Bergerot, A., Farion, R., Goury, S., et al. (2007). The ammonium-induced increase in rat brain lactate concentration is rapid and reversible and is compatible with trafficking and signaling roles for ammonium. *J. Cereb. Blood Flow Metab.* 27, 1830–1840. doi: 10.1038/sj.jcbfm.9600480
- Qu, H., Eloqayli, H., Unsgard, G., and Sonnewald, U. (2001). Glutamate decreases pyruvate carboxylase activity and spares glucose as energy substrate in cultured cerebellar astrocytes. *J. Neurosci. Res.* 66, 1127–1132. doi: 10.1002/jnr.10032
- Reina-De La Torre, F., Rodriguez-Baeza, A., and Sahuquillo-Barris, J. (1998). Morphological characteristics and distribution pattern of the arterial vessels in human cerebral cortex: a scanning electron microscope study. *Anat. Rec.* 251, 87–96.
- Robinson, M. (2002). Regulated trafficking of neurotransmitter transporters: common notes but different melodies. *J. Neurochem.* 80, 1–11. doi: 10.1046/j.0022-3042.2001.00698.x
- Rolfe, D., and Brown, G. (1997). Cellular energy utilization and molecular origin of standard metabolic rate in mammals. *Physiol. Rev.* 77, 731–758.
- Rothman, D. L., Novotny, E., Shulman, G. I., Howseman, A., Petroff, O., Mason, G. F., et al. (1992). <sup>1</sup>H-[<sup>13</sup>C] NMR measurements of [4-<sup>13</sup>C]glutamate turnover in human brain. *Proc. Natl. Acad. Sci. U.S.A.* 89, 9603–9606. doi: 10.1073/pnas.89.20.9603
- Schaller, B., Mekle, R., Xin, L., Kunz, N., and Gruetter, R. (2013). Net increase of lactate and glutamate concentration in activated human visual cortex detected with magnetic resonance spectroscopy at 7 tesla. *J. Neurosci. Res.* 91, 1076–1083. doi: 10.1002/jnr.23194
- Schaller, B., Xin, L., O’Brien, K., Magill, A., and Gruetter, R. (2014). Are glutamate and lactate increases ubiquitous to physiological activation? A <sup>1</sup>H functional MR spectroscopy study during motor activation in human brain at 7 Tesla. *Neuroimage* 93(Pt 1), 138–145. doi: 10.1016/j.neuroimage.2014.02.016
- Schroeder, M., Atherton, H., Ball, D., Cole, M., Heather, L., Griffin, J., et al. (2009). Real-time assessment of Krebs cycle metabolism using hyperpolarized <sup>13</sup>C magnetic resonance spectroscopy. *FASEB J.* 23, 2529–2538. doi: 10.1096/fj.09-129171
- Shen, J., Petersen, K., Behar, K. L., Brown, P., Nixon, T., Mason, G. F., et al. (1999). Determination of the rate of the glutamate/glutamine cycle in the human brain by *in vivo* <sup>13</sup>C NMR. *Proc. Natl. Acad. Sci. U.S.A.* 96, 8235–8240. doi: 10.1073/pnas.96.14.8235
- Shestov, A., Valette, J., Deelchand, D., Uğurbil, K., and Henry, P. G. (2012). Metabolic modeling of dynamic brain <sup>13</sup>C NMR multiplet data: concepts and simulations with a two-compartment neuronal-glial model. *Neurochem. Res.* 37, 2388–2401. doi: 10.1007/s11064-012-0782-5
- Shulman, R. G., and Rothman, D. L. (1998). Interpreting functional imaging studies in terms of neurotransmitter cycling. *Proc. Natl. Acad. Sci. U.S.A.* 95, 11993–11998. doi: 10.1073/pnas.95.20.11993
- Sibson, N., Dhankhar, A., Mason, G. F., Rothman, D. L., Behar, K. L., and Shulman, R. G. (1998). Stoichiometric coupling of brain glucose metabolism and glutamatergic neuronal activity. *Proc. Natl. Acad. Sci. U.S.A.* 95, 316–321. doi: 10.1073/pnas.95.1.316
- Sibson, N., Mason, G. F., Shen, J., Cline, G., Herskovits, A., Wall, J., et al. (2001). *In vivo* <sup>13</sup>C NMR measurement of neurotransmitter glutamate cycling, anaplerosis and TCA cycle flux in rat brain during [2-<sup>13</sup>C]glucose infusion. *J. Neurochem.* 76, 975–989. doi: 10.1046/j.1471-4159.2001.00074.x
- Sickmann, H., Waagepetersen, H., Schousboe, A., Benie, A., and Bouman, S. (2012). Brain glycogen and its role in supporting glutamate and GABA homeostasis in a type 2 diabetes rat model. *Neurochem. Int.* 60, 267–275. doi: 10.1016/j.neuint.2011.12.019
- Sickmann, H., Walls, A., Schousboe, A., Bouman, S., and Waagepetersen, H. (2009). Functional significance of brain glycogen in sustaining glutamatergic neurotransmission. *J. Neurochem.* 109, 80–86. doi: 10.1111/j.1471-4159.2009.05915.x
- Siesjö, B. (1978). Brain metabolism and anaesthesia. *Acta Anaesthesiol. Scand. Suppl.* 70, 56–59.
- Simpson, I. A., Carruthers, A., and Vannucci, S. J. (2007). Supply and demand in cerebral energy metabolism: the role of nutrient transporters. *J. Cereb. Blood Flow Metab.* 27, 1766–1791. doi: 10.1038/sj.jcbfm.9600521
- Sokoloff, L. (1978). Local cerebral energy metabolism: its relationships to local functional activity and blood flow. *Ciba Found. Symp.* 56, 171–197. doi: 10.1002/978047020370.ch10
- Sokoloff, L. (2004). “Energy metabolism in neural tissues *in vivo* at rest and in functionally altered states,” in *Brain Energetics and Neuronal Activity*, eds R. G. Shulman and D. L. Rothman (Wiley), 11–30. doi: 10.1002/0470020520.ch2
- Sonnay, S., Duarte, J. M. N., Just, N., and Gruetter, R. (2016). Compartmentalised energy metabolism supporting glutamatergic neurotransmission in response to increased activity in the rat cerebral cortex: A <sup>13</sup>C MRS study *in vivo* at 14.1 T. *J. Cereb. Blood Flow Metab.* 36, 928–940. doi: 10.1177/0271678X16629482
- Sonnay, S., Duarte, J. M. N., Just, N., and Gruetter, R. (2017). Energy metabolism in the rat cortex under thiopental anaesthesia measured *in vivo* by <sup>13</sup>C MRS. *J. Neurosci. Res.* doi: 10.1002/jnr.24032. [Epub ahead of print].
- Sonnay, S., Just, N., Duarte, J. M. N., and Gruetter, R. (2015). Imaging of prolonged BOLD response in the somatosensory cortex of the rat. *NMR Biomed.* 28, 414–421. doi: 10.1002/nbm.3263
- Sonnewald, U. (2014). Glutamate synthesis has to be matched by its degradation - where do all the carbons go? *J. Neurochem.* 131, 399–406. doi: 10.1111/jnc.12812
- Sonnewald, U., Westergaard, N., Jones, P., Taylor, A., Bachelard, H., and Schousboe, A. (1996). Metabolism of [ $U\text{-}^{13}\text{C}_5$ ] glutamine in cultured astrocytes studied by NMR spectroscopy: first evidence of astrocytic pyruvate recycling. *J. Neurochem.* 67, 2566–2572. doi: 10.1046/j.1471-4159.1996.67062566.x
- Sotelo-Hitschfeld, T., Niemeyer, M., Mächler, P., Ruminot, I., Lerchundi, R., Wyss, M., et al. (2015). Channel-mediated lactate release by K<sup>+</sup>-stimulated astrocytes. *J. Neurosci.* 35, 4168–4178. doi: 10.1523/JNEUROSCI.5036-14.2015
- Stenovec, M., Kreft, M., Grilc, S., Pangrsic, T., and Zorec, R. (2008). EAAT2 density at the astrocyte plasma membrane and Ca<sup>2+</sup>-regulated exocytosis. *Mol. Membr. Biol.* 25, 203–215. doi: 10.1080/09687680701790925
- Stevens, E., Esguerra, M., Kim, P., Newman, E., Snyder, S., Zahs, K., et al. (2003). D-serine and serine racemase are present in the vertebrate retina and contribute to the physiological activation of NMDA receptors. *Proc. Natl. Acad. Sci. U.S.A.* 100, 6789–6794. doi: 10.1073/pnas.1237052100

- Suzuki, A., Stern, S., Bozdagi, O., Huntley, G., Walker, R., Magistretti, P., et al. (2011). Astrocyte-neuron lactate transport is required for long-term memory formation. *Cell* 144, 810–823. doi: 10.1016/j.cell.2011.02.018
- Suzuki, Y., Huang, M., Lederis, K., and Rorstad, O. P. (1988). The role of adenylate cyclase in relaxation of brain arteries: studies with forskolin. *Brain Res.* 457, 241–245. doi: 10.1016/0006-8993(88)90691-9
- Swanson, R., Morton, M., Sagar, S., and Sharp, F. (1992). Sensory stimulation induces local cerebral glycogenolysis: demonstration by autoradiography. *Neuroscience* 51, 451–461. doi: 10.1016/0306-4522(92)90329-Z
- Takahashi, S., Driscoll, B., Law, M., and Sokoloff, L. (1995). Role of sodium and potassium ions in regulation of glucose metabolism in cultured astroglia. *Proc. Natl. Acad. Sci. U.S.A.* 92, 4616–4620. doi: 10.1073/pnas.92.10.4616
- Tekkōk, S., Brown, A., Westenbroek, R., Pellerin, L., and Ransom, B. (2005). Transfer of glycogen-derived lactate from astrocytes to axons via specific monocarboxylate transporters supports mouse optic nerve activity. *J. Neurosci. Res.* 81, 644–652. doi: 10.1002/jnr.20573
- Thorens, B. (2015). GLUT2 glucose sensing and glucose homeostasis. *Diabetologia* 58, 221–232. doi: 10.1007/s00125-014-3451-1
- Tiret, B., Shestov, A., Valette, J., and Henry, P.-G. (2015). Metabolic modeling of dynamic  $^{13}\text{C}$  NMR isotopomer data in the brain *in vivo*: fast screening of metabolic models using automated generation of differential equations. *Neurochem. Res.* 40, 2482–2492. doi: 10.1007/s11064-015-1748-1
- Tiwari, V., Ambadipudi, S., and Patel, A. B. (2013). Glutamatergic and GABAergic TCA cycle and neurotransmitter cycling fluxes in different regions of mouse brain. *J. Cereb. Blood Flow Metab.* 33, 1523–1531. doi: 10.1038/jcbfm.2013.114
- Tsapopoulos, M., Poitry-Yamate, C., Poitry, S., Perrottet, P., and Veuthey, A. (1997). The nutritive function of glia is regulated by signals released by neurons. *Glia* 21, 84–91.
- Uffmann, K., and Gruetter, R. (2007). Mathematical modeling of  $^{13}\text{C}$  label incorporation of the TCA cycle: the concept of composite precursor function. *J. Neurosci. Res.* 85, 3304–3317. doi: 10.1002/jnr.21392
- van den Berg, C., and Garfinkel, D. (1971). A simulation study of brain compartments. Metabolism of glutamate and related substances in mouse brain. *Biochem. J.* 123, 211–218. doi: 10.1042/bj1230211
- Van den Berg, C., Krzalić, L., Mela, P., and Waelsch, H. (1969). Compartmentation of glutamate metabolism in brain. Evidence for the existence of two different tricarboxylic acid cycles in brain. *Biochem. J.* 113, 281–290. doi: 10.1042/bj1130281
- Virchow, R. (1856). *Gesammelte Abhandlungen zur wissenschaftlichen Medicin*. Frankfurt: Meidinger Sohn.
- Voet, D., and Voet, G. (1995). *Biochemistry*, 2nd Edn. New York, NY: John Wiley and Sons.
- Volterra, A., and Meldolesi, J. (2005). Astrocytes, from brain glue to communication elements: the revolution continues. *Nat. Rev. Neurosci.* 6, 626–640. doi: 10.1038/nrn1722
- Waagepetersen, H., Qu, H., Schousboe, A., and Sonnewald, U. (2001). Elucidation of the quantitative significance of pyruvate carboxylation in cultured cerebellar neurons and astrocytes. *J. Neurosci. Res.* 66, 763–770. doi: 10.1002/jnr.10061
- Wan, B., LaNoue, K., Cheung, J., and Scaduto, R. J. (1989). Regulation of citric acid cycle by calcium. *J. Biol. Chem.* 264, 13430–13439.
- Wang, H., Hitron, I., Iadecola, C., and Pickel, V. (2005). Synaptic and vascular associations of neurons containing cyclooxygenase-2 and nitric oxide synthase in rat somatosensory cortex. *Cereb. Cortex* 15, 1250–1260. doi: 10.1093/cercor/bhi008
- Wilson, J., Peters, C., Sitar, S., Daoust, P., and Gelb, A. (2000). Glutamate stimulates ascorbate transport by astrocytes. *Brain Res.* 858, 61–66. doi: 10.1016/S0006-8993(99)02433-6
- Wolin, M. (1996). Reactive oxygen species and vascular signal transduction mechanisms. *Microcirculation* 3, 1–17. doi: 10.3109/10739689609146778
- Wyss, M., Jolivet, R., Buck, A., Magistretti, P., and Weber, B. (2011). *In vivo* evidence for lactate as a neuronal energy source. *J. Neurosci.* 31, 7477–7485. doi: 10.1523/JNEUROSCI.0415-11.2011
- Wyss, M., Weber, B., Treyer, V., Heer, S., Pellerin, L., Magistretti, P., et al. (2009). Stimulation-induced increases of astrocytic oxidative metabolism in rats and humans investigated with  $^{1-11}\text{C}$ -acetate. *J. Cereb. Blood Flow Metab.* 29, 44–56. doi: 10.1038/jcbfm.2008.86
- Yang, J., Xu, S., and Shen, J. (2009). Fast isotopic exchange between mitochondria and cytosol in brain revealed by relayed  $^{13}\text{C}$  magnetization transfer spectroscopy. *J. Cereb. Blood Flow Metab.* 29, 661–669. doi: 10.1038/jcbfm.2008.170
- Zhu, X. H., Du, F., Zhang, N., Zhang, Y., Lei, H., Zhang, X., et al. (2009). Advanced *In vivo* Heteronuclear MRS approaches for studying brain bioenergetics driven by mitochondria. *Methods Mol. Biol.* 489, 317–357. doi: 10.1007/978-1-59745-543-5\_15
- Zonta, M., Angulo, M., Gobbo, S., Rosengarten, B., Hossmann, K., Pozzan, T., et al. (2003). Neuron-to-astrocyte signaling is central to the dynamic control of brain microcirculation. *Nat. Neurosci.* 6, 43–50. doi: 10.1038/nn980
- Zwingmann, C., and Leibfritz, D. (2003). Regulation of glial metabolism studied by  $^{13}\text{C}$ -NMR. *NMR Biomed.* 16, 370–399. doi: 10.1002/nbm.850

**Conflict of Interest Statement:** The authors declare that the research was conducted in the absence of any commercial or financial relationships that could be construed as a potential conflict of interest.

Copyright © 2017 Sonny, Gruetter and Duarte. This is an open-access article distributed under the terms of the Creative Commons Attribution License (CC BY). The use, distribution or reproduction in other forums is permitted, provided the original author(s) or licensor are credited and that the original publication in this journal is cited, in accordance with accepted academic practice. No use, distribution or reproduction is permitted which does not comply with these terms.



# Graded Hypercapnia-Calibrated BOLD: Beyond the Iso-metabolic Hypercapnic Assumption

Ian D. Driver<sup>1\*</sup>, Richard G. Wise<sup>1</sup> and Kevin Murphy<sup>1,2</sup>

<sup>1</sup> Cardiff University Brain Research Imaging Centre, School of Psychology, Cardiff University, Cardiff, United Kingdom,

<sup>2</sup> School of Physics and Astronomy, Cardiff University, Cardiff, United Kingdom

## OPEN ACCESS

### Edited by:

Federico Giove,  
Centro Fermi, Italy

### Reviewed by:

Jean Chen,  
University of Toronto, Canada  
Stefan Posse,  
University of New Mexico,  
United States

### \*Correspondence:

Ian D. Driver  
Driverl@cardiff.ac.uk

### Specialty section:

This article was submitted to  
Brain Imaging Methods,  
a section of the journal  
*Frontiers in Neuroscience*

**Received:** 31 January 2017

**Accepted:** 28 April 2017

**Published:** 18 May 2017

### Citation:

Driver ID, Wise RG and Murphy K  
(2017) Graded  
Hypercapnia-Calibrated BOLD:  
Beyond the Iso-metabolic  
Hypercapnic Assumption.  
*Front. Neurosci.* 11:276.  
doi: 10.3389/fnins.2017.00276

Calibrated BOLD is a promising technique that overcomes the sensitivity of conventional fMRI to the cerebrovascular state; measuring either the basal level, or the task-induced response of cerebral metabolic rate of oxygen consumption (CMRO<sub>2</sub>). The calibrated BOLD method is susceptible to errors in the measurement of the calibration parameter *M*, the theoretical BOLD signal change that would occur if all deoxygenated hemoglobin were removed. The original and most popular method for measuring *M* uses hypercapnia (an increase in arterial CO<sub>2</sub>), making the assumption that it does not affect CMRO<sub>2</sub>. This assumption has since been challenged and recent studies have used a corrective term, based on literature values of a reduction in basal CMRO<sub>2</sub> with hypercapnia. This is not ideal, as this value may vary across subjects and regions of the brain, and will depend on the level of hypercapnia achieved. Here we propose a new approach, using a graded hypercapnia design and the assumption that CMRO<sub>2</sub> changes linearly with hypercapnia level, such that we can measure *M* without assuming prior knowledge of the scale of CMRO<sub>2</sub> change. Through use of a graded hypercapnia gas challenge, we are able to remove the bias caused by a reduction in basal CMRO<sub>2</sub> during hypercapnia, whilst simultaneously calculating the dose-wise CMRO<sub>2</sub> change with hypercapnia. When compared with assuming no change in CMRO<sub>2</sub>, this approach resulted in significantly lower *M*-values in both visual and motor cortices, arising from significant dose-dependent hypercapnia reductions in basal CMRO<sub>2</sub> of  $1.5 \pm 0.6\%/\text{mmHg}$  (visual) and  $1.8 \pm 0.7\%/\text{mmHg}$  (motor), where mmHg is the unit change in end-tidal CO<sub>2</sub> level. Variability in the basal CMRO<sub>2</sub> response to hypercapnia, due to experimental differences and inter-subject variability, is accounted for in this approach, unlike previous correction approaches, which use literature values. By incorporating measurement of, and correction for, the reduction in basal CMRO<sub>2</sub> during hypercapnia in the measurement of *M*-values, application of our approach will correct for an overestimation in both CMRO<sub>2</sub> task-response values and absolute CMRO<sub>2</sub>.

**Keywords:** fMRI, calibrated BOLD, CMRO<sub>2</sub>, hypercapnia, arterial spin labeling

## INTRODUCTION

Blood oxygenation level dependent (BOLD) functional MRI (fMRI) signal contrast is widely used as a surrogate measure of underlying neuronal activity (Kwong et al., 1992; Ogawa et al., 1992). The BOLD signal is dependent on the concentration of deoxygenated hemoglobin in blood, which is modulated by changes in cerebral blood flow (CBF), cerebral blood volume (CBV), and cerebral metabolic rate of oxygen consumption (CMRO<sub>2</sub>). Significant inter-region and inter-subject variability in the BOLD response arises due to vascular factors (Chiarelli et al., 2007a; Lu et al., 2008), which could confound interpretation of the underlying neuronal activity from BOLD results. The technique termed calibrated BOLD was developed to address this variability (Davis et al., 1998; Hoge et al., 1999). A calibration parameter ( $M$ ), defined as the theoretical BOLD signal change that would occur if all deoxygenated hemoglobin were removed, incorporates basal hemodynamic parameters, along with parameters that are dependent on the specific MRI acquisition scheme. This calibration parameter allows for calculation of either absolute CMRO<sub>2</sub> (Bulte et al., 2012; Gauthier and Hoge, 2012; Wise et al., 2013), or the task-dependent relative change in CMRO<sub>2</sub> (Davis et al., 1998; Hoge et al., 1999). CMRO<sub>2</sub> directly reflects tissue metabolism, so is widely considered a more direct measurement of underlying neuronal activity than the cerebrovascular CBF and CBV responses. However, this approach is sensitive to errors in the measurement of  $M$  (Hoge et al., 1999; Chiarelli et al., 2007b).

The original and most popular method for calculating  $M$  uses hypercapnia (an increase in arterial CO<sub>2</sub>). Typically, hypercapnia is presented through inhalation of gas mixtures including CO<sub>2</sub>, or through reductions in breathing depth and/or pace (e.g., breath hold). The cerebral vasculature is sensitive to changes in partial pressure of carbon dioxide dissolved in arterial blood (PaCO<sub>2</sub>), such that hypercapnia is a potent vasodilator, causing increases in CBF and CBV (Kety and Schmidt, 1948; Ito et al., 2003; Noth et al., 2006; Chen and Pike, 2010b; Ho et al., 2011). For calibrated BOLD, hypercapnia is assumed to be a purely vascular stimulus, providing a change in CBF and CBV without a change in CMRO<sub>2</sub> (Davis et al., 1998). However, this iso-metabolic assumption is the subject of controversy (Yablonskiy, 2011), with literature indicating increases, decreases and no change in basal CMRO<sub>2</sub> with hypercapnia (Kety and Schmidt, 1948; Kliefoth et al., 1979; Rhodes et al., 1981; Hoffman et al., 1982; Horvath et al., 1994; Jones et al., 2005; Sicard and Duong, 2005; Chen and Pike, 2010a; Jain et al., 2011; Xu et al., 2011). Recent human MRI studies (Chen and Pike, 2010a; Jain et al., 2011; Xu et al., 2011) have shown mixed results, calculating CMRO<sub>2</sub> using the Fick principle to combine CBF (phase contrast MRI) and OEF (either T<sub>2</sub>- or susceptibility-based venous blood oxygenation

measurements). Xu et al. found a significant  $13.4 \pm 2.3\%$  decrease with a 5% CO<sub>2</sub> hypercapnic challenge, whilst Chen and Pike and Jain et al. found no significant change in basal CMRO<sub>2</sub> with hypercapnia. Whilst these contrasting findings may arise due to methodological differences, any CMRO<sub>2</sub> change with hypercapnia appears to be on the order of the measurement accuracy of these methods. Despite this limited sensitivity, recent calibrated BOLD studies have begun to correct for an assumed reduction in basal CMRO<sub>2</sub> with hypercapnia (Bulte et al., 2012), based on these literature values (Xu et al., 2011). An appropriate choice of CMRO<sub>2</sub> response (or lack thereof) to hypercapnia is important for calibrated BOLD experiments due to the sensitivity of the method to propagation of errors in  $M$  through to the endpoint CMRO<sub>2</sub> calculation (Hoge et al., 1999; Chiarelli et al., 2007b; Blockley et al., 2015).

With measurement sensitivity on the order of the changes observed, current MR techniques are unsuited to fully characterize the relationship between PaCO<sub>2</sub> and CMRO<sub>2</sub>. However, electrophysiological measurements appear to have more sensitivity to investigate the dynamic range of mild hypercapnia PaCO<sub>2</sub> values. Studies in both non-human primates and, more recently, in humans show reductions in spontaneous neuronal oscillatory power with hypercapnia (Jones et al., 2005; Zappe et al., 2008; Hall et al., 2011; Xu et al., 2011). We have recently observed a linear relationship between PaCO<sub>2</sub> and spontaneous neuronal oscillatory power (Driver et al., 2016). Whilst there is currently no direct relationship established between CMRO<sub>2</sub> and neuronal oscillatory power, they may share similar underlying neurochemical mechanisms for their responses to hypercapnia, specifically extracellular pH changes modulating ATP channels (Dulla et al., 2005). Therefore, in the following paragraphs, we explore the addition to the calibrated BOLD technique of an assumption of a linear relationship between hypercapnia level and CMRO<sub>2</sub>.

In this work, we present a new approach, relaxing the iso-metabolic hypercapnia assumption in the calibrated BOLD technique. By acquiring multiple levels of hypercapnia,  $M$  and the dose-wise CMRO<sub>2</sub> response to hypercapnia are solved for as two unknowns in a set of simultaneous equations (one equation for each hypercapnia level). We apply this approach to data presented previously (Murphy et al., 2013), measuring both the calibration parameter  $M$  and the dose-wise CMRO<sub>2</sub> response to a graded hypercapnia challenge.

## MATERIALS AND METHODS

### Theory

The calibrated BOLD equation, as proposed by Davis et al. (1998) and elegantly restated by Hoge et al. (1999) can be used to model the BOLD signal change during hypercapnia:

$$\frac{\Delta BOLD_{HC}}{BOLD_0} = M \left[ 1 - \left( \frac{CBF_{HC}}{CBF_0} \right)^{\alpha-\beta} \cdot \left( \frac{CMRO_{2,HC}}{CMRO_{2,0}} \right)^\beta \right] \quad (1)$$

Where  $M$  is the calibration parameter,  $\Delta$  denotes the difference between the current state and baseline state, subscripts HC and 0 denote hypercapnia and baseline (normocapnia) conditions,

**Abbreviations:** ASL, arterial spin labeling; BOLD, blood oxygenation level dependent (fMRI signal contrast); CMRO<sub>2</sub>, cerebral metabolic rate of oxygen consumption; CBF, cerebral blood flow; CBV, cerebral blood volume; fMRI, functional magnetic resonance imaging; PaCO<sub>2</sub>, partial pressure of carbon dioxide dissolved in arterial blood; PETCO<sub>2</sub>, end-tidal partial pressure of carbon dioxide; ROI, region of interest.

respectively. The exponent  $\alpha$  describes an assumed coupling relationship between CBF and CBV (Grubb et al., 1974; Chen and Pike, 2010b), whilst  $\beta$  is a power-law relationship between venous blood oxygenation and transverse relaxation rate (Ogawa et al., 1993; Boxerman et al., 1995; Driver et al., 2010; Croal et al., 2017). If the iso-metabolic assumption were used, the  $CMRO_2$  term would reduce to 1, with numerator and denominator being equal.  $M$  could then be calculated from Equation (1) using measured values for the relative changes in BOLD and CBF due to hypercapnia.

We propose to remove the iso-metabolic assumption, such that the  $CMRO_2$  term becomes an unknown parameter to be solved alongside  $M$ . To do this, we measure BOLD and CBF responses to two levels of hypercapnia, setting up two versions of Equation (1). Since the  $CMRO_2$  term may change between the two equations, we assume a linear relationship between  $CMRO_2$  and hypercapnia level. A new parameter  $\kappa$  is defined as the dose-wise fractional  $CMRO_2$  change to a unit (1 mmHg) change in end-tidal partial pressure of carbon dioxide ( $P_{ETCO_2}$ ), a surrogate measure for  $PaCO_2$ .

$$\frac{CMRO_{2,HC}}{CMRO_{2,0}} = 1 + \kappa \cdot \Delta P_{ETCO_2} \quad (2)$$

Substituting Equation 2 into Equation 1:

$$\frac{\Delta BOLD_{HC}}{BOLD_0} = M \left[ 1 - \left( \frac{CBF_{HC}}{CBF_0} \right)^{\alpha-\beta} \cdot (1 + \kappa \cdot \Delta P_{ETCO_2})^\beta \right] \quad (3)$$

Therefore, with  $P_{ETCO_2}$  measured by sampling exhaled gas,  $M$  and  $\kappa$  are two unknowns, which can be solved for using two equations, one for each hypercapnia level.

## Data Acquisition

Fifteen subjects (7M/8F, age range 21–36 years) participated in 2 sessions in which scans were acquired using a 3 T whole body MRI system (GE Excite HDx, Milwaukee, WI, USA) with an eight-channel receive coil. The School of Psychology, Cardiff University Ethics Committee approved this study and subjects gave written informed consent prior to participating.

Data were acquired using a pulsed arterial spin labeling (ASL) proximal inversion and control for off-resonance effects (PICORE), quantitative imaging of perfusion using a single subtraction (PICORE QUIPSS II) (Wong et al., 1998) imaging sequence. This sequence used a dual-echo gradient echo readout (Liu et al., 2002) and spiral-out k-space acquisition [Glover, 1999; 490 repetitions (image volumes), TE1 = 3.3 ms TE2 = 29 ms, TR = 2,200 ms, flip angle 90°, FOV 22 cm, matrix 64 × 64, 12 slices of 7 mm thickness with an inter-slice gap of 1 mm, TI1 = 600 ms, TI2 = 1,500 ms for the most proximal slice, 10 cm inversion slab thickness, adiabatic hyperbolic secant inversion pulse, 10 mm gap between labeling slab and bottom slice, 10 cm QUIPSS II saturation band thickness]. Additionally, whole brain  $T_1$ -weighted structural scan (fast spoiled gradient recalled echo, 1 × 1 × 1 mm voxels, TI/TR/TE = 450/7.8/3 ms) was acquired for segmentation of gray matter.

Participants were presented with hypercapnia levels of +4 and +8 mmHg  $\Delta P_{ETCO_2}$  above their normal resting level. End-tidal CO<sub>2</sub> levels were changed at 2-min intervals between baseline, +4 and +8 mmHg values, in a randomized order. This provided three 2-min blocks for each condition, across the 18 min ASL scan. Gas mixtures were delivered to the subject through a tight-fitting face-mask (Quadralite, Intersurgical, Wokingham, Berkshire, UK). Flow rates of two gas mixtures, namely medical air (21% O<sub>2</sub>, 79% N<sub>2</sub>) and a 5% CO<sub>2</sub> mixture (5% CO<sub>2</sub>, 20% O<sub>2</sub>, 75% N<sub>2</sub>), were manually adjusted to provide an inspired gas mixture of 30 L/min. The respiratory circuit included a reservoir on the expired limb to permit re-breathing in the event that the instantaneous inspiratory rate exceeded 30 L/min. Expired gas concentrations were sampled from the face-mask and  $P_{ETCO_2}$  and  $P_{ETO_2}$  (end-tidal pO<sub>2</sub>) were measured using rapidly responding gas analyzers (AEI Technologies, Pittsburgh, PA, USA). A manual feedback procedure was used to reach each hypercapnia level, whereby the respective flow rates of medical air and the 5% CO<sub>2</sub> mixture were adjusted to reach the  $P_{ETCO_2}$  target.

A combined visual and motor task was simultaneously performed, consisting of blocks of 8 Hz flashing checkboard and right-handed self-paced finger tapping with a range of block durations between 20 and 30 s. These blocks were interspersed with 20–30 s blocks of rest. The range in task and rest block durations were chosen so that the visual, motor and CO<sub>2</sub> tasks had minimal correlation with each other. The task data was used to define primary visual and motor cortex ROIs.

## Data Analysis

CBF time series were calculated from the first echo by separating tag and control time series, interpolating to the TR and subtracting. A similar procedure using averaging rather than subtraction yielded BOLD time series from the second echo.  $R_2^*$  was also calculated by performing an exponential fit across the two echo times, separately for tag and control time series, then combining tag and control  $R_2^*$  values by surround averaging. A gray matter (GM) ROI was calculated for each subject by segmenting their anatomical image into three tissue types (gray matter, white matter and cerebrospinal fluid) using FSL's *fast*. The GM map was resampled to the functional data resolution. Visual and motor ROIs were calculated by including CO<sub>2</sub>, visual and motor timings in a voxel-wise GLM for both the BOLD and CBF data. The results for each subject were transformed into MNI space and a voxel-wise *t*-test against 0 across subject was performed. The *t*-test maps were FDR thresholded at  $p = 0.05$ . The resulting BOLD and CBF activation maps were transformed back into individual subject space. The visual and motor ROIs were then calculated for each subject by taking an *intersection* map between the BOLD activation map, the CBF activation map and the individual GM ROI. Therefore, a voxel was only included in the motor ROI if it significantly responded to the motor task in both the BOLD and CBF data and was present in the individual's GM mask. A similar procedure was used for the visual ROI. Once the ROIs were defined, the BOLD and CBF time series were averaged over the visual,

motor, and GM ROIs, then linear detrending was performed using baseline periods, before averaging across sessions for each subject.

BOLD and CBF responses to each hypercapnia level (relative to baseline) were input into +4 and +8 mmHg versions of Equation (3), then these two equations were solved simultaneously for  $M$  and  $\kappa$ , using a two-parameter non-linear fitting routine (*lsqcurvefit*, Matlab, The MathWorks, Natick, USA). Subjects that reached the boundary conditions of the non-linear fitting routine were removed from further analysis (boundary conditions  $1 < M < 20\%$ ;  $-5 < \kappa < +5\%/\text{mmHg}$ ). For comparison with the iso-metabolic assumption, the same two equations as above (+4 and +8 mmHg versions of Equation 3) were solved simultaneously using a one-parameter fit, to calculate  $M$  whilst fixing  $\kappa = 0$ .

Optimized values of  $\alpha = 0.14$  and  $\beta = 0.91$  were used (Griffith and Buxton, 2011), hereafter referred to as the *empirically derived  $\alpha/\beta$  pairing*. To ensure that our findings were not biased by choice of this  $\alpha/\beta$  pairing, we also repeated the non-linear fitting with the following two alternative  $\alpha/\beta$  pairings that have been used previously for calibrated BOLD experiments at 3 T. Values of  $\alpha = 0.2$  and  $\beta = 1.3$  have been used at 3 T (Bulte et al., 2012), hereafter referred to as the *3 T specific  $\alpha/\beta$  pairing*. Finally, a simplified model has been proposed recently, substituting  $\alpha/\beta$  for a single parameter  $\theta = 0.06$  at 3 T (Merola et al., 2016). In this case, this simplified model is equivalent to  $\alpha = 0.06$  and  $\beta = 1$ , hereafter referred to as the *simplified model  $\alpha/\beta$  pairing*.

## RESULTS

The two levels of hypercapnia resulted in  $\Delta_{\text{PET}}\text{CO}_2$  increases of  $4.8 \pm 0.3$  and  $8.4 \pm 0.4$  mmHg (mean  $\pm$  SEM across subjects). BOLD and CBF responses to the two levels of hypercapnia and the respective task (where applicable) are presented for visual, motor cortices and the remaining GM in **Table 1**. To assess BOLD sensitivity at the 29 ms TE, baseline  $R_2^*$  is also reported for each ROI in **Table 1**. Group-average maps (MNI space) of the BOLD and CBF responses to the two levels of hypercapnia are shown in **Figure 1**.

For results presented based on either the two- or one-parameter fits, the number of subjects included after discarding those that reached the boundary conditions are presented in the form ( $N = \# / 15$ ), where  $\#$  corresponds to the number of subjects included. The two-parameter fit with the empirically derived  $\alpha/\beta$  pairing (0.14/0.91) gave  $M = 9.6 \pm 1.3\%$  ( $N = 14/15$ ) and  $M = 4.7 \pm 0.6\%$  ( $N = 13/15$ ), in the visual and motor cortices respectively and  $M = 8.6 \pm 0.9\%$  ( $N = 15/15$ ) in the remaining GM. The dose-dependent hypercapnia CMRO<sub>2</sub> parameter  $\kappa = -1.5 \pm 0.6\%/\text{mmHg}$ ,  $\kappa = -1.8 \pm 0.7\%/\text{mmHg}$  and  $\kappa = -1.3 \pm 0.4\%/\text{mmHg}$  showed significant reductions in CMRO<sub>2</sub> with hypercapnia level (Wilcoxon  $p = 0.04$ ,  $p = 0.03$ , and  $p = 0.002$ ). The two-parameter fit resulted in significantly lower  $M$ -values than the one-parameter fit for subjects that did not reach the boundary conditions for both fits [**Figure 2**; visual  $p = 0.04$ , ( $N = 9/15$ ); motor  $p = 0.008$ , ( $N = 13/15$ ); GM  $p = 0.001$ , ( $N = 14/15$ )].

**TABLE 1 | BOLD and CBF responses (% change from baseline) for the two hypercapnia levels and for the visual and motor tasks (mean  $\pm$  SEM across subjects).**

ROI	$\Delta_{\text{PET}}\text{CO}_2(\text{mmHg})$	%BOLD	%CBF	Baseline $R_2^*$ ( $\text{s}^{-1}$ )
Visual	4.8 $\pm$ 0.3	0.9 $\pm$ 0.3	13 $\pm$ 3	31.3 $\pm$ 1.6
	8.4 $\pm$ 0.4	1.7 $\pm$ 0.3	19 $\pm$ 4	
	0 (+ Task)	1.7 $\pm$ 0.1	33 $\pm$ 3	
Motor	4.8 $\pm$ 0.3	0.8 $\pm$ 0.1	30 $\pm$ 15	22.3 $\pm$ 0.7
	8.4 $\pm$ 0.4	1.4 $\pm$ 0.2	43 $\pm$ 16	
	0 (+ Task)	1.3 $\pm$ 0.1	73 $\pm$ 19	
GM	4.8 $\pm$ 0.3	1.0 $\pm$ 0.1	13 $\pm$ 2	31.7 $\pm$ 0.9
	8.4 $\pm$ 0.4	1.6 $\pm$ 0.1	17 $\pm$ 3	

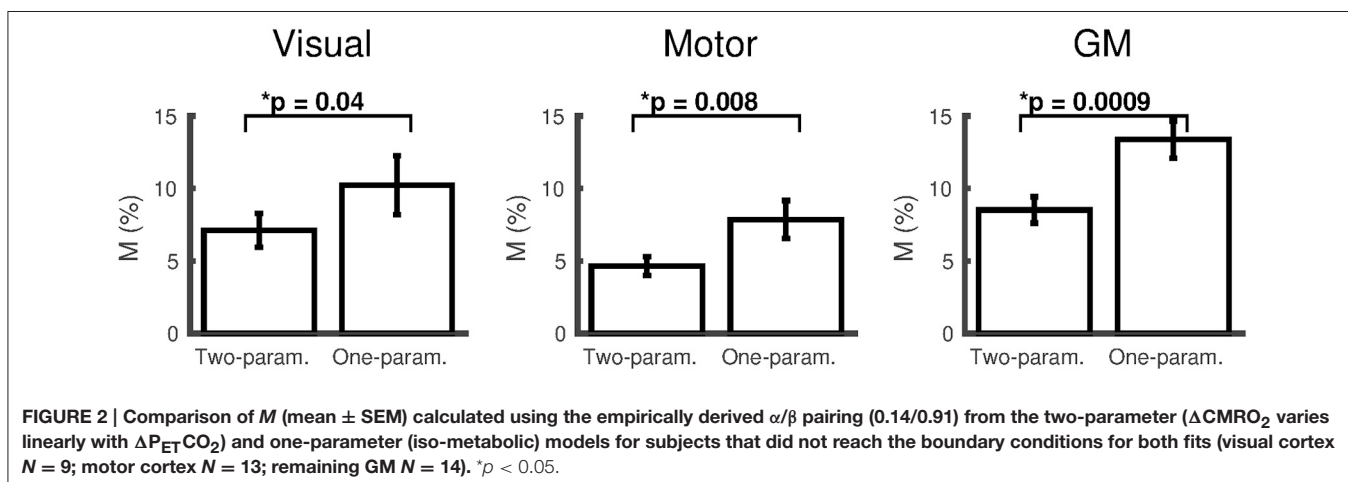
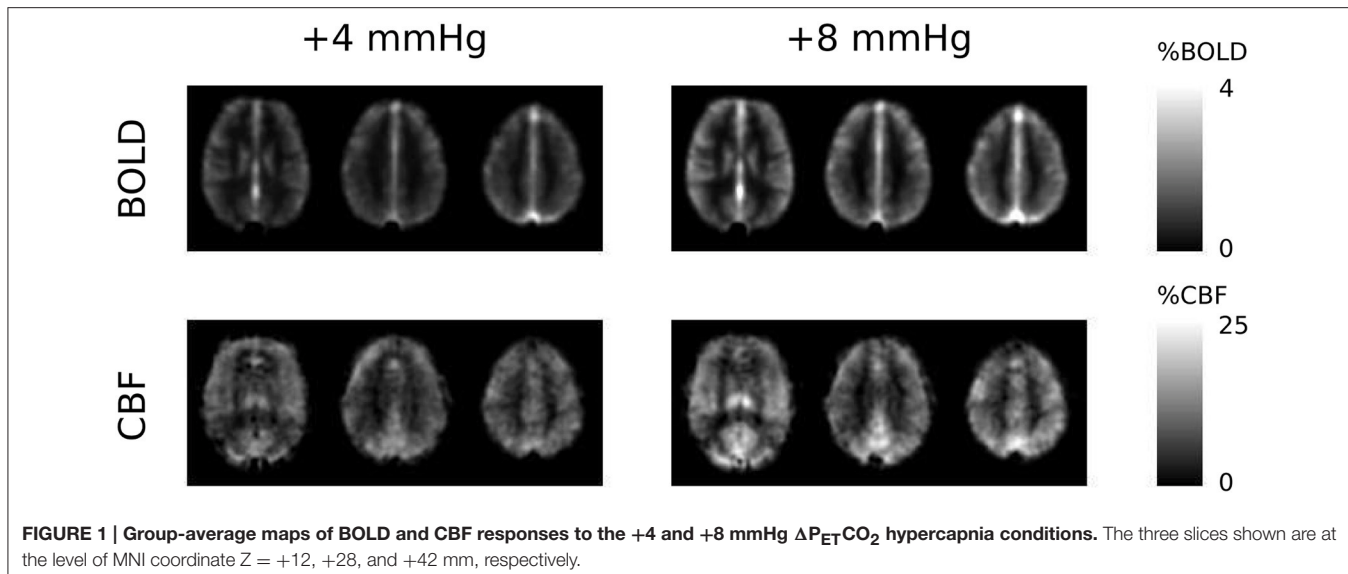
Baseline  $R_2^*$  values are also presented for each ROI.

The effect of changing the  $\alpha/\beta$  pairing is assessed in **Figures 3, 4**. **Figure 3** shows a scatter plot of  $\kappa$  across subjects for each  $\alpha/\beta$  pairing and each region of interest, with mean  $\pm$  SEM across subjects presented above. The group-averaged  $\kappa$ -values remain stable across  $\alpha/\beta$  pairings, indicating a robust decrease in CMRO<sub>2</sub> during hypercapnia. **Figure 4** presents  $M$  values across  $\alpha/\beta$  pairings. Despite the amplitude of  $M$  varying with  $\alpha/\beta$  pairing,  $M$  calculated using the two-parameter fit was consistently lower than that calculated using the one-parameter (iso-metabolic) fit.

## DISCUSSION

Through use of a graded hypercapnia gas challenge, we are able to remove the bias caused by a reduction in basal CMRO<sub>2</sub> during hypercapnia, whilst simultaneously calculating the dose-wise CMRO<sub>2</sub> change with hypercapnia. We observed consistently lower  $M$ -values when calculated from our new approach, compared to those calculated using an iso-metabolic hypercapnia assumption, evidence for a systematic overestimation of  $M$  when using the iso-metabolic assumption. In terms of studies calculating the relative change in CMRO<sub>2</sub> to a task, this overestimation in  $M$  would result in an overestimation in the CMRO<sub>2</sub> task response (see Equation 1, replacing hypercapnia terms with the equivalent task response terms). In terms of studies investigating absolute CMRO<sub>2</sub> measurements, the overestimation in  $M$  would lead to an overestimation of absolute CMRO<sub>2</sub> (Blockley et al., 2015).

In this study, we define a dose-wise CMRO<sub>2</sub> response to hypercapnia,  $\kappa$ . Our findings suggest a decrease in CMRO<sub>2</sub> with hypercapnia in the primary visual and motor cortices, as well as in the remaining GM. The scale of the CMRO<sub>2</sub> reduction is broadly similar to that observed by Xu et al. (2011), where their 5% CO<sub>2</sub> challenge resulted in a 13.4% decrease in global CMRO<sub>2</sub>. Based on the reported average  $\Delta_{\text{PET}}\text{CO}_2$  of 8.7 mmHg, this is equivalent to  $\kappa = -1.5\%/\text{mmHg}$ . This is within the range of the GM value that we measured of  $\kappa = -1.3 \pm 0.4\%/\text{mmHg}$ . Unlike previous work, which measured the global CMRO<sub>2</sub> response



to hypercapnia, our approach can provide measurements that are localized to specific brain regions. Our initial findings hint at some spatial heterogeneity in the CMRO<sub>2</sub> response to hypercapnia, with the hypercapnia CMRO<sub>2</sub> reduction appearing to be greater in the motor than visual cortex. However, this dataset does not have the sensitivity to resolve whether this is a significant difference (see inter-subject variability in **Figure 3**). Likewise, the paradigm used here is not optimized for voxelwise mapping of  $M$  and  $\kappa$ , however with a suitably optimized graded hypercapnia paradigm design that enhances voxelwise sensitivity, this approach could be translated to mapping  $M$  and  $\kappa$ , for application in mapping absolute CMRO<sub>2</sub>. The potential spatial heterogeneity of the CMRO<sub>2</sub> response to hypercapnia will be investigated in future studies, incorporating a specifically optimized hypercapnia paradigm and a more sophisticated fitting algorithm (Germuska et al., 2016). This approach for mapping the CMRO<sub>2</sub> response to hypercapnia should be considered in the context of a potential alternative, O-15 PET. There is an extensive literature on mapping CBF and CMRO<sub>2</sub> using O-15

PET (e.g., Mintun et al., 1984; Ter-Pogossian and Herscovitch, 1985; Kudomi et al., 2013). Whilst there are many studies to use O-15 PET to measure the CBF response to hypercapnia (e.g., Ito et al., 2003), the O-15 PET literature on mapping the CMRO<sub>2</sub> response to hypercapnia is limited, with no change in CMRO<sub>2</sub> measured in anesthetized dogs (Rhodes et al., 1981). The steady-state variant of the CMRO<sub>2</sub> measurement used in that work may also be biased by not accounting for intravascular <sup>15</sup>O<sub>2</sub> (Lammertsma and Jones, 1983; Lammertsma et al., 1983; Ter-Pogossian and Herscovitch, 1985). Whilst our method is constrained by the accuracy of the assumptions associated with the calibrated BOLD technique (Hoge et al., 1999; Chiarelli et al., 2007b; Chen and Pike, 2010b; Blockley et al., 2015; Croal et al., 2017), it is non-invasive, not requiring use of radioactive tracers. It also has the potential for finer temporal and spatial resolution than O-15 PET.

The approach we present here requires an assumption as to the form of the relationship between CMRO<sub>2</sub> and PaCO<sub>2</sub>; in this case, the assumption is of a linear relationship. Beyond the linear

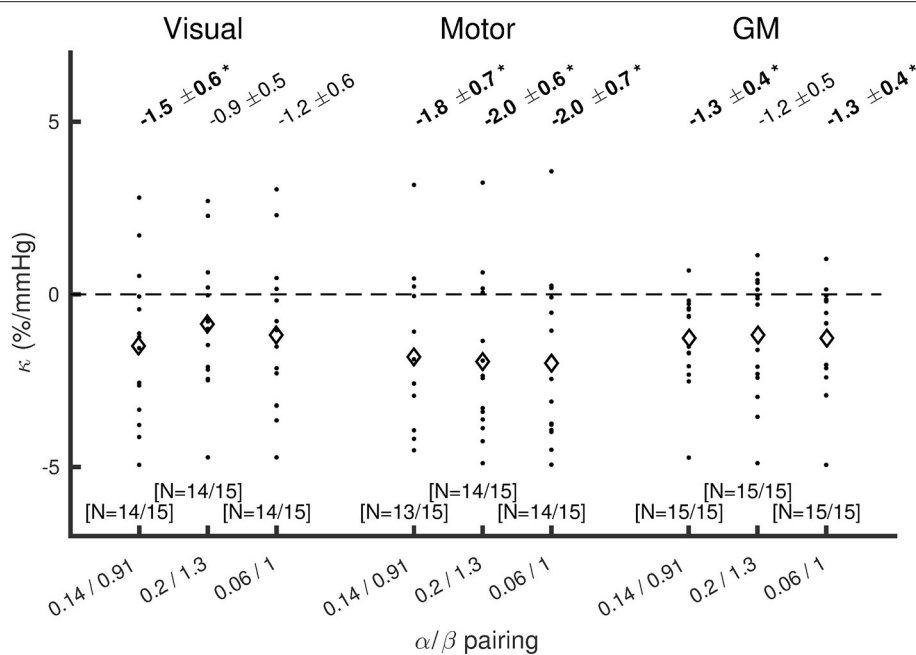


**FIGURE 3 | Plot of  $\kappa$  across subjects for each  $\alpha/\beta$  pairing, for visual cortex, motor cortex, and the remaining GM.** Diamonds show mean  $\kappa$  across subjects. The values presented at the top are mean  $\pm$  SEM across subjects for  $\kappa$ , with bold text and \*indicating  $p(\kappa \neq 0) < 0.05$  (Wilcoxon sign rank test). The numbers of subjects included after discarding those that reached the boundary conditions are presented in the form ( $N = \# / 15$ ) at the bottom of each plot.

relationship, no prior assumption is made as to whether  $\text{CMRO}_2$  increases, decreases or remains constant with hypercapnia. This linear assumption is also implicitly made as part of the iso-metabolic assumption, or when using previous literature values for a  $\text{CMRO}_2$  decrease. The linear relationship between  $\text{CMRO}_2$  and hypercapnia level is based on our recent observations of a linear relationship between hypercapnia level and spontaneous neuronal oscillatory power (Driver et al., 2016). Whilst there is currently no direct relationship established between  $\text{CMRO}_2$  and neuronal oscillatory power, they may share similar underlying neurochemical mechanisms for their responses to hypercapnia, specifically extracellular pH changes modulating ATP channels (Dulla et al., 2005). Even if the relationship includes some non-linearity, bias introduced by a linear correction will be smaller than the bias from no correction.

The constrained non-linear fitting performed here to solve for  $M$  and  $\kappa$  imposed boundary conditions on these parameters. These boundary conditions  $1 < M < 20\%$ ;  $-5 < \kappa < +5\%/\text{mmHg}$  were chosen to be sufficiently broad to include the range of values that would be reasonably expected when averaging across these regions of interest, based on previous literature (Leontiev and Buxton, 2007; Chiarelli et al., 2007a; Mark et al., 2011; Xu et al., 2011). Therefore, where the fitting algorithms returned values that reached these boundary conditions, this is likely to be due to noise in the data, most likely the ASL data, rather than being an actual physiological outlier. It is for this reason that we chose to discard results where the boundary condition was reached, an approach we have taken previously (Murphy et al., 2013; Wise et al., 2013). Out of the 18 versions of

the non-linear fitting (three ROIs over three  $\alpha/\beta$  pairings for each of the two- and one-parameter fits), 14 had either one or no subjects reaching the boundary condition. There were 3 occasions where more than two subjects reached the boundary condition, all occurring in the visual ROI for the one-parameter fit, 5 subjects each for the 0.14/0.91 and 0.2/1.3  $\alpha/\beta$  pairings and 4 subjects for the 0.06/1  $\alpha/\beta$  pairing. This is consistent with the visual ROI dataset containing more variance than the motor and remaining GM ROIs (see errorbars in Figure 4). Further, a BOLD-weighted second echo time of 29 ms used here has been optimized previously for BOLD contrast, based on GM-averaged  $R_2^*$  (Wise et al., 2013; Germuska et al., 2016). The 29 ms echo time is optimal for BOLD contrast for the  $R_2^*$  values measured here in visual and GM ROIs (Table 1), however the smaller  $R_2^*$  measured in the motor ROI means that BOLD contrast in this ROI is  $\sim 10\%$  lower than it would have been if a longer echo time, specifically optimized for the motor ROI, were used. However, since the BOLD contrast is significantly above the noise, this lower BOLD contrast in the motor ROI will have a negligible impact on BOLD sensitivity and will be incorporated into  $M$ , not impacting on quantification of  $\text{CMRO}_2$ .

In conclusion, we present a new approach to calibrated BOLD, relaxing the iso-metabolic hypercapnia assumption, whilst measuring the dose-wise change in  $\text{CMRO}_2$  due to hypercapnia. This approach can map local  $\text{CMRO}_2$  responses to hypercapnia, so may be suitable for measuring spatial heterogeneity in these responses. This approach may be especially applicable in studies including metabolic pathology, such as diabetes, dementia, and

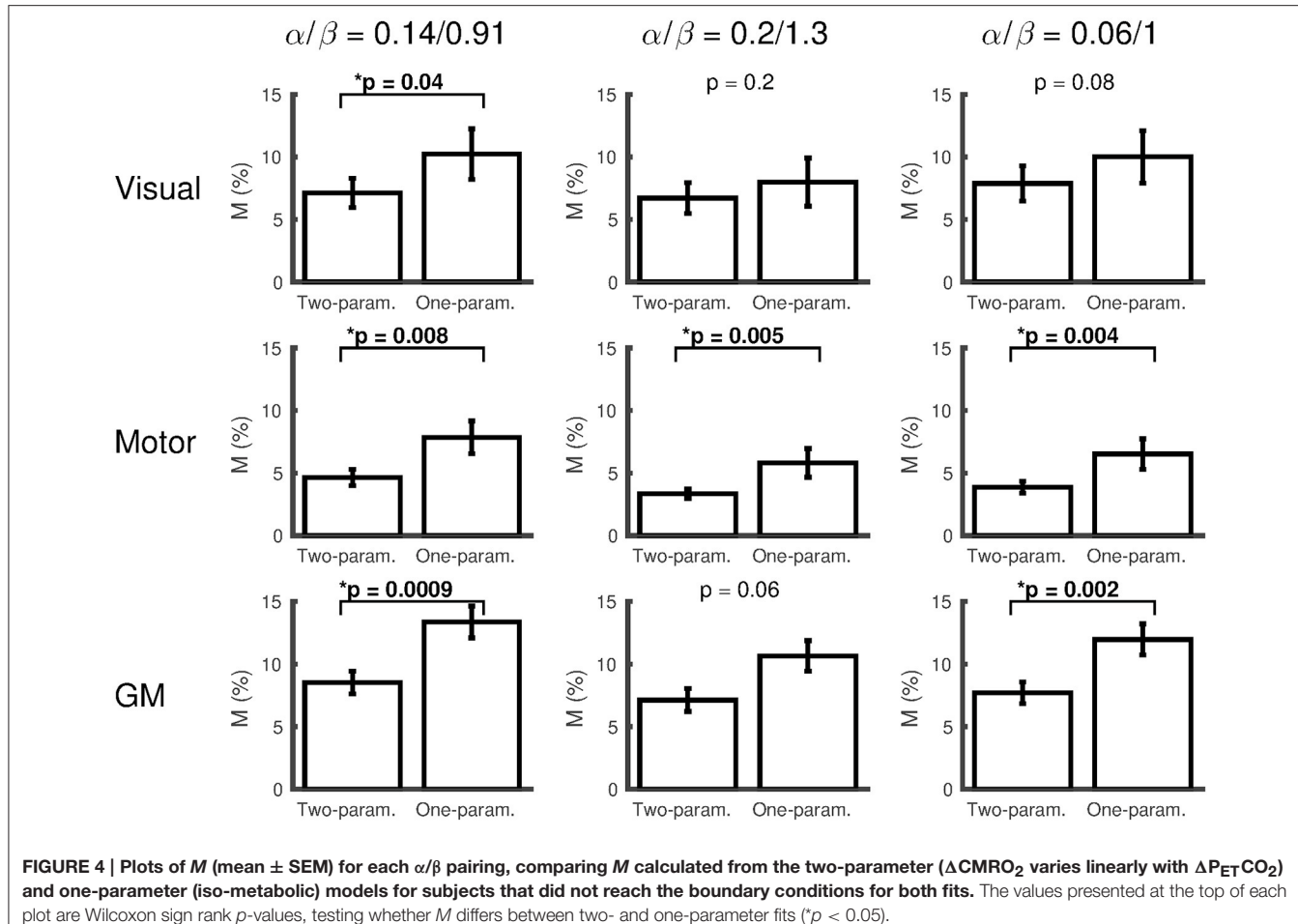


**FIGURE 4 |** Plots of  $M$  (mean  $\pm$  SEM) for each  $\alpha/\beta$  pairing, comparing  $M$  calculated from the two-parameter ( $\Delta CMRO_2$  varies linearly with  $\Delta P_{ET}CO_2$ ) and one-parameter (iso-metabolic) models for subjects that did not reach the boundary conditions for both fits. The values presented at the top of each plot are Wilcoxon sign rank  $p$ -values, testing whether  $M$  differs between two- and one-parameter fits (\* $p < 0.05$ ).

multiple sclerosis, where there may be inter- and/or intra-subject differences in the CMRO<sub>2</sub> response to hypercapnia. Further, as well as the calibrated BOLD endpoints of measuring task-dependent CMRO<sub>2</sub>, or absolute CMRO<sub>2</sub>, the measurement of the CMRO<sub>2</sub> response to hypercapnia could become a tool for investigating cerebral metabolic health in its own right.

## AUTHOR CONTRIBUTIONS

ID and KM developed the idea. KM and RW designed the experiment. KM and RW acquired the data. ID and KM

performed data analysis. ID, RW, and KM interpreted the results. ID drafted the manuscript. ID, RW, and KM revised the manuscript.

## ACKNOWLEDGMENTS

The authors wish to thank Ashley Harris for contributing to the data acquisition. ID and KM acknowledge salary support from the Wellcome Trust [WT090199; WT200804]. RW acknowledges the support of the Higher Education Funding Council for Wales (HEFCW).

## REFERENCES

- Blockley, N. P., Griffeth, V. E., Stone, A. J., Hare, H. V., and Bulte, D. P. (2015). Sources of systematic error in calibrated BOLD based mapping of baseline oxygen extraction fraction. *Neuroimage* 122, 105–113. doi: 10.1016/j.neuroimage.2015.07.059
- Boxerman, J. L., Hamberg, L. M., Rosen, B. R., and Weisskoff, R. M. (1995). MR contrast due to intravascular magnetic susceptibility perturbations. *Magn. Reson. Med.* 34, 555–566. doi: 10.1002/mrm.1910340412
- Bulte, D. P., Kelly, M., Germuska, M., Xie, J., Chappell, M. A., Okell, T. W., et al. (2012). Quantitative measurement of cerebral physiology using respiratory-calibrated MRI. *Neuroimage* 60, 582–591. doi: 10.1016/j.neuroimage.2011.12.017
- Chen, J. J., and Pike, G. B. (2010a). Global cerebral oxidative metabolism during hypercapnia and hypocapnia in humans: implications for BOLD fMRI. *J. Cereb. Blood Flow Metab.* 30, 1094–1099. doi: 10.1038/jcbfm.2010.42
- Chen, J. J., and Pike, G. B. (2010b). MRI measurement of the BOLD-specific flow-volume relationship during hypercapnia and hypocapnia in humans. *Neuroimage* 53, 383–391. doi: 10.1016/j.neuroimage.2010.07.003

- Chiarelli, P. A., Bulte, D. P., Gallichan, D., Piechnik, S. K., Wise, R., and Jezzard, P. (2007a). Flow-metabolism coupling in human visual, motor, and supplementary motor areas assessed by magnetic resonance imaging. *Magn. Reson. Med.* 57, 538–547. doi: 10.1002/mrm.21171
- Chiarelli, P. A., Bulte, D. P., Piechnik, S., and Jezzard, P. (2007b). Sources of systematic bias in hypercapnia-calibrated functional MRI estimation of oxygen metabolism. *Neuroimage* 34, 35–43. doi: 10.1016/j.neuroimage.2006.08.033
- Croal, P. L., Driver, I. D., Francis, S. T., and Gowland, P. A. (2017). Field strength dependence of grey matter  $R_2^*$  on venous oxygenation. *Neuroimage* 146, 327–332. doi: 10.1016/j.neuroimage.2016.10.004
- Davis, T. L., Kwong, K. K., Weisskoff, R. M., and Rosen, B. R. (1998). Calibrated functional MRI: mapping the dynamics of oxidative metabolism. *Proc. Natl. Acad. Sci. U.S.A.* 95, 1834–1839. doi: 10.1073/pnas.95.4.1834
- Driver, I., Blockley, N., Fisher, J., Francis, S., and Gowland, P. (2010). The change in cerebrovascular reactivity between 3 T and 7 T measured using graded hypercapnia. *Neuroimage* 51, 274–279. doi: 10.1016/j.neuroimage.2009.12.113
- Driver, I. D., Whittaker, J. R., Bright, M. G., Muthukumaraswamy, S. D., and Murphy, K. (2016). Arterial CO<sub>2</sub> fluctuations modulate neuronal rhythmicity: implications for MEG and fMRI studies of resting-state networks. *J. Neurosci.* 36, 8541–8550. doi: 10.1523/JNEUROSCI.4263-15.2016
- Dulla, C. G., Dobelis, P., Pearson, T., Frenguelli, B. G., Staley, K. J., and Masino, S. A. (2005). Adenosine and ATP link PCO<sub>2</sub> to cortical excitability via pH. *Neuron* 48, 1011–1023. doi: 10.1016/j.neuron.2005.11.009
- Gauthier, C. J., and Hoge, R. D. (2012). Magnetic resonance imaging of resting OEF and CMRO(2) using a generalized calibration model for hypercapnia and hyperoxia. *Neuroimage* 60, 1212–1225. doi: 10.1016/j.neuroimage.2011.12.056
- Germuska, M., Merola, A., Murphy, K., Babic, A., Richmond, L., Khot, S., et al. (2016). A forward modelling approach for the estimation of oxygen extraction fraction by calibrated fMRI. *Neuroimage* 139, 313–323. doi: 10.1016/j.neuroimage.2016.06.004
- Glover, G. H. (1999). Simple analytic spiral K-space algorithm. *Magn. Reson. Med.* 42, 412–415. doi: 10.1002/(SICI)1522-2594(199908)42:2<412::AID-MRM2>3.0.CO;2-U
- Griffith, V. E. M., and Buxton, R. B. (2011). A theoretical framework for estimating cerebral oxygen metabolism changes using the calibrated-BOLD method: modeling the effects of blood volume distribution, hematocrit, oxygen extraction fraction, and tissue signal properties on the BOLD signal. *Neuroimage* 58, 198–212. doi: 10.1016/j.neuroimage.2011.05.077
- Grubb, R. L. Jr., Raichle, M. E., Eichling, J. O., and Ter-Pogossian, M. M. (1974). The effects of changes in PaCO<sub>2</sub> on cerebral blood volume, blood flow, and vascular mean transit time. *Stroke* 5, 630–639. doi: 10.1161/01.STR.5.5.630
- Hall, E. L., Driver, I. D., Croal, P. L., Francis, S. T., Gowland, P. A., Morris, P. G., et al. (2011). The effect of hypercapnia on resting and stimulus induced MEG signals. *Neuroimage* 58, 1034–1043. doi: 10.1016/j.neuroimage.2011.06.073
- Ho, Y. C., Petersen, E. T., Zimine, I., and Golay, X. (2011). Similarities and differences in arterial responses to hypercapnia and visual stimulation. *J. Cereb. Blood Flow Metab.* 31, 560–571. doi: 10.1038/jcbfm.2010.126
- Hoffman, W. E., Miletich, D. J., and Albrecht, R. F. (1982). Cerebrovascular and cerebral metabolic responses of aged rats to changes in arterial PCO<sub>2</sub>. *Neurobiol. Aging* 3, 141–143. doi: 10.1016/0197-4580(82)90010-0
- Hoge, R. D., Atkinson, J., Gill, B., Crelier, G. R., Marrett, S., and Pike, G. B. (1999). Investigation of BOLD signal dependence on cerebral blood flow and oxygen consumption: the deoxyhemoglobin dilution model. *Magn. Reson. Med.* 42, 849–863. doi: 10.1002/(SICI)1522-2594(199911)42:5<849::AID-MRM4>3.0.CO;2-Z
- Horvath, I., Sandor, N. T., Ruttner, Z., and McLaughlin, A. C. (1994). Role of nitric oxide in regulating cerebrocortical oxygen consumption and blood flow during hypercapnia. *J. Cereb. Blood Flow Metab.* 14, 503–509. doi: 10.1038/jcbfm.1994.62
- Ito, H., Kanno, I., Ibaraki, M., Hatazawa, J., and Miura, S. (2003). Changes in human cerebral blood flow and cerebral blood volume during hypercapnia and hypcapnia measured by positron emission tomography. *J. Cereb. Blood Flow Metab.* 23, 665–670. doi: 10.1097/01.WCB.0000067721.64998.F5
- Jain, V., Langham, M. C., Floyd, T. F., Jain, G., Magland, J. F., and Wehrli, F. W. (2011). Rapid magnetic resonance measurement of global cerebral metabolic rate of oxygen consumption in humans during rest and hypercapnia. *J. Cereb. Blood Flow Metab.* 31, 1504–1512. doi: 10.1038/jcbfm.2011.34
- Jones, M., Berwick, J., Hewson-Stoate, N., Gias, C., and Mayhew, J. (2005). The effect of hypercapnia on the neural and hemodynamic responses to somatosensory stimulation. *Neuroimage* 27, 609–623. doi: 10.1016/j.neuroimage.2005.04.036
- Kety, S. S., and Schmidt, C. F. (1948). The effects of altered arterial tensions of carbon dioxide and oxygen on cerebral blood flow and cerebral oxygen consumption of normal young men. *J. Clin. Invest.* 27, 484–492. doi: 10.1172/JCII101995
- Klefioth, A. B., Grubb, R. L. Jr., and Raichle, M. E. (1979). Depression of cerebral oxygen utilization by hypercapnia in the rhesus monkey. *J. Neurochem.* 32, 661–663. doi: 10.1111/j.1471-4159.1979.tb00404.x
- Kudomi, N., Hirano, Y., Koshino, K., Hayashi, T., Watabe, H., Fukushima, K., et al. (2013). Rapid quantitative CBF and CMRO(2) measurements from a single PET scan with sequential administration of dual (15)O-labeled tracers. *J. Cereb. Blood Flow Metab.* 33, 440–448. doi: 10.1038/jcbfm.2012.188
- Kwong, K. K., Belliveau, J. W., Chesler, D. A., Goldberg, I. E., Weisskoff, R. M., Poncelet, B. P., et al. (1992). Dynamic magnetic resonance imaging of human brain activity during primary sensory stimulation. *Proc. Natl. Acad. Sci. U.S.A.* 89, 5675–5679. doi: 10.1073/pnas.89.12.5675
- Lammertsma, A. A., and Jones, T. (1983). Correction for the presence of intravascular oxygen-15 in the steady-state technique for measuring regional oxygen extraction ratio in the brain: 1. Description of the method. *J. Cereb. Blood Flow Metab.* 3, 416–424. doi: 10.1038/jcbfm.1983.67
- Lammertsma, A. A., Wise, R. J., Heather, J. D., Gibbs, J. M., Leenders, K. L., Frackowiak, R. S., et al. (1983). Correction for the presence of intravascular oxygen-15 in the steady-state technique for measuring regional oxygen extraction ratio in the brain: 2. Results in normal subjects and brain tumour and stroke patients. *J. Cereb. Blood Flow Metab.* 3, 425–431. doi: 10.1038/jcbfm.1983.68
- Leontiev, O., and Buxton, R. B. (2007). Reproducibility of BOLD, perfusion, and CMRO<sub>2</sub> measurements with calibrated-BOLD fMRI. *Neuroimage* 35, 175–184. doi: 10.1016/j.neuroimage.2006.10.044
- Liu, T. T., Wong, E. C., Frank, L. R., and Buxton, R. B. (2002). Analysis and design of perfusion-based event-related fMRI experiments. *Neuroimage* 16, 269–282. doi: 10.1006/nimg.2001.1038
- Lu, H., Zhao, C., Ge, Y., and Lewis-Amezua, K. (2008). Baseline blood oxygenation modulates response amplitude: physiologic basis for intersubject variations in functional MRI signals. *Magn. Reson. Med.* 60, 364–372. doi: 10.1002/mrm.21686
- Mark, C. I., Fisher, J. A., and Pike, G. B. (2011). Improved fMRI calibration: precisely controlled hyperoxic versus hypercapnic stimuli. *Neuroimage* 54, 1102–1111. doi: 10.1016/j.neuroimage.2010.08.070
- Merola, A., Murphy, K., Stone, A. J., Germuska, M. A., Griffith, V. E., Blockley, N. P., et al. (2016). Measurement of oxygen extraction fraction (OEF): an optimized BOLD signal model for use with hypercapnic and hyperoxic calibration. *Neuroimage* 129, 159–174. doi: 10.1016/j.neuroimage.2016.01.021
- Mintun, M. A., Raichle, M. E., Martin, W. R., and Herscovitch, P. (1984). Brain oxygen utilization measured with O-15 radiotracers and positron emission tomography. *J. Nucl. Med.* 25, 177–187.
- Murphy, K., Harris, A. D., and Wise, R. G. (2013). “Measuring the influence of hypercapnia on absolute CMRO<sub>2</sub> in humans,” in *Proceedings ISMRM*, (Salt Lake City, UT), 3342.
- Noth, U., Meadows, G. E., Kotajima, F., Deichmann, R., Corfield, D. R., and Turner, R. (2006). Cerebral vascular response to hypercapnia: determination with perfusion MRI at 1.5 and 3.0 Tesla using a pulsed arterial spin labeling technique. *J. Magn. Reson. Imaging* 24, 1229–1235. doi: 10.1002/jmri.20761
- Ogawa, S., Menon, R. S., Tank, D. W., Kim, S. G., Merkle, H., Ellermann, J. M., et al. (1993). Functional brain mapping by blood oxygenation level-dependent contrast magnetic resonance imaging. A comparison of signal characteristics with a biophysical model. *Biophys. J.* 64, 803–812. doi: 10.1016/S0006-3495(93)81441-3
- Ogawa, S., Tank, D. W., Menon, R., Ellermann, J. M., Kim, S. G., Merkle, H., et al. (1992). Intrinsic signal changes accompanying sensory stimulation: functional brain mapping with magnetic resonance imaging. *Proc. Natl. Acad. Sci. U.S.A.* 89, 5951–5955. doi: 10.1073/pnas.89.13.5951
- Rhodes, C. G., Lenzi, G. L., Frackowiak, R. S., Jones, T., and Pozzilli, C. (1981). Measurement of CBF and CMRO<sub>2</sub> using the continuous inhalation of C15O<sub>2</sub>

- and 15O. Experimental validation using CO<sub>2</sub> reactivity in the anaesthetised dog. *J. Neurol. Sci.* 50, 381–389. doi: 10.1016/0022-510X(81)90150-7
- Sicard, K. M., and Duong, T. Q. (2005). Effects of hypoxia, hyperoxia, and hypercapnia on baseline and stimulus-evoked BOLD, CBF, and CMRO<sub>2</sub> in spontaneously breathing animals. *Neuroimage* 25, 850–858. doi: 10.1016/j.neuroimage.2004.12.010
- Ter-Pogossian, M. M., and Herscovitch, P. (1985). Radioactive oxygen-15 in the study of cerebral blood flow, blood volume, and oxygen metabolism. *Semin. Nucl. Med.* 15, 377–394. doi: 10.1016/S0001-2998(85)80015-5
- Wise, R. G., Harris, A. D., Stone, A. J., and Murphy, K. (2013). Measurement of OEF and absolute CMRO<sub>2</sub>: MRI-based methods using interleaved and combined hypercapnia and hyperoxia. *Neuroimage* 83, 135–147. doi: 10.1016/j.neuroimage.2013.06.008
- Wong, E. C., Buxton, R. B., and Frank, L. R. (1998). Quantitative imaging of perfusion using a single subtraction (QUIPSS and QUIPSS II). *Magn. Reson. Med.* 39, 702–708. doi: 10.1002/mrm.1910390506
- Xu, F., Uh, J., Brier, M. R., Hart, J. Jr., Yezhuvath, U. S., Gu, H., et al. (2011). The influence of carbon dioxide on brain activity and metabolism in conscious humans. *J. Cereb. Blood Flow Metab.* 31, 58–67. doi: 10.1038/jcbfm.2010.153
- Yablonskiy, D. A. (2011). Cerebral metabolic rate in hypercapnia: controversy continues. *J. Cereb. Blood Flow Metab.* 31, 1502–1503. doi: 10.1038/jcbfm.2011.32
- Zappe, A. C., Uludag, K., Oeltermann, A., Ugurbil, K., and Logothetis, N. K. (2008). The influence of moderate hypercapnia on neural activity in the anesthetized nonhuman primate. *Cereb. Cortex* 18, 2666–2673. doi: 10.1093/cercor/bhn023

**Conflict of Interest Statement:** The authors declare that the research was conducted in the absence of any commercial or financial relationships that could be construed as a potential conflict of interest.

Copyright © 2017 Driver, Wise and Murphy. This is an open-access article distributed under the terms of the Creative Commons Attribution License (CC BY). The use, distribution or reproduction in other forums is permitted, provided the original author(s) or licensor are credited and that the original publication in this journal is cited, in accordance with accepted academic practice. No use, distribution or reproduction is permitted which does not comply with these terms.



# Reconstruction of Arm Movement Directions from Human Motor Cortex Using fMRI

Seungkyu Nam and Dae-Shik Kim \*

*Brain Reverse Engineering and Imaging Lab, School of Electrical Engineering, Korea Advanced Institute of Science and Technology, Daejeon, South Korea*

Recent advances in functional magnetic resonance imaging (fMRI) have been used to reconstruct cognitive states based on brain activity evoked by sensory or cognitive stimuli. To date, such decoding paradigms were mostly used for visual modalities. On the other hand, reconstructing functional brain activity in motor areas was primarily achieved through more invasive electrophysiological techniques. Here, we investigated whether non-invasive fMRI responses from human motor cortex can also be used to predict individual arm movements. To this end, we conducted fMRI studies in which participants moved their arm from a center position to one of eight target directions. Our results suggest that arm movement directions can be distinguished from the multivoxel patterns of fMRI responses in motor cortex. Furthermore, compared to multivoxel pattern analysis, encoding models were able to also reconstruct unknown movement directions from the predicted brain activity. We conclude for our study that non-invasive fMRI signal can be utilized to predict directional motor movements in human motor cortex.

## OPEN ACCESS

**Edited by:**

Itamar Ronen,  
Leiden University, Netherlands

**Reviewed by:**

Michael Hanke,  
Otto-von-Guericke University  
Magdeburg, Germany  
Baxter P. Rogers,  
Vanderbilt University, United States

**\*Correspondence:**

Dae-Shik Kim  
daeshik@kaist.ac.kr

**Specialty section:**

This article was submitted to  
Brain Imaging Methods,  
a section of the journal  
*Frontiers in Neuroscience*

**Received:** 27 January 2017

**Accepted:** 14 July 2017

**Published:** 27 July 2017

**Citation:**

Nam S and Kim D-S (2017)  
Reconstruction of Arm Movement  
Directions from Human Motor Cortex  
Using fMRI. *Front. Neurosci.* 11:434.  
doi: 10.3389/fnins.2017.00434

**Keywords:** fMRI, reconstruction, classification, decoding, encoding, directional movement

## INTRODUCTION

Recent fMRI studies have successfully discriminated visual object categories (Haxby et al., 2001; Cox and Savoy, 2003), hand gestures (Dinstein et al., 2008), and visual features such as orientation and motion direction (Kamitani and Tong, 2005, 2006) from patterns of activity across an array of voxels. Similar methods have been used to reconstruct visual stimuli such as images or movies by modeling the brain activity in each voxel evoked by the visual stimuli (Thirion et al., 2006; Miyawaki et al., 2008; Naselaris et al., 2009; Nishimoto et al., 2011). On the other hand, decoding brain activity in motor areas usually require more invasive techniques. For example, invasive electrophysiological techniques have demonstrated that neuronal activities in human primary motor cortex (M1) can be used to control an artificial devices (Hochberg et al., 2006, 2012; Truccolo et al., 2008; Collinger et al., 2013). Such invasive techniques have been found to be more precise and intuitive when used to control an external effector using neuronal signals related to arm movements. Nonetheless, these methods inevitably involved considerable risks associated with surgical procedures and potential inflammations. Therefore, we used functional magnetic resonance imaging (fMRI) to measure brain signals non-invasively and investigated whether the recent decoding methods were applicable to motor areas.

Neurons in the macaque M1 are known to be broadly tuned to directional arm movements (Georgopoulos et al., 1982). This type of directional tuning is known as a basic functional property of neuronal activity in M1. Previous studies also demonstrated that human M1 neurons are sensitive to the movement direction based on electrophysiological signals

(Hochberg et al., 2006; Truccolo et al., 2008). Furthermore, fMRI responses in human M1 suggested sensitivity to movement directions although each voxel contains a large number of neurons, where each of them has different selectivities (Eisenberg et al., 2010; Fabbri et al., 2010). Given that each voxel in motor cortex is directionally tuned, and despite the fact that the sensitivity of a voxel is weak, spatial patterns of fMRI response may be distinguishable for different movement directions. To this end, previous fMRI studies have used multivoxel pattern analysis (MVPA) based on linear classifier to discriminate cognitive states based on spatial patterns of fMRI responses (Mitchell et al., 2004; Haynes and Rees, 2006; Norman et al., 2006; Hansen, 2007; De Martino et al., 2008; Formisano et al., 2008; Haynes, 2009).

In this study, participants performed a center-out reaching task during fMRI scan. The participants moved their arm from a center position toward one of eight target positions repeatedly according to visual instructions. To investigate how head motions induced by repeated reaching movements have an effect on the identification of different movement directions, we also compared contralateral motor cortex with ipsilateral motor cortex which uninvolved in the center-out reaching task. The results demonstrated that reaching-out movements toward eight directions can be discriminated based on spatial patterns of fMRI responses in M1, although it was influenced by head motion artifacts. However, these methods were restricted to predicting sensory, cognitive, or motor information. In this model, spatial patterns of fMRI response are used to identify a specific task from a known stimulus set. To reconstruct an unknown stimulus, decoding methods using encoding model are applied. Encoding models use given stimuli to estimate corresponding brain activity in each voxel, and then are used to reconstruct unknown stimuli using the estimated fMRI responses. Here, we used the directional tuning properties in human M1 to estimate the brain activity evoked by directional motor movements in each voxel. The responses of each voxel were characterized as a linear combination of idealized directional tuning curves (Brouwer and Heeger, 2009). The identification and reconstruction of movement directions were performed using that linear encoding model. In the identification, the encoding model demonstrated similar performance compared to MVPA. To determine the feasibility of reconstructing all possible directional motor movements from a limited amount of pre-specified movement directions, we compared the reconstruction performance capabilities in the case when movement directions were used to estimate the encoding model with when they were not used.

## MATERIALS AND METHODS

### Participants

Eight healthy right-handed subjects (mean age, 24.25; range, 21–30 years) participated in the experiments, which consisted of functional scanning sessions for center-out reaching task along with a high-resolution anatomical scanning session. All subjects had normal visual acuity and no neurological or psychiatric history. They provided written informed consent regarding their participation. The experimental procedures were

in compliance with the safety guidelines for MRI research and were approved by the Institutional Review Board for research involving human subjects at the Korea Advanced Institute of Science and Technology.

### MRI Acquisition

The experiments were performed at 3T MR scanner (Siemens Magnetom Verio, Germany). The functional images were acquired with a T2\*-weighted gradient recalled echo-planar imaging (EPI) sequence (TR, 1,000 ms; TE, 20 ms; flip angle, 90°; FOV: 64 × 64 mm; voxel size, 3 × 3 × 5.5 mm, number of slices, 21). T1-weighted magnetization-prepared rapid-acquisition gradient echo (MPRAGE) images were also acquired (TR, 1,800 ms; TE, 2.52 ms; FA, 9°; FOV, 256 × 256 mm; voxel size, 1 × 1 × 1 mm).

### Experimental Design

Each subject performed a center-out movement task. This task involved a total of six runs. In the task, subjects were instructed to move their right arm from a center position to one of eight target positions along a route carved into an acrylic panel (**Figures 1A,B**). The reaching movement was performed five times in each run, along with five no movement trials on the center position. Each run involved 40 trials for the reaching movements and 5 trials for the no-movement cases. No movement trials were pseudorandomly interleaved between reaching movement trials. The reaching movements in the experiment accounted for 240 trials in total (30 trials per each direction). Each trial lasted 12 s. One run lasted 9 min and 24 s.

In each trial, we showed the participants a gray circle in the center and eight gray circles on the periphery of the center circle on a screen. Initially, they were instructed to hold their arm at the center position which was the initial position before reaching their arm to the target position. After 4 s, one of the eight gray targets turned blue, which indicated the target direction to which to move. The participants had to move their arm toward the blue target position for 2 s. After reaching the target position, they were instructed to keep their arms still at the target position for 4 s. When the circle in the center turned blue, they moved their arm back to the initial center position (**Figure 1C**). The visual task was programmed with MATLAB Psychtoolbox-3 for windows (Brainard, 1997). The visual cues were presented with MR-compatible video goggles (Nordic Neuro Lab, Norway).

Before performing a center-out movement task, each participant was sufficiently trained to become familiar with the reaching movement inside the scanner and instructed to move smoothly and consistently. To perform reaching movements on the acrylic panel without moving their head, shoulder, or upper arm, the subject's head was stabilized with foam paddings inside the head coil and cushioned head stabilizers placed on each side of the head coil to reduce head motion. The subject's upper arms and shoulder were stabilized with a strap wrapping across the chest and shoulder (**Figure 1A**).

### Data Preprocessing

Data preprocessing was performed using custom software written in Matlab (The MathWorks, Inc., USA). The first four

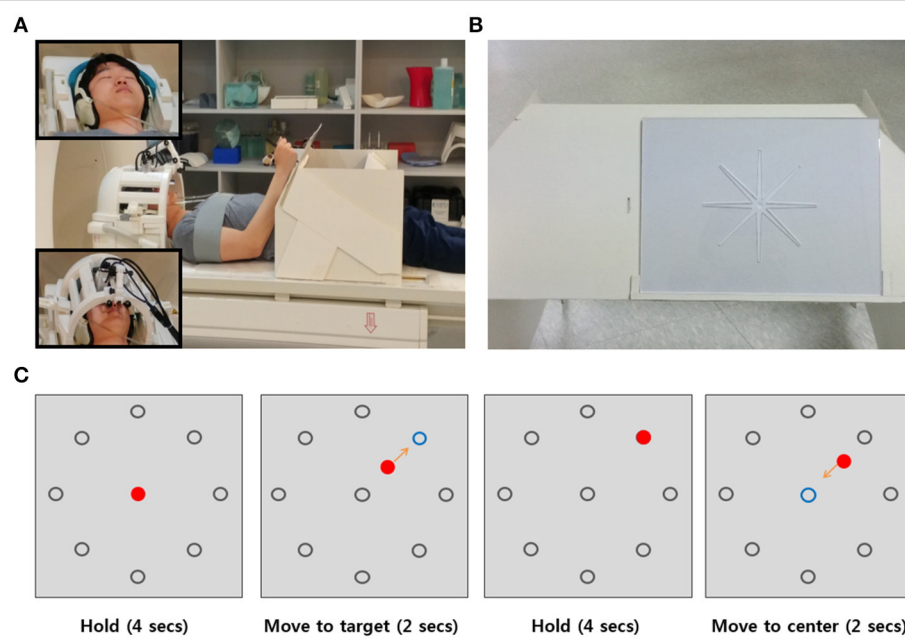


**FIGURE 1 |** Setup and Experimental Design. **(A)** Participants laid in the scanner and put their arm on the arm-rest table to perform a center-out reaching task. To perform the task without moving their head, shoulder, or upper arm, the participant's head was stabilized with foam padding inside the head coil (upper left corner in **(A)**) and fixed using cushioned head stabilizers placed on each side of the head coil (bottom left corner in **(A)**). As additional precautions against head movements and shoulder, the participant's shoulder was stabilized with a strap wrapping across the chest and shoulder. **(B)** The acrylic panel for the reaching movement. The carved route served to maintain a constant reaching direction for each trial. **(C)** Example sequence of a trial. There were eight gray target circles in the periphery of the center. The blue circle indicated the target position which to move and the red circle indicated the movement trajectory the participant used to move toward the target direction.

volumes of each run were discarded automatically during the scanning process. We performed three-dimensional motion correction using the first volume as a reference, and the T2 anatomical image was coregistered to the functional image data by SPM5 (<http://www.fil.ion.ucl.ac.uk/spm>). No spatial smoothing was applied. The left primary motor cortex (M1) ROI was individually defined for each participant by converting the left M1 ROI of the standard MNI brain (Maldjian et al., 2003) to that of an individual brain using the SPM5 deformation toolbox. Voxels with extremely low signal intensity levels were removed. The fMRI signals were linearly detrended and passed through a high-pass filter using a cutoff frequency of 0.01 Hz within each run to remove low-frequency drift. We regressed out residual motion effects from the fMRI signals using six motion parameters (three translational parameters and three rotational parameters). The parameters were estimated using rigid body transformation between each functional image and a reference image during motion correction procedure by SPM. Signal intensities were normalized by removing the baseline from the fMRI signal of each voxel within each run and were averaged within each reaching movement trial after shifting the data by 3–5 s to compensate for hemodynamic delays in each case. We selected relevant voxels within the left M1 using sparse multinomial logistic regression (SMLR)-based feature selection. In a typical fMRI experiment, there are too many voxels in the brain compared to the number of samples that can be obtained. Too many voxels or features can lead to poor generalization

performance by overfitting the learning model if all voxels are used as input features. Support vector machine (SVM) we used in this study for classification can avoid this problem by maximizing the margin and minimizing the classification error. However, the generalization performance of SVM is also decreased if too many irrelevant features are used to train the model. Therefore, we used one of voxel selection methods that can be used as a stand-alone tool box for voxel selection to improve the model performance by removing the irrelevant voxels. SMLR-based voxel selection was based on the classification performance and selection frequency as selection counting value (SC-value). Irrelevant voxels which have 0 SC-value obtained by SMLR-based feature selection were removed. SMLR-based feature selection was implemented by SLR toolbox (Miyawaki et al., 2008; Yamashita et al., 2008).

## Classification Using Multivoxel Pattern Analysis

We investigated whether human M1 voxels show directional sensitivity and whether the spatial patterns of the fMRI responses in M1 evoked by directional movements could be discriminable using MVPA based on linear classifier (Norman et al., 2006). The classification was performed with a linear support vector machine (SVM) classifier, one of the most popular classifiers in MVPA literature. The SVM was implemented by the LIBSVM toolbox (Chang and Lin, 2011) and we applied all of the default parameters of linear SVM ( $C = 1$ ). The fMRI responses of voxels in left M1 ROI evoked by reaching movements were used for the

classification. We evaluated the classification performance of the SVM using a leave-one-run-out cross-validation procedure. In each cross validation, one run (40 trials, 5 trials in each movement direction) was retained as a test dataset while the remaining five runs (200 trials, 25 trials in each movement direction) were used to remove the irrelevant voxels using the SMLR-based feature selection and to train the SVM classifier using the responses of selected voxels. This procedure was repeated 6 times until all runs were used as a test dataset. The classification performance was obtained by averaging the prediction accuracies across runs.

## Classification Using Encoding Model

To characterize the responses of each voxel, we used a simple linear encoding model (Brouwer and Heeger, 2009) that has been used for color decoding in visual cortical areas. Recent evidence has showed that neurons in human M1 are directionally tuned (Hochberg et al., 2006, 2012; Truccolo et al., 2008; Collinger et al., 2013). The fMRI responses in human M1 were also found to be sensitive to movement directions (Eisenberg et al., 2010; Fabbri et al., 2010). Therefore, we could characterize the directional tuning of the response of each voxel. To characterize the directional tuning of each voxel, we assumed that the neurons in human M1 were directionally tuned, and the activity shape of the directionally tuned neurons was modeled as a half-wave rectified sinusoidal curve. The negative values of the tuning curve were set to 0 (Figure 2A). Given that there are a large number of neurons in each voxel, we also assumed a relationship between the fMRI responses and the neuronal activity. Previous studies provides evidence that fMRI responses are linearly related to the sum of the activity of all neurons within a voxel (Heeger et al., 2000; Rees et al., 2000). Although it was an oversimplification, we assumed a linear relationship between the fMRI response and the local neuronal activity. Therefore, the response of a voxel was the result of summing up responses of all neurons distributed in that voxel. The tuning function of the voxel then characterized as a linear combination of six half-wave rectified tuning curves. The six directional tuning curves is shown in Figure 2B. The tuning curve served as a basis function of the linear encoding model. The directional movement stimulus was an angular variable ranging from 0 to  $2\pi$ .

The classification performance of the encoding model was also evaluated using a leave-one-run-out cross-validation procedure. In each cross validation, five of the six runs ( $R_1$ , 200 trials, 25 trials in each movement direction) were used to remove the irrelevant voxels and to fit the encoding model using the responses of selected voxels, while the remaining one run ( $R_2$ , 40 trials, 5 trials in each movement direction) was used to predict the movement directions using the fitted encoding model. The selected voxel responses  $R_1$  could be expressed as the weighted sum of six basis functions. The linear encoding model was given by

$$R_1 = Sw,$$

where  $R_1(m \times n)$  is the measured voxel response matrix,  $S(m \times k)$  is a response matrix of the six basis functions related to the reaching movement stimulus, and  $w(k \times n)$  is a linear weight matrix. Let  $m$  denote the number of reaching movement trials,

$n$  denote the number of voxels, and  $k$  denote the number of the basis functions.

The weight matrix  $w$  was obtained using a regularized linear regression procedure to find an optimal weight to fit the encoding model more robust. The optimal weight matrix was given by

$$\hat{w} = (S^T S + \lambda I_k)^{-1} S^T R_1,$$

where  $I_k$  is the  $k$ -dimensional identity matrix and  $\lambda$  is the regularization parameter used. The lowest Bayesian information criterion (BIC) (Schwarz, 1978) was used to find the optimal value of the regularization parameter  $\lambda$  through a bootstrap method (Efron and Tibshirani, 1994). The parameter  $\lambda$  was optimized by using a regression function in RBF networks toolbox (Orr, 1996a,b).

The model was fit to the voxels individually using the linear combination of a set of basis functions. Therefore, we could estimate the response of each voxel and the spatially distributed pattern of the response across voxels activated by each movement direction. The reaching movement direction for which the predicted spatial pattern of voxel responses could be decoded by matching the most similar one with the observed spatial patterns of voxel responses. However, since there exists substantial variation in the measured voxel responses due to noise, we used the estimated response of the basis functions to match with the responses of the basis functions associated with a movement stimulus. The responses of basis function  $\hat{S}$  were predicted using the estimated weight  $\hat{w}$  and test data  $R_2$  as follows:

$$\hat{S} = R_2 \hat{w}^T (\hat{w} \hat{w}^T)^{-1}$$

Because  $\hat{w} \hat{w}^T$  was close to singular in some cases, the inverse of  $\hat{w} \hat{w}^T$  was unstable. Therefore, we used regularization to estimate the inverse. The movement direction could then be predicted by comparing the estimated response patterns of basis functions  $\hat{S}$  with known responses of the basis functions evoked by each of eight directional movements, and selecting the most similar patterns through an assessment of Pearson's  $r$ -values. Cross-validation step was repeated 6 times for all of the runs. The results based on the encoding model show the averaged classification accuracies across runs.

## Reconstruction Using Encoding Model

MVPA and the encoding model were used to identify the movement directions. Furthermore, using the encoding model, the reconstruction of the movement direction was also performed by creating response of the basis functions for all possible movement directions from 0 to  $360^\circ$ . The reconstructed direction was estimated by matching the estimated response pattern  $\hat{S}$  with the most similar one from the created response pattern. The reconstruction was also tested using a leave-one-run-out procedure. Five of the six runs (200 trials, 25 trials in each direction of movement) were used to remove the irrelevant voxels and to fit the encoding model using the responses of selected voxels. The remaining run (40 trials, 5 trials in each direction of movement) was used to test the reconstruction performance.

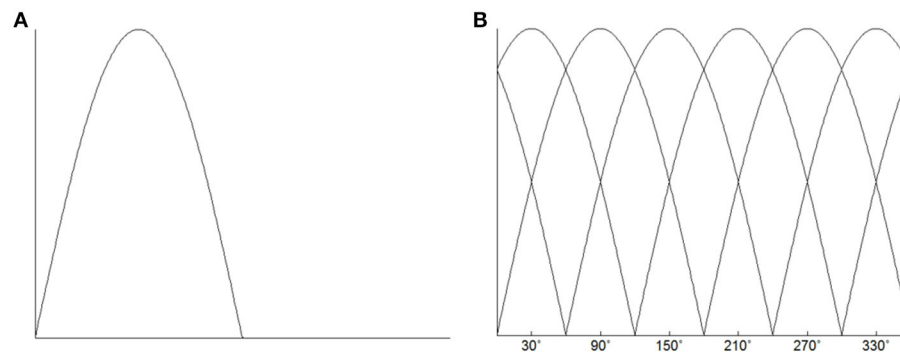


**FIGURE 2 | (A)** Directional tuning curve. The basis tuning shape was modeled as a half-wave rectified sinusoidal curve. **(B)** Six directional tuning curves were used to characterize the response of each voxel. The response of the voxel could be fitted by a linear combination of the six half-wave rectified sinusoidal curves.

We further tested the reconstruction performance in the case when movement directions were not used to fit the encoding model in order to determine the feasibility of reconstruction for unknown movement directions. To this end, the reconstruction was tested using a leave-one-direction-out procedure. One of the eight directional movements (30 trials) was remained to test the reconstruction performance as the unknown direction. The other seven directions (210 trials, 30 trials in each direction of movement) were used to select the relevant voxels using the SMLR-based feature selection and then to fit the encoding model using the responses of selected voxels. This procedure was repeated 8 times to test the reconstruction of all of eight directional movements.

The reconstructed directions for each directional movement trials were spread out from the actual movement direction. Therefore, we used the angular variance (AV) to quantify the measurement of the angular dispersion of reconstructed directions. The AV was defined as  $AV = 1 - \|r\|$ , where  $\|r\|$  is the length of the mean angular direction which is obtained by means of vector addition of reconstructed directions. The quantity of AV lies in the interval [0, 1]. It is indicative of the spread in reconstructed directions. If the reconstructed directions were spread out evenly around all directions, the AV would be close to maximal, otherwise the reconstructed directions were concentrated completely in the actual movement direction.

To compare the reconstruction performance capabilities in the case when movement directions were used to fit the encoding model with when they were not used, we investigated the association between the results of the two reconstructed directions by computing the circular correlation coefficient  $\rho$  (Jammalamadaka and Sengupta, 2001), as follows,

$$\rho = \frac{\sum_i \sin(\alpha_i - \bar{\alpha}) \sin(\beta_i - \bar{\beta})}{\sqrt{\sum_i \sin^2(\alpha_i - \bar{\alpha}) \sin^2(\beta_i - \bar{\beta})}}$$

In this equation,  $\alpha$  and  $\beta$  denote the reconstructed directions,  $\bar{\alpha}$  and  $\bar{\beta}$  denote the mean angular directions, and  $i$  denotes the number of reconstructed directions for each target direction. The correlations were obtained separately for each direction and by combining all directions for each subject.

To evaluate the reconstruction performance how they are reconstructed correctly to the actual movement directions, we computed the mean absolute error (MAE) between the reconstructed and actual movement directions across all of the reconstructed directions for individual subject. This is also computed in both cases when movement directions was included in fitting the encoding model and when they were used as unknown movement directions to compare the reconstruction performances. In this study, the reconstruction was performed based on single-trial directional movement. To investigate performance improvements when the directional movement was executed repeatedly, we computed MAE values of the mean angular directions obtained by averaging all reconstructed directions and compared the performances between the reconstruction based on single-trial and the trial-averaged reconstruction.

## Head Motion Effects

In fMRI experiments, head motion associated with motor tasks is a prominent source of noise which leads to fMRI data artifact, false detections, and misinterpretations of brain signals (Friston et al., 1996; Thesen et al., 2000; Yang et al., 2005; Culham et al., 2006). In this study, participants performed reaching-out movement task from a center to one of eight target directions. These repeated arm movements could have an effect on head motion sufficiently by generating constant movement patterns. Therefore, we investigated how head motion induced by participant-active reaching movements has an influence on the classification of directional movements. We used left M1 as a region of interest (ROI) because all reaching movements by right-handed participants were performed with the right hand. Movements performed with the dominant hand was associated with a greater activation compared with those of the non-dominant hand in the contralateral motor cortex. (Dassonville et al., 1997; Fabbri et al., 2010; Grabowska et al., 2012). Moreover, although highest directional selectivity in the right parietal reach region for both left and right hand movements was observed, executed movements performed with the right hand as well as observed and imagined movements led to non-significant activations in the ipsilateral motor cortex (Dassonville et al., 1997; Fabbri et al., 2010). The movement activation in the

right M1 would have been trivial even though it reflects any neural motion related signal by hemispheric interactions. The activation in ipsilateral M1 uninvolving in the task would reflect the head motion effects dominantly rather than hemispheric interactions. Therefore, we chose the right M1 as a control region to identify the head motion effect by the reaching movement. The performance of the control region would yield some evidence for residual head motion. The classification using MVPA and the encoding model was conducted from the right M1. The procedures were exactly identical, except for the spatial prior mask from the MNI atlas left and right M1.

## RESULTS

### Classification Performance

We evaluated the classification performance of MVPA based on SVM classifier and the encoding model via a leave-one-out cross-validation scheme. We excluded one run (40 trials) from the set of six runs to test the performance and trained the SVM classifier or the encoding model using the remaining five runs (200 trials). The classification result indicated that reaching movements toward eight different directions could be decoded from the spatially distributed patterns of the voxel responses. The classification performances of both MVPA and the encoding model were significantly greater than the chance level of 12.5% in all participants (**Figure 3**). Each point indicates the classification performance of each run which was used as test dataset during cross validation. Average accuracies across all participants for the MVPA and the encoding model were 41.8 and 36.1%, respectively. In comparison, MVPA outperformed the encoding model. These results indicated that decoding approaches using the linear classifier outperform the encoding model when used to classify brain states evoked by certain executed movements. However, such a classification-based technique shows limitations when used for decoding complex motor actions. It is impractical to measure brain activity given many states which are possible. Compared to classification-based technique, the encoding model is more applicable to decode the complex motor actions by being able to predict unknown brain states as well as to identify known states.

In the encoding model, the classification performance was less than that of MVPA. Reaching directions were predicted by matching the estimated response pattern  $\hat{S}$  with the highest correlated one among response patterns by each of eight directional movements through an assessment of Pearson's  $r$ -values. The decision boundary used to classify the reaching movement directions was not optimized in the encoding model. Therefore, we further investigated the performance validity of the encoding model by combining the encoding model with the SVM classifier. To use the SVM classifier in the encoding model, we trained the SVM classifier using the estimated response pattern of basis functions from the encoding model that was fitted by training data and then tested the classification performance capabilities. The average performance across all participants improved from 36.1 to 42.8% (**Figure 3**). There were no statistically significant performance differences between MVPA and the combined model. These results indicated that the

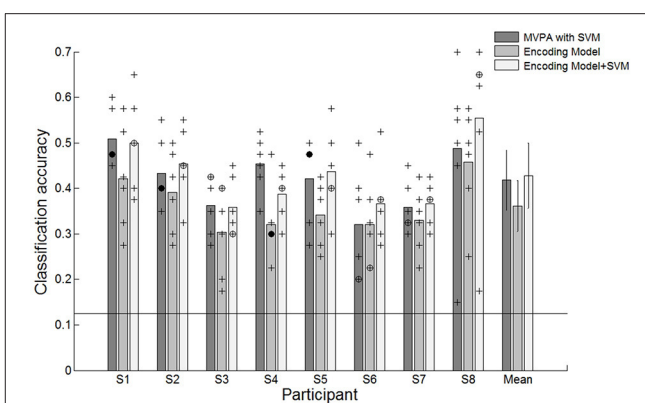


**FIGURE 3 |** Classification accuracies for individual participants and average accuracies across all participants using the conventional decoding approach based on the linear SVM classifier, the linear encoding model and combination of the encoding model and the SVM classifier. + Indicated the performance of each run which was used test dataset during cross validation.  $\oplus$  Indicates the performance of each run was overlapped twice. \* Indicates the performance of each run was overlapped three times. The solid line indicates the chance level of 12.5%. The error bars in averaged accuracies (mean) indicate the SDs across participants.

encoding model could be used to decode which direction had been moved, and these performances confirmed the validity of the encoding model for classification.

### Reconstruction Performance

The result of reconstructed direction for the first subject (S1) is shown in **Figure 4A**. The red arrows represent each actual movement direction to which the subject moved. Each black point indicates all reconstructed directions across all runs (30 trials per each movement direction). The blue arrows represent the mean angular direction for all reconstructed direction trials. The results indicated that most of the reconstructed directions were clustered near each actual movement direction and that some reconstructed directions had large errors.

We further investigated the reconstruction capabilities of when unknown directions are used. This reconstruction result is shown in **Figure 4B**. The results of the reconstructed direction indicated patterns similar to those of the reconstructed directions used to train the encoding model (**Figure 4A**). Even so some reconstructed directions had large errors showed similar patterns. To quantify this, we investigated the association between the results of the two reconstructed directions using the circular correlation coefficient  $\rho$ . The correlation result for the first subject (S1) is illustrated in **Figure 5**. For this subject, the reconstructed directions of when movement directions are used to fit the model were highly correlated with the reconstructed directions of when the movement directions are not used to fit the model for each target direction. The distributed pattern of the combined reconstructed directions over all directions also showed a highly significant correlation of  $\rho = 0.92$ . This result confirmed that the reconstructed directions by the encoding model revealed a similar pattern regardless of whether or not the

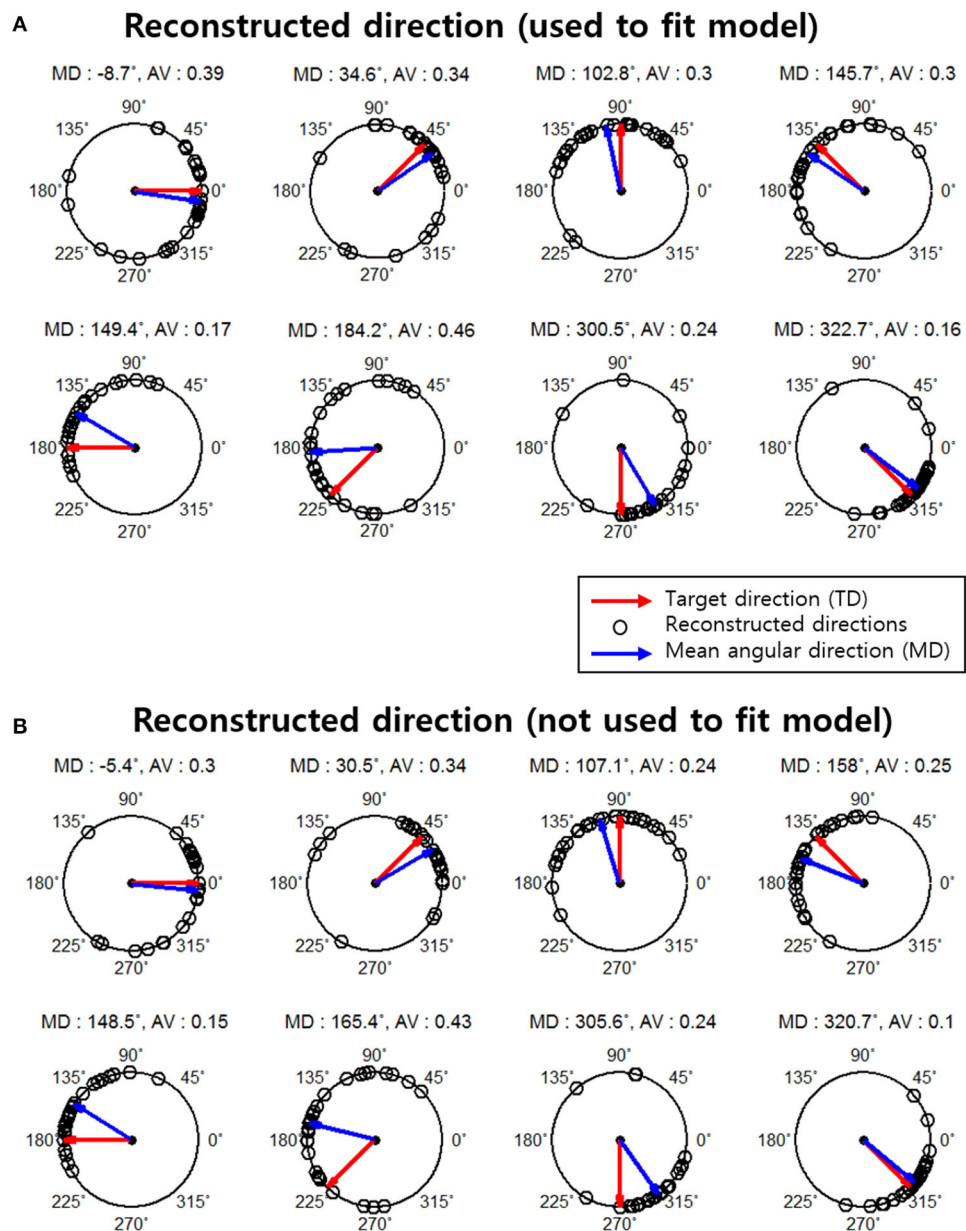


**FIGURE 4 |** Reconstruction results for subject 1. The red arrows indicate the actual movement directions (target directions). Black points indicate the reconstructed directions on a single-trial basis (total 30 reconstructed directions in each movement direction). The blue arrows represent the mean angular direction for all reconstructed directions in each target direction. The mean angular direction was obtained by means of vector addition. The angular variance (AV) was defined as  $AV = 1 - \frac{1}{N} \sum_{i=1}^N \|r_i\|^2$  and the interval of the AV was  $[0, 1]$ .  $\|r\|$  indicates the length of the mean angular direction. **(A)** Results of the reconstructed directions that were used to fit the encoding model. **(B)** Results of reconstructed direction that were not used to fit the encoding model.

reaching directions were included when fitting the model. The correlation results for all subjects are shown in **Table 1**.

To evaluate the reconstruction performance capabilities of when unknown directions are used and not used, we computed the absolute error and mean absolute error (MAE) between the reconstructed and actual movement directions (target directions) across all of the reconstructed directions for individual subject and the MAE across all subjects.

When unknown directions were used as test directions for the reconstruction, the errors were larger than when known directions were used (**Figure 6A**). That is, the reconstruction accuracy when unknown directions were used was less than the accuracy when known directions were used. However, there were no significantly different reconstruction errors between both cases. The shape of skewed distribution toward target directions also showed that the reconstructed directions were

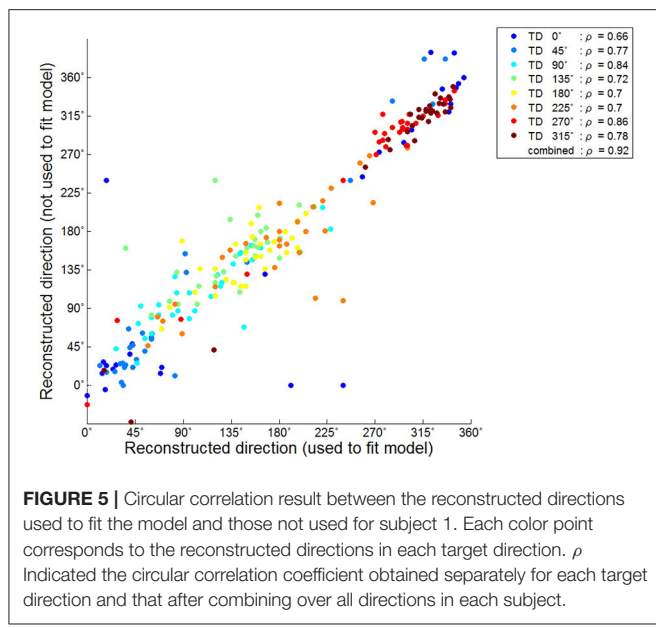


**TABLE 1 |** Circular correlation coefficients.

Target direction	S1	S2	S3	S4	S5	S6	S7	S8
0°	0.66	0.33	0.66	0.19	0.86	0.32	0.5	0.66
45°	0.77	0.77	0.53	0.47	0.5	0.31	0.35	0.82
90°	0.84	0.77	0.77	0.53	0.91	0.55	0.53	0.46
135°	0.72	0.8	0.75	0.2	0.71	0.79	0.49	0.7
180°	0.7	0.79	0.77	0.07	0.81	0.56	0.17	0.68
225°	0.7	0.46	0.68	0.54	0.15	0.23	0.63	0.29
270°	0.86	0.82	0.77	0.75	0.76	0.75	0.45	0.44
315°	0.78	0.67	0.89	0.29	0.72	0.78	0.51	0.52
Combined	0.92	0.9	0.7	0.58	0.8	0.7	0.81	0.71

clustered near the target directions. The angular dispersion of reconstructed directions when unknown movement directions were used as the test directions was also similar to the dispersion of reconstructed directions when known directions were used (**Figure 6B**). These reconstruction results confirmed the validity of the encoding model to reconstruct unknown movement directions. Furthermore, to compare the performance between the reconstruction based on each trials and the trial-averaged reconstruction, we also computed the MAE values of the mean angular direction obtained by averaging all reconstructed trials. The trial-averaged reconstructed performances were much higher than the performances based on the single trials (**Figure 6C**). The average MAE of the mean directions across all participants reduced from 49.8 to 26.6° when known directions were used to test the reconstruction and from 51.9 to 31.6° when unknown directions were used. This indicated that the trial-averaged reconstruction approach could more efficiently improve the reconstruction performance than the single-trial approach.

## Head Motion Effects

We evaluated the classification performance from the right M1 ROI via a leave-one-out cross-validation to identify head motion effects by the reaching movement task. One run (40 trials, 5 trials in each movement direction) from the set of six runs was excluded to test the performance. Remaining runs were used to train the SVM classifier and encoding model (200 trials, 25 trials in each movement direction). It was repeated 6 times until all runs were used to test the performance. The classification performance compared the left M1 and the right M1 is shown in **Figure 7**. The average accuracies across all participants for the left and right M1 based on MVPA were 41.8 and 18.9%, respectively, and the average accuracies for the left and right M1 based on encoding model were 36.1 and 16.4%, respectively. The small discriminability in right M1 could have been influenced by a residual motion signal that was not captured by the rigid body transformation for motion correction. Because each fMRI volume is slice-wise assembled over time, the rigid body transformation may not properly estimate the actual head movements between and within slice acquisition. Compared to average performances of the right M1 across participants, the left M1 is significantly higher than the right M1 for both MVPA and encoding model. The results indicated that the directional movements measured on the right M1 were insufficient for discrimination. Therefore, the effect of head motion does not have a significant effect on the classification and reconstruction performance.

## DISCUSSION

It is well known that motor cortical neurons encode various movement features, such as directions of movement (Georgopoulos et al., 1982), hand positions (Georgopoulos et al., 1984), velocities (Moran and Schwartz, 1999), and force (Taira et al., 1996; Sergio and Kalaska, 1998) to generate a variety of complex motor actions. The directional tuning of motor cortical neurons is one of the most important factors related to reaching movements. In this study, we investigated whether an approach using the directional tuning could be applied to fMRI responses to reconstruct movement directions non-invasively. The responses of voxels reflect pooled activity of neuronal populations because a large number of neurons with different movement selectivities are distributed within each fMRI voxel. Thus, the directional sensitivity of the overall response would be weaker than that of single motor neurons by averaging out the sensitivity and adding the noise. Nevertheless, the pooled response of the neurons consistently characterized with directional sensitivity due to the spatial distribution of the neurons not being uniform. This generates distinct spatial patterns of responses across multiple voxels for the reaching movements and makes it possible to decode the directional movements from the distributed response patterns. Earlier fMRI work was also revealed that individual voxels in human M1 have directional tuning properties by computing the coefficient of variation of five directions of reaching movements for each voxel (Eisenberg et al., 2010). In this study, we verified that when

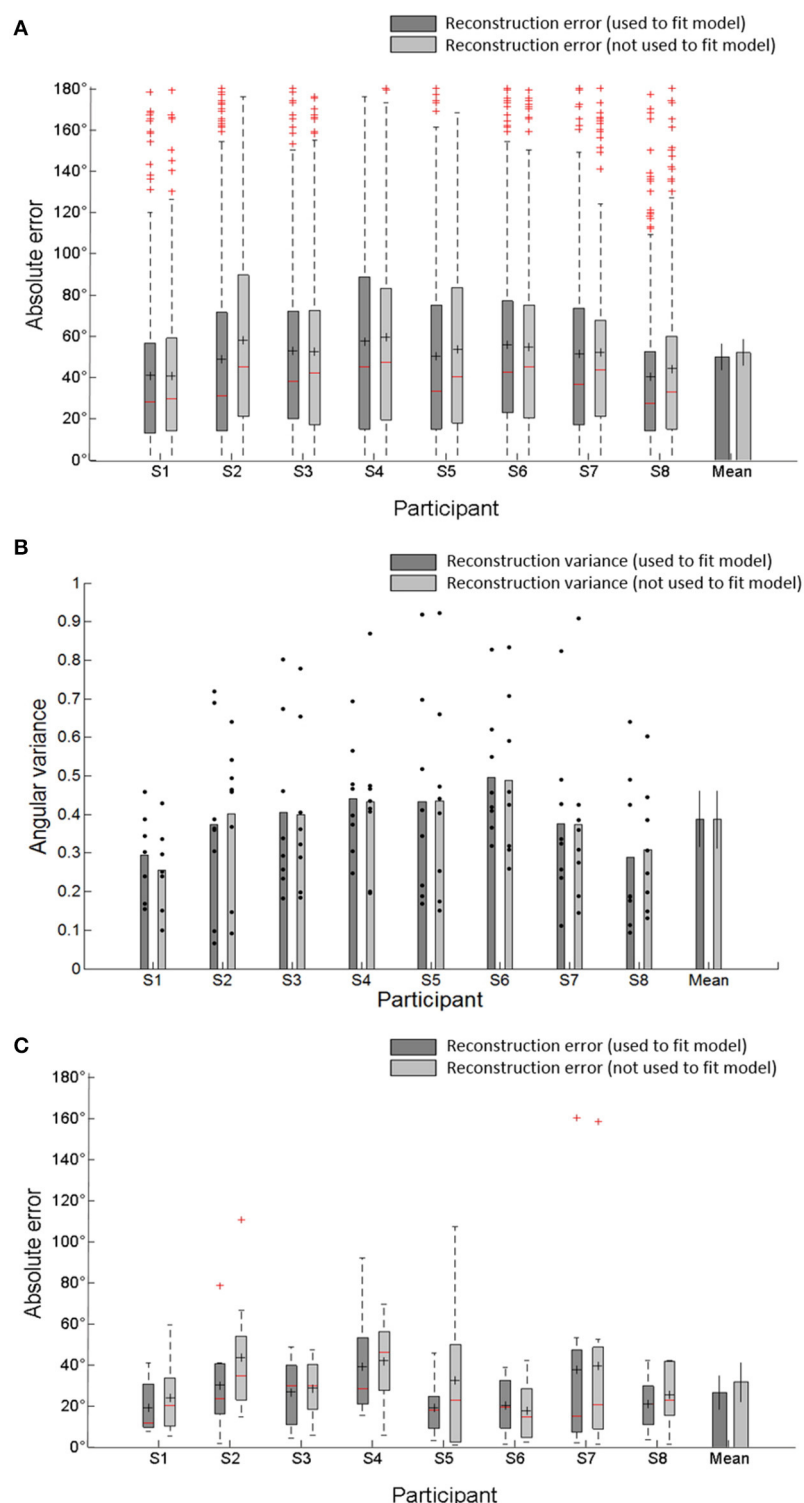


**FIGURE 6 | (A)** Absolute error between the reconstructed directions and the target directions by combining all reconstructed directions in each subject. It represents the distribution of reconstructed direction errors in each subject. The central red line in central boxes indicate the median of the reconstruction errors. Black + in the central box indicate the mean of reconstruction's absolute errors (MAE). The central box represents the central 50% of the absolute errors. Its lower and upper boundary lines are at the 25%/75% quantile of the errors. Vertical lines from the central box indicate the remaining data outside the central box except outliers (red +). Bar plot indicates average MAE and SD across all participants. **(B)** Angular variance (AV) of reconstructed directions. Black dots indicated angular variance of each target directions which was used to reconstruct movement directions. The error bars in averaged variance (mean) indicate the SDs across participants. **(C)** Absolute error between mean angular directions obtained by averaging all reconstructed directions and target directions in each subject and the average MAE and SD across all participants.

using decoding approaches based on a linear classifier, reaching movements toward eight directions were distinguishable with high accuracy from the spatially distributed patterns of responses across an array of voxels measured in human M1. Although fMRI signals were influenced by head motion effect, this indicated that responses of M1 voxel were directionally sensitive for movement directions. Therefore, we assumed that directional tuning was encoded in M1 voxel. The responses of each voxel could be simply modeled using the directional tuning property of the motor cortical neurons. The directional tuning in each voxel was estimated by a linear combination of the six sinusoidal curves. Thus, directional movements could also be predicted using the estimated responses of M1 voxels.

As a result of the classification of reaching movement directions, the encoding model also demonstrated high performance capabilities for all participants which were also comparable to MVPA. Although the classification performance of MVPA was better than that of the encoding model, the encoding model is more applicable to predict complex motor information. The classification-based decoding approaches are used to classify brain activity into a specific experimental stimuli or tasks, while the encoding model could predict brain activity without any prior stimulus. To this end, we performed the reconstruction of unknown directional movements and compared the reconstruction results of the encoding model which was fitted by seven directional movements with those of the encoding model which was fitted by all eight directional movements. The reconstruction results demonstrated that they were clustered around the target direction to which the subject moved. Furthermore, the distributed patterns of reconstructed directions showed a highly significant correlation regardless of whether the encoding model was estimated by seven or eight movement directions. This indicated the potential feasibility of decoding any possible directions over the eight movement directions given during experiment task.

Recent fMRI studies have advanced beyond the classification of cognitive states from experimentally predefined stimulus. However, such advanced fMRI studies have mostly been conducted using visual stimuli such as visual images (Kay et al., 2008; Miyawaki et al., 2008; Naselaris et al., 2009) and dynamic natural movies (Nishimoto et al., 2011). Thus, we applied such decoding methods to predict motor information about directional motor movements in human motor cortex. In the present study, we used an intuitive and simple encoding model to classify and reconstruct the movement directions. The encoding model was defined based on directional tuning properties in human motor cortex to estimate fMRI responses in each voxel evoked by a center-out reaching task. We could perform the identification and the reconstruction of movement directions using the encoding model. During the reaching task, head motions by repeated reaching movements could have an influence on the identification performance. However, the left M1 showed significantly higher performance than the right M1, and the performance from the right M1 was closed to chance level. This implies that motor information associated with directional motor movements is encoded in the responses of voxels, and fMRI responses in human M1

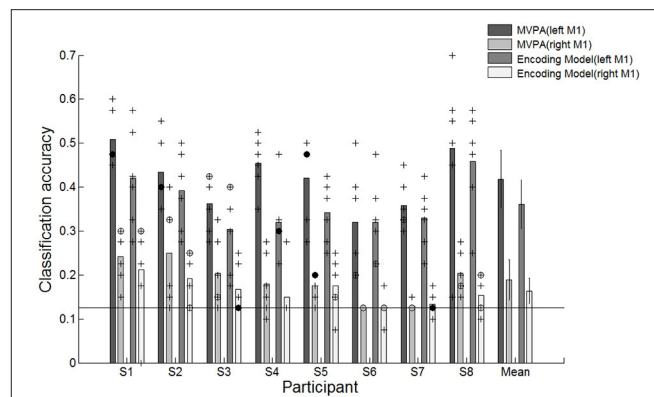


**FIGURE 7 |** Classification accuracies for individual participants and average accuracies across all participants using different motor cortex regions (left and right M1). + Indicates the performance of each run which was used test dataset during cross validation. ⊕ Indicates the performance of each run was overlapped twice. \* Indicates the performance of each run was overlapped three times. # Indicates the performance of each run was overlapped over four times. The solid line indicates the chance level of 12.5%. The error bars in averaged accuracies (mean) indicate the SDs across participants.

are directionally selective. Therefore, this result suggests that decoding approaches based on the encoding model could be applied to use motor information. Nonetheless, precise and detailed encoding models for decoding complex motor actions in real life can be considered to be used more practically. In the present study, the identification and reconstruction were performed based on single-trial basis. Reconstructed directions based on single-trial were spread out around target directions. It could cause a lot of errors to use motor information practically. Thus, using the mean angular direction predicted by averaging movement trials could reduce the reconstruction error much more than using reconstructed directions on the single-trial basis. To improve the decoding accuracy even more, a trial-averaged procedure in which movement executions are repeatedly performed is not suitable. Therefore, in the place of movement executions, decoding approaches based on motor imagery could be considered as future work. Furthermore, a future investigation with the encoding model would need to consider a variety of features related to complex movements such as directions, velocities, positions, and force.

## AUTHOR CONTRIBUTIONS

SN performed a design of the fMRI experiment, the acquisition of the data, analysis, and interpretation of data for the work. He wrote manuscript. DK performed a conception of the work, editing draft of manuscript, final approval of the version to be submitted.

## FUNDING

This research was supported by MSIP (Ministry of Science, ICT and Future Planning), Korea, under the Grand Information

Technology Research Center support program (IITP-2017-2015-0-00742) supervised by the IITP (Institute for Information and communications Technology Promotion), and by the Brain

Research Program through the National Research Foundation of Korea funded by the Ministry of Science, ICT and Future Planning (NRF-2010-0018837).

## REFERENCES

- Brainard, D. H. (1997). The psychophysics toolbox. *Spat. Vis.* 10, 433–436. doi: 10.1163/156856897X00357
- Brouwer, G. J., and Heeger, D. J. (2009). Decoding and reconstructing color from responses in human visual cortex. *J. Neurosci.* 29, 13992–14003. doi: 10.1523/JNEUROSCI.3577-09.2009
- Chang, C. C., and Lin, C. J. (2011). LIBSVM: a library for support vector machines. *ACM Trans. Intel. Sys. Technol.* 2, 1–27. doi: 10.1145/1961189.1961199
- Collinger, J. L., Wodlinger, B., Downey, J. E., Wang, W., Tyler-Kabara, E. C., Weber, D. J., et al. (2013). High-performance neuroprosthetic control by an individual with tetraplegia. *Lancet* 381, 557–564. doi: 10.1016/S0140-6736(12)61816-9
- Cox, D. D., and Savoy, R. L. (2003). Functional magnetic resonance imaging (fMRI) “brain reading”: detecting and classifying distributed patterns of fMRI activity in human visual cortex. *Neuroimage* 19, 261–270. doi: 10.1016/S1053-8119(03)00049-1
- Culham, J. C., Cavina-Pratesi, C., and Singhal, A. (2006). The role of parietal cortex in visuomotor control: what have we learned from neuroimaging? *Neuropsychologia* 44, 2668–2684. doi: 10.1016/j.neuropsychologia.2005.11.003
- Dassonville, P., Zhu, X. H., Ugurbil, K., Kim, S. G., and Ashe, J. (1997). Functional activation in motor cortex reflects the direction and the degree of handedness. *Proc. Natl. Acad. Sci. U.S.A.* 94, 14015–14018. doi: 10.1073/pnas.94.25.14015
- De Martino, F., Valente, G., Staeren, N., Ashburner, J., Goebel, R., and Formisano, E. (2008). Combining multivariate voxel selection and support vector machines for mapping and classification of fMRI spatial patterns. *Neuroimage* 43, 44–58. doi: 10.1016/j.neuroimage.2008.06.037
- Dinstein, I., Gardner, J. L., Jazayeri, M., and Heeger, D. J. (2008). Executed and observed movements have different distributed representations in human aIPS. *J. Neurosci.* 28, 11231–11239. doi: 10.1523/JNEUROSCI.3585-08.2008
- Efron, B., and Tibshirani, R. J. (1994). *An Introduction to the Bootstrap*. New York, NY: Chapman & Hall/CRC Press.
- Eisenberg, M., Shmuelof, L., Vaadia, E., and Zohary, E. (2010). Functional organization of human motor cortex: directional selectivity for movement. *J. Neurosci.* 30, 8897–8905. doi: 10.1523/JNEUROSCI.0007-10.2010
- Fabbri, S., Caramazza, A., and Lingnau, A. (2010). Tuning Curves for movement direction in the human visuomotor system. *J. Neurosci.* 30, 13488–13498. doi: 10.1523/JNEUROSCI.2571-10.2010
- Formisano, E., De Martino, F., and Valente, G. (2008). Multivariate analysis of fMRI time series: classification and regression of brain responses using machine learning. *Magn. Reson. Imaging* 26, 921–934. doi: 10.1016/j.mri.2008.01.052
- Friston, K. J., Williams, S., Howard, R., Frackowiak, R. S., and Turner, R. (1996). Movement-related effects in fMRI time-series. *Magn. Reson. Med.* 35, 346–355. doi: 10.1002/mrm.1910350312
- Georgopoulos, A. P., Caminiti, R., and Kalaska, J. F. (1984). Static spatial effects in motor cortex and area-5 - quantitative relations in a two-dimensional space. *Exp. Brain Res.* 54, 446–454. doi: 10.1007/BF00235470
- Georgopoulos, A. P., Kalaska, J. F., Caminiti, R., and Massey, J. T. (1982). On the relations between the direction of two-dimensional Arm movements and cell discharge in primate motor cortex. *J. Neurosci.* 2, 1527–1537.
- Grabowska, A., Gut, M., Binder, M., Forsberg, L., Rymarczyk, K., and Urbanik, A. (2012). Switching handedness: fMRI study of hand motor control in right-handers, left-handers and converted left-handers. *Acta Neurobiol. Exp.* 72, 439–451.
- Hansen, L. K. (2007). Multivariate strategies in functional magnetic resonance imaging. *Brain Lang.* 102, 186–191. doi: 10.1016/j.bandl.2006.12.004
- Haxby, J. V., Gobbini, M. I., Furey, M. L., Ishai, A., Schouten, J. L., and Pietrini, P. (2001). Distributed and overlapping representations of faces and objects in ventral temporal cortex. *Science* 293, 2425–2430. doi: 10.1126/science.1063736
- Haynes, J. D. (2009). Decoding visual consciousness from human brain signals. *Trends Cogn. Sci.* 13, 194–202. doi: 10.1016/j.tics.2009.02.004
- Haynes, J. D., and Rees, G. (2006). Decoding mental states from brain activity in humans. *Nat. Rev. Neurosci.* 7, 523–534. doi: 10.1038/nrn1931
- Heeger, D. J., Huk, A. C., Geisler, W. S., and Albrecht, D. G. (2000). Spikes versus BOLD: what does neuroimaging tell us about neuronal activity? *Nat. Neurosci.* 3, 631–633. doi: 10.1038/76572
- Hochberg, L. R., Bacher, D., Jarosiewicz, B., Masse, N. Y., Simmerl, J. D., Vogel, J., et al. (2012). Reach and grasp by people with tetraplegia using a neurally controlled robotic arm. *Nature* 485, 372–375. doi: 10.1038/nature11076
- Hochberg, L. R., Serruya, M. D., Friesch, G. M., Mukand, J. A., Saleh, M., Caplan, A. H., et al. (2006). Neuronal ensemble control of prosthetic devices by a human with tetraplegia. *Nature* 442, 164–171. doi: 10.1038/nature04970
- Jammalamadaka, S. R., and Sengupta, A. (2001). *Topics in Circular Statistics*. World Scientific. Singapore: World Scientific.
- Kamitani, Y., and Tong, F. (2005). Decoding the visual and subjective contents of the human brain. *Nat. Neurosci.* 8, 679–685. doi: 10.1038/nn1444
- Kamitani, Y., and Tong, F. (2006). Decoding seen and attended motion directions from activity in the human visual cortex. *Curr. Biol.* 16, 1096–1102. doi: 10.1016/j.cub.2006.04.003
- Kay, K. N., Naselaris, T., Prenger, R. J., and Gallant, J. L. (2008). Identifying natural images from human brain activity. *Nature* 452, 352–355. doi: 10.1038/nature06713
- Maldjian, J. A., Laurienti, P. J., Kraft, R. A., and Burdette, J. H. (2003). An automated method for neuroanatomic and cytoarchitectonic atlas-based interrogation of fMRI data sets. *Neuroimage* 19, 1233–1239. doi: 10.1016/S1053-8119(03)00169-1
- Mitchell, T. M., Hutchinson, R., Niculescu, R. S., Pereira, F., Wang, X. R., Just, M., et al. (2004). Learning to decode cognitive states from brain images. *Mach. Learn.* 57, 145–175. doi: 10.1023/B:MACH.0000035475.85309.1b
- Miyawaki, Y., Uchida, H., Yamashita, O., Sato, M. A., Morito, Y., Tanabe, H. C., et al. (2008). Visual image reconstruction from human brain activity using a combination of multiscale local image decoders. *Neuron* 60, 915–929. doi: 10.1016/j.neuron.2008.11.004
- Moran, D. W., and Schwartz, A. B. (1999). Motor cortical representation of speed and direction during reaching. *J. Neurophysiol.* 82, 2676–2692.
- Naselaris, T., Prenger, R. J., Kay, K. N., Oliver, M., and Gallant, J. L. (2009). Bayesian reconstruction of natural images from human brain activity. *Neuron* 63, 902–915. doi: 10.1016/j.neuron.2009.09.006
- Nishimoto, S., Vu, A. T., Naselaris, T., Benjamini, Y., Yu, B., and Gallant, J. L. (2011). Reconstructing visual experiences from brain activity evoked by natural movies. *Curr. Biol.* 21, 1641–1646. doi: 10.1016/j.cub.2011.08.031
- Norman, K. A., Polyn, S. M., Detre, G. J., and Haxby, J. V. (2006). Beyond mind-reading: multi-voxel pattern analysis of fMRI data. *Trends Cogn. Sci.* 10, 424–430. doi: 10.1016/j.tics.2006.07.005
- Orr, M. (1996b). *MATLAB Routines for Subset Selection and Ridge Regression in Linear Neural Networks*. Centre of Cognitive Science, University of Edinburgh, Scotland.
- Orr, M. J. (1996a). *Introduction to Radial Basis Function Networks*. Technical Report, Center for Cognitive Science, University of Edinburgh, Scotland.
- Rees, G., Friston, K. J., and Koch, C. (2000). A direct quantitative relationship between the functional properties of human and macaque V5. *Nat. Neurosci.* 3, 716–723. doi: 10.1038/76673
- Schwarz, G. (1978). Estimating the dimension of a model. *Ann. Statist.* 6, 461–464. doi: 10.1214/aos/1176344136
- Sergio, L. E., and Kalaska, J. F. (1998). Changes in the temporal pattern of primary motor cortex activity in a directional isometric force versus limb movement task. *J. Neurophysiol.* 80, 1577–1583.
- Taira, M., Boline, J., Smyrnis, N., Georgopoulos, A. P., and Ashe, J. (1996). On the relations between single cell activity in the motor cortex and the direction and magnitude of three-dimensional static isometric force. *Exp. Brain Res.* 109, 367–376. doi: 10.1007/BF00229620
- Thesen, S., Heid, O., Mueller, E., and Schad, L. R. (2000). Prospective acquisition correction for head motion with image-based tracking for

- real-time fMRI. *Magn. Reson. Med.* 44, 457–465. doi: 10.1002/1522-2594(200009)44:3<457::AID-MRM17>3.0.CO;2-R
- Thirion, B., Duchesnay, E., Hubbard, E., Dubois, J., Poline, J. B., Lebihan, D., et al. (2006). Inverse retinotopy: inferring the visual content of images from brain activation patterns. *Neuroimage* 33, 1104–1116. doi: 10.1016/j.neuroimage.2006.06.062
- Truccolo, W., Friehs, G. M., Donoghue, J. P., and Hochberg, L. R. (2008). Primary motor cortex tuning to intended movement kinematics in humans with tetraplegia. *J. Neurosci.* 28, 1163–1178. doi: 10.1523/JNEUROSCI.4415-07.2008
- Yamashita, O., Sato, M., Yoshioka, T., Tong, F., and Kamitani, Y. (2008). Sparse estimation automatically selects voxels relevant for the decoding of fMRI activity patterns. *Neuroimage* 42, 1414–1429. doi: 10.1016/j.neuroimage.2008.05.050
- Yang, S. L., Ross, T. J., Zhang, Y. Q., Stein, E. A., and Yang, Y. H. (2005).

Head motion suppression using real-time feedback of motion information and its effects on task performance in fMRI. *Neuroimage* 27, 153–162. doi: 10.1016/j.neuroimage.2005.02.050

**Conflict of Interest Statement:** The authors declare that the research was conducted in the absence of any commercial or financial relationships that could be construed as a potential conflict of interest.

Copyright © 2017 Nam and Kim. This is an open-access article distributed under the terms of the Creative Commons Attribution License (CC BY). The use, distribution or reproduction in other forums is permitted, provided the original author(s) or licensor are credited and that the original publication in this journal is cited, in accordance with accepted academic practice. No use, distribution or reproduction is permitted which does not comply with these terms.

# Advantages of publishing in Frontiers



## OPEN ACCESS

Articles are free to read for greatest visibility and readership



## FAST PUBLICATION

Around 90 days from submission to decision



## HIGH QUALITY PEER-REVIEW

Rigorous, collaborative, and constructive peer-review



## TRANSPARENT PEER-REVIEW

Editors and reviewers acknowledged by name on published articles



## REPRODUCIBILITY OF RESEARCH

Support open data and methods to enhance research reproducibility



## DIGITAL PUBLISHING

Articles designed for optimal readership across devices



FOLLOW US  
@frontiersin



IMPACT METRICS  
Advanced article metrics track visibility across digital media



EXTENSIVE PROMOTION  
Marketing and promotion of impactful research



LOOP RESEARCH NETWORK  
Our network increases your article's readership

### Frontiers

Avenue du Tribunal-Fédéral 34  
1005 Lausanne | Switzerland

Visit us: [www.frontiersin.org](http://www.frontiersin.org)

Contact us: [info@frontiersin.org](mailto:info@frontiersin.org) | +41 21 510 17 00